On the mechanics of strain localization in plasticity

Isotropic and orthotropic, cohesive and frictional, associated and non-associated models

Sungchul Kim

Doctoral Degree in Civil Engineering

Thesis submitted as a compendium of publications

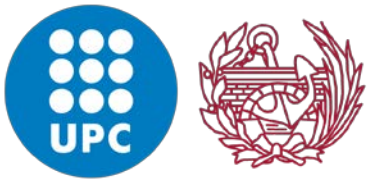

Technical University of Catalonia

School of Civil Engineering

Supervisors: Prof. Miguel Cervera

Prof. Michele Chiumenti

Barcelona, July 2021

El que lee mucho y anda mucho,

ve mucho y sabe mucho

from *Don Quijote de La Mancha*

Miguel de Cervantes Saavedra

(1547 – 1616)

Acknowledgements

I am deeply grateful for the dedicated and detailed guidance and encouragement of my supervisors, Prof. Miguel Cervera and Prof. Michele Chiumenti. In addition to studying, they helped me a lot with my life in Barcelona, Spain. I would like to thank you again.

I would like to thank Prof. Jian-Ying Wu and Dr. Savvas Saloustros for working with me. And I would also like to thank all the professors in the department for their thoughtful advice.

I wish to acknowledge the financial aid from the AGAUR (Agència de Gestió d'Ajuts Universitaris i de Recerca) and the ESF (European Social Fund) through FI grants during my Ph.D. studies.

Also, I would like to thank all members of COMET team. In particular, Gabriel Barbat Vlad is a great friend who helped and took care of me a lot from the first time I came to Barcelona. With his help, I was able to settle well in Barcelona. Thank you all, Narges, Carlos (of whom there are several), Xufei, Henning, Iván, Pau and Manuel.

In addition to the members of the research team, there are many people to thank, such as the great people in the Ph.D. management office, researchers from the C1, C2, B0 buildings, TUM (Technische Universität München) and Politecnico di Torino. Riccardo, Alessandro, Ruben, Vicente, Inocencio, Samuel, Laura, Riccardo, Marc, Nicola, Camilla, Raul, Carlos (Charlie), Uxue, Agustina, Oscar, Massimiliano, Alejandro, Sergio, Raphel, Marco, Ignacio, Pau, Sebastian, Javier, Saman, Hauke, Duolan, Barbara, Elisa, Anna, Gabriele, Bodhinanda, Simon, Mengjie, Manuel, Carles, Jordi, Chiara, Simona, Waleed, Andrea, Giacomo and many more people.

Despite the COVID-19 pandemic, thanks to all of you, I am able to get through difficult times together. Sometimes, it can be depressing and frustrating. Contact me anytime. As much as I am grateful, I want to listen to your difficulties and help you.

Finally, I am deeply grateful to my family and their love. A parent's unconditional love that cannot even be expressed. I am grateful for that grace and will live as a filial son. I hope that everyone, including my parents, my sister, brother-in-law and nephew, are all staying healthy and safe.

어떠한 말로 표현할 수 없는 부모님의 무조건적인 사랑에 마음 깊이 감사 드립니다. 그 은혜에 감사하며 효도하며 살겠습니다. 우리 가족 모두 건강하고, 안전하게 지내기를 바랍니다.

Sungchul Kim

Barcelona, July, 2021

Abstract

In this thesis, two main topics have been covered: the mechanics of strain localization in plasticity and the performance of several mixed finite elements subjected to plastic strain localization.

Throughout the thesis, incompressible and cohesive-frictional, isotropic and orthotropic, elasto- and rigid-plastic solids are analyzed using associated or non-associated flow rules, both in the continuum and the discrete settings.

Plastic yielding, strain bifurcation and strain localization are identified in the failure process prior to conducting a detailed analysis of strain localization.

The mechanics of strain localization in the continuum and discrete settings, including the constitutive relations, the kinematics for strong and weak discontinuities, and the strain localization conditions are presented. Maxwell's kinematic condition, the traction rate continuity and the stress rate constraints are explained, thereby distinguishing the correlations and differences between strain bifurcation and strain localization conditions.

The analytical prediction of strain localization derived from the stress boundedness condition is proposed and numerically verified through independent simulations. Unlike predicted in classical strain bifurcation analysis, strain localization is independent from the elasticity behavior and is only related to plastic flow. Specifically, the strain localization angle depends on the stress state and plastic potential but not on the yield surface.

Uniaxial computational experiments on strips subjected to uniaxial stretching and compressing in plane stress and plane strain to assess the theoretical analysis and Prandtl's flat punch tests are performed.

Numerical results for incompressible and cohesive-frictional, isotropic and orthotropic, associated and non-associated plasticity, with or without inclination angles between the material local axes and the global axes are compelling evidence for the proposed theoretical framework.

Various mixed finite elements are used in this thesis. By comparing the numerical outputs, the advantages and disadvantages of the performance of the several mixed finite elements are shown regarding enhanced accuracy, computational efficiency, mesh sensitivity and stress locking.

Resumen

En esta tesis trata dos temas principales: la mecánica de la localización de deformaciones en plasticidad y el funcionamiento de varios elementos finitos mixtos sometidos a la localización de deformaciones plásticas.

A lo largo de la tesis, se estudian sólidos incompresibles y cohesivo-friccionales, isotrópos y ortótropos, elasto- y rígidos-plásticos, utilizando reglas de flujo asociadas o no asociadas, tanto a en formato continuo como discreto.

En un análisis detallado del proceso de localización de la deformación, se identifican los puntos de plastificación, bifurcación y localización de la deformación.

Se presentan los mecanismos de la localización de deformaciones a nivel continuo y discreto, incluyendo las relaciones constitutivas, la cinemática de las discontinuidades fuertes y débiles y las condiciones de localización de la deformación. Se explican la condición cinemática de Maxwell, la condición de continuidad del incremento de tracción y la condición acotabilidad del incremento de la tensión, su relevancia en la bifurcación de la deformación y las condiciones de localización de la deformación.

Se propone y se verifica numéricamente mediante simulaciones independientes la predicción analítica de la localización de la deformación a partir de la condición de acotabilidad de la tensión. A diferencia de lo que predice en el análisis clásico de localización de deformaciones, ésta es independiente del comportamiento elástico y está únicamente relacionada con el flujo plástico. Específicamente, el ángulo de localización de la deformación depende del estado de la tensión y del potencial plástico, pero no de las constantes elásticas ni de la superficie de fluencia.

Se realizan experimentos computacionales en placas sometidas a tracción y compresión uniaxial en tensión y deformación plana para evaluar el análisis teórico, así como en tests de punzonamiento de Prandtl.

Los resultados numéricos con plasticidad incompresible y cohesivo-friccional, isotrópa y ortotrópica, asociada y no asociada, con o sin ángulos de inclinación entre los ejes locales materiales y los ejes globales proporcionan evidencias convincentes para el marco teórico propuesto.

En esta tesis se utilizan varios elementos finitos mixtos. Al comparar los resultados numéricos, se muestran las ventajas y desventajas del funcionamiento de varios elementos finitos mixtos con respecto a su precisión, la eficiencia computacional, la sensibilidad respecto a la alineación de la malla y el bloqueo de tensiones.

Contents

Chapter 1

Introduction

The motivation, state of the art, objectives, scope and outline of the thesis are presented in this chapter. Specifically, the motivation and state of the art for the analysis of the strain localization in plasticity of orthotropic materials using the finite element method (FEM) are discussed. Lastly, a description of the research dissemination is included.

1.1 Motivation

The main objective of this thesis is to study the phenomenon of plastic strain localization in orthotropic materials using FEM. The motivation for orthotropic materials, plasticity, strain localization and FEM is discussed in this section.

1.1.1 Orthotropic materials

Wood, easily found in nature, is an orthotropic material very much used because of its light weight and hardness. Rock, often displaying orthotropic mechanical behavior, is also a traditional building material. From natural orthotropic materials such as wood and rocks to artificial orthotropic materials such as rolled metals and polymer composites developed in modern times, engineering progresses with the use of orthotropic materials. Many materials predominantly applied in civil engineering, such as wood, geo-materials, masonry, reinforced concrete and fiber-reinforced polymers, are orthotropic materials. Orthotropic composite materials including fiber-reinforced polymer are applied to various other applications such as aircrafts, trains, vehicles, etc. Therefore, to design and build long-lasting civil structures, it is rewarding to study and characterize orthotropic materials

Compared to isotropic materials, orthotropic materials may exhibit enhanced mechanical performance regarding specific loading conditions. However, there are several difficulties in interpreting the properties of orthotropic materials and their experimental characterization. Also, composite orthotropic materials present specific failure mechanisms such as delamination.

In recent years, Additive Manufacturing (AM) is becoming increasingly common. Numerous materials are used in numerous applications of AM technology. For example, concrete is used in 3D building construction, metals are used to produce vehicles and medical materials are used for artificial bones. AM products are orthotropic when the stacking technique is used to manufacture them. With the development of Computer-Aided Engineering (CAE), testing a product using a virtual model instead of fabricating the real product has become possible. Virtual testing before production minimizes defects and enables faster product development. Thus, it is important to achieve accurate simulations that are close to the real products.

Owing to the aforementioned reasons, further research is required on the mechanics and performance of orthotropic materials.

1.1.2 Plasticity, strain localization and failure

In structural analysis, plastic deformation of a material often causes phenomena such as cracks and necking. In the field of civil engineering, for example, the plasticity of geo-materials causes landslides. In particular, designs that induce ductile failure, wherein the failure develops progressively, are preferable over those that induce brittle failure, which occurs suddenly and unexpectedly. Hence, failure modes need to be considered when designing structures and products.

In addition, plastic deformation has been used in manufacturing and molding by plastic forming process, from the production of weapons by forging and hammering in the Bronze and Iron Age to modern automated production by rolling and stamping. For plastic forming processes, the accurate analysis of plastic deformation is essential, and various techniques have been proposed according to the development of the materials.

Strain localization as a precursor to failure is often observed in narrow areas where plastic deformation is concentrated. Strain localization can be observed easily for a wide range of scales, from small material cracks to large slip lines (slip surfaces) on the Earth's crust.

Strain localization has been classically studied based on discontinuous bifurcation analysis, because the onset of strain localization requires the occurrence of strain bifurcation. Several analysis methods have been proposed over the last 50 years, related to the loss of material ellipticity with and the eigen-analysis of the elastoplastic acoustic tensor.

However, these analyses present two shortcomings:

(*i*) Classical strain localization analysis does not apply to rigid-plastic solids since they do not develop elastic strain and the stiffness tensor is undefined. This makes the classical analysis unseemly since the elastoplastic acoustic tensor is no longer well-defined.

(*ii*) As the elastoplastic acoustic tensor depends on the hardening/softening modulus H, so do the bifurcation condition and the resulting discontinuity orientation. Though the initial bifurcation point corresponding to the largest hardening/softening modulus H_b can be uniquely determined, strain localization is still indefinite and it can occur at any instant for $H \leq H_b$. Moreover, even if the hardening/softening modulus H is specified a priori in an *ad hoc* manner, there may exist several solutions that fulfill the bifurcation condition.

To overcome these shortcomings, more stringent conditions have to be identified, and studies on the analysis of strain localization that can be used consistently in a given material model are needed.

Additionally, consideration of isotropic plasticity was often sufficient for Subtractive Manufacturing. However, orthotropic plasticity needs to be considered for Additive Manufacturing and more modern applications; thus, the need for research on orthotropic plasticity is increasing, and, subsequently, there is also a need for research on strain localization of orthotropic plasticity.

1.1.3 The Finite Element Method

In modern times, a variety of advanced materials such as alloys and composite materials are used in production and considered in design. To analyze the behavior of the products, the Finite Element Method (FEM) is used. Therefore, FEM is becoming an indispensable process for new product development because engineers can contribute to shortening the development period, improving productivity and securing product quality.

FEM can be used in fields such as stress analysis, buckling, dynamics and heat conduction. Furthermore, irregularly shaped structures made of various composite materials can be modelled using the FEM. However, depending on the element types, unreliable results may be obtained.

Standard finite elements (FEs) are the basis of most FE software and are conveniently used for the analysis of most engineering structures.

However, despite their advantages, standard FEs pose several obstacles that reduce the accuracy of the FE solution under certain conditions such as the discretization, geometry and material properties.

Typical examples are mesh distortion such as irregular shapes and warped elements, volumetric locking in incompressible materials, and membrane locking during the bending of thin shells or thin plates. The lower accuracy of displacement calculation by these obstacles has an immediate negatively effect on stress calculation and analysis of the engineering structures.

Although beam, plate and shell elements are available, the use of solid elements for modelling structural elements has always been attractive due to their versatile use for modelling arbitrary geometries (e.g. linear/curved, thin/thick), construction details (e.g. element-stiffeners, web-perforated steel beams, layered elements), as well as transitions between different structural elements. Solid elements allow for the use of general strain-driven constitutive relationships and they avoid the introduction of rotational degrees of freedom and awkward boundary conditions alternatives (“soft” and “hard” supports), as well as compatibility issues when the structural model requires more than one type of element. Additionally, the discretization of a structural element with solid elements avoids the introduction of additional kinematical hypotheses (e.g. planar sections, shear stresses and warping through the thickness, etc.).

Numerous studies have been conducted over the last decades to overcome these shortcomings and obtain a solution of greater accuracy. For examples, solid-shell elements have been developed with assumed enhanced method to include higher order modes and assumed natural strain method to avoid shear and membrane locking. However, for those elements that are stable, these enhancements cannot achieve a higher asymptotic rate of convergence of displacements than that of the underlying lineal element. Interpolating with the full quadratic polynomial would be

required for achieving this. Convergence of strains, obtained by discrete differentiation of the displacement field, is one order lower, resulting in turn in a poor convergence of stresses.

In short, the challenges to overcome with FE development using independent interpolation are obvious; a greater rate of convergence, enhanced accuracy, locking-free and insensibility to mesh distortion.

For the accurate and locking-free structural analysis of strain localization in orthotropic plasticity, it is necessary to develop new solid elements that overcome these challenges.

1.2 State of the Art

1.2.1 Orthotropic elasto-plastic behavior

Failure degrades the performance and usability of engineering products and structures. Unexpected failure may threaten safety not only in engineering fields, but also in any aspect of life. In order to analyze or predict the failure of products and structures, studies in many engineering fields are conducted, and the development of research on plastic deformation is one of the most remarkable among them.

The study of plasticity has a wide range of applications, from plastic forming during the manufacturing processes to predicting and preventing the bridge collapse. Because plasticity is encountered in many fields of engineering, numerous studies on this topic have been conducted from the past to the present.

The study of plasticity has progressed gradually since the Industrial Revolution. Iron and steel are used in many factories and structures; hence, the need for accurate and reliable plastic forming of iron steel products has encouraged active research on plasticity.

The contribution of early researchers made it possible to analyze the elastic behavior of materials. Hooke's law, which expresses the relationship between stress and strain, was formulated in 1678 [1]. In 1750, the theory of elasticity in continuum was developed by Leonhard Euler [2]. In 1823, the concept of stress and the general form of the linear elastic relation was developed by Augustin–Louis Cauchy [3]; In addition, Cauchy laid the foundation for the finite-strain hypothesis. In 1831, Poisson’s ratio as one of the elastic properties was defined by Siméon Denis Poisson [4]. In 1773, Charles–Augustin de Coulomb proposed the first yield criterion for soils in his essay which was published in 1776 [5]. Coulomb’s work may have influenced Tresca's work. Henri Tresca had made considerable contributions to the study of plasticity. The Tresca yield criterion when the shear stress reaches a critical value, well known as the maximum shear stress theory, was proposed in 1864 [6]. Starting with Tresca's research, study on plasticity was expanded in various ways. A constitutive equation for perfectly plastic materials was developed by Adhémar Jean Claude Barré de Saint–Venant in 1870 [7].

Subsequently, Maurice Lévy introduced plastic strain rates to replace the plastic strains in de Saint–Venant’s equation corresponding to stresses [8].

As an alternative to considering the critical shear stress, the maximum distortion energy criterion, known as the von Mises yield criterion, was proposed for isochoric plastic strain in 1913 [9].

The Tresca yield criterion forms a hexagonal prism in the Haigh–Westergaard (HW) stress space. Unlike the maximum shear stress, which is expressed as a linear equation, the von Mises yield

criterion is expressed as a quadratic equation and appears as an elliptical cylinder in the HW stress space. In addition, when the material properties are identical, the surfaces in the HW stress space of the Tresca and von Mises yield criteria remain in contact. In 1924, Heinrich Hencky accidentally discovered that the von Mises yield criterion was related to distortion strain energies [10].

Ludwig Prandtl analyzed rigid-plastic flat punch tests under plane strain conditions. Prandtl's punch problem is excellent for expressing and analyzing complex stresses; furthermore, it can be used in slip line analysis [11].

The Prandtl–Reuss theory using the flow rule was developed by Reuss based on Hencky's deformation theory and Prandtl's previous work [12]. In this work, it is suggested that a method wherein the constitutive tensor is divided into deviatoric plastic and volumetric elastic parts.

Hill's quadratic yield criterion was developed for orthotropic incompressible plastic deformation based on the von Mises model [13]. In addition, twenty-nine years after Prandtl's slip line analysis, Hill proposed another slip-line for the punch test [14].

The von Mises and Hill yield criteria were only for isochoric plastic materials. There was a need to develop yield criteria for pressure dependent plastic material. The Mohr–Coulomb yield criterion, influenced by Tresca and Coulomb, was developed in 1900 [15]. This criterion is a model wherein friction and cohesion are considered for brittle materials such as soil, rock and concrete.

After half a century, the Drucker–Prager yield criterion was developed to analyze the pressure dependent model [16]. Similar to the relationship between the Tresca and von Mises yield criteria, there are similarities between the Mohr–Coulomb and Drucker–Prager yield criteria. In addition to the linear Drucker–Prager model, various forms of the extended Drucker–Prager models (exponential, hyperbolic and parabolic Drucker–Prager [17–19]) were suggested.

Hoffman and Tsai–Wu yield criteria were suggested for orthotropic pressure dependent plastic materials. The two yield criteria are the models wherein the difference between the tensile and compressive strengths are considered in hydrostatic stresses. And the two yield criteria are similar to each other but only the interaction terms were different. The Hoffman yield criterion was proposed for brittle materials; uniaxial test data were required [20]. Tsai and Wu developed the Tsai–Wu yield criterion for orthotropic, unidirectional composite materials [21].

Incompressible plastic models that are pressure insensitive and yield an isochoric plastic flow, such as the Tresca, von Mises and Hill yield criteria, are suitable for metallic material models. Conversely, pressure dependent plastic models, such as the Mohr–Coulomb, Drucker–Prager, Hoffman and Tsai–Wu models, are appropriate for simulating geological materials such as soils, rocks and concrete.

Various yield criteria have been proposed over the years as extensions of the aforementioned yield criteria for different applications. The Bresler–Pister yield criterion, an extension of the Drucker-Prager yield criterion that takes into account multiaxial hydrostatic stresses, was proposed for concrete and foam in 1958 [22]. The Podgórski yield criterion for isotropic brittle and granular materials was proposed in 1984 [23] and contain different isotropic yield criteria such as the von Mises, Tresca, Mohr–Coulomb and Drucker–Prager yield criteria as particular cases. In 1991, Barlat's yield criterion was proposed for anisotropic materials [24]. Studies on various types of crystal were carried out, particularly on aluminium alloy sheets based on a crystal plasticity model [25–26]. The Bigoni–Piccolroaz yield criterion, a function of seven non-negative material parameters, was proposed in 2004 for quasi-brittle materials [27]. Bigoni–Piccolroaz yield criterion includes various other yield criteria as particular cases.

Due to the development of AM technology, a number of advanced materials such as polymer are used. Additive manufacturing techniques based on filament deposition or powder bed fusion introduce different levels of orthotropy in the mechanical stiffness and strength of the fabricated components. Associated elasto-plastic cohesive-frictional models such as the Drucker–Prager, Hoffman and Tsai–Wu models are suitable for simulating polymeric materials such as PVC H100, H250 and carbon fiber composites [28–31] with isotropic and orthotropic behavior, as these materials show distinct strengths under tensile and compressive loading. Geomaterials like soils, concrete, masonry and rocks are also modelled with pressure-sensitive plasticity models; non-associated plasticity is often used for these materials in order to better approximate the real dilatant behavior.

1.2.2 Strain bifurcation and localization

As the load imposed on plastic materials increases beyond the yield point, plastic strains tend to concentrate in narrow zones. This is called strain localization (shear band); it is a typical phenomenon of localized failure in solids and structures [32].

Strain localization leads to strain (weak) discontinuities or even displacement (strong) discontinuities across lines in a two-dimensional space or surfaces in a three-dimensional space, and may cause the fracture of solid materials and the collapse of the structure.

For structural assessment, it is necessary to accurately predict failure mechanisms. Therefore, Failure Mechanics is a field that has been actively studied in the last century; several analytical, experimental and numerical research efforts have been invested in the fields of plasticity, damage and fracture mechanics. Recently, computational mechanics has addressed strain localization in plasticity and related analytical and numerical problems.

In the past, Prandtl [11], Hencky [10, 33] and Mandel [34] interpreted the slip lines of rigid-plastic materials and the related failure mechanisms. The scope of strain localization analysis was broadened from rigid-plastic solids to elasto-plastic solids by Hill [35–36], Thomas [37] and Rice [38] as a strain bifurcation problem.

Hill [35] proposed the theory of material uniqueness and stability, which became the basis of classical bifurcation analysis for the onset of strain localization. As the onset of strain localization in plastic solids was presumed to coincide with strain bifurcation, a strain bifurcation analysis based on the loss of uniqueness was used to predict strain localization.

Moreover, Rice [39] expanded on the topic of interpreting non-associative plasticity and anisotropic rigid plasticity. Rudnicki and Rice [40] investigated the general conditions for the localization in pressure-sensitive dilatant materials and introduced the acoustic tensor derived from the tangent stiffness tensor. Based on his experimental results, Rice and coworkers [41–42] presented a general theoretical framework including the loss of ellipticity as bifurcation criterion.

Bigoni and Hueckel [43–44] investigated the uniqueness of the incremental response for associated and non-associated elastoplastic models by considering the loss of strong ellipticity. Nielsen and Schreyer [45] studied bifurcations in associated and non-associated elasto-plasticity and also used the loss of strong ellipticity as a necessary condition for localization.

General bifurcation such as buckling and necking can be caused by loss of uniqueness. However, bifurcation related to strain jumps may not occur when uniqueness is lost. Rudnicki and Rice [40] proposed the loss of ellipticity condition to predict material instability related to strain jumps.

This bifurcation condition associated to the singularity of the elastoplastic acoustic tensor is derived from the combination of Maxwell's kinematics and traction rate continuity condition across the discontinuity lines

In order to explain the localization phenomenon that occurs before the occurrence of loss of ellipticity in non-associated plastic materials, Bigoni and Hueckel [43] proposed the loss of strong ellipticity condition. The loss of ellipticity condition and the loss of strong ellipticity condition are the same in associated elasto-plasticity due to symmetric tangent stiffness tensor. Runesson and Ottosen [46] studied the directions of bifurcation and the corresponding critical hardening modulus derived for non-associated flow rules.

Leroy and Ortiz performed a numerical simulation of the strain localization in frictional materials, such as clays, soils, rocks and concrete, using FEM [47]. Borja extensively studied strain localization with large deformations and strong discontinuities [48–49]. The simulation of strain localization in aluminum foams under compression force was performed by Forest [50]. William Prager studied the elasto-plastic localization properties of a non-associated Drucker–Prager model [51–52]. Zhang [53] investigated strain localization in damaged geomaterials, and Vrech [54] developed a geometrical localization method for cohesive-frictional materials with localization properties. Tasan [55] examined induced damage in dual-phase steels through experiments and simulations.

Bifurcation analysis has been applied to both weak (strain) and strong (displacement) discontinuities.

Simó, Oliver and Armero [56] studied strong discontinuities induced by strain softening analytically and numerically modeled in rate-independent inelastic solids. The analysis shows that the softening law must be re-interpreted in a distributional sense for the continuum solutions to make mathematical sense and provides a precise physical interpretation to the softening modulus.

Subsequently, Oliver [57–60] studied strong discontinuities emerging from softening damage and elastoplastic models and found that the traction continuity condition is essential to determine the stress jump in the discontinuity analytically and numerically. Stress boundedness is explicitly considered.

Oliver, Cervera and Manzoli [61–62] introduced the *Strong Discontinuity Approach* (SDA) for the analysis and simulation of strong discontinuities in solids using continuum plasticity models. They investigated under what conditions typical elasto-plastic continuum constitutive equations induce strong discontinuities having physical meaning and the link of the *Strong Discontinuity Approach*, based on the use of continuum (stress-strain) models, with the *discrete discontinuity approach* which considers a non-linear fracture mechanics environment and uses stress vs displacement-jump constitutive equations to model the de-cohesive behavior of the discontinuous interface [63–65].

In this work, the kinematics of weak and strong discontinuities were rigorously stablished, and a regularized kinematic state of discontinuity was proposed as a mean to model the formation of a strong discontinuity as the collapsed state of a weak discontinuity (with a characteristic bandwidth) induced by a bifurcation of the strain field. It is shown that, in general, such a bifurcation can only appear under the form of a weak discontinuity (non-zero bandwidth) and, if strong discontinuities are to be modeled, an additional ingredient is required. They propose a variable bandwidth model to characterize the transition between the weak and strong discontinuity regimes.

The strong discontinuity analysis also shows that the strong discontinuity kinematics induces from any standard stress-strain constitutive equation a discrete (traction-vector vs displacement-jump) constitutive equation at the strong discontinuity once this is formed. This provides a fundamental

link to the classical non-linear fracture mechanics, as the discrete constitutive equation can be regarded as the stress-jump constitutive equations used in fracture mechanics to rule the decohesive behavior at the interface [63]. The discrete hardening/softening parameter is related to the fracture energy concept.

Further, Oliver and coworkers [66] studied the analytical and numerical resolution of the so-called discontinuous bifurcation problem for finding the conditions for onset and orientation of strain localization.

Cervera, Michele and Di Capua [67] studied J_2 softening plasticity in plane stress and plane strain conditions and noted that that the bifurcation conditions (loss of uniqueness and loss of ellipticity) were insufficient to determine the occurrence of strain localization and proposed a more stringent strain localization condition by enforcing stress boundedness. The introduction of this strain localization condition allows evaluating the orientations of slip lines analytically. The analytical predictions were independently confirmed by numerical experiments performed using mixed displacement/pressure finite elements.

Cervera, Michele and Wu [68–71] successfully applied the stress (rate) boundedness condition to the prediction of strain localization of isotropic elastoplastic models and also to strain-based damage models with general failure criteria. As a follow-up, Cervera, Wu, Michele and Kim [72–73] applied the proposed localization condition to the orthotropic elastoplastic models with yield criteria. Extensive numerical simulations [61,68,71] confirmed the analytical solutions with no a priori known information in the finite element simulations.

Cervera and Wu [68–69] proved that not only the discontinuity orientation but also the localized model that emerges upon strain localization, i.e., constitutive relations, evolution equations, traction-based failure criterion, softening functions, etc., can be determined consistently from a given material model.

Remarkably, for isotropic and orthotropic elasto-plastic materials with associated evolution laws, the discontinuity orientation predicted from the stress (rate) boundedness condition depends exclusively on the plastic flow tensor, being independent from the elastic properties, the yield criterion and the hardening/softening modulus.

1.2.3 Mixed Finite Elements

The Finite Element Method (FEM) is a numerical analysis method that discretizes the target structure into several elements and obtains a discrete solution, interpolated from the computed values at the nodes. The FEM, which has been developed since the 1950s, is being used today in many fields of engineering.

With the contribution of advances in computer hardware technology, finite element modelling has been widely used in the design and assessment (or evaluation) of engineering structures. In the design and assessment processes, it is necessary to predict the mechanical behaviors such as displacement and stress of engineering structures under the design load. Simulation results obtained using the FEM can be used for decision making.

FEM applications in use today, like early stage of FEM applications in 1950s, are based on the displacement-based FEs (referred hereafter to as standard FEs) [74]. Standard FEs have a single primal variable, which is the displacement field at the nodes. Standard FEs, on which most commercial and research FEM programs are based, are convenient used to analyze all structures.

Despite convenient use of standard FEs, standard FEs pose significant inefficiencies that affect the accuracy of the solution under to certain conditions such as the discretization, geometry and material properties. Owing to these certain conditions, standard FEs pose numerical problems, such as element locking (volumetric, shear and membrane locking) and stress oscillation problems [75]. Element locking is the most common phenomenon that disturbs the accuracy of the solution in FEM. And element locking fundamentally occurs with lower order elements as the element's kinematics is not sufficient to obtain the correct solution [76–78].

To overcome these numerical difficulties, Fraeijs de Veubeke and Herrmann proposed mixed elements, based on the Hellinger–Reissner (two-field) principle for incompressible and nearly incompressible elasticity [79–80] with pressure as an additional unknown field.

With two primal variables instead of one as in standard FEs, the present element is included in the multi-field FE approaches, and particularly in the mixed FE approaches [81–82]. Mixed models with stress variables, rather than pressure variables, were studied by Pian and Yamamoto [83–84]. Pian [83] derived the element stiffness matrices for assumed stress and applied the matrices on bending of plates and shells problems. Yamamoto [84] suggested methods to obtain approximation of displacement in each element with a simple polynomial and hybrid displacement elements.

Stolarski and Belytschko [85] presented the Hu–Washizu (three-field) based mixed method, similar to the Hellinger–Reissner based mixed FE method. Simo and coworkers [86–89] studied mixed assumed strain method of incompatible modes for nonlinear analysis and improved enhanced assumed strain (EAS) methods for elasticity. Kasper and Taylor [90] investigated nearly incompressible elasticity and thin shell structures with assumed strain method.

Doherty and coworkers developed the concept of selective integration elements for stress analysis of axisymmetric solids [91]. Subsequently, Zienkiewicz and coworkers [92–93] suggested reduced integration elements for accuracy, widely applicability and efficiency in plates and shells. Prathap and coworkers [94–96] introduced field-consistent elements used to free shear locking, membrane locking, Poisson’s locking and stress oscillation.

Hughes and coworkers [81–82,97–98] proposed selective reduced integration elements (SRI) and B-bar method to treat anisotropic elastic materials. And Zienkiewicz and Taylor [99–101] developed B-bar method for isotropic (nearly) incompressible solids. The B-bar and SRI methods are nearly similar. Both methods use the separation of the stiffness matrix into volumetric and deviatoric parts. SRI method computes pressure integration as a constant using only one integration point in the center of the element. In contrast, the B-bar method computes a constant mean stress in terms of the average volumetric strain. The SRI method is difficult to extend to finite strain problems, while B-bar method can be easily applied.

The combination of solid elements and shell elements was also studied: the solid elements with the advantage of their ease of use and the shell elements with the advantage of significant computational cost savings as they allow to model thin structures with fewer elements.

Wriggers and coworkers [102–104] developed concept of solid-shell elements for combining the advantages of easy-to-use solid elements and solid elements. Hauptmann, Schweizerhof and coworkers [105–106] proposed solid-shell concept incorporates only displacement degrees of freedom for considering large deformations (stretching and bending) and nearly incompressible materials. Sze and coworkers [107] proposed that hybrid stress eight-node (hexahedral) solid-shell elements make use of the Assumed Natural Strain (ANS) method including higher order for improving the bending behavior. Additionally, ANS was also used to avoid shear and membrane locking [105,107–110]. Besides, Reese and coworkers [111–113] solved the elastic large deformation, incompressibility, hourglass and bending problems using the stabilization concept

of EAS and reduction integration. Piltner and Joseph [114] used hexahedral EAS solid-shell elements for avoiding locking and improving the accuracy of the solution. Areias and coworkers [115] investigated numerous examples of nearly incompressibility, beam and shell bending issues that are prone to locking in elasticity and plasticity with hexahedral EAS solid-shell elements. These successfully developed solid-shell elements rely on improvements in the discrete strain field by adding selected strain modes that are temporarily designed to allow the enhanced element to exhibit the desired performance. However, for such stable elements, these enhancements cannot achieve a higher asymptotic rate of displacement convergence than the underlying linear element. For achieving the higher convergence rate, the elements have to be interpolated with the full quadratic polynomial. Convergence of strains, obtained by discrete differentiation of the displacement field, is one order lower, resulting in turn in a poor convergence of stresses. For these reasons, the development mixed finite elements with interpolation for higher convergence rate and locking free become more needed.

Brezzi and coworkers [116–117] addressed that mixed elements can overcome all the above deficiencies of the standard formulation, providing accurate and locking-free solutions in both displacements and stresses. Cervera and coworkers [118] presents that increasing degrees of freedom contributes to a faster rate of convergence with mixed displacement-strain finite elements.

Cervera and coworkers [119–122] investigated mixed formulations with both displacement and stress interpolations as primary variables. In the problem of linear elasticity, nonlinear plasticity and strain localization, numerical results were analyzed taking into account stability and convergence of mixed finite elements. Recently, Cervera and coworkers [123–125] have presented mixed strain/displacement FEs involving the B-bar method or the pressure field to achieve enhanced stress accuracy and no stress locking in quasi-incompressible situations and in the incompressible limit.

1.3 Objectives

The main objectives of this work are:

To develop, implement and validate a general orthotropic elasto-plastic material model considering the orientation of the material.

- Elasto-plastic constitutive models for incompressible materials (von Mises and Hill yield criteria) are used to model various volume-preserving materials, such as metals, polymers and certain composites, whose behavior is pressure-independent.
- Elasto-plastic constitutive models for pressure-dependent materials (parabolic Drucker–Prager, Hoffman and Tsai–Wu yield criteria) are used to model pressure-sensitive materials such as rock, concrete, polymers and foam.
- All the constitutive models are combined into a general orthotropic constitutive model, also considering non-associated plasticity.

To develop and implement mixed ε/B-bar u finite elements for higher accuracy and cost efficiency.

- B-bar finite elements allow the solving of problems wherein the materials are quasi-incompressible. However, this method works only for quadrilateral meshes.
- Mixed $\boldsymbol{u}/p$ FEs enable solving problems involving incompressibility for any type of mesh, but their strain and stress accuracy is the same as standard FEs.
- Mixed $\boldsymbol{\varepsilon/u}$ FEs provide results with a significant improvement in strain and stress accuracy and can be used with any type of mesh, not only quadrilaterals.
- Mixed $\boldsymbol{\varepsilon}$/B-bar $\boldsymbol{u}$ FEs are developed to include the advantages of both B-bar and mixed $\boldsymbol{\varepsilon/u}$ FEs.

To analyze the Strain localization resulting from orthotropic elasto-plasticity, both in the continuous and discrete settings.

- The conditions of plastic yielding, strain bifurcation and strain localization are investigated.
- The strain localization condition is derived from Maxwell's kinematics, the plastic flow rule and the boundedness of the stress rate.
- The analytical results are obtained and numerically verified.

1.4 Thesis outline

In this thesis, two main topics have been covered: the mechanics of strain localization in plasticity and the performance of several mixed finite elements subjected to plastic strain localization.

Chapter 1 introduces the work, its motivation, State of the Art, objectives, thesis and research dissemination. Chapter 2 introduces the constitutive laws for isotropic and orthotropic elasto-plastic models with a description of the material model, Hooke's law and yield criteria. Chapter 3 presents the each scientific contribution of the thesis by compendium of publications. The publications present the analytical framework (constitutive relations, kinematics for strong and weak discontinuities), strain localization conditions, as well as the analytical results and numerical verification of the strain localization angles under plane stress and plane strain. Chapter 4 introduces the mixed finite formulations and presents a numerical comparison of different finite elements (standard elements, B-bar finite elements, mixed $\boldsymbol{u}/p$ finite elements, mixed $\boldsymbol{\varepsilon}/\boldsymbol{u}$ finite elements and mixed $\boldsymbol{\varepsilon}$/B-bar $\boldsymbol{u}$ finite elements with a publication about the performance of mixed $\boldsymbol{\varepsilon}/\boldsymbol{u}$ and mixed $\boldsymbol{\varepsilon}$/B-bar $\boldsymbol{u}$ finite elements in the compendium. Chapter 5 concludes the thesis with a discussion of the conclusions and future scope of the research. Then, details of all in-text references included in the thesis are given. Finally, the articles included in this doctoral thesis by a compendium of publications are provided.

1.5 Research dissemination

Publications in International Peer-Reviewed Journals

The doctoral Thesis is presented as a compendium of the following three publications

- M. Cervera, J.Y. Wu, M. Chiumenti and S. Kim. "**Strain localization analysis of Hill's orthotropic elastoplasticity: Analytical results and numerical verification**" (2020) *Computational Mechanics*, 65, 533–554. https://doi.org/10.1007/s00466-019-01782-4
- S. Saloustros, M. Cervera, S. Kim and M. Chiumenti. "**Accurate and locking-free analysis of beams, plates and shells using solid elements**" (2021) *Computational Mechanics*, 67, 883–914. https://doi.org/10.1007/s00466-020-01969-0
- S. Kim, M. Cervera, J.Y. Wu and M. Chiumenti. "**Strain Localization of Orthotropic Elasto-Plastic Cohesive-Frictional Materials: Analytical Results and Numerical Verification**" (2021) *Materials*, 14(8), 2040. https://doi.org/10.3390/ma14082040

In addition, one more paper has been prepared and incorporated into the thesis. The following manuscript is still under review on the submission date of the thesis.

- M. Cervera, J.Y. Wu, S. Kim, and M. Chiumenti. "**On the mechanics of strain localization in plasticity: Isotropic and orthotropic, elasto- and rigid-plastic, associated and non-associated models**" (2021) Submitted to Mechanics of Materials

Presentations in International Conferences

Research during the doctoral degree program has been presented in the following international conference.

- S. Kim, M. Cervera, M. Chiumenti and J.Y. Wu. "**Strain localization analysis of Hill‘s orthotropic elastoplasticity: analytical and numerical appraisal**" (2019) *COMPLAS 2019: XV International Conference on Computational Plasticity: Fundamentals and Applications*. ISBN/ISSN: 978-84-949194-7-3.

Chapter 2

Constitutive Equations for Elasto-plastic Orthotropic Materials

In this Chapter, the material models used in the thesis are presented.

Elastic, plastic, compressible and incompressible materials are described, in 3D as well as plane strain and plane stress conditions. Explanations of the elasto-plastic constitutive equations are presented in detail using Hooke's Law and the several yield criteria used for orthotropic materials.

A material model is an idealized representation of the actual behavior of a material based on certain experiments or theories and aims to suggest that such an idealization typically lies within a certain accuracy range. Notably, models do not fundamentally represent a strict description of the material. Because simulations are model-based, they do not represent reality; instead, they represent a model of reality.

Therefore, a deeper understanding of such models is required for more accurate simulation analyzes to be performed

2.1 Material

Materials are classified according to their orientation-dependent physical properties (such as Young's modulus or thermal conductivity). In the following sections, the subscript $(\cdot)_{\text{axis}}$ denotes the axis of orientation. According to this, there are:

Isotropic materials, if the mechanical properties are the same in all directions. Examples are glass, metals, mortar, concrete and epoxy.

Anisotropic materials: The mechanical properties of the material change depending on the direction. Examples are rock-forming minerals, single crystals and biological tissues.

Orthotropic material: The mechanical properties of the material are different each along three orthogonal axes. Examples include rolled metals and wood.

In recent years, Additive Manufacturing (AM), a manufacturing process to create 3D objects by stacking, is gaining considerable interest. In AM, the material properties the in-plane and out of plane of the stacking face are significantly different. Thus, the created 3D objects have the orthotropic properties.

2.1.1 Material properties

2.1.1.1 Elasticity

An elastic material returns to its original shape and size after the force applied to the material is withdrawn.

Young's modulus, Poisson's ratio, shear modulus and bulk modulus are examples of elastic material properties.

Young's Modulus

Young's modulus, denoted by E, refers to the mechanical property that relates tensile stress, denoted by σ, and axial strain, denoted by ε. $E = \sigma/\varepsilon$.

In orthotropic materials, the Young's moduli in the x, y and z directions are E_x, E_y and E_z, respectively.

Poisson's ratio

Poisson's ratio, denoted by ν, is the negative ratio of transverse to the axial strain as the material is stretched. Orthotropic Poisson's ratios (ν_{xy}, ν_{xz} and ν_{yz}) are defined as

$$\nu_{xy} = -\frac{\varepsilon_{yy}}{\varepsilon_{xx}}, \qquad \nu_{xz} = -\frac{\varepsilon_{zz}}{\varepsilon_{xx}}, \qquad \nu_{yz} = -\frac{\varepsilon_{zz}}{\varepsilon_{yy}}, \tag{2.1}$$

respectively.

For isotropic materials, $\nu = \nu_{xy} = \nu_{xz} = \nu_{yz}$.

Most isotropic materials have Poisson's ratio ranging from 0 to 0.5. This follows from thermodynamic reasons, i.e., the positivity of the shear and bulk moduli. However, there are exceptions; for example, auxetics are materials with a negative Poisson's ratio. When stretched, auxetics thicken perpendicular to the applied force. This behavior is due to their particular internal structure.

It should be noted that in orthotropic materials. The following relations must hold for thermodynamic reasons (symmetry of the elastic tensor):

$$\frac{\nu_{yx}}{E_y} = \frac{\nu_{xy}}{E_x}, \qquad \frac{\nu_{zx}}{E_z} = \frac{\nu_{xz}}{E_x}, \qquad \frac{\nu_{yz}}{E_y} = \frac{\nu_{zy}}{E_z} \tag{2.2}$$

As it can be seen in Eq. (2.2), some anisotropic or orthotropic materials may have one or more Poisson's ratios greater than 0.5.

Shear Modulus

Shear modulus, denoted by $\mu \; or \; G$, is the ratio of the shear stress to the shear strain. Orthotropic shear moduli (G_{xy}, G_{xz} and G_{yz}) are defined as

$$G_{xy} = \frac{E_x}{2(1+\nu_{xy})}, \qquad G_{xz} = \frac{E_x}{2(1+\nu_{xz})}, \qquad G_{yz} = \frac{E_y}{2(1+\nu_{yz})} \tag{2.3}$$

For isotropic materials, $G = G_{xy} = G_{xz} = G_{yz} = \frac{E}{2(1+\nu)}$.

Bulk Modulus

Bulk modulus, denoted by K, is the rate of change the volume when the material is subjected to uniform pressure p.

$$K = -\frac{p}{\frac{dV}{V}} = -\frac{p}{1-(1+\varepsilon_x)(1+\varepsilon_y)(1+\varepsilon_z)} \approx \frac{p}{\varepsilon_x+\varepsilon_y+\varepsilon_z} = \frac{p}{e_{vol}} \tag{2.4}$$

where $e_{vol} = \varepsilon_x + \varepsilon_y + \varepsilon_z$ is the volumetric strain and p is the pressure, or mean stress,

$p = \frac{1}{3}(\sigma_x + \sigma_y + \sigma_z)$.

For isotropic materials, $K = \frac{\mathrm{E}}{3(1-2\nu)}$.

When the Poisson's ratio approaches 0.5, the bulk modulus tends to infinite and isotropic materials are referred to as nearly incompressible materials. In the limit, the bulk modulus of an incompressible isotropic material would be infinity.

The compressibility modulus, denoted by β, is the reciprocal of the bulk modulus. Therefore, incompressible materials have zero compressibility.

2.1.1.2 Plasticity

A plastic material cannot return to its original shape and size after the force applied to the material is withdrawn. This permanent and irreversible change is known as plastic deformation.

A plastic material is characterized by its yield stress and its post-yielding behavior.

Yield Stress

Yield Stress, denoted by σ^Y, is the stress value at the yield strength; it indicates the beginning of plastic deformation.

Perfect Plasticity occurs if the material undergoes plasticity without any increase or decrease of the stress.

Hardening occurs if the material undergoes plasticity with an increase in the stress or applied load.

Softening occurs if the material undergoes plasticity with a decrease in the stress.

In Figure 2.1, the green, blue and red curves represent perfect plasticity, linear softening and linear hardening behavior, respectively.

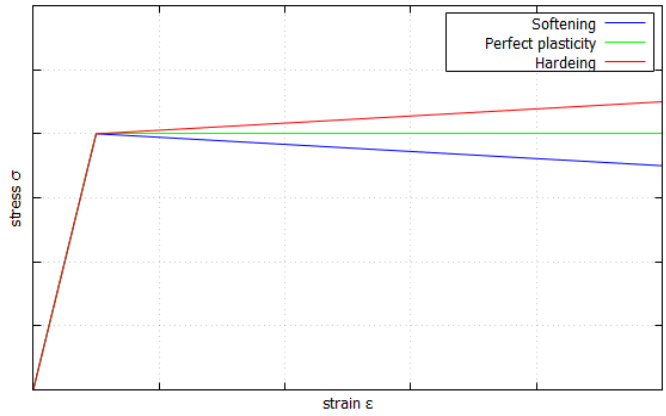

Figure 2.1 Stress–strain curves

Orthotropic plasticity

Materials with different yield stresses along three orthogonal axes are called orthotropic elasto-plastic materials. Examples are masonry, rolled metals, alloy, polymeric material and carbon fiber composites. The Hill, Hoffman and Tsai–Wu yield criteria are employed in this thesis to characterized orthotropic elasto-plastic materials.

2.1.2 Plane strain and plane stress conditions

If the 3D mechanical problem satisfies the following two planar continuum conditions, it can be expressed as a 2D model:

1. The cross-section is constant along a longitudinal direction.

2. The boundary conditions, loading and material properties are constant along the longitudinal direction.

Plane Stress Condition

Plane stress refers to the condition wherein the stress through the thickness of a material (vertical and shear) is zero (but not the strain). Plane stress is applicable to significantly thin flat plates; for examples, aircraft wing films, cantilever beams, pressure vessels, shell and membrane structures.

Plane Strain Condition

Plane strain refers to the condition wherein the strain through the thickness of a material (vertical and shear) is zero (but not the stress). Plane strain is applicable to considerably long or thick structures; for example, in the longitudinal direction of line pipes with internal pressure or long straight gravity dams.

Table 2.1 summarizes the stress and strain variables used in plane stress and plane strain.

Table 2.1. Comparison of Plane Stress and Plane Strain

	Plane Stress	Plane Strain
Stress Variables	$\sigma_{zz} = \sigma_{xz} = \sigma_{yz} = 0$ $\sigma_{xx}, \sigma_{yy}, \sigma_{xy} \neq 0$	$\sigma_{xz} = \sigma_{yz} = 0$ $\sigma_{xx}, \sigma_{yy}, \sigma_{xy} \neq 0$
Strain Variables	$\varepsilon_{xz} = 0, \varepsilon_{yz} = 0$ $\varepsilon_{xx}, \varepsilon_{yy}, \varepsilon_{zz}, \varepsilon_{xy} \neq 0$	$\varepsilon_{zz} = \varepsilon_{xz} = \varepsilon_{yz} = 0$ $\varepsilon_{xx}, \varepsilon_{yy}, \varepsilon_{xy} \neq 0$

2.2 Constitutive equation

In this section, the constitutive equation in elasto-plastic media is addressed.

Tensor notation is used in the following. Inner product with single contraction and double contraction is denoted by '$\cdot$' and ':', respectively, and the dyadic operator is denoted by '$\otimes$'.

For an elasto-plastic model, the constitutive equation is expressed in total form as

$$\boldsymbol{\varepsilon} = \boldsymbol{\varepsilon}^e + \boldsymbol{\varepsilon}^p, \qquad \boldsymbol{\sigma} = \mathbf{D}^0 : \boldsymbol{\varepsilon}^{\mathrm{e}} = \mathbf{D}^0 : (\boldsymbol{\varepsilon} - \boldsymbol{\varepsilon}^p) \tag{2.5}$$

where the second-order strain tensor $\boldsymbol{\varepsilon}$ is decomposed into its elastic and plastic parts, $\boldsymbol{\varepsilon}^e$ and $\boldsymbol{\varepsilon}^p$, respectively. The second-order stress tensor $\boldsymbol{\sigma}$ is proportional to the elastic strain tensor $\boldsymbol{\varepsilon}^e$, through the fourth-order elasticity tensor $\mathbf{D}^0$. All the tensors involved are symmetric. The elastic properties may be isotropic, orthotropic or anisotropic. $\mathbf{D}^0$ is addressed in detail in Section 2.3.

The admissible stress domain is determined by the yield criterion

$$\Phi(\boldsymbol{\sigma}, \zeta) = \phi(\boldsymbol{\sigma}) - q(\zeta) \leq 0 \tag{2.6}$$

defined in terms of the equivalent stress $\phi(\boldsymbol{\sigma})$, a stress-like internal variable $q(\zeta)$ and the equivalent plastic strain ζ, which determine the shape and size of the domain, respectively. Yield criteria for orthotropic elasto-plasticity are discussed in Section 2.4.

The plastic strain is defined in rate form; its direction is derived from the plastic potential. In associated plasticity, the plastic potential is equal to the yield function; therefore,

$$\dot{\boldsymbol{\varepsilon}}^p = \dot{\lambda} \frac{\partial \phi}{\partial \boldsymbol{\sigma}} = \dot{\lambda}\, \boldsymbol{\Lambda} \tag{2.7}$$

where $\dot{\lambda} \geq 0$ denotes the plastic multiplier; $(\dot{\ })$ is the time derivative, and the plastic flow tensor $\boldsymbol{\Lambda} = \partial\phi \,/\, \partial\boldsymbol{\sigma}$ is normal to the yield function $\Phi = 0$. Similarly, the evolution of equivalent plastic strain is

$$\dot{\zeta} = \dot{\lambda} \frac{\partial \phi}{\partial q} = -\dot{\lambda} \tag{2.8}$$

The constitutive equation in rate form follows from Eq. (2.5) as follows:

$$\dot{\boldsymbol{\sigma}} = \mathbf{D}^0 : \dot{\boldsymbol{\varepsilon}}^e = \mathbf{D}^0 : (\dot{\boldsymbol{\varepsilon}} - \dot{\boldsymbol{\varepsilon}}^p) = \mathbf{D}^{ep} : \dot{\boldsymbol{\varepsilon}} \tag{2.9}$$

where the fourth-order elasto-plasticity tangent tensor $\mathbf{D}^{ep}$ is obtained from the Kuhn–Tucker and consistency conditions as

$$\mathbf{D}^{ep} = \frac{\mathrm{d}\boldsymbol{\sigma}}{\mathrm{d}\boldsymbol{\varepsilon}} = \mathbf{D}^0 - \frac{\mathbf{D}^0 : \boldsymbol{\Lambda} \otimes \mathbf{D}^0 : \boldsymbol{\Lambda}}{H + \boldsymbol{\Lambda} : \mathbf{D}^0 : \boldsymbol{\Lambda}} \tag{2.10}$$

where $H = \partial q \,/\, \partial \zeta$ is the hardening or softening modulus. Note that $\mathbf{D}^{ep}$ is symmetric.

For perfect plasticity, $q = q_0$, and $H = 0$. It should be noted that, in associative plasticity, the elasto-plastic tangent tensor is symmetric.

For non-associated plasticity, a plastic potential $\psi = \psi(\boldsymbol{\sigma})$ is defined, so that

$$\boldsymbol{\Lambda}_\phi = \frac{\partial \phi}{\partial \boldsymbol{\sigma}}, \qquad \boldsymbol{\Lambda}_\psi = \frac{\partial \psi}{\partial \boldsymbol{\sigma}} \tag{2.11}$$

where $\phi(\boldsymbol{\sigma})$ is the equivalent stress used in the yield surface and $\psi(\boldsymbol{\sigma})$ in the plastic potential

$$\dot{\boldsymbol{\varepsilon}}^p = \dot{\lambda}\, \boldsymbol{\Lambda}_\psi, \qquad \mathbf{D}^{ep} = \mathbf{D}^0 - \frac{\mathbf{D}^0 : \boldsymbol{\Lambda}_\psi \otimes \mathbf{D}^0 : \boldsymbol{\Lambda}_\phi}{H + \boldsymbol{\Lambda}_\phi : \mathbf{D}^0 : \boldsymbol{\Lambda}_\psi} \tag{2.12}$$

Note that $\mathbf{D}^{ep}$ is non-symmetric in this case.

2.3 Hooke's law in stiffness form

Hooke's Law expresses a linear relationship between stress and strain.

For linear springs, Hooke's law states that $\mathrm{F} = k\mathrm{x}$, where applied force F is linearly proportional to the displacement or change in length x. The proportionality constant, k, is the stiffness of the spring.

For continuous media, Hooke's law is given as $\boldsymbol{\sigma} = \mathbf{D}^0 : \boldsymbol{\varepsilon}^e$, where the second-order stress tensor $\boldsymbol{\sigma}$ is equal to the fourth-order stiffness tensor (elasticity tensor) $\mathbf{D}^0$ multiplied by the second-order strain tensor $\boldsymbol{\varepsilon}^e$. Because of the symmetry of the strain, stress and elasticity tensors, Voigt's notation, transforming tensors to matrices, is used in the following.

2.3.1 Anisotropic materials

In anisotropic materials, the fourth-order stiffness tensor $\mathbf{D}^0$ has 36 stiffness matrix components. As the stiffness matrix needs to be symmetric for thermodynamical reasons, $\mathbf{D}^0$ has only 21 independent matrix components.

$$\begin{bmatrix} \sigma_{xx} \\ \sigma_{yy} \\ \sigma_{zz} \\ \sigma_{xy} \\ \sigma_{xz} \\ \sigma_{yz} \end{bmatrix} = \begin{bmatrix} \mathrm{D}_{11} & \mathrm{D}_{12} & \mathrm{D}_{13} & \mathrm{D}_{14} & \mathrm{D}_{15} & \mathrm{D}_{16} \\ \mathrm{D}_{21} & \mathrm{D}_{22} & \mathrm{D}_{23} & \mathrm{D}_{24} & \mathrm{D}_{25} & \mathrm{D}_{26} \\ \mathrm{D}_{31} & \mathrm{D}_{32} & \mathrm{D}_{33} & \mathrm{D}_{34} & \mathrm{D}_{35} & \mathrm{D}_{36} \\ \mathrm{D}_{41} & \mathrm{D}_{42} & \mathrm{D}_{43} & \mathrm{D}_{44} & \mathrm{D}_{45} & \mathrm{D}_{46} \\ \mathrm{D}_{51} & \mathrm{D}_{52} & \mathrm{D}_{53} & \mathrm{D}_{54} & \mathrm{D}_{56} & \mathrm{D}_{56} \\ \mathrm{D}_{61} & \mathrm{D}_{62} & \mathrm{D}_{63} & \mathrm{D}_{64} & \mathrm{D}_{65} & \mathrm{D}_{66} \end{bmatrix} \begin{bmatrix} \varepsilon_{xx} \\ \varepsilon_{yy} \\ \varepsilon_{zz} \\ \varepsilon_{xy} \\ \varepsilon_{xz} \\ \varepsilon_{yz} \end{bmatrix} \tag{2.13}$$

2.3.2 Isotropic material

In isotropic materials, the fourth-order stiffness tensor $\mathbf{D}^0$ requires only two independent elastic constants (E and ν).

$$\begin{bmatrix}\sigma_{xx}\\ \sigma_{yy}\\ \sigma_{zz}\\ \sigma_{xy}\\ \sigma_{xz}\\ \sigma_{yz}\end{bmatrix} = 2G\begin{bmatrix}\varepsilon_{xx}\\ \varepsilon_{yy}\\ \varepsilon_{zz}\\ \varepsilon_{xy}\\ \varepsilon_{xz}\\ \varepsilon_{yz}\end{bmatrix} + \lambda\,\mathrm{tr}(\varepsilon)\mathrm{I}$$
$$= \frac{E}{(1+\nu)(1-2\nu)}\begin{bmatrix}1-\nu & \nu & \nu & 0 & 0 & 0\\ \nu & 1-\nu & \nu & 0 & 0 & 0\\ \nu & \nu & 1-\nu & 0 & 0 & 0\\ 0 & 0 & 0 & 1-2\nu & 0 & 0\\ 0 & 0 & 0 & 0 & 1-2\nu & 0\\ 0 & 0 & 0 & 0 & 0 & 1-2\nu\end{bmatrix}\begin{bmatrix}\varepsilon_{xx}\\ \varepsilon_{yy}\\ \varepsilon_{zz}\\ \varepsilon_{xy}\\ \varepsilon_{xz}\\ \varepsilon_{yz}\end{bmatrix} \tag{2.14}$$

The conversion formulas for the alternative material properties are:

$$\lambda = \frac{E\nu}{(1+\nu)(1-2\nu)}, \qquad G = \frac{E}{2(1+\nu)}, \qquad \mathrm{K} = \frac{E}{3(1-2\nu)} \tag{2.15}$$

2.3.3 Orthotropic materials

In orthotropic materials, the fourth-order stiffness tensor $\mathbf{D}^0$ requires 9 independent elastic constants, namely, 3 Young's moduli, 3 Poisson's ratios and 3 shear moduli.

$$\begin{bmatrix}\sigma_{xx}\\ \sigma_{yy}\\ \sigma_{zz}\\ \sigma_{xy}\\ \sigma_{xz}\\ \sigma_{yz}\end{bmatrix} = \begin{bmatrix}\frac{1-\nu_{yz}\nu_{zy}}{E_yE_z\Delta} & \frac{\nu_{xy}+\nu_{xz}\nu_{yz}}{E_xE_z\Delta} & \frac{\nu_{xz}+\nu_{xy}\nu_{yz}}{E_xE_y\Delta} & 0 & 0 & 0\\ \frac{\nu_{xy}+\nu_{xz}\nu_{yz}}{E_xE_z\Delta} & \frac{1-\nu_{xz}\nu_{zx}}{E_xE_z\Delta} & \frac{\nu_{yz}+\nu_{xz}\nu_{yx}}{E_xE_y\Delta} & 0 & 0 & 0\\ \frac{\nu_{xz}+\nu_{xy}\nu_{yz}}{E_xE_y\Delta} & \frac{\nu_{yz}+\nu_{xz}\nu_{yx}}{E_xE_y\Delta} & \frac{1-\nu_{xy}\nu_{yx}}{E_xE_y\Delta} & 0 & 0 & 0\\ 0 & 0 & 0 & 2G_{xy} & 0 & 0\\ 0 & 0 & 0 & 0 & 2G_{xz} & 0\\ 0 & 0 & 0 & 0 & 0 & 2G_{yz}\end{bmatrix}\begin{bmatrix}\varepsilon_{xx}\\ \varepsilon_{yy}\\ \varepsilon_{zz}\\ \varepsilon_{xy}\\ \varepsilon_{xz}\\ \varepsilon_{yz}\end{bmatrix} \tag{2.16}$$

$$\Delta = \frac{1-\nu_{xy}\nu_{yx}-\nu_{yz}\nu_{zy}-\nu_{zx}\nu_{xz}-2\nu_{xy}\nu_{yz}\nu_{zx}}{E_xE_yE_z}$$

2.4 Generalized yield criteria

The yield criterion is used to determine the occurrence of yielding under combined stress states; it is specified in relation to the material yield stress or stresses.

Accordingly, if the stress state lies within the yield criterion, the stress state is said to be elastic; otherwise, it is said to be plastic.

This section presents a general yield criterion which may include the von Mises, the Drucker–Prager, Hill, Hoffman and Tsai–Wu yield criteria, among others.

Orthotropic cohesive-frictional yield criteria of the form

$$\Phi(\boldsymbol{\sigma}, \zeta) = \phi(\boldsymbol{\sigma}) - q(\zeta) \leq 0 \tag{2.17}$$

are now considered. $\phi = \phi(\boldsymbol{\sigma})$ is the equivalent stress, $q(\zeta)$ is a stress-like internal variable and ζ is the equivalent plastic strain. Let (1,2,3) be the material orthotropy axes and

$$\boldsymbol{\sigma}^{\mathrm{T}} = [\sigma_{11}, \sigma_{22}, \sigma_{33}, \sigma_{12}, \sigma_{13}, \sigma_{23}] \tag{2.18}$$

Voigt's representation of the symmetric second-order stress tensor in those axes.

The equivalent stress $\phi(\boldsymbol{\sigma})$ is expressed as

$$\phi(\boldsymbol{\sigma}) = \sqrt{\frac{3}{2}(\boldsymbol{\sigma}^{\mathrm{T}} \cdot \mathbf{P} \cdot \boldsymbol{\sigma} + \mathbf{Q}^{\mathbf{T}} \cdot \boldsymbol{\sigma})} \tag{2.19}$$

The generalized orthotropic matrix **P** and **Q** vector read

$$\mathbf{P} = \frac{1}{F+G+H}\begin{bmatrix} F+G & -\tilde{F} & -\tilde{G} & 0 & 0 & 0 \\ -\tilde{F} & F+H & -\tilde{H} & 0 & 0 & 0 \\ -\tilde{G} & -\tilde{H} & G+H & 0 & 0 & 0 \\ 0 & 0 & 0 & 2L & 0 & 0 \\ 0 & 0 & 0 & 0 & 2M & 0 \\ 0 & 0 & 0 & 0 & 0 & 2N \end{bmatrix}, \mathbf{Q} = \frac{1}{F+G+H}\begin{bmatrix} I \\ J \\ K \\ 0 \\ 0 \\ 0 \end{bmatrix} \tag{2.20}$$

where the material parameters F, G, H, $\tilde{F}$, $\tilde{G}$, $\tilde{H}$, L, M, N, I, J and K are given in terms of by the material strengths f (with superscripts c and t denoting compression and tension, and with subscript denoting the material axis (1,2,3), respectively):

$$\begin{aligned} F &= \frac{1}{2}\left[\frac{1}{f_1^c f_1^t} + \frac{1}{f_2^c f_2^t} - \frac{1}{f_3^c f_3^t}\right], G = \frac{1}{2}\left[\frac{1}{f_1^c f_1^t} - \frac{1}{f_2^c f_2^t} + \frac{1}{f_3^c f_3^t}\right], H \\ &= \frac{1}{2}\left[-\frac{1}{f_1^c f_1^t} + \frac{1}{f_2^c f_2^t} + \frac{1}{f_3^c f_3^t}\right] \end{aligned} \tag{2.21}$$

$$L = \frac{1}{2}\left(\frac{1}{f_{12}}\right)^2, M = \frac{1}{2}\left(\frac{1}{f_{13}}\right)^2, N = \frac{1}{2}\left(\frac{1}{f_{23}}\right)^2 \tag{2.22}$$

$$I = \frac{1}{f_1^t} - \frac{1}{f_1^c}, J = \frac{1}{f_2^t} - \frac{1}{f_2^c}, K = \frac{1}{f_3^t} - \frac{1}{f_3^c} \tag{2.23}$$

Unless otherwise stated:

$$\tilde{F} = F, \quad \tilde{G} = G, \quad \tilde{H} = H \tag{2.24}$$

The initial stress threshold is defined as

$$q_0^2 = \frac{3}{2}[F + G + H]^{-1} \tag{2.25}$$

Different well-known quadratic isotropic and orthotropic yield criteria are obtained by appropriately selecting the material parameters:

- **The von Mises Yield criterion**

$$f = f_1^c = f_2^c = f_3^c = f_1^t = f_2^t = f_3^t, \quad \frac{f}{\sqrt{3}} = f_{12} = f_{13} = f_{23} \tag{2.26}$$

- **The parabolic Drucker–Prager (DP) Yield criterion**

$$f^c = f_1^c = f_2^c = f_3^c, \quad f^t = f_1^t = f_2^t = f_3^t, \quad \frac{\sqrt{f^c f^t}}{\sqrt{3}} = f_{12} = f_{13} = f_{23} \tag{2.27}$$

- **The Hill Yield criterion**

$$f_1 = f_1^c = f_1^t, f_2 = f_2^c = f_2^t, f_3 = f_3^c = f_3^t \text{ and } I = J = K = 0 \tag{2.28}$$

- **The Hoffman Yield criterion**

$$\widetilde{F} = F, \quad \widetilde{G} = G, \quad \widetilde{H} = H \tag{2.29}$$

- **The Tsai–Wu Yield criterion**

$$\tilde{F} = \frac{1}{2}\frac{1}{\sqrt{f_1^c f_1^t f_2^c f_2^t}}, \quad \tilde{G} = \frac{1}{2}\frac{1}{\sqrt{f_1^c f_1^t f_3^c f_3^t}}, \quad \tilde{H} = \frac{1}{2}\frac{1}{\sqrt{f_2^c f_2^t f_3^c f_3^t}} \tag{2.30}$$

Orthotropic criteria cannot be represented graphically in the Haigh–Westergaard (HW) stress space because they depend on the six stress components. A partial graphical representation can be obtained by considering them projected into the HW space when the principal stresses act on the material axis, that is, no shear stress appears on the material system. Such representation, generally as an elliptic paraboloid is offered in Figure 2.2 and Figure 2.3. All strengths are scaled to 1.

Figure 2.2 shows two incompressible yield criteria, tensile and compressive strength are equal; Figure 2.2a shows isotropic von Mises cylinder with $f_1/f_2 = f_1/f_3 = 1$ and Figure 2.2b shows orthotropic Hill cylinder with $f_1/f_2 = f_1/f_3 = 1.5$.

Figure 2.3 shows three cohesive-frictional yield criteria. Figure 2.3a shows isotropic parabolic Drucker–Prager for compressive to tensile strength ratio $\kappa = f^c/f^t = 1.5$. Figure 2.3b,c show the orthotropic Hoffman and Tsai–Wu criteria, respectively, for $\kappa = f_1^c/f_1^t = 1.5$ and $f_2^c/f_2^t = f_3^c/f_3^t = 1.0$.

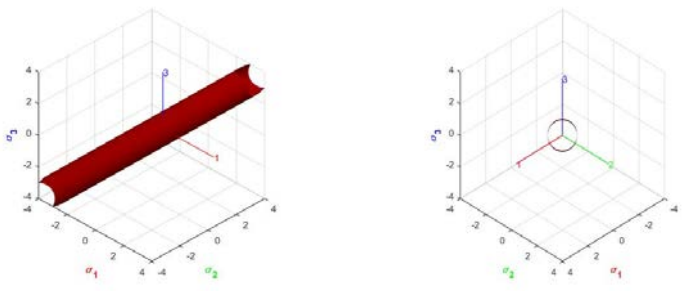

(**a**)

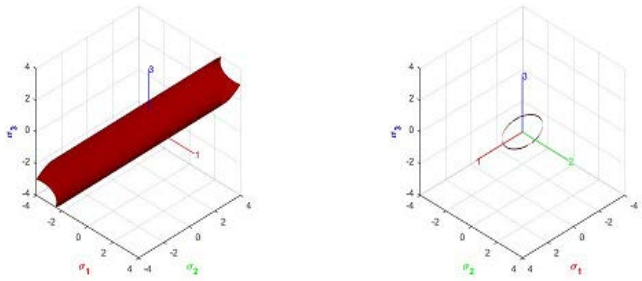

(**b**)

Figure 2.2 Yield criteria in HW stress space, lateral and view from the hydrostatic axis:

(a) von Mises; (b) Hill

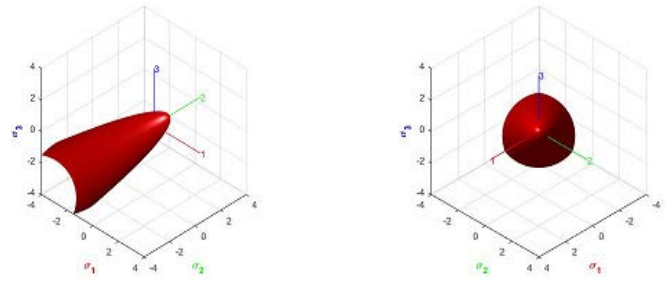

(a)

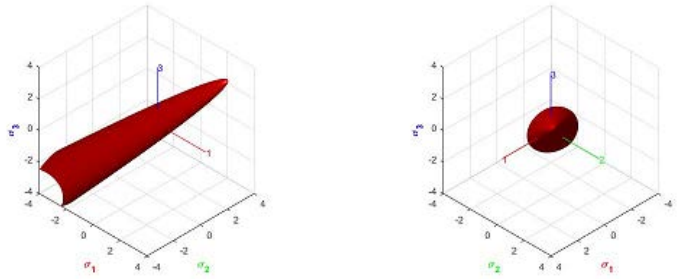

(b)

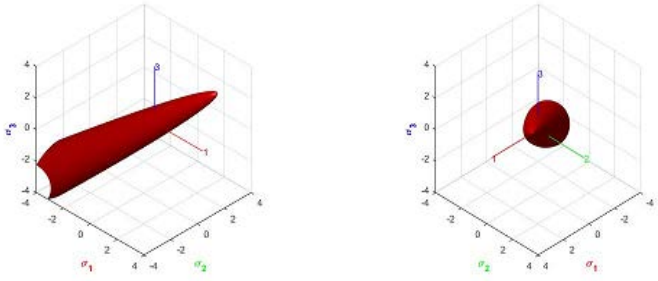

(c)

Figure 2.3 Yield criteria in HW stress space, lateral and view from the hydrostatic axis:

(a) Parabolic Drucker–Prager; (b) Hoffman; (c) Tsai–Wu.

Chapter 3

Strain Localization in Plasticity

In this chapter, the main topic of the thesis, the mechanics of strain localization in elasto-plastic materials, is addressed. Isotropic and orthotropic, incompressible and cohesive-frictional, associative and non-associative flows are studied. Analytical results are obtained for problems where the far field stress state is known. Independent numerical FE analyses are performed to confirm the analytical predictions.

The outline of the Chapter is as follow. Section 3.1 presents the concepts regarding strain bifurcation and strain localization analysis used in this thesis. Section 3.2 summarizes a published journal paper on the strain localization analysis of Hill's orthotropic elasto-plasticity. Section 3.3 provides complementarily results on the dependence of the analytical strain localization angles on the degree of orthotropy. Section 3.4 summarizes a published journal paper on the strain localization of orthotropic elasto-plastic cohesive-frictional materials. Section 3.5 provides complementarily results on the dependence of the analytical strain localization angles on the degree of friction. Section 3.6 summarizes a paper under review on the mechanics of strain localization in plasticity.

3.1 Strain bifurcation and strain localization analysis

3.1.1 Failure analysis: continuous, localized and discrete failure

Let $\Omega \subset \mathrm{R}^{\boldsymbol{n_{dim}}}$ $(n_{\mathrm{dim}} = 1, 2, 3)$ be an elasto-plastic solid domain where the evolution of the deformation process leads to failure, with the reference position vector $\boldsymbol{x} \subset \mathrm{R}^{\boldsymbol{n_{dim}}}$. Deformations of the solid are characterized by the displacement field $\boldsymbol{u}(\boldsymbol{x})$ and the infinitesimal strain field $\boldsymbol{\varepsilon}(\boldsymbol{x}) = \nabla^{\mathrm{sym}}\boldsymbol{u}(\boldsymbol{x})$, where $\nabla^{\mathrm{sym}}(\,\cdot\,)$ is the symmetric gradient operator. Displacement rate jumps and strain rate jumps are denoted by $[\![\dot{\boldsymbol{u}}]\!]$ and $[\![\dot{\boldsymbol{\varepsilon}}]\!]$, respectively.

According to the continuity of displacement and strain fields, three stages can be identified in the failure: continuous failure, localized failure and discrete failure. They are schematically represented in Figure 3.1.

Continuous failure. The standard continuum compatibility conditions hold during the deformation progressing to failure; that is, the displacement and strain rate jumps do not emerge as the displacement and strain (rate) fields are continuous. $[\![\dot{\boldsymbol{u}}]\!] = 0$, $[\![\dot{\boldsymbol{\varepsilon}}]\!] = 0$.

Localized failure. The standard kinematic compatibility conditions in the continuum body are partially violated by the strain field during the deformation progressing to failure; namely, the displacement (rate) jump does not emerge, but strain (rate) jump occurs $[\![\dot{\boldsymbol{u}}]\!] = 0$, $[\![\dot{\boldsymbol{\varepsilon}}]\!] \neq 0$.

Discrete failure. The displacement and strain fields appear discontinuous, resulting in fracture; namely, displacement and strain (rate) jumps emerge. $[\![\dot{\boldsymbol{u}}]\!] \neq 0$, $[\![\dot{\boldsymbol{\varepsilon}}]\!] \neq 0$.

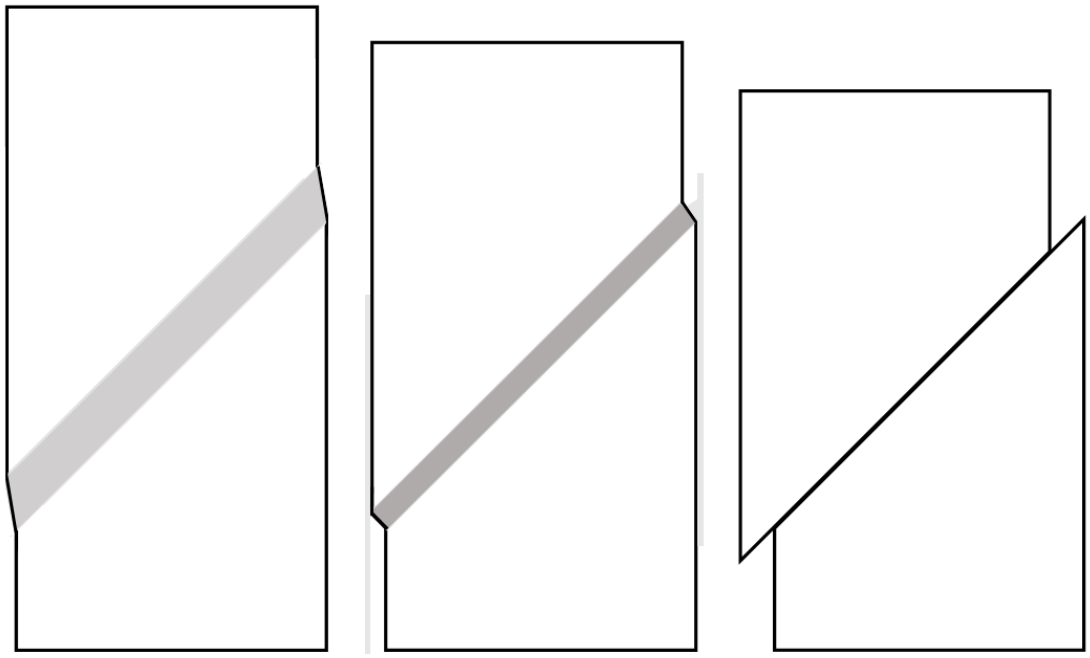

(a) **(b)** **(c)**

Figure 3.1 Stages of failure: (a) continuous failure, (b) localized failure and (c) discrete failure

For each type of failure to occur, there are necessary requirements that hold. The necessary conditions can be used as identifiers to diagnose the respective stage of failure.

In the following, the general setting of strong and regularized discontinuities and the necessary conditions for these to appear (the strain bifurcation, strain localization and stress boundedness conditions) are discussed.

In this chapter, tensor notation is used. The inner products with single and double contractions are denoted by '$\cdot$' and ':', respectively, while the dyadic operator is signified by '$\otimes$'.

3.1.2 General setting of discontinuities

Kinematics of discontinuities. Maxwell's compatibility condition

In the early stages of the loading and deformation process of an elasto-plastic solid, standard kinematics applies and both the displacement rate and strain rate fields are continuous. However, in softening and associated perfect plasticity, and even in hardening non-associated plasticity, slip lines (in 2D) or slip surfaces (in 3D) may form. Across these, the deformation can grow unbounded, displacement and/or strain discontinuities may appear.

Figure 3.2a shows the elasto-plastic solid domain Ω split by a displacement discontinuity $\boldsymbol{S}$ (the slip line or slip surface) into two parts Ω^+ and Ω^-. The orientation of the discontinuity is denoted with the unit normal vector $\boldsymbol{n}$ with direction from Ω^- to Ω^+. Let L be a characteristic size of the domain.

For the analysis of strain localization in the continuum setting and also for its numerical verification using FEM, it is convenient to consider a *regularized discontinuity*, as shown in Figure 3.2b. Here, subdomains Ω^+ and Ω^- are separated by a regularized discontinuity band $\boldsymbol{B}$ of finite width b, as the distance between surfaces $\boldsymbol{S}^+$ and $\boldsymbol{S}^-$; these are weak (strain) discontinuities. The bandwidth b is small compared to the characteristic size of the domain L, so that $b/L << 1$.

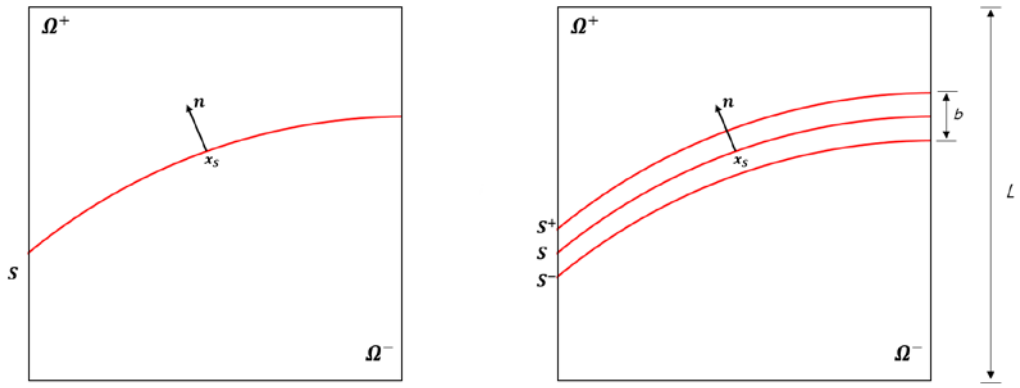

Figure 3.2 (a) Strong and (b) regularized discontinuities in an elasto-plastic solid.

Figure 3.3a shows the corresponding kinematics of a strong discontinuity: the velocity and strain rate fields are not regular. There is a discontinuity of the displacement rate at $\boldsymbol{S}$ of value $\dot{\boldsymbol{w}}$. From Maxwell's compatibility condition, the jump of strain rate at $\boldsymbol{S}$ is

$$[\![\dot{\boldsymbol{\varepsilon}}]\!] = \dot{\boldsymbol{\varepsilon}}_{\text{int}} - \dot{\boldsymbol{\varepsilon}}_{\text{ext}} = (\dot{\boldsymbol{w}} \otimes \boldsymbol{n})^{\text{sym}} \delta_S \tag{3.1}$$

where $\dot{\boldsymbol{\varepsilon}}_{\text{int}}$ is strain rate inside $\boldsymbol{S}$ and $\dot{\boldsymbol{\varepsilon}}_{\text{ext}}$ is strain rate outside $\boldsymbol{S}$ and δ_S denotes the Dirac delta function. Note that this strain rate jump is unbounded and has a very definite structure determined by the direction of the discontinuity surface, as it allows for unbounded strain rate components at $\boldsymbol{S}$ due to the discontinuity of the displacement in the normal direction $\boldsymbol{n}$, but not in those directions tangential to $\boldsymbol{S}$.

Figure 3.3b shows the corresponding regularized kinematics. Note that the strain localizes in the regularized band $\boldsymbol{B}$. The jump of strain rate inside and outside of the localization band can be expressed in terms of the deformation rate vector inside the band, $\dot{\boldsymbol{e}} = \dot{\boldsymbol{w}}/b$, as

$$[\![\dot{\boldsymbol{\varepsilon}}]\!] = \dot{\boldsymbol{\varepsilon}}_{\text{int}} - \dot{\boldsymbol{\varepsilon}}_{\text{ext}} = (\dot{\boldsymbol{e}} \otimes \boldsymbol{n})^{\text{sym}} \tag{3.2}$$

This strain rate jump is bounded and has the same structure than (3.1).

Note that for the band width $b \to 0$, the strain rate in the discontinuity band $\boldsymbol{B}$ tends to the strain rate in the strong discontinuity $\boldsymbol{S}$. Reversely, a localization band $\boldsymbol{B}$ of width b bounded by two weak discontinuities can be viewed as a regularized strong discontinuity $\boldsymbol{S}$,

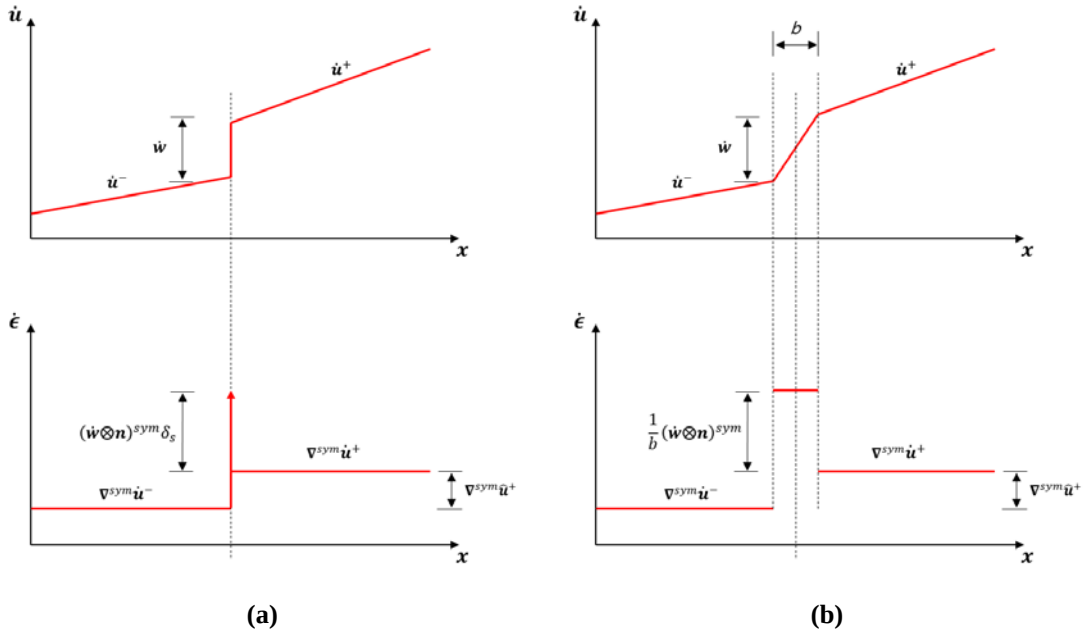

(a) **(b)**

Figure 3.3 Kinematics of (a) strong and (b) regularized discontinuities.

Stress–strain relationship

For elastoplastic models, the constitutive equation and generalized yield criteria are outlined in Section 2.2 and 2.4, respectively.

The yield criterion is denoted by $\Phi(\boldsymbol{\sigma}, \zeta) = \phi(\boldsymbol{\sigma}) - q(\zeta) \leq 0$, where the equivalent stress $\phi(\boldsymbol{\sigma})$, a stress-like internal variable $q(\zeta)$ and the equivalent plastic strain ζ. And plastic strain rate $\dot{\boldsymbol{\varepsilon}}^p = \dot{\lambda}\frac{\partial \phi}{\partial \boldsymbol{\sigma}} = \dot{\lambda}\,\boldsymbol{\Lambda}$, where the plastic multiplier $\dot{\lambda} \geq 0$; the time derivative $(\dot{\ })$ and the plastic flow tensor $\boldsymbol{\Lambda} = \partial\phi \,/\, \partial\boldsymbol{\sigma}$ is normal to the yield function $\Phi = 0$.

The constitutive equation in rate form is expressed as $\dot{\boldsymbol{\sigma}} = \mathbf{D}^0 : \dot{\boldsymbol{\varepsilon}}^e = \mathbf{D}^0 : (\dot{\boldsymbol{\varepsilon}} - \dot{\boldsymbol{\varepsilon}}^p) = \mathbf{D}^{ep} : \dot{\boldsymbol{\varepsilon}}$, where second-order stress rate tensor $\dot{\boldsymbol{\sigma}}$ and the fourth-order elasto-plasticity tangent tensor

$$\mathbf{D}^{ep} = \frac{\mathrm{d}\boldsymbol{\sigma}}{\mathrm{d}\boldsymbol{\varepsilon}} = \mathbf{D}^0 - \frac{\mathbf{D}^0 : \boldsymbol{\Lambda} \otimes \mathbf{D}^0 : \boldsymbol{\Lambda}}{H + \boldsymbol{\Lambda} : \mathbf{D}^0 : \boldsymbol{\Lambda}} \tag{2.12}$$

for the hardening or softening modulus $H = \partial q \,/\, \partial\zeta$.

3.1.3 Strain bifurcation (SB) condition

The strain bifurcation condition is usually associated to the stationarity of the stress ($\dot{\boldsymbol{\sigma}} = 0$). Because of the constitutive equation in rate form, the stationary condition implies that the elasto-plasticity tangent tensor $\mathbf{D}^{\mathbf{ep}}(H)$ is singular. That is, the determinant of the tangent tensor has to be zero:

$$\det(\mathbf{D}^{\mathbf{ep}}(H, \boldsymbol{\Lambda})) = 0. \tag{3.3}$$

This is the *loss of uniqueness* condition. Note that $\mathbf{D}^{\mathbf{ep}}$ depends on the softening parameter H and flow tensor $\boldsymbol{\Lambda}$.

Loss of uniqueness is a necessary condition for bifurcation to occur, as it implies the existence of a limit or stationary stress point and two alternative possible solutions obtained by perturbing the stationary situation, one in which all material points continue to load and another in which some point load while some other points unload.

However, the loss of uniqueness condition ($\det(\mathbf{D}^{\mathbf{ep}}(H,\boldsymbol{\Lambda})) = 0$) is not sufficient for bifurcation, because it would be satisfied at an inflection point of the constitutive relation, if such point existed and this would not imply loss of uniqueness.

The necessary condition for (continuous, localized or discrete) failure to emerge is that there are strain rates $\dot{\boldsymbol{\varepsilon}}$, such that $\dot{\boldsymbol{\varepsilon}}:\dot{\boldsymbol{\sigma}} \leq 0$, thus:

$$\dot{\boldsymbol{\varepsilon}}:\mathbf{D}^{\mathbf{ep}}(H,\boldsymbol{\Lambda}):\dot{\boldsymbol{\varepsilon}} \leq 0. \tag{3.4}$$

Note that Eq. (3.3) is obtained by restricting Eq. (3.4) to the equality case for the symmetric elasto-plasticity tangent tensor $\mathbf{D}^{\mathbf{ep}}(H,\boldsymbol{\Lambda})$.

3.1.4 Strain localization (SL) condition

The localization condition detects the formation of a discontinuity $\boldsymbol{S}$ (the slip line or slip surface) along material surfaces defined by a unit normal vector $\boldsymbol{n}$. The localization condition applies to both weak and strong discontinuities depending on the severity of the jumps in the displacement and strain fields.

According to Maxwell's condition (3.2), the strain rate jump can be expressed $[\![\dot{\boldsymbol{\varepsilon}}]\!] = (\dot{\boldsymbol{e}}\otimes\boldsymbol{n})^{\mathrm{sym}}$; from Eq. (3.2). According to Cauchy's stress theorem, the traction rate jump across the discontinuity $\boldsymbol{S}$ can be obtained, $[\![\dot{\boldsymbol{t}}]\!] = 0$. Being $\dot{\boldsymbol{t}} = \boldsymbol{n}\cdot\dot{\boldsymbol{\sigma}}$ be the traction rate and assuming a linear comparison solid, this is shown to imply the singularity of the acoustic tensor in elasto-plasticity $\mathbf{Q}^{\mathbf{ep}}(\boldsymbol{n},H,\boldsymbol{\Lambda}) = \boldsymbol{n}\cdot\mathbf{D}^{\mathbf{ep}}(H,\boldsymbol{\Lambda})\cdot\boldsymbol{n}$, that is,

$$\det(\mathbf{Q}^{\mathbf{ep}}(\boldsymbol{n},H,\boldsymbol{\Lambda})) = 0 \tag{3.5}$$

This is called the *loss of ellipticity condition* and is a necessary condition for a weak discontinuity to appear and localized failure to occur. This is why the loss of ellipticity condition is called the *continuous bifurcation condition*. The case $\det(\mathbf{Q}^{\mathbf{ep}}(\boldsymbol{n},\boldsymbol{\Lambda},H)) \leq 0$ is called the *discontinuous bifurcation condition*. [41–42]

Classically, the problem of determining the onset of discontinuous bifurcation consists in, for a given stress state $\boldsymbol{\sigma}$ and the corresponding flow tensor $\boldsymbol{\Lambda}$, finding the first instant (maximum hardening or softening coefficient H_{cr}) of the loading process and the corresponding direction of the discontinuity $\boldsymbol{n}_{cr}$ was used. The discontinuous bifurcation condition satisfies that $\det(\mathbf{Q}^{\mathbf{ep}}(\boldsymbol{n}_{cr},H_{cr},\boldsymbol{\Lambda})) \leq 0$

However, the loss of ellipticity condition (3.5) is necessary but not sufficient for localization; see references [60–62] for additional details on discontinuous bifurcation analysis.

Let us consider the discontinuous bifurcation scenario where the material is in plastic loading ($\dot{\lambda} \geq 0$) inside the discontinuity band $\boldsymbol{B}$ and in elastic unloading ($\dot{\lambda} = 0$) outside of the band $\boldsymbol{B}$, so that

$$\dot{\boldsymbol{\sigma}}_{\text{ext}} = \mathbf{D}^0 : \dot{\boldsymbol{\varepsilon}}_{\text{ext}} \tag{3.6}$$

$$\dot{\boldsymbol{\sigma}}_{\text{int}} = \mathbf{D}^0 : (\dot{\boldsymbol{\varepsilon}}_{\text{int}} - \dot{\boldsymbol{\varepsilon}}^p) \tag{3.7}$$

where $\dot{\boldsymbol{\sigma}}_{\text{int}}$ is the stress rate inside $\boldsymbol{S}$ and $\dot{\boldsymbol{\sigma}}_{\text{ext}}$ is the stress rate outside $\boldsymbol{S}$

Hence, the jump in the stress rate reads:

$$[\![\dot{\boldsymbol{\sigma}}]\!] = \dot{\boldsymbol{\sigma}}_{\text{int}} - \dot{\boldsymbol{\sigma}}_{\text{ext}} = \mathbf{D}^0 : ([\![\dot{\boldsymbol{\varepsilon}}]\!] - \dot{\boldsymbol{\varepsilon}}^p) = \mathbf{D}^0 : \left((\dot{\boldsymbol{e}} \otimes \boldsymbol{n})^{\text{sym}} - \dot{\lambda}\, \boldsymbol{\Lambda}\right) \tag{3.8}$$

where the Maxwell's compatibility condition (3.2) has been used.

Considering the traction rate jump and Cauchy's stress theorem, $[\![\dot{\boldsymbol{t}}]\!] = \boldsymbol{n} \cdot [\![\dot{\boldsymbol{\sigma}}]\!] = 0$, Eq. (3.8) reads:

$$\boldsymbol{n} \cdot \left[\mathbf{D}^0 : \left[(\dot{\boldsymbol{e}} \otimes \boldsymbol{n})^{\text{sym}} - \dot{\lambda}\, \boldsymbol{\Lambda}\right]\right] = 0 \tag{3.9}$$

Eq. (3.9) is alternative expression for the discontinuous bifurcation condition (3.5).

Using the elastic acoustic tensor $\mathbf{Q}^0 = \boldsymbol{n} \cdot \mathbf{D}^0 \cdot \boldsymbol{n}$, the deformation vector rate can be obtained as

$$\dot{\boldsymbol{e}} = \dot{\lambda}\, (\mathbf{Q}^0)^{-1} (\boldsymbol{\Lambda} : \mathbf{D}^0 \cdot \boldsymbol{n}) \tag{3.10}$$

Stress (rate) boundedness condition

Upon strain bifurcation inside the band, and ongoing deformation, the deformation vector rate in the band, $\dot{\boldsymbol{e}} = \dot{\boldsymbol{w}}/b$, the strain rate jump, $[\![\dot{\boldsymbol{\varepsilon}}]\!]$, and the plastic strain rate in the band, $\dot{\boldsymbol{\varepsilon}}^{\text{p}}_{\text{int}}$, the variables inside of the band will grow much larger than the total strain rate outside the band, $\dot{\boldsymbol{\varepsilon}}_{\text{ext}}$, and the corresponding plastic strain rate, $\dot{\boldsymbol{\varepsilon}}^{\text{p}}_{\text{ext}}$, that may even vanish (on elastic unloading); this ensures boundedness of the stress rate outside the band, $\dot{\boldsymbol{\sigma}}_{\text{ext}}$.

For the sake of simplicity, let us here consider the loading/unloading case; the loading\loading case is considered in Paper #4. Then, Eqs. (3.6), (3.7) and (3.8) may be rewritten, with the terms that will grow upon strain localization, inversely proportional to the bandwidth *b*, underlined.

$$\dot{\boldsymbol{\sigma}}_{\text{ext}} = \mathbf{D}^0 : \dot{\boldsymbol{\varepsilon}}_{\text{ext}}, \qquad \dot{\boldsymbol{\sigma}}_{\text{int}} = \mathbf{D}^0 : \left(\underline{\dot{\boldsymbol{\varepsilon}}_{\text{int}}} - \underline{\dot{\boldsymbol{\varepsilon}}^p}\right) \tag{3.11}$$

$$[\![\dot{\boldsymbol{\sigma}}]\!] = \dot{\boldsymbol{\sigma}}_{\text{int}} - \dot{\boldsymbol{\sigma}}_{\text{ext}} = \mathbf{D}^0 : \left(\underline{[\![\dot{\boldsymbol{\varepsilon}}]\!]} - \underline{\dot{\boldsymbol{\varepsilon}}^p}\right) = \mathbf{D}^0 : \left[\underline{(\dot{\boldsymbol{e}} \otimes \boldsymbol{n})}^{\text{sym}} - \underline{\dot{\lambda}}\, \boldsymbol{\Lambda}\right] \tag{3.12}$$

Inside the localization band, elasto-plastic behavior and satisfaction of the yield criterion ensure that the stress rate remains bounded even if the strain rate is not. Consequently, the jump of the stress rate in Eq. (3.12), but it is bounded; therefore, stress rate boundedness, together with Maxwell's compatibility (3.2), require that

$$(\dot{\boldsymbol{e}} \otimes \boldsymbol{n})^{\text{sym}} = \dot{\lambda}\, \boldsymbol{\Lambda} \tag{3.13}$$

The entire jump of the strain rate is due to the plastic strain rate inside the band. This a necessary condition for strain localization to occur.

Remark 3.1: Regarding the determination of the discontinuity orientation $\boldsymbol{n}$, Eq. (3.13) fully determines $\boldsymbol{n}$. The discontinuity orientations that satisfy the discontinuous bifurcation condition $\det(\mathbf{Q}^{\mathbf{ep}}(\boldsymbol{n}, H, \boldsymbol{\Lambda})) \leq 0$, do not necessarily guarantee stress (rate) boundedness.

Remark 3.2: The discontinuity orientation $\boldsymbol{n}$ in the discontinuous bifurcation condition $\det(\mathbf{Q}^{\mathbf{ep}}(\boldsymbol{n}, H, \boldsymbol{\Lambda})) \leq 0$ is affected by the softening parameter H and plastic flow tensor $\boldsymbol{\Lambda}$. In contrast, the discontinuity orientation $\boldsymbol{n}$ in Eq. (3.13) is only affected by plastic flow tensor $\boldsymbol{\Lambda}$.

Remark 3.3: As can be seen in Eq. (3.13), the discontinuity orientation $\boldsymbol{n}$ depends only on the plastic flow tensor $\boldsymbol{\Lambda}$ and the specific stress state, but does not depend on elastic properties. Application to materials in rigid-plasticity can be implied from this independence. This is not the case with classical conditions related to strain bifurcation.

Remark 3.4: Eq. (3.13) holds for small finite bandwidths b, as in regularized discontinuities and standard FEM simulations. The condition for strong discontinuities follows for the limit case of vanishing bandwidth $b \to 0$.

Remark 3.5: Eq. (3.13) does not necessarily hold on plastic yielding or strain bifurcation. Therefore, a transition stage may be necessary in most situations during which plastic behavior happens without strain localization. Only when the localization condition is fulfilled, might true strain localization happen.

3.1.5 Orientation of the discontinuity

Strain localization plastic flow vector and tensor

In the following, the subscript $(\cdot)_{\text{int}}$ will be omitted for the sake of simplicity, as all quantities refer to points inside the localization band.

From Eq. (3.13), a plastic flow localization vector, $\boldsymbol{\gamma}$, can be defined so that the deformation rate vector $\dot{\boldsymbol{e}}$ and the plastic flow tensor $\boldsymbol{\Lambda}$ are written as

$$\dot{\boldsymbol{e}} = \dot{\lambda}\boldsymbol{\gamma}, \qquad \boldsymbol{\Lambda} = (\boldsymbol{\gamma} \otimes \boldsymbol{n})^{\text{sym}} \tag{3.14}$$

where $\boldsymbol{n}$ is the unit vector normal to the discontinuity $\boldsymbol{S}$. Note that $\boldsymbol{\Lambda}$ is a second order tensor, while $\dot{\boldsymbol{e}}$, $\boldsymbol{\gamma}$ and $\boldsymbol{n}$ are vectors.

Let $\boldsymbol{m}$ and $\boldsymbol{p}$ be unit vectors on the plane of the discontinuity $\boldsymbol{S}$ such that $(\boldsymbol{n}, \boldsymbol{m}, \boldsymbol{p})$ is a basis of orthonormal vectors. Then, the plastic flow localization vector, $\boldsymbol{\gamma}$, can be equivalently defined so that

$$\boldsymbol{\gamma} = 2\boldsymbol{n} \cdot \boldsymbol{\Lambda} - \Lambda_{nn}\boldsymbol{n} = \gamma_n \boldsymbol{n} + \gamma_m \boldsymbol{m} + \gamma_p \boldsymbol{p} \tag{3.15}$$

The components of the plastic flow localization vector $\boldsymbol{\gamma} = (\gamma_n, \gamma_m, \gamma_p)$ are determined

so that

$$\gamma_n = \boldsymbol{\gamma} \cdot \boldsymbol{n} = \Lambda_{nn}, \gamma_m = \boldsymbol{\gamma} \cdot \boldsymbol{m} = 2\Lambda_{nm}, \gamma_p = \boldsymbol{\gamma} \cdot \boldsymbol{p} = 2\Lambda_{np} \tag{3.16}$$

$$\boldsymbol{\gamma} = \Lambda_{nn}\boldsymbol{n} + 2\Lambda_{nm}\boldsymbol{m} + 2\Lambda_{np}\boldsymbol{p} \tag{3.17}$$

Accordingly, the other components of the strain localization plastic flow tensor are zero:

$$\Lambda_{mm} = 0, \quad \Lambda_{pp} = 0, \quad \Lambda_{mp} = 0 \tag{3.18}$$

From these equations the orientation of the slip surface may be derived.

Orientation of strain localization

The orientation of the slip lines is analytically obtained for orthotropic and pressure-dependent plastic solids subjected to plane strain and plane stress conditions. The strain localization angle is measured counter-clockwise $\theta_{\text{cr}} \in [-\frac{\pi}{2}, \frac{\pi}{2}]$ as the angle between the vector $\boldsymbol{n}$ normal to the discontinuity and the material axis 1; see Figure 3.4.

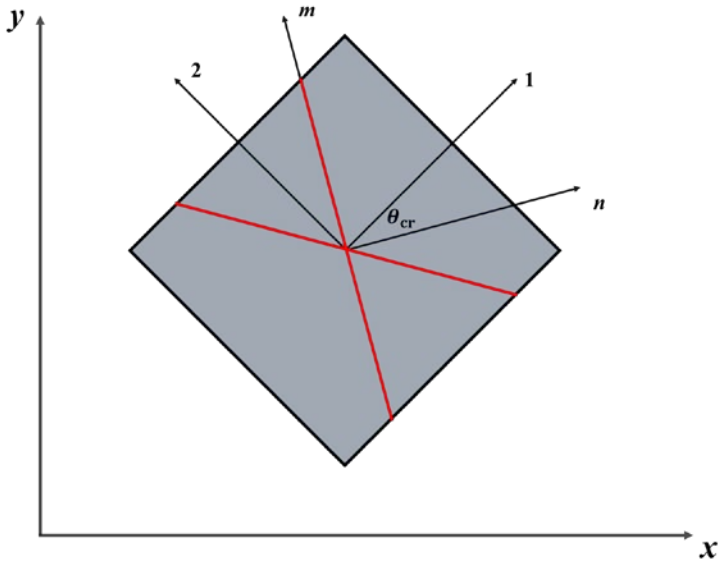

Figure 3.4 Definition of the localization angle θ_{cr}.

Let $(\boldsymbol{n}, \boldsymbol{m}, \boldsymbol{p})$ be the basis formed by the orthonormal vectors normal and tangential to the discontinuity $\boldsymbol{S}$, such that vectors $\boldsymbol{n}$ and $\boldsymbol{m}$ are respectively normal and tangential to the trace of $\boldsymbol{S}$ in the reference plane *xy* and vector $\boldsymbol{p}$ points in the out-of-plane *z* direction, as shown in Figure 3.4.

The strain localization Eq. (3.19) requires the flow tensor the plastic flow tensor $\boldsymbol{\Lambda} = \partial\phi / \partial\boldsymbol{\sigma}$ to be expressed in this system. Let θ^{cr} be the angle between the material system (1, 2, 3) and the $(\boldsymbol{n}, \boldsymbol{m}, \boldsymbol{p})$ system. Then

$$\Lambda_{mm} = \Lambda_{11} \sin^2 \theta^{\text{cr}} + \Lambda_{22} \cos^2 \theta^{\text{cr}} + 2\Lambda_{12} \sin \theta^{\text{cr}} \cos \theta^{\text{cr}} \tag{3.19}$$

$$\Lambda_{pp} = \Lambda_{33} \tag{3.20}$$

$$\Lambda_{mp} = 0 \tag{3.21}$$

The strain localization angle θ^{cr} is obtained from the kinematic constraints in Eq. (3.19), that is, equating these components to zero. Solving $\Lambda_{mm}(\theta^{\text{cr}}) = 0$ for $\tan \theta^{\text{cr}}$:

$$\tan \theta^{\text{cr}} = -\frac{\Lambda_{12}}{\Lambda_{11}} \pm \sqrt{\left(\frac{\Lambda_{12}}{\Lambda_{11}}\right)^2 - \frac{\Lambda_{22}}{\Lambda_{11}}} \tag{3.22}$$

As can be seen, the strain localization angle θ^{cr} depends on the stress state upon strain localization. The condition $\Lambda_{pp}(\theta^{cr}) = \Lambda_{33} = 0$ Eqs. (3.20) – (3.22) needs to be imposed in plane stress and plane strain conditions.

Remark 3.6: For the case of $\Lambda_{12} = 0$, where the no shear stress acts on the material axes, Eq. (3.23) simplifies to

$$\tan\theta^{\mathrm{cr}} = \pm\sqrt{-\frac{\Lambda_{22}}{\Lambda_{11}}} \tag{3.23}$$

Remark 3.7: The angle of the slip lines (counter-clockwise from 1-axis) is $\theta^{slip} = \frac{\pi}{2} - \theta^{cr}$:

$$\tan\theta^{\mathrm{slip}} = (\tan\theta^{\mathrm{cr}})^{-1} \tag{3.24}$$

Remark 3.8: The above expressions are obtained for the stress expressed in the material system. These are obtained from the stresses in the global (x,y,z) system by standard transformation. For instance, in plane strain conditions

$$\begin{bmatrix}\sigma_{11}\\ \sigma_{22}\\ \sigma_{33}\\ \sigma_{12}\end{bmatrix} = \begin{bmatrix}\cos^2\alpha & \sin^2\alpha & 0 & -2\cos\alpha\sin\alpha\\ \sin^2\alpha & \cos^2\alpha & 0 & 2\cos\alpha\sin\alpha\\ 0 & 0 & 1 & 0\\ \cos\alpha\sin\alpha & -\cos\alpha\sin\alpha & 0 & \cos^2\alpha-\sin^2\alpha\end{bmatrix}\begin{bmatrix}\sigma_{xx}\\ \sigma_{yy}\\ \sigma_{zz}\\ \sigma_{xy}\end{bmatrix} \tag{3.25}$$

where α is the tilt angle between the global axis x and the material local axis 1 measured counter-clockwise.

3.2 Strain localization analysis of Hill's orthotropic elastoplasticity: Analytical results and numerical verification

Article Data:

Title: **Strain localization analysis of Hill's orthotropic elastoplasticity: Analytical results and numerical verification.**

Authors: M. Cervera, J.Y. Wu, M. Chiumenti and S. Kim

Journal : Computational Mechanics, 65, 533–554 (2020)

https://doi.org/10.1007/s00466-019-01782-4

Scientific Contribution:

In this paper, the strain localization analysis of Hill's orthotropic plasticity is addressed. In particular, the localization condition derived from the boundedness of stress rates together with Maxwell's kinematics is employed. Similarly to isotropic plasticity considered in our previous work, the plastic flow components on the discontinuity surface vanish upon strain localization. Compared to the classical work based on the discontinuous bifurcation analysis, the resulting localization angles in orthotropic plastic materials are independent from the elastic constants, but rather, they depend exclusively on the material parameters involved in the plastic flow in the material axes. This turns out to be coincident with Hill's results for strictly incompressible rigid-plastic problems, extending them to general elasto-plastic materials.

Application of the above localization condition to Hill's orthotropic plasticity in 2-D plane stress and plane strain conditions yields closed-form solutions of the localization angles. It is found that the two discontinuity lines in plane strain conditions are always perpendicular to each other, and for the states of no shear stresses, the localization angle depends only on the tilt angle of the material axes with respect to the global ones.

The analytical results are then validated by independent numerical simulations. Being the plastic flow purely isochoric, the B-bar finite element is employed to deal with the incompressibility of plastic flow.

For a strip regarding a horizontal slit under vertical stretching in plane stress and plane strain as well as Prandtl's problem of indentation by a flat rigid die in plane strain, numerical results are presented for both isotropic and orthotropic plasticity models with or without tilt angle. The influence of various parameters is studied. In all cases, the critical angles predicted from the localization condition coincide with the numerical results, giving compelling supports to the analytical prognosis.

Interestingly, as for Prandtl's punch test in plane strain the material right under the rigid footing is almost free of shear stresses, the localization angles are also independent from the stress state and can be determined as those for a slit under vertical stretching.

3.3 Hill's orthotropic elasto-plasticity: dependence of the strain localization angles on the degree of orthotropy

In this section, a complementary analytical study on the dependence of the strain localization angles on the degree of orthotropy for Hill's orthotropic elasto-plasticity is presented.

The von Mises and Hill yield criteria are used; for the sake of clearness, no tilt between the material and the global axes is considered. Both plane strain and plane stress conditions are contemplated. For purely cohesive models, tensile and compression tests lead to identical results; thus, only vertical uniaxial tensile loading is studied, along material direction 2. All material strengths are scaled to 1. The degree of orthotropy is studied in terms of ratio $\alpha = f_1/f_2$. The von Mises criterion corresponds to α = 1.0.

Cross sections of the von Mises and Hill yield criteria for strength ratio α = 1.25 and α = 0.8 under plane stress and plane stress are shown in Figures 3.5 and 3.6, respectively. From these, the strain localization angles can be measured in a counter–clockwise manner from the 1–axis. See the geometrical interpretation of the strain localization angle in the Section 3.4 of Paper #3.

For plane strain, Figure 3.5 depicts both yield criteria as parallel straight lines; strain localization angles ensue at 45°.

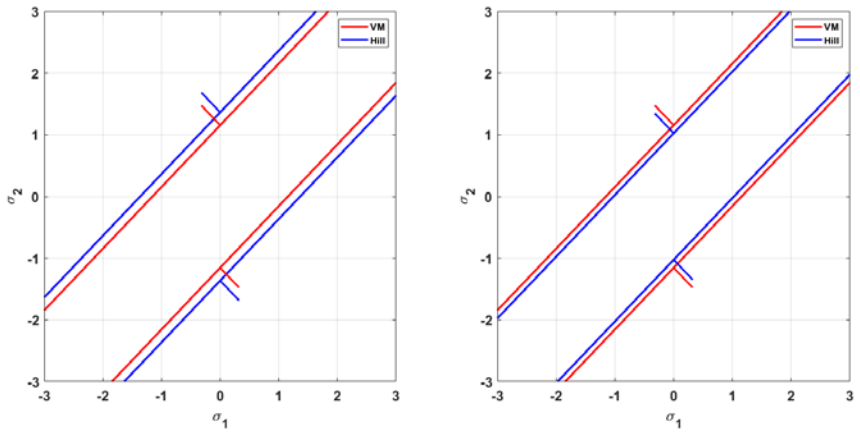

(a) **(b)**

Figure 3.5 Cross sections of the von Mises and Hill yield criteria under plane strain:

(a) $\alpha = 1.25$ for the Hill yield criterion and (b) $\alpha = 0.8$ for the Hill yield criterion

For plane stress, Figure 3.6 depicts both yield criteria as ellipses; different strain localization angles follow depending on the strength ratio α. This dependence may be analytically deduced, as follows.

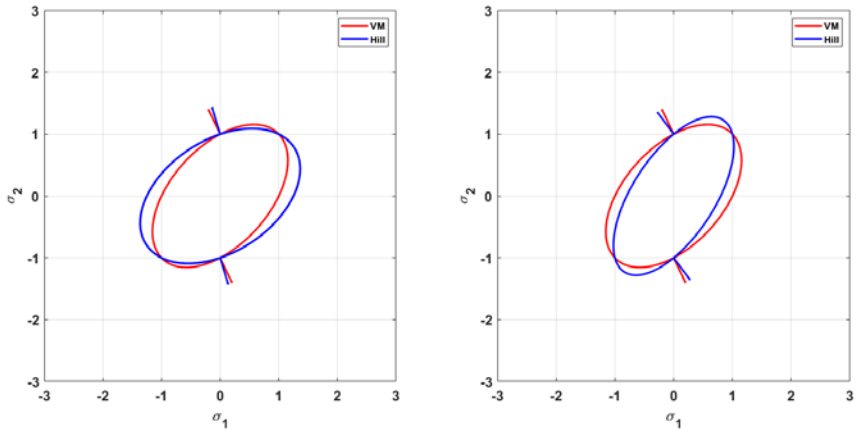

(a) **(b)**

Figure 3.6 Cross sections of the von Mises and Hill yield criteria under plane stress: (a) $\alpha = 1.25$ for the Hill yield criterion and (b) $\alpha = 0.8$ for the Hill yield criterion

From Eq. (48) of Paper #3, the stress state for uniaxial tension under plane stress is

$$\sigma_{11} = 0, \qquad \sigma_{22} = \sigma > 0, \qquad \sigma_{12} = 0, \qquad \sigma_{33} = 0 \tag{3.26}$$

From Eq. (49) of Paper #3, strain localization angles under plane stress are obtained as

$$\tan\theta^{\text{slip}} = (\tan\theta^{\text{cr}})^{-1} = \pm\sqrt{-\frac{\Lambda_{11}}{\Lambda_{22}}} = \pm\sqrt{\frac{2F\sigma_{22} - I}{2(F+H)\sigma_{22} + J}} \tag{3.27}$$

where *F*, *H*, *I* and *J* are the matrix coefficient in Eq. (2.20).

Let be the strength ratio $\alpha = f_1/f_2$ and $f_3 = f_2$ =1 for the Hill yield criterion. Then, $F = \frac{1}{2\alpha^2}$, $G = \frac{1}{2\alpha^2}$, $H = 1 - \frac{1}{2\alpha^2}$, $I = J = 0$ are obtained from Eqs. (2.21) – (2.24) and (2.28).

Then:

$$\tan\theta^{\text{slip}} = \pm\sqrt{\frac{F}{F+H}} = \pm\sqrt{\frac{1}{2\alpha^2}} = \pm\frac{1}{\sqrt{2}\alpha} \tag{3.28}$$

It is observed that, for plane stress, the tangent value of strain localization angles and the strength ratio α are inversely proportional .This is shown in Figures 3.7.

Figure 3.8 shows the strain localization angle versus the strength ratio α both for plane strain and plane stress.

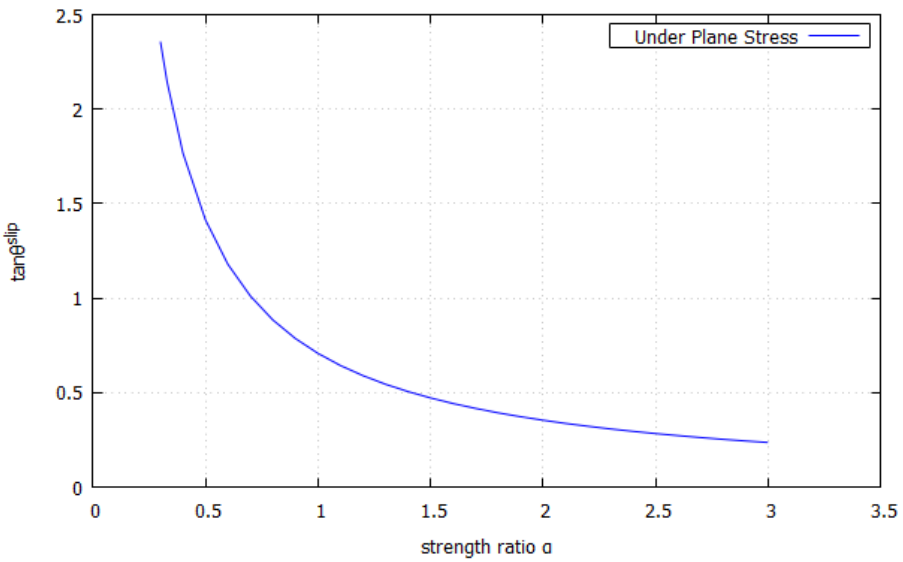

Figure 3.7 Curve of tangent of strain localization angle – strength ratio α under plane stress

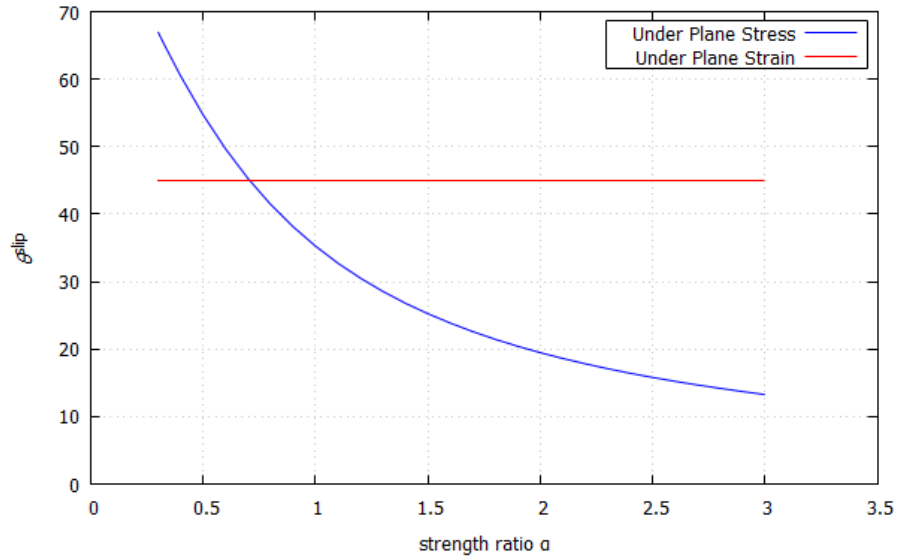

Figure 3.8 Curves of strain localization angle – strength ratio α

3.4 Strain Localization of Orthotropic Elasto-Plastic Cohesive-Frictional Materials: Analytical Results and Numerical Verification

Article Data:

Title: **Strain Localization of Orthotropic Elasto-Plastic Cohesive-Frictional Materials: Analytical Results and Numerical Verification.**

Authors: S. Kim, M. Cervera, J.Y. Wu and M. Chiumenti

Journal : Materials, 14 (8), 2040 (2021)

https://doi.org/10.3390/ma14082040

Scientific Contribution:

In this paper, strain localization analysis for orthotropic-associated plasticity in cohesive-frictional materials is addressed. Specifically, the necessary localization condition is derived from Maxwell's kinematics, the plastic flow rule and the boundedness of stress rates. The analysis is applicable to strong and regularized discontinuity settings.

Contrariwise to the usually studied conditions for strain bifurcation, these proffer requirements that do not depend on the elastic properties of the medium, but only on the plastic flow provided by the adopted plastic potential. Expanding on previous works, the quadratic orthotropic Hoffman and Tsai–Wu models are investigated and compared to pressure insensitive and sensitive models such as von Mises, Hill and Drucker–Prager.

Application of the above localization conditions to isotropic and orthotropic cohesive-frictional plastic models derives analytical solutions for the strain localization angle and the slopes of the ensuing slip lines. The distinct effects of compressive and tensile loading are also evaluated.

Analytical localization angles are obtained in uniaxial tension and compression under plane stress and plane strain conditions. These are only dependent on the plastic potential adopted; ensuing, a geometrical interpretation in the stress space is offered.

The analytical results are then validated by independent numerical simulations. The B-bar finite element is used to deal with the limiting incompressibility in the purely isochoric plastic flow. For a strip under vertical stretching in plane stress and plane strain and Prandtl's problem of indentation by a flat rigid die in plane strain, numerical results are presented for both isotropic and orthotropic plasticity models with or without tilting angle between the material axes and the applied loading. In the first problem, the far field stress state is known, and the analytical results can be verified directly from the numerical simulations. In the second problem, once the failure mechanism and the corresponding stress field are computationally evaluated, these are shown to conform precisely with those anticipated by the strain localization condition.

The influence of frictional behavior is studied. In all the investigated cases, the numerical results provide compelling support to the analytical prognosis.

3.5 Cohesive-frictional models: dependence of the localization angles on the degree of friction

In this section, a complementarily analytical study on the dependence of the strain localization angles on the degree of friction for cohesive-frictional elasto-plasticity is presented.

The Drucker–Prager, Hoffman and Tsai–Wu yield criteria are used; for the sake of clearness, no tilt between the material and the global axes is considered. Both plane strain and plane stress conditions are contemplated. For cohesive-frictional models, behavior under compression and tension is different; thus, both vertical uniaxial tensile and compressive loadings are studied, along material direction 2. All material strengths are scaled to 1. The degree of friction is studied in terms of ratio $\kappa = f_1^c / f_1^t$. The von Mises criterion corresponds to $\kappa = 1.0$.

Cross sections of Drucker–Prager, Hoffman and Tsai–Wu yield criteria with $\kappa = 1.25$ and 0.8 under plane strain and plane stress are shown in Figures 3.9 and 3.10, respectively. From these, strain localization angles can be measured in a counter–clockwise manner from the 1–axis. See the geometrical interpretation of the strain localization angle in the Section 3.4 of Paper #3.

For plane strain, Figure 3.9 depicts all the yield criteria as parabolas. The friction ratio κ determines the location of the vertex of the parabola, different for $\kappa > 1$ and $0 < \kappa < 1$. The cross sections of the yield criteria are parallel lines. When friction ratio $\kappa = 1$, as for the von Mises and Hill yield criteria.

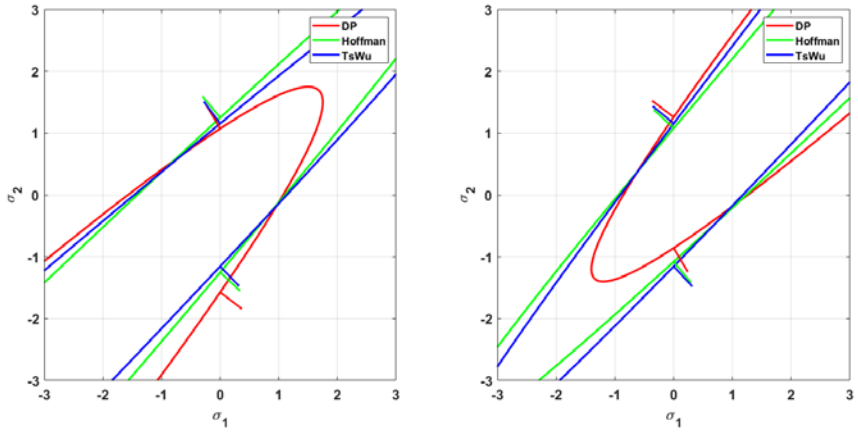

(a) **(b)**

Figure 3.9 Cross sections of the Drucker–Prager, Hoffman and Tsai–Wu yield criteria under plane strain: (a) $\kappa = 1.25$ and (b) $\kappa = 0.8$

For plane stress, Figure 3.10 depicts yield criteria as ellipses; material strengths define the intersections with the 1–axis and 2–axis.

For both plane strain and plane stress, different strain localization angles follow depending on the friction ratio κ. This dependence may be analytically deduced, as follows.

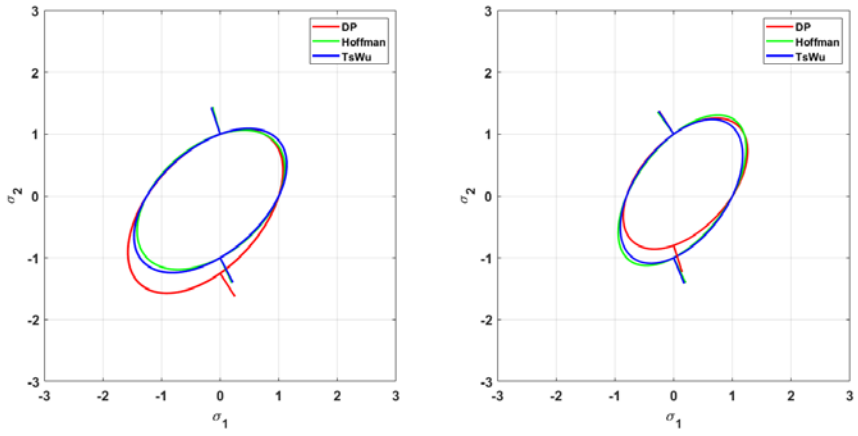

(a) **(b)**

Figure 3.10 Cross sections of the Drucker–Prager, Hoffman and Tsai–Wu yield criteria under plane stress: (a) $\kappa = 1.25$ and (b) $\kappa = 0.8$

From Eq. (48) of Paper #3, the stress state for uniaxial tension under plane stress is

$$\sigma_{11} = 0, \qquad \sigma_{22} = \sigma > 0, \qquad \sigma_{12} = 0, \qquad \sigma_{33} = 0 \tag{3.26}$$

From Eq. (49) of Paper #3, strain localization angles under plane stress are obtained as

$$\tan\theta^{\text{slip}} = (\tan\theta^{\text{cr}})^{-1} = \pm\sqrt{-\frac{\Lambda_{11}}{\Lambda_{22}}} = \pm\sqrt{\frac{2F\sigma_{22} - I}{2(F+H)\sigma_{22} + J}} \tag{3.27}$$

where F, H, I and J are the matrix coefficient in Eq. (2.20).

Let be the friction ratio $\kappa = f_1^c/f_1^t$, $f_1^c = f_2^c = f_3^c = \kappa$ and $f_1^t = f_2^t = f_3^t = 1$ for the Drucker–Prager yield criterion. Then, $F = H = \frac{1}{2\kappa}$ and $I = J = 1 - \frac{1}{\kappa}$ are obtained by Eqs. (2.21) – (2.24) and (2.27).

Then,

$$\tan\theta^{\text{slip}} = \pm\sqrt{\frac{2F\sigma_{22} - I}{2(F+H)\sigma_{22} + J}} \pm \sqrt{\frac{2F\sigma - I}{4F\sigma + I}} = \pm\sqrt{\frac{2-\kappa}{\kappa+1}} \tag{3.29}$$

Additionally, let us consider the case with a reciprocal friction ratio $\frac{1}{\kappa}$ under uniaxial compression. Then, $f_1^t = f_2^t = f_3^t = \kappa$, $f_1^c = f_2^c = f_3^c = 1$, $\sigma_{22} = -\sigma$, $F = H = \frac{1}{2\kappa}$ and $I = J = \frac{1}{\kappa} - 1$. As a result, $\tan\theta^{\text{slip}} = \pm\sqrt{\frac{2F\sigma - I}{4F\sigma + I}} = \pm\sqrt{\frac{2-\kappa}{\kappa+1}}$ in uniaxial compression is the same as that in Eq. (3.29).

It is observed that, for plane stress, the strain localization angle of the Drucker–Prager yield criterion for the friction ratio κ in compressive loading is identical to that for $\frac{1}{\kappa}$ in the tensile loading. The strain localization angles under plane strain can be similarly obtained.

Figure 3.11 shows the strain localization angle versus the friction ratio κ under plane strain in both tensile and compressive loading. A negative correlation is found in tension and a positive correlation is found in compression between the strain localization angles and the friction ratio κ. It is also observed that difference of the three criteria to friction is quite different.

Figure 3.12 shows the strain localization angle versus the friction ratio κ under plane stress in both tensile and compressive loading. Again, a negative correlation is found in tension and a positive correlation is found in compression.

Note that Hoffman's criterion is insensitive to friction in compression.

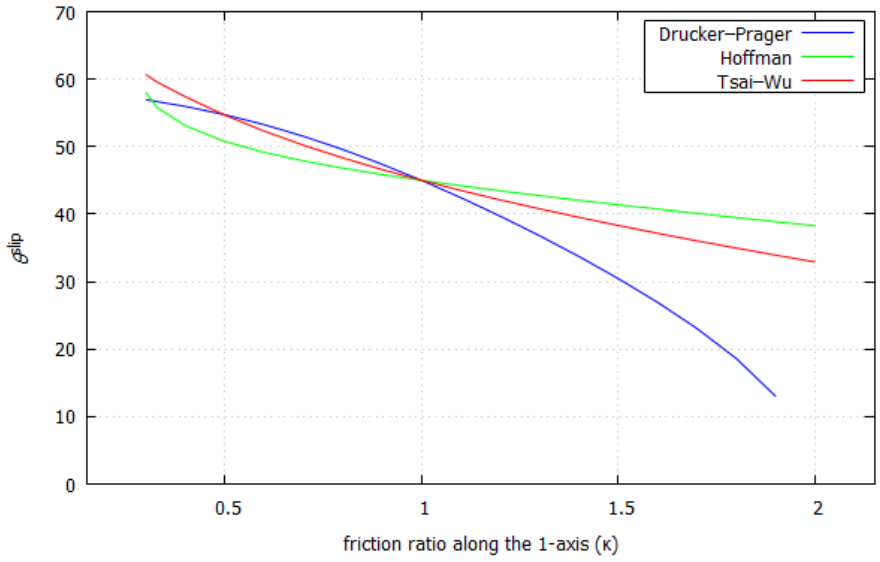

(a)

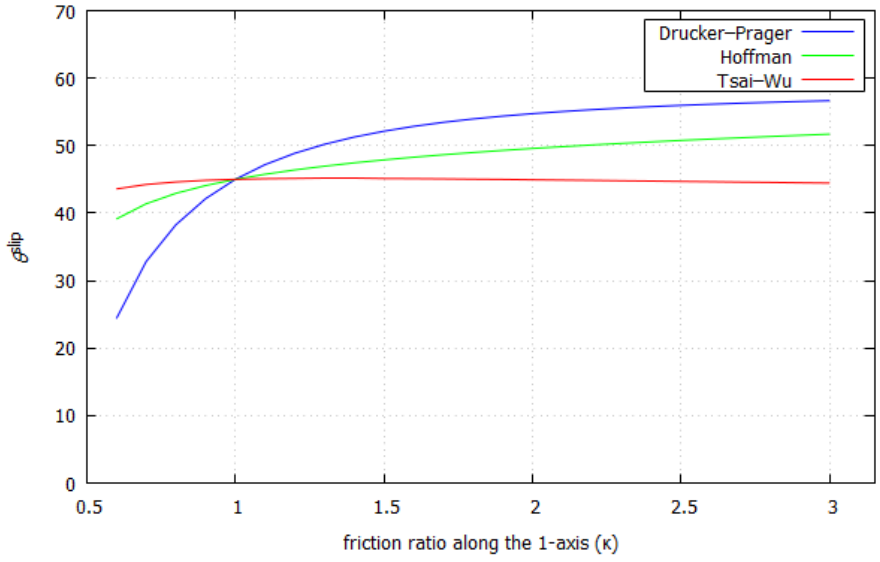

(b)

Figure 3.11 Curves of strain localization angle – friction ratio κ under plane strain: (a) Tension and (b) Compression

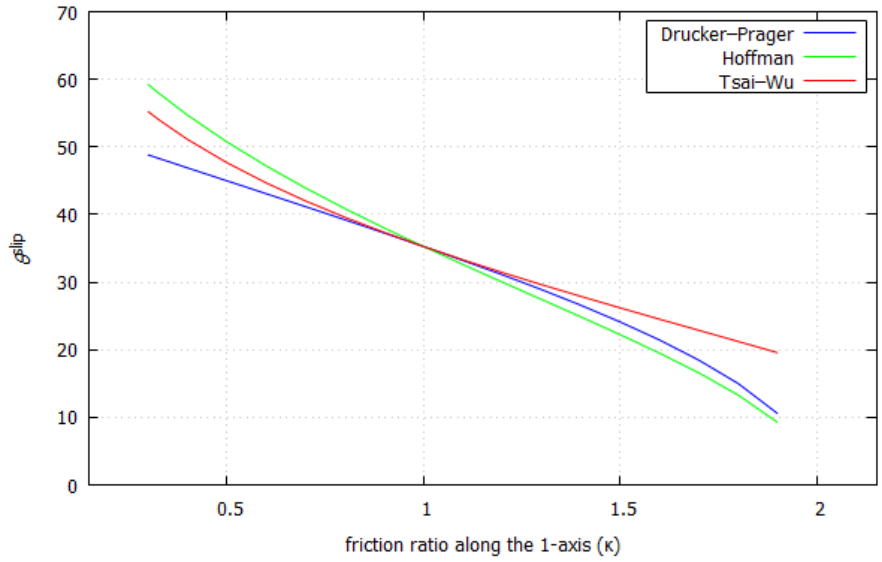

(a)

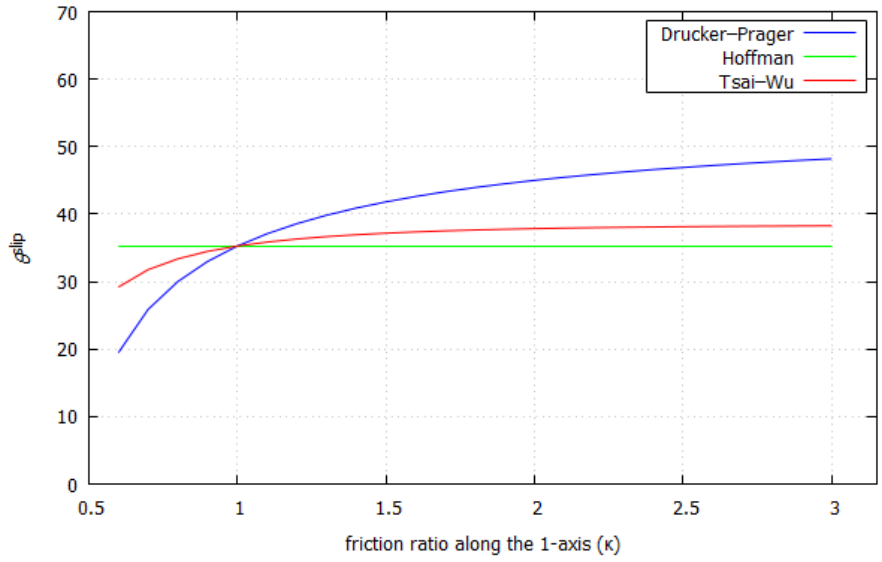

(b)

Figure 3.12 Curves of strain localization angle – friction ratio κ under plane stress: (a) Tension and (b) Compression

3.6 On the mechanics of strain localization in plasticity: Isotropic and orthotropic, elasto- and rigid-plastic, associated and non-associated models

Article Data:

Title: **On the mechanics of strain localization in plasticity: Isotropic and orthotropic, elasto- and rigid-plastic, associated and non-associated models.**

Authors: M. Cervera, J.Y. Wu, S. Kim and M. Chiumenti

Journal : International Journal of Solids and Structures (Under review)

Scientific Contribution:

As strain localization is usually prognostics of localized failure in solids and structures, prediction of its occurrence and quantification its adverse effects are of both theoretical and practical significance. Regarding plastic solids, onset of strain localization was presumed to be coincident with strain bifurcation, and the discontinuous bifurcation analysis was usually adopted to determine the discontinuity orientation though it does not apply to rigid-plastic solids.

However, recent studies indicate that strain bifurcation and localization correspond to distinct stages of localized failure and should be dealt with separately. In this paper, the mechanics of strain localization is addressed for perfect and softening plasticity in the most general context. Both isotropic and orthotropic, elasto- and rigid-plastic solids with associated and non-associated flow rules are analytically considered and numerically validated, extending our previous work on softening plasticity with associated evolution laws. In addition to Maxwell's kinematics and continuity of the traction rate for strain bifurcation, a novel necessary condition, i.e., the stress rate objectivity (independent from the discontinuity bandwidth), and the resulting kinematic and static constraints, are derived for the occurrence of strain localization. In particular, the localization angles of the discontinuity band (surface) depend only on the specific stress state and the plastic flow tensor, relevant neither to the material elastic constants nor to the plastic yield function.

Moreover, it is found that a transition stage generally exists in the case of plane strain during which the orientation of plastic flow rotates progressively such that strain localization may occur. Back-to-back numerical predictions of some benchmark problems, involving both perfect and softening plasticity, sufficiently justify the analytical results.

Consequently, strain localization is more demanding than the classical continuous/discontinuous strain bifurcation, though both accounts for the plastic loading/unloading and loading/loading scenarios. For the plane strain condition, there generally exists a transition stage between plastic yielding/strain bifurcation and strain localization. Moreover, regarding the stress (rate) within the discontinuity band, the boundedness condition and the continuity condition, both assuming plastic loading/unloading with associated evolution laws in strain softening solids, are recovered as particular cases of strong discontinuities with a vanishing bandwidth and of regularized ones with a finite bandwidth, respectively.

The concept of "slip-line" or "zero rate of extension" is also incorporated for rigid-plastic solids and soils). The kinematic and static constraints upon strain localization were then derived analytically. In particular, the localization angles of the discontinuity band (surface) depend only

on the specific stress state and the plastic flow tensor, relevant neither to the elastic material constants nor to the plastic yield function. During the transition stage the orientation of the discontinuity band (surface) rotates progressively to the localization angle. For the plane strain condition, the yield function affects evolution process upon which the out-of-plane stress for strain localization is achieved and consequently the transition stage, but not the localization angle.

The above strain localization condition and analytical results for the localization angle are validated numerically by several benchmark examples. The stabilized mixed finite element formulation is adopted to deal with the quasi-incompressible deformations resulting from the von Mises and Hill potential functions. It is found that for perfectly and softening plastic solids with either associated or non-associated evolution laws, upon strain localization and thereafter the stresses inside the discontinuity band are indeed independent of the bandwidth, validating the postulated assumption.

Moreover, similarly to our previous work on plastic or damaging solids, the numerically predicted localization angles are coincident with those given by the analytical results, further justifying the proposed strain localization condition. As it applies to isotropic and orthotropic rigid-/elasto-plastic solids with associated or non-associated flow rules, the proposed strain localization condition can be used to determine the discontinuity orientation in the numerical modeling of localized failure in solids.

Chapter 4

Irreducible and Mixed Finite Element formulations

In this chapter, several irreducible and mixed finite element formulations are compared with regard to their performance concerning strain approximation in:

- accurate and locking-free analysis of beams, plates and shells using solid elements, and
- strain localization stemming from plastic flow concentrating in narrow bands.

The outline of the Chapter is as follows. Section 4.1 presents the various finite element formulations used in this Thesis. Section 4.2 summarizes a published paper on the accuracy of mixed strain/displacement finite elements on the analysis of beams, plates and shells. Section 4.3 presents some results regarding strain localization in incompressible and frictional plastic flow.

4.1 Irreducible and Mixed Finite Elements

This section summarizes the formulation of 5 irreducible and mixed finite element formulations:

- Irreducible $\boldsymbol{u}$ finite elements
- B-bar finite elements
- Mixed $\boldsymbol{u}/p$ finite elements
- Mixed $\boldsymbol{\varepsilon}/\boldsymbol{u}$ finite elements
- Mixed $\boldsymbol{\varepsilon}$/B-bar $\boldsymbol{u}$ finite elements

For each of formulation the continuous strong and variational forms and the corresponding discrete finite element form are discussed.

4.1.1 Irreducible $\boldsymbol{u}$ finite elements

Irreducible strong form

In standard FE formulations, the strong form of the nonlinear solid mechanics problem is written in terms of the displacement $\boldsymbol{u}$ field.

In 3D analysis, following Voigt's notation, $\boldsymbol{u}$ is a vector of 3 components. The displacements $\boldsymbol{u} = (u, v, w)^T$ can be linked to the total strain $\boldsymbol{\varepsilon} = \left(\varepsilon_x, \varepsilon_y, \varepsilon_z, \varepsilon_{xy}, \varepsilon_{yz}, \varepsilon_{xz}\right)^T$ through the compatibility equation

$$\boldsymbol{\varepsilon} = \mathbf{S}\boldsymbol{u} \tag{4.1}$$

where **S** is the differential symmetric gradient operator, defined as

$$\mathbf{S} = \begin{bmatrix} \partial_x & 0 & 0 & \partial_y & 0 & \partial_z \\ 0 & \partial_y & 0 & \partial_x & \partial_z & 0 \\ 0 & 0 & \partial_z & 0 & \partial_y & \partial_x \end{bmatrix}^T \tag{4.2}$$

And the stress vector $\boldsymbol{\sigma} = \left(\sigma_x, \sigma_y, \sigma_z, \tau_{xy}, \tau_{yz}, \tau_{xz}\right)^T$ can be related to the body forces $\mathbf{f} = \left(f_x, f_y, f_z\right)^T$ through Cauchy's equilibrium equation

$$\mathbf{S}^T\boldsymbol{\sigma} + \mathbf{f} = \mathbf{0} \tag{4.3}$$

where $\mathbf{S}^T$ is the differential divergence operator, adjoint to the **S** in (4.1).

The stress vector $\boldsymbol{\sigma}$ and the strain vector $\boldsymbol{\varepsilon}$ are connected by the constitutive equation:

$$\boldsymbol{\sigma} = \mathbf{D}_s\boldsymbol{\varepsilon} \tag{4.4}$$

where $\mathbf{D}_s$ is the secant constitutive matrix.

Substituting Eq. (4.1) and (4.4) into Eq. (4.3) yields Navier's equation, in terms of the displacement field $\boldsymbol{u}$ only:

$$\mathbf{S}^T\mathbf{D}_s\,\mathbf{S}\,\boldsymbol{u} + \mathbf{f} = \mathbf{0} \tag{4.5}$$

To be solved with the appropriate Dirichlet's and Newman's boundary conditions, where the boundary of the domain Γ comprises the union of the Dirichlet's boundary Γ_u and the Newman's boundary Γ_t, such that $\Gamma = \Gamma_u \cup \Gamma_t$ and $\{\emptyset\} = \Gamma_u \cap \Gamma_t$.

Irreducible variational form

The variational form of the problem is then obtained as follows. Firstly, Eq. (4.5) is pre-multiplied by an arbitrary virtual displacement $\delta\boldsymbol{u}$ and integrated over the spatial domain:

$$\int_\Omega \delta\boldsymbol{u}^T[\mathbf{S}^T\mathbf{D}_s\mathbf{S}\,\boldsymbol{u}]\,\mathrm{d}\Omega + \int_\Omega \delta\boldsymbol{u}^T\mathbf{f}\,\mathrm{d}\Omega = 0 \quad \forall\delta\boldsymbol{u} \tag{4.6}$$

The virtual displacement $\delta\boldsymbol{u}$ conforms with the boundary conditions, so that $\delta\boldsymbol{u} = \mathbf{0}$ in Γ_u.

Then, the Divergence Theorem is considered in the first term of Eq. (4.6), so that

$$\int_{\Omega} (\boldsymbol{S}\delta\boldsymbol{u})^{\mathrm{T}}(\mathbf{D}_s\mathbf{S}\,\boldsymbol{u})\mathrm{d}\Omega = \int_{\Omega} \delta\boldsymbol{u}^{\mathrm{T}}\mathbf{f}\mathrm{d}\Omega + \int_{\Gamma_t} \delta\boldsymbol{u}^{\mathrm{T}}\bar{\boldsymbol{t}}\mathrm{d}\Gamma \quad \forall\delta\boldsymbol{u} \tag{4.7}$$

FE approximation

Then, as usual, the FE discrete problem is derived by discretizing the spatial domain in FE, such that $\Omega = \cup\, \Omega_e$, and by taking discrete FE approximations of the displacements $\boldsymbol{u}$

$$\boldsymbol{u} \cong \widehat{\boldsymbol{u}} = \boldsymbol{N}_u\boldsymbol{U} \tag{4.8}$$

where $\boldsymbol{U}$ is a vectors comprising the values of the displacements at the nodes of the finite element mesh. $\boldsymbol{N}_u$ are the matrices containing the interpolation functions adopted in the FE approximation.

In the Galerkin method, the same approximation is taken for the discrete virtual displacements so that

$$\delta\boldsymbol{u} \cong \delta\widehat{\boldsymbol{u}} = \boldsymbol{N}_u\delta\boldsymbol{U} \tag{4.9}$$

The submatrices of $\boldsymbol{N}_u$ are diagonal matrices and the corresponding components are $N_u^{(i)}$ $i$nterpolation functions, (i) being the node counter.

Introducing these approximations, Eq. (4.7) becomes:

$$\int_{\Omega} \delta\boldsymbol{U}^T\boldsymbol{B}_u^T\,(\mathbf{D}_s\boldsymbol{B}_u\,\boldsymbol{U})\,\mathrm{d}\Omega = \widehat{W}(\delta\boldsymbol{U}) \quad \forall\delta\boldsymbol{U} \tag{4.10}$$

where $\boldsymbol{B}_u$ is the discrete strain-displacement matrix defined as

$$\boldsymbol{B}_u = \boldsymbol{S}\boldsymbol{N}_u \tag{4.11}$$

The submatrices of $\boldsymbol{B}_u$ have the structure corresponding to the **S** operator in Eq. (4.2), and their components are the Cartesian derivatives of the $N_u^{(i)}$ interpolation functions $\left(\frac{\partial N^{(i)}}{\partial x}; \frac{\partial N^{(i)}}{\partial y}; \frac{\partial N^{(i)}}{\partial z}\right)$, (i) being the node counter.

In Eq. (4.10), $\widehat{W}(\delta\boldsymbol{U})$ is the work done by the tractions $\bar{\boldsymbol{t}}$ and body forces **f** defined as

$$\widehat{W}(\delta\boldsymbol{U}) = \int_{\Omega} \delta\boldsymbol{U}^T\boldsymbol{N}_u^T\mathbf{f}\,\mathrm{d}\Omega + \int_{\Gamma_t} \delta\boldsymbol{U}^T\boldsymbol{N}_u^T\bar{\boldsymbol{t}}\,\mathrm{d}\Gamma \tag{4.12}$$

In (4.10) and henceforth, integrals over the domain are understood as the sum of the integrals over the elements in the FE mesh

$$\int_{\Omega} (\cdot)\,d\Omega = \sum_e \int_{\Omega_e} (\cdot)\,\mathrm{d}\Omega_e \tag{4.13}$$

Also, with some abuse of notation, $\boldsymbol{U}$ (and $\delta\boldsymbol{U}$) are to be considered as the nodal values over the whole FE mesh. This implies the corresponding assembling operations for elemental matrices and vectors into global entities.

The virtual displacement $\delta\boldsymbol{U}$ are arbitrary nodal vectors that appear in the system of equations (4.10). Therefore, the system of equations for the Galerkin method becomes

$$\boldsymbol{K}\boldsymbol{U} = \boldsymbol{F} \tag{4.14}$$

with

$$\boldsymbol{K} = \int_{\Omega} \boldsymbol{B}_u^T \mathbf{D}_s \boldsymbol{B}_u \mathrm{d}\Omega \tag{4.15}$$

$$\boldsymbol{F} = \int_{\Omega} \boldsymbol{N}_u^{\mathrm{T}} \mathbf{f} \mathrm{d}\Omega + \int_{\Omega} \boldsymbol{N}_u^{\mathrm{T}} \bar{\boldsymbol{t}} \mathrm{d}\Gamma \tag{4.16}$$

4.1.2 B-bar finite elements

Volumetric and deviatoric strain

The strain tensor is split into its volumetric and deviatoric components as:

$$\boldsymbol{\varepsilon} = \frac{1}{3} e_{vol} \mathbf{I} + \boldsymbol{e} \tag{4.17}$$

where e_{vol} and $\boldsymbol{e}$ are the volumetric strain and the deviatoric strain vector, respectively, defined as

$$e_{vol} = \varepsilon_x + \varepsilon_y + \varepsilon_z \tag{4.18}$$

$$\boldsymbol{e} = \left(\varepsilon_x - \frac{1}{3} e_{vol}, \varepsilon_y - \frac{1}{3} e_{vol}, \varepsilon_z - \frac{1}{3} e_{vol}, \varepsilon_{xy}, \varepsilon_{yz}, \varepsilon_{xz} \right)^T \tag{4.19}$$

and $\mathbf{I} = (1 \quad 1 \quad 1 \quad 0 \quad 0 \quad 0)^T$ is the second order identity tensor expressed in Voigt's notation.

The volumetric strain e_{vol} can be computed as the divergence of the displacements $\boldsymbol{u}$

$$e_{vol} = \mathbf{G}^T \boldsymbol{u} \tag{4.20}$$

where $\mathbf{G}^T = \left(\partial_x, \partial_y, \partial_z \right)$ is the divergence operator and is the adjoint gradient operator. Then

$$\frac{1}{3} e_{vol} \mathbf{I} = \frac{1}{3} \mathbf{I} (\mathbf{G}^T \boldsymbol{u}) = \frac{1}{3} \mathbf{H} \boldsymbol{u} \tag{4.21}$$

where **H** is the matrix operator

$$\mathbf{H} = \mathbf{I}\mathbf{G}^T = \begin{bmatrix} \partial_x & \partial_x & \partial_x & 0 & 0 & 0 \\ \partial_y & \partial_y & \partial_y & 0 & 0 & 0 \\ \partial_z & \partial_z & \partial_z & 0 & 0 & 0 \end{bmatrix}^T \tag{4.22}$$

Similarly, the deviatoric strains can be computed from the displacements $\boldsymbol{u}$:

$$\boldsymbol{e} = \mathbf{S}\boldsymbol{u} - \frac{1}{3} \mathbf{H} \boldsymbol{u} = \mathbf{W} \boldsymbol{u} \tag{4.23}$$

where **W** is the matrix operator

$$\mathbf{W} = \mathbf{S} - \frac{1}{3} \mathbf{H} = \frac{1}{3} \begin{bmatrix} 2\partial_x & -\partial_x & -\partial_x & 3\partial_y & 0 & 3\partial_z \\ -\partial_y & 2\partial_y & -\partial_y & 3\partial_x & 3\partial_z & 0 \\ -\partial_z & -\partial_z & 2\partial_z & 0 & 3\partial_y & 3\partial_x \end{bmatrix}^T \tag{4.24}$$

Note that

$$\mathbf{S} = \frac{1}{3} \mathbf{H} + \mathbf{W} \tag{4.25}$$

The discrete strain-displacement matrix $\boldsymbol{B}_u$ can be correspondingly split in its volumetric and deviatoric components as follows

$$\boldsymbol{B}_u = \mathbf{S}\,\boldsymbol{N}_u = \frac{1}{3}\mathbf{H}\boldsymbol{N}_u + \mathbf{W}\boldsymbol{N}_u = \boldsymbol{B}_u^{\mathrm{vol}} + \boldsymbol{B}_u^{\mathrm{dev}} \tag{4.26}$$

The B-bar element

The B-bar element is a particular implementation of the mixed displacement/pressure quadrilateral Q1P0 element in which the constant pressure has been eliminated at element level at the expense of renouncing the incompressible limit. This is accomplished by evaluating the constant mean stress in terms of the mean volumetric strain, the latter computed from the nodal displacements.

The standard discrete strain-displacement $\boldsymbol{B}_u$ matrix, computed at each integration point from the Cartesian derivatives of the nodal shape functions, is split into its volumetric and deviatoric parts

$$\boldsymbol{B}_u = \boldsymbol{B}_u^{\mathrm{vol}} + \boldsymbol{B}_u^{\mathrm{dev}} \tag{4.27}$$

A mean volumetric sub-matrix $\bar{\boldsymbol{B}}^{\mathrm{vol}}$ is computed as

$$\bar{\boldsymbol{B}}_{\boldsymbol{u}}^{\mathrm{vol}} = \frac{1}{\mathrm{n_g}}\sum_{k=1}^{\mathrm{n_g}} \left(\boldsymbol{B}_u^{\mathrm{vol}}\right)_k \tag{4.28}$$

where $\mathrm{n_g}$ is the number of integration points in the element.

The B-bar discrete strain-displacement matrix is obtained as

$$\bar{\boldsymbol{B}}_u = \bar{\boldsymbol{B}}_u^{\mathrm{vol}} + \boldsymbol{B}_u^{\mathrm{dev}} \tag{4.29}$$

Adopting the B-bar operator in Eq. (4.28), requires, correspondingly, averaging the mean stress over the finite element, so that the elemental stiffness matrix is symmetrical. This is further justified in Section 1.1.3, with regard the Q1P0 $\boldsymbol{u}/p$ elements.

The system of equations to be solver for the stabilized B-bar element is

$$\boldsymbol{K}\boldsymbol{U} = \boldsymbol{F} \tag{4.30}$$

with

$$\boldsymbol{K} = \int_{\Omega} (\bar{\boldsymbol{B}}_u)^{\boldsymbol{T}} \mathbf{D}_{\boldsymbol{s}} \bar{\boldsymbol{B}}_u \, d\Omega \tag{4.31}$$

$$\boldsymbol{F} = \int_{\Omega} \boldsymbol{N}_u^{\mathrm{T}} \boldsymbol{f}\, \mathrm{d}\Omega + \int_{\Omega} \boldsymbol{N}_u^{\mathrm{T}} \bar{\boldsymbol{t}}\, \mathrm{d}\Gamma \tag{4.32}$$

By design, the B-bar element has some zero-energy modes that may show as spurious hour-glassing in some instances. This may be avoided by using

$$\bar{\boldsymbol{B}}_u^{\mathrm{stab}} = \bar{\boldsymbol{B}}_u + (1-\tau)\left[\boldsymbol{B}_u^{\mathrm{vol}} - \bar{\boldsymbol{B}}_u^{\mathrm{vol}}\right] \tag{4.33}$$

For $\tau = 1$, then $\bar{\boldsymbol{B}}_u^{\mathrm{stab}} = \bar{\boldsymbol{B}}_u^{\mathrm{vol}} + \boldsymbol{B}_u^{\mathrm{dev}} = \bar{\boldsymbol{B}}_u$ is identical to the B-bar formulation. For $\tau = 0$, then $\bar{\boldsymbol{B}}_u^{\mathrm{stab}} = \boldsymbol{B}_u^{\mathrm{vol}} + \boldsymbol{B}_u^{\mathrm{dev}}$ is identical to the standard $\boldsymbol{u}$ formulation.

4.1.3 Mixed $\boldsymbol{u/p}$ finite elements

Volumetric and deviatoric stress and split constitutive equation

Similarly to the strain tensor, the stress tensor is split into its volumetric and deviatoric components as:

$$\boldsymbol{\sigma} = p\mathbf{I} + \boldsymbol{s} \tag{4.34}$$

where p and $\boldsymbol{s}$ are the pressure and the deviatoric stress vector respectively, defined as

$$p = \frac{1}{3}(\sigma_x + \sigma_y + \sigma_z) \tag{4.35}$$

$$\boldsymbol{s} = (\sigma_x - p, \sigma_y - p, \sigma_z - p, \tau_{xy}, \tau_{yz}, \tau_{xz})^T \tag{4.36}$$

Now, a volumetric/deviatoric split constitutive law is contemplated so that:

$$p = Ke_{vol} \tag{4.37}$$

$$\boldsymbol{s} = \mathbf{D}_s^{\text{dev}}\boldsymbol{\varepsilon} \tag{4.38}$$

where K is the secant bulk modulus and $\mathbf{D}_s^{\text{dev}}$is the secant deviatoric constitutive matrix.

Mixed $\boldsymbol{u/p}$ strong form

In mixed $\boldsymbol{u/p}$ FE formulations, the strong form of the nonlinear solid mechanics problem is written in terms of the displacement $\boldsymbol{u}$ and pressure p fields.

The split of the stresses in Eq. (4.34) is introduced in Cauchy's equilibrium equation in Eq. (4.3):

$$\mathbf{S}^T\boldsymbol{s} + \mathbf{G}p + \mathbf{f} = \mathbf{0} \tag{4.39}$$

where $\mathbf{S}^T\mathbf{I} = \mathbf{G}$ has been substituted. Eqs. (4.38) and (4.1) are used to yield:

$$\mathbf{S}^T\left(\mathbf{D}_s^{\text{dev}}\mathbf{S}\boldsymbol{u}\right) + \mathbf{G}p + \mathbf{f} = \mathbf{0} \tag{4.40}$$

Then, by introducing Eq. (4.20) in Eq. (4.37) it is possible to write

$$\mathbf{G}^T\boldsymbol{u} = \frac{p}{K} \tag{4.41}$$

Eqs. (4.39) and (4.41) constitute the mixed u/p strong form:

$$\mathbf{S}^T\left(\mathbf{D}_s^{\text{dev}}\mathbf{S}\boldsymbol{u}\right) + \mathbf{G}p + \mathbf{f} = \mathbf{0} \tag{4.42}$$

$$\mathbf{G}^T\boldsymbol{u} - \frac{p}{K} = 0 \tag{4.43}$$

to be solved with the appropriate Dirichlet's and Newman's boundary conditions.

Mixed $\boldsymbol{u/p}$ variational form

The variational form of the mixed $\boldsymbol{u/p}$ problem is then obtained as follows. Firstly, Eq. (4.42) is pre-multiplied by an arbitrary virtual strain displacement $\delta\boldsymbol{u}$ and integrated over the spatial

domain; also, the Divergence Theorem is considered in the two terms on the left hand side. Secondly, Eq. (4.43) is pre-multiplied by an arbitrary virtual pressure vector δp and integrated over the spatial domain.

The resulting mixed $\boldsymbol{u}/p$ variational form is:

$$\int_{\Omega} (\mathbf{S}\delta\boldsymbol{u})^T\left(\mathbf{D}_s^{\text{dev}}\mathbf{S}\boldsymbol{u}\right)\mathrm{d}\Omega + \int_{\Omega} (\mathbf{S}\delta\boldsymbol{u})^T(p\boldsymbol{I})\mathrm{d}\Omega = \int_{\Omega} \delta\boldsymbol{u}^T\mathbf{f}\,\mathrm{d}\Omega + \int_{\Gamma_t} \delta\boldsymbol{u}^T\bar{\boldsymbol{t}}\,\mathrm{d}\Gamma \quad \forall\delta\boldsymbol{u} \tag{4.44}$$

$$\int_{\Omega} \delta p^T(\mathbf{G}^T\boldsymbol{u})\,\mathrm{d}\Omega - \int_{\Omega} \delta p^T\frac{p}{K}\,\mathrm{d}\Omega = 0 \quad \forall\delta p \tag{4.45}$$

The mixed problem to be solved is to find the unknowns $\boldsymbol{u}$ and p that verify the system of Eqs. (4.44) – (4.45) and that comply with the boundary conditions.

FE approximation

The FE discrete problem is derived by discretizing the spatial domain in FE, such that $\Omega = \cup\,\Omega_e$, and by taking discrete FE approximations of the displacements $\boldsymbol{u}$ and the pressure p:

$$\boldsymbol{u} \cong \widehat{\boldsymbol{u}} = \boldsymbol{N}_u\boldsymbol{U} \tag{4.46}$$

$$p \cong \hat{p} = \boldsymbol{N}_p\boldsymbol{P} \tag{4.47}$$

where $\boldsymbol{U}$ and $\boldsymbol{P}$ are vectors comprising the values of the displacements and pressures at the nodes of the finite element mesh. $\boldsymbol{N}_u$and $\boldsymbol{N}_p$ are the matrices containing the interpolation functions adopted in the FE approximation.

In the Galerkin method, the same approximation is taken for the discrete virtual displacements, and virtual pressure so that

$$\delta\boldsymbol{u} \cong \delta\widehat{\boldsymbol{u}} = \boldsymbol{N}_u\delta\boldsymbol{U} \tag{4.48}$$

$$\delta p \cong \delta\hat{p} = \boldsymbol{N}_p\delta\boldsymbol{P} \tag{4.49}$$

The submatrices of $\boldsymbol{N}_u$and $\boldsymbol{N}_p$ are diagonal matrices and the corresponding components are $N_u^{(i)}$, $N_e^{(i)}$ and $N_p^{(i)}$ interpolation functions, (i) being the node counter.

Introducing these approximations, the system of Eqs. (4.44) – (4.45) becomes:

$$\int_{\Omega} \delta\boldsymbol{U}^T\boldsymbol{B}_u^T\left(\mathbf{D}_s^{\text{dev}}\boldsymbol{B}_u\boldsymbol{U}\right)\mathrm{d}\Omega + \int_{\Omega} \delta\boldsymbol{U}^T\boldsymbol{B}_u^T\left(\boldsymbol{N}_p\boldsymbol{P}\mathbf{I}\right)\mathrm{d}\Omega = \widehat{W}(\delta\boldsymbol{U}) \quad \forall\delta\boldsymbol{U} \tag{4.50}$$

$$\int_{\Omega} \delta\boldsymbol{P}^T\boldsymbol{N}_p^T(\mathbf{G}^T\boldsymbol{N}_u\boldsymbol{U})\,\mathrm{d}\Omega - \int_{\Omega} \delta\boldsymbol{P}^T\boldsymbol{N}_p^T\frac{\boldsymbol{N}_p\boldsymbol{P}}{K}\,\mathrm{d}\Omega = 0 \quad \forall\delta p \tag{4.51}$$

In (4.50) – (4.51), the remarks made in Eqs. (4.11), (4.12) and (4.13) apply. Also, with some abuse of notation, $\boldsymbol{U}$ and $\boldsymbol{P}$ (and $\delta\boldsymbol{U}$ and $\delta\boldsymbol{P}$**)** are to be considered as the nodal values over the whole FE mesh.

Note that the second term in Eq. (4.50) can also be rewritten as

$$\int_{\Omega} \delta\boldsymbol{U}^T\boldsymbol{B}_u^T\left(\boldsymbol{N}_p\boldsymbol{P}\mathbf{I}\right)d\Omega = \int_{\Omega} \delta\boldsymbol{U}^T\boldsymbol{N}_u^T\mathbf{S}^T\mathbf{I}\boldsymbol{N}_p\boldsymbol{P}d\Omega = \int_{\Omega} \delta\boldsymbol{U}^T\boldsymbol{N}_u^T\mathbf{G}\boldsymbol{N}_p\boldsymbol{P}d\Omega \tag{4.52}$$

where $\mathbf{G} = \mathbf{S}^T\mathbf{I}$ is used again. This shows that the resulting problem is symmetric.

The virtual displacement $\delta\boldsymbol{U}$ and virtual pressure $\delta\boldsymbol{P}$ are arbitrary; therefore, the system of equations for the mixed Galerkin method becomes

$$\begin{bmatrix} \boldsymbol{K}^{\mathrm{dev}} & \boldsymbol{Q} \\ \boldsymbol{Q}^T & -\boldsymbol{M} \end{bmatrix} \begin{bmatrix} \boldsymbol{U} \\ \boldsymbol{P} \end{bmatrix} = \begin{bmatrix} \boldsymbol{F} \\ \boldsymbol{0} \end{bmatrix} \tag{4.53}$$

where $[\boldsymbol{U} \quad \boldsymbol{P}]^T$ is the array of nodal values of displacements and pressure and

$$\boldsymbol{K}^{\mathrm{dev}} = \int_{\Omega} \boldsymbol{B}_u^T \mathbf{D}_s^{\mathrm{dev}} \boldsymbol{B}_u \mathrm{d}\Omega \tag{4.54}$$

$$\boldsymbol{M} = \int_{\Omega} \boldsymbol{N}_p^T \frac{1}{K} \boldsymbol{N}_p \mathrm{d}\Omega \tag{4.55}$$

$$\boldsymbol{Q} = \int_{\Omega} \boldsymbol{N}_u^T \mathbf{G} \boldsymbol{N}_p \mathrm{d}\Omega \tag{4.56}$$

$$\boldsymbol{F} = \int_{\boldsymbol{\Omega}} \boldsymbol{N}_{\boldsymbol{u}}^{\boldsymbol{T}} \mathbf{f}\, \mathrm{d}\Omega + \int_{\boldsymbol{\Gamma}_{\boldsymbol{t}}} \boldsymbol{N}_{\boldsymbol{u}}^{\boldsymbol{T}} \bar{\boldsymbol{t}}\, \mathrm{d}\Gamma \tag{4.57}$$

Note that the Galerkin problem is symmetric.

Note also that if $1/K \neq 0$, the second equation in Eq. (4.53) may be solved for $\boldsymbol{P} = \boldsymbol{M}^{-1}\boldsymbol{Q}^T\boldsymbol{U}$ and substituted into the first one to yield:

$$\left(\boldsymbol{K}^{\mathrm{dev}} + \boldsymbol{Q}\boldsymbol{M}^{-1}\boldsymbol{Q}^{\boldsymbol{T}}\right)\boldsymbol{U} = \boldsymbol{F} \tag{4.58}$$

which may be solved for $\boldsymbol{U}$. This procedure is impractical if $\boldsymbol{M}$ and $\boldsymbol{Q}$ are global matrices.

Discontinuous pressure interpolation

If the selected interpolation for the pressure is inter-element discontinuous, then the second equation in Eq. (4.53) may be solved element-by-element and the substitution in Eq. (4.58) can be carried out in practice.

In particular, for a bilinear quadrilateral element, if the pressure is constant over the element, the Q1P0 element is obtained, where

$$\boldsymbol{K} = \boldsymbol{K}^{\mathrm{dev}} + \boldsymbol{K}^{\mathrm{vol}} \tag{4.59}$$

$$\boldsymbol{K}^{\mathrm{dev}} = \int_{\Omega} \left(\boldsymbol{B}_u^{\mathrm{dev}}\right)^{\boldsymbol{T}} \boldsymbol{D}_{\boldsymbol{s}}\, \boldsymbol{B}_u^{\mathrm{dev}} \mathrm{d}\Omega \tag{4.60}$$

$$\boldsymbol{K}^{\mathrm{vol}} = \int_{\Omega} \left(\bar{\boldsymbol{B}}_u^{\mathrm{vol}}\right)^{\boldsymbol{T}} \boldsymbol{D}_{\boldsymbol{s}}\, \bar{\boldsymbol{B}}_u^{\mathrm{vol}} \mathrm{d}\Omega \tag{4.61}$$

Because of the orthogonality between deviatoric and volumetric operator, the $\boldsymbol{K}$ matrix in Eq. (4.64) is identical to that in Eq. (4.31).

VMS stabilization

The interpolation functions in Eqs. (4.46) – (4.47) must satisfy the Inf-Sup condition [116] to ensure the stability of the solution obtained in the system of equations (4.53). Unfortunately, this condition is not verified if equal order interpolations are used for all the unknown fields. In such case, the solution is unstable and a suitable stabilization method is needed.

In this work, linear approximations in all the interpolation functions are used together with a stabilization procedure which circumvents the strictness of the Inf-Sup condition. The stabilization procedure consists in the modification of the discrete variational form using the Variational Multiscale Stabilization (VMS) Method, introduced in [126–127].

The basic idea of the stabilization procedure is to enhance the FE approximation of the continuous solution in Eqs. (4.46) – (4.47) by adding to the discrete fields $\boldsymbol{u}_h$ and p_h a term approximating the finer sub-grid scale that cannot be captured a priori at the FE scale $\tilde{\boldsymbol{u}}$ and $\tilde{p}$:

$$\boldsymbol{u} \cong \hat{\boldsymbol{u}} = \boldsymbol{u}_h + \tilde{\boldsymbol{u}} \tag{4.62}$$

$$p \cong \hat{p} = p_h + \tilde{p} \tag{4.63}$$

The subscales are computed in terms of the residuals of the discrete solution, so that,

$$\tilde{\boldsymbol{u}} = \tau_u \left[\mathbf{S}^T \left(\mathbf{D}_s^{\mathrm{dev}} \mathbf{S} \boldsymbol{u}_h\right) + \mathbf{G} p_h + \mathbf{f}\right] \tag{4.64}$$

$$\tilde{p} = \tau_p \left[\mathbf{G}^T \boldsymbol{u}_h - \frac{p_h}{K}\right] \tag{4.65}$$

Here the stabilization parameters τ_u and τ_p are chosen to obtain optimal convergence rate upon mesh refinement [119,125].

$$\tau_u = c_u \frac{h^2}{2G_s} \tag{4.66}$$

$$\tau_p = c_p \frac{2}{3} G_s \left(\frac{1+\nu}{1-\nu}\right) \tag{4.67}$$

where G_s is the effective (secant) shear modulus and c_u, c_p are *O(1)* coefficients.

Introducing the multiscale approximations in Eqs. (4.62) – (4.63), together with the subscales in Eqs. (4.64) – (4.65) into the variational form in Eqs. (4.44) – (4.45) results in the stabilized algebraic system:

$$\begin{bmatrix} \boldsymbol{K}^{\mathrm{dev}} + \tau_p \boldsymbol{K}_u & \left(1 - \frac{\tau_p}{K}\right) \boldsymbol{Q} \\ \left(1 - \frac{\tau_p}{K}\right) \boldsymbol{Q}^T & -\left(1 - \frac{\tau_p}{K}\right) \boldsymbol{M} - \tau_u \boldsymbol{K}_p \end{bmatrix} \begin{bmatrix} \boldsymbol{U} \\ \boldsymbol{P} \end{bmatrix} = \begin{bmatrix} \boldsymbol{F} \\ \boldsymbol{0} \end{bmatrix} \tag{4.68}$$

where $[\boldsymbol{U} \quad \boldsymbol{P}]^T$ is the array of nodal values of displacements and pressure and the new matrices are

$$\boldsymbol{K}_u = \int_\Omega \boldsymbol{N}_u^T \mathbf{G} \mathbf{G}^T \boldsymbol{N}_u \mathrm{d}\Omega \tag{4.69}$$

$$\boldsymbol{K}_p = \int_\Omega \boldsymbol{N}_p^T \mathbf{G}^T \mathbf{G} \boldsymbol{N}_p \, \mathrm{d}\Omega \tag{4.70}$$

Note that the VMS stabilized problem is symmetric.

The stabilization used is variationally consistent, because residual-based stabilization procedures do not introduce any consistency error. For a converged solution, when the size of the element h tends to zero, $h \to 0$, the stabilization terms vanish. For non-converged solutions, the added stabilization terms are small, as they depend on the residuals of the discrete solution.

For a given FE mesh, using different values of the stabilization procedure produces slightly different results. This is akin to use different FE interpolations of the same order of convergence with the same nodal arrangement.

4.1.4 Mixed $\boldsymbol{\varepsilon/u}$ finite elements

Mixed *ε/u* strong form

In mixed ***ε/u*** FE formulations, the strong form of the nonlinear solid mechanics problem is written in terms of the strain $\boldsymbol{\varepsilon}$ and displacement $\boldsymbol{u}$ fields.

The displacements $\boldsymbol{u}$ are related to the total strains $\boldsymbol{\varepsilon}$ through the compatibility equation

$$\boldsymbol{\varepsilon} = \mathbf{S}\boldsymbol{u} \tag{4.71}$$

where $\mathbf{S}$ is the differential symmetric gradient operator, and the stress vector $\boldsymbol{\sigma}$ is related to the body forces $\mathbf{f}$ through Cauchy's equilibrium equation

$$\mathbf{S}^T\boldsymbol{\sigma} + \mathbf{f} = \mathbf{0} \tag{4.72}$$

where $\mathbf{S}^T$ is the differential divergence operator. The stress vector $\boldsymbol{\sigma}$ and the strain vector $\boldsymbol{\varepsilon}$ are connected by the constitutive equation:

$$\boldsymbol{\sigma} = \mathbf{D}_s\boldsymbol{\varepsilon} \tag{4.73}$$

where $\mathbf{D}_s$ is the secant constitutive matrix.

By combining Eqs. (4.74) – (4.75), the symmetrical mixed ***ε/u*** strong form of the problem is as:

$$-\mathbf{D}_s\boldsymbol{\varepsilon} + \mathbf{D}_s\mathbf{S}\boldsymbol{u} = 0 \tag{4.74}$$

$$\boldsymbol{S}^T(\mathbf{D}_s\boldsymbol{\varepsilon}) + \mathbf{f} = 0 \tag{4.75}$$

to be solved with the appropriate Dirichlet's and Newman's boundary conditions.

Mixed *ε/u* variational form

The corresponding weak form of the problem is obtained through three steps. First, Eqs. (4.74) and (4.75) are multiplied by an arbitrary virtual strain vector $\delta\boldsymbol{\varepsilon}$ and arbitrary virtual displacement vector $\delta\boldsymbol{u}$, respectively. Second, each of the multiplied equations is integrated over the domain Ω. Third, the Divergence Theorem is applied in the first term of the second equation.

The resulting mixed ***ε/u*** variational form is:

$$-\int_\Omega \delta\boldsymbol{\varepsilon}^T\mathbf{D}_s\boldsymbol{\varepsilon}\mathrm{d}\Omega + \int_\Omega \delta\boldsymbol{\varepsilon}^T\mathbf{D}_s\mathbf{S}\boldsymbol{u}\mathrm{d}\Omega = 0 \quad \forall\delta\boldsymbol{\varepsilon} \tag{4.76}$$

$$\int_{\Omega}(\boldsymbol{S}\delta\boldsymbol{u})^{T}(\mathbf{D}_{s}\boldsymbol{\varepsilon})\mathrm{d}\Omega=\int_{\Omega}\delta\boldsymbol{u}^{\mathrm{T}}\mathbf{f}\mathrm{d}\Omega+\int_{\Gamma_{t}}\delta\boldsymbol{u}^{\mathrm{T}}\bar{\boldsymbol{t}}\mathrm{d}\Gamma\quad\forall\delta\boldsymbol{u} \tag{4.77}$$

The mixed problem to be solved is to find the unknowns $\boldsymbol{\varepsilon}$ and $\boldsymbol{u}$ that verify the system of Eqs. (4.76) – (4.77) and that comply with the boundary conditions.

FE approximation

The mixed finite approximation is similar to the Standard FEs described previously, only the strain field needs to be considered. The domain is discretized into finite elements (Ω_e), such that $\Omega \cong \Sigma\Omega_e$; displacements $\boldsymbol{u}$ and strains $\boldsymbol{\varepsilon}$ are approximated by taking the discrete FE interpolations:

$$\boldsymbol{u}\cong\widehat{\boldsymbol{u}}=\boldsymbol{N}_{u}\boldsymbol{U} \tag{4.78}$$

$$\boldsymbol{\varepsilon}\cong\hat{\boldsymbol{\varepsilon}}=\boldsymbol{N}_{\varepsilon}\boldsymbol{E} \tag{4.79}$$

where $\boldsymbol{U}$ and $\boldsymbol{E}$ are the displacement and strain vectors representing the nodal discrete displacements $\widehat{\boldsymbol{u}}$ and nodal discrete strain $\hat{\boldsymbol{\varepsilon}}$ values in the finite element mesh.

In the Galerkin method, the same approximation is taken for the discrete virtual displacements, and virtual strains so that

$$\delta\boldsymbol{u}\cong\delta\widehat{\boldsymbol{u}}=\boldsymbol{N}_{u}\delta\boldsymbol{U} \tag{4.80}$$

$$\delta\boldsymbol{\varepsilon}\cong\delta\hat{\boldsymbol{\varepsilon}}=\boldsymbol{N}_{\varepsilon}\delta\boldsymbol{E} \tag{4.81}$$

The submatrices of $\boldsymbol{N}_{u}$ and $\boldsymbol{N}_{\varepsilon}$ are diagonal matrices and the corresponding components are $N_{u}^{(i)}$ and $N_{\varepsilon}^{(i)}$ interpolation functions, (i) being the node counter.

Introducing these approximations, the system of Eqs. (4.76) – (4.77) becomes:

$$-\int_{\Omega}\delta\boldsymbol{E}^{T}\boldsymbol{N}_{\varepsilon}^{T}\mathbf{D}_{s}\boldsymbol{N}_{\varepsilon}\boldsymbol{E}\mathrm{d}\Omega+\int_{\Omega}\delta\boldsymbol{E}^{T}\boldsymbol{N}_{\varepsilon}^{T}\mathbf{D}_{\boldsymbol{s}}\boldsymbol{B}_{u}\boldsymbol{U}\mathrm{d}\Omega=0\qquad\forall\delta\boldsymbol{E} \tag{4.82}$$

$$\int_{\Omega}\delta\boldsymbol{U}^{T}\boldsymbol{B}_{u}^{T}\mathbf{D}_{\boldsymbol{s}}\boldsymbol{N}_{\varepsilon}\boldsymbol{E}\mathrm{d}\Omega=\widehat{W}(\delta\boldsymbol{U})\qquad\forall\delta\boldsymbol{U} \tag{4.83}$$

In Eqs. (4.82) – (4.83), the remarks made in Eqs. (4.11), (4.12) and (4.13) apply. Also, with some abuse of notation, $\boldsymbol{U}$ and $\boldsymbol{E}$ (and $\delta\boldsymbol{U}$ and $\delta\boldsymbol{E}$**)** are to be considered as the nodal values over the whole FE mesh.

The virtual displacement $\delta\boldsymbol{U}$ and virtual pressure $\delta\boldsymbol{E}$ are arbitrary; therefore, the system of equations for the mixed Galerkin method becomes

$$\begin{bmatrix}-\boldsymbol{M} & \boldsymbol{Q}\\ \boldsymbol{Q}^{\mathrm{T}} & \mathbf{0}\end{bmatrix}\begin{bmatrix}\boldsymbol{E}\\ \boldsymbol{U}\end{bmatrix}=\begin{bmatrix}\mathbf{0}\\ \boldsymbol{F}\end{bmatrix} \tag{4.84}$$

where $[\boldsymbol{E}\quad\boldsymbol{U}]^{T}$ is the array of nodal values of strains and displacements and

$$\boldsymbol{M}=\int_{\Omega}\boldsymbol{N}_{\varepsilon}^{T}\mathbf{D}_{\boldsymbol{s}}\boldsymbol{N}_{\varepsilon}\mathrm{d}\Omega \tag{4.85}$$

$$\boldsymbol{Q}=\int_{\Omega}\boldsymbol{N}_{\varepsilon}^{\mathrm{T}}\mathbf{D}_{\boldsymbol{s}}\boldsymbol{B}_{u}\mathrm{d}\Omega \tag{4.86}$$

$$\boldsymbol{F}=\int_{\Omega}\boldsymbol{N}_{u}^{T}\mathbf{f}\mathrm{d}\Omega+\int_{\Omega}\boldsymbol{N}_{u}^{T}\bar{\boldsymbol{t}}\mathrm{d}\Gamma \tag{4.87}$$

Note that the Galerkin problem is symmetric.

Note that if $\mathbf{D}_s$ is not singular, the first equation in Eq. (4.84) may be solved for $\boldsymbol{E} = \boldsymbol{M}^{-1}\boldsymbol{Q}^T\boldsymbol{U}$ and substituted into the second one to yield:

$$(\boldsymbol{Q}\boldsymbol{M}^{-1}\boldsymbol{Q}^T)\boldsymbol{U} = \boldsymbol{F} \tag{4.88}$$

which may be solved for $\boldsymbol{U}$. This procedure is impractical if $\boldsymbol{M}$ and $\boldsymbol{Q}$ are global matrices. However, if the selected interpolation for the strains is inter-element discontinuous, then the first equation in Eq. (4.84) may be solved element-by-element and the substitution in Eq. (4.94) can be carried out in practice. This is the design of many successful strain-enhanced finite elements.

VMS stabilization

The interpolation functions in Eqs. (4.78) – (4.79) must satisfy the Inf-Sup condition [116] to ensure the stability of the solution obtained in the system of equations (4.84). In this work, linear approximations are used together with a VMS stabilization procedure which circumvents the strictness of the Inf-Sup condition.

The FE approximation of the continuous solution in Eqs. (4.78) – (4.79) is enhanced by adding to the discrete fields $\boldsymbol{u}_h$ and $\boldsymbol{\varepsilon}_h$ a subscale term, $\tilde{\boldsymbol{u}}$ and $\tilde{\boldsymbol{\varepsilon}}$, respectively, approximating the finer sub-grid scale that cannot be captured a priori at the FE scale:

$$\boldsymbol{u} \cong \hat{\boldsymbol{u}} = \boldsymbol{u}_h + \tilde{\boldsymbol{u}} \tag{4.89}$$

$$\boldsymbol{\varepsilon} \cong \hat{\boldsymbol{\varepsilon}} = \boldsymbol{\varepsilon}_h + \tilde{\boldsymbol{\varepsilon}} \tag{4.90}$$

The subscales are computed in terms of the residuals of the discrete solution, so that, is adopted herein, corresponding to the residual based sub-grid approach

$$\tilde{\boldsymbol{u}} = \tau_u \left[\mathbf{S}^T\mathbf{D}_s\boldsymbol{\varepsilon}_h + \mathbf{f}\right] \tag{4.91}$$

$$\tilde{\boldsymbol{\varepsilon}} = \tau_\varepsilon[\mathbf{S}\boldsymbol{u}_h - \boldsymbol{\varepsilon}_h] \tag{4.92}$$

Here the stabilization parameters τ_u and τ_ε are chosen to obtain optimal convergence rate upon mesh refinement [119,125].

$$\tau_u = c_u \frac{h^2}{2G_s} \tag{4.93}$$

$$\tau_\varepsilon = c_\varepsilon \frac{h}{L} \tag{4.94}$$

where G_s is the effective (secant) shear modulus, L is a characteristic length of the problem and c_u, c_ε are *O(1)* coefficients.

It is worth noting that the stabilized approximation of the strain field in Eq. (4.90), substituting the interpolation in Eq. (4.81) and the subscale in Eq. (4.92), reads

$$\boldsymbol{\varepsilon} \cong \hat{\boldsymbol{\varepsilon}} = \boldsymbol{N}_\varepsilon\boldsymbol{E} + \tau_\varepsilon(\boldsymbol{B}_u\boldsymbol{U} - \boldsymbol{N}_\varepsilon\boldsymbol{E}) = (1-\tau_\varepsilon)\boldsymbol{N}_\varepsilon\boldsymbol{E} + \tau_\varepsilon\boldsymbol{B}_u\boldsymbol{U} \tag{4.95}$$

where $0 \le \tau_\varepsilon \le 1$ and $\boldsymbol{B}_u = \mathbf{S}\boldsymbol{N}_u$ is the standard compatibility matrix. Note that $\tau_\varepsilon = 0$ corresponds to the strain interpolation of the non-stabilized problem, while $\tau_\varepsilon = 1$ corresponds to the strain interpolation from the standard displacement-based formulation.

Introducing the multiscale approximations in Eqs.(4.89) – (4.90), together with the subscales in Eqs. (4.91) – (4.92) into the variational form in Eqs. (4.76) – (4.77) results in the stabilized algebraic system:

$$\begin{bmatrix} -(1-\tau_\varepsilon)\boldsymbol{M} - \tau_u \boldsymbol{L} & (1-\tau_\varepsilon)\boldsymbol{Q} \\ (1-\tau_\varepsilon)\boldsymbol{Q}^T & \tau_\varepsilon \boldsymbol{K} \end{bmatrix} \begin{bmatrix} \boldsymbol{E} \\ \boldsymbol{U} \end{bmatrix} = \begin{bmatrix} \boldsymbol{0} \\ \boldsymbol{F} \end{bmatrix} \tag{4.96}$$

where

$$\boldsymbol{K} = \int_\Omega \boldsymbol{B}_u^T \mathbf{D}_{\boldsymbol{s}} \boldsymbol{B}_u \mathrm{d}\Omega \tag{4.97}$$

$$\boldsymbol{L} = \int_\Omega (\boldsymbol{N}_e^T \mathbf{D}_s^T)(\mathbf{D}_s \boldsymbol{N}_e)\, \mathrm{d}\Omega \tag{4.98}$$

Note that the VMS stabilized problem is symmetric.

Note also that if $\mathbf{D}_{\boldsymbol{s}}$ is not singular, the substitution procedure outlined in Eq. (4.88) is formally applicable to the VMS stabilized problem, even if it practical application has to be carefully considered if the matrices involved are globally defined.

The remarks about the consistency of residual-based stabilization methods made in the previous Section with regard the stabilized ***u***/*p* elements are relevant here with regard the stabilized ***ε/u*** elements.

4.1.5 Mixed ***ε***/B-bar ***u*** finite elements

The mixed ***ε***/B-bar ***u*** finite element is a particular implementation of the mixed displacement/strain/pressure quadrilateral Q1Q1P0 element in which the constant pressure has been eliminated at element level at the expense of renouncing the incompressible limit. This is accomplished by evaluating the constant mean stress in terms of the mean volumetric strain, the latter computed from the nodal displacements.

The implementation of the mixed ***ε***/B-bar ***u*** element is similar to the irreducible B-bar element. It consists in substituting the standard discrete strain-displacement $\boldsymbol{B}_u$ matrix, computed at each integration point from the Cartesian derivatives of the nodal shape functions, by the B-bar discrete strain-displacement matrix $\overline{\boldsymbol{B}}_u$ computed as

$$\overline{\boldsymbol{B}}_u = \overline{\boldsymbol{B}}_u^{\mathrm{vol}} + \boldsymbol{B}_u^{\mathrm{dev}} \tag{4.99}$$

where the constant $\overline{\boldsymbol{B}}_u^{\mathrm{vol}}$ is computed as

$$\overline{\boldsymbol{B}}_{\boldsymbol{u}}^{\mathrm{vol}} = \frac{1}{\mathrm{n_g}} \sum_{k=1}^{\mathrm{n_g}} (\boldsymbol{B}_u^{\mathrm{vol}})_k \tag{4.100}$$

where $\mathrm{n_g}$ is the number of integration points in the element.

Adopting the B-bar operator in Eqs. (4.99) – (4.100), matrices $\boldsymbol{Q}$ and $\boldsymbol{K}$ read

$$\boldsymbol{Q} = \int_\Omega \boldsymbol{N}_\varepsilon^T \mathbf{D}_{\boldsymbol{s}} \overline{\boldsymbol{B}}_u \mathrm{d}\Omega \tag{4.101}$$

$$\boldsymbol{K} = \int_\Omega \overline{\boldsymbol{B}}_u^T \mathbf{D}_{\boldsymbol{s}}\, \overline{\boldsymbol{B}}_u \mathrm{d}\Omega \tag{4.102}$$

4.1.6 Secant matrix for plasticity

In the previous Sections it is assumed that the constitutive relationship between strains and stresses is written in secant form as:

$$\boldsymbol{\sigma} = \mathbf{D}_s \boldsymbol{\varepsilon} \tag{4.103}$$

where $\mathbf{D}_s$ is the secant constitutive matrix.

In plasticity, the constitutive equation is written as:

$$\boldsymbol{\sigma} = \mathbf{D}_o \left(\boldsymbol{\varepsilon} - \boldsymbol{\varepsilon}_p \right) \tag{4.104}$$

where $\mathbf{D}_o$ is the elastic constitutive matrix and $\boldsymbol{\varepsilon}_p$ is the plastic strain. Both expressions are equivalent with $\mathbf{D}_s$ as the symmetric matrix

$$\mathbf{D}_s = \mathbf{D}_o - \frac{\left(\mathbf{D}_o \boldsymbol{\varepsilon}_p \right)^{\boldsymbol{T}} \left(\mathbf{D}_o \boldsymbol{\varepsilon}_p \right)}{\boldsymbol{\varepsilon}^{\boldsymbol{T}} \mathbf{D}_o \boldsymbol{\varepsilon}_p} \tag{4.105}$$

4.2 Accurate and locking-free analysis of beams, plates and shells using solid elements

Article Data:

Title: **Accurate and locking-free analysis of beams, plates and shells using solid elements.**

Authors: S. Saloustros, M. Cervera, S. Kim and M. Chiumenti

Journal : Computational Mechanics, 67, 883–914 (2021)

https://doi.org/10.1007/s00466-020-01969-0

Scientific Contribution:

This paper investigates the capacity of solid finite elements with independent interpolations for displacements and strains to address shear, membrane and volumetric locking in the analysis of beam, plate and shell structures. The performance of the proposed strain/displacement formulation is compared to the standard one through a set of eleven benchmark problems. In addition to the relative performance of both finite element formulations, the paper studies the effect of discretization and material characteristics. The first refers to different solid element typologies (hexahedra, prisms) and shapes (regular, skewed, warped configurations). The second refers to isotropic, orthotropic and layered materials, and nearly incompressible states. For the analysis of nearly incompressible cases, the B-bar method is employed in both standard and strain/displacement formulations. Numerical results show the enhanced accuracy of the proposed strain/displacement formulation in predicting stresses and displacements, as well as producing locking-free discrete solutions, which converge asymptotically to the corresponding continuous problems.

The paper presents the use of solid finite elements with independent displacement and strain interpolations for addressing element locking problems under common load, geometrical and material conditions found in engineering structures. The accuracy of the present FE formulation is investigated in terms of displacements and stresses through the analysis of a set of eleven benchmarks problems of beam, shell and plate structures. All problems are analyzed using solid finite elements, which are available at all FE codes and can be conveniently used for the modelling of any type of structure and with any type of general constitutive model.

The performance of the present FE is investigated considering several modelling choices, such as different element typologies (hexahedra and prisms) and mesh configurations (regular, skewed, warped). The effect of material properties is studied by considering isotropic and orthotropic cases, as well as compressible and nearly incompressible materials. For the latter, the use of the B-bar method as a way to address volumetric locking is investigated. Laminated multi-layered orthotropic material distribution is also investigated.

Numerical results demonstrate that $\boldsymbol{\varepsilon/u}$ FEs far outperform the corresponding standard ones in estimating displacements and stresses, providing locking membrane and shear free solutions. The use of the B-bar method is beneficial for the performance of the present formulation in the incompressibility limit, guaranteeing convergence in displacements and stresses. The simulated cases studied here show that FEs with independent interpolations for displacements and strains are an effective alternative for simulating complex stress states in beam, shell and plate structures with enhanced accuracy.

4.3 On the performance of different FE formulations with regard strain localization

In this Section, the performance of the different finite FE formulations introduce in Section 4.1 is assessed with regard their relative merits for modelling strain localization induced by plastic flow.

For doing this, a benchmark problem is selected: a strip subjected to uniaxial tension via imposed vertical displacements at the top and bottom ends; the horizontal movement is not restrained. As shown in Figure 4.1, the strip has dimensions 10 m × 20 m (width × height). A sharp horizontal slit (2 m) is inserted in the center of strip to introduce the perturbation necessary to trigger strain localization. Plane strain conditions are investigated.

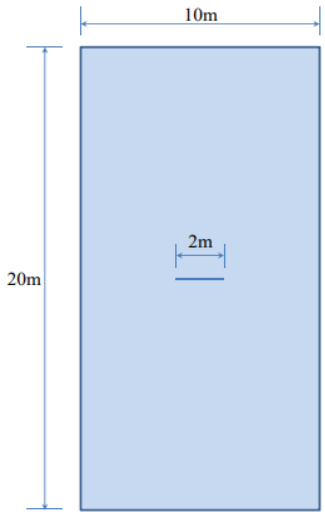

Figure 4.1 Dimensions of the strip stretching test

In this problem the far field stress state is:

$$\sigma_x = 0, \qquad \sigma_y = \sigma > 0, \qquad \tau_{xy} = 0$$

The sharp horizontal slit causes a stress concentration that triggers the onset of plastic behavior and strain localization; subsequently, straight slip lines stem from these and cross the strip at well-defined slopes that must follow the angles predicted from the localization analysis.

The following material properties are used: Young's modulus E = 1.0 ×10^7 MPa, Poisson's ratio ν = 0.2. Isotropic elasto-plastic models with pressure independent von Mises (VM) and pressure dependent Drucker-Prager (DP) yield criteria are investigated. Perfect plasticity is assumed.

Due to the double symmetry of the strip and the boundary conditions, only a quarter of the domain needs to be analyzed. Structured meshes of regular triangles and quadrilaterals are employed. Square elements (0.1 m × 0.1 m) are arranged 50 horizontally and 100 vertically, with a total of 5,000 elements used for plane strain 2D simulations. Triangular meshes are constructed by halving the square elements; the nodal arrangement is preserved. In all cases, 500 time steps are performed to complete the analyses.

The constitutive laws and finite elements used have been implemented in the COMET finite element program, developed at the International Center for Numerical Methods in Engineering (CIMNE). Pre- and post-processing are done with GiD, also developed at CIMNE.

The following cases are compared:

Tris FE, VM: irreducible ***u***, mixed ***u***/*p* and mixed ***ε/u*** FEs

Quads FE, VM: irreducible ***u***, B-bar, mixed ***u***/*p*, mixed ***ε/u*** and mixed ***ε/***B-bar ***u*** FEs

Quads FE, DP: irreducible ***u***, B-bar, mixed ***ε/u*** and mixed ***ε/***B-bar ***u*** FEs

For each FE simulation, a Figure shows the computed failure mechanism and the corresponding contour fills of: (a) vertical y-displacement [0 : 0.4] m, (b) equivalent plastic strain [0 : 2.0], (c) Lode's angle [0° : 60°], (d) J_2 stress [0 : 10000] MPa, (d) mean stress [-3000 : 7000] MPa and (e) vertical σ_y stress [-5000 : 15000] MPa. Ranges used in the figures are indicated in brackets.

4.3.1 Triangles, von Mises: irreducible u, mixed u/p and mixed ε/u FEs

Isotropic von Mises J2 plasticity with yield strength $\sigma^Y = 1.0 \times 10^4$ MPa is now considered. Insensitive to pressure, under plane strain, uniaxial tensile tests show localization angles at + 45° from the horizontal axis, measured in a counter-clockwise manner.

The vertical reaction–displacement curves for the ***u,*** mixed ***u***/*p* and mixed ***ε/u*** triangular meshes are shown in Figure 4.2. As you can see, the global responses for all three are satisfactory, and no signs pressure locking are observed.

Figure 4.3 shows the results corresponding to the triangular irreducible ***u*** FEs. Because of the favorable mesh alignment of the triangles, the contour fills of the (a) vertical displacement and (b) equivalent plastic strain indicate the correct strain localization. Note that the displacement jump and the strain localization occur across one single element.

Lode's angle (c) is correctly evaluated as 30° inside and in the vicinity of the localization band. However, clear signs of pressure locking are observed in the results of the mean stress (e) that reflect also on the contour-fills of the vertical σ_y stress (f). This affects also the J_2 stresses (d), but this is not obvious in the figure.

These results are due to the isochoric character of the plastic flow of the von Mises model are the inability of the standard elements to reproduce a purely sliding behavior even if the mesh is favorably aligned.

Figure 4.4 shows the results corresponding to the triangular mixed ***u***/*p* FEs. For this particular case, the triangular ***u***/*p* FEs perform admiringly. The contour fills of the (a) vertical displacement and (b) equivalent plastic strain and Lode's angle correspond to the expected results. Also, no sign of pressure locking is observed in the results of the mean stress (e) nor the vertical σ_y stress (f) or the J_2 stresses (d). Note that the displacement jump and the strain localization occur across one single element.

Figure 4.5 shows the results corresponding to the triangular mixed ***ε/u*** FEs. Again, the contour fills of the (a) vertical displacement and (b) equivalent plastic strain and Lode's angle correspond to the expected results. Note that in this case, the displacement jump and the strain localization occur across three elements, due to the continuity of the strain interpolation. As for the irreducible elements, the incompressible plastic flow induces pressure locking in the results of the mean stress (e) and the vertical σ_y stress (f).

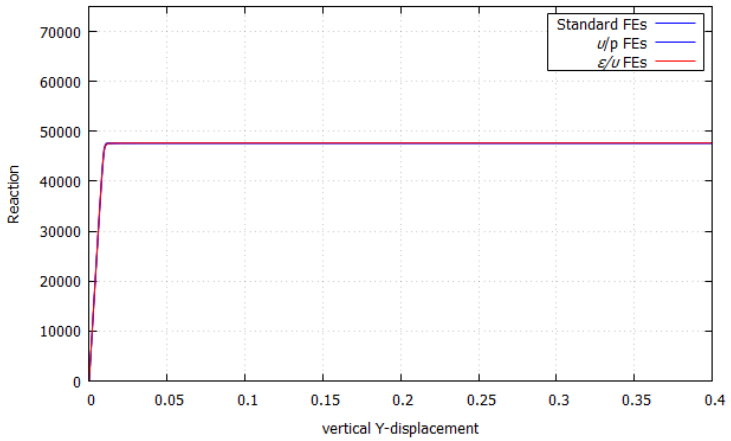

Figure 4.2 Evolution curves of vertical reaction–displacement for Tris FE for the von Mises yield criterion

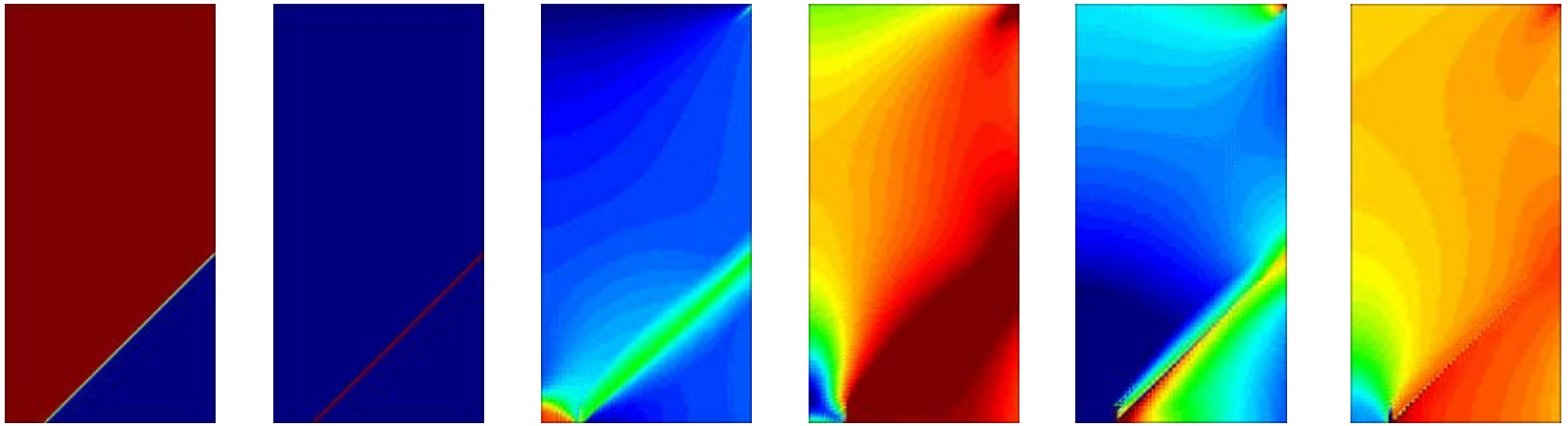

(a) (b) (c) (d) (e) (f)

Figure 4.3 Contour fills for triangular irreducible FE, von Mises: (a) Y-disp, (b) Equiv. plast. strain, (c) Lode angle, (d) J2 stress, (e) Mean stress, (f) Y-stress

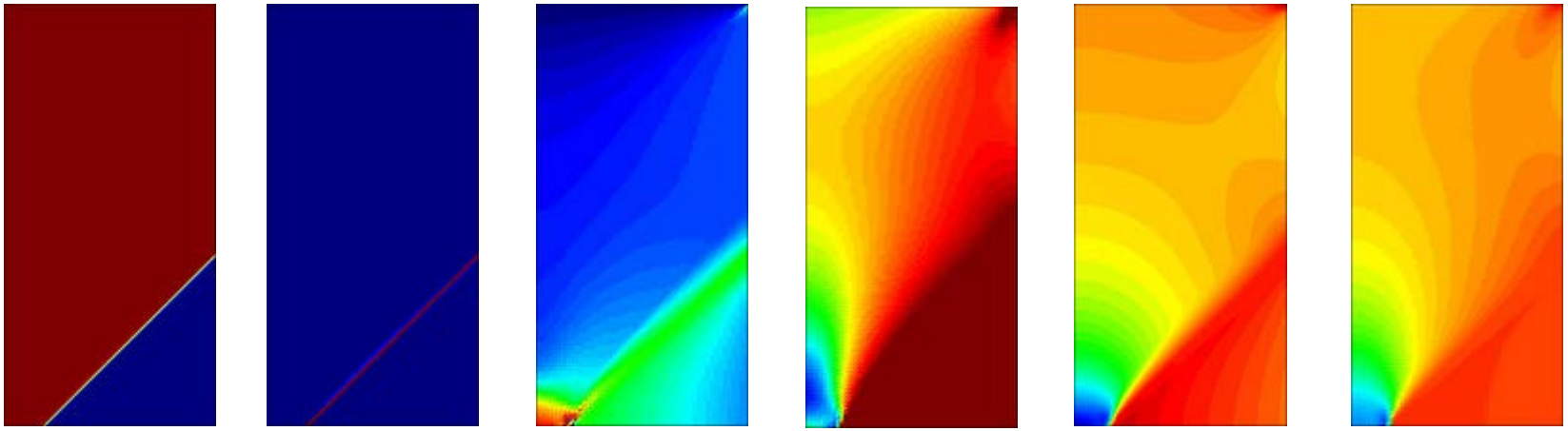

(a) (b) (c) (d) (e) (f)

Figure 4.4 Contour fills for triangular mixed *u*/*p*, FE, von Mises: (a) Y-disp, (b) Equiv. plast. strain, (c) Lode angle, (d) J2 stress, (e) Mean stress, (f) Y-stress

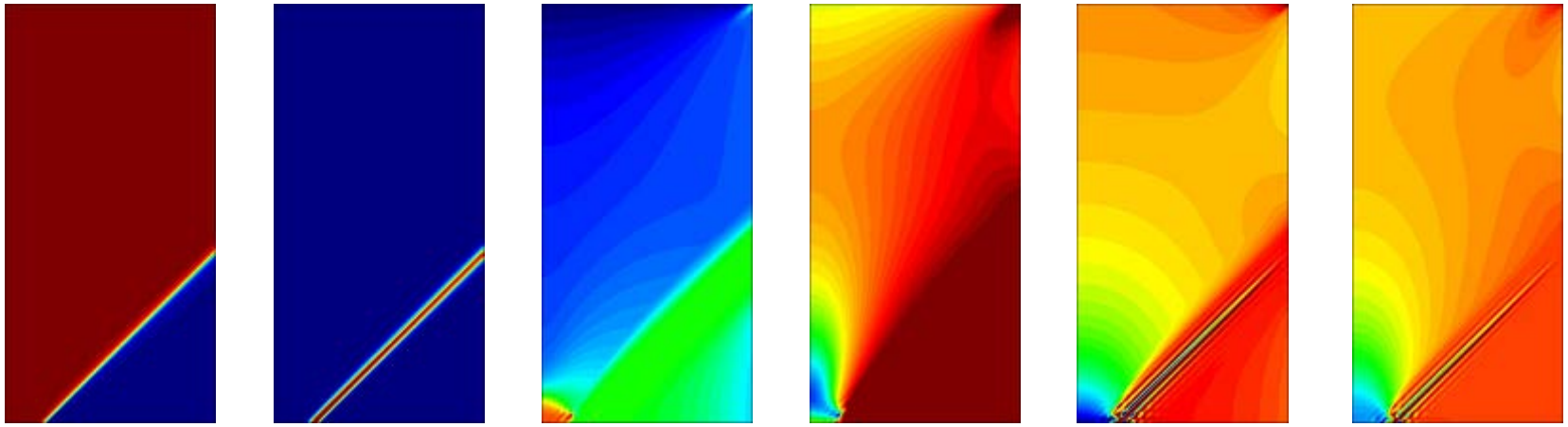

(a) (b) (c) (d) (e) (f)

Figure 4.5 Contour fills for triangular mixed *ε/u* FE, von Mises: (a) Y-disp, (b) Equiv. plast. strain, (c) Lode angle, (d) J2 stress, (e) Mean stress, (f) Y-stress

4.3.2 Quadrilaterals, von Mises: irreducible $\boldsymbol{u}$, B-bar, mixed $\boldsymbol{u/p}$, mixed $\boldsymbol{\varepsilon/u}$ and mixed $\boldsymbol{\varepsilon}$/B-bar $\boldsymbol{u}$ FEs

The vertical reaction–displacement curves for Quads FE for the von Mises yield criterion are shown in Figure 4.6. In some cases, pressure locking leads to overstiff responses. The global response of irreducible $\boldsymbol{u}$ quadrilaterals and mixed $\boldsymbol{\varepsilon/u}$ quadrilaterals is much stiffer than the global responses of the other FEs, which do not show signs of pressure locking.

Figure 4.7 shows the results corresponding to the quadrilateral irreducible $\boldsymbol{u}$ FEs. Results are completely pressure locked, to the extent that no strain localization band can be identified. Note that the results are far worse than those obtained with the triangular mesh; this is only attributable to the favorable orientation of the triangles.

Figure 4.8 shows the results corresponding to the B-bar quadrilateral FEs. The beneficial effect of the selective integration of the volumetric strain and stress introduced by the B-bar procedure is immediately obvious. Good agreement is found with the $\boldsymbol{u/p}$ solution in Figure 4.4, although two differences are noted. One is the wider spread of the displacement jump and the strain localization in the quadrilateral mesh and the other is the obvious piece-wise constant interpolation of the mean-stress, which also shows in the vertical stress.

Figure 4.9 shows the results corresponding to the $\boldsymbol{u/p}$ quadrilateral FEs. These are very similar to those of the B-bar element, apart from displaying an inter-element continuous interpolation of the pressure.

Figure 4.10 shows the results for the mixed $\boldsymbol{\varepsilon/u}$ quadrilaterals. Like for their triangular counterparts, the solution appears to be significantly pressure-locked.

Finally, Figure 4.11 shows the results for the mixed $\boldsymbol{\varepsilon}$/B-bar $\boldsymbol{u}$ quadrilaterals. As for their irreducible B-bar counterpart, pressure locking is overcome and the results are satisfactory.

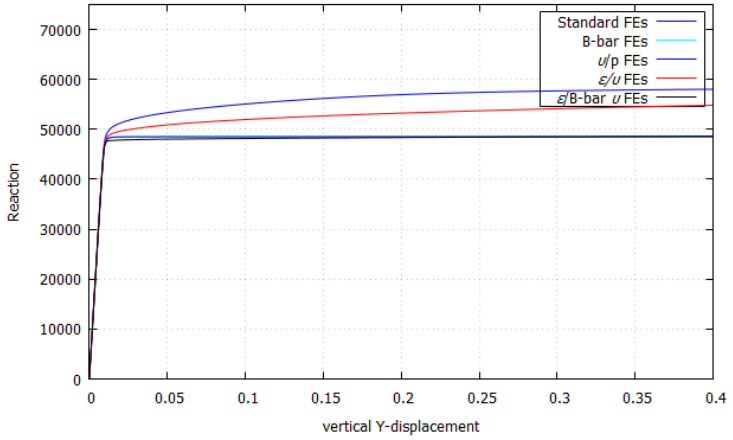

Figure 4.6 Evolution curves of vertical reaction–displacement for Quads FE for the von Mises yield criterion

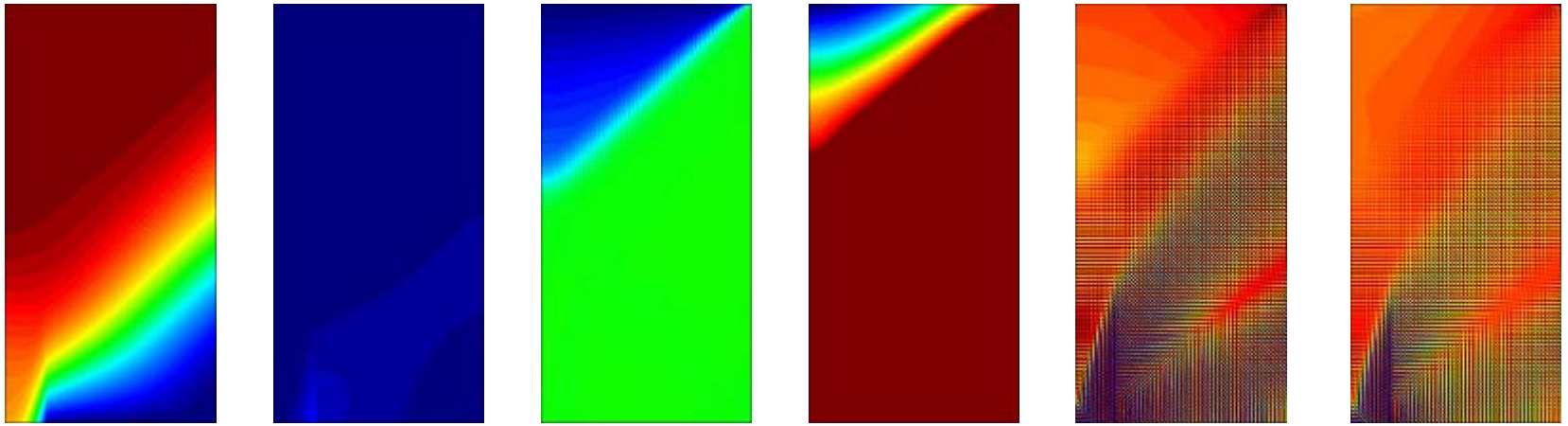

(a) (b) (c) (d) (e) (f)

Figure 4.7 Contour fills for quadrilaterals irreducible FE, von Mises: (a) Y-disp, (b) Equiv. plast. strain, (c) Lode angle, (d) J2 stress, (e) Mean stress, (f) Y-stress

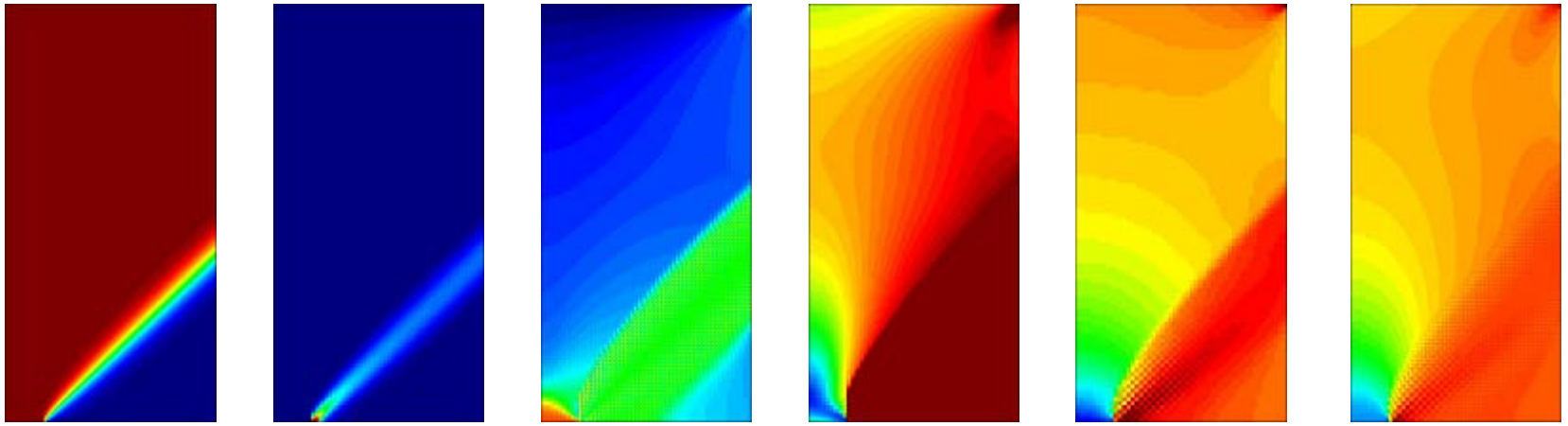

(a) (b) (c) (d) (e) (f)

Figure 4.8 Contour fills for quadrilaterals B-bar FE, von Mises: (a) Y-disp, (b) Equiv. plast. strain, (c) Lode angle, (d) J2 stress, (e) Mean stress, (f) Y-stress

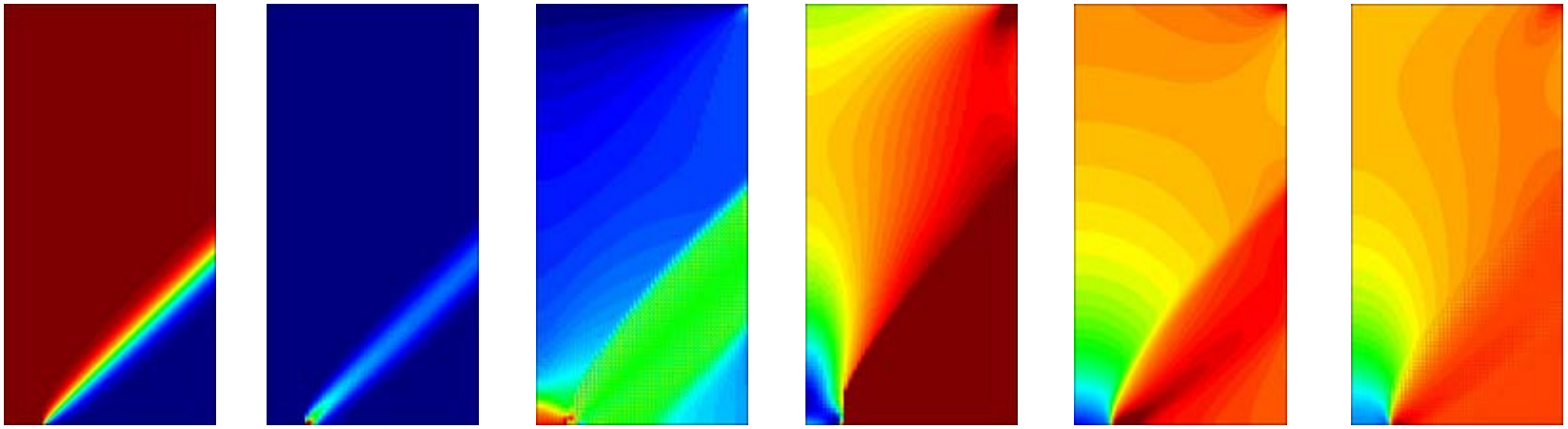

(a) (b) (c) (d) (e) (f)

Figure 4.9 Contour fills for quadrilaterals mixed *u/p* FE, von Mises: (a) Y-disp, (b) Equiv. plast. strain, (c) Lode angle, (d) J2 stress, (e) Mean stress, (f) Y-stress

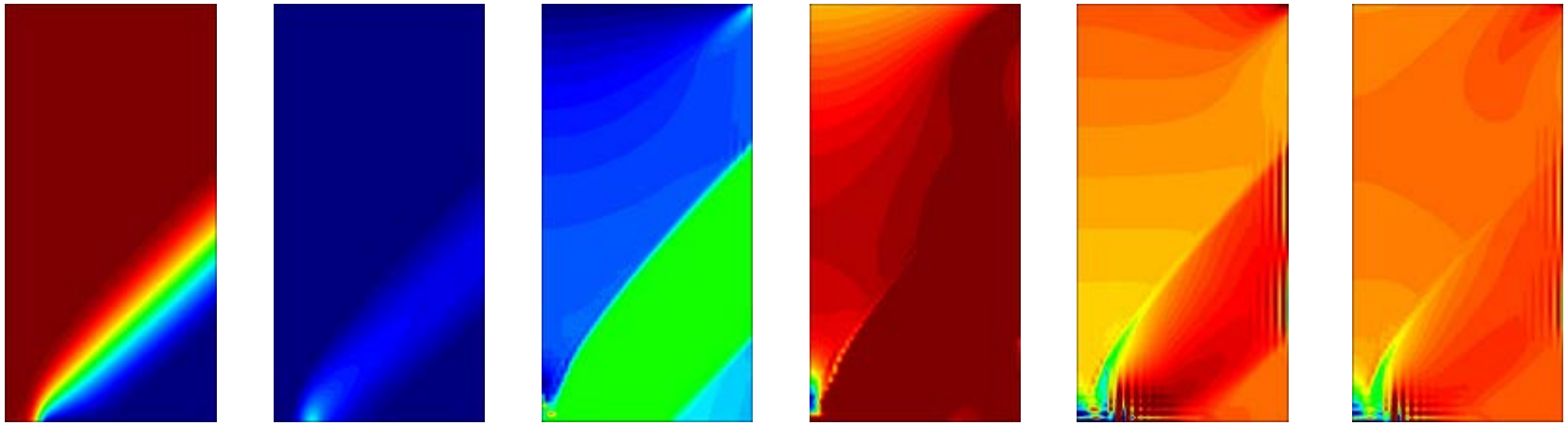

(a) (b) (c) (d) (e) (f)

Figure 4.10 Contour fills for quadrilaterals mixed *ε/u* FE, von Mises: (a) Y-disp, (b) Equiv. plast. strain, (c) Lode angle, (d) J2 stress, (e) Mean stress, (f) Y-stress

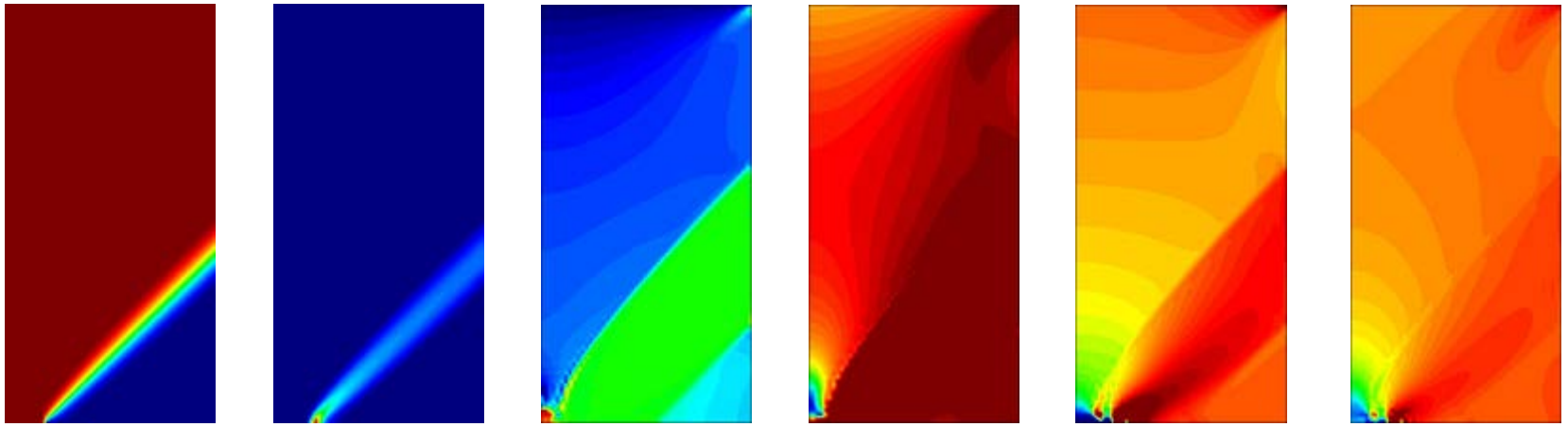

(a) (b) (c) (d) (e) (f)

Figure 4.11 Contour fills for quads mixed *ε/B-bar u* FE, von Mises: (a) Y-disp, (b) Equiv. plast. strain, (c) Lode angle, (d) J2 stress, (e) Mean stress, (f) Y-stress

4.3.3 Quadrilaterals, Drucker-Prager: irreducible $\boldsymbol{u}$, B-bar, mixed $\boldsymbol{\varepsilon/u}$ and mixed $\boldsymbol{\varepsilon}$/B-bar $\boldsymbol{u}$ FEs

Isotropic Ducker–Prager plasticity with compressive strength f^c = 1.5 × 10⁴ MPa and tensile strength f^t = 1.0 × 10⁴ MPa is now considered. Under plane strain, uniaxial tensile tests show localization angles at + 24.0948° from the horizontal axis, measured in a counter-clockwise manner.

The vertical reaction–displacement curves for Quads FE for the Ducker–Prager yield criterion are shown in Figure 4.12. The global responses of all FEs are satisfactory, and no signs pressure locking are observed.

Figure 4.13 shows the results corresponding to the quadrilateral irreducible $\boldsymbol{u}$ FEs. The plastic flow is frictional and not isochoric; therefore, no pressure locking occurs and the failure mechanism and strain localization band are properly obtained. However, the poor capacity of the standard quadrilateral to approximate the localized strain field and the ensuing stress field shows in all the contour-fills related to the stresses.

Figure 4.14 shows the results corresponding to the B-bar quadrilaterals. They are almost identical to those of Figure 4.13, because the poor results of the standard elements are not related to volumetric locking.

Figure 4.15 shows the results for the mixed $\boldsymbol{\varepsilon/u}$ quadrilaterals. Here the solution is remarkably satisfactory is all the represented fields.

Finally, Figure 4.16 shows the results for the mixed ε/B-bar u quadrilaterals. They are practically identical to those in Figure 4.14.

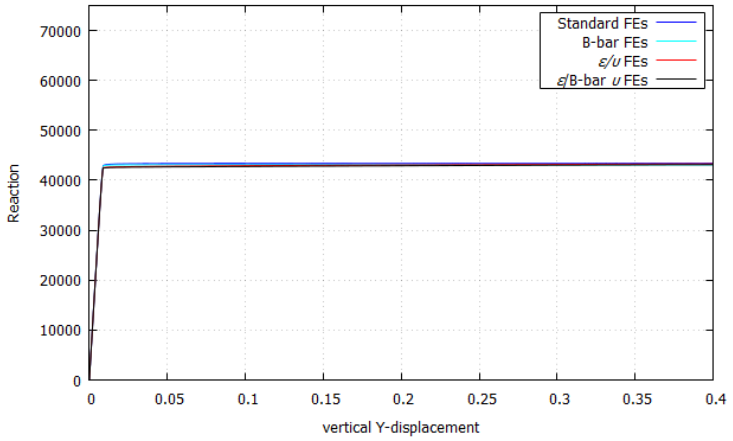

Figure 4.12 Evolution curves of vertical reaction–displacement for Quads FE for the Ducker–Prager yield criterion

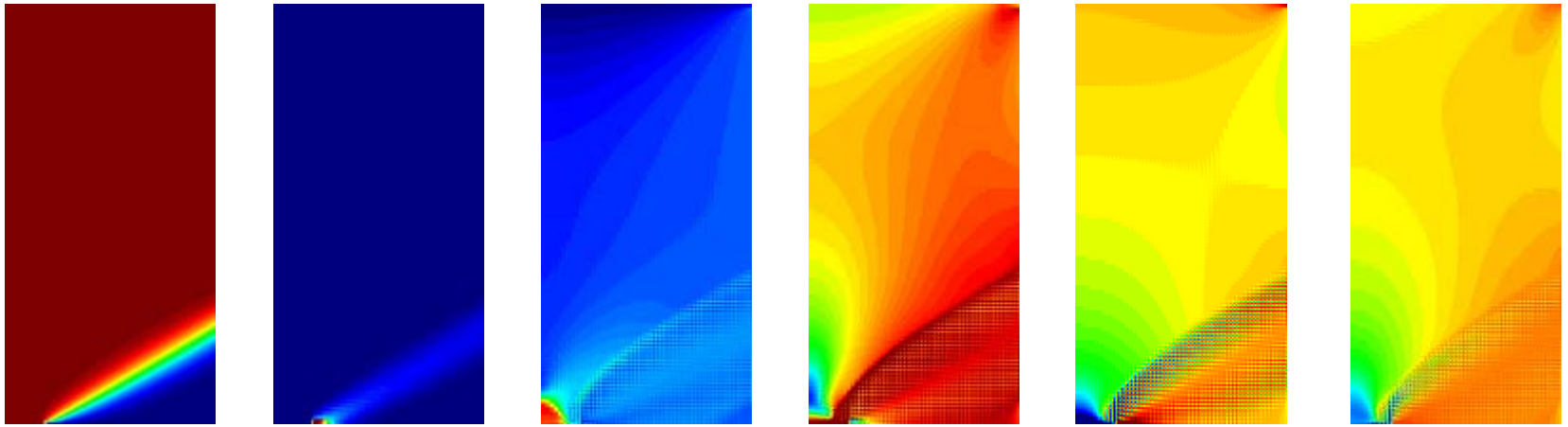

(a) (b) (c) (d) (e) (f)

Figure 4.13 Contour fills for quads irreducible FE, Drucker-Prager: (a) Y-disp, (b) Equiv. plast. strain, (c) Lode angle, (d) J2 stress, (e) Mean stress, (f) Y-stress

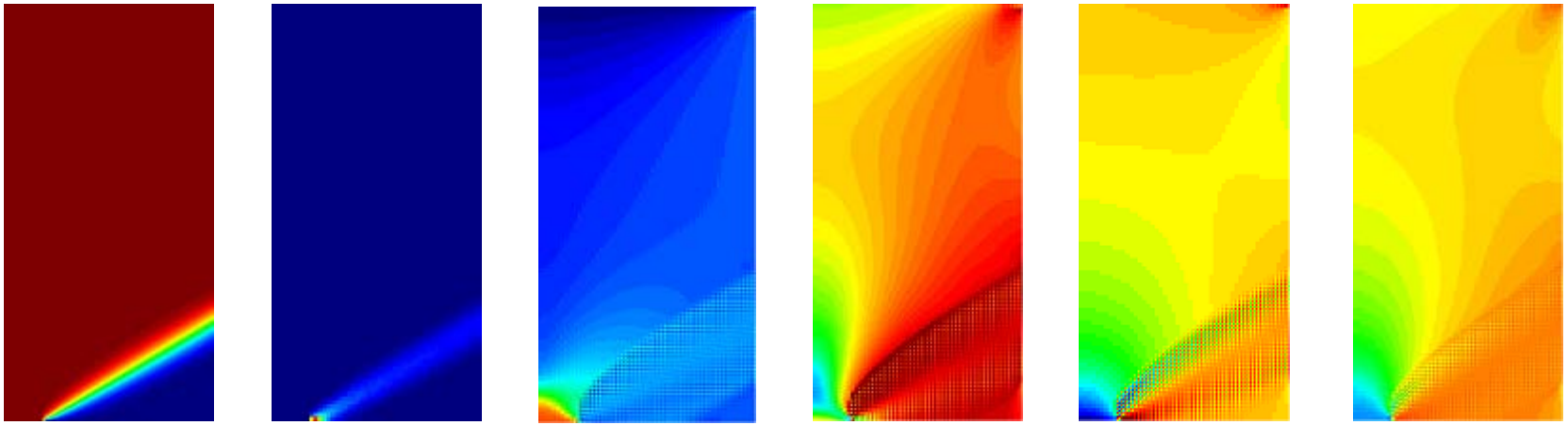

(a) (b) (c) (d) (e) (f)

Figure 4.14 Contour fills for quads B-bar FE, Drucker-Prager: (a) Y-disp, (b) Equiv. plast. strain, (c) Lode angle, (d) J2 stress, (e) Mean stress, (f) Y-stress

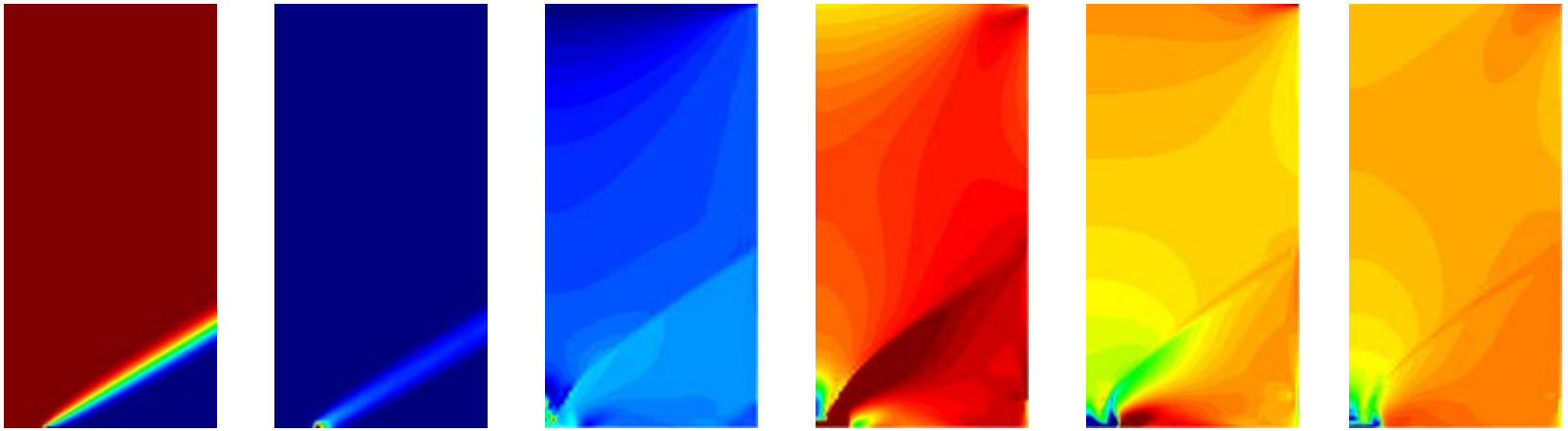

(a) (b) (c) (d) (e) (f)

Figure 4.15 Contour fills for quads mixed *ε/ u* FE, , Drucker-Prager: (a) Y-disp, (b) Equiv. plast. strain, (c) Lode angle, (d) J2 stress, (e) Mean stress, (f) Y-stress

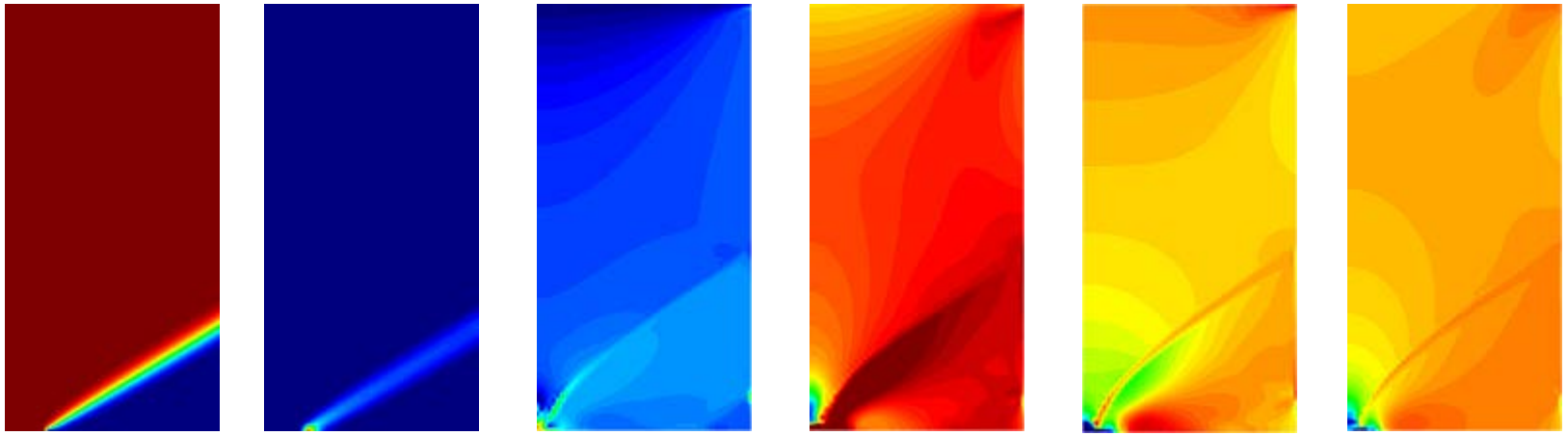

(a) (b) (c) (d) (e) (f)

Figure 4.16 Contour fills for quads mixed *ε/B-bar u* FE, Drucker-Prager: (a) Y-disp, (b) Eq.. plast. strain, (c) Lode angle, (d) J2 stress, (e) Mean stress, (f) Y-stress

Chapter 5

Conclusion

The outline of this concluding Chapter is as follows. Section 5.1 summarizes this doctoral thesis. Section 5.2 lists the conclusions of the work. Section 5.3 presents main contributions. Section 5.4 suggests the lines for future research.

5.1 Summary

In this doctoral thesis, Chapter 2 briefly introduces elastic, plastic, compressible and incompressible material behavior, in 3D as well as plane strain and plane stress conditions. The elasto-plastic constitutive equations are summarized and the several yield criteria used for orthotropic materials are presented in a unified format. Additionally, the yield criteria are graphically represented in HW stress space.

Chapter 3 introduces the topic of strain bifurcation and localization in elasto-plastic materials, summarizes the scientific contributions of three papers and presents some complementary contents on the topic of the dependence of the strain localization angles on the degree of orthotropy and friction.

The mechanics of strain localization is addressed analytically and numerically in isotropic and orthotropic materials, with cohesive and frictional plastic flows, following associated and non-associated flow rules, both in the continuous and the discrete settings.

Plastic yielding and strain bifurcation are identified in the failure process as prior to the strain localization. The necessary conditions for their occurrence and their respective correlations and differences are described. Stress rate boundedness is established as a necessary condition for the occurrence of strain localization, in addition to Maxwell's discontinuity kinematics and traction rate continuity, classical conditions for strain bifurcation.

The strain localization angles can be analytically derived from the strain localization condition in a relatively straight-forward manner. These localization angles depend exclusively on the plastic flow tensor, but are not related to the elastic moduli or the yield surface. This applies equally to

isotropic and orthotropic, cohesive and frictional materials using associated or non-associated flow rules. And it is contrasting with the conclusions drawn from the classical bifurcation condition, where the directions for strain bifurcation are derived from the eigen-analysis of the elasto-plastic acoustic tensor.

When the localization condition is not fulfilled at the same time as strain bifurcation occurs, a transition stage ensues in-between. During the transition phase, the plastic flow evolves to match the strain localization condition.

The analytical strain localization angles derived from the strain localization condition are verified through independent numerical simulations. In the discrete setting, localization angles do not depend on mesh bias or resolution. All the analytical conditions for strain localization from the continuous setting are met on mesh refinement. All this is compelling evidence of the relevance and applicability of the strain localization condition.

Chapter 4 compares several irreducible and mixed finite element formulations with regard to their performance concerning strain approximation in the accurate and locking-free analysis of beams, plates and shells using solid elements, and in strain localization stemming from plastic flow concentrating in narrow bands.

Regarding the analysis of beams, plates and shells, it is known from antique that standard finite elements pose difficulties such as lack of accuracy, mesh sensitivity or stress locking phenomena in those particular instances. A contributed paper shows that the proposed mixed $\boldsymbol{\varepsilon}/\boldsymbol{u}$ and mixed $\boldsymbol{\varepsilon}$/B-bar $\boldsymbol{u}$ finite elements largely overcome those difficulties. Stabilization methods and parameters in mixed formulations are described and appropriate stabilization parameters are suggested. Furthermore, the influence of the stabilization parameter is investigated. In addition, the proposed mixed FEs are compared with the previously developed solid-shell and EAS FEs.

The chapter includes complementary contents on the performance of the different finite element formulations with regard to strain localization. These show that the orientation of the strain localization of plasticity can be predicted with the proposed mixed $\boldsymbol{\varepsilon}$/B-bar $\boldsymbol{u}$ FEs used.

5.2 Conclusions

The following conclusions can be drawn from the work presented in this thesis:

Conclusions on the strain localization in plasticity

- The distinct conditions for plastic yielding, strain bifurcation and strain localization are investigated. In addition to Maxwell's kinematics and continuity of the traction rate for strain bifurcation, an additional condition stating the objectivity (and boundedness) of the stress rate is necessary for strain localization condition.
- The condition for strain localization is more restrictive than the classical continuous/discontinuous strain bifurcation, though both account for the plastic loading/unloading and loading/loading scenarios.
- The angles of the directions at which strain localization occurs can be analytically derived from the proposed strain localization condition. This derivation is applicable to isotropic and orthotropic, cohesive and frictional, associated and non-associated elastoplastic models. The analytical results are numerically verified through independent simulations.

- The localization angles of the discontinuity band (surface) depend only on the specific stress state and the corresponding plastic flow tensor in the material axes; neither he material elastic properties nor the yield function are relevant to their determination.
- The dependence of the analytical localization angles on the degree of orthotropy and on friction is investigated. It is found that the tangent of the strain localization angle and the f_x/f_y ratio of orthotropic strengths are inversely proportional for Hill's orthotropic plasticity. For the Drucker–Prager yield criterion, the strain localization angles under uniaxial tension and compression are identical for reciprocal values of the compressive to tensile strengths ratios.
- The failure mechanisms formed in isotropic and orthotropic plasticity are numerically reproduced considering associated and non-associated plasticity. The numerical results match the analytical predictions remarkably.
- For perfectly and softening plastic solids with either associated or non-associated evolution laws, upon strain localization and thereafter, the stresses inside the discontinuity band are indeed independent of the discrete localization bandwidth.
- The stress rate inside the discontinuity band is independent from the mesh size and the resulting discontinuity bandwidth.
- During the stage in-between strain bifurcation and strain localization, the plastic flow changes progressively in order to meet the strain localization condition.
- In evolving problems the accumulated plastic strain may affect the final failure mechanism.

Conclusions on the performance of different finite elements formulations

- The mixed ***ε/u*** FEs far outperforms the corresponding standard FEs in displacement and stress estimation, providing shear and membrane locking-free solutions.
- The mixed ***ε/u*** FEs also perform well with different element typologies (hexahedra and prisms) and mesh configurations (regular, skewed and warped).
- The use of the B-bar method is beneficial to the performance of the The mixed ***ε/u*** formulation in quasi-incompressible situations, guaranteeing convergence of displacements and stresses.
- FEs with independent interpolation for displacement and strain are an effective alternative that can provide simulation of complex stress states of beam, shell and plate structures with improved accuracy.

5.3 Scientific contributions

The main contributions of the thesis are:

- An in-depth study on the mechanics of the strain localization in isotropic and orthotropic material models considering plastic incompressibility was carried out. Such mechanics apply to metals, which behave as incompressible plastic materials.

- An in-depth study on the mechanics of the strain localization in isotropic and orthotropic material models considering frictional–cohesive plasticity was carried out. Such mechanics apply to rock, concrete, polymers, foams and other materials whose behavior depends on pressure can be modeled.
- An in-depth study on the mechanics of the strain localization in isotropic and orthotropic material models considering associated and non-associated plasticity was carried out. Such mechanics apply to, for example, soft clay, sand and rock.
- The Lode angle was used for identification of the strain localization condition.
- A comparative study of several FE formulations was conducted with regards to of beams, plates and shells behavior.
- A comparative study of several FEs was conducted with regard to their strain localization capabilities.
- All contributions were developed and implemented in the in-house FE code COMET (COupled MEchanical and Thermal analysis)

5.4 Lines of future research

In this thesis, strain localization analysis for plasticity and mixed FEs were investigated. The following lines of future research need to be pursued:

- **Softening plasticity.** The current research mainly considers perfect plasticity. Additional research is needed to assess the effect of softening in the failure mechanism of elasto-plastic solids.
- **Hardening plasticity.** Strain bifurcation may occur in non-associate elasto-plastic solid. The corresponding effect on strain bifurcation needs to be investigated.
- **Damage–plasticity.** In this thesis, only the plasticity is considered in the mechanics of strain localization. Coupled damage and plasticity is of interest in several applications, and the present framework may be easily extended to include it.
- **Failure under alternate loading.** In a cohesive-frictional material, different plastic flows will stem from loading in tension and compression. Under alternate loading, these two plastic flows interact in a non-evident fashion.
- **Large strains.** The use of nonlinear kinematics need to be studied with regard strain localization because of two distinct reasons. First, because kinematics after strain localization occurs are expected to be nonlinear. Second, to study strain localization conditions in materials that experience nonlinear kinematics before failure occurs.

References

[1] Hooke, R. De Potentia Restitutiva, or, of spring Explaining the Power of Springing Bodies, London, **1678**.

[2] L. Euler, Mémoires de l'académie des sciences de Berlin **1752**, Volume 6, pp. 185–217.

[3] Cauchy, A. Résumé des leçons sur le calcul infinitesimal, Ellipses, **1823**.

[4] Poisson, S. Mémoire sur les équations générales de l'équilibre et du mouvement des corps solides élastiques et des fluids, *Journal de l'École polytechnique* **1831**.

[5] Coulomb, C.A. Essai sur une application des regles de maximis et minimis quelques problemes de statique, relatits a l'architecture. *Memoires de Mathematique de l'Academie Royale de Science 7*, Paris, **1776**.

[6] Tresca, H. Mémoire sur l'écoulement des corps solides soumis à de fortes pressions. *Comptes rendus hebdomadaires des séances de l'Académie des Sciences* **1864**, Volume 18, Issue 59, pp. 754–758.

[7] de Saint-Venant, B.: Sur l'établissement des équations des mouvements intérieurs operes dans les corps solides ductiles au delà des limites où l'élasticité pourrait les ramener à leur premier état. *Comptes Rendus des Séances de l'Académie des Sciences. Paris* **1870**, pp. 368–369.

[8] Lévy, M. Mémoire sur les équations générales des mouvements intérieurs des corps solides ductiles au delà des limites où l'élasticité pourrait les ramener à leur premierétat. *Comptes Rendus des Séances de l'Académie des Sciences Paris* **1870**, pp. 1323–1325.

[9] von Mises, R. Mechanik der festen Körper im plastisch-deformablen Zustand. *Nachrichten von der Gesellschaft der Wissenschaften zu Göttingen, Mathematisch-Physikalische Klasse* **1913**, Volume 1, pp. 582–592.

[10] Hencky, H. Zur Theorie plastischer Deformationen und der hierdurch im Material hervorgerufenen Nachspannungen. *Zeitschrift für Angewandte Mathematik und Mechanik* **1924**, Volume 4, Issue 4, pp. 323–334 (In German). https://doi.org/10.1002/zamm.19240040405

[11] Prandtl, L. Über die Härte plastischer Körper. *Nachrichten der Gesellschaft der Wissenschaften zu Göttingen, Mathematisch physikalische Klasse* **1920**, pp. 74–85 (In German). https://doi.org/10.1007/978-3-662-11836-8_7

[12] Reuss, A. Berücksichtigung der elastischen Formänderung in der Plastizitätstheorie. *ZAMM-Journal of Applied Mathematics and Mechanics/Zeitschrift für Angewandte Mathematik und Mechanik* **1930**, Volume 10, Issue 3, pp. 266–274.

[13] Hill, R. A theory of the yielding and plastic flow of anisotropic metals. *Proceedings of the Royal Society A: Mathematical, Physical and Engineering Sciences* **1948**, London, Volume 193, Issue 1033, pp. 281–297. https://doi.org/10.1098/rspa.1948.0045

[14] Hill, R. The plastic yielding of notched bars under tension. *The Quarterly Journal of Mechanics and Applied Mathematics* **1949**, Volume 2, Issue 1, pp. 40–52. https://doi.org/10.1093/qjmam/2.1.40

[15] Mohr, O. Welche Umstände bedingen die Elastizitätsgrenze und den Bruch eines Materials? *Zeitschrift des Vereins Deutscher Ingenieure* **1900**, Volume 24, pp. 1524–1530 and 1572–1577.

[16] Drucker, D.C; Prager, W; Greenberg, H. Extended limit design theorems for continuous media. *Quarterly of Applied Mathematics* **1952**, Volume 9, pp. 381–389. https://doi.org/10.1090/qam/45573

[17] Raghava, R.; Caddell, R.M.; Yeh, G.S. The Macroscopic Yield Behaviour of Polymers. *Journal of Materials Science* **1973**, Volume 8, pp. 225–232. https://doi.org/10.1007/BF00550671

[18] Iordache, M.M.; Willam, K. Localized failure analysis in elastoplastic Cosserat continua. *Computer Methods in Applied Mechanics and Engineering* **1998**, Volume 151, Issues 3–4, pp. 559–586. https://doi.org/10.1016/S0045-7825(97)00166-7

[19] Hansen, E.; Willam, K.; Carol, I. A two-surface anisotropic damage/plasticity model for plain concrete, *Fracture mechanics of concrete materials de Borst, R. (Ed.), A.A. Balkema, Rotterdam* **2001**, pp. 549–556.

[20] Hoffman, O. The Brittle Strength of Orthotropic Materials, *Journal of Composite Materials* **1967**, Volume 1, Issue 2, pp. 200–206. https://doi.org/10.1177/002199836700100210

[21] Tsai, S.; Wu, E. A general theory of strength for anisotropic materials. *Journal of Composite Materials* **1971**, Volume 5, Issue 1, pp. 58–80. https://doi.org/10.1177/002199837100500106

[22] Bresler, B.; Pister, K.S. Strength of concrete under combined stresses, *ACI Journal Proceedings* **1958**, Volume 551, Issue 9, pp. 321–345.

[23] Podgórski, J. Limit state condition and the dissipation function for isotropic materials, *Archives of Mechanics* **1984**, Volume 36, Issue 3, pp. 323–342.

[24] Barlat, F.; Lege, D.J.; Brem, J.C. A six-component yield function for anisotropic materials. *International Journal of Plasticity* **1991**, Volume 7, Issue 7, pp. 693–712. https://doi.org/10.1016/0749-6419(91)90052-Z

[25] Barlat, F.; Lian, J. Plastic behavior and stretchability of sheet metals. Part I: A yield function for orthotropic sheets under plane stress conditions. *International Journal of Plasticity* **1989**, Volume 5, Issue 1, pp. 51–66. https://doi.org/10.1016/0749-6419(89)90019-3

[26] Barlat, F.; Brem, J. C.; Yoon, J. W.; Chung, K.; Dick, R.E.; Lege, D. J.; Pourboghrat, F.; Choi, S.H.; Chu, E. Plane stress yield function for aluminum alloy sheets—part 1: theory. *International Journal of Plasticity* **2003**, Volume 19, Issue 9, pp. 1297–1319. https://doi.org/10.1016/S0749-6419(02)00019-0

[27] Bigoni, D.; Piccolroaz, A. Yield criteria for quasibrittle and frictional materials, *International Journal of Solids and Structures* **2004**, Volume 41, Issues 11–12, pp. 2855–2878. https://doi.org/10.1016/j.ijsolstr.2003.12.024

[28] Gdoutos, E.E.; Abot, J.L. Indentation of a PVC Cellular Foam. *Recent Advances in Experimental Mechanics* **2002**, pp. 55–64. https://doi.org/10.1007/0-306-48410-2_6

[29] Gdoutos, E.; Daniel, I.; Wang, K.-A. Failure of cellular foams under multiaxial loading. *Composites Part A: Applied Science and Manufacturing* **2002**, Volume 33, Issue 2, pp. 163–176. https://doi.org/10.1016/S1359-835X(01)00110-5

[30] Qiao, Y.; Bisagni, C.; Bai, Y. Experimental investigation and numerical simulation of unidirectional carbon fiber composite under multi-axial loadings. *Composites Part B: Engineering* **2017**, Volume 124, pp. 190–206. https://doi.org/10.1016/j.compositesb.2017.05.034

[31] Zhong, C. Pressure Chamber Experiments to Determine Triaxial Material Properties of Polymer Foams. Ph.D. Thesis, University of Akron, Akron, OH, USA, 2019.

[32] Galavi, V; Schweiger, H.F. Nonlocal Multilaminate Model for Strain Softening Analysis. *International Journal of Geomechanics* **2010**, Volume 10, Issue 1, pp. 30–44. https://doi.org/10.1061/(ASCE)1532–3641(2010)10:1(30)

[33] Hencky, H. Über Einige Statisch Bestimmte Fälle Des Gleichgewichts In Plastischen Körpern. *Zeitschrift für Angewandte Mathematik und Mechanik* **1923**, Volume 3, Issue 4, pp. 241–251 (In German). https://doi.org/10.1002/zamm.19230030401

[34] Mandel J. Sur les équilibres par tranches planes des corps solides à la limite d'écoulement. Thèses de docteur ès-sciences, Université de Lyon, Lyon, 1942. (In French) http://www.numdam.org/issue/THESE_1942__251__1_0.pdf

[35] Hill, R. A general theory of uniqueness and stability in elastic-plastic solids. *Journal of the Mechanics and Physics of Solids* **1958**, Volume 6, Issue 3, pp. 236–249. https://doi.org/10.1016/0022-5096(58)90029-2

[36] Hill, R. Acceleration waves in solids. *Journal of the Mechanics and Physics of Solids* **1962**, Volume 10, Issue 1, pp. 1–16. https://doi.org/10.1016/0022-5096(62)90024-8

[37] Thomas, T.Y. *Plastic Flow and Fracture of Solids*. Academic Press, New York, USA, **1961**.

[38] Rice, J.R. A path independent integral and the approximate analysis of strain concentration by notches and cracks. *Journal of Applied Mechanics* **1968**, Volume 35, Issue 2, pp. 379–386. https://doi.org/10.1115/1.3601206

[39] Rice, J.R. Plane strain slip line theory for anisotropic rigid/plastic materials. *Journal of the Mechanics and Physics of Solids* **1973**, Volume 21, Issue 2, pp. 63–74. https://doi.org/10.1016/0022-5096(73)90030-6

[40] Rudnicki, J.W., Rice, J.R. Conditions for the localization of deformation in pressure-sensitive dilatant materials. *Journal of the Mechanics and Physics of Solids* **1975**, Volume 23, Issue 6, pp. 371–394. https://doi.org/10.1016/0022-5096(75)90001-0

[41] Rice, J.R. The localization of plastic deformation. *Proc. of the 14th International Congress on Theoretical and Applied Mechanics* **1976**, North-Holland Publishing Co., Delft, Netherlands, pp. 207–220.

[42] Rice, J.R.; Rudnicki, J.W. A note on some features of the theory of localization of deformation. *International Journal of Solids and Structures* **1980**, Volume 16, Issue 7, pp. 597–605. https://doi.org/10.1016/0020-7683(80)90019-0

[43] Bigoni, D.; Hueckel, T. Uniqueness and localization— I. Associative and non-associative elastoplasticity. *International Journal of Solids and Structures* **1991**, Volume 28, Issue 2, pp. 197–213. https://doi.org/10.1016/0020-7683(91)90205-T

[44] Bigoni, D.; Hueckel, T. Uniqueness and localization—II. Coupled elastoplasticity. *International Journal of Solids and Structures* **1991**, Volume 28, Issue 2, pp. 215–224. https://doi.org/10.1016/0020-7683(91)90206-U

[45] Neilsen, M.K.; Schreyer, H.L. Bifurcations in elastic-plastic materials. *International Journal of Solids and Structures* **1993**, Volume 30, Issue 4, pp. 521–544. https://doi.org/10.1016/0020-7683(93)90185-A

[46] Ottosen, N.S.; Runesson, K. Properties of discontinuous bifurcation solutions in elasto-plasticity, *International Journal of Solids and Structures* **1991**, Volume 27, Issue 4, pp. 401–421.

[47] Leroy, Y.; Ortiz, M. Finite element analysis of transient strain localization phenomena in frictional solids. *International journal for numerical and analytical methods in geomechanics* **1990**, Volume 14, Issue 2, pp. 93–124. https://doi.org/10.1002/nag.1610140203

[48] Borja, R.I. A finite element model for strain localization analysis of strongly discontinuous fields based on standard Galerkin approximation. *Computer Methods in Applied Mechanics and Engineering* **2000**. Volume 190, Issues 11–12, pp. 1529–1549. https://doi.org/10.1016/S0045-7825(00)00176-6

[49] Borja, R.I. Finite element simulation of strain localization with large deformation: capturing strong discontinuity using a Petrov–Galerkin multiscale formulation. *Computer Methods in Applied Mechanics and Engineering* **2002**. Volume 191, Issues 27–28, pp. 2949–2978. https://doi.org/10.1016/S0045-7825(02)00218-9

[50] Forest, S.; Blazy, J.-S.; Chastel, Y.; Moussy, F. Continuum modeling of strain localization phenomena in metallic foams. *Journal of Materials Science* **2005**, Volume 40, Issue 22, pp. 5903–5910. https://doi.org/10.1007/s10853-005-5041-6

[51] Kuhl, E; Ramm, E; Willam, K. Failure analysis of elasto-plastic material models on different levels of observation, *International Journal of Solids and Structures* **2000**, Volume 37, Issues 48–50, pp. 7259–7280. https://doi.org/10.1016/S0020-7683(00)00198-0

[52] Liebe, T.; Willam, K. Localization Properties of Generalized Drucker-Prager Elastoplasticity. *Journal of Engineering Mechanics* **2001**, Volume 127, Issue 6, pp. 616–619. https://doi.org/10.1061/(ASCE)0733-9399(2001)127:6(616)

[53] Zhang, Y.Q.; Lu, Y.; Qiang, H.F. Influence of damage on properties of strain localization in geomaterials at plane stress and plane strain. *Archive of Applied Mechanics* **2004**, Volume 74, Issues 1–2, pp. 102–117. https://doi.org/10.1007/BF02637212

[54] Vrech, S.M.; Etse, G. Geometrical localization analysis of gradient-dependent parabolic Drucker–Prager elastoplasticity. *International Journal of Plasticity* **2006**, Volume 22, Issue 5, pp. 943–964. https://doi.org/10.1016/j.ijplas.2005.07.002

[55] Tasan, C.C.; Hoefnagels, J.P.M.; Diehl, M.; Yan, D.; Roters, F.; Raabe, D. Strain localization and damage in dual phase steels investigated by coupled in-situ deformation experiments and crystal plasticity simulations. *International Journal of Plasticity* **2014**, Volume 63, pp. 198–210. https://doi.org/10.1016/j.ijplas.2014.06.004

[56] Simo, J.C.; Oliver, J.; Armero, F. An analysis of strong discontinuities induced by strain-softening in rate-independent inelastic solids. *Computational Mechanics* **1993**, Volume 12, Issues 5, pp. 277–296. https://doi.org/10.1007/bf00372173

[57] Oliver, J. Modelling strong discontinuities in solid mechanics via strain softening constitutive equations. Part 1: Fundamentals. *International Journal for Numerical Methods in* Engineering **1996**, Volume 39, Issues 21, pp. 3575–3600. https://doi.org/10.1002/(SICI)1097-0207(19961115)39:21<3575::AID-NME65>3.0.CO;2-E

[58] Oliver, J. Modelling strong discontinuities in solid mechanics via strain softening constitutive equations. Part 2: Numerical simulation. *International Journal for Numerical Methods in Engineering* **1996**, Volume 39, Issues 21, pp. 3601–3623. https://doi.org/10.1002/(SICI)1097-0207(19961115)39:21<3601::AID-NME64>3.0.CO;2-4

[59] Oliver, J. On the discrete constitutive models induced by strong discontinuity kinematics and continuum constitutive equations. *International Journal of Solids and Structures* **2000**, Volume 37, Issues 48–50, pp. 7207–7229. https://doi.org/10.1016/S0020-7683(00)00196-7

[60] Oliver, J. Topics on failure mechanics. *Monograph M68, Centre Internacional de Mètodes Numèrics en Enginyeria (CIMNE)*, Barcelona, **2002**.

[61] Oliver, J.; Cervera, M; Manzoli. On the Use of Strain-Softening Models for the Simulation of Strong Discontinuities in Solids. IUTAM Symposium **1997**, pp. 107–123.

[62] Oliver, J.; Cervera, M; Manzoli, O. Strong discontinuities and continuum plasticity models: the strong discontinuity approach. *International Journal of Plasticity* **1999**, Volume 15, Issue 3, pp. 319–351. https://doi.org/10.1016/S0749-6419(98)00073-4

[63] Hillerborg, A. The theoretical basis of a method to determine the fracture energyG_F of concrete. *Materials and Structures* **1985**, Volume 18, Issue 4, pp. 291–296. https://doi.org/10.1007/BF02472919

[64] Dvorkin, E.N.; Cuitiño, A.M.; Gioia, G. Finite elements with displacement interpolated embedded localization lines insensitive to mesh size and distortions. *International Journal for Numerical Methods in Engineering* **1990**, Volume 30, Issue 3, pp. 541–564. https://doi.org/10.1002/nme.1620300311

[65] Lotfi, H.R.; Shing, P.B. Embedded representation of fracture in concrete with mixed finite elements. *International Journal for Numerical Methods in Engineering* **1995**, Volume 38, Issue 8, pp. 1307–1325. https://doi.org/10.1002/nme.1620380805

[66] Oliver, J.; Huespe, A.E.; Cante, J.C.; Díaz, G. On the numerical resolution of the discontinuous material bifurcation problem. *International Journal for Numerical Methods in Engineering* **2010**, Volume 83, pp. 786–804. https://doi.org/10.1002/nme.2870

[67] Cervera, M; Chiumenti, M.; Capua, D.D. Benchmarking on bifurcation and localization in J2 plasticity for plane stress and plane strain conditions. *Computer Methods in Applied Mechanics and Engineering* **2012**, Volumes 241–244, pp. 206–224. https://doi.org/10.1016/j.cma.2012.06.002

[68] Wu, J.; Cervera, M. Strain localization and failure mechanics for elastoplastic damage solids. *Monograph M147, Centre Internacional de Mètodes Numèrics en Enginyeria (CIMNE)*, Barcelona, **2014**. ISBN 978-84-943307-0-4.

[69] Wu, J.Y.; Cervera, M. On the equivalence between traction- and stress-based approaches for the modeling of localized failure in solids. *Journal of the Mechanics and Physics of Solids* **2015**, Volume 82, pp. 137–163. https://doi.org/10.1016/j.jmps.2015.05.016

[70] Wu, J.Y.; Cervera, M. A thermodynamically consistent plastic-damage framework for localized failure in quasi-brittle solids: Material model and strain localization analysis. *International Journal of Solids and Structures* **2016**, Volumes 88–89, Issues 227–247. https://doi.org/10.1016/j.ijsolstr.2016.03.005

[71] Wu, J.Y.; Cervera, M. Strain Localization of Elastic-Damaging Frictional-Cohesive Materials: Analytical Results and Numerical Verification. *Materials* **2017**, Volume 10, Issue 4, pp. 434. https://doi.org/10.3390/ma10040434

[72] Cervera, M.; Wu, J.Y.; Chiumenti, M; Kim, S. Strain localization analysis of Hill's orthotropic elastoplasticity: analytical results and numerical verification. *Computational Mechanics* **2020**, Volume 65, pp. 533–554. https://doi.org/10.1007/s00466-019-01782-4

[73] Kim, S.; Cervera, M.; Wu, J.Y; Chiumenti, M. Strain Localization of Orthotropic Elasto-Plastic Cohesive-Frictional Materials: Analytical Results and Numerical Verification. *Materials* **2021**, Volume 14, pp. 2040. https://doi.org/10.3390/ma14082040

[74] Gatewood, B.E. *Virtual Principles in Aircraft Structures*. Springer, Dordrecht, Netherlands, **1989**.

[75] Bower, A.F. *Applied Mechanics of Solids.* CRC Press, Boca Raton, FL, United States, **2009**.

[76] Prathap, G. The poor bending response of the four-node plane stress quadrilateral. *International Journal for Numerical Methods in Engineering* **1985**, Volume 21, Issue 5, pp. 825–835. https://doi.org/10.1002/nme.1620210505

[77] Bathe, K.J. *Finite element procedures*. Englewood Cliffs, New Jersey, United States, **1996**.

[78] Crisfield, M.A.; Tassoulas, J.L. Non-Linear Finite Element Analysis of Solids and Structures, Volume 1, *Journal of Engineering Mechanics* **1993**, Volume 119, Issue 7, pp. 1504–1505. https://doi.org/10.1061/(asce)0733-9399(1993)119:7(1504)

[79] Zienkiewicz , O.C. Displacement and equilibrium models in the finite element method by B. Fraeijs de Veubeke, Chapter 9, Pages 145–197 of Stress Analysis, Edited by O. C. Zienkiewicz and G. S. Holister, Published by John Wiley & Sons, *International Journal for Numerical Methods in Engineering* **1965**, Volume 52, Issue 3, pp. 287–342. https://doi.org/10.1002/nme.339

[80] Herrmann, L. Elasticity equations for incompressible and nearly incompressible materials by a variational theorem. *American Institute of Aeronautics and Astronautics Journal* **1965**, Volume 3, Issue 10, pp. 1896–1900. https://doi.org/10.2514/3.3277

[81] Hughes, T. J. R.; Cohen, M.; Haroun, M. Reduced and selective integration techniques in the finite element analysis of plates. *Nuclear Engineering and Design* **1978**, Volume 46, Issue 1, pp. 203–222. https://doi.org/10.1016/0029-5493(78)90184-X

[82] Malkus, D.S.; Hughes, T.J.R. Mixed finite element methods — Reduced and selective integration techniques: A unification of concepts. *Computer Methods in Applied Mechanics and Engineering* **1978**, Volume 15, Issue 1, pp. 63–81. https://doi.org/10.1016/0045-7825(78)90005-1

[83] Pian, T. H. H. Derivation of element stiffness matrices by assumed stress distributions. *American* Institute *of Aeronautics and Astronautics Journal* **1964**, Volume 2, Issue 7, pp. 1333–1336. https://doi.org/10.2514/3.2546.

[84] Yamamoto, Y. A Formulation of Matrix Displacement Method. Dept. of Aeronautics and Astronautics, Massachusetts Institute of Technology **1966**.

[85] Stolarski, H.; Belytschko, T. Limitation principles for mixed finite elements based on the Hu-Washizu variational formulation. *Computer Methods in Applied Mechanics and Engineering* **1987**, Volume 60, Issue 2, pp. 195–216. https://doi.org/10.1016/0045-7825(87)90109-5

[86] Simo, J.C.; Rifai, M.S. A class of mixed assumed strain methods and the method of incompatible modes. *International Journal for Numerical Methods in Engineering* **1990**, Volume 29, Issue 8, pp. 1595–1638. https://doi.org/10.1002/nme.1620290802.

[87] Simo, J. C.; Armero, F. Geometrically non-linear enhanced strain mixed methods and the method of incompatible modes. *International Journal for Numerical Methods in Engineering* **1992**, Volume 33, Issue 7, pp. 1413–1449. https://doi.org/10.1002/nme.1620330705

[88] Simo, J.; Armero, F.; Taylor, R. Improved versions of assumed enhanced strain trilinear elements for 3D finite deformation problems. *Computer Methods in Applied Mechanics and Engineering* **1993**, Volume 110, Issue 3, pp. 359–386. https://doi.org/10.1016/0045-7825(93)90215-J

[89] Reddy, B.; Simo, J. Stability and convergence of a class of enhanced strain methods. *SIAM Journal on Numerical Analysis* **1995**, Volume 32, Issue 6, pp. 1705–1728. https://doi.org/10.1137/0732077

[90] Kasper, E.P.; Taylor, R.L. A mixed-enhanced strain method: Part I: Geometrically linear problems. *Computers & Structures* **2000**, Volume 75, Issue 3, pp. 237–250. https://doi.org/10.1016/S0045-7949(99)00134-0

[91] Doherty, W.P.; Wilson, E.L.; Taylor, R.L. *Stress analysis of axisymmetric solids utilizing higher-order quadrilateral finite elements*. University of California, Structural Engineering Laboratory, Berkeley, CA, USA, **1969**.

[92] Zienkiewicz, O.C.; Taylor, R.L.; Too, J.M. Reduced integration technique in general analysis of plates and shells. *International Journal for Numerical Methods in Engineering* **1971**, Volume 3, Issue 2, pp. 275–290. https://doi.org/10.1002/nme.1620030211

[93] Zienkiewicz, O.C.; Bauer, J.; Morgan, K.; Onate, E. A simple and efficient element for axisymmetric shells. *International Journal for Numerical Methods in Engineering* **1977**, Volume 11, Issue 10, pp. 1545–1558. https://doi.org/10.1002/nme.1620111006

[94] Prathap, G. Field-consistency — toward a science of constrained multi-strain-field finite element formulations. *Sadhana* **1986**, Volume 9, Issue 4, pp. 319–343. https://doi.org/10.1007/BF02811972

[95] Prathap, G.; Babu, C.R. A field consistent three-noded quadratic curved axisymmetric shell element. *International Journal for Numerical Methods in Engineering* **1986**, Volume 23, Issue 4, pp. 711–723. https://doi.org/10.1002/nme.1620230413

[96] Chandra, S. Prathap, G. A field-consistent formulation for the eight-noded solid finite element. *Computers & Structures* **1989**, Volume 33, Issue 2, pp. 345–355. https://doi.org/10.1016/0045-7949(89)90005-9

[97] Hughes, T.J.R. Generalization of selective integration procedures to anisotropic and nonlinear media. *International Journal for Numerical Methods in Engineering* **1980**, Volume 15, Issue 9, pp. 1413–1418. https://doi.org/10.1002/nme.1620150914

[98] Hughes, T.J.R. *The Finite Element Method: Linear Static and Dynamic Finite Element Analysis*, Prentice-Hall, San Diego, CA, USA, **1987**, ISBN:9780133170252.

[99] Zienkiewicz, O.C.; Taylor R.L. *The Finite Element Method - 5th edition, Volume 1 – The Basis*. Butterworth-Heinemann, Oxford, UK, **2000**.

[100] Zienkiewicz, O.C.; Taylor R.L. *The Finite Element Method - 5th edition, Volume 2 – Solid Mechanics*. Butterworth-Heinemann, Oxford, UK, **2000**.

[101] Zienkiewicz, O.C.; Taylor R.L. *The Finite Element Method - 5th edition, Volume 3 – Fluid Dynamics*. Butterworth-Heinemann, Oxford, UK, **2000**.

[102] Wriggers, P.; Eberlein, R.; Reese, S. A comparison of three-dimensional continuum and shell elements for finite plasticity. *International Journal of Solids and Structures* **1996**, Volume 33, Issues 20-22, pp. 3309–3326. https://doi.org/10.1016/0020-7683(95)00262-6

[103] Korelc, J.; Wriggers, P. An efficient 3D enhanced strain element with Taylor expansion of the shape functions. *Computational Mechanics* **1996**, Volume 19, Issue 2, pp. 30–40. https://doi.org/10.1007/BF02757781

[104] Wriggers, P. Korelc, J. On enhanced strain methods for small and finite deformations of solids. *Computional Mechanics* **1996**, Volume 18, Issue 6, pp. 413–428. https://doi.org/10.1007/BF00350250

[105] Hauptmann, R.; Schweizerhof, K. A systematic development of "solid-shell" element formulations for linear and non-linear analyses employing only displacement degrees of freedom. *International Journal for Numerical Methods in Engineering* **1998**, Volume 42, Issue 1, pp. 49–69. https://doi.org/10.1002/(SICI)1097-0207(19980515)42:1%3C49::AID-NME349%3E3.0.CO;2-2

[106] Hauptmann, R.l Doll, S.; Harnau, M.; Schweizerhof, K. `Solid-shell' elements with linear and quadratic shape functions at large deformations with nearly incompressible materials. *Computers & Structures* **2001**, Volume 79, Issue 18, pp. 1671–1685.

https://doi.org/10.1016/S0045-7949(01)00103-1

[107] Sze, K.Y.; Yao, L.Q. A hybrid stress ANS solid-shell element and its generalization for smart structure modelling. Part I—solid-shell element formulation. *International Journal for Numerical Methods in Engineering* **2000**, Volume 48, Issue 4, pp. 545–564. https://doi.org/10.1002/(SICI)1097-0207(20000610)48:4%3C545::AID-NME889%3E3.0.CO;2-6

[108] Kim, K.D.; Liu, G.Z.; Han, S. C. A resultant 8-node solid-shell element for geometrically nonlinear analysis. *Computational Mechanics* **2004**, Volume 35, Issue 5, pp. 315–331. https://doi.org/10.1007/s00466-004-0606-9

[109] Schwarze, M.; Reese, S. A reduced integration solid-shell finite element based on the EAS and the ANS concept-Geometrically linear problems. *International Journal for Numerical Methods in Engineering* **2009**, Volume 80, Issue 10, pp. 1322–1355. https://doi.org/10.1002/nme.2653

[110] Huang, J.; Cen, S.; Li, Z.; Li, C.-F. An unsymmetric 8-node hexahedral solid-shell element with high distortion tolerance: Linear formulations. *International Journal for Numerical Methods in Engineering* **2018**, Volume 116, Issues 12–13, pp. 759–783. https://doi.org/10.1002/nme.5945

[111] Reese, S.; Wriggers, P.; Reddy, B.D. A new locking-free brick element technique for large deformation problems in elasticity. *Computers & Structures* **2000**, Volume 75, Issue 3, pp. 291–304. https://doi.org/10.1016/S0045-7949(99)00137-6

[112] Reese, S. A large deformation solid-shell concept based on reduced integration with hourglass stabilization. *International Journal for Numerical Methods in Engineering* **2007**, Volume 69, Issue 8, pp. 1671–1716. https://doi.org/10.1002/nme.1827

[113] Wulfinghoff, S.; Bayat, H.R.; Alipour, A.; Reese, S. A low-order locking-free hybrid discontinuous Galerkin element formulation for large deformations. *Computer Methods in Applied Mechanics and Engineering* **2017**, Volume 323, pp. 353–372. https://doi.org/10.1016/j.cma.2017.05.018

[114] Piltner, R.; Joseph, D.S. A mixed finite element for plate bending with eight enhanced strain modes. *Communications in Numerical Methods in Engineering* **2001**, Volume 17, Issue 7, pp. 443–454. https://doi.org/10.1002/cnm.416

[115] Areias, P.M.A.; César de Sá, J.M.A.; António, C.A.C.; Fernandes, A.A. Analysis of 3D problems using a new enhanced strain hexahedral element. *International Journal for Numerical Methods in Engineering* **2003**, Volume 58, Issue 11, pp. 1637–1682. https://doi.org/10.1002/nme.835

[116] Brezzi, F; Fortin, M. *Mixed and Hybrid Finite Element Methods*. Springer-Verlag, New York, USA, **1991**.

[117] Boffi, D.; Brezzi, F; Fortin, M. *Mixed Finite Element Methods and Applications*. Springer-Verlag, New York, USA, **2013**.

[118] Lafontaine N.M.; Rossi, R.; Cervera, M.; Chiumenti, M. Explicit mixed strain–displacement finite element for dynamic geometrically non-linear solid mechanics. *Computational Mechanics* **2015**, Volume 55, Issue 3, pp. 543–559. https://doi.org/10.1007/s00466-015-1121-x

[119] Cervera, M.; Chiumenti, M.; Codina, R. Mixed stabilized finite element methods in nonlinear solid mechanics: Part I: Formulation. *Computer Methods in Applied Mechanics and Engineering* **2010**, Volume 199, Issues 37–40, pp. 2559–2570. https://doi.org/10.1016/j.cma.2010.04.006

[120] Cervera, M.; Chiumenti, M.; Codina, R. Mixed stabilized finite element methods in nonlinear solid mechanics: Part II: Strain localization. *Computer Methods in Applied Mechanics and Engineering* **2010**, Volume 199, Issues 37–40, pp. 2571–2589. https://doi.org/10.1016/j.cma.2010.04.005

[121] Cervera, M.; Chiumenti, M.; Codina, R. Mesh objective modeling of cracks using continuous linear strain and displacement interpolations. *International Journal for Numerical Methods in Engineering* **2011**, Volume 87, Issue 10, pp. 962–987. https://doi.org/10.1002/nme.3148

[122] Cervera, M.; Chiumenti, M.; Benedetti, L.; Codina, R. Mixed stabilized finite element methods in nonlinear solid mechanics. Part III: Compressible and incompressible plasticity. *Computer Methods in Applied Mechanics and Engineering* **2015**, Volume 285, pp. 752–775. https://doi.org/10.1016/j.cma.2014.11.040

[123] Chiumenti, M.; Cervera, M.; Codina, R. A mixed three-field FE formulation for stress accurate analysis including the incompressible limit. *Computer Methods in Applied Mechanics and Engineering* **2015**, Volume 283, pp. 1095–1116. http://dx.doi.org/10.1016/j.cma.2014.08.004

[124] S. Kim; M. Cervera; J.Y. Wu; M. Chiumenti. Strain Localization of Orthotropic Elasto-Plastic Cohesive-Frictional Materials: Analytical Results and Numerical Verification. *Materials* **2021**, Volume 14, pp. 2040. https://doi.org/10.3390/ma14082040

[125] Chiumenti, M.; Cervera, M.; Moreira, C.A.; Barbat, G.B. Stress, strain and dissipation accurate 3-field formulation for inelastic isochoric deformation. *Finite Elements in Analysis and Design* **2021**, Volume 192, pp. 103534. https://doi.org/10.1016/j.finel.2021.103534

[126] Hughes, T.J.R.; Feijoo, G.R.; Mazzei, L.; Quincy, J.B. The variational multiscale method-a paradigm for computational mechanics. *Computer Methods in Applied*

Mechanics and Engineering **1998**, Volume 166, Issues 1–2, pp. 3–28. https://doi.org/10.1016/S0045-7825(98)00079-6

[127] Codina, R. Stabilization of incompressibility and convection through orthogonal sub-scales in finite element methods. *Computer Methods in Applied Mechanics and Engineering* **2000**, Volume 190, Issues 13–14, pp. 1579–1599. https://doi.org/10.1016/S0045-7825(00)00254-1

Publications included in the compendium

Strain localization analysis of Hill's orthotropic elastoplasticity: Analytical results and numerical verification

M. Cervera, J.Y. Wu, M. Chiumenti and S. Kim

Computational Mechanics

Volume 65, pp. 533–554 (2020)

Editor-in-Chief: Prof. Dr. Peter Wriggers

PRINT ISSN: 0178-7675

Journal Editors - Springer

https://doi.org/10.1007/s00466-019-01782-4

Computational Mechanics manuscript No.
(will be inserted by the editor)

Strain localization analysis of Hill's orthotropic elastoplasticity

Analytical results and numerical verification

Miguel Cervera[1], Jian-Ying Wu[*2], Michele Chiumenti[1], Sungchul Kim[1]

[1] CIMNE, Technical University of Catalonia, Edificio C1, Campus Norte, Jordi Girona 1-3, 08034 Barcelona, Spain.

[2] State Key Laboratory of Subtropic Building Science, South China Univeristy of Technology, 510641 Guangzhou, China.

Received: date / Revised version: date

Abstract In this work the strain localization analysis of Hill's orthotropic plasticity is addressed. In particular, the localization condition derived from the boundedness of stress rates together with Maxwell's kinematics is employed. Similarly to isotropic plasticity considered in our previous work, the plastic flow components on the discontinuity surface vanish upon strain localization. The resulting localization angles in orthotropic plastic materials are independent from the elastic constants, but rather, depend on the material parameters involved in the plastic flow in the material axes. Application of the above localization condition to Hill's orthotropic plasticity in 2-D plane stress and plane strain conditions yields closed-form solutions of the localization angles. It is found that the two discontinuity lines in plane strain conditions are always perpendicular to each other, and for the states of no shear stresses, the localization angle depends only on the tilt angle of the material axes with respect to the global ones. The analytical results are then validated by *independent* numerical simulations. The B-bar finite element is employed to deal with the incompressibility due to the purely isochoric plastic flow. For a strip under vertical stretching in plane stress and plane strain as well as Prandtl's problem of indentation by a flat rigid die in plane strain, numerical results are presented for both isotropic and orthotropic plasticity models with or without tilt angle. The influence of various parameters is studied. In all cases, the critical angles

predicted from the localization condition coincide with the numerical results, giving compelling supports to the analytical prognoses.

1 Introduction

Strain localization in solids is characterized by highly localized deformations and manifested by diverse phenomena of distinct length scales, e.g., dislocations of orders of microns in metals, cracks of order of millimeters in concrete, and shear bands of order ranging from millimeters to kilometers in granular and geological problems, etc. Being strain localization a prognosis of structural failure, it is of utmost significance to determine when strain localization occurs and quantify its adverse effects on the global response of structures.

Regarding rigid-plastic problems and shear driven, pressure independent flows, seminal works of Prandtl [1], Hencky [2,3] and Mandel [4] assumed the existence of "slip lines" and determined their directions by the "zero rate of extension" criterion. Later, Hill [5] revisited the similar problem and interpreted the family of "slip lines" as the characteristic curves (along which small disturbances propagate) of the hyperbolic plastic governing equations. With this method, the field of slip lines for typical metallurgical problems, e.g., sheet drawing and extrusion, piercing, strip-rolling, etc., were determined [6]. Note that in these early studies, elastic deformations were explicitly ignored, and perfectly incompressible behavior prior to shear driven plastic yielding was assumed.

For general elasto-plastic materials, as strain localization inevitably induces strain (weak) or even displacement (strong) discontinuities, the discontinuous bifurcation condition set forth by [7,8,9,10] is customarily employed. More specifically, the necessary condition for strain localization in elastoplastic materials is identified upon the assumption of linear comparison solids (i.e., inelastic loading both inside and outside the localization band) and traction continuity [11,12,13]. Closed-form results for the localization angles have been obtained for 2-D plane stress and plane strain conditions in this way [13]. One noteworthy property of such results is that the localization angle depends on the elastic constants, e.g., Poisson's ratio.

The classical discontinuous bifurcation analysis has been applied not only to weak discontinuities, but also to strong ones. For instance, [14,15] used it to determine the discontinuity orientation, such that strong discontinuities can be embedded in standard finite elements. However, it was soon found that this discontinuous bifurcation condition by itself does not necessarily guarantee the occurrence of strong discontinuities, unless the strong discontinuity is properly regularized, involving also stress boundedness [14,15,16,17]. In particular, the fact that material points inside the discontinuity band undergo inelastic loading while those outside it unload elastically, is inconsistent with the assumption of linear comparison solids in which inelastic loading is assumed in both the bulk and localization band. Furthermore, due to the singular strain field caused by displacement discontinuities, the traction continuity condition alone is sufficient to guarantee neither stress locking-free results or the decohesion limit due to the mis-prediction of the discontinuity orientation [18,19].

In order to overcome the above crucial but generally overlooked issue, the authors [18] proposed further exploiting the kinematic compatibility condition resulting from stress boundedness to determine the discontinuity orientation of von Mises (J_2) plastic materials. It turns out that the condition for stress boundedness is more constrictive for the orientation of discontinuities than the localization condition based on singularity of the acoustic tensor. More specifically, a given discontinuity orientation $\boldsymbol{n}$ that satisfies the localization condition $\det \boldsymbol{Q}_{\text{ep}}(H, \boldsymbol{n}) = 0$ for a given maximum softening parameter $H < 0$, guarantee neither stress boundedness nor full decohesion in the final stage of the deformation process. Reversely, stress boundedness implies both satisfaction of the classical discontinuous bifurcation condition and also perfect decohesion in the softening or perfect plasticity cases.

Remarkably, for elasto-plastic materials the above kinematic compatibility based localization condition predicts localization angles which depend exclusively on the components of the flow strain tensor. This incorporates as a particular case Hills zero rate of extension" for the classical slip-line theory for rigid-plastic problems. Compared to those given by the discontinuous bifurcation condition, the localization angles are independent of the elastic constants as well as of the softening parameter, as the tangent elasto plastic tensor is not involved in the analysis.

More recently, the authors [20,21,22] have successfully extended the above strain localization analysis to a unified stress-based plastic-damage model with general (e.g., Rankine, von Mises, Mohr-Coulomb, Drucker-Prager, and more complex elliptic, parabolic, hyperbolic, etc.) failure criteria and to strain-based elastic-damage models. The closed-form results were remarkably confirmed by independent numerical simulations [23] in which the analytical results are not used in finite element analyses. Moreover, not only the discontinuity orientation but also the corresponding localized cracking model, i.e., constitutive relations, evolution equations, traction-based failure criterion, softening functions, etc., can be determined consistently from a given material model. With these work, the gap between continuous and discontinuous approaches for the modeling of localized failure in solids [20] has been largely bridged.

In many industrial applications, e.g., additive manufacturing, automotive rolling, etc., engineering materials like steel sheets, aluminum, wood, paper and stratified rocks, composites with oriented fibers, etc., exhibit strongly orthotropic behavior. Ever since the pioneering work of Hill [7], plasticity models with orthotropic yield functions, e.g., Hoffman model [24] and Tsai-Wu model [25], among many others, have been extensively studied; see [26]. However, most of the aforementioned work considered only strain localization in isotropic materials and very rare references deal with orthotropic ones. To the authors' best knowledge, it is only in [27] that strain localization in orthotropic plasticity models is considered to determine the upper bound load capacity of such materials. Nevertheless, the closed-form results for the localization angle are not available. Consequently, the failure modes have to be calibrated from finite element simulations. This deficiency is sometimes not acceptable since the numerical results can be sensitive to the mesh alignment, leading to ill-predictions of failure modes and global responses [28,29,30,31].

For these reasons, this work addresses strain localization analysis in orthotropic elastoplastic materials. The objectives are four-fold: (*i*) to show that our previously established localization condition also applies to materials with orthotropic elastic and plastic behavior; (*ii*) to analyze strain localization of orthotropic plastic models and, in particular, to determine the localization angles in 2-D plane stress and plane strain conditions; (*iii*) to numerically verify the analytical results through independent finite element simulations, and (*iv*) to

investigate the influence of various material parameters on strain localization in orthotropic materials. Though other orthotropic yield functions can be considered, Hill's quadratic one is adopted in this work as the prototype example due to its wide application.

The remainder of this paper is structured as follows. Section 2 addresses the localization condition of elasto-plastic solids based on the boundedness of stress rates together with Maxwell's kinematics. Section 3 is devoted to the application of the derived localization condition to Hill's orthotropic plasticity. In particular, closed-form results of the localization angles under 2-D conditions of plane stress and plane strain are given. Numerical verification of the analytical results is presented in Section 4 using the B-bar finite elements to deal with the isochoric nature of the plastic flow. A horizontal slit under vertical stretch and the Prandtl punch test, with or without tilt angle between the material local axes and the global ones, are considered. The influence of various parameters on the localization angles is also studied. The most relevant conclusions are drawn in Section 5 to close the paper.

Notation. Compact tensor notation is used in the theoretical part of this paper. As general rules, scalars are denoted by italic light-face Greek or Latin letters (e.g. a or λ); vectors, second- and fourth-order tensors are signified by italic boldface minuscule, majuscule and blackboard-bold majuscule characters like $\boldsymbol{a}$, $\boldsymbol{A}$ and $\mathbb{A}$, respectively. The inner products with single and double contractions are denoted by '$\cdot$' and ':', respectively, while the dyadic operator is signified by '$\otimes$'. The Voigt notation of vectors and second-order tensors is denoted by boldface minuscule and majuscule letters like $\mathbf{a}$ and $\mathbf{A}$, respectively.

2 Strain localization of elastoplastic solids

In this section, our previous work on strain localization in inelastic solids is briefly recalled and then particularized to elastoplastic materials. The resulting solution extends Hill's results for strictly incompressible rigid-plastic materials to general associated elasto-plastic materials, incompressible or not. Compared to the classical discontinuous bifurcation analysis [7,8,9,11,12,13], not only traction continuity but also stress boundedness are guaranteed [18,20,21,22] by reproducing Maxwell's discontinuity kinematics.

Let us consider the domain $\Omega \subset \mathbb{R}^{n_{\text{dim}}}$ ($n_{\text{dim}} = 1, 2, 3$) occupied by an elastoplastic solid with reference position vector $\boldsymbol{x} \in \mathbb{R}^{n_{\text{dim}}}$. The boundary is denoted by $\Gamma \subset \mathbb{R}^{n_{\text{dim}}-1}$, with an external unit normal vector $\boldsymbol{n}^*$. Deformations of the solid are characterized by the displacement field $\boldsymbol{u} : \Omega \to \mathbb{R}^{n_{\text{dim}}}$ and the infinitesimal strain field $\boldsymbol{\epsilon} := \nabla^{\text{sym}}\boldsymbol{u}$, with $\nabla(\cdot)$ being the spatial gradient operator.

2.1 Elastoplasticity model

For an elastoplastic model, the constitutive relation is expressed in total form as

$$\boldsymbol{\epsilon} = \boldsymbol{\epsilon}^{\text{e}} + \boldsymbol{\epsilon}^{\text{p}}, \qquad \boldsymbol{\sigma} = \mathbb{E}^0 : \boldsymbol{\epsilon}^{\text{e}} = \mathbb{E}^0 : \left(\boldsymbol{\epsilon} - \boldsymbol{\epsilon}^{\text{p}}\right) \tag{2.1}$$

where the second-order tensors $\boldsymbol{\epsilon}^{\text{e}}$ and $\boldsymbol{\epsilon}^{\text{p}}$ represent the elastic and plastic parts of the strain $\boldsymbol{\epsilon}$, respectively; the second-order stress tensor $\boldsymbol{\sigma}$ is related to the elastic strain $\boldsymbol{\epsilon}^{\text{e}}$ by fourth-order elasticity tensor $\mathbb{E}^0$. Note that $\mathbb{E}^0$ may be isotropic or orthotropic in this work.

For the classical associated evolution law, the plastic strain rate is given by

$$\dot{\boldsymbol{\epsilon}}^{\text{p}} = \dot{\lambda}\boldsymbol{\Lambda}, \qquad \dot{\kappa} = \dot{\lambda}h \tag{2.2}$$

where $\dot{\lambda} \geq 0$ denotes the plastic multiplier, with $\dot{(\cdot)}$ being the time derivative; the derivatives $\boldsymbol{\Lambda} := \partial\phi/\partial\boldsymbol{\sigma}$ and $h := \partial\phi/\partial q$ are normal to the yield surface $\phi(\boldsymbol{\sigma}, q) = 0$, with q being a stress-like internal variable (yield stress). In this work, Hill's orthotropic yield function is considered later in Eq. (3.1).

The corresponding constitutive relation in rate form then reads

$$\dot{\boldsymbol{\sigma}} = \mathbb{E}^0 : \left(\dot{\boldsymbol{\epsilon}} - \dot{\boldsymbol{\epsilon}}^{\text{p}}\right) = \mathbb{E}^{\text{ep}} : \dot{\boldsymbol{\epsilon}} \tag{2.3}$$

where the fourth-order elastoplasticity tensor $\mathbb{E}^{\text{ep}}$ is expressed as

$$\mathbb{E}^{\text{ep}} = \mathbb{E}^0 - \frac{\mathbb{E}^0 : \boldsymbol{\Lambda} \otimes \boldsymbol{\Lambda} : \mathbb{E}^0}{\boldsymbol{\Lambda} : \mathbb{E}^0 : \boldsymbol{\Lambda} + h \cdot H \cdot h} \tag{2.4}$$

for the hardening/softening modulus $H := \partial q/\partial\kappa$.

2.2 Discontinuity kinematics

At the early stage of the deformation process, the standard continuum kinematics applies, in which both the velocity and strain rate fields are continuous and regular (bounded). For a perfectly or softened plastic solid, upon satisfaction of the yield condition $\phi(\boldsymbol{\sigma}, q) = 0$, the deformation can grow unbounded. In particular, two orthogonal families of curves (surfaces in 3D) form in 2-D conditions. These so-called slip lines or surfaces represent macroscopic phenomena occurring at the micro- or meso-level associated with strain localization and induce jumps in the strain rate or even velocity fields.

Velocity jumps can be described by strong discontinuities. As depicted in Figure 1(a), the interface $\mathcal{S}$ splits the solid Ω into two parts Ω^+ and Ω^-, located "ahead of" and "behind" $\mathcal{S}$, respectively. The discontinuity orientation is characterized by a unit normal vector $\boldsymbol{n}$, pointing from Ω^- to Ω^+ and fixed along time, i.e., $\dot{\boldsymbol{n}} = \boldsymbol{0}$, with $\dot{(\,)}$ being the time derivative. Alternatively, strain discontinuities can be characterized by a discontinuity band $\mathcal{B}$ of finite width b, delimited by two surfaces $\mathcal{S}^+$ and $\mathcal{S}^-$ parallel to the discontinuity $\mathcal{S}$ as shown in Figure 1(b). As the bandwidth b is a regularization parameter that can be made as small as desired, the strong discontinuity can be regarded as the limit of a regularized one, with a vanishing bandwidth $b \to 0$. Reciprocally, a discontinuity band can be regarded as the convenient regularization of a strong discontinuity.

Upon the above setting, the strain rate fields $\dot{\boldsymbol{\epsilon}}_{\text{int}}$ and $\dot{\boldsymbol{\epsilon}}_{\text{ext}}$ inside and outside the discontinuity band $\mathcal{B}$ verify the following Maxwell's compatibility condition [9]

$$\dot{\boldsymbol{\epsilon}}_{\text{int}} = \dot{\boldsymbol{\epsilon}}_{\text{ext}} + \left(\dot{\boldsymbol{e}} \otimes \boldsymbol{n}\right)^{\text{sym}} \tag{2.5}$$

or, equivalently,

$$[\![\dot{\boldsymbol{\epsilon}}]\!] := \dot{\boldsymbol{\epsilon}}_{\text{int}} - \dot{\boldsymbol{\epsilon}}_{\text{ext}} = \left(\dot{\boldsymbol{e}} \otimes \boldsymbol{n}\right)^{\text{sym}} \tag{2.6}$$

where the inelastic deformation rate vector $\dot{\boldsymbol{e}} := \dot{\boldsymbol{w}}/b$ is defined as the apparent velocity jump $\dot{\boldsymbol{w}}$ across the discontinuity band $\mathcal{B}$ normalized by the regularization length b; see Figure 2(a) for the strong discontinuity and Figure 2(b) for a regularized one, respectively. Note that the jump of strain rate, $[\![\dot{\boldsymbol{\epsilon}}]\!]$, is inversely proportional to b for a regularized discontinuity or unbounded for a strong one.

2.3 Strain localization condition

Upon strain localization, material points inside the discontinuity (band) undergo inelastic loading while those outside it unload elastically [16,18]. Accordingly, it follows from the constitutive relation (2.3) that

$$\dot{\boldsymbol{\sigma}}_{\text{int}} = \mathbb{E}^0 : \left(\dot{\boldsymbol{\epsilon}}_{\text{int}} - \dot{\boldsymbol{\epsilon}}^{\text{p}}\right), \qquad \dot{\boldsymbol{\sigma}}_{\text{ext}} = \mathbb{E}^0 : \dot{\boldsymbol{\epsilon}}_{\text{ext}} \tag{2.7}$$

The resulting jump in the stress rate, $[\![\dot{\boldsymbol{\sigma}}]\!]$, is given by

$$[\![\dot{\boldsymbol{\sigma}}]\!] = \dot{\boldsymbol{\sigma}}_{\text{int}} - \dot{\boldsymbol{\sigma}}_{\text{ext}} = \mathbb{E}^0 : \left[\left(\dot{\boldsymbol{e}} \otimes \boldsymbol{n}\right)^{\text{sym}} - \dot{\boldsymbol{\epsilon}}^{\text{p}}\right] \tag{2.8}$$

The stress tensors and their rates have to remain bounded during the failure process to guarantee their physical significance. Being $\dot{\boldsymbol{\sigma}}_{\text{int}}$ and $\dot{\boldsymbol{\sigma}}_{\text{ext}}$ both bounded, so is the jump $[\![\dot{\boldsymbol{\sigma}}]\!]$. Accordingly, the difference $\left(\dot{\boldsymbol{e}} \otimes \boldsymbol{n}\right)^{\text{sym}} - \dot{\boldsymbol{\epsilon}}^{\text{p}}$ has to be bounded, too. As the bandwidth b is a regularization parameter that can be made as small as desired, the stress boundedness condition requires [18,21]

$$\boxed{[\![\dot{\boldsymbol{\epsilon}}]\!] = \dot{\boldsymbol{\epsilon}}^{\text{p}} = \left(\dot{\boldsymbol{e}} \otimes \boldsymbol{n}\right)^{\text{sym}}} \tag{2.9}$$

That is, upon strain localization *stress boundedness* requires that ***the strain rate jump, defined as the difference in the strain rate fields between the interior/exterior points of the discontinuity (band) and characterized by Maxwell's compatibility condition, has to be completely plastic***.

Remark 2.1 The kinematic constraint (2.9) implies that even though the corresponding strains are not, the stresses inside and outside the discontinuity band are continuous, i.e., $[\![\dot{\boldsymbol{\sigma}}]\!] = \boldsymbol{0}$. In this case, the traction continuity $[\![\dot{\boldsymbol{t}}]\!] = \boldsymbol{n} \cdot [\![\dot{\boldsymbol{\sigma}}]\!]$ is also guaranteed. □

Remark 2.2 This stress boundedness/continuity holds for softened plasticity [18,20,21] and also for perfect plastic flows (incremental full decohesion). Similarly, the same condition guarantees that full decohesion ($\dot{\boldsymbol{\sigma}} = \boldsymbol{0}$) can be fulfilled with large plastic straining inside the discontinuity; see [18] for details. □

2.4 Strain localization of plastic solids

The kinematic constraint (2.9) implies the existence of a *plastic flow vector* $\boldsymbol{\gamma}$ satisfying

$$\dot{\boldsymbol{e}} = \dot{\lambda}\boldsymbol{\gamma} \qquad \Longrightarrow \qquad \boxed{\boldsymbol{\Lambda} = \big(\boldsymbol{\gamma} \otimes \boldsymbol{n}\big)^{\text{sym}}} \tag{2.10}$$

Let (n, m, p) be discontinuity local axes, with $\boldsymbol{n}$, $\boldsymbol{m}$ and $\boldsymbol{p}$ being the normal vector, the in-plane and out-of-plane tangential ones of the discontinuity $\mathcal{S}$, respectively. It then follows that [17,20,21]

$$\boldsymbol{\gamma} = 2\boldsymbol{n} \cdot \boldsymbol{\Lambda} - \boldsymbol{n}\Lambda_{nn} = \gamma_n \boldsymbol{n} + \gamma_m \boldsymbol{m} + \gamma_p \boldsymbol{p} \tag{2.11}$$

where the components $(\gamma_n, \gamma_m, \gamma_p)$ of the plastic flow vector $\boldsymbol{\gamma}$ are determined as

$$\gamma_n := \boldsymbol{\gamma} \cdot \boldsymbol{n} = \Lambda_{nn}, \qquad \gamma_m := \boldsymbol{\gamma} \cdot \boldsymbol{m} = 2\Lambda_{nm}, \qquad \gamma_p := \boldsymbol{\gamma} \cdot \boldsymbol{p} = 2\Lambda_{np} \tag{2.12}$$

Substitution of the above plastic flow vector $\boldsymbol{\gamma}$ back into the relation $(2.10)_2$ yields [20,21]

$$\Lambda_{mm}(\boldsymbol{\theta}^{\text{cr}}) = 0, \qquad \Lambda_{pp}(\boldsymbol{\theta}^{\text{cr}}) = 0, \qquad \Lambda_{mp}(\boldsymbol{\theta}^{\text{cr}}) = 0 \tag{2.13}$$

where $\boldsymbol{\theta}^{\text{cr}}$ denote the localization angles upon which the kinematic constraint (2.10) is satisfied. Note that the components $\Lambda_{mm}, \Lambda_{pp}$ and Λ_{mp} depend on the specific yield function $\phi(\boldsymbol{\sigma}, q)$; see Section 3.1 for the application to Hill's criterion.

Remark 2.3 As can be seen from Eq. (2.13), upon strain localization the plastic flow tensor evolves into a particular structure in terms of a localized flow vector and the discontinuity orientation. Accordingly, the tensorial flow components in the directions orthogonal to the discontinuity orientation have to vanish so that the consistent loading/unloading deformation states upon strain localization are correctly represented and slip lines or surfaces eventually form. This result is an extension of Hill's criterion of "zero rate of extension" for incompressible rigid-plastic materials [5,6] to general elasto-plastic ones. In the following, we apply this procedure to determine the localization angle for Hill's orthotropic plastic materials. □

Remark 2.4 In the case of plane strain, the strain localization condition $\Lambda_{33} = \Lambda_{pp} = 0$ is not necessarily fulfilled at the onset of plastic yield $\phi(\boldsymbol{\sigma}, q) = 0$ with the out-of-plane stress given by $\epsilon_{33} = 0$. Accordingly, except for very particular cases, strain localization cannot occur at the onset of plastic yielding. Rather, some (continuous) inelastic deformations and substantial rotation of the principal strain directions have to occur, until the localization condition $\Lambda_{33} = \Lambda_{pp} = 0$ is fulfilled such that strain localization is set in motion and a strong (regularized) discontinuity forms; see the numerical results presented in [18] for the case of von Mises (J_2) model with isotropic linear elasticity. □

Remark 2.5 The above localization conditions allow developing a traction-based plastic model for the discontinuity (band). Both the orientation and the traction-based failure criterion can be determined *a posteriori* from the given stress-based counterpart; see [32,20,21,22] for the details. However, this extra procedure is not considered in this work. □

3 Application to Hill's orthotropic plastic materials

In this section the above strain localization condition is applied to Hill's orthotropic perfectly plastic materials [33]. In particular, closed-form solutions are obtained for the localization angle in the 2-D plane stress and plane strain conditions. Similarly, Hill [5] considered only the plane stress condition for rigid-plastic materials.

3.1 Hill's orthotropic plasticity

Without loss of generality, let us consider Hill's orthotropic yield criterion of the following form [33]

$$\phi(\boldsymbol{\sigma}) = F\big(\sigma_{11} - \sigma_{22}\big)^2 + G\big(\sigma_{11} - \sigma_{33}\big)^2 + H\big(\sigma_{22} - \sigma_{33}\big)^2 + 2L\sigma_{12}^2 + 2M\sigma_{13}^2 + 2N\sigma_{23}^2 - 1 \leq 0 \tag{3.1}$$

with the material parameters F, G, H, L, M and N given by

$$F = \frac{1}{2}\left[\left(\frac{1}{\sigma_{Y,11}}\right)^2 + \left(\frac{1}{\sigma_{Y,22}}\right)^2 - \left(\frac{1}{\sigma_{Y,33}}\right)^2\right], \qquad L = \frac{1}{2}\left(\frac{1}{\sigma_{Y,12}}\right)^2 \tag{3.2a}$$

$$G = \frac{1}{2}\left[\left(\frac{1}{\sigma_{Y,11}}\right)^2 + \left(\frac{1}{\sigma_{Y,33}}\right)^2 - \left(\frac{1}{\sigma_{Y,22}}\right)^2\right], \qquad M = \frac{1}{2}\left(\frac{1}{\sigma_{Y,13}}\right)^2 \tag{3.2b}$$

$$H = \frac{1}{2}\left[\left(\frac{1}{\sigma_{Y,22}}\right)^2 + \left(\frac{1}{\sigma_{Y,33}}\right)^2 - \left(\frac{1}{\sigma_{Y,11}}\right)^2\right], \qquad N = \frac{1}{2}\left(\frac{1}{\sigma_{Y,23}}\right)^2 \tag{3.2c}$$

where $\sigma_{11}, \sigma_{22}, \sigma_{33}, \sigma_{12}, \sigma_{13}$ and σ_{23} denote the stress components in the material local axes $(1, 2, 3)$, with those entities embellished by subscripts "Y" representing the corresponding yield strengths.

The components Λ_{ij} of the flow tensor $\boldsymbol{\Lambda} := \mathrm{d}\phi/\mathrm{d}\boldsymbol{\sigma}$ are then expressed as

$$\Lambda_{11} = \frac{\mathrm{d}\phi}{\mathrm{d}\sigma_{11}} = 2\big(F+G\big)\sigma_{11} - 2F\sigma_{22} - 2G\sigma_{33} \tag{3.3a}$$

$$\Lambda_{22} = \frac{\mathrm{d}\phi}{\mathrm{d}\sigma_{22}} = 2\big(F+H\big)\sigma_{22} - 2F\sigma_{11} - 2H\sigma_{33} \tag{3.3b}$$

$$\Lambda_{33} = \frac{\mathrm{d}\phi}{\mathrm{d}\sigma_{33}} = 2\big(G+H\big)\sigma_{33} - 2G\sigma_{11} - 2H\sigma_{22} \tag{3.3c}$$

$$\Lambda_{12} = \Lambda_{21} = \frac{1}{2}\frac{\mathrm{d}\phi}{\mathrm{d}\sigma_{12}} = 2L\sigma_{12} \tag{3.3d}$$

$$\Lambda_{13} = \Lambda_{31} = \frac{1}{2}\frac{\mathrm{d}\phi}{\mathrm{d}\sigma_{13}} = 2M\sigma_{13} \tag{3.3e}$$

$$\Lambda_{23} = \Lambda_{32} = \frac{1}{2}\frac{\mathrm{d}\phi}{\mathrm{d}\sigma_{23}} = 2N\sigma_{23} \tag{3.3f}$$

Note that the identity $\mathrm{tr}\boldsymbol{\Lambda} = \Lambda_{11} + \Lambda_{22} + \Lambda_{33} = 0$ always holds. That is, Hill's yield function leads to an isochoric (purely deviatoric) plastic flow.

Remark 3.1 von Mises's isotropic yield criterion is recovered for

$$F = G = H = \frac{1}{2}\left(\frac{1}{\sigma_Y}\right)^2, \qquad L = M = N = \frac{3}{2}\left(\frac{1}{\sigma_Y}\right)^2 \tag{3.4}$$

for the yield strength σ_Y. □

3.2 Localization angles

In this section strain localization of a 2-D Hill's plastic solid $\Omega \subset \mathbb{R}^2$ is considered. In such 2-D cases, the discontinuity orientation can be characterized by the inclination angle (counter-clockwise) $\theta \in [-\pi/2, \pi/2]$

between the normal vector $\boldsymbol{n}$ and the material axis 1; see Figure 3. Accordingly, the flow components $\Lambda_{mm}, \Lambda_{pp}$ can be expressed in terms of $\Lambda_{11}, \Lambda_{22}, \Lambda_{33}, \Lambda_{12}$ in the material local axes as follows

$$\Lambda_{mm} = \Lambda_{11} \sin^2\theta + \Lambda_{22} \cos^2\theta + 2\Lambda_{12} \cos\theta \sin\theta, \qquad \Lambda_{pp} = \Lambda_{33} \tag{3.5}$$

Our objective is to derive explicitly the discontinuity angle $\theta^{\rm cr}$ upon strain localization.

For a given stress-based failure criterion $\phi \leq 0$, the critical angle $\theta^{\rm cr}$ can be determined explicitly from the projection relation (2.10) or, more specifically, from the kinematic constraints (2.13) applied to the flow components (3.5), i.e.,

$$\Lambda_{mm}(\theta^{\rm cr}) = \cos^2\theta^{\rm cr}\left(\Lambda_{11} \tan^2\theta^{\rm cr} + 2\Lambda_{12} \tan\theta^{\rm cr} + \Lambda_{22}\right) = 0 \tag{3.6a}$$

$$\Lambda_{pp}(\theta^{\rm cr}) = \Lambda_{33} = 0 \tag{3.6b}$$

Note that in 2-D cases the other constraint $\Lambda_{mp}(\theta^{\rm cr}) = 0$ is automatically satisfied.

It then follows from Eq. (3.6a) that

$$\tan\theta^{\rm cr} = -\frac{\Lambda_{12}}{\Lambda_{11}} \pm \sqrt{\left(\frac{\Lambda_{12}}{\Lambda_{11}}\right)^2 - \frac{\Lambda_{22}}{\Lambda_{11}}} \tag{3.7}$$

where the flow components Λ_{11} and Λ_{22} given in Eq. (3.3) are further constrained by the condition (3.6b).

As can be seen, the above discontinuity angle $\theta^{\rm cr}$ depends on the ratios $\Lambda_{22}/\Lambda_{11}$ and/or $\Lambda_{12}/\Lambda_{11}$, or equivalently, the stress state, upon strain localization. In particular, the distinction between plane stress and plane strain states has to be made regarding the condition (3.6b).

Remark 3.2 For the above stress-based failure criterion, the resulting localization angle $\theta^{\rm cr}$ does not depend on the elastic constants like Young's modulus and Poisson's ratio. This is in strong contrast to the results given from classical discontinuous bifurcation analysis [11,12,13]. In orthotropic materials, the elastic properties may well be orthotropic. The localization angle $\theta^{\rm cr}$ does not depend on this feature either. □

Remark 3.3 For the case of $\Lambda_{12} = 0$, it follows that

$$\tan\theta^{\rm cr} = \pm\sqrt{-\frac{\Lambda_{22}}{\Lambda_{11}}} \tag{3.8}$$

This is the result we previously obtained for isotropic plasticity models [18,20,21]. Note that for orthotropic materials, the analysis needs to be considered in the material local axes. □

Remark 3.4 The above discontinuity angle $\theta^{\rm cr}$ is expressed in terms of the flow components (or stresses) in the material local axes. Though the localization analysis is independent of the frame of reference, it is sometimes more convenient to use those stresses in the global axes (x, y, z). To this end, we can considered the following transformation relation

$$\begin{Bmatrix} \sigma_{11} \\ \sigma_{22} \\ \sigma_{33} \\ \sigma_{12} \end{Bmatrix} = \begin{bmatrix} \cos^2\alpha & \sin^2\alpha & 0 & -2\cos\alpha\sin\alpha \\ \sin^2\alpha & \cos^2\alpha & 0 & 2\cos\alpha\sin\alpha \\ 0 & 0 & 1 & 0 \\ \cos\alpha\sin\alpha & -\cos\alpha\sin\alpha & 0 & \cos^2\alpha - \sin^2\alpha \end{bmatrix} \begin{Bmatrix} \sigma_{xx} \\ \sigma_{yy} \\ \sigma_{zz} \\ \sigma_{xy} \end{Bmatrix} \tag{3.9}$$

for the counter-clockwise tilt angle α between the global axis x and the material local axis 1. □

3.2.1 Plane stress Let us consider plane stress conditions with $\sigma_{33} = \sigma_{pp} = 0$. In this case, the relevant flow components in Eq. (3.3) become

$$\Lambda_{11} = 2\big(F + G\big)\sigma_{11} - 2F\sigma_{22} \tag{3.10a}$$

$$\Lambda_{22} = 2\big(F + H\big)\sigma_{22} - 2F\sigma_{11} \tag{3.10b}$$

$$\Lambda_{12} = 2L\sigma_{12} \tag{3.10c}$$

As the condition (3.6b) is automatically satisfied, strain localization occurs at the same instant as the initial failure surface $\phi = 0$ is reached and the localization angle $\theta^{\rm cr}$ is determined straightforwardly from Eq. (3.7) together with the relations (3.10). It is seen from the transformation (3.9) that the localization angle $\theta^{\rm cr}$ depends on the stresses in the global axes and on the tilt.

3.2.2 Plane strain In this case, the condition (3.6b) yields

$$\Lambda_{pp} = \Lambda_{33} = 0 \qquad \Longrightarrow \qquad \sigma_{33} = \frac{G\sigma_{11} + H\sigma_{22}}{G + H}, \qquad \Lambda_{11} + \Lambda_{22} = -\Lambda_{33} = 0 \tag{3.11}$$

Accordingly, Eq. (3.7) becomes

$$\tan\theta^{\rm cr} = -\frac{\Lambda_{12}}{\Lambda_{11}} \pm \sqrt{\left(\frac{\Lambda_{12}}{\Lambda_{11}}\right)^2 + 1} \tag{3.12}$$

where the flow components are expressed as

$$\Lambda_{11} = -\Lambda_{22} = 2\frac{FG+FH+GH}{G+H}\big(\sigma_{11}-\sigma_{22}\big), \qquad \Lambda_{12} = 2L\sigma_{12} \tag{3.13}$$

or, equivalently,

$$\frac{\Lambda_{12}}{\Lambda_{11}} = \frac{(G+H)L}{FG+FH+GH}\cdot\frac{\sigma_{12}}{\sigma_{11}-\sigma_{22}} \tag{3.14}$$

Therefore, the localization angle $\theta^{\rm cr}$ depends on the ratio $\sigma_{12}/(\sigma_{11}-\sigma_{22})$; see Remark 3.7.

Remark 3.5 It follows from Eq. (3.12) that

$$\tan\theta_1^{\rm cr}\cdot\tan\theta_2^{\rm cr} = -1 \qquad \Longrightarrow \qquad \big|\theta_1^{\rm cr}-\theta_2^{\rm cr}\big| = 90^\circ \tag{3.15}$$

Accordingly, the discontinuity lines are perpendicular to each other. □

Remark 3.6 For the case of $\Lambda_{12}=0$, Eq. (3.12) becomes

$$\tan\theta^{\rm cr} = 1 \qquad \Longrightarrow \qquad \theta^{\rm cr} = \pm 45^\circ \tag{3.16}$$

This is exactly the result obtained for isotropic plasticity [18,20,21]. □

Remark 3.7 It follows from the transformation (3.9) that

$$\frac{\sigma_{12}}{\sigma_{11}-\sigma_{22}} = \frac{1}{2}\frac{\big(\sigma_{xx}-\sigma_{yy}\big)\sin(2\alpha)+2\sigma_{xy}\cos(2\alpha)}{\big(\sigma_{xx}-\sigma_{yy}\big)\cos(2\alpha)-2\sigma_{xy}\sin(2\alpha)} \tag{3.17}$$

Regarding the stresses in the global axes, the following two cases are of interest

$$\frac{\sigma_{12}}{\sigma_{11}-\sigma_{22}} = \begin{cases} \dfrac{1}{2}\tan(2\alpha) & \sigma_{xy}=0 \\[2ex] \dfrac{1}{2\tan(2\alpha)} & \sigma_{xx}=\sigma_{yy} \end{cases} \tag{3.18}$$

In the first case, the principal directions are aligned with the global axes, while in the second one, they are at 45° with respect to the global reference. In both cases, the localization angle $\theta^{\rm cr}$ depends only on the tilt angle α of the material axes. □

3.3 Particular examples

In order to make the above results more clear, let us consider the stress state of vertical stretching, i.e.,

$$\sigma_{xx} = 0, \qquad \sigma_{yy} = \sigma, \qquad \sigma_{xy} = 0 \tag{3.19}$$

along axis y.

For the plane stress condition, it follows from Eqs. (3.9) and (3.10) that

$$\frac{\Lambda_{22}}{\Lambda_{11}} = \frac{(F+H)\cos^2\alpha - F\sin^2\alpha}{(F+G)\sin^2\alpha - F\cos^2\alpha} \tag{3.20a}$$

$$\frac{\Lambda_{12}}{\Lambda_{11}} = -\frac{L\cos\alpha\sin\alpha}{(F+G)\sin^2\alpha - F\cos^2\alpha} \tag{3.20b}$$

The localization angle θ^{cr} is then determined from Eq. (3.7). In particular, for the case $\alpha = 0$, it follows that

$$\tan\theta^{\mathrm{cr}} = \pm\sqrt{-\frac{\Lambda_{22}}{\Lambda_{11}}} = \pm\sqrt{\frac{F+H}{F}} \tag{3.21}$$

which depends only on the material plastic parameters F and H. This result is coincident with that in [5] obtained from the "zero rate of extension".

For the plane strain condition, the localization angle θ^{cr} is determined from Eq. (3.12)

$$\frac{\Lambda_{12}}{\Lambda_{11}} = \frac{1}{2}\frac{(G+H)L}{FG+FH+GH}\tan(2\alpha) \tag{3.22}$$

For the case $\alpha = 0$, it follows that

$$\tan\theta^{\mathrm{cr}} = \pm 1 \qquad \Longrightarrow \qquad \theta^{\mathrm{cr}} = \pm 45^\circ \tag{3.23}$$

4 Numerical verifications

In this section the analytical results presented in Section 3 are numerically verified. It is stressed that the numerical verification is totally independent from the analytical results. That is, these results are not used in any way in finite element simulations. Perfect plasticity with null modulus $H = 0$ is considered in this work, though the present strain localization analysis applies also to plastic-damage models with softening regimes.

This is because the equations from which the localization angle is obtained, Eq. (2.13) and Eq. (3.7), depend only on the plastic flow components in the material local system; they do not depend on the softening modulus. Compelling results for isotropic elastoplastic models with softening regimes are shown in reference [21].

As seen in previous Sections, Hill's plastic flow is isochoric by definition, and for strain localization to take place the plastic flow needs to be well developed and, at that stage, the (incompressible) plastic component of the deformation is dominant over the elastic part. Standard displacement-based finite elements are not well suited to cope with this quasi-incompressibility situation and this blunder is more evident if low order finite elements are used. Mixed displacement/pressure ($\mathbf{u}/p$) finite element formulations are far more suitable to tackle (quasi)-incompressible problems [34]. In previous works, the authors have used mixed displacement-pressure elements [35,18] and strain-displacement ones [22] in the solution of strain localization problems in isochoric and quasi-isochoric situations.

In this work, orthotropic elasticity is addressed as well as orthotropic plasticity. In orthotropic elasticity, two interesting questions arise in contrast to isotropic elasticity. On the one hand, there is no simple scalar relation between the pressure (or mean stress) and the volumetric strain. This renders inapplicable most developments related to mixed $\mathbf{u}/p$ formulations. This is also the case of some related elements, like the widely used $Q1P0$, where the discontinuous constant pressure is eliminated at element level to yield a final formulation in terms of displacements only. On the other hand, the term "incompressible material" results a contentious matter when referred to anisotropic solids, see [36] for a discussion on this subject. Fortunately, the B-bar method can be introduced to deal with anisotropic and non-linear media [37,38]. This method is adopted in this work.

4.1 B-bar finite element

In the standard displacement based finite element method, the strain field $\boldsymbol{\epsilon}$ inside an element is related to the nodal displacements $\mathbf{a}$ by the strain-displacement matrix $\mathbf{B}$ (discrete symmetric gradient operator)

$$\boldsymbol{\epsilon} = \mathbf{B}\mathbf{a} \tag{4.1}$$

where matrix $\mathbf{B}$ is expressed as

$$\mathbf{B} = \left[\mathbf{B}_1, ..., \mathbf{B}_i, ..., \mathbf{B}_{n_n}\right] \tag{4.2}$$

for $1 \leq i \leq n_n$, with n_n being the number of nodes in the element. In general 3D cases, sub-matrix $\mathbf{B}_i$ and its volumetric part $\mathbf{B}_i^{\text{vol}}$ are expressed in Voigt's notation as

$$\mathbf{B}_i = \begin{bmatrix} \partial N_{i,1} & 0 & 0 \\ 0 & \partial N_{i,2} & 0 \\ 0 & 0 & \partial N_{i,3} \\ \partial N_{i,2} & \partial N_{i,1} & 0 \\ \partial N_{i,3} & 0 & \partial N_{i,1} \\ 0 & \partial N_{i,3} & \partial N_{i,2} \end{bmatrix}, \qquad \mathbf{B}_i^{\text{vol}} = \frac{1}{3} \begin{bmatrix} \partial N_{i,1} & \partial N_{i,2} & \partial N_{i,3} \\ \partial N_{i,1} & \partial N_{i,2} & \partial N_{i,3} \\ \partial N_{i,1} & \partial N_{i,2} & \partial N_{i,3} \\ 0 & 0 & 0 \\ 0 & 0 & 0 \\ 0 & 0 & 0 \end{bmatrix} \tag{4.3}$$

where N_i is the shape function of node i and $\partial N_{i,j}$ is its derivative with respect to the j^{th} $(1 \leq j \leq 3)$ Cartesian coordinate. The corresponding deviatoric part is then given by

$$\mathbf{B}_i^{\text{dev}} = \mathbf{B}_i - \mathbf{B}_i^{\text{vol}} \tag{4.4}$$

With these definitions, it follows that

$$\boldsymbol{\epsilon} = \mathbf{B}\mathbf{a} = \left(\mathbf{B}^{\text{dev}} + \mathbf{B}^{\text{vol}}\right)\mathbf{a} = \boldsymbol{\epsilon}^{\text{dev}} + \frac{1}{3}\epsilon^{\text{vol}}\mathbf{1} \tag{4.5}$$

where $\boldsymbol{\epsilon}^{\text{dev}} = \text{dev}\boldsymbol{\epsilon}$ and $\epsilon^{\text{vol}} = \text{tr}\boldsymbol{\epsilon} = \nabla \cdot \mathbf{u}$ are the deviatoric and volumetric strains, respectively.

Now, let n_g be the number of integration points used to sample the strains and stresses and to integrate the internal nodal forces in the finite element. Then the average of the strain-displacement sub-matrices, $\bar{\mathbf{B}}_i^{\text{vol}}$, corresponding to node i, can be computed as

$$\bar{\mathbf{B}}_i^{\text{vol}} = \frac{1}{n_g} \sum_{k=1}^{n_g} \mathbf{B}_i^{\text{vol}} \tag{4.6}$$

The modified B-bar strain-displacement matrix is then defined as

$$\bar{\mathbf{B}}_i = \mathbf{B}_i^{\text{dev}} + \bar{\mathbf{B}}_i^{\text{vol}} \tag{4.7}$$

As explained in [37], the B-bar method is equivalent to the use of reduced integration for the volumetric part of the strain energy, while full integration is retained for the deviatoric contribution. Under given circumstances, a B-bar $Q1$ element is identical to the mixed $Q1P0$ element, but obtained through the deviatoric/volumetric split of the strains rather than the stresses.

4.2 Example: Strip under vertical stretching

In this section, a strip under vertical stretching is considered as shown in Figure 4. Following Hill [5] where characteristics are defined as "curves along which small disturbances propagates, a sharp horizontal slit is inserted in the strip to introduce the perturbation necessary to trigger strain localization. The far field stress state corresponds exactly to that given in Eq. (3.19). The analytical results presented in Section 3.3 are compared to the corresponding numerical ones.

4.2.1 Isotropic and orthotropic elasticity with von Mises plasticity. Let us consider the reference material of J_2 perfect plasticity, and isotropic elastic behavior with Young's modulus $E_0 = 1.0 \times 10^7$ MPa, Poisson's ratio $\nu_0 = 0.2$ and the yield strength $\sigma_Y = 1.0 \times 10^4$ MPa.

Due to the facts $\sigma_{12} = 0$ and $\Lambda_{12} = 0$, the localization angle is given from Eq. (3.8), i.e.,

$$\tan\theta^{\rm cr} = \begin{cases} \pm\sqrt{2} & \text{Plane stress} \\ \pm 1 & \text{Plane strain} \end{cases} \quad \Longrightarrow \quad \theta^{\rm cr} = \begin{cases} \pm 54.74^\circ & \text{Plane stress} \\ \pm 45^\circ & \text{Plane strain} \end{cases} \tag{4.8}$$

The above results were obtained and numerically validated in previous works [18,21].

As shown in Figures 5 and 6 for the plane stress cases and Figures 7 and 8 for the plane strain cases, the localization angle $\theta^{\rm cr}$ depends neither on Young's modulus nor on Poisson's ratio, even if they are varied in an orthotropic fashion.

4.2.2 Othotropic Hill material with no tilt. The Hill orthotropic plasticity material with the local axis 1 coincident with the global one x, i.e., $\alpha = 0$, is considered. In this case, the analytical localization angle $\theta^{\rm cr}$ is given by Eqs. (3.21) and (3.23), respectively.

Table 1 A strip under plane stress vertical stretching: Localization angles for various $\sigma_{Y,11}$ while $\sigma_{Y,22} = \sigma_{Y,33} = \sigma_Y$ are fixed.

Yield strength $\sigma_{Y,11}$	F	H	$\tan\theta^{\rm cr}$	$\theta^{\rm cr}$	Angles of slip lines
$0.75\sigma_Y$	$\frac{8}{9}\left(\frac{1}{\sigma_Y}\right)^2$	$\frac{1}{9}\left(\frac{1}{\sigma_Y}\right)^2$	$\pm\sqrt{\frac{9}{8}}$	$\pm46.69^\circ$	$\pm43.31^\circ$
σ_Y (Isotropic)	$\frac{1}{2}\left(\frac{1}{\sigma_Y}\right)^2$	$\frac{1}{2}\left(\frac{1}{\sigma_Y}\right)^2$	$\pm\sqrt{2}$	$\pm54.74^\circ$	$\pm35.26^\circ$
$1.50\sigma_Y$	$\frac{2}{9}\left(\frac{1}{\sigma_Y}\right)^2$	$\frac{7}{9}\left(\frac{1}{\sigma_Y}\right)^2$	$\pm\sqrt{\frac{9}{2}}$	$\pm64.76^\circ$	$\pm25.24^\circ$

Table 2 A strip under plane stress vertical stretching: Localization angles for various $\sigma_{Y,22}$ while $\sigma_{Y,11} = \sigma_{Y,33} = \sigma_Y$ are fixed.

Yield strength $\sigma_{Y,22}$	F	H	$\tan\theta^{\rm cr}$	$\theta^{\rm cr}$	Angles of slip lines
$0.75\sigma_Y$	$\frac{8}{9}\left(\frac{1}{\sigma_Y}\right)^2$	$\frac{8}{9}\left(\frac{1}{\sigma_Y}\right)^2$	$\pm\sqrt{2}$	$\pm54.74^\circ$	$\pm35.26^\circ$
σ_Y (Isotropic)	$\frac{1}{2}\left(\frac{1}{\sigma_Y}\right)^2$	$\frac{1}{2}\left(\frac{1}{\sigma_Y}\right)^2$	$\pm\sqrt{2}$	$\pm54.74^\circ$	$\pm35.26^\circ$
$1.50\sigma_Y$	$\frac{2}{9}\left(\frac{1}{\sigma_Y}\right)^2$	$\frac{2}{9}\left(\frac{1}{\sigma_Y}\right)^2$	$\pm\sqrt{2}$	$\pm54.74^\circ$	$\pm35.26^\circ$

– Plane stress: Let us first alter the yield strength $\sigma_{Y,11}$ while the other two ones $\sigma_{Y,22}$ and $\sigma_{Y,33}$ are both fixed as σ_Y. The analytical results are summarized in Tables 1 and 2, against the numerical contours of the equivalent plastic strain shown in Figure 9.

  As can be seen, the alteration of the yield strength $\sigma_{Y,11}$ yields distinct localization angles for the slit under vertical stretching. Comparatively, alteration of $\sigma_{Y,22}$ does not vary the localization angle since the slit is stretched along axis y.

– Plane strain: It follows from the analytical result Eq. (3.23) that the localization angle $\theta^{\rm cr}$ is fixed as 45° regardless the alteration of the material yield strengths. This conclusion is validated from the numerical contours presented in Figure 10.

For all cases, the analytical results are coincident with the numerical ones as expected.

4.2.3 Othotropic Hill material with tilt. Let us now discuss the Hill orthotropic plasticity with the material local axis 1 different from the global one x, i.e., $\alpha \neq 0$. Similarly, the plane stress and plane strain conditions have to be discriminated.

– Plane stress: The analytical localization angle $\theta^{\rm cr}$ is given by Eq. (3.7) together with the ratios (3.20). In particular, some analytical results are summarized in Tables 3, 4, 5 and 6. The numerical contours of the equivalent plastic strain are shown in Figures 11 to 14.

  As can be seen, variation of the yield strengths in both directions yields distinct localization angles.

– Plane strain: Some of the analytical localization angles $\theta^{\rm cr}$ given by Eq. (3.12) together with the ratios (3.22) are summarized in Tables 7 and 8. The corresponding numerical contours of the equivalent plastic strain are shown in Figures 15 and 16.

  Compared to the results of plane stress, the variation of the yield strength in both directions has the same influences on the localization angles.

In all cases, the analytical results are reproduced by the numerical ones. Note again that the above results given from localization analyses are independent of the frame of reference. However, if the material axes are not aligned with the direction of straining, the strip is no longer of uniaxial straining in the material axes. Accordingly, considering material tilting with respect to the direction of straining verifies the results obtained for multi-directional straining.

4.3 Example: Indentation by a flat rigid die

The second example is the indentation by a flat rigid die shown in Figure 17. This is a well-known 2-D plane strain problem usually used in the literature to test the ability of plasticity model to capture the failure modes; see also [5].

Table 3 A strip under plane stress vertical stretching: Localization angles for $\sigma_{Y,11} = 1.50\sigma_Y$ at various tilts α.

Tilt α	$\tan\theta^{\rm cr}$	$\theta^{\rm cr}$	$\theta^{\rm cr}+\alpha$	Angles of slip lines
0°	$-2.1213;\ 2.1213$	$64.8^\circ;\ -64.8^\circ$	$64.8^\circ;\ -64.8^\circ$	$-25.2^\circ;\ 25.2^\circ$
30°	$-23.906;\ 0.5229$	$-87.6^\circ;\ 27.6^\circ$	$57.6^\circ;\ -57.6^\circ$	$-32.4^\circ;\ 32.4^\circ$
45°	$0.2644;\ 13.236$	$14.8^\circ;\ 85.7^\circ$	$59.8^\circ;\ 130.7^\circ$	$-30.2^\circ;\ 40.7^\circ$
60°	$0.0651;\ 4.6115$	$3.7^\circ;\ 77.8^\circ$	$63.7^\circ;\ 137.8^\circ$	$-26.3^\circ;\ 47.8^\circ$

Table 4 A strip under plane stress vertical stretching: Localization angles for $\sigma_{Y,11} = 0.75\sigma_Y$ at various tilts α.

Tilt α	$\tan\theta^{\rm cr}$	$\theta^{\rm cr}$	$\theta^{\rm cr}+\alpha$	Angles of slip lines
0°	$-1.0607;\ 1.0607$	$46.7^\circ;\ -46.7^\circ$	$46.7^\circ;\ -46.7^\circ$	$-43.3^\circ;\ 43.3^\circ$
30°	$-6.2271;\ 0.3814$	$-80.9^\circ;\ 20.9^\circ$	$50.9^\circ;\ -50.9^\circ$	$-39.1^\circ;\ 39.1^\circ$
45°	$0.0375;\ 3.3375$	$2.1^\circ;\ 73,3^\circ$	$47.1^\circ;\ 118.3^\circ$	$-42.9^\circ;\ 28.3^\circ$
60°	$-0.2620;\ 1.4312$	$-14.7^\circ;\ 55.1^\circ$	$45.3^\circ;\ 115.1^\circ$	$-44.7^\circ;\ 25.1^\circ$

Table 5 A strip under plane stress vertical stretching: Localization angles for $\sigma_{Y,22} = 1.50\sigma_Y$ at various tilts α.

Tilt α	$\tan\theta^{\rm cr}$	$\theta^{\rm cr}$	$\theta^{\rm cr}+\alpha$	Angles of slip lines
0°	$-1.1414;\ 1.1414$	$54.7^\circ;\ -54.7^\circ$	$54.7^\circ;\ -54.7^\circ$	$-35.3^\circ;\ 35.3^\circ$
30°	$0.2169;\ 15.3716$	$12.2^\circ;\ 86.3^\circ$	$42.2^\circ;\ 116.3^\circ$	$-47.8^\circ;\ 26.3^\circ$
45°	$0.0756;\ 3.7816$	$4.3^\circ;\ 75.2^\circ$	$49.3^\circ;\ 120.2^\circ$	$-40.7^\circ;\ 30.2^\circ$
60°	$-0.0418;\ 1.9124$	$-2.4^\circ;\ 62.4^\circ$	$57.6^\circ;\ 122.4^\circ$	$-32.4^\circ;\ 32.4^\circ$

Table 6 A strip under plane stress vertical stretching: Localization angles for $\sigma_{Y,22} = 0.75\sigma_Y$ at various tilts α.

Tilt α	$\tan\theta^{\rm cr}$	$\theta^{\rm cr}$	$\theta^{\rm cr}+\alpha$	Angles of slip lines
0°	$-1.1414;\ 1.1414$	$54.7^\circ;\ -54.7^\circ$	$54.7^\circ;\ -54.7^\circ$	$-35.3^\circ;\ 35.3^\circ$
30°	$-3.8164;\ 0.6987$	$-75.3^\circ;\ 34.9^\circ$	$-45.3^\circ;\ 64.9^\circ$	$44.7^\circ;\ -25.1^\circ$
45°	$0.2996;\ 26.700$	$16.7^\circ;\ 87.9^\circ$	$61.7^\circ;\ 132.9^\circ$	$-28.3^\circ;\ 42.9^\circ$
60°	$-0.1606;\ 2.6219$	$-9.1^\circ;\ 69.1^\circ$	$50.9^\circ;\ 129.1^\circ$	$39.1^\circ;\ 39.1^\circ$

Table 7 A strip under plane strain vertical stretching: Localization angles for $\sigma_{Y,11} = 1.50\sigma_Y$ or $\sigma_{Y,22} = 1.50\sigma_Y$ at various tilts α.

Tilt α	$\tan\theta^{\rm cr}$	$\theta^{\rm cr}$	$\theta^{\rm cr}+\alpha$	Angles of slip lines
0°	$-1.0000;\ 1.0000$	$45.0^\circ;\ -45.0^\circ$	$45.0^\circ;\ -45.0^\circ$	$-45.0^\circ;\ 45.0^\circ$
30°	$-6.7251;\ 0.1487$	$-81.5^\circ;\ 8.5^\circ$	$-51.5^\circ;\ 38.5^\circ$	$38.5^\circ;\ -51.5^\circ$
45°	$0;\ -\infty$	$0.0^\circ;\ -90.0^\circ$	$45.0^\circ;\ -45.0^\circ$	$-45.0^\circ;\ 45.0^\circ$
60°	$-0.1487;\ 6.7251$	$-8.5^\circ;\ 81.5^\circ$	$51.5^\circ;\ 141.5^\circ$	$-38.5^\circ;\ 51.5^\circ$

Table 8 A strip under plane strain vertical stretching: Localization angles for $\sigma_{Y,11} = 0.75\sigma_Y$ or $\sigma_{Y,22} = 0.75\sigma_Y$ at various tilts α.

Tilt α	$\tan\theta^{\rm cr}$	$\theta^{\rm cr}$	$\theta^{\rm cr}+\alpha$	Angles of slip lines
0°	$-1.0000;\ 1.0000$	$45.0^\circ;\ -45.0^\circ$	$45.0^\circ;\ -45.0^\circ$	$-45.0^\circ;\ 45.0^\circ$
30°	$-2.9675;\ 0.3370$	$-71.4^\circ;\ 18.6^\circ$	$-41.4^\circ;\ 48.6^\circ$	$48.6^\circ;\ -41.4^\circ$
45°	$0;\ -\infty$	$0.0^\circ;\ -90.0^\circ$	$45.0^\circ;\ -45.0^\circ$	$-45.0^\circ;\ 45.0^\circ$
60°	$-0.3370;\ 2.9675$	$-18.6^\circ;\ 71.4^\circ$	$41.4^\circ;\ 131.4^\circ$	$-48.6^\circ;\ 41.4^\circ$

As shown in Figure 18, the material right under the rigid die is almost under uniaxial vertical loading in the global axes, i.e., $\sigma_{xy} = 0$. In accordance with Remark 3.7, the localization angle $\theta^{\rm cr}$ is determined from Eq. (3.12) with the following ratio

$$\frac{\Lambda_{12}}{\Lambda_{11}} = \frac{1}{2}\frac{(G+H)L}{FG+FH+GH}\tan(2\alpha) \tag{4.9}$$

for the tilt α.

4.3.1 Isotropic von Mises material. Similarly as before, let us first consider the reference isotropic material of J_2 perfect plasticity, with Young's modulus $E_0 = 1.0 \times 10^7$ MPa, Poisson's ratio $\nu_0 = 0.2$ and the yield strength $\sigma_Y = 1.0 \times 10^4$ MPa.

As shown in Figure 19, the localization angle is fixed $\theta^{\rm cr} = 45^\circ$ regardless of the elastic constants. It is worthy noting that the failure modes are symmetric and corresponds to the claimed Prandtl's solution.

4.3.2 Orthotropic Hill material with no tilt. It follows from $\alpha = 0$ that $\Lambda_{12}/\Lambda_{11} = 0$. Accordingly, the localization angle is also fixed as $\theta^{\rm cr} = 45^\circ$ regardless of the material yield strength; see Figure 20 for the numerical results.

4.3.3 Orthotropic Hill material with tilt. As the localization angle depends only on the tilt, regardless of the stresses, the results coincide with those for the slit under plane strain vertical stretching. Therefore, the analytical localization angles summarized in Tables 7 and 8 also apply here. The numerical results presented in Figures 21 and 22 validate this conclusion.

As can be seen, due to the tilt of the material axes the failure modes are no longer symmetric. Note that the results for $\alpha = 45^\circ$ are identical to those for $\alpha = 0^\circ$ and the results for $\alpha = 30^\circ$ are symmetric to those for $\alpha = 60^\circ$ in both figures.

Note that in all cases the obtained results agree with those of Hill [5] for rigid-plastic materials.

5 Conclusions

In this work the strain localization analysis of Hill's orthotropic plasticity is addressed. Similarly to our previous work on isotropic plastic or damage models, the localization condition is derived from the boundedness of stress rates together with Maxwell's kinematics. That is, the plastic flow components perpendicular to the discontinuity normal vector vanish upon strain localization. Compared to the classical work based on the discontinuous bifurcation analysis, in the material axes the localization angles are independent from the elastic constants, but rather, they depend exclusively on the material parameters involved in the plastic yield function. This turns out

to be coincident with Hill's results for strictly incompressible rigid-plastic problems, extending them to general elasto-plastic materials.

In 2-D plane stress and plane strain situations, application of the above localization condition to Hill's orthotropic plasticity yields closed-form solutions of the localization angles. In particular, the discontinuity lines in plane strain conditions are always perpendicular to each other, and the localization angle depends only on the tite angle of the material axes for the case of shear stress free states.

The analytical results are validated independently by numerical simulations. Being the plastic flow purely isochoric, the B-bar finite element is employed to deal with the incompressibility of the plastic flow. Regarding a horizontal slit under vertical stretching and Prandtl's punch test in plane strain, numerical results are presented for both the isotropic plasticity and the orthotropic one with or without tilt angle between the material axes and the global ones. In all cases, the critical angles predicted from the localization condition coincide with those given by numerical simulations. Interestingly, as for Prandtl's punch test in plane strain the material right under the rigid footing is almost free of shear stresses, the localization angles are also independent from the stress state and can be determined as those for a slit under vertical stretching.

6 Acknowledgments

Financial support from the Spanish Government-MINECO-Proyectos de I + D (Excelencia)-DPI2017-85998-P-ADaMANT-Computational Framework for Additive Manufacturing of Titanium Alloy and the Catalan Government ACCIÓ - Ris3cat Transport and PRO^2 Project is gratefully acknowledged. This work is also supported by the National Natural Science Foundation of China (51878294; 51678246), the State Key Laboratory of Subtropical Building Science (2018ZC04) and the Funding for Central Universities (2018PY20) to J.Y. Wu.

References

1. L. Prandtl. Über die häete plastistischer körper. *Nachr. Ges. Wisensch, Göttingen, math. phys. Klasse*, pages 74–85, 1920.

2. H. Hencky. Über einige statisch bestimmte fälle des gleichgewichts in plastischen körpern. *Z. Angew. Math. Mech.*, 3:241–251, 1923.
3. H. Hencky. Zur theorie plastischer deformationen und der hierdurch im material hervorgerufenen nachspannungen. *Z. Angew. Math. Mech.*, 4:323–334, 1924.
4. J. Mandel. *Equilibre par trasches planes des solides à la limite d'écoulement.* PhD thesis, Thèse, Paris, 1942.
5. R. Hill. *The Mathematical Theory of Plasticity.* Oxford University Press, New York, 1950.
6. R. Hill. On discontinuous plastic states, with special reference to localized necking in thin sheets. *J. Mech. Phys. Solids*, 1:19–30, 1952.
7. R. Hill. General theory of uniqueness and stability of elasto-plastic solids. *J. Mech. Phys. Solids*, 6:236–249, 1958.
8. R. Hill. Acceleration waves in solids. *J. Mech. Phys. Solids*, 10:1–16, 1962.
9. T.Y. Thomas. *Plastic Flow and Fracture of Solids.* Academic Press, New York, 1961.
10. J. R. Rice. A path independent integral and the approximate analysis of strain cncentrations by notches and cracks. *J. Appl. Mech.-T. ASME*, 35:379–386, 1968.
11. J. W. Rudnicki and J. R. Rice. Conditions of the localization of deformation in pressure-sensitive dilatant material. *J. Mech. Phys. Solids*, 23:371–394, 1975.
12. J. R. Rice and J. W. Rudnicki. A note on some features of the theory of localization of deformation. *Int. J. Solids Structures*, 16:597–605, 1980.
13. K. Runesson, N.S. Ottosen, and D. Peric. Discontinuous bifurcations of elastic-plastic solutions at plane stress and plane strain. *Int. J. Plast.*, 7:99–121, 1991.
14. J.C. Simó, J. Oliver, and F. Armero. An analysis of strong discontinuities induced by strain-softening in rate-independent inelastic solids. *Comput. Mech.*, 12:277–296, 1993.
15. J. Oliver. Modeling strong discontinuities in solid mechanics via strain softening constitutive equations. part i: Fundamentals; part ii: Numerical simulation. *International Journal for Numerical Methods in Engineering*, 39:3575–3600; 3601–3623, 1996.
16. J. Oliver, M. Cervera, and O. Manzoli. Strong discontinuities and continuum plasticity models: the strong discontinuity approach. *Int. J. Plast.*, 15:319–351, 1999.
17. J. Oliver. On the discrete constitutive models induced by strong discontinuity kinematics and continuum constitutive equations. *International Journal of Solids and Structures*, 37:7207–7229, 2000.

18. M. Cervera, M. Chiumenti, and D. Di Capua. Benchmarking on bifurcation and localization in j_2 plasticity for plane stress and plane strain conditions. *Comput. Methods Appl. Mech. Eng.*, 241244:206224, 2012.

19. J. Oliver, A. E. Huespe, and I. F. Dias. Strain localization, strong discontinuities and material fracture: Matches and mismatches. *Comput. Methods Appl. Mech. Eng.*, 241:323–336, 2006.

20. J. Y. Wu and M. Cervera. On the equivalence between traction- and stress-based approaches for the modeling of localized failure in solids. *Journal of the Mechanics and Physics of Solids*, 82:137–163, 2015.

21. J. Y. Wu and M. Cervera. A thermodynamically consistent plastic-damage framework for localized failure in quasi-brittle solids: Material model and strain localization analysis. *International Journal of Solids and Structures*, 88-89:227–247, 2016.

22. J. Y. Wu and M. Cervera. Strain localization of elastic-damaging frictional-cohesive materials: Analytical results and numerical verification. *Materials*, 10:434; doi:10.3390/ma10040434, 2017.

23. M. Cervera, M. Chiumenti, L. Benedetti, and R. Codina. Mixed stabilized finite element methods in nonlinear solid mechanics. part iii: Compressible and incompressible plasticity. *Comput. Methods Appl. Mech. Eng.*, 285:752–775, 2015.

24. O. Hoffman. The brittle strength of orthotropic materials. *J. Comp. Mater.*, 1:200–206, 1967.

25. S. W. Tsai and E. M. Wu. A general theory of strength for anisotropic materials. *J. Comp. Mater.*, 5:58–80, 1971.

26. S. Oller, E. Car, and J. Lubliner. Definition of a general implicit orthotropic yield criterion. *Comput. Methods Appl. Mech. Engrg.*, 192:895–912, 2003.

27. M. Li, J. Füssl, M. Lukacevic, and J. Eberhardsteiner. A numerical upper bound formulation with sensibly-arranged velocity discontinuities and orthotropic material strength behavior. *Journal of Theoretical and Applied Mechanics*, 56(2):417–433, 2018.

28. J.G. Rots, P. Nauta, G.M.A. Kusters, and J. Blaauwendraad. Smeared crack approach and fracture localization in concrete. *Heron*, 30:1–47, 1985.

29. M. Jirásek and T. Zimmermann. Analysis of rotating crack model. *J. Eng. Mech., ASCE*, 124(8):842–851, 1998.

30. M. Cervera. A smeared-embedded mesh-corrected damage model for tensile cracking. *Int. J. Numer. Meth. Engng.*, 76:1930–1954, 2008.

31. M. Cervera. An orthotropic mesh corrected crack model. *Comput. Methods Appl. Mech. Engrg.*, 197:1603–1619, 2008.

32. J. Y. Wu and M. Cervera. *Strain localization and failure mechanics for elastoplastic damage solids*. Monograph CIMNE M147, Barrcelona, Spain, 2014.

33. R. Hill. A theory of the yielding and plastic flow of anisotropic metals. *Proc. Roy. Soc. A*, 193:281–297, 1948.

34. J.C. Simó and T.J.R. Hughes. *Computational inelasticity*. Springer, New York, 1998.

35. M. Cervera and M. Chiumenti. Size effect and localization in j_2 plasticity. *International Journal of Solids and Structures*, 46:3301–3312, 2009.

36. C. A. Felippa and E. Oñate. Stress, strain and energy splittings for anisotropic solids under volumetric constraints. *Computers & Structures*, 81(13):1343–1357, 2003.

37. T. J. R. Hughes. Generalization of selective intertegration procedures to anisotropic and nonlinear media. *International Journal for Numerical Methods in Engineering*, 15(9):1413–1418, 1980.

38. T.R.J. Hughes. *The finite element method. Linear Static and Dynamic Finite Element Analysis*. Dover Publications Inc., Mineaola, New York, 2000.

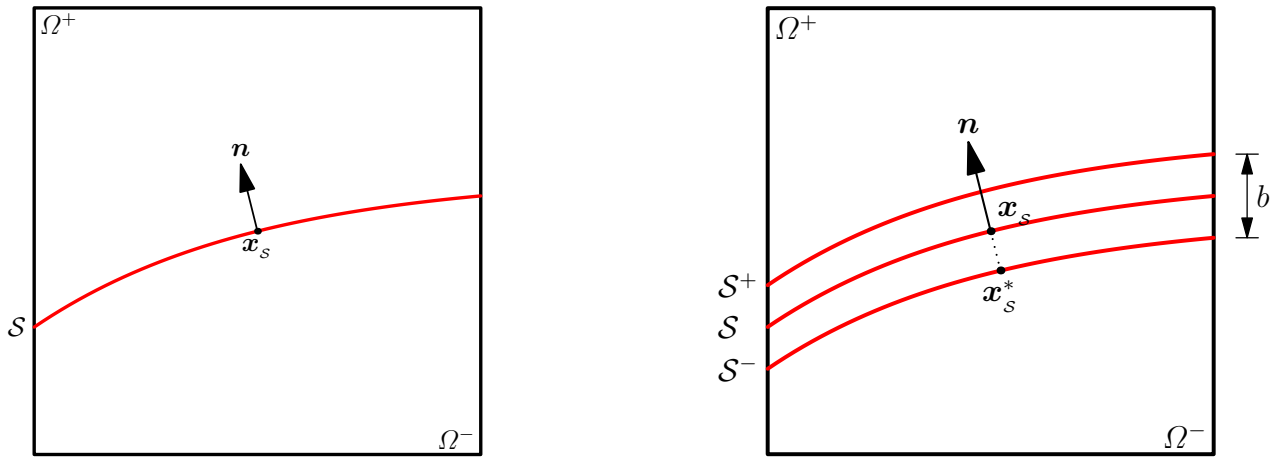

(a) Strong discontinuity

(b) Regularized discontinuity

Fig. 1 Strong and regularized discontinuities in a solid

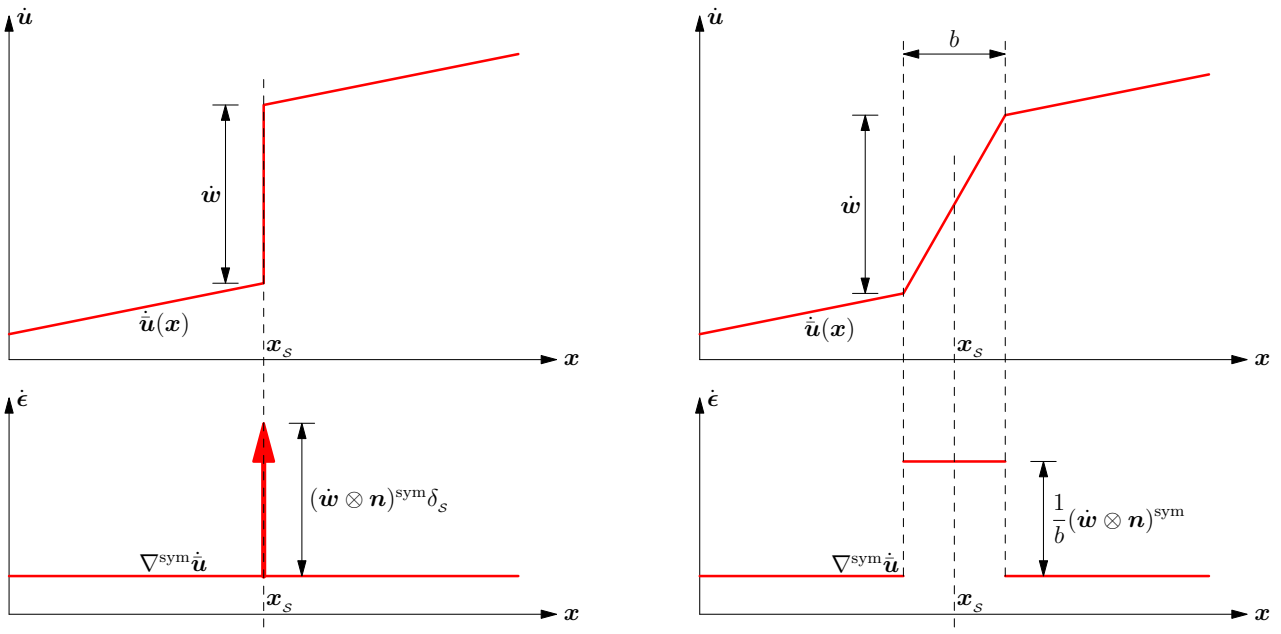

(a) Velocity/strain rate fields around a strong discontinuity

(b) Velocity/strain rate fields around a regularized discontinuity

Fig. 2 Kinematics of strong and regularized discontinuities

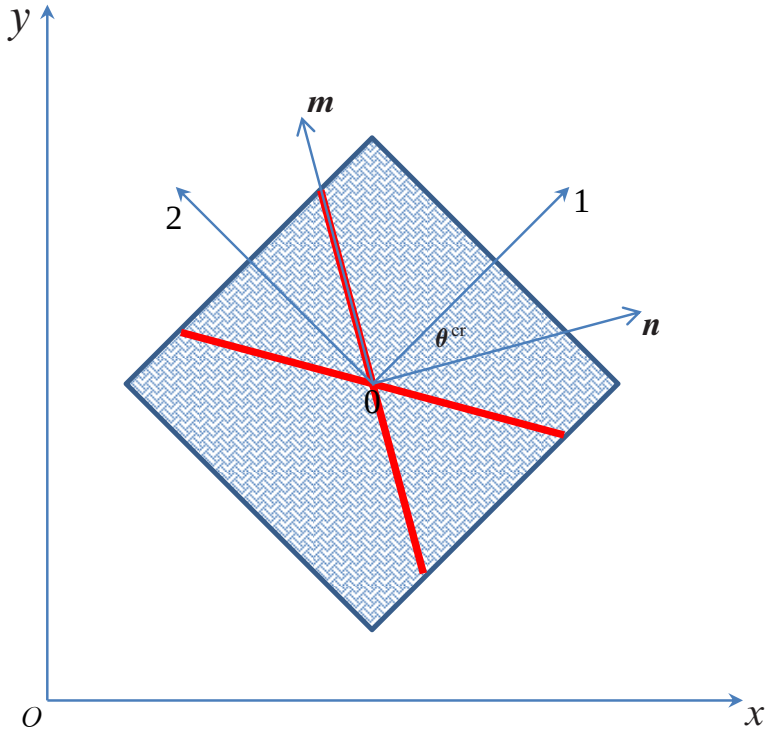

Fig. 3 Definition of the localization angle θ^{cr} between the normal vector $\boldsymbol{n}$ of the discontinuity and the material local axis 1.

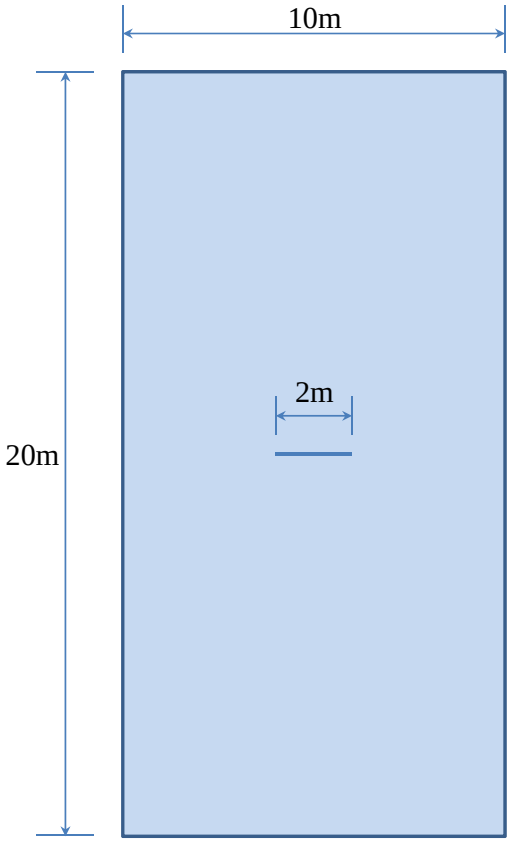

Fig. 4 A strip under vertical stretching: Dimensions. The bottom and top edges are vertically stretched along opposite directions but with equal magnitude.

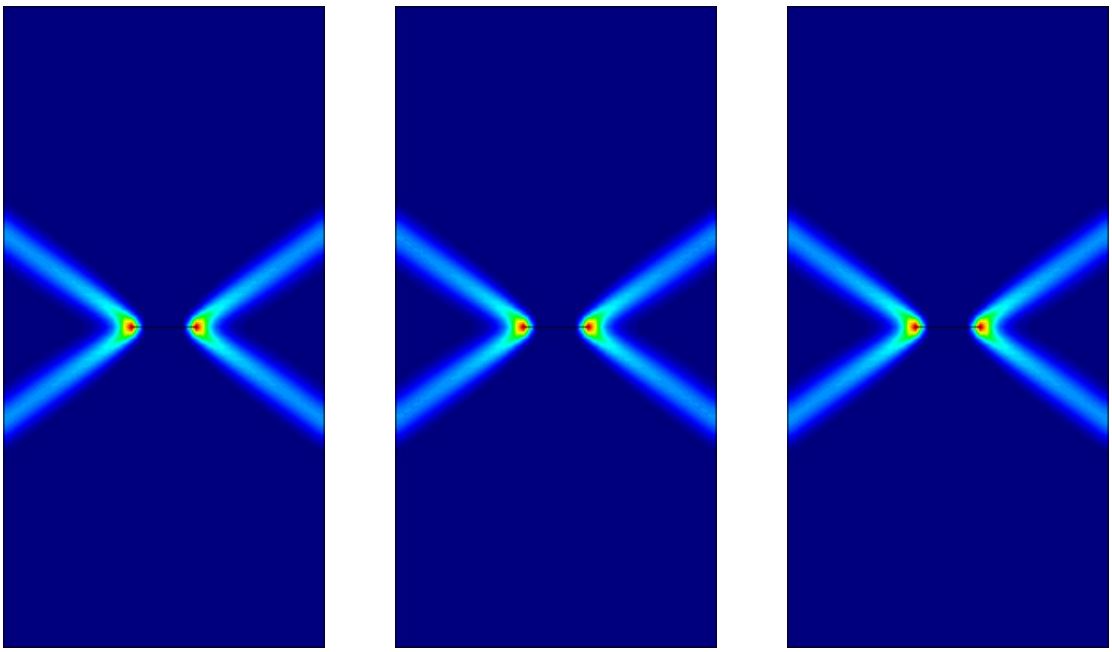

(a) $E_{11} = 1.5E_0$ (b) $E_{11} = E_{22} = E_0$ (c) $E_{22} = 1.5E_0$

Fig. 5 A strip under vertical stretching (plane stress): Influence of Young's moduli on the localization angle $\theta^{\text{cr}} = 54.7°$

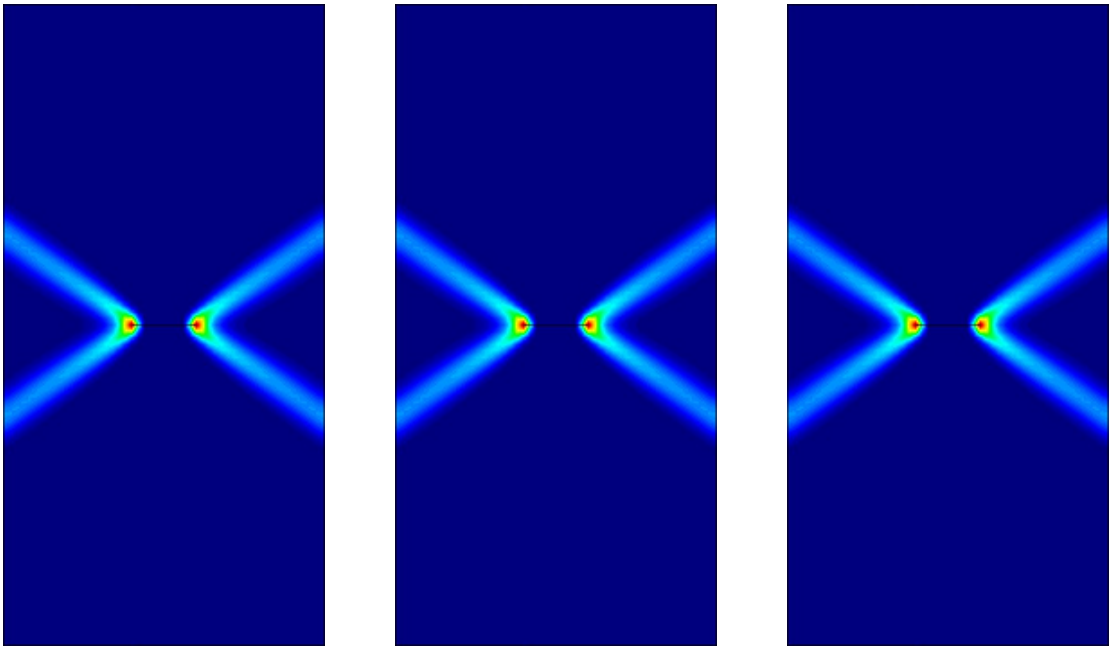

(a) $\nu_0 = 0.0$ (b) $\nu_0 = 0.2$ (c) $\nu_0 = 0.4$

Fig. 6 A strip under vertical stretching (plane stress): Influence of Poisson's ratio on the localization angle $\theta^{\text{cr}} = 54.7°$

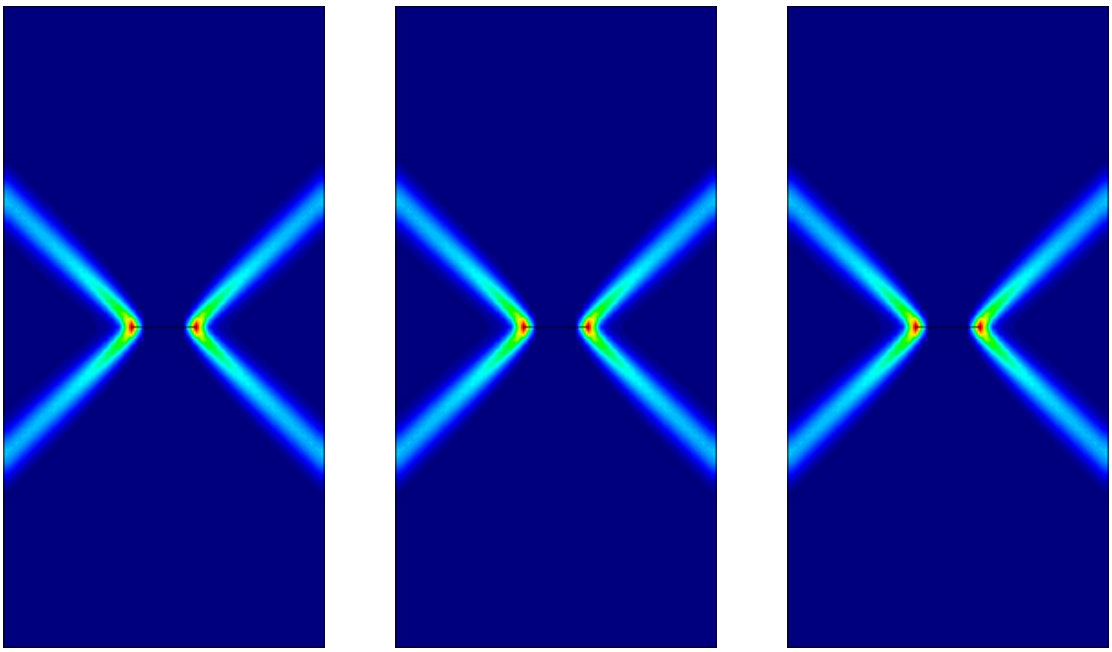

(a) $E_{11} = 1.5E_0$ (b) $E_{11} = E_{22} = E_0$ (c) $E_{22} = 1.5E_0$

Fig. 7 A strip under vertical stretching (plane strain): Influence of Young's moduli on the localization angle $\theta^{\text{cr}} = 45^\circ$

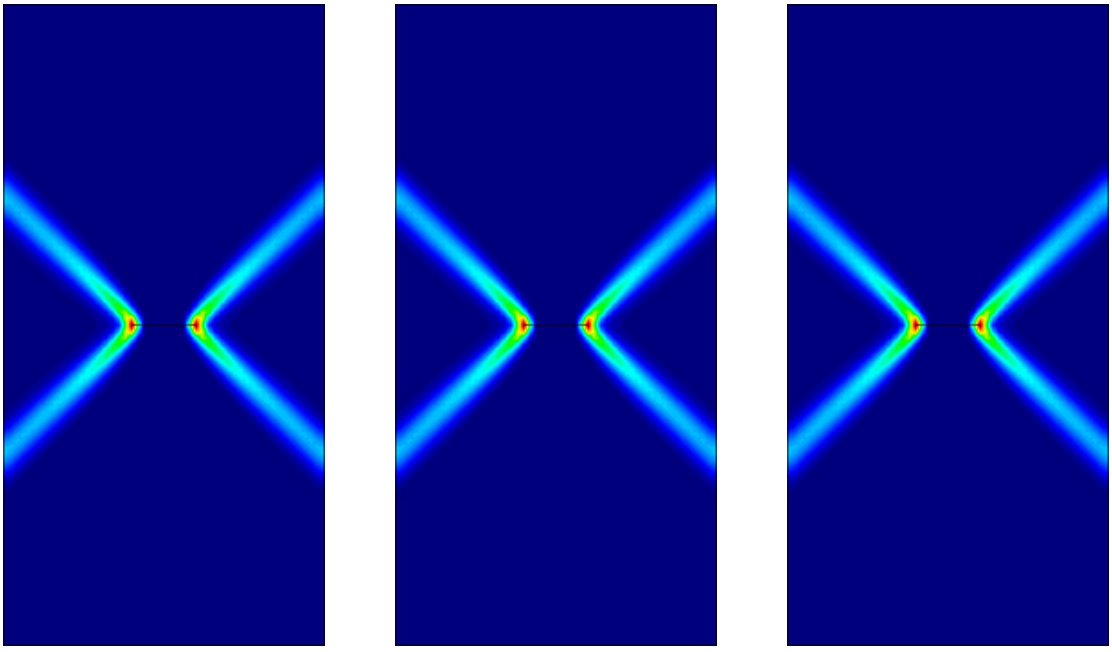

(a) $\nu_0 = 0.0$ (b) $\nu_0 = 0.2$ (c) $\nu_0 = 0.4$

Fig. 8 A strip under vertical stretching (plane strain): Influence of Poisson's ratio on the localization angle $\theta^{\text{cr}} = 45^\circ$

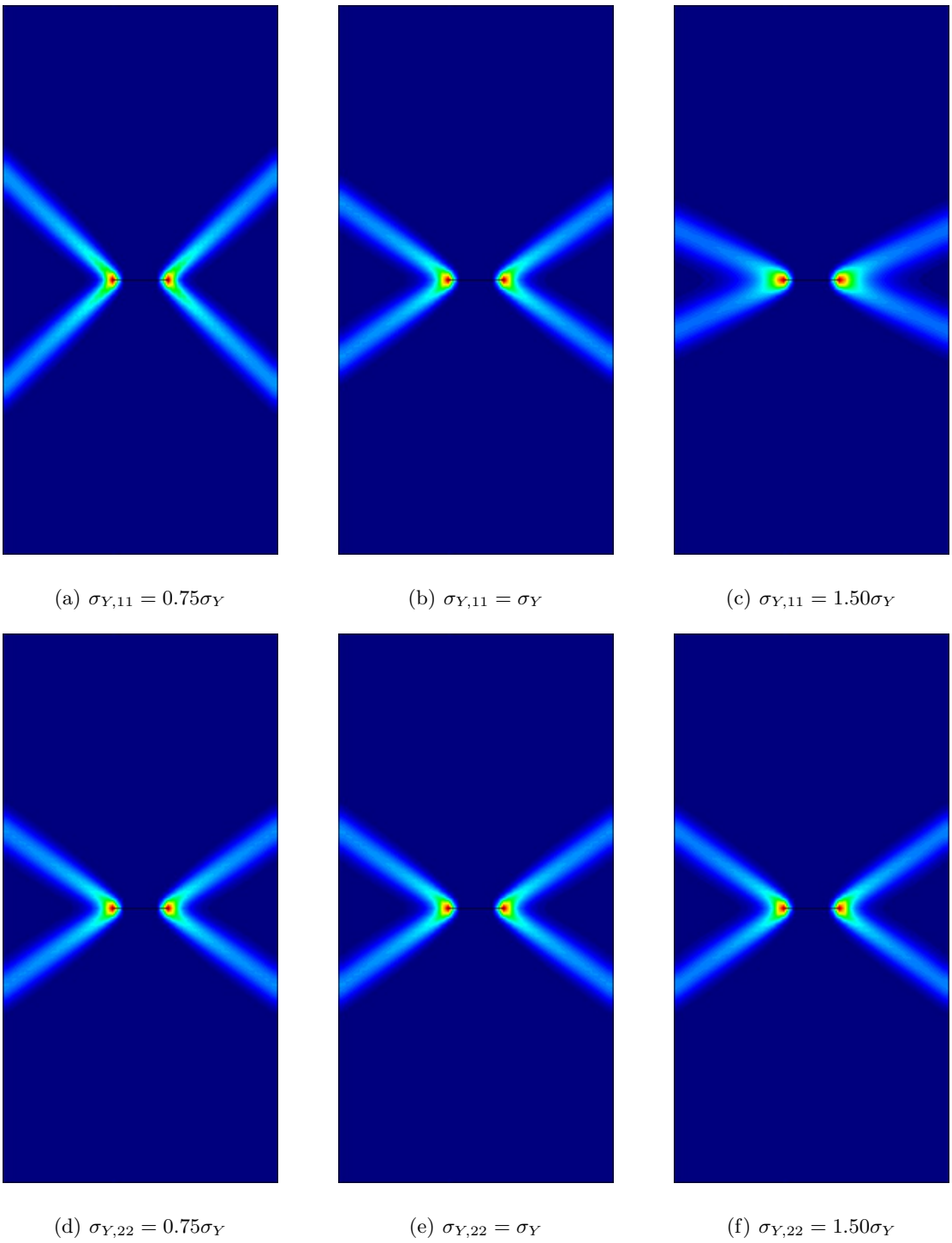

(a) $\sigma_{Y,11} = 0.75\sigma_Y$ (b) $\sigma_{Y,11} = \sigma_Y$ (c) $\sigma_{Y,11} = 1.50\sigma_Y$

(d) $\sigma_{Y,22} = 0.75\sigma_Y$ (e) $\sigma_{Y,22} = \sigma_Y$ (f) $\sigma_{Y,22} = 1.50\sigma_Y$

Fig. 9 A strip under vertical stretching (plane stress): Influence of the yield strengths $\sigma_{Y,11}$ and $\sigma_{Y,22}$ on the localization angle $\theta^{\mathrm{cr}} = 54.7^\circ$

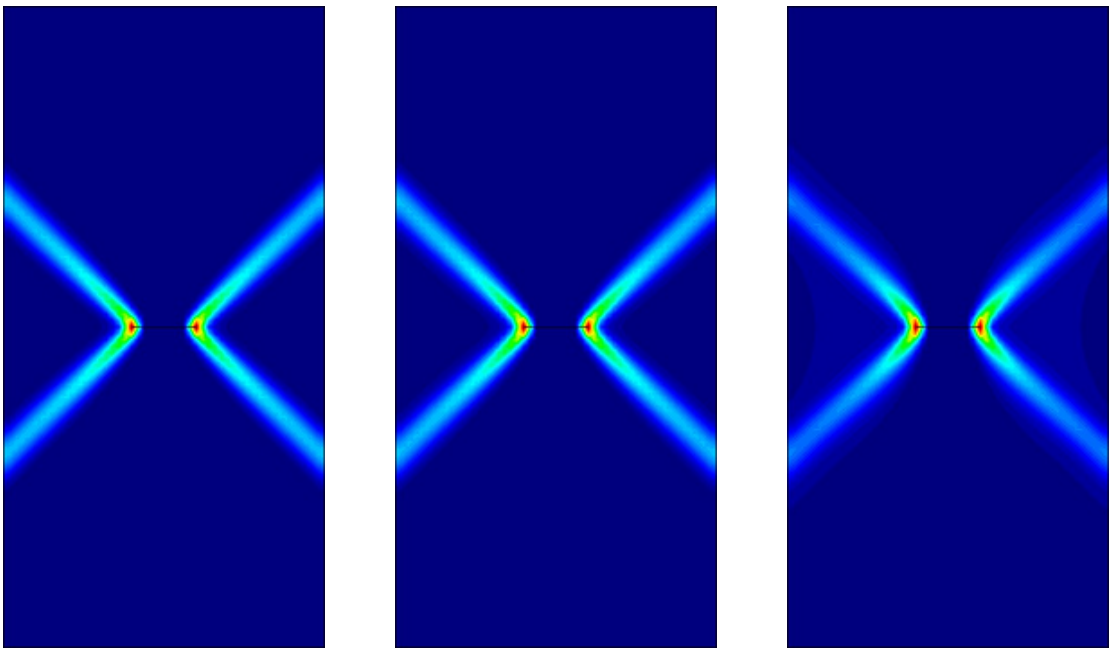

(a) $\sigma_{Y,11} = 0.75\sigma_Y$ (b) $\sigma_{Y,11} = \sigma_Y$ (c) $\sigma_{Y,11} = 1.50\sigma_Y$

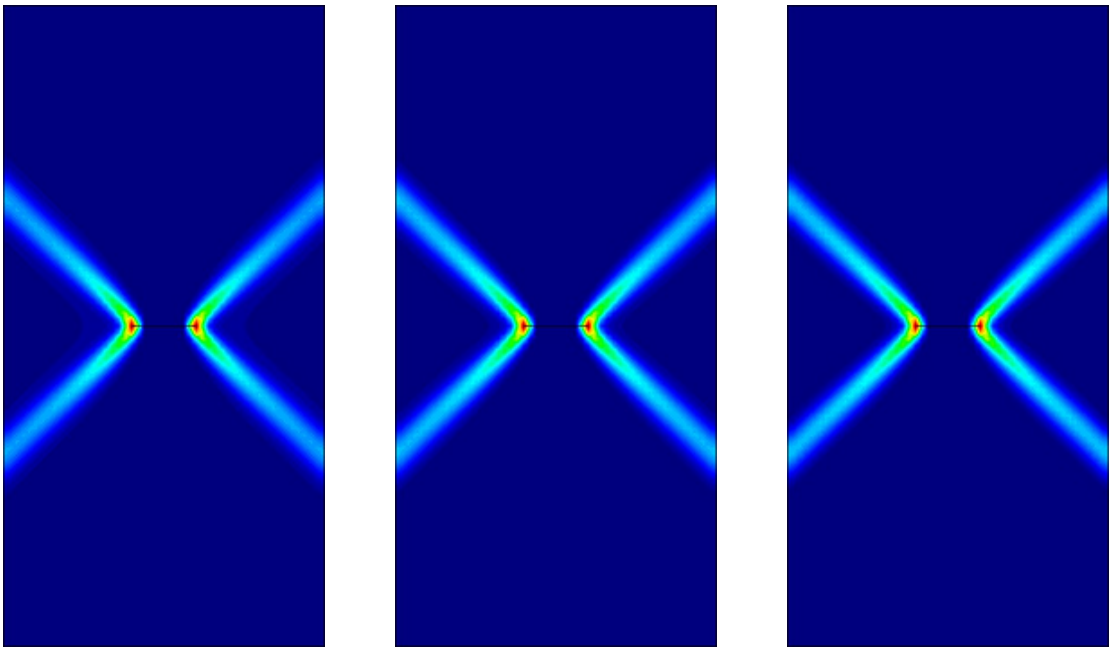

(d) $\sigma_{Y,22} = 0.75\sigma_Y$ (e) $\sigma_{Y,22} = \sigma_Y$ (f) $\sigma_{Y,22} = 1.50\sigma_Y$

Fig. 10 A strip under vertical stretching (plane strain): Influence of the yield strength $\sigma_{Y,11}$ and $\sigma_{Y,22}$ on the localization angle $\theta^{\rm cr} = 45^\circ$.

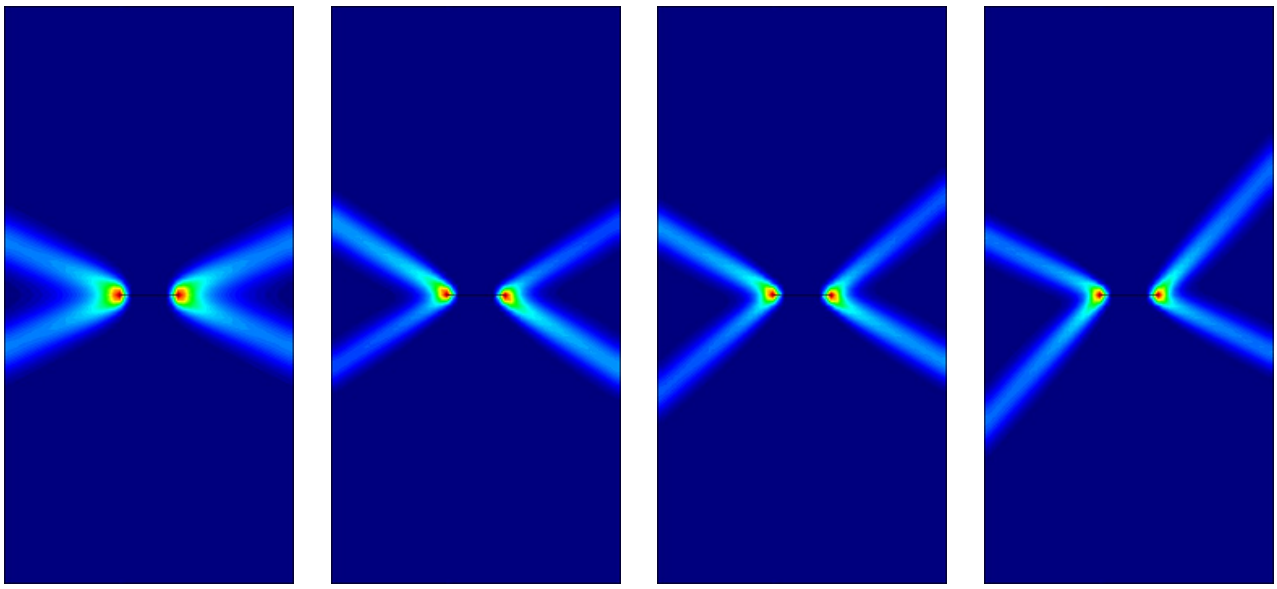

(a) $\alpha = 0^\circ$ (b) $\alpha = 30^\circ$ (c) $\alpha = 45^\circ$ (d) $\alpha = 60^\circ$

Fig. 11 A strip under vertical stretching (plane stress): Influence of the yield strength $\sigma_{Y,11} = 1.5\sigma_Y$ on the localization angle θ^{cr}.

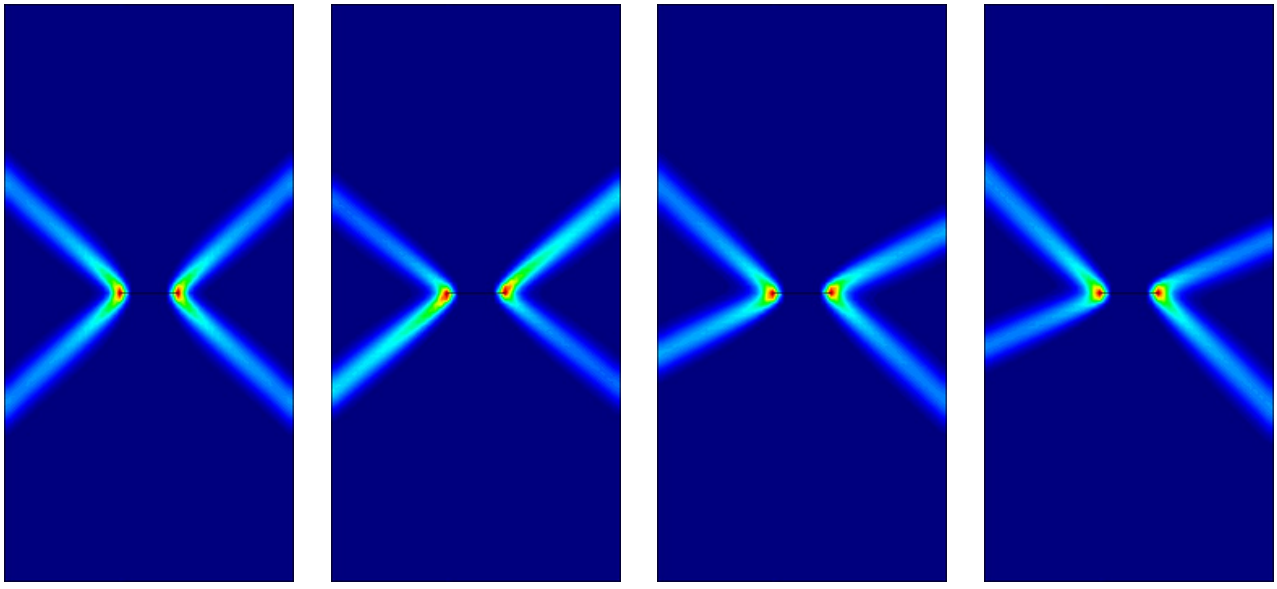

(a) $\alpha = 0^\circ$ (b) $\alpha = 30^\circ$ (c) $\alpha = 45^\circ$ (d) $\alpha = 60^\circ$

Fig. 12 A strip under vertical stretching (plane stress): Influence of the yield strength $\sigma_{Y,11} = 0.75\sigma_Y$ on the localization angle θ^{cr}.

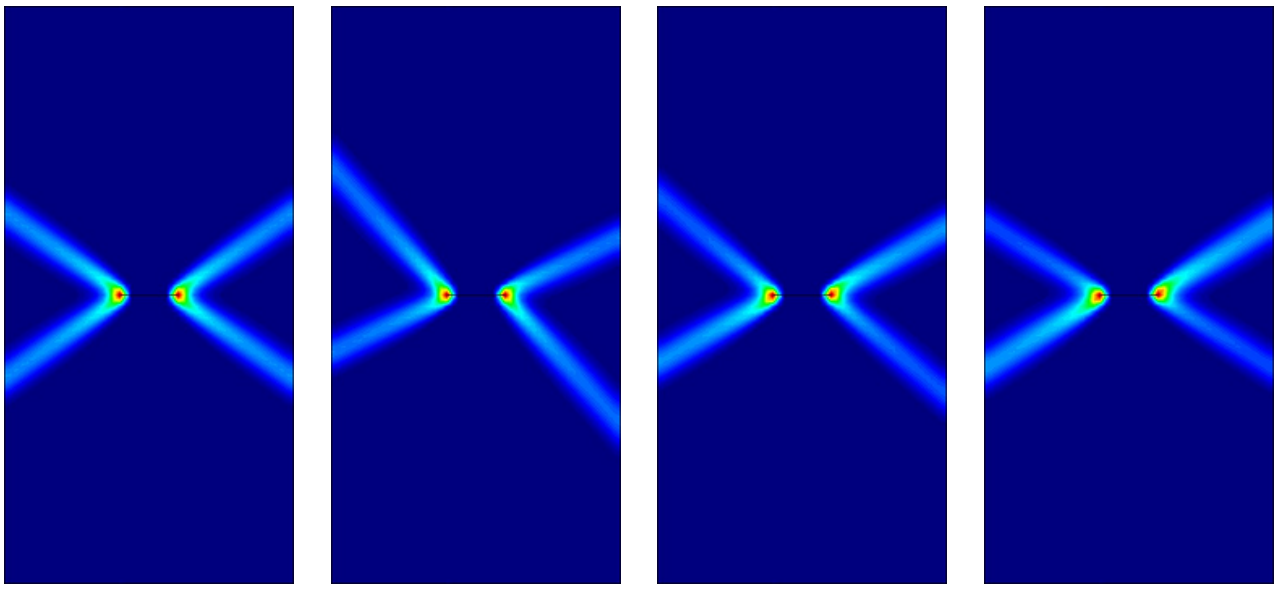

(a) $\alpha = 0^\circ$ (b) $\alpha = 30^\circ$ (c) $\alpha = 45^\circ$ (d) $\alpha = 60^\circ$

Fig. 13 A strip under vertical stretching (plane stress): Influence of the yield strength $\sigma_{Y,22} = 1.5\sigma_Y$ on the localization angle $\theta^{\rm cr}$.

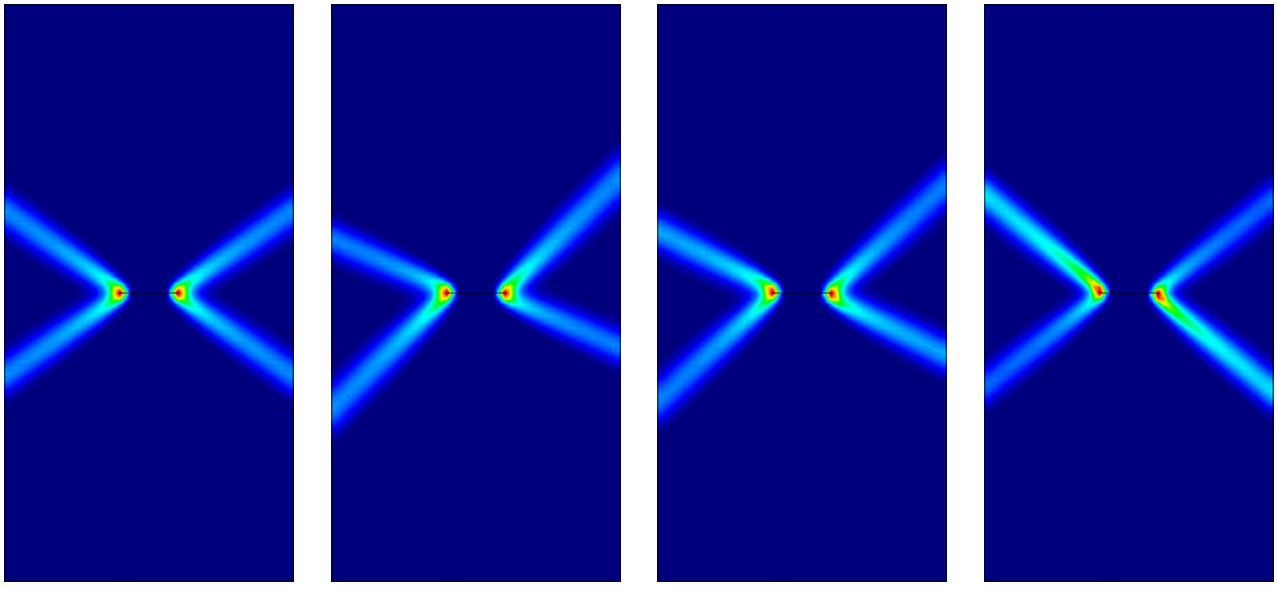

(a) $\alpha = 0^\circ$ (b) $\alpha = 30^\circ$ (c) $\alpha = 45^\circ$ (d) $\alpha = 60^\circ$

Fig. 14 A strip under vertical stretching (plane stress): Influence of the yield strength $\sigma_{Y,22} = 0.75\sigma_Y$ on the localization angle $\theta^{\rm cr}$.

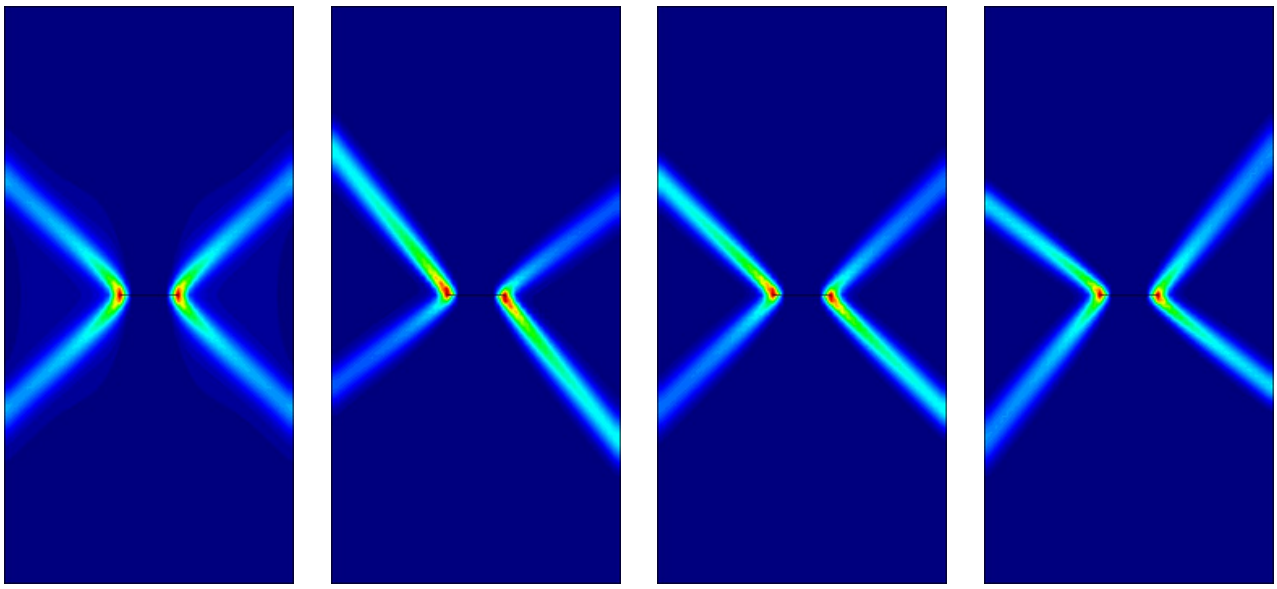

(a) $\alpha = 0^\circ$ (b) $\alpha = 30^\circ$ (c) $\alpha = 45^\circ$ (d) $\alpha = 60^\circ$

Fig. 15 A strip under vertical stretching (plane strain): Influence of the yield strength $\sigma_{Y,11} = 1.5\sigma_Y$ or $\sigma_{Y,22} = 1.5\sigma_Y$ on the localization angle θ^{cr}.

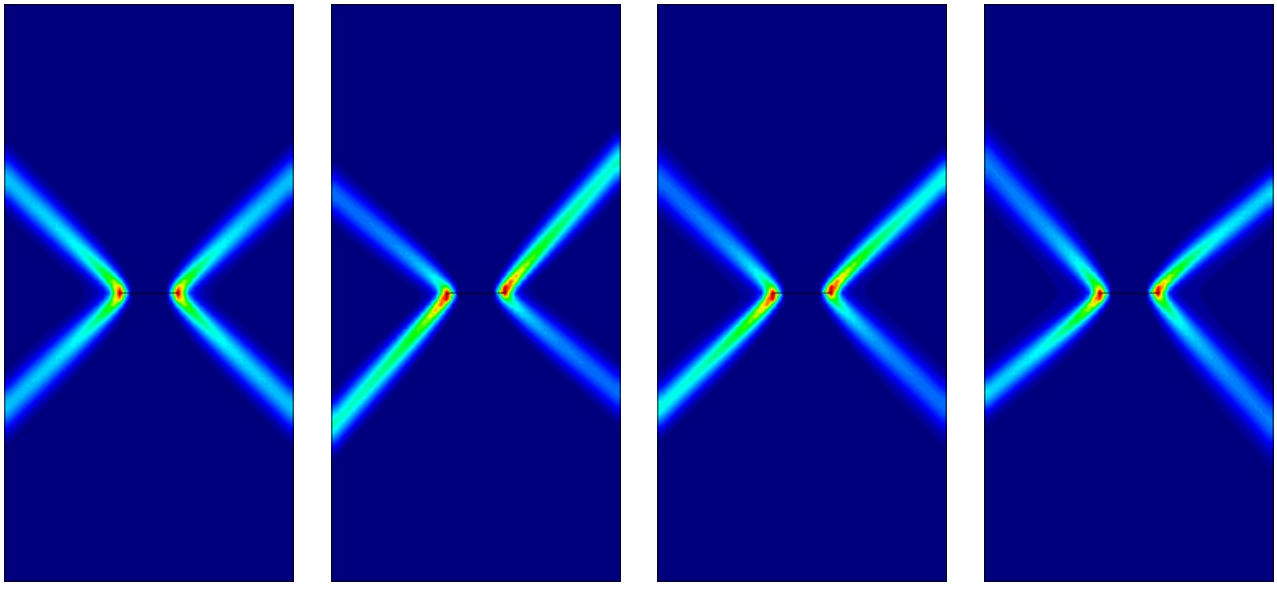

(a) $\alpha = 0^\circ$ (b) $\alpha = 30^\circ$ (c) $\alpha = 45^\circ$ (d) $\alpha = 60^\circ$

Fig. 16 A strip under vertical stretching (plane strain): Influence of the yield strength $\sigma_{Y,11} = 0.75\sigma_Y$ or $\sigma_{Y,22} = 0.75\sigma_Y$ on the localization angle θ^{cr}.

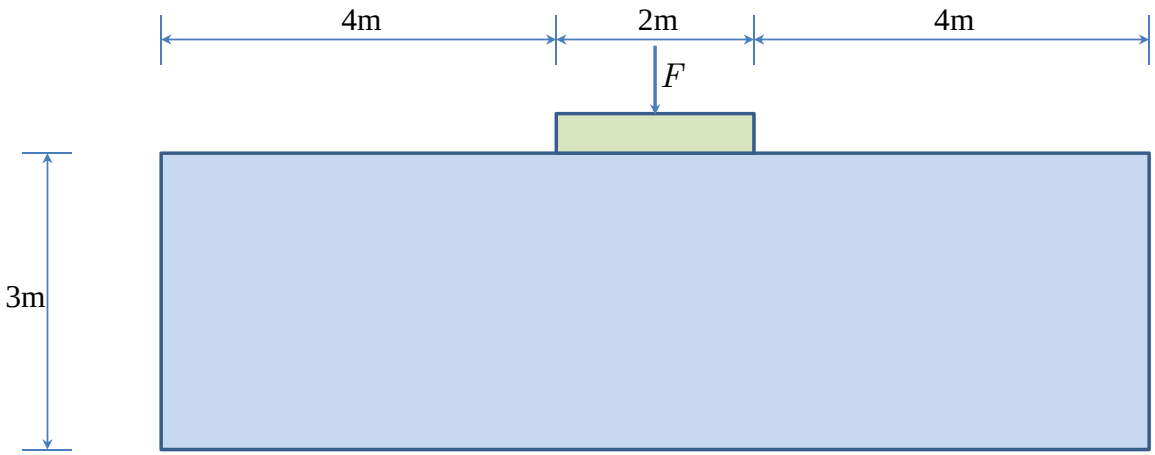

Fig. 17 Indentation by a flat rigid die: Dimensions and loading. The bottom edge is fixed in both direction, while the left and right edges are constrained along the horizontal direction.

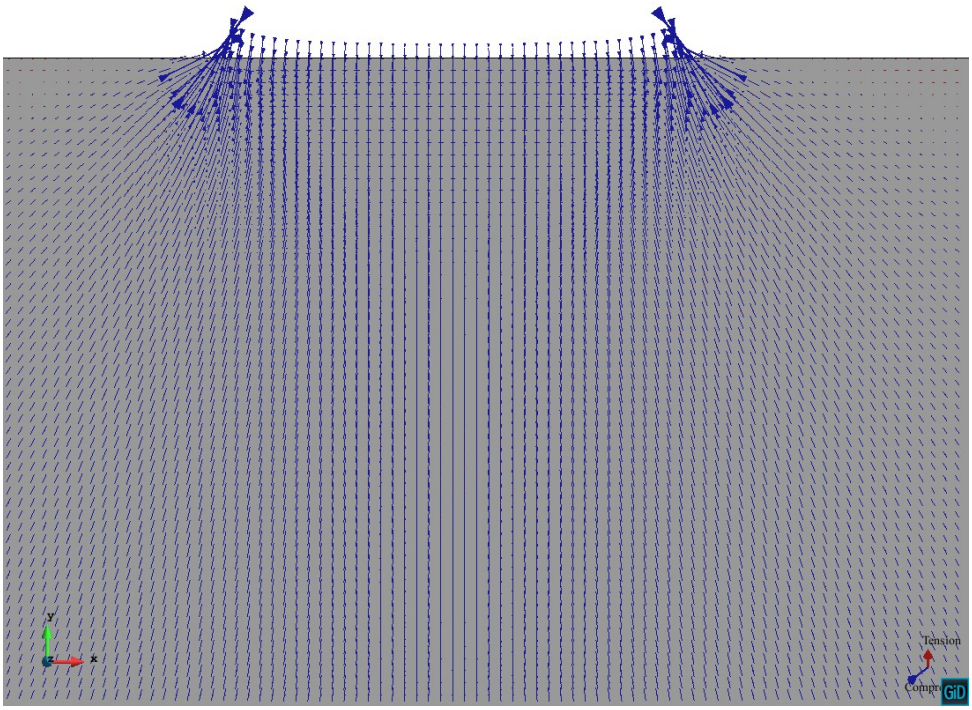

Fig. 18 Indentation by a flat rigid die: Directions of principal stresses around the rigid footing.

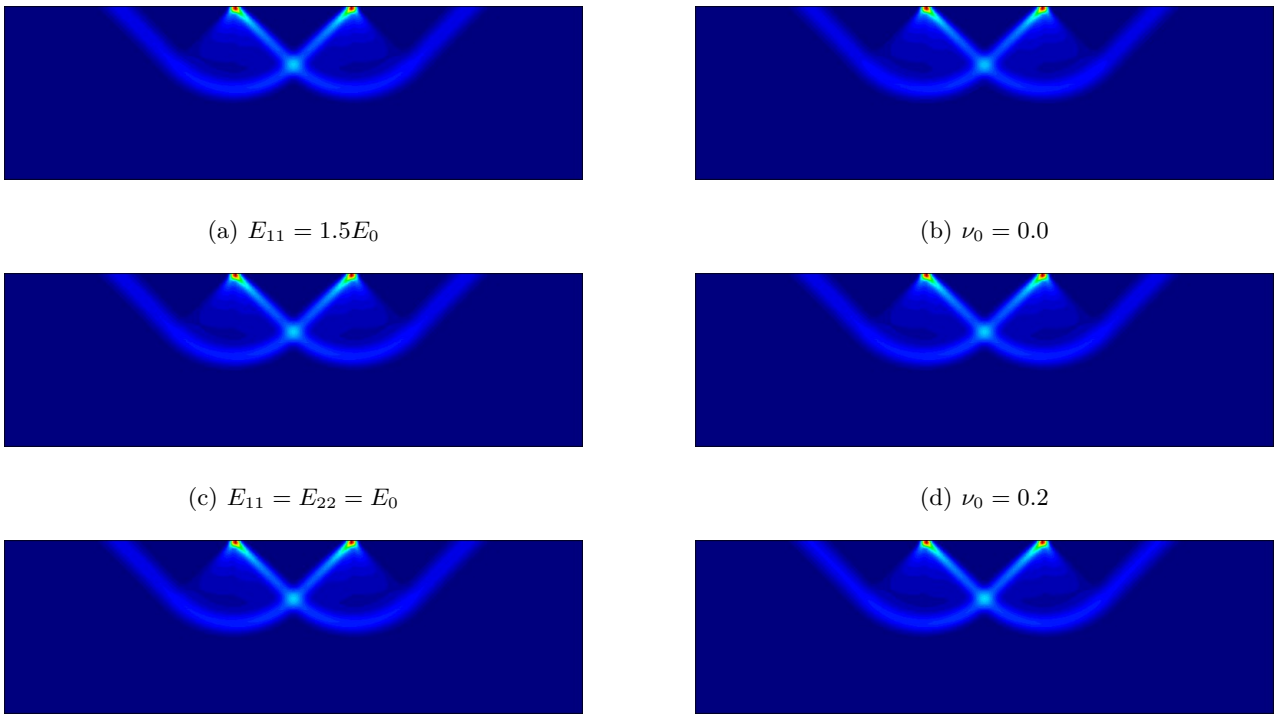

(a) $E_{11} = 1.5E_0$ (b) $\nu_0 = 0.0$

(c) $E_{11} = E_{22} = E_0$ (d) $\nu_0 = 0.2$

(e) $E_{22} = 1.5E_0$ (f) $\nu_0 = 0.4$

Fig. 19 Indentation by a flat rigid die: Influence of Young's modulus and Poisson's ratio on the localization angle θ^{cr}.

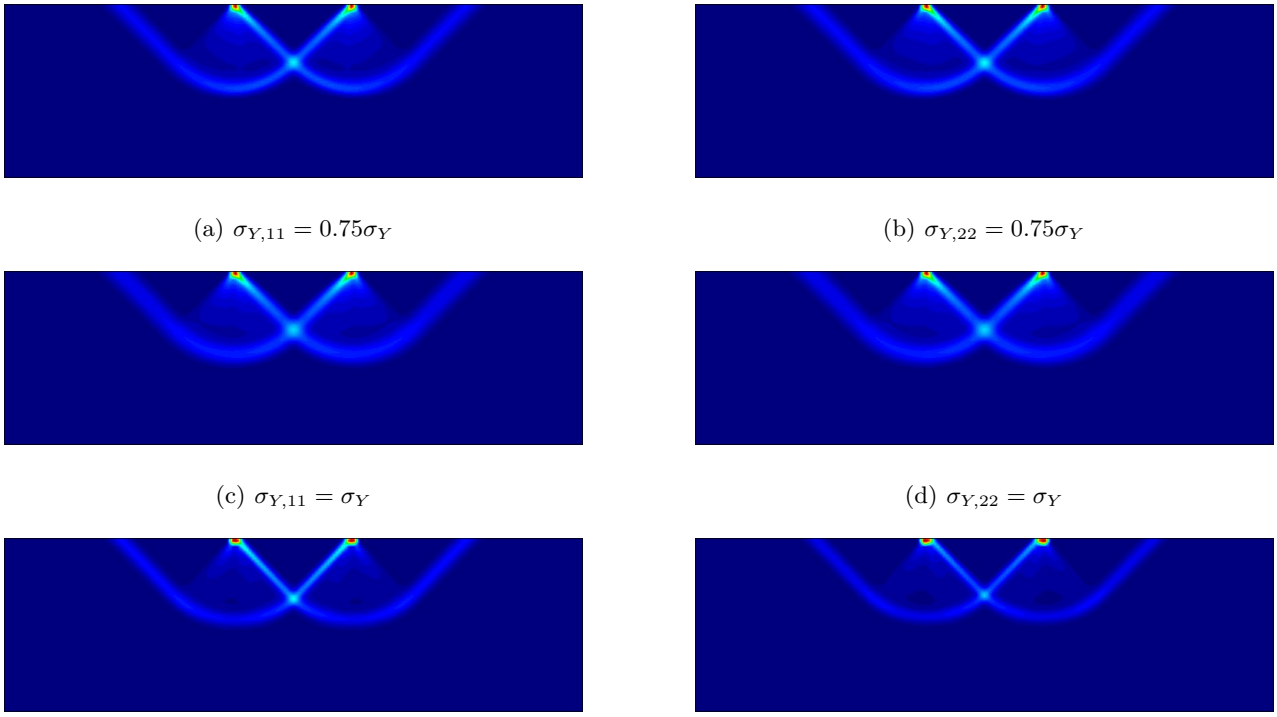

(a) $\sigma_{Y,11} = 0.75\sigma_Y$ (b) $\sigma_{Y,22} = 0.75\sigma_Y$

(c) $\sigma_{Y,11} = \sigma_Y$ (d) $\sigma_{Y,22} = \sigma_Y$

(e) $\sigma_{Y,11} = 1.50\sigma_Y$ (f) $\sigma_{Y,22} = 1.50\sigma_Y$

Fig. 20 Indentation by a flat rigid die: Influence of the material yield strengths $\sigma_{Y,11}$ and $\sigma_{Y,22}$ on the localization angle θ^{cr}.

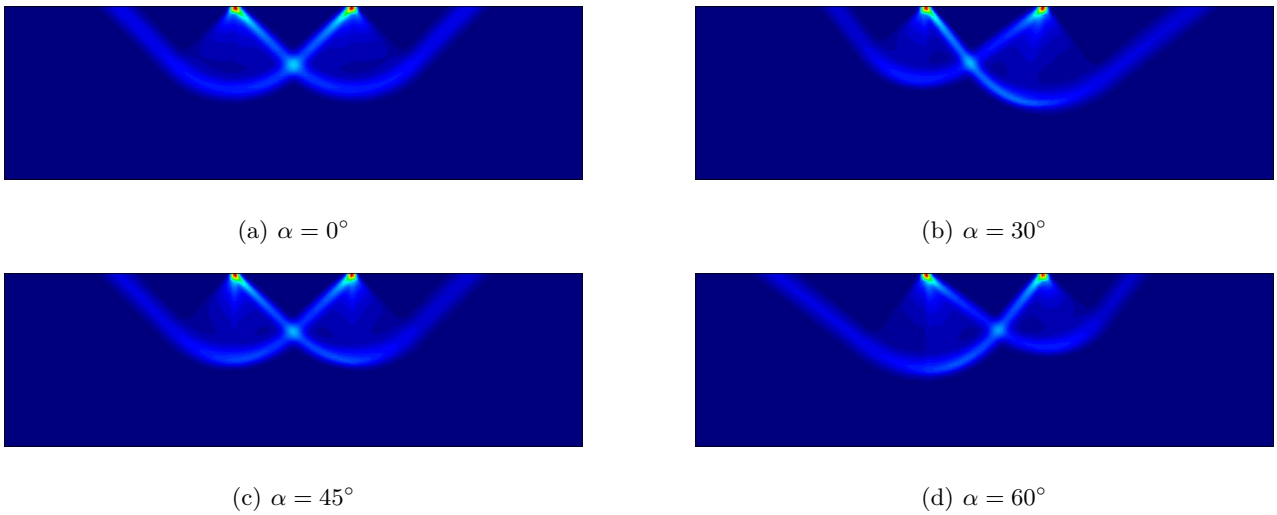

(a) $\alpha = 0^\circ$ (b) $\alpha = 30^\circ$

(c) $\alpha = 45^\circ$ (d) $\alpha = 60^\circ$

Fig. 21 Indentation by a flat rigid die: Influence of the material yield strengths $\sigma_{Y,11} = 1.5\sigma_Y$ or $\sigma_{Y,22} = 1.5\sigma_Y$ on the localization angle $\theta^{\rm cr}$.

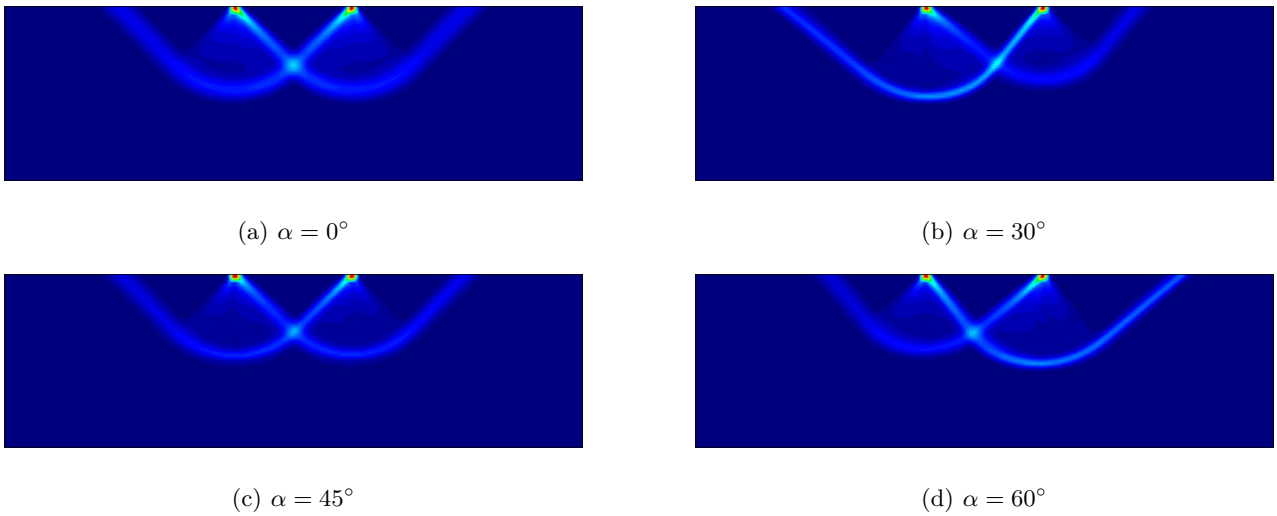

(a) $\alpha = 0^\circ$ (b) $\alpha = 30^\circ$

(c) $\alpha = 45^\circ$ (d) $\alpha = 60^\circ$

Fig. 22 Indentation by a flat rigid die: Influence of the material yield strengths $\sigma_{Y,11} = 0.75\sigma_Y$ and $\sigma_{Y,22} = 0.75\sigma_Y$ on the localization angle $\theta^{\rm cr}$.

Accurate and locking-free analysis of beams, plates and shells using solid elements

S. Saloustros, M. Cervera, S. Kim and M. Chiumenti

Computational Mechanics

Volume 67, pp. 883–914 (2021)

Editor-in-Chief: Prof. Dr. Peter Wriggers

PRINT ISSN: 0178-7675

Journal Editors - Springer

https://doi.org/10.1007/s00466-020-01969-0

Author's version of paper published in *Computational Mechanics*

Accurate and locking-free analysis of beams, plates and shells using solid elements

Savvas Saloustros[a] · **Miguel Cervera**[a,b] · **Sungchul Kim**[a] · **Michele Chiumenti**[a,b]

Accepted: 28 December 2020

Abstract This paper investigates the capacity of solid finite elements with independent interpolations for displacements and strains to address shear, membrane and volumetric locking in the analysis of beam, plate and shell structures. The performance of the proposed strain/displacement formulation is compared to the standard one through a set of eleven benchmark problems. In addition to the relative performance of both finite element formulations, the paper studies the effect of discretization and material characteristics. The first refers to different solid element typologies (hexahedra, prisms) and shapes (regular, skewed, warped configurations). The second refers to isotropic, orthotropic and layered materials, and nearly incompressible states. For the analysis of nearly incompressible cases, the B-bar method is employed in both standard and strain/displacement formulations. Numerical results show the enhanced accuracy of the proposed strain/displacement formulation in predicting stresses and displacements, as well as producing locking-free discrete solutions, which converge asymptotically to the corresponding continuous problems.

a. Department of Civil and Environmental Engineering
Universitat Politècnica de Catalunya (UPC-BarcelonaTech)
Jordi Girona 1-3, 08034 Barcelona, Spain.

b. International Center for Numerical Methods in Engineering (CIMNE)
Gran Capità, S/N, 08034 Barcelona, Spain.

E-mail: savvas.saloustros@upc.edu
E-mail: miguel.cervera@upc.edu
E-mail: sungchul.kim@upc.edu
E-mail: michele@cimne.upc.edu

Keywords finite element method · mixed finite elements · nearly incompressible · anisotropic materials · plate structures · shell structures · beam structures

1 Introduction

Finite element modelling is a common practice today in the design and structural assessment of new and existing engineering structures. It has been a long way to come to this point with important milestones including: technological advances in computer hardware, making personal computers with large processing capacities accessible to engineering offices; incorporation of Finite Element (FE) method courses into engineering curricula, training new engineers on the use of FE models; and continuous research on the further development of FE technologies (e.g. finite elements, constitutive models, etc.), enhancing the reliability on the accuracy of FE solutions. Despite the important changes in the used tools and training in the engineering practice, the FE formulations employed today and those of the first FEM applications in the 1950s share a common standpoint; the use of (standard) displacement based finite elements.

Displacement based finite elements (referred hereafter to as *standard FEs*) have a single primal variable, which is the displacement field at the nodes. Standard elements are conveniently used for the analysis of any engineering structure and form the basis of the vast majority of commercial and research FE software. Nevertheless, under certain conditions related to the material properties, the geometry and the discretization, standard FEs suffer from important inefficiencies that influence the accuracy of the FE solution. Element locking is one of the most common pathologies, referring

to the computation of displacements that are orders of magnitude lower than the actual solution [1, 2, 3]. Element locking is common under certain loading (e.g. shear locking under bending), geometry (e.g. locking of thin plates) and material conditions (e.g. volumetric locking in incompressible materials). Additionally, the accuracy of standard FEs is sensitive to mesh distortion (e.g. warped elements, small aspect ratios, irregular shapes).

The lower accuracy in the computation of displacements has an immediate effect in the calculation of stresses, and thus in the structural analysis of engineering structures. For instance, the design of a new shell structure or the structural assessment of an existing one depends on the capacity to identify accurately the compressive and tensile stress fields within them. This is especially important for shell structures made from materials with low tensile capacity, as for instance masonry, the equilibrium of which relies in the formation of a system of compressive thrusts within the thickness of the shell [4, 5, 6]. Membrane locking is a common pathology when modelling curved thin shells under bending with standard FEs [7, 8, 9, 10], attributed to the poor choice of the displacement interpolation space and thus the inability to model pure bending modes. The result of membrane locking is an artificial increase in the stiffness and the erroneous estimation of displacement and stress fields. Similarly, standard FEs used for the modelling of thin plates under bending exhibit severe shear locking manifested again as a spurious increase of the transverse shear strains resulting in an overstiff response [9, 2, 3]. Standard FEs suffer also from volumetric locking in quasi-incompressible situations, such as when Poisson's ratio approaches a value of 0.5 [2].

The use of solid elements for modelling structural elements, such as beams, plates and shells, has always been attractive due to their versatile use for modelling arbitrary geometries (e.g. linear/curved, thin/thick), construction details (e.g. element-stiffeners, web-perforated steel beams, layered elements), as well as transitions between different structural elements. Solid elements allow for the use of general strain-driven constitutive relationships and they avoid the introduction of rotational degrees of freedom and awkward boundary conditions alternatives ("soft" and "hard" supports), as well as compatibility issues when the structural model requires more than one type of element. Additionally, the discretization of a structural element with solid elements avoids the introduction of additional kinematical hypotheses (e.g. planar sections, shear stresses and warping through the thickness, etc.).

The above motivated the development of the solid-shell concept by Wriggers and coworkers [11, 12, 13], Hauptmann et al. [14, 15] and Sze et al. [16], which used only displacement degrees of freedom and proved to be locking-free in many situations. Having as their objective the material and geometrical non-linear modelling of shells and deep drawing processes of metal sheets, solid-shell elements make use of the assumed enhanced method (EAS) to include higher order modes, which standard linear FE quadrilateral elements do not possess, in order to improve their bending behavior. EAS, introduced by Simo and Rifai [17] and extended by Simo, Armero, Taylor and Pister [18, 19, 19, 20], is conceived as a mixed method in which the additional strain modes are discontinuous and defined elementwise, so that they can be solved at element level, thus yielding only displacement degrees of freedom at the nodes. The enhancing modes were firstly termed as *incompatible* modes, and later as *non-conforming* modes. Additionally, the Assumed Natural Strain method (ANS) was called into play to circumvent shear and membrane locking [14, 16, 21, 22, 23]. In parallel, hexahedral elements with reduced integration and hourglass stabilization were also used in this context [24, 25]. These successful elements rely in the improvement of the discrete strain field with the addition of selected strain modes, which are devised ad-hoc so that the enhanced element shows the desired performance. However, for those elements that are stable, these enhancements cannot achieve a higher asymptotic rate of convergence of displacements than that of the underlying lineal element. Interpolating with the full quadratic polynomial would be required for achieving this. Convergence of strains, obtained by discrete differentiation of the displacement field, is one order lower, resulting in turn in a poor convergence of stresses. Wriggers and Korelc [13] give an early road map for later developments and Kim et al. [21] offer an overview of them.

In this work, we present a thoroughly different approach for the analysis of structural elements under the aforementioned conditions in which standard displacement based FEs fall short in accuracy and reliability: the use of finite elements with independent interpolations for strains and displacements (referred hereafter to as ε/u FEs). This procedure is closely related to using the mixed Hu-Washizu and Hellinger-Reissner variational principles [26]. Both interpolated fields, displacements and strains, are *complete* and *continuous*, or *fully compatible* and *conforming*, and their respective values are solved at the nodes of the mesh. In fact, equal interpolations are used for both of them. Consequently, this work does not present a new element technology, but the assessment of a mixed solid finite

element formulation applied to the challenging problem of shell behavior.

The advantages of such setting are manifold: (i) the corresponding continuum and discrete variational formulations are fully general and straight-forwardly derived from the strong form of the problem, (ii) beam, plate or shell behavior hypotheses are not invoked or enforced, (iii) the ε/u FEs can be used in 2D and 3D, and they can be of any shape (triangular, quadrilateral, tetrahedral, hexahedral, prismatic) and support any degree of interpolation (linear, quadratic, etc.), (iv) standard full numerical integration rules are used, (iv) the ensuing FE formulation, if stability is ensured, displays not only better displacement accuracy, but more importantly, a higher strain and stress asymptotic rate of convergence than the corresponding standard FE, (vi) sensibility to mesh distortion is very small, and (vii) due to the choice of an independent interpolation of the strains, rather than the stresses, the ε/u FEs are readily available for nonlinear analysis, as most of the constitutive models used in FE practice are strain-driven [27].

The use of two primal variables instead of one, as in standard FEs, positions the present element in the category of *multifield* FE approaches and in particular in the *mixed* FE approaches [28]. Once the problems related to the stability of mixed formulations are satisfactorily addressed [29, 30], they are able to overcome all the above deficiencies of the standard formulation, providing accurate and locking-free solutions in both displacements and stresses [31]. Evidence is provided to show that the increase in the number of degrees of freedom is overturned by the greater rate of convergence.

The paper presents the use of ε/u FEs in the analysis of eleven benchmark problems of beam, shell and plate structures. These benchmark tests are those commonly used in FE literature to test elements in the situations of interest and they cover several aspects influencing the accuracy of standard FEs. The first one concerns loading situations inducing element locking, such as bending of thin plates and shells. The second one refers to different discretization choices, such as element types (hexahedra vs. prisms) and shapes (regular vs. distorted meshes).The third one is the simulation of isotropic, orthotropic and layered materials. Finally, the last investigated aspect is related to the analysis of nearly incompressible materials ($\nu \approx 0.5$). In this latter case, we employ the use of the B-bar method [32, 33, 34] to address volumetric locking.

The paper is structured in the following way. Section 2 presents the finite element formulation with independent strain/displacement interpolations, and section 3 the implementation in a Finite Element (FE) framework. The use of the B-bar method in both standard and ε/u FEs is described in section 4. Section 5 presents the application of ε/u and standard formulations in a set of eleven problems of beam, shell and plate structures. The paper closes with some concluding remarks in section 6. Five appendices at the end of the paper present the details related to the implementation and the numerical parameters of the ε/u FEs, as well as a comparison with different solid-shell and solid FE formulations.

2 Independent $\boldsymbol{\varepsilon/u}$ finite element interpolation

This section presents the finite element formulation with independent ε/u interpolations in compact form adopting Voigt's convention for symmetric tensors. The detailed form of the vectors and matrices used hereafter is reported in Appendix A. The present finite element formulation belongs in the family of *mixed* formulations that simultaneously resolve multiple fields of interest [30], the displacements and the strains in this case.

The mechanical boundary value problem of interest is defined in terms of the displacement $\boldsymbol{u}$, the strain $\boldsymbol{\varepsilon}$, the stress $\boldsymbol{\sigma}$ and the force $\boldsymbol{f}$ vectors. The compatibility equation (1) establishes the local relationship between the strain and displacements fields as

$$\boldsymbol{\varepsilon} = \boldsymbol{\mathcal{S}}\boldsymbol{u} \tag{1}$$

where $\boldsymbol{\mathcal{S}}$ is the symmetric gradient operator. Cauchy's equilibrium equation (2) relates the local stresses with the body forces as

$$\boldsymbol{\mathcal{S}}^T\boldsymbol{\sigma} + \boldsymbol{f} = 0 \tag{2}$$

where $\boldsymbol{\mathcal{S}}^T$ is the differential divergence operator, adjoint to $\boldsymbol{\mathcal{S}}$ in Eq. (1). Finally, the constitutive equation (3) associates the stress and strain vectors as

$$\boldsymbol{\sigma} = \boldsymbol{D_s}\,\boldsymbol{\varepsilon} \tag{3}$$

with $\boldsymbol{D_s}$ standing for the secant constitutive matrix.

Some manipulation of Eqs. (1)-(3) gives the symmetric strong form of the boundary value problem in terms of $\boldsymbol{\varepsilon}$ and $\boldsymbol{u}$. In particular, pre-multiplying Eq. (1) by the secant constitutive matrix $\boldsymbol{D_s}$ and introducing Eq. (3) into Eq. (2) we obtain

$$-\boldsymbol{D_s}\,\boldsymbol{\varepsilon} + \boldsymbol{D_s}\,\boldsymbol{\mathcal{S}}\boldsymbol{u} = \boldsymbol{0} \tag{4}$$

$$\boldsymbol{\mathcal{S}}^T\,(\boldsymbol{D_s}\,\boldsymbol{\varepsilon}) + \boldsymbol{f} = \boldsymbol{0}, \tag{5}$$

which together with the proper boundary conditions define the strong form of the ε/u independent interpolation formulation.

The boundary conditions are imposed on the boundary of the body Γ and are applied in Γ_u and Γ_t, corresponding to Dirichlet's boundary conditions (prescibed displacements) and Newman's boundary conditions (prescribed tractions), such that $\Gamma = \Gamma_u \cup \Gamma_t$ and $\{\oslash\} = \Gamma_u \cap \Gamma_t$.

Observe that the introduction of Eq. (4) into Eq. (5) would eliminate the strains as independent unknowns, yielding the standard *irreducible* formulation in terms of displacements only.

The variational formulation is obtained in two steps. First, we pre-multiply Eq. (4) by an arbitrary virtual strain vector $\delta\boldsymbol{\varepsilon}$ and integrate over the spatial domain Ω. Second, we pre-multiply Eq. (5) by an arbitrary virtual displacement vector $\delta\boldsymbol{u}$ and integrate over the spatial domain Ω. Then, we apply in the latter equation the Divergence Theorem, assuming that the boundary conditions vanish on Γ_u, i.e. $\delta\boldsymbol{u} = \boldsymbol{0}$ on Γ_u (see Appendix B). With the above manipulations, the variation form of the ε/u independent formulation is expressed by the following two equations

$$-\int_\Omega \delta\boldsymbol{\varepsilon}^T \boldsymbol{D_s}\boldsymbol{\varepsilon}\, d\Omega + \int_\Omega \delta\boldsymbol{\varepsilon}^T \boldsymbol{D_s}\boldsymbol{\mathcal{S}}\boldsymbol{u}\, d\Omega = 0 \quad \forall\delta\boldsymbol{\varepsilon} \tag{6}$$

$$\int_\Omega \left(\boldsymbol{\mathcal{S}}\delta\boldsymbol{u}\right)^T \left(\boldsymbol{D_s}\boldsymbol{\varepsilon}\right) d\Omega = \int_\Omega \delta\boldsymbol{u}^T \boldsymbol{f}\, d\Omega + \int_{\Gamma_t} \delta\boldsymbol{u}^T \bar{\boldsymbol{t}}\, d\Gamma \tag{7}$$

Equation (6) corresponds to the weak form of the constitutive and compatibility relationships and equation (7) to the Principle of Virtual Work, as the right hand side term represents the virtual work done by the tractions $\bar{\boldsymbol{t}} = \bar{\boldsymbol{G}}^T \boldsymbol{D_s}\boldsymbol{\varepsilon}$ and the body forces $\boldsymbol{f}$, with $\bar{\boldsymbol{G}}^T$ being the projection matrix (see Appendix A). The nontrivial case with prescribed displacements $\boldsymbol{u} = \bar{\boldsymbol{u}}$ on Γ_u can be accomodated following standard arguments. Note that eqs. (6)-(7) are symmetric.

Summarizing, the symmetric weak form statement of the presented boundary value problem is to find the unknown displacements $\boldsymbol{u}$ and strains $\boldsymbol{\varepsilon}$ that verify the system of equations (6)-(7) and the boundary conditions imposed on Γ_u and Γ_t.

Note that in view of equation (3), for constant $\boldsymbol{D_s}$, the system of equations (6)-(7) can be understood as the stationary conditions of the classical Hellinger-Reissner functional. For non-constant or non-uniform $\boldsymbol{D_s}$, the present formulation is closely related, but not identical, to classical Hellinger-Reissner methods.

3 Finite Element approximation

In the FE approximation of the above boundary value problem, the domain is discretized in finite elements (Ω_e), so that $\Omega \cong \sum \Omega_e$ and displacements $\boldsymbol{u}$ and strains $\boldsymbol{\varepsilon}$ are approximated as $\hat{\boldsymbol{u}}$ and $\hat{\boldsymbol{\varepsilon}}$ defined as

$$\boldsymbol{u} \cong \hat{\boldsymbol{u}} = \boldsymbol{N}_u \boldsymbol{U} \tag{8}$$

$$\boldsymbol{\varepsilon} \cong \hat{\boldsymbol{\varepsilon}} = \boldsymbol{N}_\varepsilon \boldsymbol{E} \tag{9}$$

where $\boldsymbol{U}$ and $\boldsymbol{E}$ are displacement and strain vectors representing the values of $\hat{\boldsymbol{u}}$ and $\hat{\boldsymbol{\varepsilon}}$, respectively, at the nodes of the finite element mesh. $\boldsymbol{N}_u$ and $\boldsymbol{N}_\varepsilon$ are the matrices containing the interpolation functions adopted in the FE approximation. The submatrices of $\boldsymbol{N}_u$ and $\boldsymbol{N}_\varepsilon$ are diagonal matrices and the corresponding components are $N_u^{(i)}$ and $N_\varepsilon^{(i)}$ interpolation functions, with (i) representing the node counter.

Note that equations (8)-(9) illustrate the basic difference of the current formulation compared to the standard one, which is the use of independent interpolation functions for displacements and strains. On the contrary, in the standard formulation strains are a function of the displacements computed as

$$\boldsymbol{\varepsilon} \cong \tilde{\boldsymbol{\varepsilon}} = \boldsymbol{\mathcal{S}}\boldsymbol{N}_u \boldsymbol{U} = \boldsymbol{B}_u \boldsymbol{U} \tag{10}$$

where $\boldsymbol{B}_u = \boldsymbol{\mathcal{S}} N_u$ is the discrete strain-displacement matrix. The submatrices of $\boldsymbol{B}_u$ have the structure corresponding to the $\boldsymbol{\mathcal{S}}$ operator (see Appendix A) and their components are the Cartesian derivatives of the $N_u^{(i)}$. In the $\boldsymbol{\varepsilon}/u$ independent interpolation formulation, the discrete virtual displacements $\delta\boldsymbol{u}$ and virtual strains $\delta\boldsymbol{\varepsilon}$ are described in the Galerkin method with the same approximation as

$$\delta\boldsymbol{u} \cong \delta\hat{\boldsymbol{u}} = \boldsymbol{N}_u \delta\boldsymbol{U} \tag{11}$$

$$\delta\boldsymbol{\varepsilon} \cong \delta\hat{\boldsymbol{\varepsilon}} = \boldsymbol{N}_\varepsilon \delta\boldsymbol{E}. \tag{12}$$

It is noted that in the following, integrals over the domain Ω are understood as the sum of the integrals over the elements in the finite element mesh

$$\int_\Omega (\cdot) d\Omega = \sum_e \int_{\Omega_e} (\cdot) d\Omega_e \tag{13}$$

while $\boldsymbol{U}$, $\boldsymbol{E}$, $\delta\boldsymbol{U}$ and $\delta\boldsymbol{E}$ are interpreted as the nodal values over the whole FE mesh. This implies the corresponding assembling operations for elemental matrices and vectors into global entities.

Introducing equations (8)-(12) into equations (6)-(7), the discrete weak form of the ε/u independent FE formulation becomes

$$-\int_\Omega \delta\boldsymbol{E}^T \boldsymbol{N}_\varepsilon^T \boldsymbol{D_s}\boldsymbol{N}_\varepsilon \boldsymbol{E}\, d\Omega + \int_\Omega \delta\boldsymbol{E}^T \boldsymbol{N}_\varepsilon^T \boldsymbol{D_s}\boldsymbol{B}_u \boldsymbol{U}\, d\Omega = 0 \quad \forall\delta\boldsymbol{E} \tag{14}$$

$$\int_\Omega \delta \boldsymbol{U}^T \boldsymbol{B}_u^T \left(\boldsymbol{D_s} \boldsymbol{N}_\varepsilon \boldsymbol{E}\right) d\Omega = \int_\Omega \delta \boldsymbol{U}^T \boldsymbol{N}_u^T \boldsymbol{f}\, d\Omega + \int_{\Gamma_t} \delta \boldsymbol{U}^T \boldsymbol{N}_u^T \bar{\boldsymbol{t}}\, d\Gamma \quad \forall \delta \boldsymbol{U} \tag{15}$$

The first term in equation (15) is the internal work $\hat{\boldsymbol{U}}$ done by the stresses $\hat{\sigma} = \boldsymbol{D_s}\, \boldsymbol{N}_\varepsilon\, \boldsymbol{E}$. The second term in equation (15) corresponds to the work $\hat{W}$ done by the tractions $\bar{\boldsymbol{t}}$ and body forces $\boldsymbol{f}$.

Considering that the virtual displacements $\delta \boldsymbol{U}$ and the virtual strains $\delta \boldsymbol{E}$ are arbitrary, the system of equations of the *mixed* Galerkin method becomes

$$-\left(\int_\Omega \boldsymbol{N}_\varepsilon^T \boldsymbol{D_s} \boldsymbol{N}_\varepsilon\, d\Omega\right) \boldsymbol{E} + \left(\int_\Omega \boldsymbol{N}_\varepsilon^T \boldsymbol{D_s} \boldsymbol{B}_u d\Omega\right) \boldsymbol{U} = 0 \tag{16}$$

$$\left(\int_\Omega \boldsymbol{B}_u^T \boldsymbol{D_s} \boldsymbol{N}_\varepsilon\, d\Omega\right) \boldsymbol{E} = \int_\Omega \boldsymbol{N}_u^T \boldsymbol{f}\, d\Omega + \int_{\Gamma_t} \boldsymbol{N}_u^T \bar{\boldsymbol{t}}\, d\Gamma \tag{17}$$

which can be written in matrix form as

$$\begin{bmatrix} -\boldsymbol{M} & \boldsymbol{G} \\ \boldsymbol{G}^T & 0 \end{bmatrix} \begin{bmatrix} \boldsymbol{E} \\ \boldsymbol{U} \end{bmatrix} = \begin{bmatrix} 0 \\ \boldsymbol{F} \end{bmatrix} \tag{18}$$

In the above equation, $[\boldsymbol{E}, \boldsymbol{U}]^T$ is the array of the nodal values of strains and displacements. $\boldsymbol{M}$ is a mass-like projection matrix, $\boldsymbol{G}$ is the discrete gradient matrix and $\boldsymbol{F}$ is the vector of external forces defined as

$$\boldsymbol{M} = \int_\Omega \boldsymbol{N}_\varepsilon^T \boldsymbol{D_s} \boldsymbol{N}_\varepsilon d\Omega \tag{19}$$

$$\boldsymbol{G} = \int_\Omega \boldsymbol{N}_\varepsilon^T \boldsymbol{D_s} \boldsymbol{B}_u d\Omega \tag{20}$$

$$\boldsymbol{F} = \int \boldsymbol{N}_u^T \boldsymbol{f} d\Omega + \int_{\Gamma_t} \boldsymbol{N}_u^T \bar{\boldsymbol{t}} d\Gamma. \tag{21}$$

Note again that the discrete system of equations (18) is symmetric and can be expressed only in terms of nodal displacements $\boldsymbol{U}$ in the following way. Using the first equation in (18), the nodal values for the strains can be obtained as

$$\boldsymbol{E} = \boldsymbol{M}^{-1} \boldsymbol{G} \boldsymbol{U} \tag{22}$$

which introduced in the second equation in (18) gives

$$\boldsymbol{U} = \left(\boldsymbol{G}^T \boldsymbol{M}^{-1} \boldsymbol{G}\right)^{-1} \boldsymbol{F} \tag{23}$$

where $\left(\boldsymbol{G}^T \boldsymbol{M}^{-1} \boldsymbol{G}\right)^{-1}$ is the Schur complement of $-\boldsymbol{M}$ in the system of equations (18).

It is noted that the use of equal interpolations for the displacements and strains in equations (8)-(9) does not satisfy the Inf-Sup condition [29, 35, 30], resulting in an unstable solution in which uncontrollably spurious oscilations may appear in the computed displacement field. Solid elastic FEs with independent interpolations of strain and displacement that satisfy the Inf-Sup condition are strikingly scarce [36, 37, 38]. They use ad-hoc designed interpolations of stress and displacement fields with a multiplicity of nodes, which in turn host different nodal variables. These interpolations make difficult the use of these mixed elements in practical engineering problems. Alternatively, independent interpolations may be chosen circumventing the strictness of the Inf-Sup condition using a stabilisation method to provide the necessary stability. In this way, equal order interpolation may be used, with nodes located in the usual positions and all of them hosting the same nodal variables (see Appendix C). Following this procedure, the final system of equations for the ε/u independent interpolation FE problem becomes

$$\begin{bmatrix} -\boldsymbol{M}_\tau & \boldsymbol{G}_\tau \\ \boldsymbol{G}_\tau^T & \boldsymbol{K}_\tau \end{bmatrix} \begin{bmatrix} \boldsymbol{E} \\ \boldsymbol{U} \end{bmatrix} = \begin{bmatrix} 0 \\ \boldsymbol{F} \end{bmatrix} \tag{24}$$

with

$$\boldsymbol{M}_\tau = (1 - \tau_\varepsilon) \boldsymbol{M} \tag{25}$$

$$\boldsymbol{G}_\tau^T = (1 - \tau_\varepsilon) \boldsymbol{G} \tag{26}$$

$$\boldsymbol{K}_\tau = \tau_\varepsilon \underbrace{\int_\Omega \boldsymbol{B}_u^T \boldsymbol{D_s} \boldsymbol{B}_u d\Omega}_{\boldsymbol{K}} = \tau_\varepsilon \boldsymbol{K} \tag{27}$$

where $\tau_\varepsilon = [0, 1]$ is a stabilization parameter (see Appendix C).

The nodal values $\boldsymbol{U}$ can be formally computed in the stabilized system (24) as

$$\boldsymbol{U} = \left(\boldsymbol{G}\tau^T \boldsymbol{M}_\tau^{-1} \boldsymbol{G}_\tau + \boldsymbol{K}_\tau\right)^{-1} \boldsymbol{F} \tag{28}$$

The stabilization ensures definitiveness, uniqueness and stability of the solution if $\boldsymbol{K}$ is positive definite. Observe that for $\tau_\varepsilon = 1$ the stable solution of the standard form $\boldsymbol{U} = \boldsymbol{K}^{-1} \boldsymbol{F}$ is recovered.

Linear interpolation is used in this paper for both the $\boldsymbol{E}$ and $\boldsymbol{U}$ fields. Higher order equal interpolations are identically derived.

In this work, the presented FE formulation is used for the investigation of accuracy in stress and displacements of beams, plates and shells in the linear elastic range. Its extention to geometrical and material nonlinear problems is possible as shown in [31, 39, 40].

4 B-bar finite element

The use of the B-bar method in the standard formulation with quadrilateral and hexahedral elements allows to solve quasi-incompressible problems avoiding volumetric locking. It is known to be equivalent to the underintegration of the volumetric energy and to the use of an underlying piecewise constant interpolation of the volumetric strain (and the mean-stress). It will be shown here that the B-bar method serves an identical purpose in the ε/u formulation, following the same arguments. The discrete strain displacement matrix can be split in terms of its volumetric and deviatoric components as

$$\boldsymbol{B_u} = \boldsymbol{B_u^{vol}} + \boldsymbol{B_u^{dev}}. \tag{29}$$

Let us now consider n_g as the number of integration points used in the finite element. The average of the strain-displacement sub-matrices, $\bar{\boldsymbol{B}}_u^{vol}$, can be computed as

$$\bar{\boldsymbol{B}}_u^{vol} = \frac{1}{n_g}\sum_{k=1}^{n_g} \boldsymbol{B}_{u_k}^{vol} \tag{30}$$

Using this, a modified *B-bar* discrete strain-displacement matrix is defined as

$$\bar{\boldsymbol{B}}_u = \boldsymbol{B}_u^{dev} + \bar{\boldsymbol{B}}_u^{vol}. \tag{31}$$

The above equation represents the classical form of the B-bar method for implementation in the standard irreducible FE formulation. The extension of the B-bar method to the presented formulation with ε/u independent interpolations, defined as $\bar{\boldsymbol{B}}_u^{\varepsilon}$, is straightforward

$$\begin{aligned}\bar{\boldsymbol{B}}_u^{\varepsilon} &= \boldsymbol{B}_u^{dev} + \left[\tau_\varepsilon \bar{\boldsymbol{B}}_u^{vol} + (1-\tau_\varepsilon)\boldsymbol{B}_u^{vol}\right] \\ &= \bar{\boldsymbol{B}}_u + (1-\tau_\varepsilon)\left[\boldsymbol{B}_u^{vol} - \bar{\boldsymbol{B}}_u^{vol}\right]\end{aligned} \tag{32}$$

Observe that for a $\tau_\varepsilon = 1$, $\bar{\boldsymbol{B}}_u^{\varepsilon} = \bar{\boldsymbol{B}}_u$, i.e. equation (31) is recovered.

In virtue of the above, the use of the B-bar method in the presented ε/u independent formulation is possible by using in the final system of equations (24) the following versions of $\boldsymbol{G}_\tau^T$ and $\boldsymbol{K}_\tau$ matrices

$$\boldsymbol{G}_\tau^T = (1-\tau_\varepsilon)\int_\Omega \boldsymbol{N}_\varepsilon^T \boldsymbol{D_s} \bar{\boldsymbol{B}}_u^{\varepsilon} d\Omega \tag{33}$$

$$\boldsymbol{K}_\tau = \tau_\varepsilon \int_\Omega \bar{\boldsymbol{B}}_u^{\varepsilon\,T} \boldsymbol{D_s} \bar{\boldsymbol{B}}_u^{\varepsilon} d\Omega. \tag{34}$$

5 Benchmark Tests

This section presents the use of the ε/u independent interpolation solid finite elements (called hereafter as ε/u FEs) for the analysis of eleven compressible and nearly incompressible problems in beam, shell and plate structures. The usual form of the B-matrix (see Eq. (41)) is adopted in all cases, apart from the analysis of nearly incompressible tests, where the *B-bar* method is employed (section 5.5).

For all cases, geometry, material properties and loads are given in a self-consistent set of units. The results obtained using ε/u FEs are compared in each case with those of the standard FEs and, whenever available, with reference analytical solutions. Results are represented in terms of displacements and stresses at specific locations, as well as stress distribution within the analysed structure and deformed shapes. Relative error of a quantity $[X]$ is computed as $1 - [X]_{FEM}/[X]_{ref}$. In cases where stress values are compared at a node, the values reported for standard FEs correspond to the continuous projection $P_h(\boldsymbol{D_s\varepsilon})$ evaluated at the mesh nodes, rather than the actual discontinuous stresses $\boldsymbol{D_s\varepsilon}$ evaluated at the integration points. This projection is advantageous for the standard FEs, as it results in better values than those actually computed.

5.1 Twisted beam - Warp effect

The effect of warp on solid finite elements is investigated through the twisted beam test, proposed by Macneal and Harder [41]. The problem consists in the application of a force with different directions at the free end of a cantilever twisted beam and has been analysed in the literature with solid [42, 37], shell [43] and solid-shell FEs [22, 23].

The geometry, boundary and loading conditions are defined as in [41] and are shown in Figure 1. The adopted material properties are: Young's modulus $E = 29 \times 10^6$ and Poisson's ratio $\nu = 0.22$. The reference solution for the maximum displacement at the center of the free end of the twisted beam is $u_x = -1.754$ and $u_y = -5.424$ for a unit force along the +X and +Y directions, respectively [41].

For this test, two solid finite element typologies are analysed: hexahedra and prisms. Eight mesh refinements are considered with $N = 12; 16; 32; 64; 96; 128; 144; 160$ elements along the span of the beam. Considering that the used elements have straight edges, the warp of each element diminishes from 7.5° to 0.5625° by increasing the number of elements used across the span from $N = 12$ to $N = 160$. The cross-section of the beam is discretized

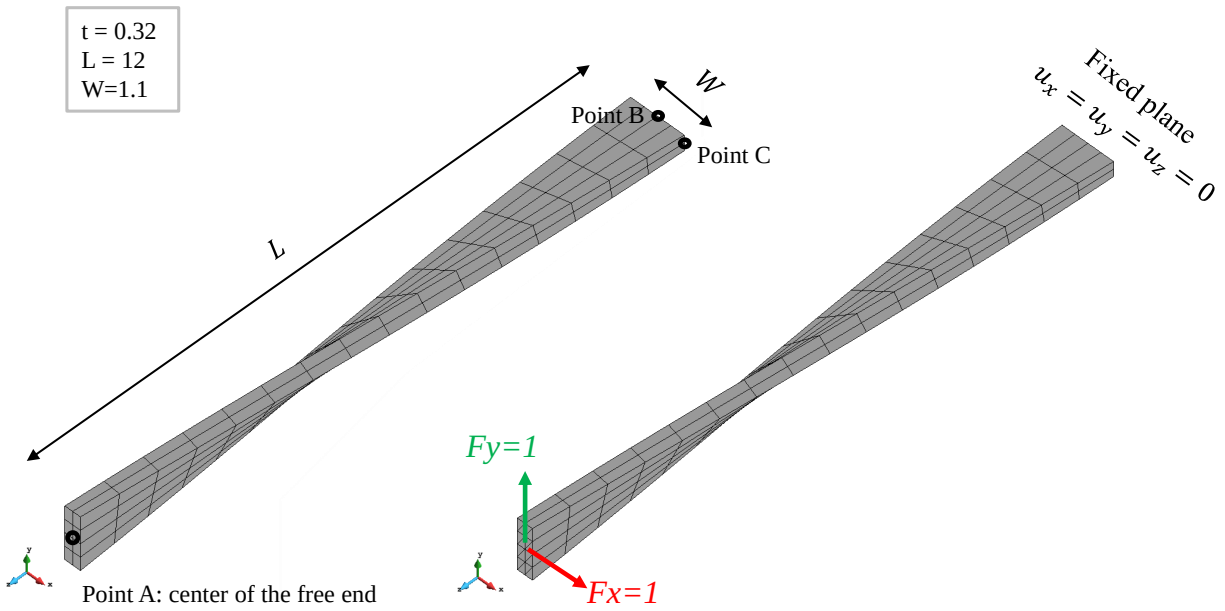

Fig. 1: Twisted beam: Geometry (left), load and boundary conditions (right) on a mesh using hexahedra (left) and prisms (right) of $N = 16$ elements per side.

in all meshes with 2×4 elements (see Figure 1). When prism elements are used, each hexahedron is divided into two prisms.

Figures 2 and 3 present the convergence of the computed horizontal and vertical displacement at the center of the free end of the twisted beam (Point A in Figure 1). The solutions with ε/u FEs are in agreement with the reference ones even for coarse meshes with $N = 12$ elements per span, with errors for both hexahedral and prism meshes below 4% and 5.5% for loading in X and Y directions, respectively. Standard FEs achieve this level of accuracy only for meshes with more than 128 elements per span (see Table 1). Prisms and hexahedra present a very similar response in both formulations, with hexahedral meshes giving a marginally better accuracy. It is noted that the converged solution of the displacement for loading in Y using ε/u FEs is slightly higher than the reference solution given by beam theory [41].

Figures 4 and 5 present the evolution of the normal stresses σ_{zz} at the middle edges of the fixed end (Points B and C in Fig. 1) for the two loading cases. The enhanced accuracy of the ε/u formulation results in a faster convergence of the normal stresses. The standard FEs converge to a lower normal stress for both

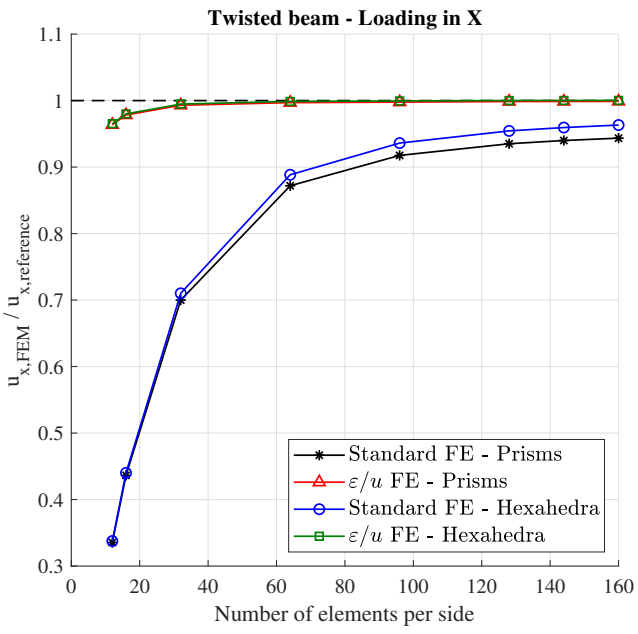

Fig. 2: Twisted beam: Horizontal displacement u_x at the center of the free end (Point A in Figure 1) normalized against the reference value versus the number of elements per side for loading in the +X direction.

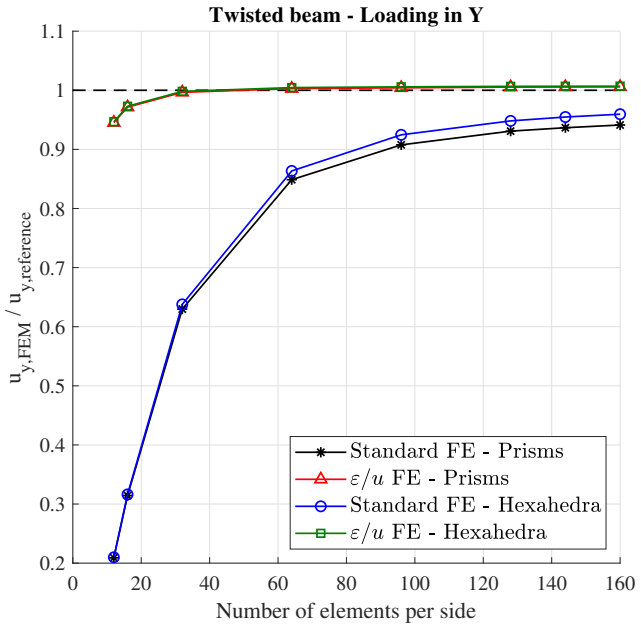

Fig. 3: Twisted beam: Vertical displacement u_y at the center of the free end (Point A in Figure 1) normalized against the reference value versus the number of elements per side for loading in the +Y direction.

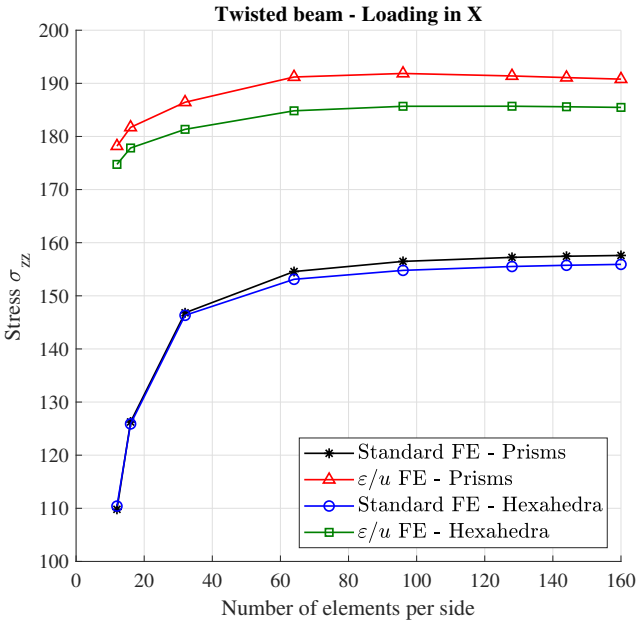

Fig. 4: Twisted beam: Normal stress σ_{zz} (compression) at the middle of the fixed end (Point C in Figure 1) versus the number of elements per side loading in +X direction.

loading directions compared to the one computed with the ε/u FEs.

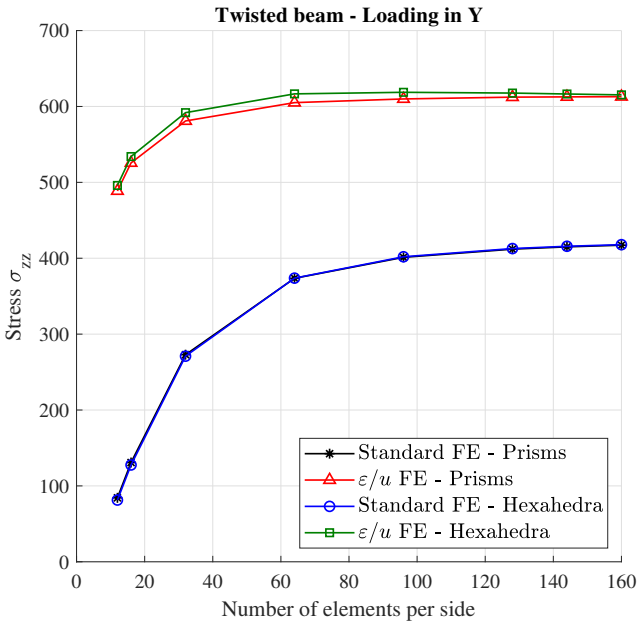

Fig. 5: Twisted beam: Normal stress σ_{zz} (compression) at the middle of the fixed end (Point B in Figure 1) versus the number of elements per side loading in +Y direction.

5.2 Simulation of shell structures

This section investigates the capacity of the ε/u FE formulation to avoid membrane locking. Membrane locking produces artificial stiffness in discrete thin shells due to the poor selection of the FE interpolation subspaces. It is common that this leads to widely understimated asymptotic stress values and altogether different failure mechanisms. Three benchmark tests are analysed: the Scordelis-Lo roof, the hemispherical shell and the pinched cylinder with diaphragm. These cases are commonly used in the literature to test the capacity of shell and solid elements in modelling shell structures [44, 41, 9, 43, 45, 37, 46].Comparison with the performance of some solid-shell elements is given in Appendix E. Note that all cases are discretized with only one element per thickness.

5.2.1 "Scordelis-Lo" roof

The Scordelis-Lo roof problem [47] is considered a benchmark test for solid [37], shell [7, 9, 43] and solid-shell FE [22, 23] formulations investigating the ability of an element to model complex states of membrane strain [9].

The problem consists in the loading under vertical pressure of a single curvature thin shell supported by rigid diaphragms in the two curved edges, while keeping free the straight ones. Figure 6 presents the geometry of the problem and the load and boundary conditions.

Table 1: Twisted beam: Relative error between numerical displacements and reference ones [41]. Error below 5% is shown in bold

		Error in u_x [%]				Error in u_y [%]			
		Prism		Hexahedra		Prism		Hexahedra	
Elements per span	Warp angle	Standard	ε/u	Standard	ε/u	Standard	ε/u	Standard	ε/u
12	7.5°	66.40	**3.64**	66.24	**3.48**	79.10	5.47	79.01	5.32
16	5.625°	56.30	**2.17**	55.99	**2.01**	68.57	**2.86**	68.37	**2.70**
32	2.8125°	29.95	**0.70**	28.99	**0.52**	37.02	**0.35**	36.22	**0.18**
64	1.406°	12.75	**0.31**	11.16	**0.13**	15.13	**-0.28**	13.65	**-0.46**
96	0.9375°	8.19	**0.23**	6.39	**0.06**	9.24	**-0.41**	7.54	**-0.58**
128	0.7031°	6.44	**0.14**	**4.56**	**-0.01**	6.91	**-0.53**	5.18	**-0.67**
144	0.625°	5.95	**0.13**	**4.05**	**-0.02**	6.33	**-0.55**	**4.52**	**-0.68**
160	0.5625°	5.59	**0.12**	**3.68**	**-0.02**	5.88	**-0.57**	**4.05**	**-0.69**

Due to symmetry, only a quarter of the shell is analysed adopting proper boundary conditions at the planes of symmetry (see Figure 6). A uniform vertical pressure of -90 per unit surface is applied on the top of the roof.

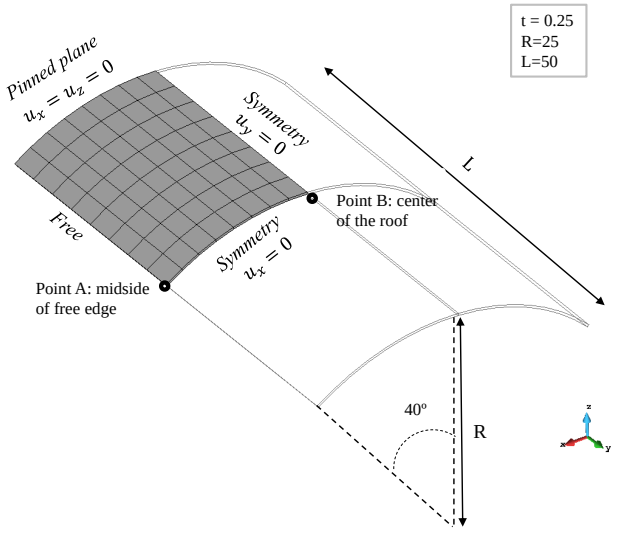

Fig. 6: Scordelis-Lo roof: Geometry and boundary conditions on a regular mesh of $N = 8$ elements per side.

The problem is analysed using six regular meshes with $N = 8; 16; 24; 32; 40; 48$ elements per edge. In all cases, the thickness of the shell is discretized using a single element. The material properties for this problem are: Young's modulus $E = 4.32 \times 10^8$ and Poisson's ratio $\nu = 0.0$. The reference solution of the vertical displacement at the center of the roof is 0.3086 from [47].

Figure 7 and Table 2 present the convergence for the displacements of the ε/u and standard formulations. ε/u FEs present a much faster convergence than standard ones with relative errors in displacements below 10% even for the most coarse mesh with $N = 8$ elements per side of the roof. The poor performance of

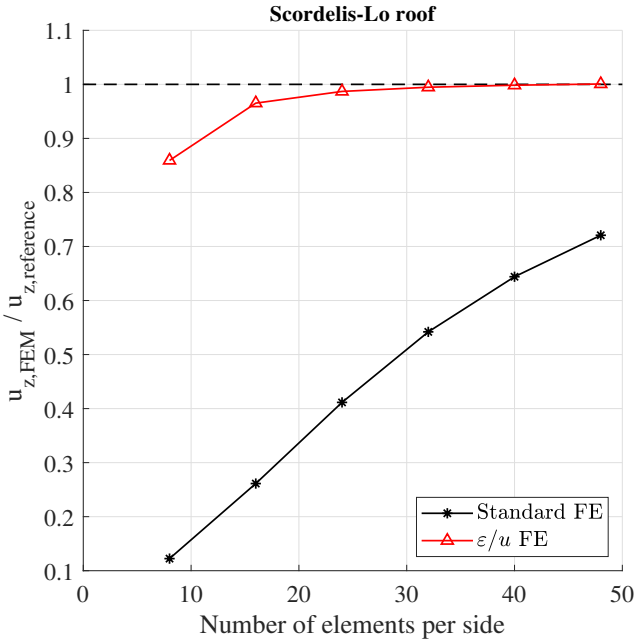

Fig. 7: Scordelis-Lo roof: Normalized vertical displacement u_z at the midpoint of the free edge (Point A in Figure 6) versus the number of finite elements per side.

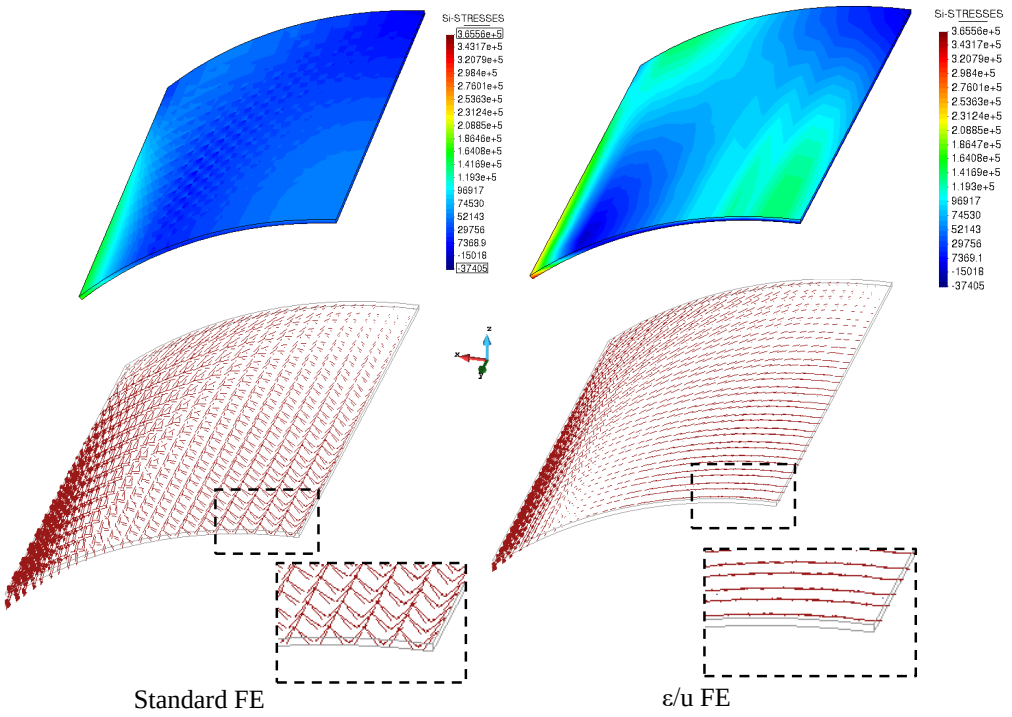

Fig. 8: Scordelis-Lo roof: Contour (top) and vectors (bottom) of the maximum principal stresses using standard (left) and ε/u FEs (right). The lower two figures present a close-up of the zones enclosed by dashed rectangles.

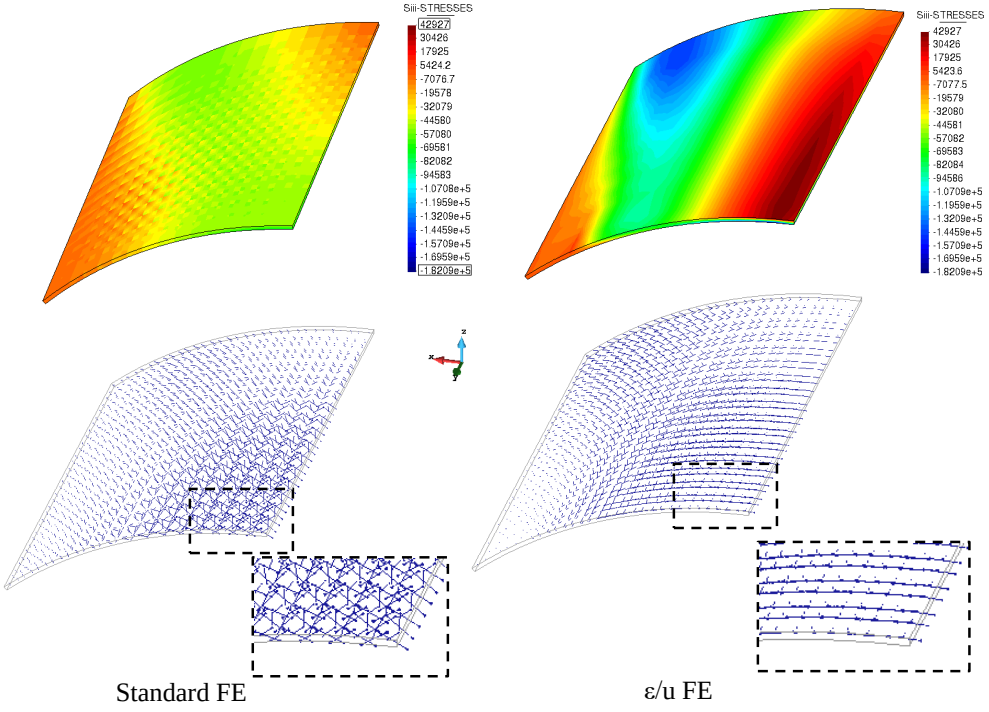

Fig. 9: Scordelis-Lo roof: Contour (top) and vectors (bottom) of the minimum principal stresses using standard (left) and ε/u FEs (right). The lower two figures present a close-up of the zones enclosed by dashed rectangles.

standard FEs is demonstrated by the high relative errors in the computed displacements, which are greater than 25% for all analysed discretizations.

The accurate computation of stresses is of primary importance in shell structures as they allow to identify the resisting mechanism within the structure, which is

not always straightforward. Table 2 presents the normal stresses at the center of the roof and Figures 8-9 present the distribution and directions of the maximum and minimum principal stresses, respectively, for the mesh with $N = 16$ elements per side of the roof. The identification of the stress flow within the shell structure is difficult using standard FEs, as the directions of the computed principal stresses vary spuriously due to membrane (and shear) locking. On the contrary, stress directions computed by the ε/u formulation allow to assess the flow of compressive and tensile stresses within the shell. The accurate prediction of the stress directions is of great interest in the analysis and design of spatial shell structures, especially of unreinforced masonry ones, where the resisting mechanism relies on the development of a system of compressive thrusts within the volume of the shell [48].

5.2.2 Hemispherical Shell

The hemispherical shell with a free edge is a typical benchmark of a double-curved shell problem, often used in the literature for the investigation of the capacity of solid [41, 20, 37, 46], shell [41, 9, 43, 49] and solid-shell [50, 51, 22, 23] elements to represent inextensional bending modes.

Figure 10 presents the geometry, load and boundary conditions. The equator edge is free and point radial loads of $F = 2.0$ alternating in sign (i.e. towards the interior or exterior of the shell) are applied at 90° on it. Due to symmetry, only a quarter of the hemisphere is analysed adopting proper boundary conditions on the symmetry planes (see Figure 10).

The problem is analysed using six regular meshes of hexahedra with $N = 8; 16; 32; 40; 64; 80$ elements per side. For all the studied meshes, the shell is discretized with a single element per thickness. The material properties for this problem are: Young's modulus $E = 6.825 \times 10^7$ and Poisson's ratio $\nu = 0.3$. The reference solution regarding the radial displacement at the load points is 0.0940, given in [41].

Figure 11 reports the convergence of the displacement results. Similar to the previous case, the convergence of the solution using standard FEs is very slow presenting errors in displacements greater than 80% even for the most refined mesh. For the ε/u case, convergence progresses rapidly with mesh refinement and errors of less than 10% are computed with meshes of $N \geq 32$ elements per side of the shell.

The enhanced accuracy of the ε/u FE in the computation of stresses is visible in the comparison of the principal stresses distribution, shown in Figures 12-13. As in Scordelis-Lo roof case, there are spurious membrane and shear stresses using standard FEs, while ε/u FEs are free from membrane (and shear) locking, making possible the identification of the stress flow within the shell.

Table 2: Scordelis-Lo roof: Deflection u_z at top midside of free edge (Point A in Figure 6) and normal stresses σ_{xx} at the top of the center of the roof (Point B in Figure 6).

	Standard FE		ε/u FE	
Elements per side	u_z	σ_{xx}	u_z	σ_{xx}
8	0.0378	7335.4	0.2652	104200
16	0.0806	19816	0.2979	139130
24	0.1270	52872	0.3046	153660
32	0.1673	82232	0.3070	161680
40	0.1987	105400	0.3081	166740
48	0.2224	122820	0.3088	170220

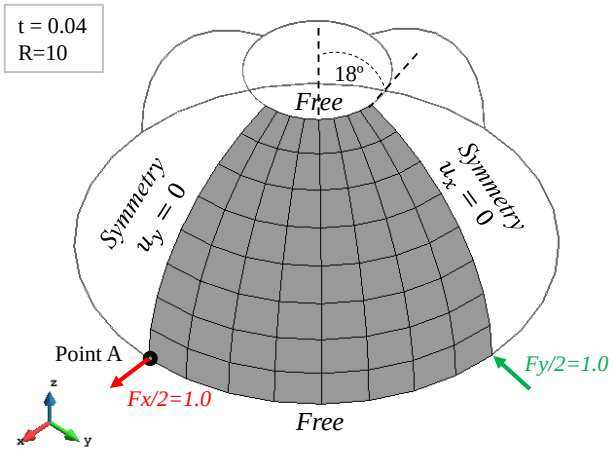

Fig. 10: Hemispherical shell: Geometry, load and boundary conditions on a regular mesh of $N = 8$ elements per side.

5.2.3 Pinched cylinder with diaphragm

The last benchmark test related to the simulation of shell behaviour is the pinched cylinder with diaphragm [52, 53, 44]. Several simulation of this test exist in the literature using solid [26, 12, 20], shell [44, 9, 43, 26, 49] and solid-shell [14, 51, 54] elements. This test is considered by Belytschko et al. [9] as "one of the most severe tests for both inextenstional bending modes and complex membrane states".

The problem consists in the application of two opposing radial loads at the center of a cylinder, which

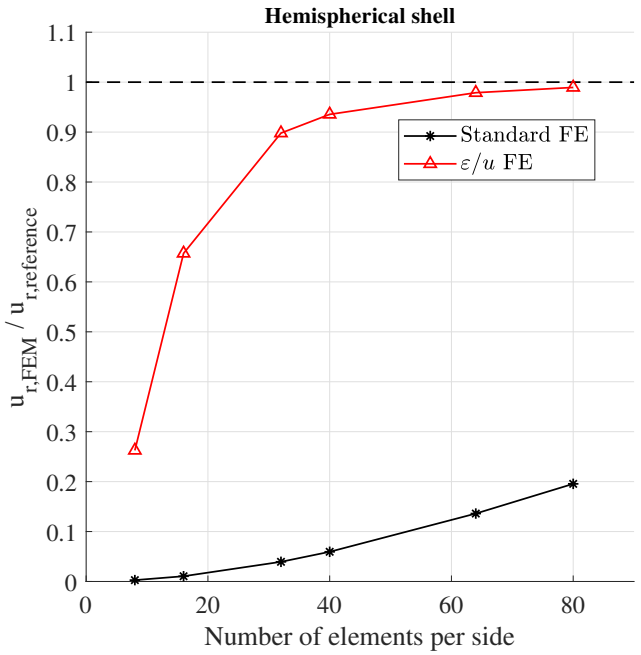

Fig. 11: Hemispherical shell: Convergence of the radial displacement at the load point (Point A in Figure 10) versus the number of finite elements per side.

Table 3: Pinched cylinder with diaphragm: Displacements and error between numerical displacements and reference value. Error below 5% is shown in bold

	Standard FE		ε/u FE	
Elements per side	u_y	Error [%]	u_y	Error [%]
4	0.0770	-95.78	0.1529	-91.62
8	0.1569	-91.40	0.7189	-60.60
16	0.3245	-82.22	1.3452	-26.28
32	0.6594	-63.86	1.6729	-8.32
48	0.9038	-48.99	1.7456	**-4.34**
64	1.1340	-37.86	1.7719	**-2.90**
80	1.2834	-29.67	1.7844	**-2.21**
96	1.3936	-23.63	1.7919	**-1.80**
128	1.5378	-15.73	1.8020	**-1.25**
144	1.5854	-13.12	1.8052	**-1.07**
160	1.6226	-11.08	1.8078	**-0.93**
176	1.6521	-9.46405	1.8100	**-0.81**

has two ends supported by rigid diaphragms. Figure 14 presents the geometry, load and boundary conditions. The ratio between the thickness and the radius of the cylinder is 1/100, so that structure can be considered as a thin shell. Due to the symmetry of the problem, only one-eighth of the cylinder is modelled.

The cylinder is analysed using twelve regular meshes with $N = 4; 8; 16; 32; 48; 64; 80; 96; 128; 144; 160; 176$ elements per side. The following material properties are considered: Young's modulus $E = 3.0 \times 10^6$ and Poisson's ratio $\nu = 0.3$. The reference solution for the deflection at the load location given by [52] based on Flügge's series solution [53] is $u_z = 0.18248 \cdot 10^{-4}$.

Figure 15 shows the convergence of the deflection at point A (see Figure 14) with mesh refinement. Similar to the previous cases, the ε/u FE converges faster than the standard one and the error in displacements drops below 5% for a mesh with $N \geq 48$ elements per side (see Table 3). For all the studied meshes, the relative error in displacements given by the standard FE is above 10%. Comparing to the rest of the shell related examples, a higher refinement is necessary to achieve errors below 2% with the ε/u FE. This supports the claim that this problem is one of the most challenging for testing the capacity of elements to represent shell behaviour. Similar to the displacements, ε/u show a faster convergence in terms of stresses compared to standard ones (see Figure 16).

5.3 Simulation of plates

This section investigates the capacity of the ε/u FE formulation to avoid shear locking in thin plates. Two benchmark plate problems [55, 17, 56, 37] are analysed: the thin square and circular plates with clamped edges. Note that in all cases the plates are discretized with two elements through the thickness.

5.3.1 Clamped square plate

The clamped square plate test consists in the loading under uniform normal pressure on the top surface of a square plate with fixed edges. This benchmark test has been analysed in the literature with solid [20, 37], plate [41, 56], shell [43, 57, 49] and solid-shell elements [14, 22].

Figure 17 shows the geometry, load and boundary conditions. A square plate with edge length $L = 2$ and thickness $t = 0.01$ is subjected to uniform pressure $p = -100$ per unit surface on its midsurface. The symmetry of the problem allows the simulation of only a quarter of the plate, considering appropriate boundary conditions. All displacements are zero at the two clamped edges, while only the normal displacements are zero at the two planes of symmetry (see Figure 17). Young's modulus is $E = 17.472 \times 10^6$ and Poisson's ratio $\nu = 0.3$. The reference solution of the vertical displacement at the middle of the plate according to Kirchhoff's plate theory is $u_z = 1.26$ [41].

The effect of the element distortion is investigated using two mesh configurations; a regular and a skewed one, with a varying number N of finite elements along

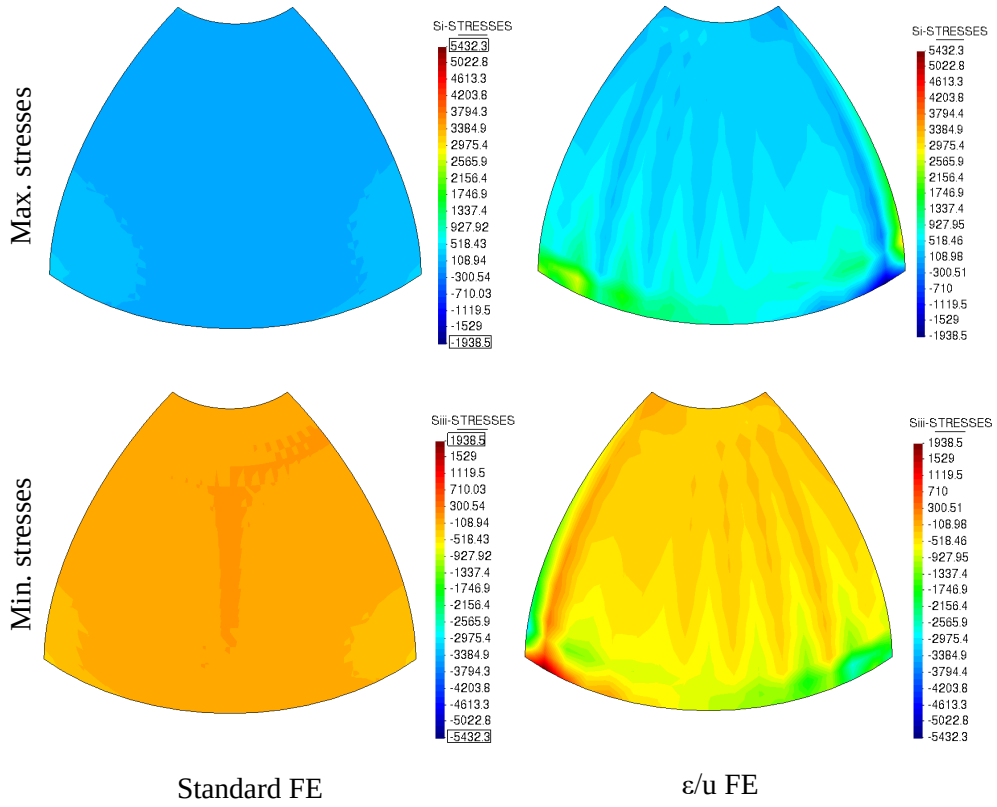

Fig. 12: Hemispherical shell: Contour of the maximum and minimum principal stresses using standard (left) and ε/u FEs (right).

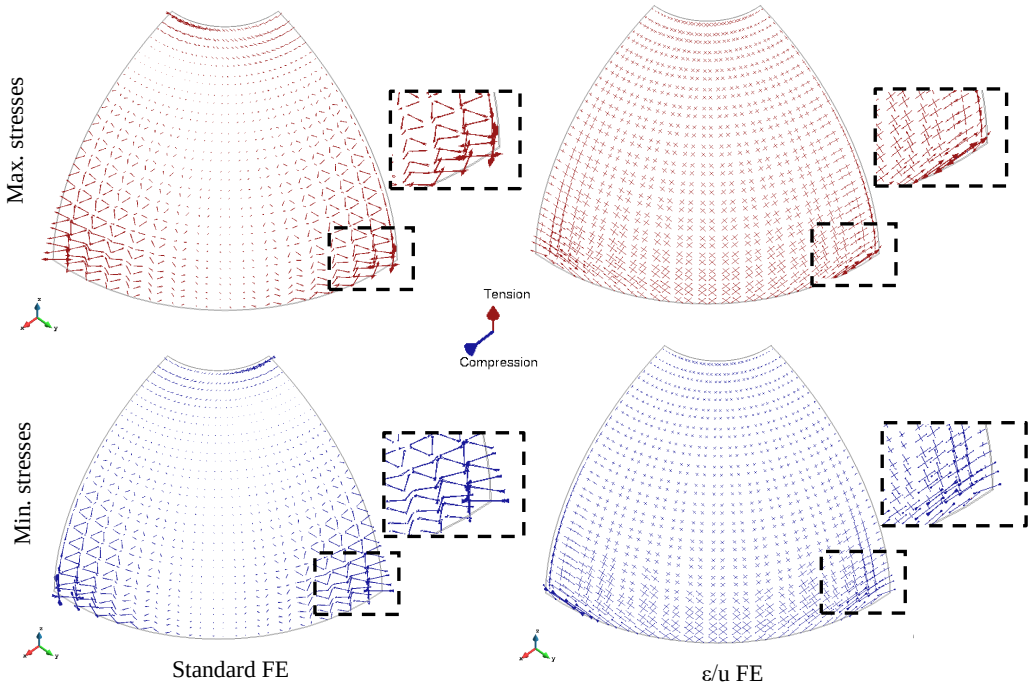

Fig. 13: Hemispherical shell: Vectors of the maximum and minimum principal stresses using standard (left) and ε/u FEs (right).

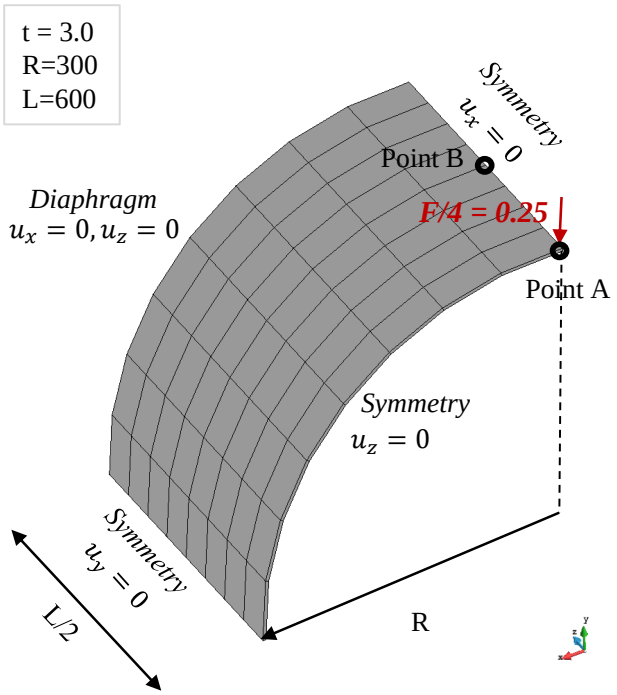

Fig. 14: Pinched cylinder with diaphragm: Geometry, load and boundary conditions on a regular mesh of $N = 8$ elements per side.

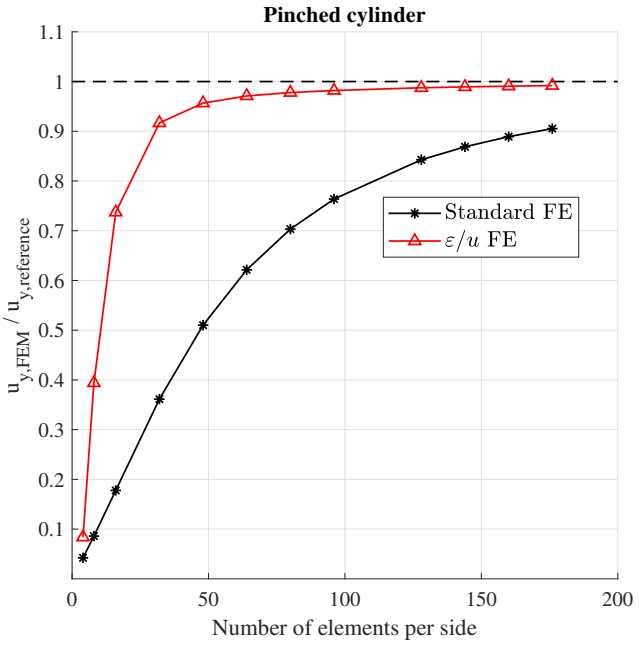

Fig. 15: Pinched cylinder with diaphragm: Normalized vertical displacement u_z at the midpoint (Point A in Figure 14) versus the number of finite elements per side.

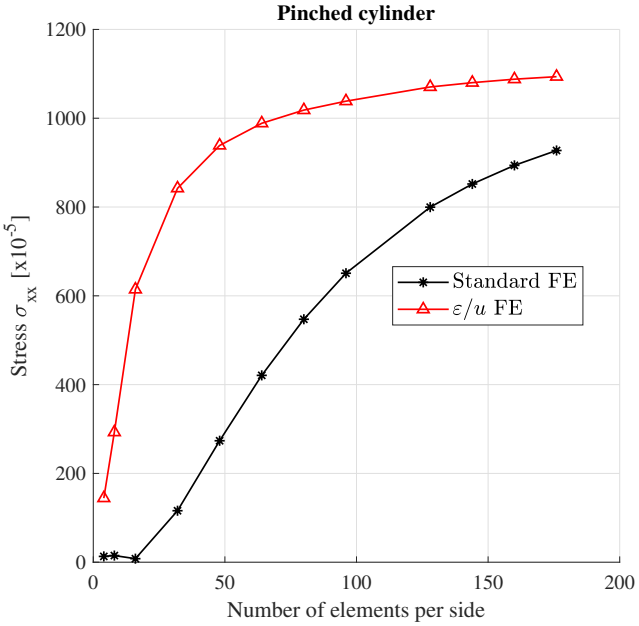

Fig. 16: Pinched cylinder with diaphragm: Normal stress (compression) at Point B (see Figure 14) versus the number of finite elements per side.

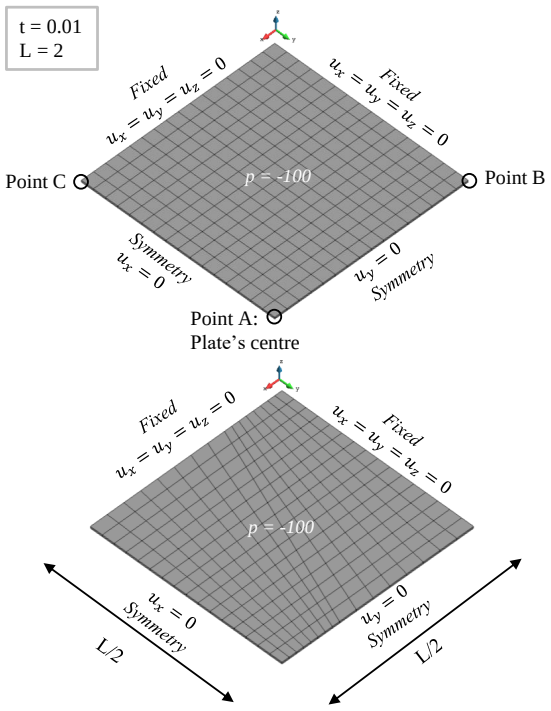

Fig. 17: Clamped square plate: Geometry, load and boundary conditions on a regular (top) and a skewed (bottom) finite element mesh with $N = 16$ elements per side.

each side of the plate. Figure 17 shows the finite element meshes for the regular and skewed configuration with $N = 16$ elements per side. Nine mesh sizes have been analysed for each mesh type with $N = 8; 10; 16; 24; 40; 64; 80; 100; 120$ elements per plate side.

For all the analyses, the plate is discretized using two finite elements per thickness.

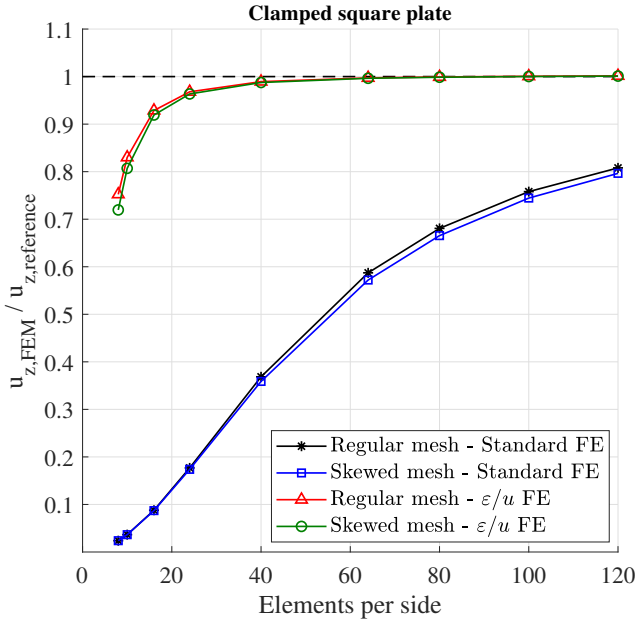

Fig. 18: Clamped square plate: Normalized vertical displacement u_z at the center of the square plate (Point A in Fig. 17) against number of elements per side.

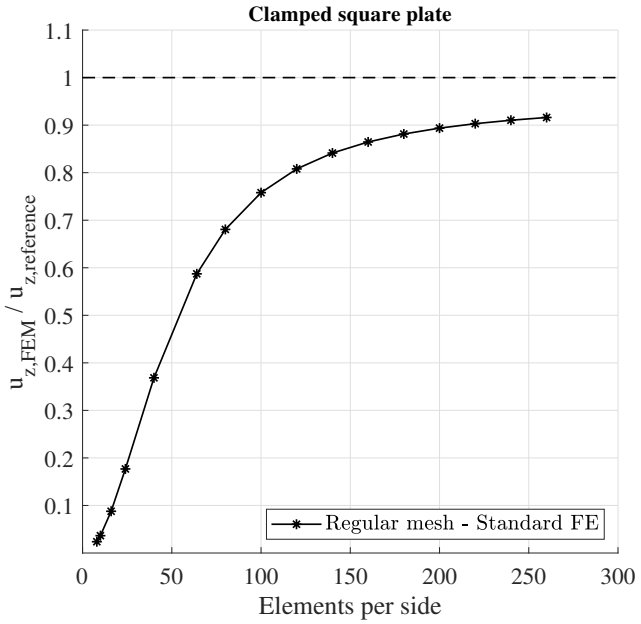

Fig. 19: Clamped square plate: Normalized vertical displacement u_z at the center of the square plate (Point A in Fig. 17) against number of elements per side for the case of the standard FE.

Figure 18 shows the relative convergence of the computed value of the vertical displacement at the center of the plate (Point A in Fig. 17). For all analysed cases, the displacement predictions by the ε/u FE outperform those of the standard one. The difference between the regular and the skewed mesh for the ε/u FE formulation is always below 5% and drops rapidly from a 4.55% for $N = 8$ to 0.18% for $N = 80$. Observe that the ε/u FE predicts the displacement with accuracy below 10% even for very stretched elements with an aspect ratio of 1:12.5 (mesh with 16 elements per edge). For the standard formulation, the relative error between the computed displacement and the reference one is above 20% for all the studied meshes. Figure 20 illustrates the difference in the computed deformation for a mesh of $N = 16$ elements per side using mixed and standard finite elements. The difference in the computed displacements for this case is of an order of magnitude. A further investigation of the convergence of the displacement for the standard element using regular meshes with $N = 140; 160; 180; 200; 220; 240; 260$ (see Figure 19) makes evident the shear locking effect, resulting in the convergence at a lower displacement compared to the analytical one. Standard FE shear locking is clear also in the stress distribution within the plate, shown in Figure 21.The inconsistent stress directions using the standard formulation illustrate the effect of spurious shear stresses; these are not present in the ε/u formulation.

5.3.2 Clamped square plate: Investigation of computational cost

When interpreting the above results, we should consider that for the same amount of finite elements, ε/u FEs have three times more degrees of freedom, i.e. three displacements and six strain components instead of only three displacements used in standard FEs. In order to have a more representative comparison in terms of cost-efficiency, Figure 22 presents the local error in displacements against the total number of degrees of freedom (DOF). It is visible that for any number of DOF (i.e. a vertical line in Figure 22), the error in displacements is always lower using the ε/u FE formulation. This means that for any size of problem (represented by the total number of DOFs), the use of ε/u FEs will result in a more accurate prediction of the displacement field compared to the use of standard FEs. In other words, and for this case, an error below 10% is achieved with a standad FE mesh of 220 FEs per side (see Figure 19) in contrast to a ε/u FE mesh of 10 FEs per side of the plate (see Figure 18). Moreover, the higher slope of the graphs corresponding to the ε/u FEs illustrates clearly

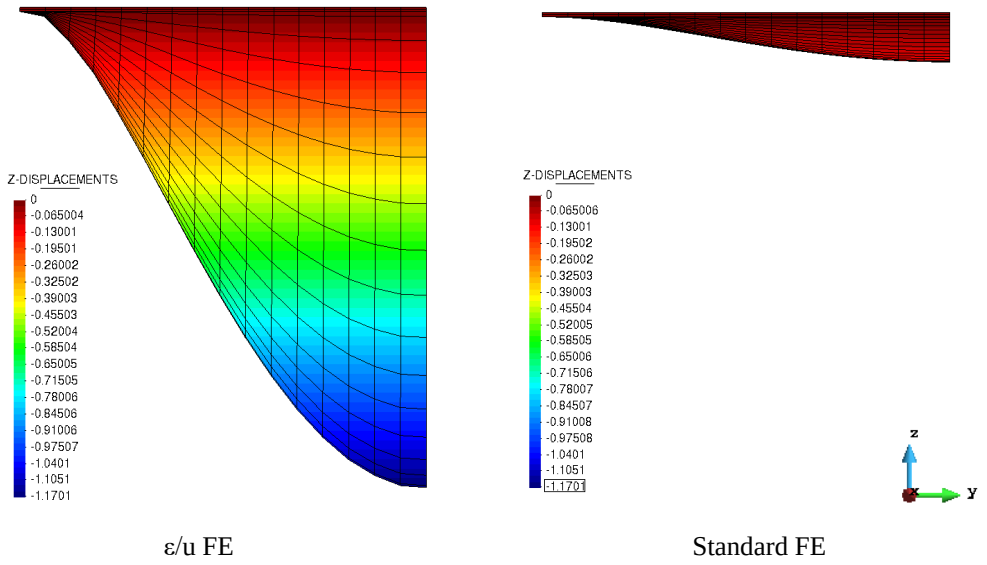

Fig. 20: Clamped square plate: Deformed shape (×1) and vertical displacement contour fill for a regular mesh with $N = 16$ elements per side using mixed (left) and standard (right) FEs.

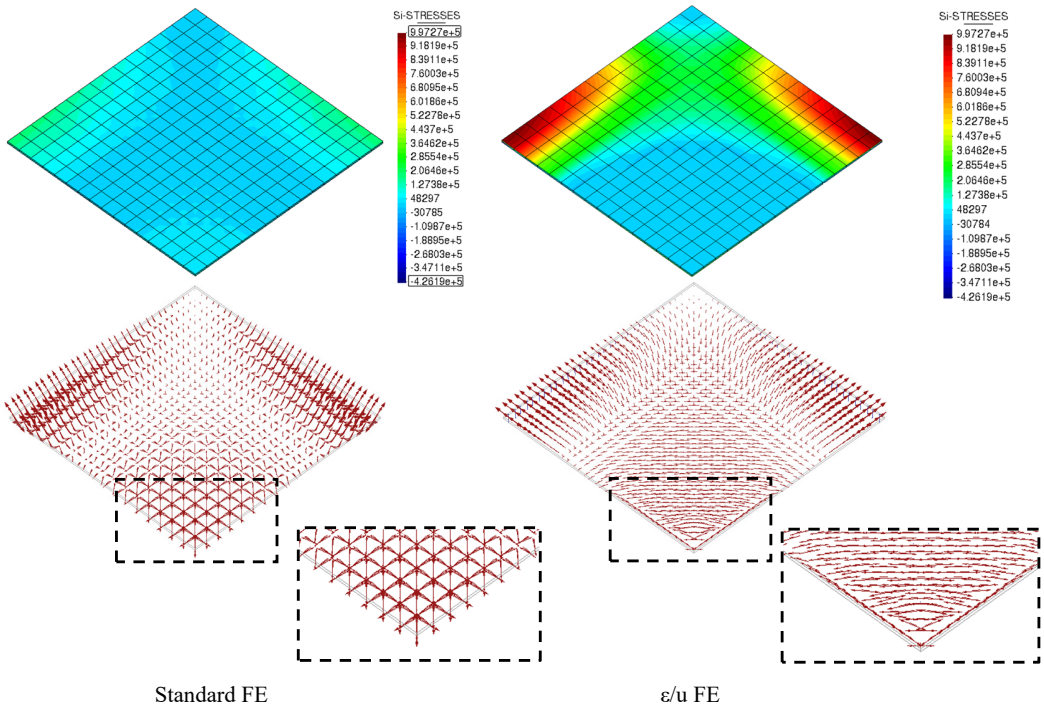

Fig. 21: Clamped square plate: Maximum principal stresses contour (top) and vectors (bottom) for standard (left) and ε/u FEs (right) in a regular mesh of 16 elements per side.

the difference in the convergence rate between the two formulations and the enhanced accuracy of ε/u FEs. Note that the small difference in the displacement estimations between regular and skewed meshes has only a minor influence in the convergence rate of each case.

In order to further illustrate the relative computational cost of the standard and the proposed ε/u formulations, Figure 23 presents the relationship between computational time and accuracy using both standard and ε/u FEs. The graph shows that for any level of

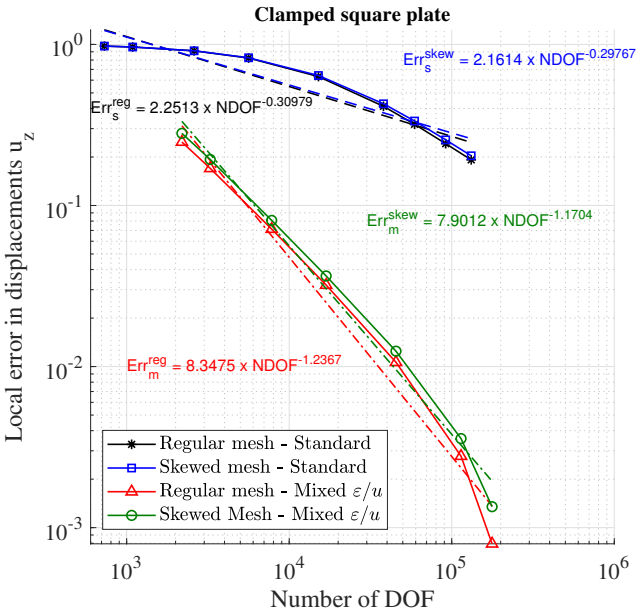

Fig. 22: Clamped square plate: Local error in displacement u_z at the center of the square plate versus the Number of Degrees of Freedom (DOF). Dashed lines correspond to the linear regression for each of the studied cases. Subscripts s and m stand for standard and mixed formulations, respectively. Superscripts *reg* and *skew* stand for regular and skewed meshes, respectively.

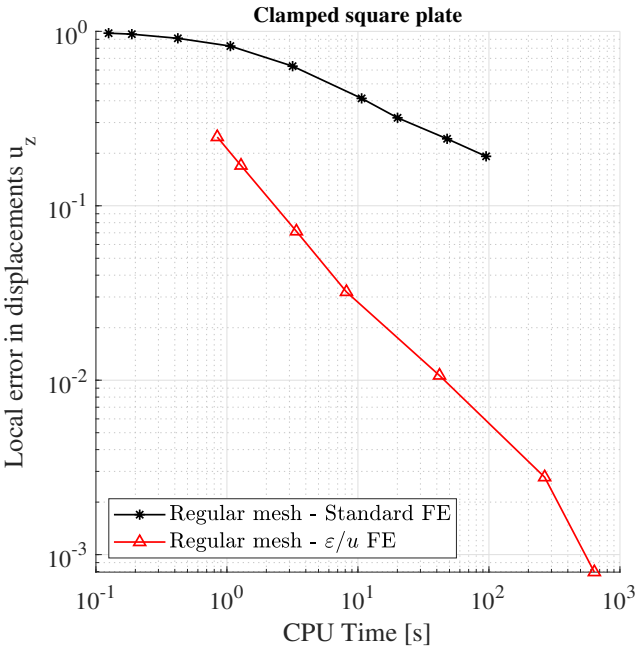

Fig. 23: Clamped square plate: Local error in displacement u_z at the center of the square plate versus the CPU time in seconds.

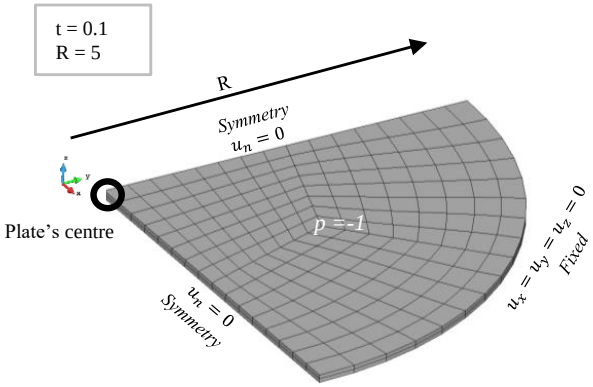

Fig. 24: Clamped circular plate: Geometry, load and boundary conditions for a finite element mesh of 16 elements per side.

accuracy, the computational time for the ε/u FE formulation is lower than that of the standard one.

5.3.3 Clamped circular plate

The second case related with the simulation of plates using the present ε/u FEs is the clamped circular plate. The test consists in the application of a uniform normal pressure at the middle surface of a cylindrical plate with fixed edges. Compared to the clamped square plate, this case allows to evaluate the performance of shell [7, 44], plate [56] and solid [37] elements in nonrectangular configurations (i.e. distorted elements).

Figure 24 presents the geometry, load and boundary conditions. As in the case of the square plate, the numerical model includes only a quadrant using appropriate symmetry boundary conditions. The plate has a radius $R = 5$ and a thickness $t = 0.1$. Young's modulus is $E = 1.092 \times 10^6$ and Poisson's ratio $\nu = 0.3$. The vertical load is applied as a uniform pressure of $p = -1$ per unit surface at the middle surface of the plate. The reference values of the vertical displacement and the radial stress at the center of the plate according to Kirchhoff's plate theory are equal to $u_z = -0.398137$ and $\sigma_{rr} = -3093.75$, given in [37].

Both standard and ε/u FE formulations are analysed using eleven finite element meshes with a varying number of elements per side $N = 8; 16; 24; 32; 40; 64; 80; 100; 120; 140; 160$. For all meshes, the thickness of the plate is discretized using two elements. The use of only hexahedral elements for the discretization of the circular plate results in distorted elements, as can be seen in Fig. 24.

The performance of both ε/u and standard FEs is similar to the square plate problem. The ε/u FE formulation predicts with increased accuracy and with a higher convergence rate both displacements and stresses compared to the standard formulation (see Figures 25-26). A mesh with 16 elements per side is suffi-

cient using ε/u FEs to compute the displacements with a difference of less than 5% compared to the analytical solution. Standards FEs do not reach this accuracy even for the most refined mesh, converging at a lower displacement (see Figure 25). This shear locking of the standard formulation results in the overestimation of the stress values, which converge at a higher value than the analytical solution (see Figure 26).

5.4 Anisotropic material

5.4.1 Clamped rectangular plate of an orthotropic material

The case of the clamped rectangular plate is investigated here considering an orthotropic material with different elastic properties along the two axes on the midplane of the plate. The geometry, loading and boundary conditions are the same as the ones shown in Figure 17. Young's modulus in the y and z directions is equal to the already analysed case $E_y = E_z = 17.472 \times 10^6$, while in the x direction is ten times greater $E_x = 174.720 \times 10^6$. Poisson's ratio is equal to $\nu = 0.3$ in all directions.

The convergence behaviour in displacements (see Figure 27) and stresses (see Figures 28-29) of the ε/u and standard formulations resemble closely the isotropic case. The σ_{xx} and σ_{yy} stresses shown in Figures 28-29 correspond to Points B and C in Figure 17.

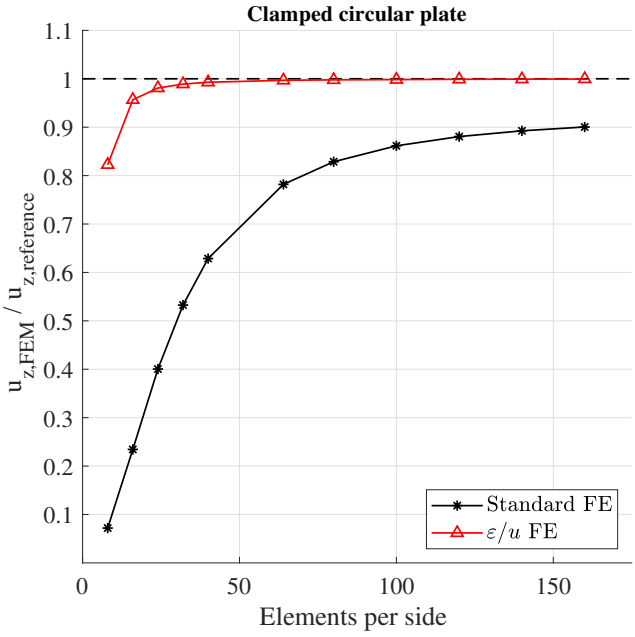

Fig. 25: Clamped circular plate: Vertical displacement u_z at the center of the circular plate versus number of finite elements per side.

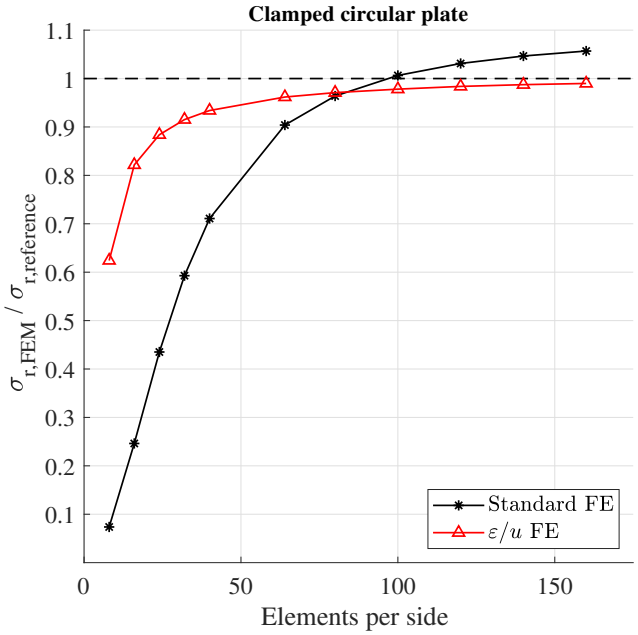

Fig. 26: Clamped circular plate: Vertical displacement u_z at the center of the circular plate versus number of finite elements per side.

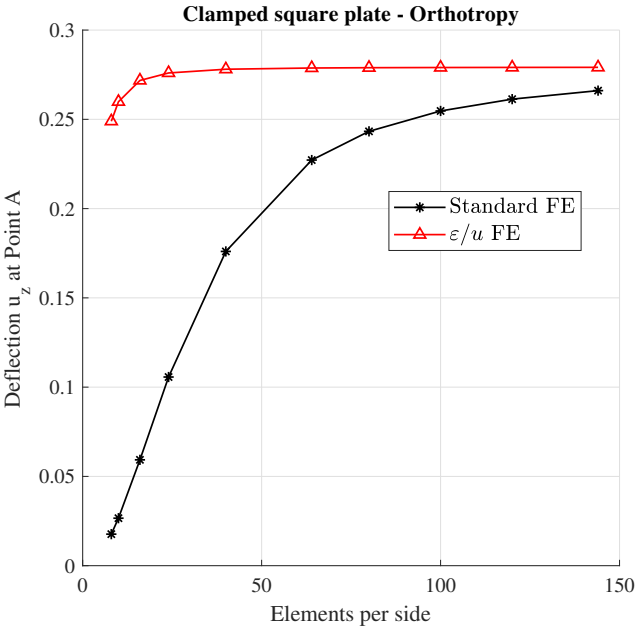

Fig. 27: Clamped square plate with orthotropy: Vertical displacement u_z at the center of the circular plate (Point A in Fig. 17) versus number of finite elements per side.

Taking the values from the most refined ε/u FE mesh as reference, $N = 144$, the ε/u formulation converges to the maximum displacement with an error below 5% for $N \geq 16$ elements per side. Regarding the stresses, the same level of convergence to the maximum normal stress occurs for $N \geq 40$ for σ_{xx} and $N \geq 64$ for σ_{yy}

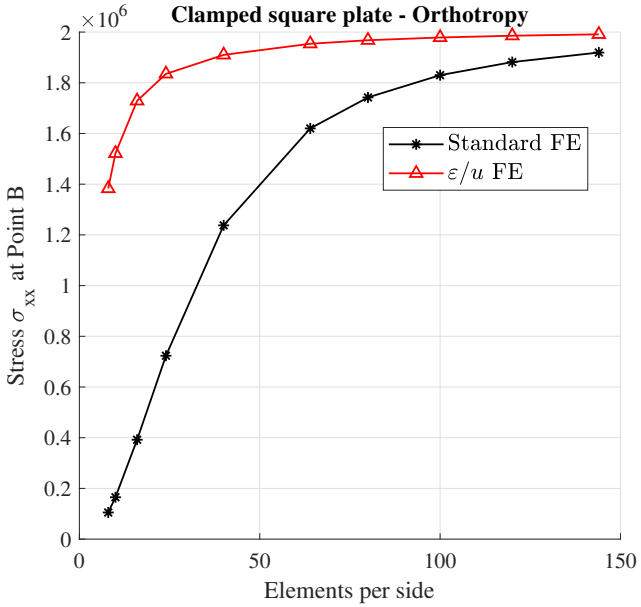

Fig. 28: Clamped square plate with orthotropy: Normal stress σ_{xx} at Point B (see Fig. 17) versus number of finite elements per side.

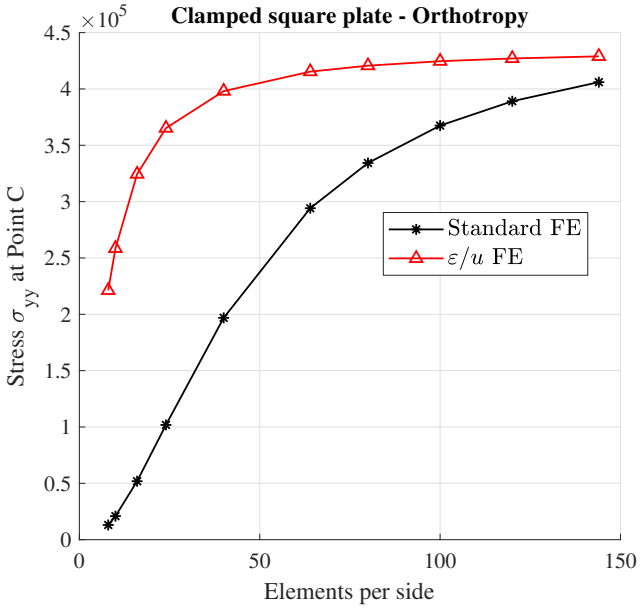

Fig. 29: Clamped square plate with orthotropy: Normal stress σ_{yy} at Point C (see Fig. 17) versus number of finite elements per side.

(see Table 4). The standard element reaches the same level of convergence in displacements and stresses only for the most refined case with $N = 144$ per side (Table 4).

The difference in the convergence rate of the stresses between standard and ε/u FEs is illustrated in Figure 30. The graphs make evident what has been observed so

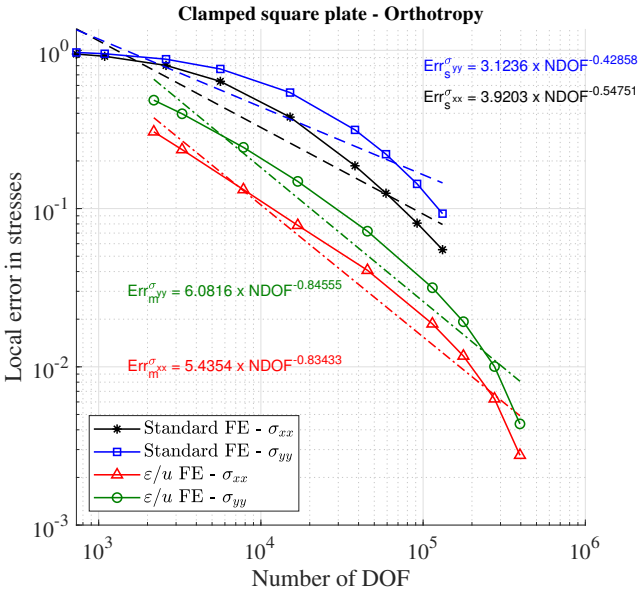

Fig. 30: Clamped square plate with orthotropy: Local error in the stresses σ_{xx}, σ_{yy} at Points B and C (see Fig.17) versus the Number of Degrees of Freedom (DOF).

far regarding the faster convergence in stresses (apart from displacements) of the ε/u FE.

Figure 31 presents the deflection along the midsides "AB" and "AC" of the orthotropic plate for the case of $N = 40$ elements per side. The increased stiffness of the plate in the x-direction (side "AB") is evident, as well as the important difference between the predicted deflections with standard and ε/u FEs.

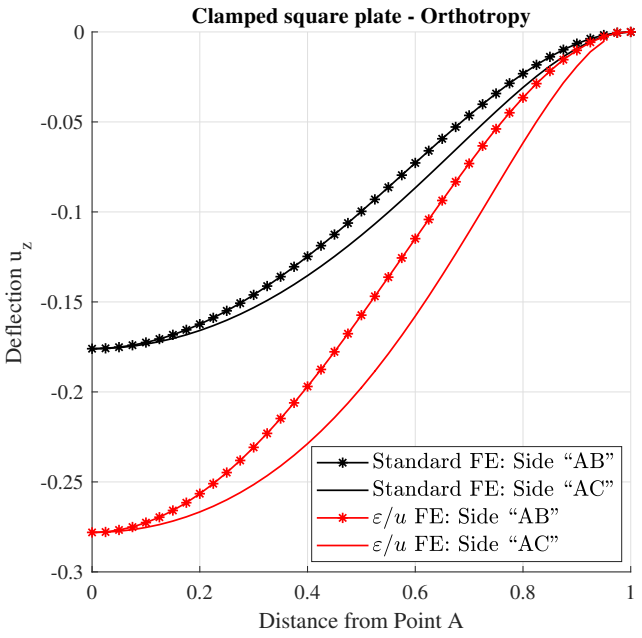

Fig. 31: Clamped square plate with orthotropy: Deflection u_z along two two midsides "AB" and "BC" (see Fig.17).

Table 4: Clamped square plate with orthotropy: Convergence study for deflection u_z and stresses σ_{xx}, σ_{yy}. Ratios above 0.95 are shown in bold.

	$u_z/u_{z,max}$		$\sigma_{xx}/\sigma_{xx,max}$		$\sigma_{yy}/\sigma_{yy,max}$	
N_{el} per side	Stand.	Mixed	Stand.	Mixed	Stand.	Mixed
8	0.063	0.892	0.053	0.694	0.030	0.516
10	0.095	0.931	0.083	0.764	0.049	0.603
16	0.212	**0.974**	0.197	0.868	0.121	0.756
24	0.379	**0.989**	0.363	0.922	0.237	0.851
40	0.631	**0.996**	0.622	**0.959**	0.459	0.928
64	0.814	**0.999**	0.814	**0.981**	0.686	**0.968**
80	0.872	**0.999**	0.875	**0.988**	0.779	**0.981**
100	0.912	**1.000**	0.919	**0.994**	0.857	**0.990**
120	0.936	**1.000**	0.945	**0.997**	0.907	**0.996**
144	**0.953**	**1.000**	**0.964**	**1.000**	0.947	**1.000**

$u_{z,max} = 0.27912, \sigma_{xx,max} = 1991100, \sigma_{yy,max} = 428940$

5.4.2 Clamped layered rectangular plate with orthotropic properties

Layered beams, plates and shells may present isotropic or orthotropic behaviour. This section investigates the case of a clamped rectangular plate constructed as a layered structure of an orthotropic material, but with different orientations of the axes of orthotropy in the two layers.

The geometry, load and boundary conditions are the same as in the previous example (see Figure 17). In this case, the plate is composed by two superimposed layers of orthotropic materials with the same thickness $t_1 = t_2 = 0.005\,m$. Young's moduli of the top layer are $E_{x,top} = 174.72 \times 10^6$ and $E_{y,top} = 17.472 \times 10^6$, while those of the lower layer are $E_{x,bottom} = 17.472 \times 10^6$ and $E_{y,bottom} = 174.72 \times 10^6$. Poisson's ratio equal to 0.3 is considered for both layers.

The plate is analysed using both standard and ε/u FEs with regular meshes of $N = 8; 10; 16; 24; 40; 64; 80; 100; 120$ per side of the plate. In all cases, each layer is discretized with one element per thickness, which makes a total of two elements per thickness of the plate.

The convergence of displacements and stresses in X and Y directions are shown in Figures 32, 33, 34, respectively. The results for this case are very similar to the previous ones, with the convergence rates in both displacements and stresses being far superior using ε/u FEs. Even for the more refined mesh with $N = 120$ elements per side of the plate, the standard FE formulation underestimates the results of both displacements and stress for more than 10%. The highest accuracy of the ε/u FE formulation can be appreciated in Figure 35, presenting the vectors of the principal stresses for the mesh of $N = 16$ elements per side. On the one hand, the shear locking present to the standard FE formulation results in the spurious orientation of the principal stress vectors within the plate, in addition to their underestimation, as shown in Figures 33 and 34. This shear locking is not present when the plate is discretized with ε/u FEs. On the other hand, the in-plane orthotropic behaviour of the two layers is perfectly represented by the ε/u formulation.

5.4.3 Clamped multi-layered rectangular plate with orthotropic properties

A multi-layered plate is now investigated. It is composed by five superimposed alternating layers of orthotropic materials with the same thickness $t = 0.002$. The geometry, load and boundary conditions are the same as in the rectangular plate example (see Figure 17), but the mechanical properties are different. Young's moduli of the odd layers are $E_{x,odd} = 174.72 \times 10^6$ and $E_{y,even} = 17.472 \times 10^6$, while for the even layers are $E_{x,even} = 17.472 \times 10^6$ and $E_{y,odd} = 174.72 \times 10^6$. Poisson's ratio equal to 0.3 is considered for all the layers.

The plate is analysed with both standard and ε/u FEs using a regular mesh of $N = 8; 10; 16; 24; 40; 64; 80$

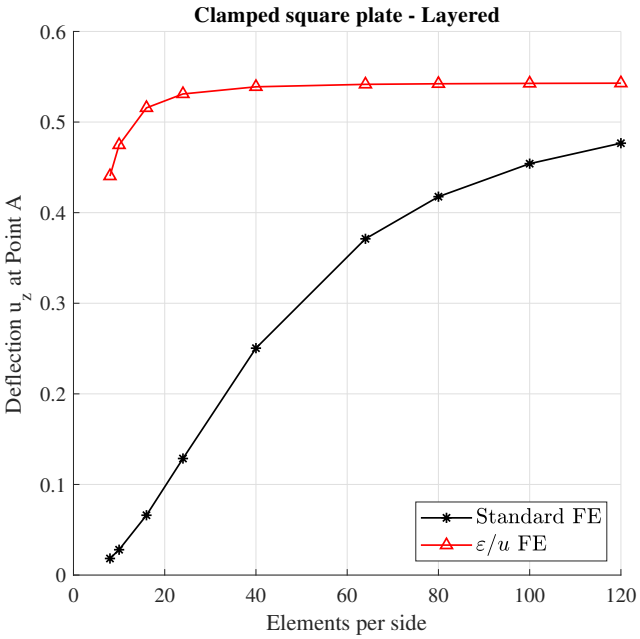

Fig. 32: Clamped square plate with two layers of orthotropic materials: Vertical displacement u_z at the center of the circular plate (Point A in Fig. 17) versus number of finite elements per side.

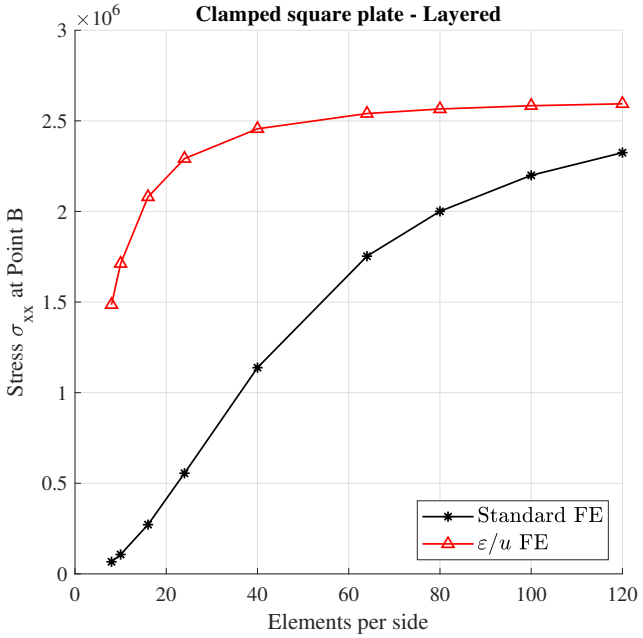

Fig. 33: Clamped square plate with two layers of orthotropic materials: Normal stress σ_{xx} at Point B on the top surface of the plate (see Fig. 17) versus number of finite elements per side.

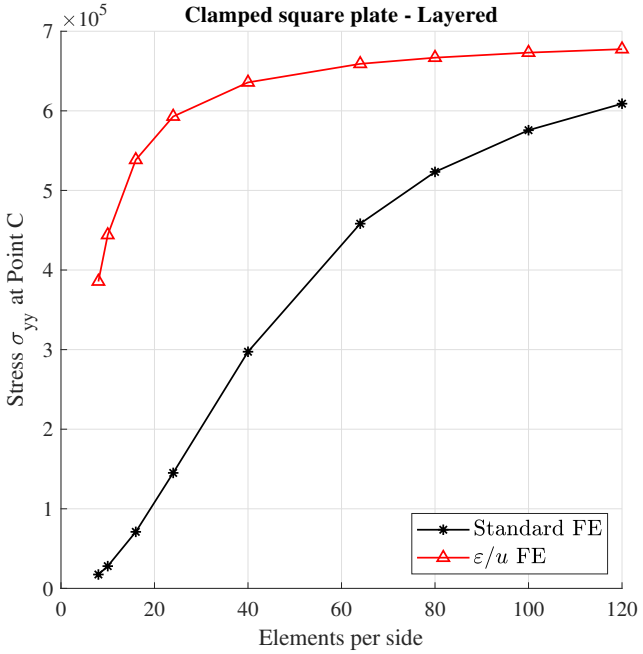

Fig. 34: Clamped square plate with two layers of orthotropic materials: Normal stress σ_{yy} at Point C on the top surface of the plate (see Fig. 17) versus number of finite elements per side.

elements per side of the plate. Each layer is discretized with 2 elements per thickness, which makes a total of 10 elements through the thickness of the plate.

Figure 36 presents the convergence behaviour in displacement and Figures 37 and 38 in stresses at Points A, B and C of the plate (see Figure 17), respectively. A comparison with the 2-layer case (Figures 32-29) shows the beneficial effect of the finer refinement through the thickness for the ε/u FEs. In fact, the use of 2 elements per layer leads to a very good estimation of both displacements and stresses, even for meshes with low numbers of finite elements per side of the plate. Contrarily, despite this refinement through the thickness, standard displacement-based FEs show a slow convergence with a difference in displacements and stresses of above 12% even for the most refined mesh with 80 elements per side.

Figure 39 shows the vectors of the principal stresses for the mesh of $N = 16$ elements per side. The same remarks as for the 2-layer plate in the previous subsection apply. Transverse shear distributions are correctly represented; no shear locking appears. Furthermore, the normal stress in the vertical direction is almost null without the need of explicitly imposing a plane stress assumption, as it corresponds to the tractions boundary conditions of the problem.

5.5 Nearly incompressible cases

This section investigates the capacity of the ε/u FE to overcome volumetric locking near the incompressibility limit ($\nu \to 0.5$). Two benchmark problems are analysed: the Cook's membrane and a square rectangular plate. For these cases, the B-bar method is employed for both standard and ε/u FEs.

5.5.1 Cook's membrane

Cook's membrane problem is considered as a standard test for investigating the performance of solid [58], shell [59] and solid-shell [50] finite elements under bending dominated stress conditions. The test considers the shear loading at a side of a tapered panel clamped on the opposide end.

Figure 40 presents the geometry, loading and boundary conditions. The material properties are: Young's modulus $E = 200 \times 10^6$, and Poisson's ratio $\nu = 0.4999$ referring to a nearly incompressible state.

The problem is analysed using five regular meshes with a varying number N of elements per side $N = 4; 8; 16; 32; 64$. Figure 40 shows the mesh for the case

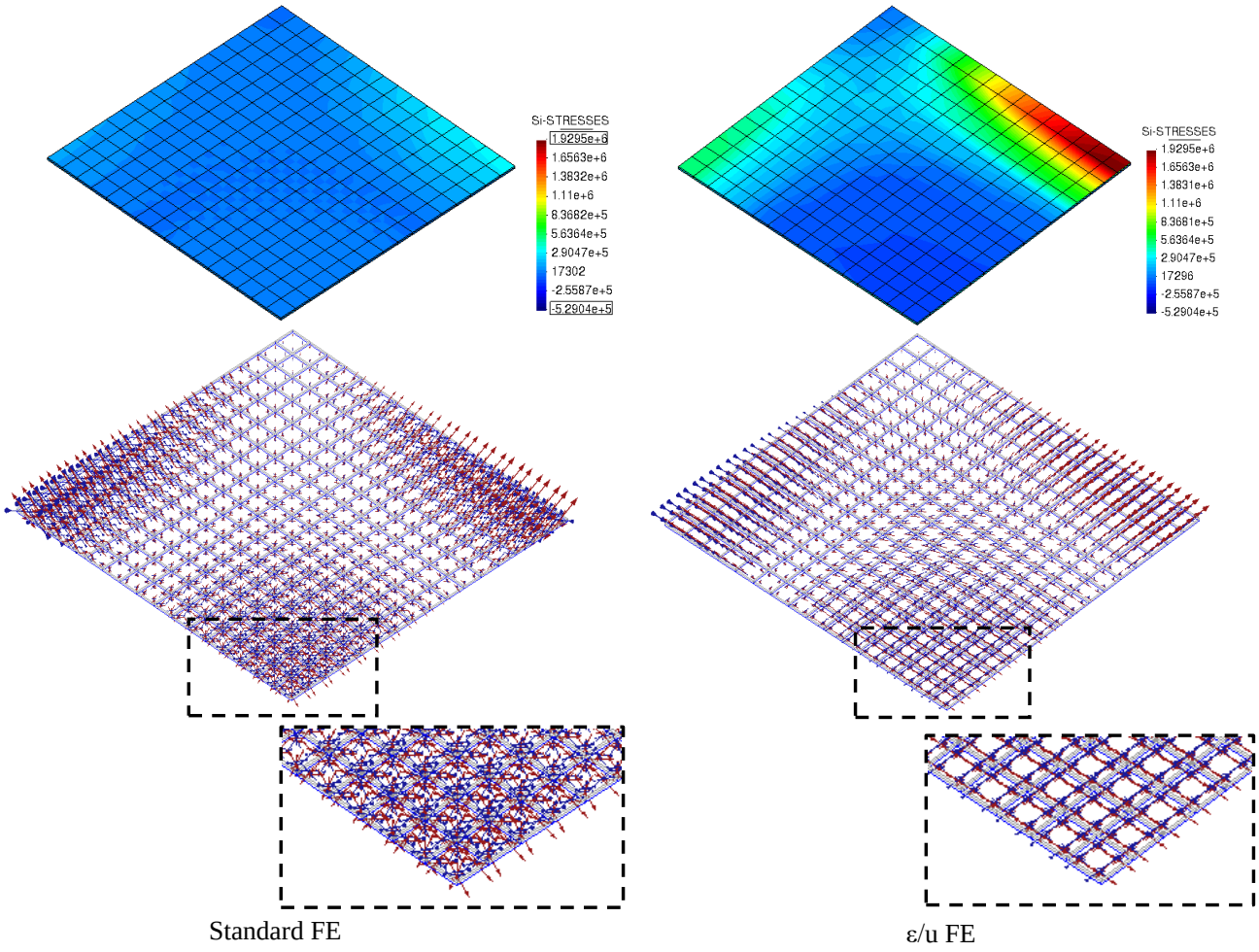

Fig. 35: Clamped square plate with two layers of orthotropic materials: Maximum principal stresses contour (top) and vectors (bottom) for standard (left) and ε/u FEs (right) in a regular mesh of 16 elements per side.

with $N = 8$ elements per side. In all meshes, the membrane is discretized with a single element per thickness (see Fig. 40).

Figure 41 presents the convergence of the vertical displacement at the top right corner of the membrane for mesh refinement using the ε/u and standard formulations with and without the B-bar method. The beneficial effect of the B-bar method in the convergence rate is evident for both formulations. It is noted that ε/u formulation converges to the same correct value with and without the B-bar method. On the contrary, convergence of the standard formulation is only possible using the B-bar method; otherwise, it is almost completely locked by the spurious volumentric strains.

Figure 42 and Figure 43 present the convergence of the pressure and J2 stress, respectively, at the middle of the lower side (Point B in Figure 40). In both cases, standard and ε/u formulations using the B-bar method converge very fast to a single value of pressure and J2 stress. The ε/u FE presents a much faster convergence and accuracy in J2 stresses compared to pressure and converges to the same value as the cases with the B-bar method for the finest mesh. On the contrary, the standard FE solution is locked as manifested by the divergence in the pressure values with mesh refinement. The same conclusions can be drawn by looking at the pressure and J2 stress contours presented in Figures 44 and 45, respectively. It is possible to observe the more accurate and continuous estimation of the pressure and J2 stress fields in the ε/u formulation, which is an immediate consequence of independent interpolation considered for the strains.

5.5.2 Clamped square plate

The second case studied near the incompressibility limit is the clamped square plate, already analysed for a compressible material using isotropic and orthotropic properties. The geometry, load and boundary conditions are

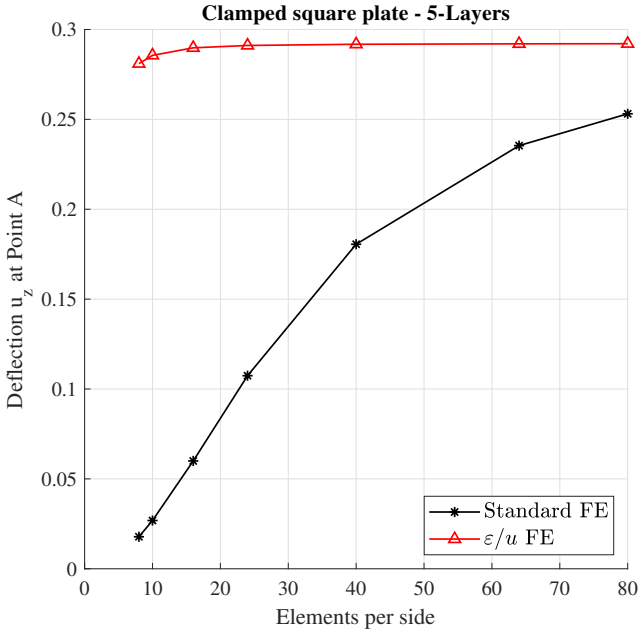

Fig. 36: Clamped square plate with five layers of orthotropic materials: Vertical displacement u_z at the center of the circular plate (Point A in Fig. 17) versus number of finite elements per side.

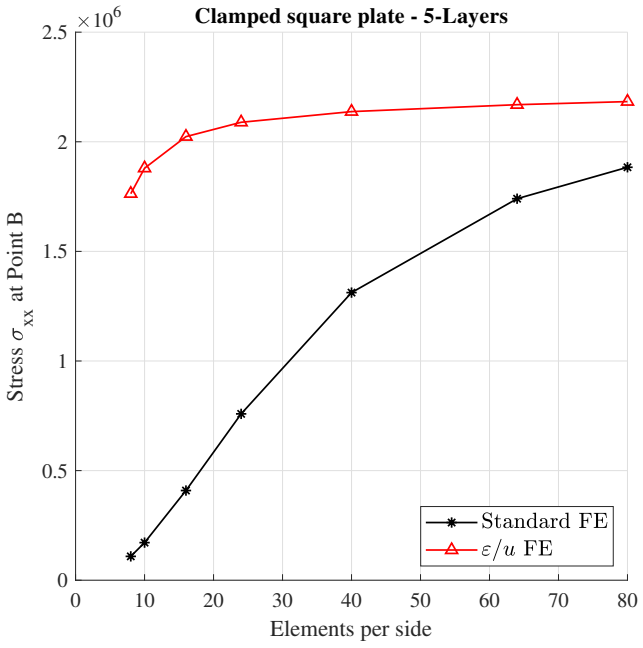

Fig. 37: Clamped square plate with five layers of orthotropic materials: Normal stress σ_{xx} at Point B on the top surface of the plate (see Fig. 17) versus number of finite elements per side.

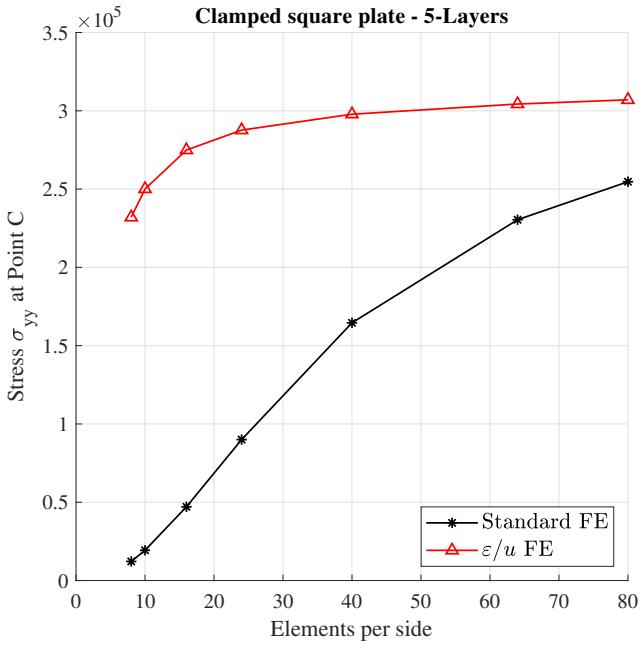

Fig. 38: Clamped square plate with five layers of orthotropic materials: Normal stress σ_{yy} at Point C on the top surface of the plate (see Fig. 17) versus number of finite elements per side.

the same to the ones presented in Figure 17. Young's modulus is $E = 17.472 \times 10^6$, while for Poisson's ratio the adopted value is $\nu = 0.4999$, representing a nearly incompressible material. For this case, the plate has been discretized using two and four elements per thickness in meshes with $N = 8; 10; 16; 24; 40; 64; 80$ elements per side. According to plate theory, the reference solution for the displacement at the center of the plate is inversely proportional to the plate regidity $D = E\,t^3/12(1-\nu^2)$ [60]. Considering that the analytical solution for $\nu = 0.3$ is equal to $u_z = 1.26$, the reference displacement for this case is $u_z = 1.04$.

Figure 46 presents the convergence of the displacements at the center of the plate. As for the previous case, the B-bar method is employed to simulate the nearly incompressible behaviour of the material. The best accuracy in terms of displacements is obtained for the ε/u FE with four elements per thickness. Observe that for the case with two ε/u FEs per thickness, the plate presents a more flexible response. This is a result of the under-integration of the mean stress by using the B-bar procedure, which is necessary to overcome the near-incompressibility constraint, but comes at the cost of the loss of some resolution across the thickness. As the results show, the accuracy of the ε/u FE solution is recovered through a more refined discretization across the thickness. Observe also that the standard FEs underestimate significantly the deflections of the plate even

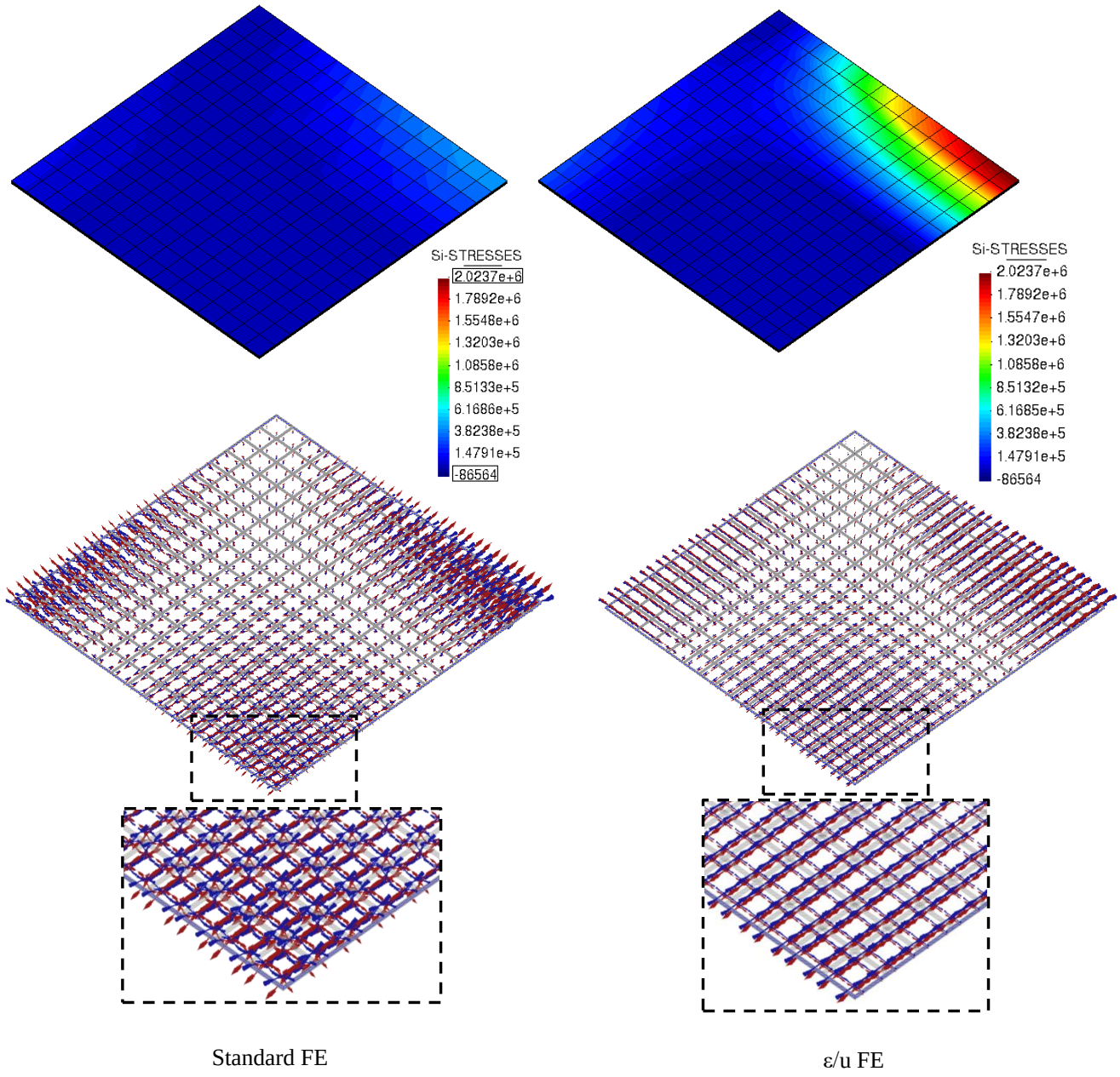

Fig. 39: Clamped square plate with 5 layers of orthotropic materials: Maximum principal stresses contour (top) and vectors (bottom) for standard (left) and ε/u FEs (right) in a regular mesh of 16 elements per side.

if the B-bar method is used. This is consistent with the results obtained for the $\nu = 0.3$ case (see Figure 18) and the layered plates (Figures 32 and 36).

6 Conclusions

This paper presents the use of solid finite elements with independent displacement and strain interpolations for addressing element locking problems under common load, geometrical and material conditions found in engineering structures. The accuracy of the present FE formulation is investigated in terms of displacements and stresses through the analysis of a set of eleven benchmarks problems of beam, shell and plate structures.

All problems are analysed using solid finite elements, which are available at all FE codes and can be conveniently used for the modelling of any type of structure and with any type of general constitutive model.

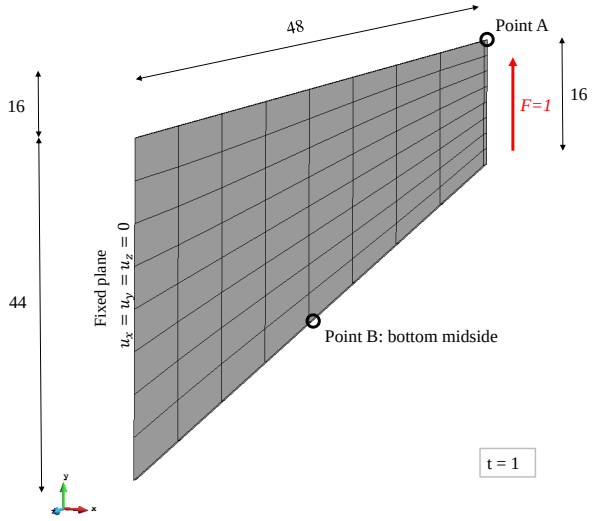

Fig. 40: Cook's membrane: Geometry, load and boundary conditions on a structured mesh of $N = 8$ elements per side.

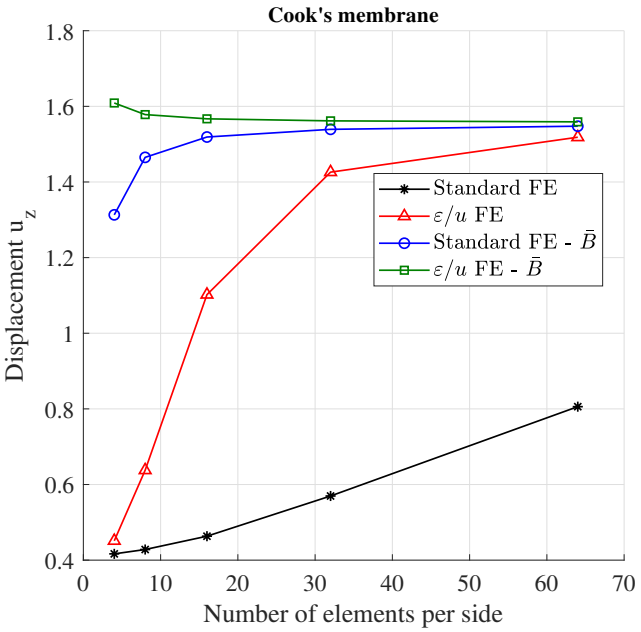

Fig. 41: Cook's membrane: Vertical displacement u_z at the top right corner of Cook's membrane (Point A in Fig. 40) versus number of finite elements per side.

The performance of the present FE is investigated considering several modelling choices, such as different element typologies (hexahedra and prisms) and mesh configurations (regular, skewed, warped). The effect of material properties is studied by considering isotropic and orthotropic cases, as well as compressible and nearly incompressible materials. For the latter, the use of the B-bar method as a way to address volumetric locking is investigated. Laminated multi-layered orthotropic material distribution is also investigated.

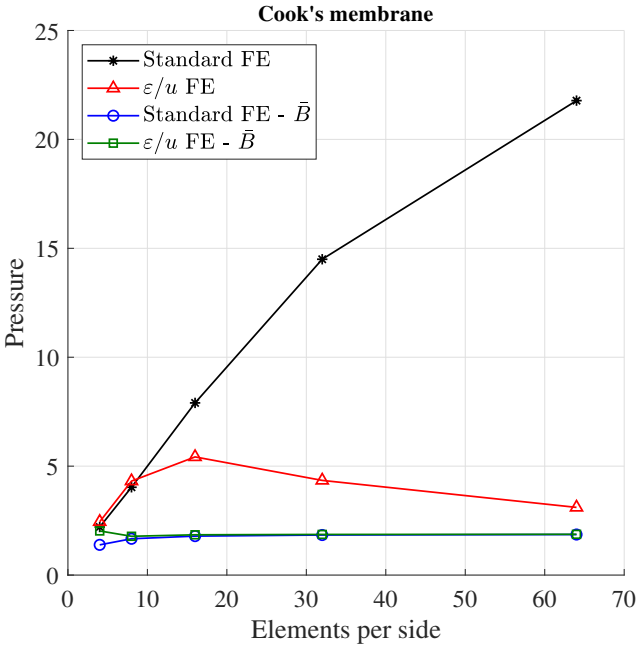

Fig. 42: Cook's membrane: Pressure at the bottom midside of Cook's membrane (Point B in Fig. 40) versus number of finite elements per side.

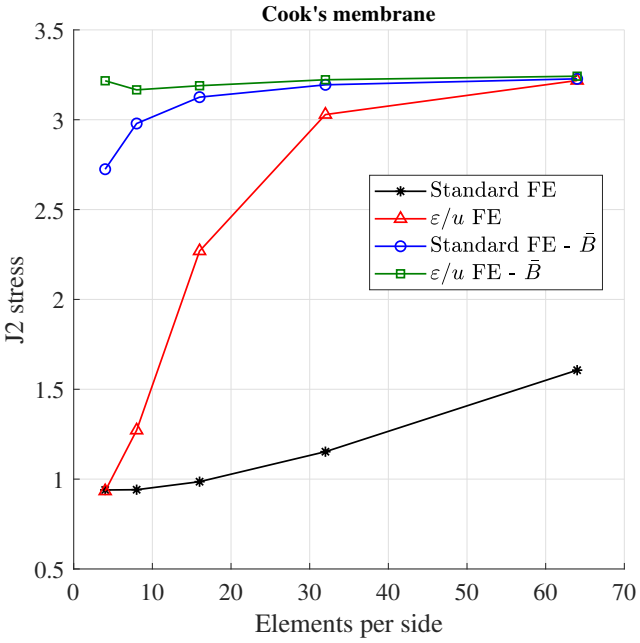

Fig. 43: Cook's membrane: J2 stress at the bottom midside of Cook's membrane (Point B in Fig. 40) versus number of finite elements per side.

Numerical results demonstrate that ε/u FEs far outperform the corresponding standard ones in estimating displacements and stresses, providing locking membrane and shear free solutions. The use of the B-bar method is beneficial for the performance of the present

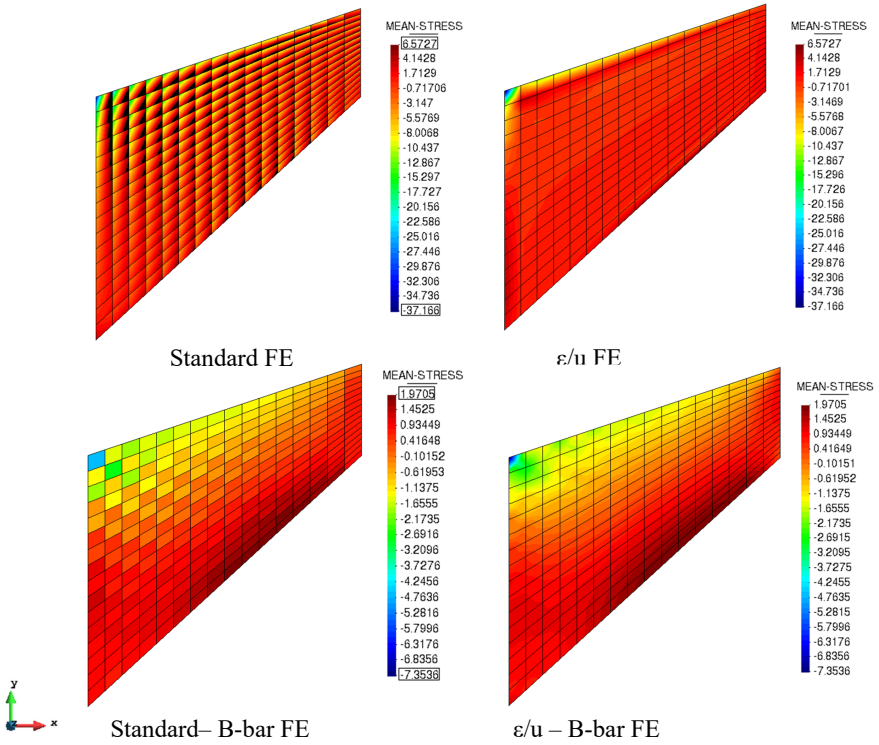

Fig. 44: Cook's membrane: Pressure contour fill for the standard (left) and mixed formulations (right) without (top) and with (bottom) the B-bar method for a mesh with 16 elements per side.

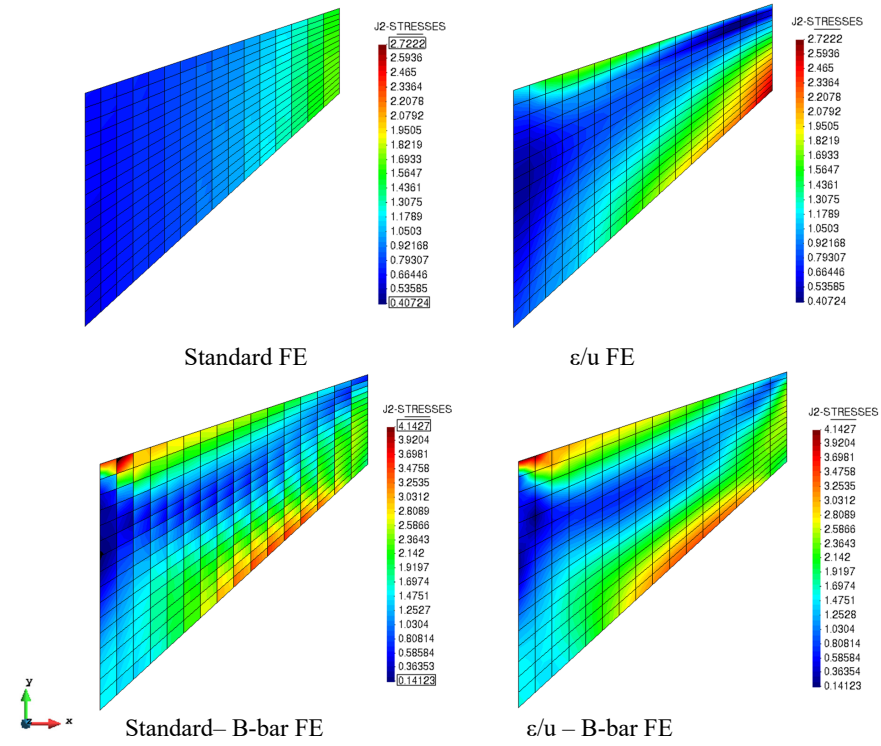

Fig. 45: Cook's membrane: Pressure contour fill for the standard (left) and mixed formulations (right) without (top) and with (bottom) the B-bar method for a mesh with 16 elements per side.

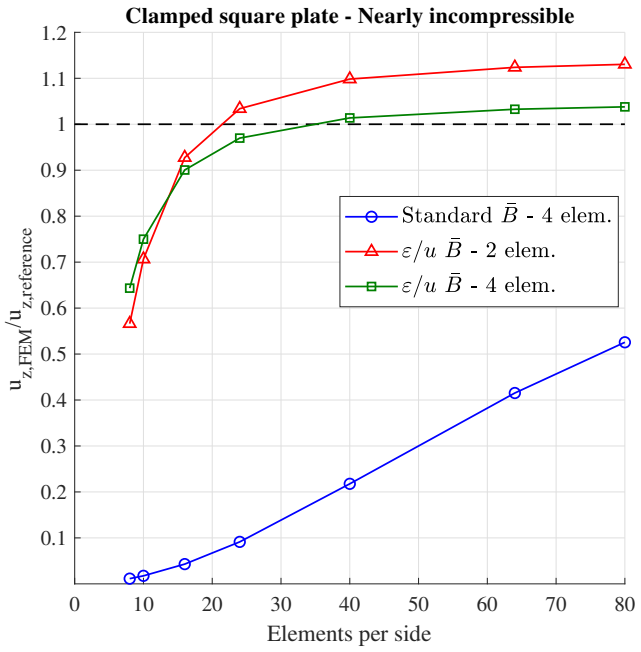

Fig. 46: Clamped square plate near incompressibility: Vertical displacement u_z at the center of the plate (Point A in Fig. 17) versus number of finite elements per side.

formulation in the incompressibility limit, guaranteeing converegence in displacements and stresses. The simulated cases studied here show that FEs with independent interpolations for displacements and strains are an effective alternative for simulating complex stress states in beam, shell and plate structures with enhanced accuracy.

Acknowledgements

The authors gratefully acknowledge the financial support from the Ministry of Science, Innovation and Universities (MCIU) via: the ADaMANT project (Computational Framework for Additive Manufacturing of Titanium Alloy, Proyectos de I+D -Excelencia-, ref. num. DPI2017-85998-P); the SEVERUS project (Multilevel evaluation of seismic vulnerability and risk mitigation of masonry buildings in resilient historical urban centres, ref. num. RTI2018-099589-B-I00); and the Severo Ochoa Programme for Centres of Excellence in R&D (CEX2018-000797-S).

Sungchul Kim gratefully acknowledges the support received from the Agència de Gestió d'Ajuts Universitaris i de Recerca (AGAUR) and the European Social Fund (ESF) through the predoctoral FI grants (ref. num. 2019FI_B00727).

A Vectors and Matrices

Displacements $\boldsymbol{u}$, strains $\boldsymbol{\varepsilon}$, stresses $\boldsymbol{\sigma}$ and forces $\boldsymbol{f}$ are represented following Voigt's notation as vectors

$$\boldsymbol{u} = (u_x, u_y, u_z)^T \tag{35}$$
$$\boldsymbol{\varepsilon} = (\varepsilon_x, \varepsilon_y, \varepsilon_z, \gamma_{xy}, \gamma_{yz}, \gamma_{xz})^T \tag{36}$$
$$\boldsymbol{\sigma} = (\sigma_x, \sigma_y, \sigma_z, \tau_{xy}, \tau_{yz}, \tau_{xz})^T \tag{37}$$
$$\boldsymbol{f} = (f_x, f_y, f_z)^T \tag{38}$$

The differential symmetric gradient operator relating the displacements with the strains has the following form

$$\boldsymbol{S}^T = \begin{bmatrix} \partial_x & 0 & 0 & \partial_y & 0 & \partial_z \\ 0 & \partial_y & 0 & \partial_x & \partial_z & 0 \\ 0 & 0 & \partial_z & 0 & \partial_y & \partial_x \end{bmatrix} \tag{39}$$

The projection matrix, introduced in Eq. (7), is

$$\bar{\boldsymbol{G}}^T = \begin{bmatrix} n_x & 0 & 0 & n_y & 0 & n_z \\ 0 & n_y & 0 & n_x & n_z & 0 \\ 0 & 0 & n_z & 0 & n_y & n_z \end{bmatrix} \tag{40}$$

where $\boldsymbol{n} = (n_x, n_y, n_z)^T$ is the outward normal vector at the boundary of the analysed domain Γ_t.

The discrete strain-displacement matrix (or discrete symmetric gradient operator) is expressed as

$$\boldsymbol{B}_u = [\boldsymbol{B}_{u_1}, \ldots, \boldsymbol{B}_{u_i}, \ldots, \boldsymbol{B}_{u_n}] \tag{41}$$

for $1 \leq i \leq n_n$, with n_n being the number of nodes in the element. The submatrix $\boldsymbol{B}_{u_i}$ and its volumetric part $\boldsymbol{B}_{u_i}^{vol}$ are expressed in Voigt's notation as

$$\boldsymbol{B}_{u_i} = \begin{bmatrix} \partial N_{i,1} & 0 & 0 \\ 0 & \partial N_{i,2} & 0 \\ 0 & 0 & \partial N_{i,3} \\ \partial N_{i,2} & \partial N_{i,1} & 0 \\ \partial N_{i,3} & 0 & \partial N_{i,1} \\ 0 & \partial N_{i,3} & \partial N_{i,2} \end{bmatrix} \tag{42}$$

$$\boldsymbol{B}_{u_i}^{vol} = \frac{1}{3} \begin{bmatrix} \partial N_{i,1} & \partial N_{i,2} & \partial N_{i,3} \\ \partial N_{i,1} & \partial N_{i,2} & \partial N_{i,3} \\ \partial N_{i,1} & \partial N_{i,2} & \partial N_{i,3} \\ 0 & 0 & 0 \\ 0 & 0 & 0 \\ 0 & 0 & 0 \end{bmatrix} \tag{43}$$

where N_i is the shape function of node i and $\partial N_{i,j}$ is its derivative with respect to the jth Cartesian coordinate ($j = [1:3]$). The deviatoric part is obtained by

$$\boldsymbol{B}_{u_i}^{dev} = \boldsymbol{B}_{u_i} - \boldsymbol{B}_{u_i}^{vol}. \tag{44}$$

B Principle of Virtual Work

This Appendix presents the derivation of equation (7) from equation (5) in two steps. First, equation (5) is premultiplied by an arbitrary virtual displacement $\delta\boldsymbol{u}$ and integrated over the spatial domain Ω

$$\int_\Omega \delta\boldsymbol{u}^T \left[\boldsymbol{S}^T (\boldsymbol{D}_{\boldsymbol{s}}\boldsymbol{\varepsilon})\right] d\Omega + \int_\Omega \delta\boldsymbol{u}^T \boldsymbol{f}\, d\Omega = 0 \quad \forall \delta\boldsymbol{u} \tag{45}$$

Then, the Divergence Theorem is applied on the first term of the above equation yielding

$$\begin{aligned}\int_\Omega \delta\boldsymbol{u}^T \left[\boldsymbol{\mathcal{S}}^T (\boldsymbol{D_s}\boldsymbol{\varepsilon})\right] d\Omega = \\ -\int_\Omega (\boldsymbol{\mathcal{S}}\delta\boldsymbol{u})^T (\boldsymbol{D_s}\boldsymbol{\varepsilon})\, d\Omega + \int_\Gamma \delta\boldsymbol{u}^T \left(\bar{\boldsymbol{G}}^T \boldsymbol{D_s}\boldsymbol{\varepsilon}\right) d\Gamma \\ = -\int_\Omega (\boldsymbol{\mathcal{S}}\delta\boldsymbol{u})^T (\boldsymbol{D_s}\boldsymbol{\varepsilon})\, d\Omega + \underbrace{\int_{\Gamma_u} \delta\boldsymbol{u}^T \left(\bar{\boldsymbol{G}}^T \boldsymbol{D_s}\boldsymbol{\varepsilon}\right) d\Gamma}_{=0} \\ + \int_{\Gamma_t} \delta\boldsymbol{u}^T \left(\bar{\boldsymbol{G}}^T \boldsymbol{D_s}\boldsymbol{\varepsilon}\right) d\Gamma \\ = -\int_\Omega (\boldsymbol{\mathcal{S}}\delta\boldsymbol{u})^T (\boldsymbol{D_s}\boldsymbol{\varepsilon})\, d\Omega + \int_{\Gamma_t} \delta\boldsymbol{u}^T \left(\bar{\boldsymbol{G}}^T \boldsymbol{D_s}\boldsymbol{\varepsilon}\right) d\Gamma \quad (46)\end{aligned}$$

In the previous derivation, equation (3) is used on the integral over Γ and adopted the assumption that the prescribed displacements vanish on the boundary Γ_u. Finally, substituting equation (46) into equation (45) the final version of the Principle of Virtual Work for the mixed ε/u formulation is obtained

$$\begin{aligned}\int_\Omega (\boldsymbol{\mathcal{S}}\delta\boldsymbol{u})^T (\boldsymbol{D_s}\boldsymbol{\varepsilon})\, d\Omega \\ = \int_\Omega \delta\boldsymbol{u}^T \boldsymbol{f}\, d\Omega + \int_{\Gamma_t} \delta\boldsymbol{u}^T \left(\bar{\boldsymbol{G}}^T \boldsymbol{D_s}\boldsymbol{\varepsilon}\right) d\Gamma \quad (47)\end{aligned}$$

presented in equation (7).

C Variational Multiscale Stabilization method

This section presents the stabilization procedure leading to the final system of equations (24) of the ε/u indepedent interpolation formulation. The stabilisation procedure adopted herein consists in the modification of the discrete variational form using the Orthogonal Subscales Method, introduced in [61] within the framework of the Variational Multiscale Stabilization methods [62, 63].

The stabilization of the problem is achieved by substituting the approximated strains in equation (9) with the following form

$$\begin{aligned}\boldsymbol{\varepsilon} \cong \hat{\boldsymbol{\varepsilon}} + \tau_\varepsilon (\tilde{\varepsilon} - \hat{\varepsilon}) \\ = \boldsymbol{N}_\varepsilon \boldsymbol{E} + \tau_\varepsilon (\boldsymbol{B}_u \boldsymbol{U} - \boldsymbol{N}_\varepsilon \boldsymbol{E}) \\ = (1-\tau_\varepsilon)\boldsymbol{N}_\varepsilon \boldsymbol{E} + \tau_\varepsilon \boldsymbol{B}_u \boldsymbol{U} \quad (48)\end{aligned}$$

where $\tau_\varepsilon = [0,1]$ is a stabilization parameter. Observe that for $\tau_\varepsilon = 0$ the stabilization effect is lost, while for $\tau_\varepsilon = 1$ the strain interpolation of the standard irreducible formulation is recovered

$$\boldsymbol{\varepsilon} \cong \tilde{\varepsilon} = \boldsymbol{B}_u \boldsymbol{U} \quad (49)$$

The use of equation (48) in equations (6)-(7) gives the final stabilized set of equations for the mixed ε/u FE formulation

$$\begin{aligned}-(1-\tau_\varepsilon)\int_\Omega \delta\boldsymbol{E}^T \boldsymbol{N}_\varepsilon^T \boldsymbol{D_s} \boldsymbol{N}_\varepsilon \boldsymbol{E}\, d\Omega \\ + (1-\tau_\varepsilon)\int_\Omega \delta\boldsymbol{E}^T \boldsymbol{N}_\varepsilon^T \boldsymbol{D_s} \boldsymbol{B}_u \boldsymbol{U}\, d\Omega = 0 \quad \forall \delta\boldsymbol{E} \quad (50)\end{aligned}$$

$$\begin{aligned}(1-\tau_\varepsilon)\int_\Omega \delta\boldsymbol{U}^T \boldsymbol{B}_u^T (\boldsymbol{D_s} \boldsymbol{N}_\varepsilon \boldsymbol{E})\, d\Omega \\ + \tau_\varepsilon \int_\Omega \delta\boldsymbol{U}^T \boldsymbol{B}_u^T \boldsymbol{D_s} \boldsymbol{B}_u \boldsymbol{U} d\Omega = \int_\Omega \delta\boldsymbol{U}^T \boldsymbol{N}_u^T \boldsymbol{f}\, d\Omega \\ + \int_{\Gamma_t} \delta\boldsymbol{U}^T \boldsymbol{N}_u^T \bar{\boldsymbol{t}}\, d\Gamma \quad \forall \delta\boldsymbol{U} \quad (51)\end{aligned}$$

Residual-based stabilisation procedures, like the one in (48) used herein, do not introduce any additional approximation nor any consistency error. For this, the stabilisation technique is variationally consistent, meaning that converging values of the unknowns $\boldsymbol{\varepsilon}$ ad $\boldsymbol{u}$ satisfying the Galerkin system (16)-(17) also satisfy the stabilized form (50)-(51). In particular, considering a converged solution, when the size of the element h tends to zero, $h \to 0$, $\boldsymbol{\varepsilon} \to \boldsymbol{N}_\varepsilon \boldsymbol{E} = \boldsymbol{B}_u \boldsymbol{U}$ and the stabilization term vanishes. Considering a non-converged situation, the added terms $\tau_\varepsilon(\boldsymbol{B}_u \boldsymbol{U} - \boldsymbol{N}_\varepsilon \boldsymbol{E})$ are small, as they depend on the difference between two approximations of different order to the same quantity. This means that for a given FE mesh, using different values of the stabilization procedure yields slightly different results (see Appendix D). Nevertheless, the consistency of the residual-based stabilization guarantees that the discrete problem converges to the unique solution. The use of different stabilization parameters on the same mesh is analogous to the use of different FE interpolations of the same order of convergence with the same nodal arrangement.

As shown in [64, 65], the optimal convergence rate in linear problems is obtained reducing the stabilization on mesh refinement, such that

$$\tau_\varepsilon = c_\varepsilon \frac{h}{L_0} \quad (52)$$

where c_ε stands for a positive number of the order $c_\varepsilon = O(1)$, h for the finite element size and L_0 is the characteristic size of the problem.

Following the above, the stabilized system of equations becomes

$$\begin{bmatrix} -\boldsymbol{M}_\tau & \boldsymbol{G}_\tau \\ \boldsymbol{G}_\tau^T & \boldsymbol{K}_\tau \end{bmatrix} \begin{bmatrix} \boldsymbol{E} \\ \boldsymbol{U} \end{bmatrix} = \begin{bmatrix} 0 \\ \boldsymbol{F} \end{bmatrix} \quad (53)$$

with

$$\boldsymbol{M}_\tau = (1-\tau_\varepsilon)\boldsymbol{M} \quad (54)$$

$$\boldsymbol{G}_\tau^T = (1-\tau_\varepsilon)\boldsymbol{G} \quad (55)$$

$$\boldsymbol{K}_\tau = \tau_\varepsilon \underbrace{\int_\Omega \boldsymbol{B}_u^T \boldsymbol{D_s} \boldsymbol{B}_u d\Omega}_{\boldsymbol{K}} = \tau_\varepsilon \boldsymbol{K} \quad (56)$$

D Influence of parameter τ_ε

This Appendix investigates the influence of the stabilization parameter τ_ε in the numerical results obtained with the ε/u FE formulation. The parameter τ_ε is defined in all the studied cases through the equation (52), in which intervenes the parameter c aside with the parameters h and L_0, associated with the finite element size and the characteristic size of the problem, respectively. Here, we investigate the influence of parameter c, with regard to the case of the clamped square plate.

Figure 47 presents the results obtained using three different values of $c = 5; 1; 1/5$ in equation (52). A value of $c = 1$ corresponds to the reference value used for this case $\tau_{\varepsilon,ref} = h/L_0$. The results show that the convergence rate is very similar for all the selected values of τ_ε, as analytically predicted [64, 65]. The fact that using different values for c (i.e. different τ_ε) produces different approximate solutions can be seen as similar to getting different approximate solutions by using meshes with different layouts, as already mentioned in Appendix C. Nevertheless, convergence to the

solution, and optimal rate of convergence, are independent from the choice of parameter c.

As can be observed, for the same mesh, the use of a higher value of τ_ε results in an increase of the estimated error. This is to be expected, as for the limit value of $\tau_\varepsilon = 1$ the standard irreducible formulation is recovered. On the other end, very small values of τ_ε fail to effectively stabilize the ε/u formulation.

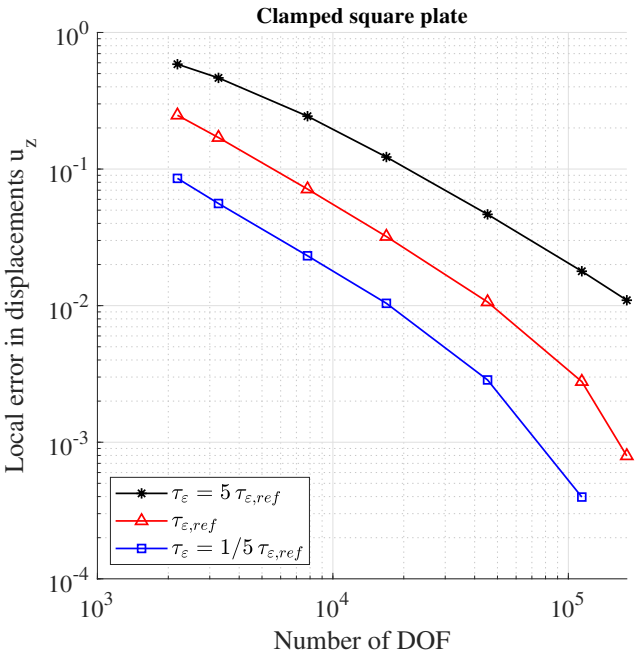

Fig. 47: Clamped square plate: Local error in displacement u_z at the center of the square plate versus the Number of Degrees of Freedom (DOF) for different values of τ_ε.

E Comparison with solid-shell and EAS FEs

This Appendix presents a comparison between the numerical results of the standard displacement based linear hexahedron (referred in the tables as Q1), the proposed ε/u FEs (referred in the tables as Q1Q1) and the reported results of several successful solid-shell and EAS elements for three benchmark shell problems: the Scordelis-Lo roof (Table 5), the hemispherical shell (Table 6) and the pinched cylinder (Table 7).

The following solid-shell and EAS elements are considered:

- Wriggers and Koralc QS/E9 [13]: 3D solid-shell enhanced strain element with 9 enhanced modes based on Taylor expansion with exact symbolic integration.
- Wriggers and Koralc QS/E12 [13]: 3D solid-shell enhanced strain element with 12 enhanced modes based on Taylor expansion with exact symbolic integration.
- Reese [51]: EAS solid-shell based on reduced integration with hourglass stabilization (QISPs).
- Kim et al. [21]: ANS solid-shell with plane stress assumption (XSolid85).
- Alves de Sousa et al. [66] : EAS solid-shell with reduced (in-plane) integration (RESS).
- Areias et al. [25]: EAS solid element with penalty stabilization.
- Kasper and Taylor [20]: Mixed-enhanced strain element with nine enhanced modes (H1/ME9).
- Schwarze and Reese [22]: Reduced integration solid-shell based on the EAS and the ANS concepts.
- Huang et al. [23]: unsymmetric 8-node hexahedral solid-shell (US-ATFHS8).
- Sze et al. [16]: hybrid stress ANS solid-shell.

It is observed that:

1 The standard general purpose FEs lock in the tested curved thick shell situations, while the proposed ε/u FEs and the solid-shell elements do not.
2 The special purpose solid-shell elements, enhanced with higher order bending modes, are more accurate than the general purpose ε/u finite elements. However, their corresponding displacement convergence rate is the same.
3 Even if the stable solid-shell elements are notoriously more accurate than the corresponding underlying linear element, the asymptotic rate of convergence of displacements is the same as they do not interpolate with the full second order polynomial needed to achieve higher order convergence.
4 Only displacement results are reported in the literature for the solid-shell elements. The mixed ε/u FEs are devised to yield enhanced strain and stress order of convergence.
5 All the reported tests are performed on hexahedral elements, as this is the shape of the solid-shell elements. Mixed ε/u FEs can be equally shaped as prisms or tetras, without loss of convergence rate.
6 All the reported tests are performed in regular meshes. EAS elements often underperform in distored meshes. Huang et al. [23] solve this quaint at the expense of using an unsymmetrical element.

Table 5: Scordelis Lo-Roof: Vertical displacement at the midpoint of the free edge normalized with the reference solution 0.3086 given in [47].

Elem. per side	u Q1	ε/u Q1Q1	Solid-shell: Schwarze and Reese [22]	Solid-shell: Areias et al. [25]	Solid-Shell: Kim et al. [21]	Solid-Shell: Alves de Sousa et al. [66]
8	0.112	0.859	0.994	1.001	0.984	0.986
16	0.261	0.965	1.000	0.992	0.999	0.993
32	0.542	0.995	1.003	0.991	-	0.996

Table 6: Hemispherical shell: Radial displacement at the load points normalized with the reference solution of 0.0940 given in [41].

Elem. per side	u Q1	ε/u Q1Q1	Solid-shell: Schwarze and Reese [22]	Solid-shell: Reese [51]	Solid-EAS: Areias et al. [25]	Solid-Mixed-EAS: Kasper and Taylor [20]	Solid-shell: Huang et al. [23]	Solid-shell: Sze et al. [16]
8	0.003	0.263	1.002	-	0.756	0.732	1.0106	1.0051
16	0.011	0.657	0.993	0.723	0.991	0.989	1.0038	0.9983
32	0.039	0.898	0.994	0.919	0.999	0.998	-	-
64	0.136	0.979	-	-	-	-	-	-

Table 7: Pinched cylinder: Vertical displacement at the midpoint normalized with the reference solution of $0.18248 \cdot 10^{-4}$ given in [53].

Elem. per side	u Q1	ε/u Q1Q1	Solid-shell QS/E9: Wriggers and Koralc [13]	Solid-shell QS/E12: Wriggers and Koralc [13]
8/9[1]	0.086	0.394	0.506	0.572
16/17[2]	0.178	0.737	0.864	0.922
30/32[3]	0.361	0.917	0.971	0.986
64	0.621	0.971	-	-

[1] 8 elements for standard and ε/u FEs and 9 elements for solid shell FEs.

[2] 16 elements for standard and ε/u FEs and 17 elements for solid shell FEs.

[3] 32 elements for standard and ε/u FEs and 30 elements for solid shell FEs.

References

1. G. Prathap, The poor bending response of the four-node plane stress quadrilateral, International Journal for Numerical Methods in Engineering 21 (5) (1985) 825–835. doi:10.1002/nme.1620210505.
2. Bathe K J., Finite Element Procedures, Englewood Cliffs New Jersey.
3. M. A. Crisfield, J. L. Tassoulas, Non-Linear Finite Element Analysis of Solids and Structures, Volume 1, Journal of Engineering Mechanics 119 (7) (1993) 1504–1505. doi:10.1061/(asce)0733-9399(1993)119:7(1504).
4. J. Heyman, The stone skeleton, International Journal of Solids and Structures 2 (2) (1966) 249–279. doi:10.1016/0020-7683(66)90018-7.
URL https://www.sciencedirect.com/science/article/abs/pii/0020768366900187{#}!

5. A. Tralli, C. Alessandri, G. Milani, Computational Methods for Masonry Vaults : A Review of Recent Results (2014) 272–286.
6. A. Feizolahbeigi, P. B. Lourenço, M. Golabchi, J. Ortega, M. Rezazadeh, Discussion of the role of geometry, proportion and construction techniques in the seismic behavior of 16th to 18th century bulbous discontinuous double shell domes in central Iran, Journal of Building Engineering 33 (2021) 101575. doi:10.1016/j.jobe.2020.101575. URL https://doi.org/10.1016/j.jobe.2020.101575
7. O. C. Zienkiewicz, R. L. Taylor, J. M. Too, Reduced integration technique in general analysis of plates and shells, International Journal for Numerical Methods in Engineering 3 (1971) 275–290. doi:10.1002/nme.1620030211.
8. H. Stolarski, T. Belytschko, Shear and membrane locking in curved C0 elements, Computer Methods in Applied Mechanics and Engineering 41 (3) (1983) 279–296. doi:10.1016/0045-7825(83)90010-5.
9. T. Belytschko, H. Stolarski, W. K. Liu, N. Carpenter, J. S. Ong, Stress projection for membrane and shear locking in shell finite elements, Computer Methods in Applied Mechanics and Engineering 51 (1-3) (1985) 221–258. doi:10.1016/0045-7825(85)90035-0.
10. J. Pitkäranta, The problem of membrane locking in finite element analysis of cylindrical shells, Numerische Mathematik 61 (1) (1992) 523–542. doi:10.1007/BF01385524.
11. P. Wriggers, R. Eberlein, S. Reese, A comparison of three-dimensional continuum and shell elements for finite plasticity, International Journal of Solids and Structures 33 (1996) 3309–3326. doi:10.1016/0020-7683(95)00262-6.
12. J. Korelc, P. Wriggers, An efficient 3D enhanced strain element with Taylor expansion of the shape functions, Computational Mechanics 19 (2) (1996) 30–40. doi:10.1007/bf02757781.
13. P. Wriggers, J. Korelc, On enhanced strain methods for small and finite deformations of solids, Computational Mechanics 18 (6) (1996) 413–428. doi:10.1007/BF00350250.
14. R. Hauptmann, K. Schweizerhof, A systematic development of 'solid-shell' element formulations for linear and non-linear analyses employing only displacement degrees of freedom, International Journal for Numerical Methods in Engineering 42 (1) (1998) 49–69. doi:10.1002/(SICI)1097-0207(19980515)42:1<49::AID-NME349>3.0.CO;2-2.
15. R. Hauptmann, S. Doll, M. Harnau, K. Schweizerhof, 'Solid-shell' elements with linear and quadratic shape functions at large deformations with nearly incompressible materials, Computers and Structures 79 (18) (2001) 1671–1685. doi:10.1016/S0045-7949(01)00103-1.
16. K. Y. Sze, L. Q. Yao, S. Yi, A hybrid stress ANS solid-shell element and its generalization for smart structure modelling. Part II - Smart structure modelling, International Journal for Numerical Methods in Engineering 48 (4) (2000) 565–582. doi:10.1002/(SICI)1097-0207(20000610)48:4<565::AID-NME890>3.0.CO;2-U.
17. J. C. Simo, M. S. Rifai, A class of mixed assumed strain methods and the method of incompatible modes, International Journal for Numerical Methods in Engineering 29 (8) (1990) 1595–1638. doi:10.1002/nme.1620290802. URL http://doi.wiley.com/10.1002/nme.1620290802
18. J. C. Simo, F. Armero, Geometrically non-linear enhanced strain mixed methods and the method of incompatible modes, International Journal for Numerical Methods in Engineering 33 (7) (1992) 1413–1449. doi:10.1002/nme.1620330705. URL http://doi.wiley.com/10.1002/nme.1620330705
19. J. C. Simo, F. Armero, R. L. Taylor, Improved versions of assumed enhanced strain tri-linear elements for 3D finite deformation problems, Computer Methods in Applied Mechanics and Engineering 110 (3-4) (1993) 359–386. doi:10.1016/0045-7825(93)90215-J.
20. E. P. Kasper, R. L. Taylor, Mixed-enhanced strain method. Part I: Geometrically linear problems, Computers and Structures 75 (3) (2000) 237–250. doi:10.1016/S0045-7949(99)00134-0.
21. K. D. Kim, G. Z. Liu, S. C. Han, A resultant 8-node solid-shell element for geometrically nonlinear analysis, Computational Mechanics 35 (5) (2005) 315–331. doi:10.1007/s00466-004-0606-9.
22. M. Schwarze, Reese, A reduced integration solid-shell finite element based on the EAS and the ANS concept-Geometrically linear problems, International Journal of Numerical Methods in Engineering 80 (2009) 1322–1355. doi:10.1002/nme.
23. J. Huang, S. Cen, Z. Li, C. F. Li, An unsymmetric 8-node hexahedral solid-shell element with high distortion tolerance: Linear formulations, International Journal for Numerical Methods in Engineering 116 (12-13) (2018) 759–783. doi:10.1002/nme.5945.
24. S. Reese, P. Wriggers, B. D. Reddy, A new locking-free brick element technique for large deformation problems in elasticity, Computers and Structures 75 (3) (2000) 291–304. doi:10.1016/S0045-7949(99)00137-6.
25. P. M. Areias, J. M. de Sé, C. A. António, Analysis of 3D problems using a new enhanced strain hexahedral element, International Journal for Numerical Methods in Engineering 58 (11) (2003) 1637–1682. doi:10.1002/nme.835.
26. P. Wriggers, R. Eberlein, S. Reese, Continuum and Shell Elements for Finite Plasticity 33 (20) (1996) 3309–3326. doi:10.1016/0020-7683(95)00262-6.
27. G. Vlachakis, M. Cervera, G. B. Barbat, S. Saloustros, Out-of-plane seismic response and failure mechanism of masonry structures using finite elements with enhanced strain accuracy, Engineering Failure Analysis 97 (2019) 534–555. doi:10.1016/J.ENGFAILANAL.2019.01.017. URL https://www.sciencedirect.com/science/article/abs/pii/S1350630718310306?via{%}3Dihub
28. D. S. Malkus, T. J. Hughes, Mixed finite element methods - Reduced and selective integration techniques: A unification of concepts, Computer Methods in Applied Mechanics and Engineering 15 (1) (1978) 63–81. doi:10.1016/0045-7825(78)90005-1.
29. I. Babuška, J. M. Melenk, The partition of unity method, International Journal for Numerical Methods in Engineering 40 (4) (1997) 727–758. doi:10.1002/(SICI)1097-0207(19970228)40:4<727::AID-NME86>3.0.CO;2-N.
30. D. Boffi, F. Brezzi, M. Fortin, Mixed Finite Element Methods and Applications, 2013. doi:10.1007/978-3-642-36519-5.
31. N. M. Lafontaine, R. Rossi, M. Cervera, M. Chiumenti, Explicit mixed strain-displacement finite element for dynamic geometrically non-linear solid mechanics, Computational Mechanics 55 (3) (2015) 543–559. doi:10.1007/s00466-015-1121-x.
32. J. C. Nagtegaal, D. M. Parks, J. R. Rice, On numerically accurate finite element solutions in the fully plastic range, Computer Methods in Applied Mechanics and Engineering 4 (2) (1974) 153–177. doi:10.1016/0045-7825(74)

90032-2.
33. S. W. Sloan, M. F. Randolph, Numerical prediction of collapse loads using finite element methods, International Journal for Numerical and Analytical Methods in Geomechanics 6 (1) (1982) 47–76. doi:10.1002/nag.1610060105.
34. T. J. Hughes, Generalization of selective integration procedures to anisotropic and nonlinear media, International Journal for Numerical Methods in Engineering 15 (9) (1980) 1413–1418. doi:10.1002/nme.1620150914.
35. F. Brezzi, on the Existence, Uniqueness and Approximation of Saddle-Point Problems Arising From Lagrangian Multipliers., Rev Fr Autom Inf Rech Oper 8 (1974) 129–151. doi:10.1051/m2an/197408R201291.
36. D. N. Arnold, R. Winther, Mixed finite elements for elasticity, Numerische Mathematik 92 (3) (2002) 401–419. doi:10.1007/s002110100348.
37. D. Mijuca, On hexahedral finite element HC8/27 in elasticity, Computational Mechanics 33 (6) (2004) 466–480. doi:10.1007/s00466-003-0546-9.
38. D. N. Arnold, G. Awanou, R. Winther, Finite elements for symmetric tensors in three dimensions, Mathematics of Computationdoi:10.1090/s0025-5718-08-02071-1.
39. M. Cervera, N. Lafontaine, R. Rossi, M. Chiumenti, Explicit mixed strainâĂŞdisplacement finite elements for compressible and quasi-incompressible elasticity and plasticity, Computational Mechanics 58 (3) (2016) 511–532. doi:10.1007/s00466-016-1305-z.
40. M. Cervera, G. B. Barbat, M. Chiumenti, Finite element modeling of quasi-brittle cracks in 2D and 3D with enhanced strain accuracy, Computational Mechanics 60 (5) (2017) 767–796. doi:10.1007/s00466-017-1438-8.
41. R. H. Macneal, R. L. Harder, A proposed standard set of problems to test finite element accuracy, Finite Elements in Analysis and Design 1 (1) (1985) 3–20. doi:10.1016/0168-874X(85)90003-4.
42. S. H. Lo, C. Ling, Improvement on the 10-node tetrahedral element for three-dimensional problems, Computer Methods in Applied Mechanics and Engineering 189 (3) (2000) 961–974. doi:10.1016/S0045-7825(99)00410-7.
43. D. W. White, J. F. Abel, Testing of shell finite element accuracy and robustness, Finite Elements in Analysis and Design 6 (2) (1989) 129–151. doi:10.1016/0168-874X(89)90040-1.
44. E. N. Dvorkin, K. J. Bathe, A continuum mechanics based four-node shell element for general nonlinear analysis, Engineering Computations 1 (1) (1984) 77–88. doi:10.1108/eb023562.
45. N. Büchter, E. Ramm, D. Roehl, Three-dimensional extension of non-linear shell formulation based on the enhanced assumed strain concept, International Journal for Numerical Methods in Engineering 37 (15) (1994) 2551–2568. doi:10.1002/nme.1620371504.
46. P. Nguyen, M. Doškár, A. Pakravan, P. Krysl, Modification of the quadratic 10-node tetrahedron for thin structures and stiff materials under large-strain hyperelastic deformation, International Journal for Numerical Methods in Engineering 114 (6) (2018) 619–636. doi:10.1002/nme.5757.
47. A. Scordelis, K. Lo, Computer Analysis of Cylindrical Shells, ACI Journal Proceedings 61 (5). doi:10.14359/7796.
48. J. Heyman, The stone skeleton, International Journal of solids and structures 2.
URL http://www.sciencedirect.com/science/article/pii/0020768366900187
49. B. A. Izzuddin, Y. Liang, A hierarchic optimisation approach towards locking-free shell finite elements, Computers and Structures 232 (2020) 105839. doi:10.1016/j.compstruc.2017.08.010.
URL https://doi.org/10.1016/j.compstruc.2017.08.010
50. S. Klinkel, F. Gruttmann, W. Wagner, A robust nonlinear solid shell element based on a mixed variational formulation, Computer Methods in Applied Mechanics and Engineering 195 (1-3) (2006) 179–201. doi:10.1016/j.cma.2005.01.013.
51. S. Reese, A large deformation solid-shell concept based on reduced integration with hourglass stabilization, International Journal for Numerical Methods in Engineering 69 (2007) 1671–1716. doi:10.1002/nme.1827.
52. G. Lindberg, M. Olson, G. Copwer, New Developments in the Finite Element Analysis of Shells, Quart. Bull. Div. Mech. Engrg. and the National Aeronautical Establishment 4, (1969) 1–38.
53. W. Flügge, Stresses in Shells., Springer, Berlin, 1973. doi:10.1007/978-3-662-01028-0.
54. S. Reese, A large deformation solid-shell concept based on reduced integration with hourglass stabilization, International Journal of nu 69 (2012) 1971–1716. doi:10.1002/nme.
URL http://onlinelibrary.wiley.com/doi/10.1002/nme.3279/full
55. T. J. Hughes, T. E. Tezduyar, Finite elements based upon mindlin plate theory with particular reference to the four-node bilinear isoparametric element, Journal of Applied Mechanics, Transactions ASME 48 (3) (1981) 587–596. doi:10.1115/1.3157679.
56. R. Piltner, D. S. Joseph, An accurate low order plate bending element with thickness change and enhanced strains, Computational Mechanics 27 (5) (2001) 353–359. doi:10.1007/s004660100247.
57. K. J. Bathe, A. Iosilevich, D. Chapelle, Inf-sup test for shell finite elements, Computers and Structures 75 (5) (2000) 439–456. doi:10.1016/S0045-7949(99)00213-8.
58. A. Chama, B. D. Reddy, New stable mixed finite element approximations for problems in linear elasticity, Computer Methods in Applied Mechanics and Engineering 256 (2013) 211–223. doi:10.1016/j.cma.2012.12.006.
59. J. C. Simo, J. Oliver, F. Armero, An analysis of strong discontinuities induced by strain-softening in rate-independent inelastic solids, Computational Mechanics 12 (5) (1993) 277–296. doi:10.1007/BF00372173.
60. S. P. Timoshenko, J. N. Goodier, H. N. Abramson, Theory of Elasticity (3rd ed.), Journal of Applied Mechanicsdoi:10.1115/1.3408648.
61. R. Codina, Stabilization of incompressibility and convection through orthogonal sub-scales in finite element methods, Computer Methods in Applied Mechanics and Engineering 190 (13-14) (2000) 1579–1599. doi:10.1016/S0045-7825(00)00254-1.
62. T. J. Hughes, L. P. Franca, M. Balestra, A new finite element formulation for computational fluid dynamics: V. Circumventing the babuška-brezzi condition: a stable Petrov-Galerkin formulation of the stokes problem accommodating equal-order interpolations, Computer Methods in Applied Mechanics and Engineering 59 (1) (1986) 85–99. doi:10.1016/0045-7825(86)90025-3.
63. T. J. Hughes, G. R. Feijóo, L. Mazzei, J. B. Quincy, The variational multiscale method - A paradigm for computational mechanics, Computer Methods in Applied Mechanics and Engineering 166 (1-2) (1998) 3–24. doi:

10.1016/S0045-7825(98)00079-6.
64. S. Badia, R. Codina, Unified Stabilized Finite Element Formulations for the Stokes and the Darcy Problems, SIAM Journal on Numerical Analysis 47 (3) (2009) 1971–2000. doi:10.1137/08072632x.
65. M. Cervera, M. Chiumenti, R. Codina, Mixed stabilized finite element methods in nonlinear solid mechanics. Part I: Formulation, Computer Methods in Applied Mechanics and Engineering 199 (37-40) (2010) 2559–2570. doi:10.1016/j.cma.2010.04.006.
URL http://dx.doi.org/10.1016/j.cma.2014.11.040http://linkinghub.elsevier.com/retrieve/pii/S0045782510001234http://dx.doi.org/10.1016/j.cma.2010.04.006
66. R. J. Alves de Sousa, R. P. Cardoso, R. A. Fontes Valente, J. W. Yoon, J. J. Grácio, R. M. Natal Jorge, A new one-point quadrature enhanced assumed strain (EAS) solid-shell element with multiple integration points along thickness: Part I - Geometrically linear applications, International Journal for Numerical Methods in Engineering 62 (7) (2005) 952–977. doi:10.1002/nme.1226.

Strain Localization of Orthotropic Elasto-Plastic Cohesive-Frictional Materials: Analytical Results and Numerical Verification

S. Kim, M. Cervera, J.Y. Wu and M. Chiumenti

Materials

Volume 14, Issue 8, pp. 2040 (2021)

Editor-in-Chief: Prof. Dr. Maryam Tabrizian

EISSN : 1996-1944

Journal Editors - MDPI

https://doi.org/10.3390/ma14082040

Strain Localization of Orthotropic Elasto-Plastic Cohesive-Frictional Materials: Analytical Results and Numerical Verification

Sungchul Kim [1], Miguel Cervera [2,*] Jian-Ying Wu [3] and Michele Chiumenti [2]

[1] Technical University of Catalonia, Edificio C1, Campus Norte, Jordi Girona 1-3, 08034 Barcelona, Spain; Sungchul.kim@upc.edu
[2] CIMNE, Technical University of Catalonia, Edificio C1, Campus Norte, Jordi Girona 1-3, 08034 Barcelona, Spain; Miguel.Cervera@upc.edu, Michele@cimne.upc.edu
[3] State Key Laboratory of Subtropical Building Science, South China University of Technology, Guangzhou 510641, China; Jywu@scut.edu.cn
* Correspondence: Miguel.cervera@upc.edu; Tel.: +34-93 401 64 92

Abstract: Strain localization analysis for orthotropic plasticity in cohesive-frictional materials is addressed in this work. Specifically, the localization condition is derived from Maxwell's kinematics, the plastic flow rule and the boundedness of stress rates. The analysis is applicable to strong and regularized discontinuity settings. Expanding on previous works, the quadratic orthotropic Hoffman and Tsai-Wu models are investigated and compared to pressure insensitive and sensitive models such as von Mises, Hill and Drucker-Prager. Analytical localization angles are obtained in uniaxial tension and compression under plane stress and plane strain conditions. These are only dependent on the plastic potential adopted; ensuing, a geometrical interpretation in the stress space is offered. The analytical results are then validated by independent numerical simulations. The B-bar finite element is used to deal with the limiting incompressibility in the purely isochoric plastic flow. For a strip under vertical stretching in plane stress and plane strain as well as Prandtl's problem of indentation by a flat rigid die in plane strain, numerical results are presented for both isotropic and orthotropic plasticity models with or without tilting angle between the material axes and the applied loading. The influence of frictional behavior is studied. In all the investigated cases, the numerical results provide compelling support to the analytical prognoses.

Keywords: localized failure; strain localization; orthotropic plasticity; cohesive-frictional materials; plasticity

1. Introduction

Orthotropic Materials such as wood and masonry have been traditionally used in construction and are very much used today. Other frequently used materials, such as rolled metals, are orthotropic because of their manufacturing process. This is also very much the case of metallic and polymeric materials and components produced layer-by-layer using modern additive manufacturing (AM) techniques, now increasingly used. In the field of geological engineering, the analysis of orthotropic materials is of interest in ground excavation, tunnel construction and landslides prevention.

Hill [1-3], a pioneer in the mathematical research of plasticity, proposed several constitutive orthotropic plasticity models for sheet metals and investigated strain localization and failure of orthotropic plastic materials. Based on Hill's works, many isotropic and orthotropic plastic criteria have been later proposed, such as the Drucker-Prager model [4-7], Hoffman model [8], Tsai-Wu model [9], and many more [10-12]. Purely cohesive models which are insensitive to pressure and yield an isochoric plastic flow, such as the von Mises and the Hill models, are appropriate for metallic materials. Instead, cohesive-frictional models such as the Drucker-Prager, Hoffman and

Tsai-Wu models are suitable for simulating geomaterials like soils, concrete and rocks, as these materials show distinct strengths under tensile and compressive loading.

In plastic materials subjected to increasing loading beyond yielding, plastic strains tend to concentrate in narrow zones called shear bands. This phenomenon, consisting of irreversible deformation concentrating in a definite thin zone, is known as strain localization [13]. Strain localization results in strain (weak) discontinuities across the surfaces limiting the shear band. If the size of the band is very small compared to the dimensions of the plastic medium, the band appears as (strong) discontinuity surface across which the displacement field is discontinuous.

Structural assessment requires the accurate prediction of failure mechanisms and peak carrying loads. Thus, Failure Mechanics has evolved in the last decades as a very active field and much analytical, experimental and computational research effort has been invested in plasticity, damage, and fracture mechanics. Lately, Computational Failure Mechanics have often addressed the problem of the phenomenon of plastic strain localization and the analytical and numerical challenges associated to it.

Early works of Prandtl [14], Hencky [15-26], and Mandel [17] determined the directions of the slip lines, and the associated failure mechanisms and loads. Hill revisited and interpreted the slip lines as the characteristic lines of the hyperbolic plastic governing equations assuming rigid-plastic and incompressible behavior preceding shear-driven plastic yielding.

Hill [18-19], Thomas [20] and Rice [21] investigated strain localization as a bifurcation problem and extended the scope from rigid-plastic to elasto-plastic solids. Rice [22] extended the plane strain slip line theory to anisotropic rigid-plastic material. Strain localization in frictional solids was researched by Leroy and Ortiz [23]. Forest [24] used continuum models for strain localization in metallic foams. Borja [25-26] extended the modeling in elasto-plastic models and soft rocks. Willam and coworkers [27-28] studied the localization properties of standard and generalized Drucker-Prager models. Vrech [29] addressed localization analysis of gradient-dependent parabolic Drucker–Prager models. Zhang [30] studied damage and strain localization in geomaterials and Tasan [31] studied strain localization and damage in dual phase steels.

The classical bifurcation analysis has been applied both to weak and strong discontinuities. Simo [32] and Oliver [33-34] studied the orientation of strong discontinuities in inelastic solids and Oliver [35-36] suggested continuum plasticity models for the modelling of such strong discontinuities. They soon found that conditions for discontinuous bifurcation do not necessarily guarantee the occurrence of strong discontinuities, unless the strong discontinuity is properly regularized and stress boundedness is invoked [33-36].

The authors [37-38] have used Maxwell's compatibility condition and stress boundedness to predict analytically the orientation of shear discontinuities for isotropic von Mises and orthotropic Hill elasto-plastic models. The analytical results have been verified numerically. This strain localization analysis has been successfully applied to other and elastic-damage models [39-41].

It turns out that the stress boundedness condition is a more constrictive necessary condition than the classical discontinuous bifurcation condition, as strain localization generally occurs after strain bifurcation has occurred. Contrarily to the strain bifurcation conditions, this strain localization condition depends entirely on the inelastic flow; remarkably, it does not depend on the elastic properties or in the yield surface. The localization angles can be analytically predicted from the inelastic flow tensor alone.

This paper addresses the analytical determination of the orientation of slip lines in orthotropic elasto-plastic cohesive-frictional materials by extending the strain localization analysis developed in previous works. The objectives are four-fold: (i) to extend the strain localization analysis to orthotropic elasto-plastic cohesive-frictional materials; (ii) to derive analytically localization angles in plane stress and plane strain conditions for these models; (iii) to verify these analytical results via independent numerical simulations; and (iv) to investigate the influence of plastic material properties on strain localization in orthotropic cohesive-frictional materials.

The paper is structured as follows. Section 2 briefly presents the analytical framework: constitutive relations, kinematics for strong and weak discontinuities, and strain localization

conditions. Section 3 introduces orthotropic plasticity and develops the analytical results for the localization angles in plane stress and plane strain conditions with some examples. In Section 4, numerical verification of the analytical results using B-bar finite elements is offered. Section 5 closes the paper with some conclusions.

2. Strain Localization in Elasto-Plastic solids

In this section, the mechanics of strain localization in elasto-plastic media is addressed. Using Maxwell's kinematics and assuming boundedness of the stresses rates, the necessary condition for strain localization in elasto-plastic materials is obtained. The results hold both for strong (displacement) discontinuities and for regularized strain localization bands limited by weak (strain) discontinuities.

Let $\boldsymbol{\Omega} \subset \mathrm{R}^{\boldsymbol{n_{dim}}}$ $(n_{\mathrm{dim}} = 1, 2, 3)$ be an elasto-plastic solid domain, with the reference position vector $\boldsymbol{x} \subset \mathrm{R}^{\boldsymbol{n_{dim}}}$. The outer boundary is denoted by $\Gamma \subset \mathrm{R}^{\boldsymbol{n_{dim}}-1}$, with the outward unit normal vector $\boldsymbol{n}^*$. Deformations of the solid are characterized by the displacement field $\boldsymbol{u}(\boldsymbol{x})$ and the infinitesimal strain field $\boldsymbol{\epsilon}(\boldsymbol{x}) = \nabla^{\mathrm{sym}}\boldsymbol{u}(\boldsymbol{x})$, where $\nabla^{\mathrm{sym}}(\cdot)$ is the symmetric gradient operator.

2.1. Elasto-Plasticity Model

For the elasto-plastic model, the constitutive equation is expressed in total form as

$$\boldsymbol{\epsilon} = \boldsymbol{\epsilon}^{\mathrm{e}} + \boldsymbol{\epsilon}^{\mathrm{p}}, \qquad \boldsymbol{\sigma} = \mathbf{E}^0 : \boldsymbol{\epsilon}^{\mathrm{e}} = \mathbf{E}^0 : (\boldsymbol{\epsilon} - \boldsymbol{\epsilon}^{\mathbf{p}}) \tag{1}$$

where the second-order strain tensor $\boldsymbol{\epsilon}$ is decomposed into its elastic and plastic parts, $\boldsymbol{\epsilon}^{\mathrm{e}}$ and $\boldsymbol{\epsilon}^{\mathrm{p}}$. The second-order stress tensor $\boldsymbol{\sigma}$ is proportional to the elastic strain tensor $\boldsymbol{\epsilon}^{\mathrm{e}}$, through the fourth-order elasticity tensor $\mathbf{E}^0$. All the tensors involved are symmetric. The elastic properties may be orthotropic.

The admissible stress domain is determined by the yield criterion $\Phi(\boldsymbol{\sigma}, \zeta) = \phi(\boldsymbol{\sigma}) - q(\zeta) \leq 0$, defined in terms of the equivalent stress $\phi(\boldsymbol{\sigma})$ and a stress-like internal variable $q(\zeta)$, which determine the shape and size of the domain, respectively. Yield criteria for orthotropic elasto-plasticity are discussed in Section 3.

The plastic strain is defined in rate form, its direction is derived from a plastic potential. In associated plasticity, the plastic potential is equal to the yield surface, so that

$$\dot{\epsilon}^{\mathrm{p}} = \dot{\lambda}\frac{\partial \phi}{\partial \boldsymbol{\sigma}} = \dot{\lambda}\,\boldsymbol{\Lambda} \tag{2}$$

where $\dot{\lambda} \geq 0$ denotes the plastic multiplier; $\dot{(\ )}$ is the time derivative and the plastic flow tensor $\boldsymbol{\Lambda} = \partial\phi \,/\, \partial\boldsymbol{\sigma}$ is normal to the yield surface $\Phi = 0$. Similarly, the evolution of the size of the yield surface is determined by

$$\dot{\zeta} = \dot{\lambda}\frac{\partial \phi}{\partial q} = -\dot{\lambda} \tag{3}$$

The constitutive equation in rate form follows from Eq. (1),

$$\dot{\boldsymbol{\sigma}} = \mathbf{E}^0 : \dot{\boldsymbol{\epsilon}}^{\mathrm{e}} = \mathrm{E}^0 : (\dot{\boldsymbol{\epsilon}} - \dot{\boldsymbol{\epsilon}}^{\mathrm{p}}) = \mathbf{E}^{\mathrm{ep}} : \dot{\epsilon} \tag{4}$$

where the fourth-order elasto-plasticity tangent tensor $\mathbf{E}^{\mathrm{ep}}$ is obtained from the Kuhn-Tucker and consistency conditions as

$$\mathbf{E}^{\mathrm{ep}} = \frac{d\boldsymbol{\sigma}}{d\boldsymbol{\epsilon}} = \mathbf{E}^0 - \frac{\mathbf{E}^0 : \boldsymbol{\Lambda} \otimes \mathbf{E}^0 : \boldsymbol{\Lambda}}{H + \boldsymbol{\Lambda} : \mathbf{E}^0 : \boldsymbol{\Lambda}} \tag{5}$$

where $H = \partial q \,/\, \partial\zeta$ is the hardening or softening modulus. For perfect plasticity, $q = q_0$, and $H = 0$. Note that in associative plasticity, the elasto-plastic tangent tensor is symmetric.

2.2. Kinematics of strong and regularized discontinuities

In the early stages of the loading and deformation process of an elasto-plastic solid, standard kinematics applies and both the displacement rate and strain rate fields are continuous. However, in

softening and associated perfect plasticity, and even in hardening non-associated plasticity, slip lines (in 2D) or slip surfaces (in 3D) may form. Across these, the deformation can grow unbounded, displacement and/or strain discontinuities may appear and Maxwell's compatibility condition needs to be considered.

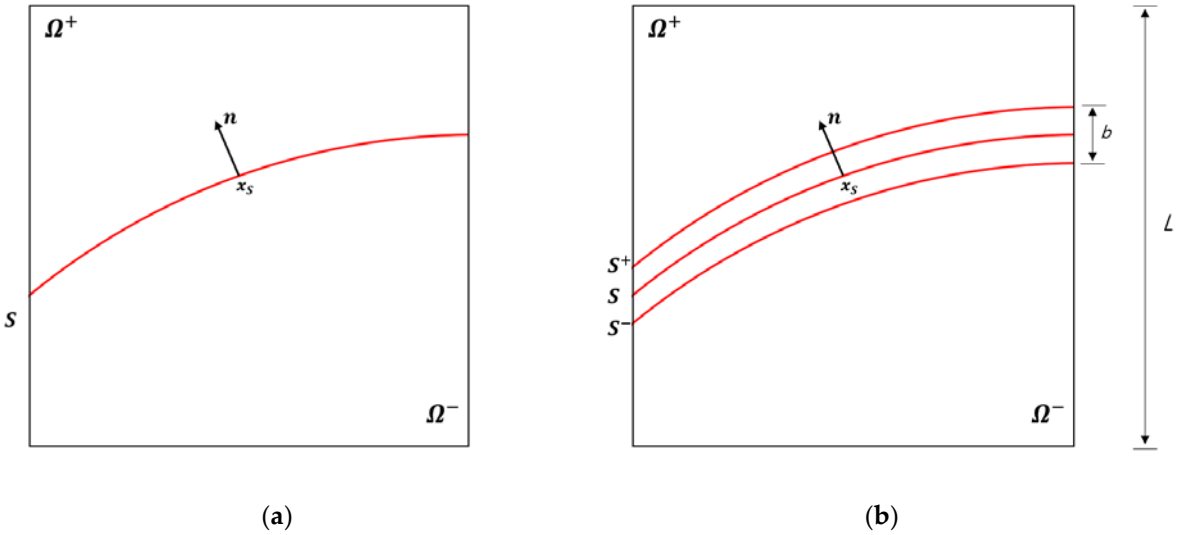

Figure 1. (**a**) Strong and (**b**) regularized discontinuities in an elasto-plastic solid.

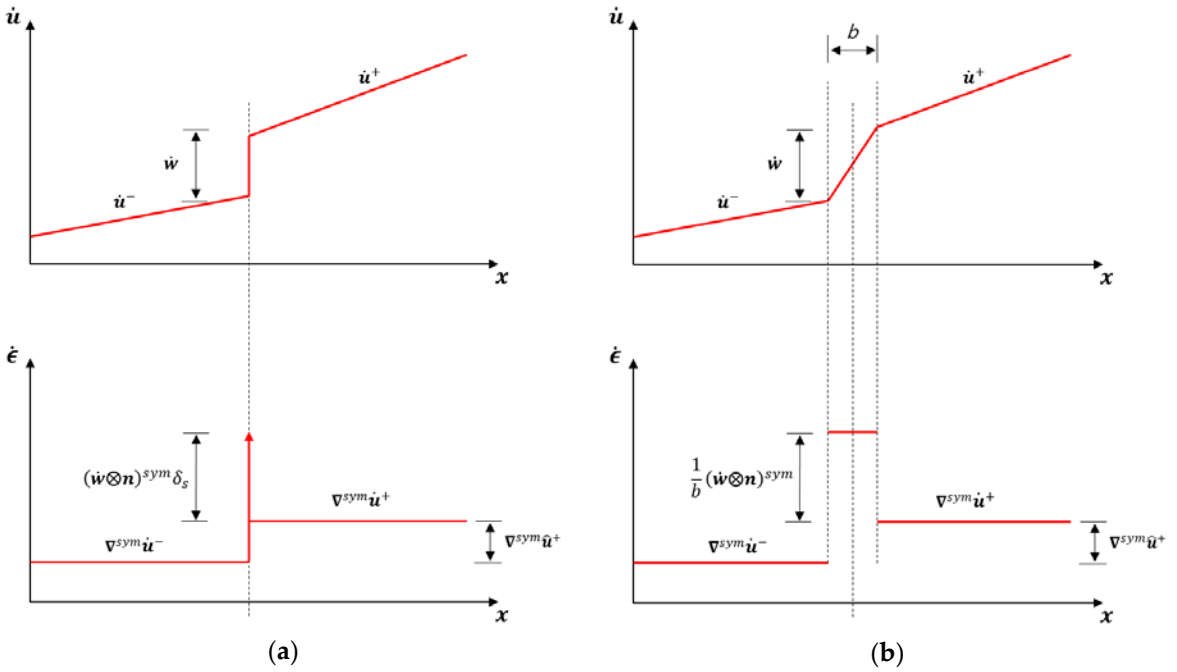

Figure 2. Kinematics of (a) strong and (b) regularized discontinuities.

Figure 1a shows the elasto-plastic solid domain $\boldsymbol{\Omega}$ split by a displacement discontinuity $\boldsymbol{S}$ (the slip line or slip surface) into two parts $\boldsymbol{\Omega}^+$ and $\boldsymbol{\Omega}^-$. The orientation of the discontinuity is denoted with the unit normal vector $\boldsymbol{n}$ with direction from $\boldsymbol{\Omega}^-$ to $\boldsymbol{\Omega}^+$. Let L be a characteristic size of the domain.

Figure 2a shows the corresponding kinematics: the velocity and strain rates fields are not regular. There is a discontinuity of the displacement rate at $\boldsymbol{S}$ of value $\dot{\boldsymbol{w}}$; correspondingly, the strain rate at $\boldsymbol{S}$ is:

$$\dot{\boldsymbol{\epsilon}}_S = (\dot{\boldsymbol{w}} \otimes \boldsymbol{n})^{\text{sym}} \delta_S \tag{6}$$

where δ_S denotes the Dirac delta function. Note that this strain rate is unbounded and has a very definite structure determined by the direction of the discontinuity surface, as it allows for unbounded strain rate components at $\boldsymbol{S}$ due to the discontinuity of the displacement in the normal direction $\boldsymbol{n}$, but not in those directions tangential to $\boldsymbol{S}$.

For the analysis of strain localization in the continuum setting and also for its numerical verification using FEM, it is convenient to consider a *regularized* discontinuity, as shown in Figure 1b. Here, subdomains $\boldsymbol{\Omega}^+$ and $\boldsymbol{\Omega}^-$ are separated by a regularized discontinuity band $\boldsymbol{B}$ of finite width b, as the distance between surfaces $\boldsymbol{S}^+$ and $\boldsymbol{S}^-$; these are weak (strain) discontinuities. The bandwidth b is small compared to the characteristic size of the domain L, so that $b/L << 1$.

Figure 2b shows the corresponding regularized kinematics. Note that the strain localizes in the regularized band $\boldsymbol{B}$**.** The deformation vector rate in the strain localization band $\dot{\boldsymbol{e}}$ is defined as the (apparent) jump of displacement rate $\dot{\boldsymbol{w}}$ across the regularized discontinuity band divided by the band width, $\dot{\boldsymbol{e}} = \dot{\boldsymbol{w}}/b$.

Let $\dot{u}$ be a characteristic displacement in domain and the jump $\dot{w}$ be of the same order. Deformations outside the localization band are or the order $\dot{\boldsymbol{e}}_{\text{ext}} = \frac{\dot{u}}{L}$, while inside the band they are of order $\dot{\boldsymbol{e}}_{\text{int}} = \dot{\boldsymbol{w}}/L$. As $b/L << 1$, $\dot{\boldsymbol{e}}_{\text{ext}}/\dot{\boldsymbol{e}}_{\text{int}} << 1$ even for a finite, small bandwidth.

Denoting by $\dot{\boldsymbol{\epsilon}}_{\text{ext}}$ and $\dot{\boldsymbol{\epsilon}}_{\text{int}}$ the strain rates inside and outside of the localization band, respectively, and being $[\![\dot{\boldsymbol{\epsilon}}]\!]$ the corresponding strain rate jump, Maxwell's compatibility condition [20] is now expressed as

$$[\![\dot{\boldsymbol{\epsilon}}]\!] = \dot{\boldsymbol{\epsilon}}_{\text{int}} - \dot{\boldsymbol{\epsilon}}_{\text{ext}} = (\dot{\boldsymbol{e}} \otimes \boldsymbol{n})^{\text{sym}} \tag{7}$$

Eq. (7) is the regularized counterpart of Eq. (6). Note that for the band width $b \to 0$, the strain rate in the regularized discontinuity band $\boldsymbol{B}$ tends to the strain rate in the strong discontinuity $\boldsymbol{S}$.

2.3. Strain localization and stress boundedness

From the constitutive relation of the elasto-plastic solids, the stress rates inside and outside of the localization band are given by

$$\dot{\boldsymbol{\sigma}}_{\text{int}} = \mathbf{E}^0 : \left(\underline{\dot{\boldsymbol{\epsilon}}_{\text{int}}} - \underline{\dot{\boldsymbol{\epsilon}}^{\text{p}}_{\text{int}}}\right), \qquad \dot{\boldsymbol{\sigma}}_{\text{ext}} = \mathbf{E}^0 : \left(\dot{\boldsymbol{\epsilon}}_{\text{ext}} - \dot{\boldsymbol{\epsilon}}^{\text{p}}_{\text{ext}}\right) \tag{8}$$

Note that plastic behavior is considered inside and outside the localization band. The jump of stress rate $[\![\dot{\boldsymbol{\sigma}}]\!]$ is expressed as

$$[\![\dot{\boldsymbol{\sigma}}]\!] = \dot{\boldsymbol{\sigma}}_{\text{int}} - \dot{\boldsymbol{\sigma}}_{\text{ext}} = \mathbf{E}^0 : \left(\underline{[\![\dot{\boldsymbol{\epsilon}}]\!]} - \underline{[\![\dot{\boldsymbol{\epsilon}}^{\text{p}}]\!]}\right) = \mathbf{E}^0 : \left[\underline{(\dot{\boldsymbol{e}} \otimes \boldsymbol{n})^{\text{sym}}} - \underline{[\![\dot{\boldsymbol{\epsilon}}^{\text{p}}]\!]}\right] \tag{9}$$

where the compatibility condition (7) has been used and the jump of plastic strain rate is

$$\underline{[\![\dot{\boldsymbol{\epsilon}}^{\text{p}}]\!]} = \underline{\dot{\boldsymbol{\epsilon}}^{\text{p}}_{\text{int}}} - \dot{\boldsymbol{\epsilon}}^{\text{p}}_{\text{ext}} = \underline{\dot{\lambda}_{\text{int}}}\, \boldsymbol{\Lambda} - \dot{\lambda}_{\text{ext}}\, \boldsymbol{\Lambda} = \underline{[\![\dot{\lambda}]\!]}\, \boldsymbol{\Lambda} \tag{10}$$

Eqs. (8)-(10) are derived from the constitutive behavior and the compatibility conditions across the weak discontinuities $\boldsymbol{S}^+$ and $\boldsymbol{S}^-$; as strain localization has not been invoked, all the terms involved are bounded.

Upon strain localization inside the band, and on-going deformation, the deformation vector rate in the band, $\dot{\boldsymbol{e}} = \dot{\boldsymbol{w}}/b$ the strain rate jump, $(\dot{\boldsymbol{e}} \otimes \boldsymbol{n})^{\text{sym}}$, and the plastic strain rate in the band, $\dot{\boldsymbol{\epsilon}}^{\text{p}}_{\text{int}}$, will grow much larger than the total strain rate outside the band, $\dot{\boldsymbol{\epsilon}}_{\text{ext}}$, and the corresponding plastic strain rate, $\dot{\boldsymbol{\epsilon}}^{\text{p}}_{\text{ext}}$, will either vanish (on elastic unloading) or remain small (on plastic loading); this ensures boundedness of the stress rate outside the band, $\dot{\boldsymbol{\sigma}}_{\text{ext}}$. Those terms that will grow upon strain localization, inversely proportional to b, are underlined in Eqs. (8)-(10).

Inside the localization band, elasto-plastic behavior and satisfaction of the yield criterion ensure that the stress rate needs to remain bounded even if the strain rate is not. Consequently, the jump of the stress rate in Eq. (9) may not be null, but it is bounded; therefore, stress rate boundedness requires that

$$[\![\dot{\boldsymbol{\epsilon}}]\!] = (\dot{\boldsymbol{e}} \otimes \boldsymbol{n})^{\mathrm{sym}} = \dot{\boldsymbol{\epsilon}}^{\mathrm{p}}_{\mathrm{int}} = \dot{\lambda}_{\mathrm{int}}\, \boldsymbol{\Lambda} \tag{11}$$

This is that the entire jump of strain rate is due to the plastic strain rate inside the band. This a necessary condition for strain localization to occur. Some Remarks are in order.

Remark 2.1: This condition holds for small finite bandwidths b, as in regularized discontinuities and standard FEM simulations. The condition for strong discontinuities follows for the limit case of vanishing bandwidth $b \to 0$.

Remark 2.2: This condition does not necessarily occur upon plastic yielding nor strain bifurcation. Therefore, a transition stage may be necessary in most situations during which plastic behavior happens without strain localization. Only when the localization condition is fulfilled, true strain localization may happen.

Remark 2.3: Only kinematic conditions depending on the plastic flow rule are implied; therefore, the condition may be extended to non-associated plasticity.

Remark 2.4: For the same reason, the condition is independent from the elastic properties. Application to rigid-plastic materials can be implied from this independence. This is not the case for classical conditions related to strain bifurcation.

Remark 2.5: Stress rate *continuity* upon strain localization follows from Eq. (9) if unloading occurs outside the band, that is, $\dot{\lambda}_{\mathrm{ext}} = 0$. In this case, $[\![\dot{\boldsymbol{\epsilon}}]\!] = [\![\dot{\boldsymbol{\epsilon}}^{\mathrm{p}}]\!]$ and $[\![\dot{\boldsymbol{\sigma}}]\!] = 0$. This is usually the case when softening plasticity is considered.

2.4. Strain localization plastic flow vector and tensor

In the following, the subscript $(\cdot)_{\mathrm{int}}$ will be omitted for the sake of simplicity, as all quantities refer to points inside the localization band. From Eq. (10), a plastic flow localization vector, $\boldsymbol{\gamma}$, can be defined so that

$$\dot{\boldsymbol{e}} = \dot{\lambda}\boldsymbol{\gamma}, \qquad \boldsymbol{\Lambda} = (\boldsymbol{\gamma} \otimes \boldsymbol{n})^{\mathrm{sym}} \tag{12}$$

or, equivalently,

$$\boldsymbol{\gamma} = 2\boldsymbol{n} \cdot \boldsymbol{\Lambda} - \Lambda_{nn}\boldsymbol{n} = \gamma_n \boldsymbol{n} + \gamma_m \boldsymbol{m} + \gamma_p \boldsymbol{p} \tag{13}$$

where $(\boldsymbol{n}, \boldsymbol{m}, \boldsymbol{p})$ is a basis of orthonormal vectors normal and tangential to the discontinuity $\boldsymbol{S}$. The components of the plastic flow localization vector $\boldsymbol{\gamma} = (\gamma_n, \gamma_m, \gamma_p)$ are determined by

$$\gamma_n = \boldsymbol{\gamma} \cdot \boldsymbol{n} = \Lambda_{nn}, \quad \gamma_m = \boldsymbol{\gamma} \cdot \boldsymbol{m} = 2\Lambda_{nm}, \quad \gamma_p = \boldsymbol{\gamma} \cdot \boldsymbol{p} = 2\Lambda_{np} \tag{14}$$

So that

$$\boldsymbol{\gamma} = \Lambda_{nn}\boldsymbol{n} + 2\Lambda_{nm}\boldsymbol{m} + 2\Lambda_{np}\boldsymbol{p} \tag{15}$$

Accordingly, the other components of the strain localization plastic flow tensor are zero

$$\Lambda_{mm} = 0, \quad \Lambda_{pp} = 0, \quad \Lambda_{mp} = 0 \tag{16}$$

From these equations the orientation of the slip surface may be derived.

3. Application to Orthotropic Cohesive-Frictional Plastic Materials

In this section, the above results for strain localization in elasto-plastic materials are purposedly applied to orthotropic cohesive-frictional plastic materials. A general form of the considered yield criteria is given that allows closed-form solutions for the orientation of the slip lines in 2-D plane strain and plane stress conditions.

3.1. Orthotropic Cohesive-Frictional plasticity

Orthotropic cohesive-frictional yield criteria of the form $\Phi(\boldsymbol{\sigma},\zeta)=\phi(\boldsymbol{\sigma})-q(\zeta)\leq 0$ are now considered. Let (1,2,3) be the material orthotropy axes and

$$\boldsymbol{\sigma}^{\mathrm{T}}=[\sigma_{11},\sigma_{22},\sigma_{33},\sigma_{12},\sigma_{13},\sigma_{23}] \tag{17}$$

Voigt's representation of the symmetric second-order stress tensor in those axes. The equivalent stress $\phi(\boldsymbol{\sigma})$ is expressed as

$$\phi(\boldsymbol{\sigma})=\sqrt{\frac{3}{2}(\boldsymbol{\sigma}^{\mathrm{T}}\cdot\mathbf{P}\cdot\boldsymbol{\sigma}+\mathbf{Q}^{\mathrm{T}}\cdot\boldsymbol{\sigma})} \tag{18}$$

The generalized orthotropic matrix $\mathbf{P}$ and $\mathbf{Q}$ vector read

$$\mathbf{P}=\frac{1}{F+G+H}\begin{bmatrix}F+G & -\tilde{F} & -\tilde{G} & 0 & 0 & 0\\ -\tilde{F} & F+H & -\tilde{H} & 0 & 0 & 0\\ -\tilde{G} & -\tilde{H} & G+H & 0 & 0 & 0\\ 0 & 0 & 0 & 2L & 0 & 0\\ 0 & 0 & 0 & 0 & 2M & 0\\ 0 & 0 & 0 & 0 & 0 & 2N\end{bmatrix},\qquad \mathbf{Q}=\frac{1}{F+G+H}\begin{bmatrix}I\\ J\\ K\\ 0\\ 0\\ 0\end{bmatrix} \tag{19}$$

where the material parameters F, G, H, $\tilde{F}$, $\tilde{G}$, $\tilde{H}$, L, M, N, I, J and K are given in terms of by the material strengths (superscripts c and t denote compression and tension, respectively):

$$F=\frac{1}{2}\left[\frac{1}{f_1^c f_1^t}+\frac{1}{f_2^c f_2^t}-\frac{1}{f_3^c f_3^t}\right],G=\frac{1}{2}\left[\frac{1}{f_1^c f_1^t}-\frac{1}{f_2^c f_2^t}+\frac{1}{f_3^c f_3^t}\right],H=\frac{1}{2}\left[-\frac{1}{f_1^c f_1^t}+\frac{1}{f_2^c f_2^t}+\frac{1}{f_3^c f_3^t}\right] \tag{20a}$$

$$L=\frac{1}{2}\left(\frac{1}{f_{12}}\right)^2,M=\frac{1}{2}\left(\frac{1}{f_{13}}\right)^2,N=\frac{1}{2}\left(\frac{1}{f_{23}}\right)^2 \tag{20b}$$

$$I=\frac{1}{f_1^t}-\frac{1}{f_1^c},J=\frac{1}{f_2^t}-\frac{1}{f_2^c},K=\frac{1}{f_3^t}-\frac{1}{f_3^c} \tag{20c}$$

Unless, otherwise stated:

$$\tilde{F}=F,\quad \tilde{G}=G,\quad \tilde{H}=H \tag{20d}$$

The initial stress threshold is defined as

$$q_0^2=\frac{3}{2}[F+G+H]^{-1} \tag{21}$$

Different well-known quadratic isotropic and orthotropic yield criteria are obtained by appropriately selecting the material parameters:

von Mises criterion:

$$f=f_1^c=f_2^c=f_3^c=f_1^t=f_2^t=f_3^t,\quad \frac{f}{\sqrt{3}}=f_{12}=f_{13}=f_{23} \tag{22a}$$

Parabolic Drucker-Prager (DP) criterion:

$$f^c = f_1^c = f_2^c = f_3^c, \qquad f^t = f_1^t = f_2^t = f_3^t, \qquad \frac{\sqrt{f^c f^t}}{\sqrt{3}} = f_{12} = f_{13} = f_{23} \tag{22b}$$

Hill criterion:

$$f_1 = f_1^c = f_1^t,\ f_2 = f_2^c = f_2^t,\ f_3 = f_3^c = f_3^t \text{ and } I = J = K = 0 \tag{22c}$$

Hoffman criterion:

$$\widetilde{F} = F, \quad \widetilde{G} = G, \quad \widetilde{H} = H \tag{22d}$$

Tsai-Wu criterion:

$$\tilde{F} = \frac{1}{2}\frac{1}{\sqrt{f_1^c f_1^t f_2^c f_2^t}}, \qquad \tilde{G} = \frac{1}{2}\frac{1}{\sqrt{f_1^c f_1^t f_3^c f_3^t}}, \qquad \tilde{H} = \frac{1}{2}\frac{1}{\sqrt{f_2^c f_2^t f_3^c f_3^t}} \tag{22e}$$

Remark 3.1: The effective stress in Eq. (18) defines a quadratic yield surface, with a quadratic dependence of the friction-angle on pressure. Alternatively, an effective stress defined as

$$\phi(\boldsymbol{\sigma}) = \sqrt{\frac{3}{2}\boldsymbol{\sigma}^{\mathrm{T}} \cdot \mathbf{P} \cdot \boldsymbol{\sigma}} + \widehat{\mathbf{Q}}^{\mathrm{T}} \cdot \boldsymbol{\sigma} \tag{23}$$

allows for a yield surface with straight meridians; the isotropic criterion would the more conventional DP cone.

Orthotropic criteria cannot be represented graphically in the Haigh–Westergaard (HW) stress space because they depend on the 6 stress components. A partial graphical representation can be obtained by considering them projected into the HW space when the principal stresses act on the material axis, that is, no shear stress appears on the material system. Such representation, generally as an elliptic paraboloid, is offered in Figure 3. All strengths are scaled to 1. Figure 3(a) shows an orthotropic Hill cylinder, with $f_1/f_2 = f_1/f_3 = 1.5$, tensile and compresive strenth are equal. Figure 3(**b**) show the isotropic parabolic Drucker-Prager for compressive to tensile strength ratio $\kappa = f^c/f^t = 1.5$. Figures 3(c) and (d) show the orthotropic Hoffman and Tsai-Wu criteria, respectively, for ratios $\kappa = f_1^c/f_1^t = 1.5$ and $f_2^c/f_2^t = f_3^c/f_3^t = 1$; all tensile strengths are taken equal to 1.

3.2. Orthotropic Plastic flow

From the effective stress in Eq. (18), the components of the plastic flow tensor plastic flow are obtained

$$\boldsymbol{\Lambda} = \frac{\partial \phi}{\partial \boldsymbol{\sigma}} = \frac{3}{4}\frac{1}{\phi(\boldsymbol{\sigma})}\,(2\,\mathbf{P} \cdot \boldsymbol{\sigma} + \mathbf{Q}^{\mathbf{T}}) \tag{24}$$

so that

$$\Lambda_{11} = \frac{\partial \phi}{\partial \sigma_{11}} = \frac{q_0^2}{2\phi}\left[2(G+F)\sigma_{11} - 2\tilde{F}\sigma_{22} - 2\tilde{G}\sigma_{33} + I\right] \tag{24a}$$

$$\Lambda_{22} = \frac{\partial \phi}{\partial \sigma_{22}} = \frac{q_0^2}{2\phi}\left[2(F+H)\sigma_{22} - 2\tilde{F}\sigma_{11} - 2\tilde{H}\sigma_{33} + J\right] \tag{24b}$$

$$\Lambda_{33} = \frac{\partial \phi}{\partial \sigma_{33}} = \frac{q_0^2}{2\phi}\left[2(G+H)\sigma_{33} - 2\tilde{G}\sigma_{11} - 2\tilde{H}\sigma_{22} + K\right] \tag{24c}$$

272

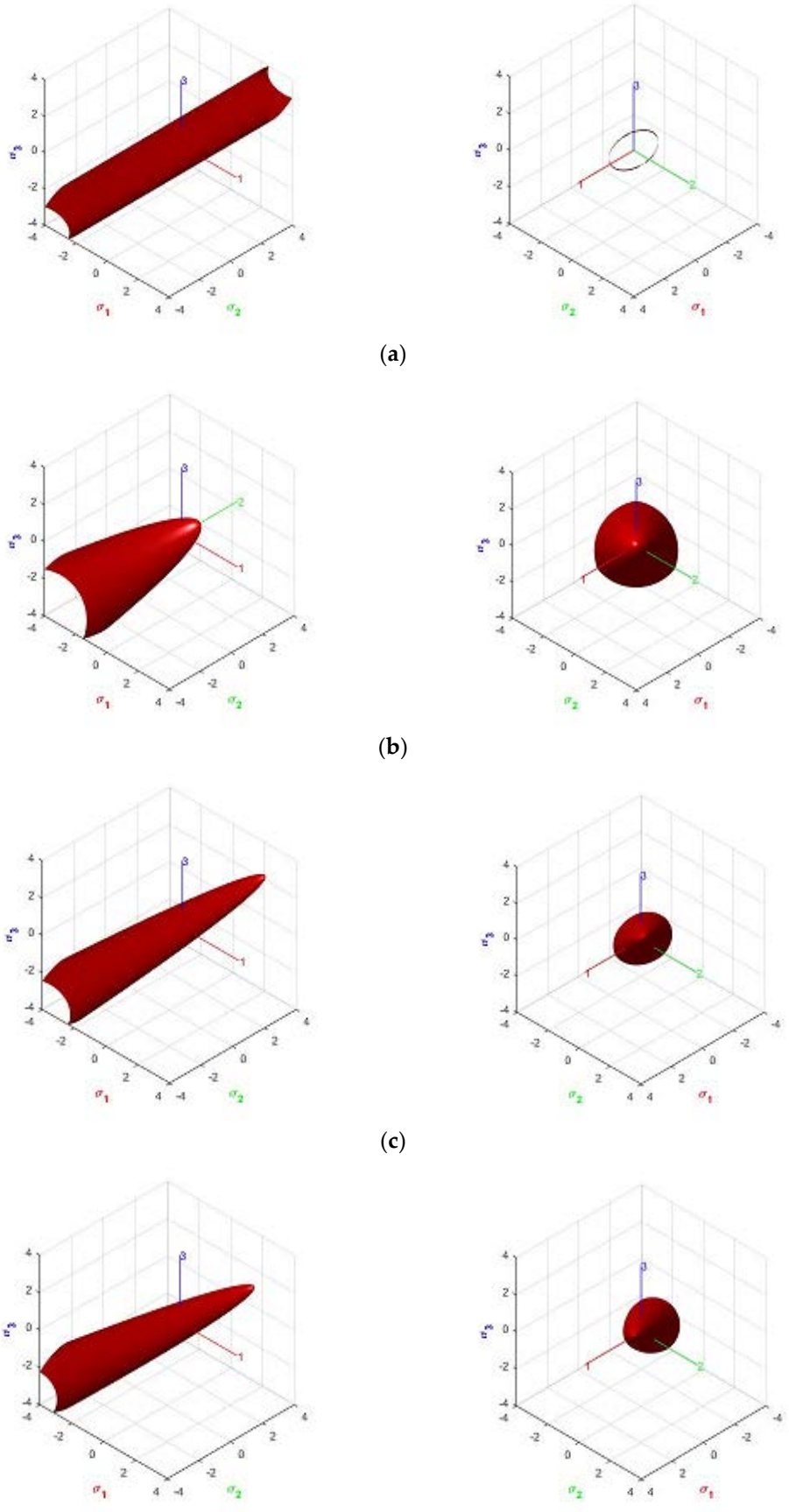

(**a**)

(**b**)

(**c**)

(**d**)

273 **Figure 3.** Yield criteria in HW stress space, lateral view from the hydrostatic axis:
274 (**a**) Hill; (**b**) Parabolic Drucker-Prager; (**c**) Hoffman; (**d**) Tsai-Wu.

$$\Lambda_{12} = \Lambda_{21} = \frac{1}{2}\frac{\partial \phi}{\partial \sigma_{12}} = \frac{q_0^2}{2\phi} L\sigma_{12} \tag{24d}$$

$$\Lambda_{13} = \Lambda_{31} = \frac{1}{2}\frac{\partial \phi}{\partial \sigma_{13}} = \frac{q_0^2}{2\phi} M\sigma_{13} \tag{24e}$$

$$\Lambda_{23} = \Lambda_{32} = \frac{1}{2}\frac{\partial \phi}{\partial \sigma_{23}} = \frac{q_0^2}{2\phi} N\sigma_{23} \tag{24f}$$

The identity $\mathrm{tr}\boldsymbol{\Lambda} = \Lambda_{11} + \Lambda_{22} + \Lambda_{33} = \frac{q_0^2}{2\phi}(I + J + K)$ holds.

3.3. Strain Localization Angle

In this section, the orientation of the slip lines is analytically obtained for orthotropic and pressure-dependent plastic solids subjected to plane strain and plane stress conditions. The strain localization angle is measured counter-clockwise $\theta_{\mathrm{cr}} \in [-\frac{\pi}{2}, \frac{\pi}{2}]$ as the angle between the vector $\boldsymbol{n}$ normal to the discontinuity and the material axis 1; see Figure 4.

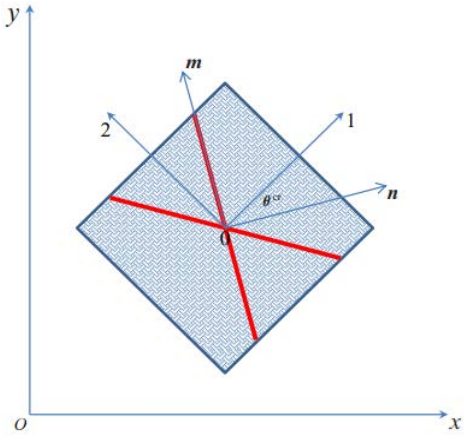

Figure 4. Definition of the localization angle θ_{cr}.

Let $(\boldsymbol{n}, \boldsymbol{m}, \boldsymbol{p})$ be the basis formed by the orthonormal vectors normal and tangential to the discontinuity $\boldsymbol{S}$. The strain localization equations (16) require the flow tensor in Eqs. (24) to be written in this system. Let θ be the angle between the material and another system. Then

$$\Lambda_{mm} = \Lambda_{11}\sin^2\theta + \Lambda_{22}\cos^2\theta + 2\Lambda_{12}\sin\theta\cos\theta \tag{25a}$$

$$\Lambda_{pp} = \Lambda_{33} \tag{25b}$$

$$\Lambda_{mp} = 0 \tag{25c}$$

The strain localization angle θ^{cr} is obtained from the kinematic constraints in Eqs. (16), that is, equating these components to zero. Solving $\Lambda_{mm}(\theta^{\mathrm{cr}}) = 0$ for $\tan\theta^{\mathrm{cr}}$

$$\tan\theta^{\mathrm{cr}} = -\frac{\Lambda_{12}}{\Lambda_{11}} \pm \sqrt{\left(\frac{\Lambda_{12}}{\Lambda_{11}}\right)^2 - \frac{\Lambda_{22}}{\Lambda_{11}}} \tag{26}$$

As can be seen, the strain localization angle θ^{cr} depends on the stress state upon strain localization. The condition $\Lambda_{pp}(\theta^{cr}) = \Lambda_{33} = 0$ (25b) needs to be imposed in plane stress and strain conditions.

Remark 3.2: For the case of $\Lambda_{12} = 0$, where the no shear stress acts on the material axes, Eq. (26) simplifies to

$$\tan\theta^{\mathrm{cr}} = \pm\sqrt{-\frac{\Lambda_{22}}{\Lambda_{11}}} \tag{27}$$

Remark 3.3: The kinematic constraints produce two alternative strain localization angle, see also Figure 3. The in-between angle that follows from Eq. (27) is

$$\tan(\theta_1^{\mathrm{cr}} - \theta_2^{\mathrm{cr}}) = \frac{\tan\theta_1^{\mathrm{cr}} - \tan\theta_2^{\mathrm{cr}}}{1 + \tan\theta_1^{\mathrm{cr}}\tan\theta_2^{\mathrm{cr}}} = \pm\left(\frac{2\sqrt{-\frac{\Lambda_{22}}{\Lambda_{11}}}}{1 + \frac{\Lambda_{22}}{\Lambda_{11}}}\right) \tag{28}$$

Remark 3.4: In purely isochoric models (von Mises, Hill), $\Lambda_{11} = -\Lambda_{22}$, and $\tan(\theta_1^{\mathrm{cr}} - \theta_2^{\mathrm{cr}}) = \pm\infty$, so $\theta_1^{\mathrm{cr}} - \theta_2^{\mathrm{cr}} = \pm 90°$

Remark 3.5: The angle of the slip lines (counter-clockwise from 1-axis) is $\theta^{\mathrm{slip}} = \frac{\pi}{2} - \theta^{\mathrm{cr}}$

$$\tan\theta^{\mathrm{slip}} = (\tan\theta^{\mathrm{cr}})^{-1} \tag{29}$$

Remark 3.6: The above expressions are obtained for the stress expressed in the material system. These are obtained from the stresses in the global (x,y,z) system by standard transformation. For instance, in plane strain conditions

$$\begin{bmatrix}\sigma_{11}\\ \sigma_{22}\\ \sigma_{33}\\ \sigma_{12}\end{bmatrix} = \begin{bmatrix}\cos^2\alpha & \sin^2\alpha & 0 & -2\cos\alpha\sin\alpha\\ \sin^2\alpha & \cos^2\alpha & 0 & 2\cos\alpha\sin\alpha\\ 0 & 0 & 1 & 0\\ \cos\alpha\sin\alpha & -\cos\alpha\sin\alpha & 0 & \cos^2\alpha - \sin^2\alpha\end{bmatrix}\begin{bmatrix}\sigma_{xx}\\ \sigma_{yy}\\ \sigma_{zz}\\ \sigma_{xy}\end{bmatrix} \tag{30}$$

where α is the tilt angle between the global axis x and the material local axis 1 measured counter-clockwise.

3.2.1. Plane Stress

In plane stress, $\sigma_{33} = \sigma_{pp} = 0$.

In this case, the non-zero plastic flow components Λ_{ij} in Eq. (27) are

$$\Lambda_{11} = \frac{q_0^2}{2\phi}[2(G+F)\sigma_{11} - 2\tilde{F}\sigma_{22} + I] \tag{31a}$$

$$\Lambda_{22} = \frac{q_0^2}{2\phi}[2(F+H)\sigma_{22} - 2\tilde{F}\sigma_{11} + J] \tag{31b}$$

$$\Lambda_{12} = \Lambda_{21} = \frac{q_0^2}{2\phi}L\sigma_{12} \tag{31d}$$

These components can be substituted in Eq. (26).

3.2.2. Plane Strain

In this case, the non-zero plastic flow components Λ_{ij} in Eq. (27) are considered with Eq. (25b).

$$\Lambda_{11} = \frac{q_0^2}{2\phi}\left[2(G+F)\sigma_{11} - 2\tilde{F}\sigma_{22} - 2\tilde{G}\sigma_{33} + I\right] \tag{32a}$$

$$\Lambda_{22} = \frac{q_0^2}{2\phi}\left[2(F+H)\sigma_{22} - 2\tilde{F}\sigma_{11} - 2\tilde{H}\sigma_{33} + J\right] \tag{32b}$$

$$\Lambda_{33} = \frac{q_0^2}{2\phi}\left[2(G+H)\sigma_{33} - 2\tilde{G}\sigma_{11} - 2\tilde{H}\sigma_{22} + K\right] \tag{32c}$$

$$\Lambda_{12} = \Lambda_{21} = \frac{q_0^2}{2\phi} L\sigma_{12} \tag{32d}$$

From the kinematical condition $\Lambda_{\mathrm{pp}}(\theta^{\mathrm{cr}}) = \Lambda_{33} = 0$, σ_{33} is obtained as

$$\sigma_{33} = \frac{2\left(\tilde{G}\sigma_{11} + \tilde{H}\sigma_{22}\right) - K}{2(G+H)} \tag{33}$$

and inserted into Eq. (32a) and Eq. (32b), and these components can be then substituted in Eq. (26).

3.4. Geometrical interpretation of the strain localization angle in the stress space

In the following, a geometrical interpretation of the strain localization angles obtained analytically is offered. As explained, Figure 3 gives a partial graphical representation of the orthotropic yield criteria projected into the HW space when the principal stresses act on the material axis, that is, no shear stress appears on the material system.

In Figure 5, a cross section of those paraboloids by a horizontal plane is given. For plane stress, the plane $\sigma_{33} = 0$ is used; for plane strain, the plane $\sigma_{33} = \left[2\left(\tilde{G}\sigma_{11} + \tilde{H}\sigma_{22}\right) - K\right] / 2(G+H)$, from Eq. (33), is used. The isotropic Drucker-Prager and the orthotropic Hoffmann and Tsai-Wu criteria are depicted for ratios $\kappa = f^c / f^t = 1.5\ and\ 3.0$ and $f_2^c / f_2^t = f_3^c / f_3^t = 1$; all tensile strengths are taken equal to 1. For plane stress, the intersected quadratic curves are ellipses; for plane strain, they are parabolas. They are more stretched for higher ratios κ.

In Figure 5, the projection of the plastic flow vector, normal to the yield surface, for uniaxial tension and compression in the 2-direction, is also plotted. See the next Section for the analytical values.

Remark 3.7: The angle $\tilde{\theta}$ between this projected flow vector and the 2-axis is related to the strain localization angle θ^{cr}, because

$$\tan\tilde{\theta} = -\frac{\Lambda_{22}}{\Lambda_{11}} = \tan^2\theta^{\mathrm{cr}} \tag{34}$$

3.5. Uniaxial tension and compression: Analytical strain localization angles

In the following, the analytical values of the strain localization angle are obtained for the uniaxial tension and compression cases illustrated in Figure 5. Material strengths are those indicated in the previous Section; with those, the coefficients for matrix **P** and vector **Q** are computed for the three different criteria (Drucker-Prager, Hoffmann and Tsai-Wu) and listed in Table 1.

Table 1. Material coefficients for matrix **P** and vector **Q**

$\boldsymbol{\kappa = 1.5}$	$\boldsymbol{F}$	$\boldsymbol{G}$	$\boldsymbol{H}$	$\boldsymbol{\tilde{F}}$	$\boldsymbol{\tilde{G}}$	$\boldsymbol{\tilde{H}}$	$\boldsymbol{I}$	$\boldsymbol{J}$	$\boldsymbol{K}$
DP	1/3	1/3	1/3	F	G	H	1/3	1/3	1/3
Hoffman	1/3	1/3	2/3	F	G	H	1/3	0	0
Tsai-Wu	1/3	1/3	2/3	$\sqrt{1/6}$	$\sqrt{1/6}$	0.5	1/3	0	0

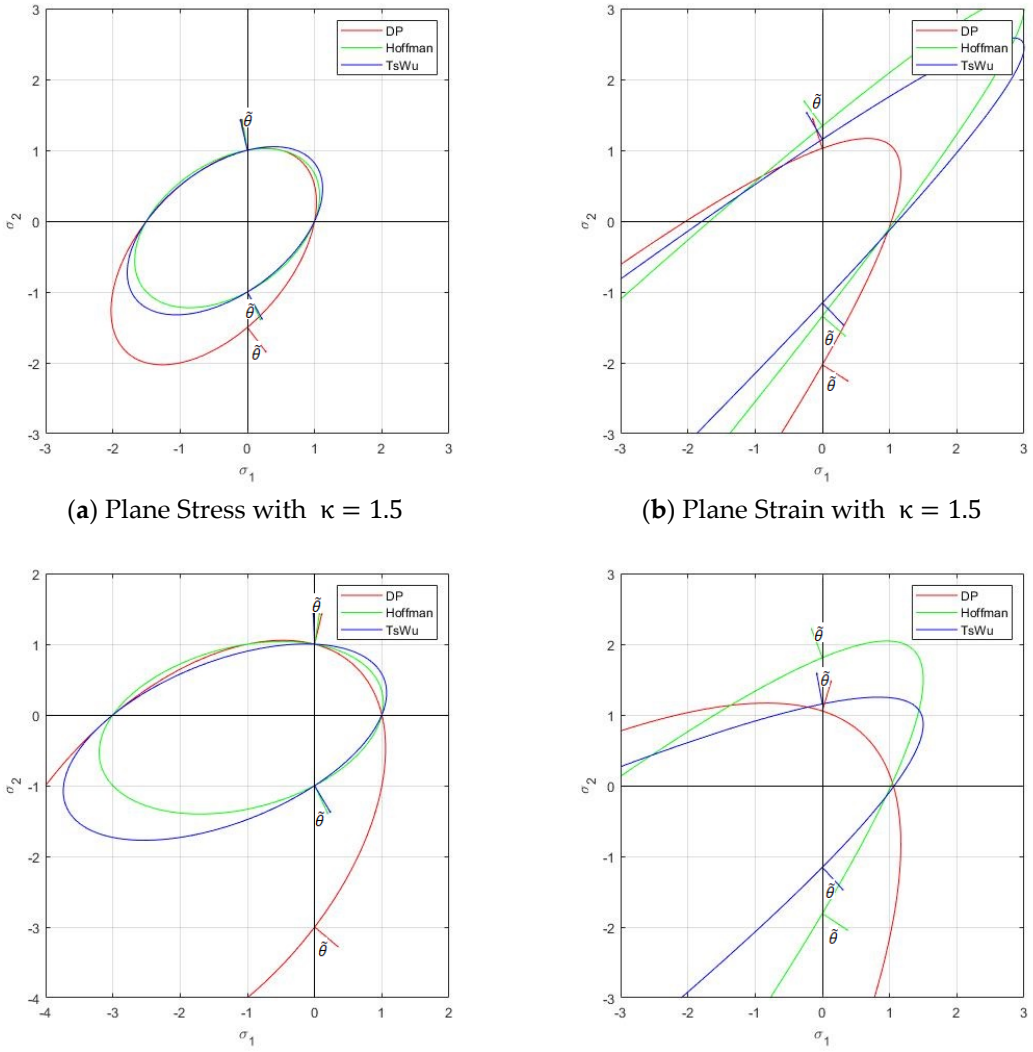

(**a**) Plane Stress with $\kappa = 1.5$ (**b**) Plane Strain with $\kappa = 1.5$

(**c**) Plane Stress with $\kappa = 3.0$ (**d**) Plane Strain with $\kappa = 3.0$

Figure 5. Cross sections of the yield criteria and strain localization angle under uniaxial tension and compression in plane stress and plane strain.

3.5.1. Plane Stress

For uniaxial tension in plane stress, the stress state is:

$$\sigma_{11} = 0, \qquad \sigma_{22} = \sigma > 0, \qquad \sigma_{12} = 0, \qquad \sigma_{33} = 0$$

Therefore, the kinematical condition $\Lambda_{33} = 0$ (25b) needs not be considered, and no extra constraint imposes on the stress state upon strain localization. Therefore, once the initial yield surface, $\Phi(\boldsymbol{\sigma}, \zeta) = 0$, is reached, strain localization occurs at the same instant, with the orientation determined from the corresponding flow tensor.

A stress $\sigma_{22} = \sigma = 1$ is taken so that the point $[0, \sigma, 0]$ is on yield surface, see Figure 5a.

As $\Lambda_{12} = 0$,

$$\tan\theta^{\text{slip}} = (\tan\theta^{\text{cr}})^{-1} = \pm\sqrt{-\frac{\Lambda_{11}}{\Lambda_{22}}} = \pm\sqrt{\frac{2\tilde{F}\sigma_{22} - I}{2(F+H)\sigma_{22} + J}}$$

The obtained values for θ^{slip} are given in Table 2. Results corresponding to uniaxial compression are also given in the Table. Note that the localization angles under tension and compression are very different and for the various yield criteria, as depicted graphically in Figure 5.

Table 2. Plane Stress: stress state and slip-lines angles for uniaxial tension and compression

$\kappa = 1.5$	Tension			Compression		
	σ_{22}	σ_{33}	θ^{slip}	σ_{22}	σ_{33}	θ^{slip}
DP	1.0000	0.0000	$\pm 24.0948°$	-1.0000	0.0000	$\pm 41.8103°$
Hoffman	1.0000	0.0000	$\pm 22.2077°$	-1.0000	0.0000	$\pm 35.2644°$
Tsai-Wu	1.0000	0.0000	$\pm 26.1746°$	-1.0000	0.0000	$\pm 37.1705°$

Remark 3.8: Note that for $I = 2\tilde{F}$ the localization angle $\theta^{\mathrm{cr}} = 0$ *for* tension, as $\sigma_{22} = \sigma = 1$. This happens if the compressive strength is sufficiently larger than the tensile strength; for instance, it happens for the ratio $\kappa = 2$ for the Drucker-Prager criterion. For larger ratios, there is no real value for the localization angles. In compression, for $\sigma_{22} = \sigma = -1$, this happens reciprocally, that is, if the compressive strength is sufficiently smaller that the tensile strength.

3.5.2. Plane Strain

In the plane strain case, the kinematical condition $\Lambda_{33} = 0$ (25b) needs to be enforced. From this,

$$\sigma_{33} = \frac{2\left(\tilde{G}\sigma_{11} + \tilde{H}\sigma_{22}\right) - K}{2(G + H)}$$

A stress $\sigma_{22} = \sigma$ is found so that the point $[0, \sigma, \sigma_{33}]$ is on the corresponding yield surface, see Figure 5a.

Then,

$$\tan\theta^{\mathrm{slip}} = (\tan\theta^{\mathrm{cr}})^{-1} = \pm\sqrt{-\frac{\Lambda_{11}}{\Lambda_{22}}} = \pm\sqrt{\frac{2\tilde{F}\sigma_{22} + 2\tilde{G}\,\sigma_{33} - I}{2(F + H)\sigma_{22} - 2\tilde{H}\sigma_{33} + J}}$$

The obtained values for θ^{slip} are given in Table 3. Results corresponding to uniaxial compression are also given. Note that the angles under tension and compression are distinct and they are also different for the various yield criteria, as shown in Figure 5.

Table 3. Plane Strain: stress state and slip-lines angles for uniaxial tension and compression

$\kappa = 1.5$	Tension			Compression		
	σ_{22}	σ_{33}	θ^{slip}	σ_{22}	σ_{33}	θ^{slip}
DP	1.0275	0.2638	$\pm 30.4411°$	-2.0275	-1.2638	$\pm 52.1384°$
Hoffman	1.3416	0.8944	$\pm 41.3843°$	-1.3416	-0.8944	$\pm 47.8857°$
Tsai-Wu	1.1547	0.5774	$\pm 38.3075°$	-1.1547	-0.5774	$\pm 45.1276°$

4. Numerical Verification

In this Section, FEM analyses are performed to numerically verify the analytical results obtained in Section 3 and derived from the strain localization analysis in Section 2.

It is emphasized that the numerical verification is totally independent from the analytical results. That is, the numerical analyses follow the standard procedure for solving the nonlinear mechanical problem and plastic behavior appears and evolves into the formation of slip lines; and the analytical results are not by any means used.

In previous works [38], it has been demonstrated that the strain localization angle is independent from the elastic properties. Therefore, the argument is not pursued here. Similarly, the localization angle does not depend on the softening behavior [40], so perfect plasticity is assumed in the following.

Although pressure dependent plasticity models are to be investigated, they are compared to the isochoric von Mises model. To avoid volumetric locking in nearly incompressible situations, B-bar finite elements [42] are used in 2D and 3D.

4.1. B-bar Finite Element

The B-bar element is a particular implementation of the mixed displacement/pressure *Q1P0* element in which the constant pressure has been eliminated at element level at the expense of renouncing the incompressible limit. This is accomplished by evaluating the constant mean stress in terms of the mean volumetric strain, the latter computed from the nodal displacements.

The standard discrete strain-displacement $\boldsymbol{B}$ matrix, computed at each integration point from the Cartesian derivatives of the nodal shape functions, is split into its volumetric and deviatoric parts

$$\boldsymbol{B} = \boldsymbol{B}^{\mathrm{vol}} + \boldsymbol{B}^{\mathrm{dev}} \tag{34}$$

A mean volumetric sub-matrix $\bar{\boldsymbol{B}}^{\mathrm{vol}}$ is computed as

$$\bar{\boldsymbol{B}}^{\mathrm{vol}} = \frac{1}{\mathrm{n_g}} \sum_{k=1}^{\mathrm{n_g}} \boldsymbol{B}_k^{\mathrm{vol}} \tag{35}$$

where $\mathrm{n_g}$ is the number of integration points in the element.

The B-bar discrete strain-displacement matrix is obtained as

$$\bar{\boldsymbol{B}} = \bar{\boldsymbol{B}}^{\mathrm{vol}} + \boldsymbol{B}^{\mathrm{dev}} \tag{36}$$

The B-bar element has some zero-energy modes that may show as spurious hour-glassing in some instances. This may be avoided by using

$$\bar{\boldsymbol{B}}^{stab} = \bar{\boldsymbol{B}} + (1-\tau)\left[\boldsymbol{B}^{\mathrm{vol}} - \bar{\boldsymbol{B}}^{\mathrm{vol}}\right] \tag{37}$$

For $\tau = 1$, then $\bar{\boldsymbol{B}}^{stab} = \bar{\boldsymbol{B}}^{\mathrm{vol}} + \boldsymbol{B}^{\mathrm{dev}} = \bar{\boldsymbol{B}}$ is identical to the B-bar formulation. For $\tau = 0$, then $\bar{\boldsymbol{B}}^{stab} = \boldsymbol{B}^{\mathrm{vol}} + \boldsymbol{B}^{\mathrm{dev}}$ is identical to the standard formulation.

4.2. Uniaxial tension and compression: Numerical verification

In this section, the above B-bar finite element is used to perform benchmark verifications in strain localization analysis. The benchmark example is a strip loaded in uniaxial tension and compression via imposed vertical displacements at the top and bottom ends; the horizontal movement is not restrained. As shown in Figure 6, the strip has dimensions $10\mathrm{m} \times 20\mathrm{m}$ (width × height). A sharp horizontal slit (2 m) is inserted in the center of strip to introduce the perturbation necessary to trigger strain localization.

In this problem the stress field is known a-priori. Plane strain and plane stress conditions are investigated. In both cases, the far field stress state corresponds exactly to those assumed for the analytical results in Section 3

$$\sigma_{11} = 0, \qquad \sigma_{22} = \sigma > 0, \qquad \sigma_{12} = 0$$

The sharp horizontal slit causes a stress concentration that triggers the onset of plastic behavior and strain localization; subsequently, straight slip lines stem from these and cross the strip at well-defined slopes that must follow the angles analytically predicted in Sections 2 and 3. The numerical results obtained in the FE analysis are used to validate the strain localization analysis in Section 2 and the analytical results in Section 3 that follows from it.

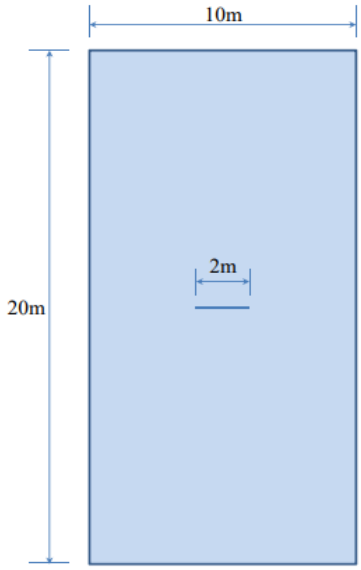

Figure 6. Geometry of a strip under vertical stretching.

The following material properties are used: Young's modulus $E = 1.0 \times 10^7$ MPa, Poisson's ratio $\nu = 0.2$. Several orthotropic elasto-plastic criteria are compared; the different plastic yield strengths along the material axes are detailed for each case. Perfect plasticity is assumed.

Structured meshes of regular quadrilateral are employed. Square elements (0.05 m × 0.05 m) are arranged 200 horizontally and 400 vertically, with a total of 80,000 elements used for plane strain 2D simulations. Plane stress cases are simulated in 3D, with as many hexahedral elements arranged in a mesh 1 element thick. In all cases, 500 time steps are performed to complete the analyses. The constitutive laws and finite elements used have been implemented in the COMET finite element program, developed by the authors at the International Center for Numerical Methods in Engineering (CIMNE). Pre and post-processing is done with GiD, also developed at CIMNE.

4.2.1. Isotropic Incompressible and Cohesive-Frictional Models

In this subsection, strain localization is first investigated for isotropic incompressible and pressure sensitive models.

Isotropic von Mises *J2* plasticity with yield strength $f = 1.0 \times 10^4$ MPa is used as reference case. Insensitive to pressure, under plane strain, tensile and compression tests show the same localization angles ($\pm 45°$), while under plane stress, the localization angles are $\pm 35.26°$ from horizontal axis, measured in a counter-clockwise manner.

Isotropic Parabolic Drucker-Prager models are also considered. A tensile strength $f^t = 1.0 \times 10^4$ MPa and different compressive strengths according to the ratio $\kappa = f^c / f^t$ are used, $\kappa = 1.25, 1.50$ for tension, $\kappa = 2, 3$ for compression; the isotropic shear strength is $\sqrt{f^c f^t / 3}$.

Some of the corresponding analytical results are given in Section 3.5. Here, the analytical and numerical results are presented for comparison in Figures 7 to 10 and Tables 4 to 7. Plane stress and plane stress results are shown both for tension and compression. For the numerical results, the numerical Lode angle is measured at the point in the slip line located 1 m to the right from the right end of the slit. The angle of the slide slip line is measured counter-clockwise from the x-axis.

For all cases, the numerical results are coincident with the analytical results. Correct angles of the slip lines are depicted in Figures 7, 8, 9, and 10. Also, the coincidence between analytical and numerical results is shown in Tables 4, 5, 6 and 7. The strain localization angle decreases with increasing ratios κ in the tensile tests (Figures 7 and 9), while the strain localization angle increases with κ in the compressive tests (Figure 8 and 10). The coincidence of the analytical and numerical Lode angles in the plane strain cases indicates that the kinematical constraint imposed by the $\Lambda_{33} = \Lambda_{zz} = 0$ condition is verified.

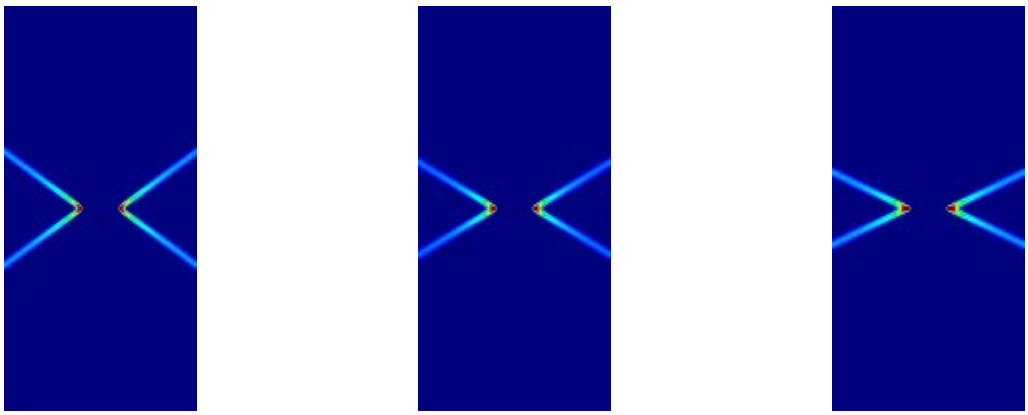

(**a**) (**b**) (**c**)

Figure 7. Strip under vertical **plane stress tension** (Parabolic Drucker-Prager): (**a**) $\kappa = 1$, identical to von Mises; (**b**) $\kappa = 1.25$; (**c**) $\kappa = 1.5$.

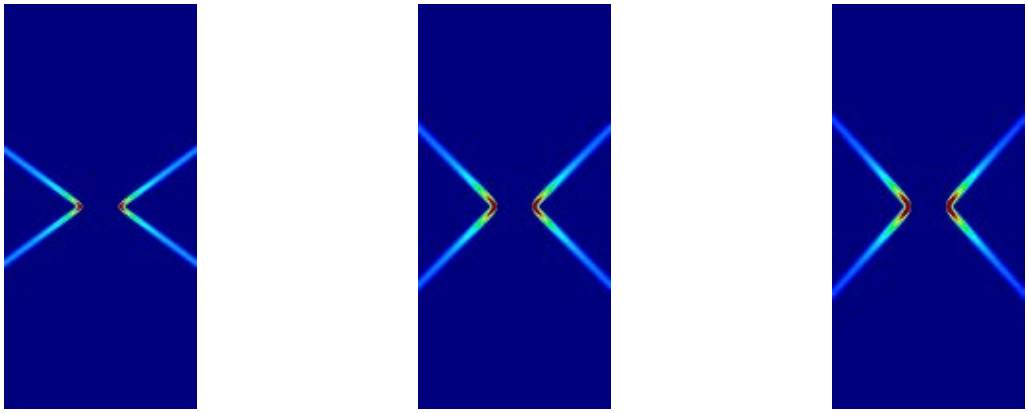

(**a**) (**b**) (**c**)

Figure 8. Strip under vertical **plane stress compression** (Parabolic Drucker-Prager): (**a**) $\kappa = 1$, identical to von Mises; (**b**) $\kappa = 2$; (**c**) $\kappa = 3$.

Table 4. Analytical and numerical Lode and strain localization angles for **isotropi**c models under **plane stress tension**

κ	ϑ_{ana}	ϑ_{num}	θ_{ana}^{slip}	θ_{num}^{slip}
VM 1.0	0.0000°	0.6459°	35.2644°	35.4699°
DP 1.25	0.0000°	0.3803°	30.0000°	30.4342°
DP 1.5	0.0000°	0.7800°	24.0948°	24.2277°

Table 5. Analytical and numerical Lode and strain localization angles for **isotropic** models under **plane stress compression**

κ	ϑ_{ana}	ϑ_{num}	θ_{ana}^{slip}	θ_{num}^{slip}
VM 1.0	60.0000°	59.3541°	35.2644°	35.4699°
DP 2.0	60.0000°	59.6989°	45.0000°	45.0000°
DP 3.0	60.0000°	59.6006°	48.1897°	48.8141°

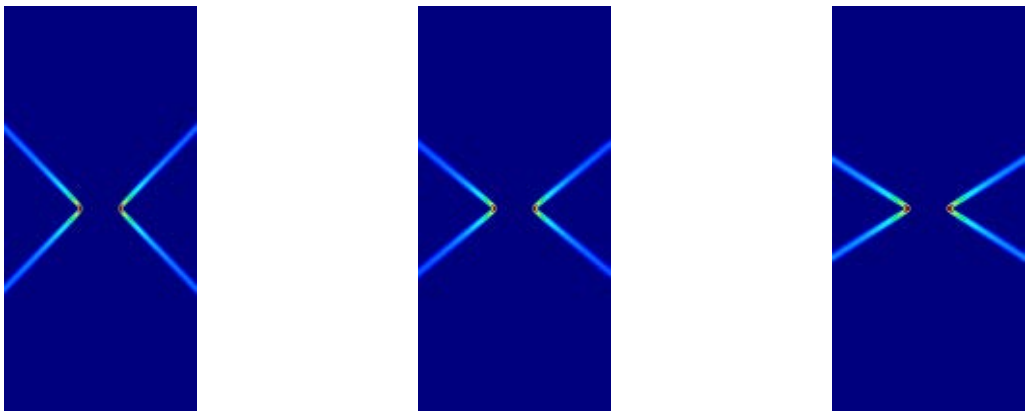

(**a**) (**b**) (**c**)

Figure 9. Strip under vertical **plane strain tension** (Parabolic Drucker-Prager): (**a**) $\kappa = 1$ identical to von-Mises; (**b**) $\kappa = 1.25$; (**c**) $\kappa = 1.5$.

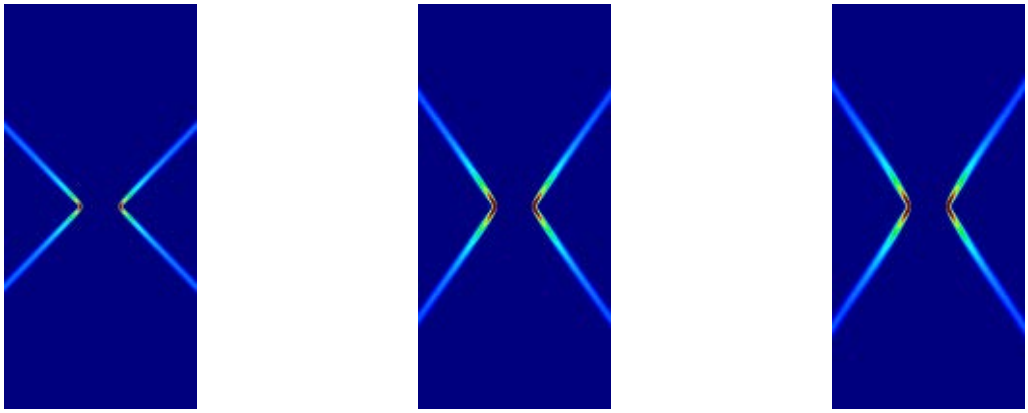

(**a**) (**b**) (**c**)

Figure 10. Strip under vertical **plane strain compression** (Parabolic Drucker-Prager): (**a**) $\kappa = 1$ identical to von-Mises; (**b**) $\kappa = 2$; (**c**) $\kappa = 3$.

Table 6. Analytical and numerical Lode and strain localization angles for **isotropic** models under **plane strain tension**

κ	ϑ_{ana}	ϑ_{num}	θ_{ana}^{slip}	θ_{num}^{slip}
VM 1.0	30.0000°	30.1669°	45.0000°	45.0000°
DP 1.25	22.3378°	23.6244°	38.2626°	39.0939°
DP 1.5	14.3077°	15.9519°	30.4411°	31.4875°

Table 7. Analytical and numerical Lode and strain localization angles for **isotropic** models under **plane strain compression**

κ	ϑ_{ana}	ϑ_{num}	θ_{ana}^{slip}	θ_{num}^{slip}
VM 1.0	30.0000°	30.1669°	45.0000°	45.0000°
DP 2.0	19.1066°	19.6359°	54.7356°	54.2934°
DP 3.0	17.1330°	17.6788°	56.6531°	57.5289°

4.2.2. Isotropic and Orthotropic Cohesive-Frictional Models

In this subsection, the formation of slip lines is now investigated for orthotropic Hoffman and Tsai-Wu pressure sensitive models and compared to the isotropic counterpart. The orthotropy material axes (1,2,3) are coincident with the global axes (x,y,z); relative tilting is investigated in Appendix B.

For the comparison, a ratio of compressive to tensile strengths $\kappa = 1.5$ is taken for the tension tests and $\kappa = 3.0$ for the compression tests. For the orthotropic models, all the yield strengths are taken as $f = 1.0 \times 10^4$ MPa, except the compressive f_x^c, which is taken to the κ ratio; shear strength $f_{xy} = \sqrt{f_x^c f_y^c / 3}$.

Some of the corresponding analytical results are given in Section 3.5. In the following, the analytical and numerical results are presented for comparison in Figures 11 to 14 and Tables 8 to 11.

As previously, for all cases, the numerical and analytical results are coincident. Note that Hoffman and Tsai-Wu models produce different outcomes for the same material properties, as they use different $\tilde{F}$, $\tilde{G}$ and $\tilde{H}$ parameters. Lode angles in plane stress are 0° under tensile loading and 60° under compressive loading; they vary in plane strain.

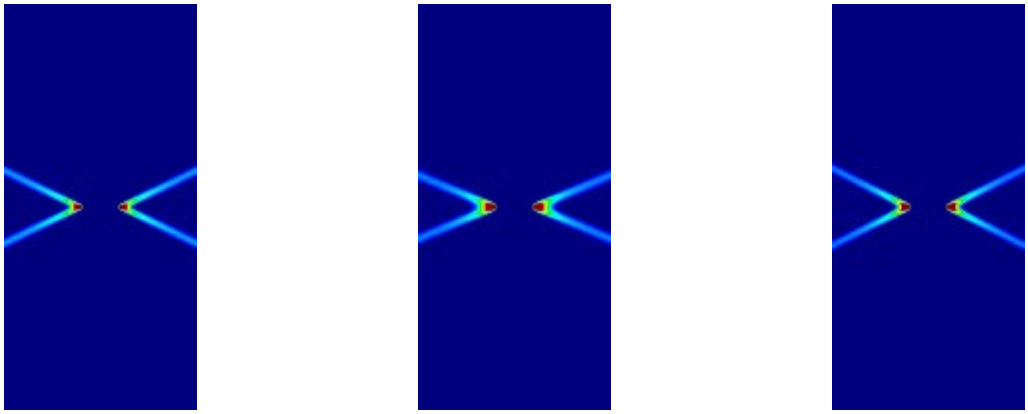

(**a**) (**b**) (**c**)

Figure 11. Strip under vertical **plane stress tension** (Cohesive-frictional models, $\kappa = 1.5$): (**a**) Parabolic Drucker-Prager; (**b**) Hoffman; (**c**) Tsai-Wu.

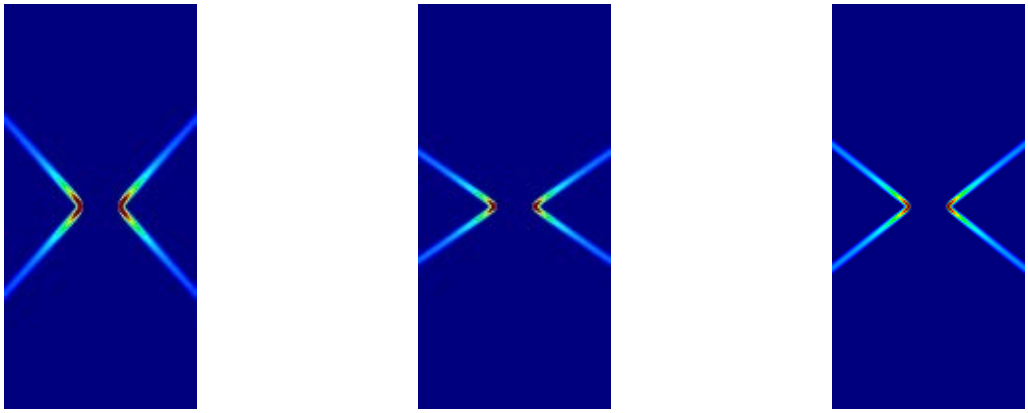

(**a**) (**b**) (**c**)

Figure 12. Strip under vertical **plane stress compression** (Cohesive-frictional models, $\kappa = 3.0$): (**a**) Parabolic Drucker-Prager; (**b**) Hoffman; (**c**) Tsai-Wu.

Table 8. Analytical and numerical Lode and strain localization angles for **frictional-cohesive** models under **plane stress tension**, $\kappa = 1.5$

$\boldsymbol{\kappa = 1.5}$	$\boldsymbol{\vartheta_{ana}}$	$\boldsymbol{\vartheta_{num}}$	$\boldsymbol{\theta_{ana}^{slip}}$	$\boldsymbol{\theta_{num}^{slip}}$
Drucker-Prager	0.0000°	0.7800°	24.0948°	24.2277°
Hoffman	0.0000°	0.5258°	22.2077°	22.1355°
Tsai-Wu	0.0000°	0.3457°	26.1746°	26.5651°

Table 9. Analytical and numerical Lode and strain localization angles for **frictional-cohesive** models under **plane stress compression**, $\kappa = 3.0$

$\boldsymbol{\kappa = 3.0}$	$\boldsymbol{\vartheta_{ana}}$	$\boldsymbol{\vartheta_{num}}$	$\boldsymbol{\theta_{ana}^{slip}}$	$\boldsymbol{\theta_{num}^{slip}}$
Drucker-Prager	60.0000°	59.6006°	48.1897°	48.8141°
Hoffman	60.0000°	58.6061°	35.2644°	35.4699°
Tsai-Wu	60.0000°	59.8503°	38.2620°	37.7757°

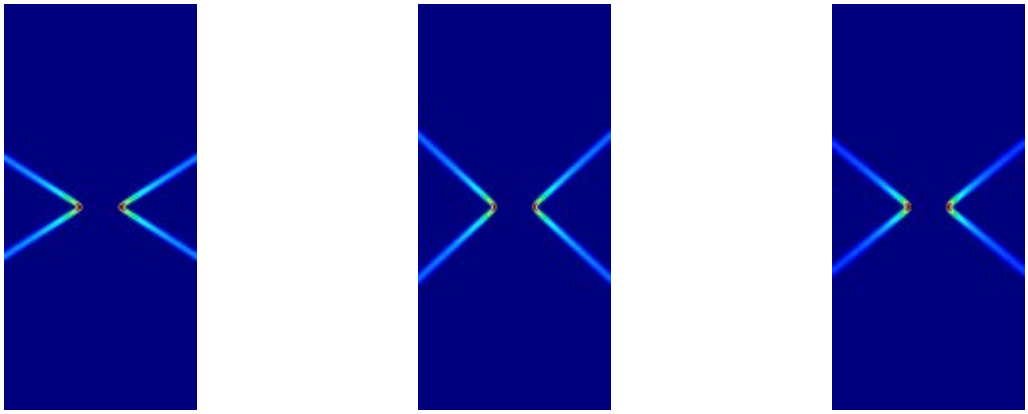

(**a**) (**b**) (**c**)

Figure 13. Strip under vertical **plane strain tension** (Cohesive-frictional models, $\kappa = 1.5$): (**a**) Parabolic Drucker-Prager; (**b**) Hoffman; (**c**) Tsai-Wu.

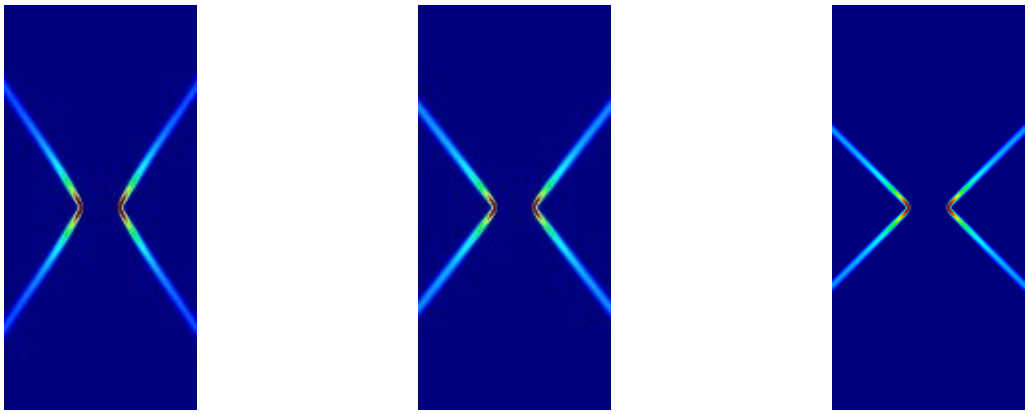

(**a**) (**b**) (**c**)

Figure 14. Strip under vertical **plane strain tension** (Cohesive-frictional models, $\kappa = 3.0$): (**a**) Parabolic Drucker-Prager; (**b**) Hoffman; (**c**) Tsai-Wu.

Table 10. Analytical and numerical Lode and strain localization angles for **frictional-cohesive** models under **plane strain tension**, $\kappa = 1.5$

$\kappa = 1.5$	ϑ_{ana}	ϑ_{num}	θ_{ana}^{slip}	θ_{num}^{slip}
Drucker-Prager	14.3077°	15.9519°	30.4411°	31.4875°
Hoffman	40.8934°	42.5043	41.3843°	41.5891°
Tsai-Wu	30.0000 °	30.7240°	38.3075°	38.2204°

Table 11. Analytical and numerical Lode and strain localization angles for **frictional-cohesive** models under **plane strain compression,** $\kappa = 3.0$

$\kappa = 3.0$	ϑ_{ana}	ϑ_{num}	θ_{ana}^{slip}	θ_{num}^{slip}
Drucker-Prager	17.1330°	17.6788°	56.6531°	57.5288°
Hoffman	8.9483°	7.8626°	51.6975°	50.7106°
Tsai-Wu	30.0000°	29.4419°	44.4488°	44.6397°

4.3. Prandtl's punch test

The second example is Prandtl's Punch test, a 2-D plane problem in which a flat rigid die punches into an elasto-plastic semi-infinite medium. Classical solutions to this problem for rigid-plastic materials are well-known.

As shown in Figure 15, the computational domain of the elasto-plastic medium is 10 m × 3 m (width × height). Boundary conditions consist of a fixed bottom edge, left and right edges horizontally restrained. Punching is applied by imposing an increasing vertical displacement at the base of the rigid die; the horizontal movement is restrained at this base.

Material properties are the same as for the strip under vertical loading. A regular mesh of 192,000 (800 × 240) square B-bar elements (0.0125 m × 0.0125 m) is used. In all cases, 1,000 time steps are performed to complete the analyses.

The mechanics of the failure are as follows. Plastic yielding starts at the singular points at the extreme ends of the rigid die. From here, two slip lines dig into the supporting elasto-plastic medium at diverging angles. Further loading causes the formation of a collapse mechanism in which the triangular wedge of material immediately under the punch moves vertically, causes the outward lateral displacement of adjoining material and the upwards displacement of the material located in the triangular wedges close to the surface and next to flat punch.

Figure 16 shows the numerically obtained failure mechanisms for the four different cases studied, depending on the plastic criterion used in each one: (**a**) isotropic pressure-independent von Mises; (**b**) isotropic pressure-dependent Parabolic Drucker-Prager, $\kappa = 3.0$; (**c**) orthotropic Hoffman, $\kappa = 3.0$ in the horizontal direction; and (**d**) orthotropic Tsai-Wu, $\kappa = 3.0$, in the horizontal direction. Associated perfect plasticity is used, so that the plastic potential coincides with the described yield criteria. The plots are zoomed in the region of interest, with identical magnification.

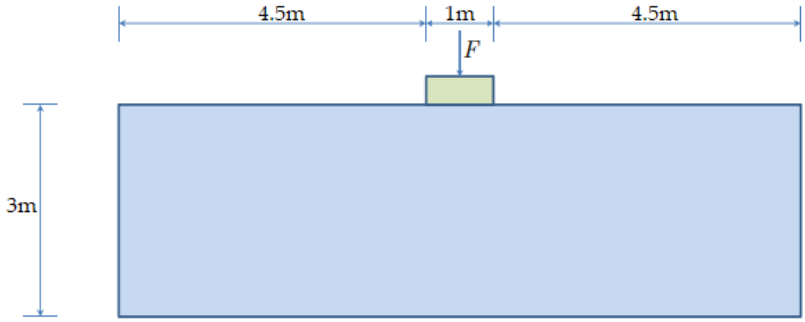

Figure 15. Geometry Prandtl's Punch test. The bottom edge is fixed in both directions, while the left and right edges are constrained along the horizontal direction.

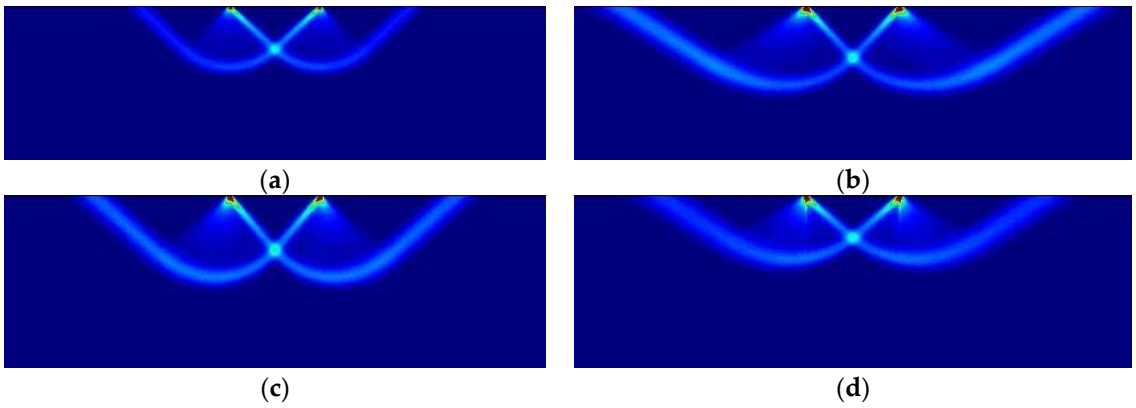

Figure 16. Prandtl's Punch test: (**a**) von Mises; (**b**) Parabolic Drucker-Prager, $\kappa = 3.0$; (**c**) Hoffman, $\kappa = 3.0$; (**d**) Tsai-Wu, $\kappa = 3.0$.

As can be observed, similar but notably different failure mechanisms form depending on the plastic potential that applies. Although the process of the formation of the slip lines and the failure mechanism is analogous in all cases, the observed discrepancies in the slopes of the slip lines, and the corresponding amounts of mobilized material, depend on the plastic material properties.

Contrariwise to the case studied in the previous Section, here the stress field is known a-priori. Furthermore, substantial stress redistribution happens in the transition between the initial elastic stage and the final elasto-plastic state in which the failure mechanism is completely formed and yielding. This can be observed in Figure 17, where the distribution of the principal stresses in the elastic (initial) and plastic (stationary) states in the region below the punch are compared for the Drucker-Prager case (b). It can be seen that the stress state in the elastic range consists mainly of vertical stress σ_{yy} and the corresponding out of plane σ_{zz} (not shown in the Figure), due to Poisson's ratio $\nu = 0.2$. In contrast, in the stationary plastic stress state, in-plane horizontal σ_{xx} have noticeably developed.

The extension and nature of this stress redistribution is further investigated in Figure 18, where the evolution of the normal stress components $\sigma_{xx}, \sigma_{yy}, \sigma_{zz}$ against the vertical displacement of the die is plotted for the four cases. The stresses are sampled at the corresponding crossing point of the slip lines, in the symmetry axis below the center of the punch. Figure 19 further summarizes the comparison of stress evolution by plotting the evolution of the stress Invariant I_1 and the Lode angle ϑ.

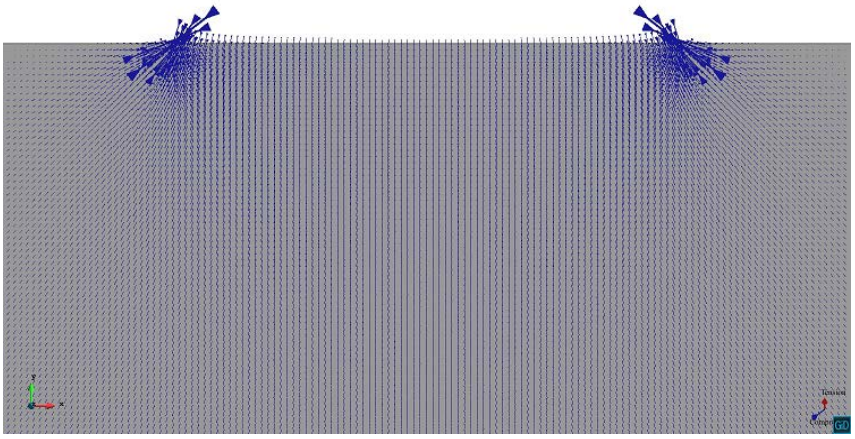

(**a**)

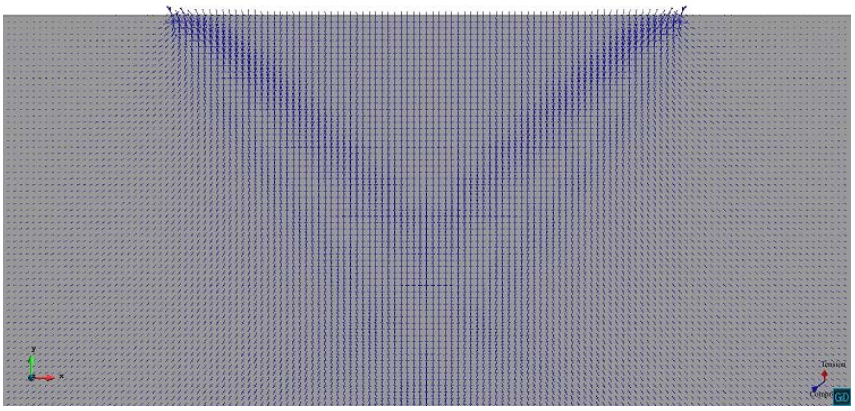

(**b**)

Figure 17. Directions of principal stresses below the rigid footing of Prandtl's Punch test (Parabolic Drucker-Prager, $\kappa = 3.0$): (**a**) Elastic stage; (**b**) Final plastic stage.

Several remarks are in order: (a) the extension of the transition phase largely differs from one case to the other; it is shorter for von Mises and longer for Drucker-Prager; (b) due to increasing vertical loading, the out of plane σ_{zz} develops due to the plane strain constraint; (c) concurrently, the in-plane horizontal σ_{xx} also develop, very much depending on the yield criterion; this later development shows the frictional and/or orthotropic nature of the plastic behavior.

It can be verified that this stress redistribution during the formation of the slip lines occurs precisely as dictated by the strain localization condition. This is done in Table 12 by comparing the value $\theta_{\text{num}}^{\text{slip}}$, measured directly from Figure 16, with the value $\theta_{\text{ana}}^{\text{slip}}$, obtained by applying the analytical condition (Section 3.2.2 and 3.5.2) to the numerically obtained values for the stresses. The correspondence between both value is remarkable.

Table 12. Stresses and localization angle in Prandtl's Punch test

$\kappa = 3$	σ_{xx}	σ_{yy}	σ_{zz}	ϑ_{num}	$\theta_{\text{num}}^{\text{slip}}$	$\theta_{\text{ana}}^{\text{slip}}$
VM	−18286	−29832	−24061	29.9902°	45.0000°	45.0000°
Drucker-Prager	−104260	−220560	−171920	24.6035°	50.1944°	49.9512°
Hoffman	−57783	−97541	−92394	6.8372°	48.9909°	48.4646°
Tsai-Wu	−72007	−69365	−56219	8.9246°	41.1859°	40.6354°

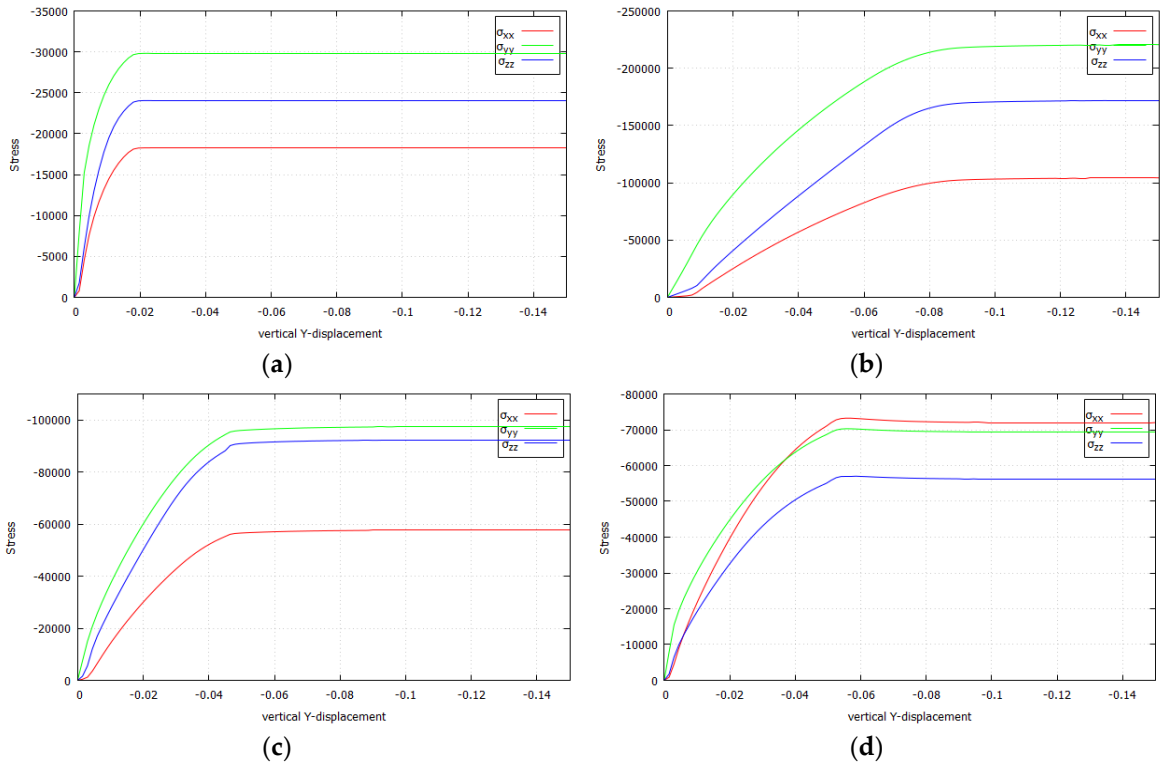

Figure 18. Stresses where the slide lines of Prandtl's Punch test (Plane Strain, $\kappa = 3.0$): (**a**) von Mises; (**b**) Parabolic Drucker-Prager; (**c**) Hoffman; (**d**) Tsai-Wu.

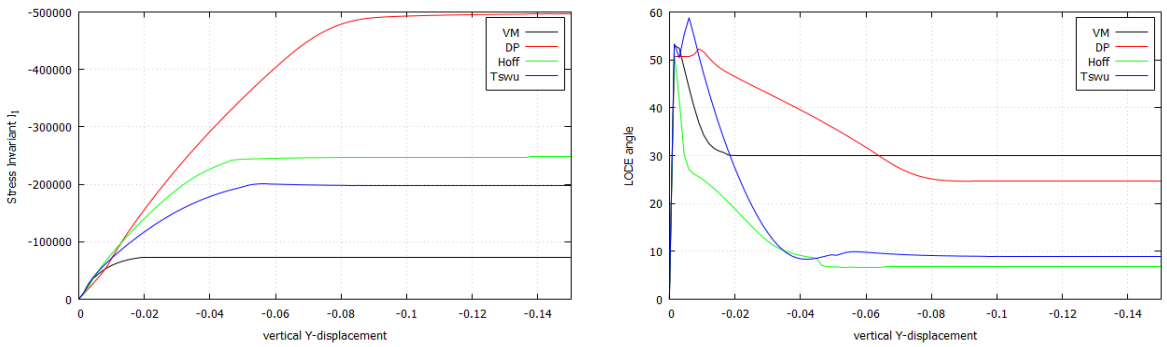

(**a**) (**b**)

Figure 19. Results comparison where the slide lines cross (Plane Strain, $\kappa = 3.0$): (**a**) Stress Invariant I_1; (**b**) Lode angle ϑ.

5. Conclusions

In this work, the strain localization analysis of cohesive-frictional elasto-plastic materials is addressed which applies to both strong and regularized slip lines and surfaces. Maxwell kinematics, stress boundedness and plastic consistency are invoked to derive the necessary strain localization conditions. Contrariwise to the usually studied conditions for strain bifurcation, these proffer requirements that do not depend on the elastic properties of the medium, but only on the plastic flow provided by the adopted plastic potential.

Expanding on previous works, application of the above localization conditions to isotropic and orthotropic cohesive-frictional plastic models derives analytical solutions for the strain localization angle and the slopes of the ensuing slip lines. The distinct effects of compressive and tensile loading are also evaluated.

The analytical results are validated independently by 2-D plane stress and plane strain FE simulations using the B-bar element; namely, a strip under vertical tension and compression tests and Prandtl's punch problem are investigated. In the first problem, the far field stress state is known and the analytical results can be verified directly from the numerical simulations. In the second problem, once the failure mechanism and the corresponding stress field are computationally evaluated, these are shown to conform precisely with those anticipated by the strain localization condition.

Author Contributions: Conceptualization and methodology, M. Cervera; software, M. Chiumenti and M. Cervera; data curation and writing—original draft preparation, S. Kim; writing—review and editing, M. Cervera and J.Wu; All authors have read and agreed to the published version of the manuscript.

Funding: Financial support from the European Union Horizon 2020 research and innovation programme (H2020-DT-2019-1 No. 872570) under the KYKLOS 4.0 Project (An Advanced Circular and Agile Manufacturing Ecosystem based on rapid reconfigurable manufacturing process and individualized consumer preferences), the Severo Ochoa Program for Centers of Excellence in R&D (CEX2018-000797-S) and the Catalan Government ACCIO - Ris3cat Transport and PRO2 Projects is gratefully acknowledged as well as the support of the Agència de Gestió d'Ajuts Universitaris i de Recerca (AGAUR) and the European Social Fund (ESF) to S. Kim through the predoctoral FI grants (ref. num.2019FI-B00727). This work is also funded by the National Natural Science Foundation of China (51878294;51678246), the State Key Laboratory of Subtropical Building Science (2018ZC04) to J.Y. Wu.

Conflicts of Interest: The authors declare no conflict of interest.

Appendix A. Stress Invariants and Lode angle

The first, second, and third invariants of the stress tensors are

$$I_1 = \sigma_{11} + \sigma_{22} + \sigma_{33} \tag{A1a}$$

$$I_2 = \sigma_{11}\sigma_{22} + \sigma_{22}\sigma_{33} + \sigma_{11}\sigma_{33} - \sigma_{12}^2 - \sigma_{23}^2 - \sigma_{31}^2 \tag{A1b}$$

$$I_3 = \sigma_{11}\sigma_{22}\sigma_{33} + 2\sigma_{12}\sigma_{23}\sigma_{31} - \sigma_{12}^2\sigma_{33} - \sigma_{23}^2\sigma_{11} - \sigma_{31}^2\sigma_{22} \tag{A1c}$$

The second and third invariants of the deviatoric stress tensors are

$$J_2 = \frac{1}{3}I_1^2 - I_2 \tag{A2a}$$

$$J_3 = \frac{2}{27}I_1^3 - \frac{1}{3}I_1 I_2 + I_3 \tag{A2b}$$

Lode Angle (positive cosine) $\left[0 \le \vartheta \le \frac{\pi}{3}\right]$ is defined from these deviatoric stress invariants as

$$\vartheta = \frac{1}{3}\arccos\left(\frac{J_3}{2}\left(\frac{3}{J_2}\right)^{3/2}\right) \tag{A3}$$

Appendix B. Tilting of the material axes with respect the global axes

In this Appendix, the effect of the tilting of the orthotropy material axes with respect the global axes and the orientation of the loading is demonstrated. The tilt angle α is measured counter-clockwise between the global x and the material 1 axes. The rotation transformation matrix was introduced in **Remark 3.6**.

Figure B1 and Table B1 show the results for the trip under vertical plane strain tension (Parabolic Drucker-Prager, κ=1.5) and different tilting; as the model is isotropic, the results are insensitive to the rotation of the material axes.

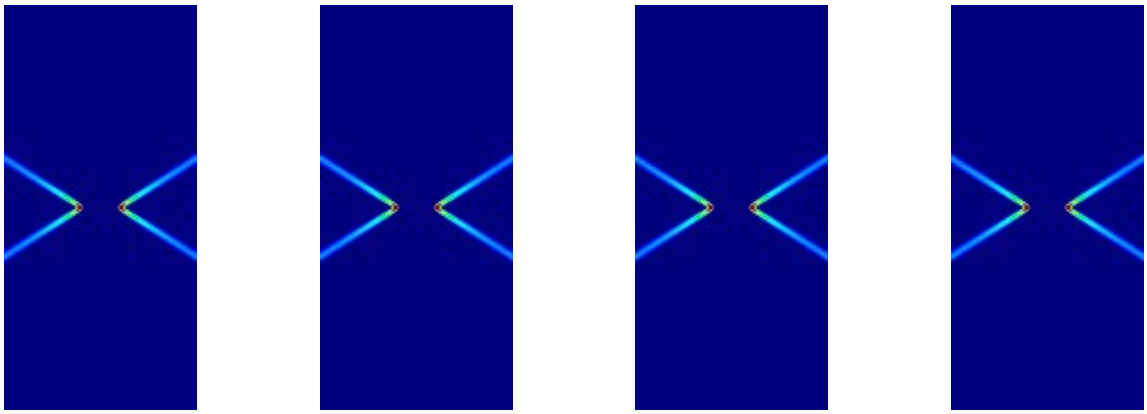

(**a**) (**b**) (**c**) (**d**)

Figure B1. Strip under vertical **plane strain tension** (Parabolic Drucker-Prager, κ = 1.5): (**a**) α = 0°; (**b**) α = 30°; (**c**) α = 45°; (**d**) α = 60°.

Table B1. Analytical and numerical Lode and strain localization angles for **Parabolic Drucker- Prager** under **plane strain tension**, κ = 1.5

α	$\vartheta_{\mathbf{ana}}$	$\vartheta_{\mathbf{num}}$	$\theta_{\mathbf{ana}}^{\mathbf{slip}}$	$\theta_{\mathbf{num}}^{\mathbf{slip}}$
0°	14.3077°	15.9519°	30.4411°	31.4875°
30°	14.3077°	15.9519°	30.4411°	31.4875°
45°	14.3077°	15.9519°	30.4411°	31.4875°
60°	14.3077°	15.9519°	30.4411°	31.4875°

Figure B2 and Table B2 show corresponding results for the orthotropic Hoffman model, $\kappa = 1.5$. Here, the effect of the tilting of the material axes is evident. Analytical and numerical results coincide for all slip lines.

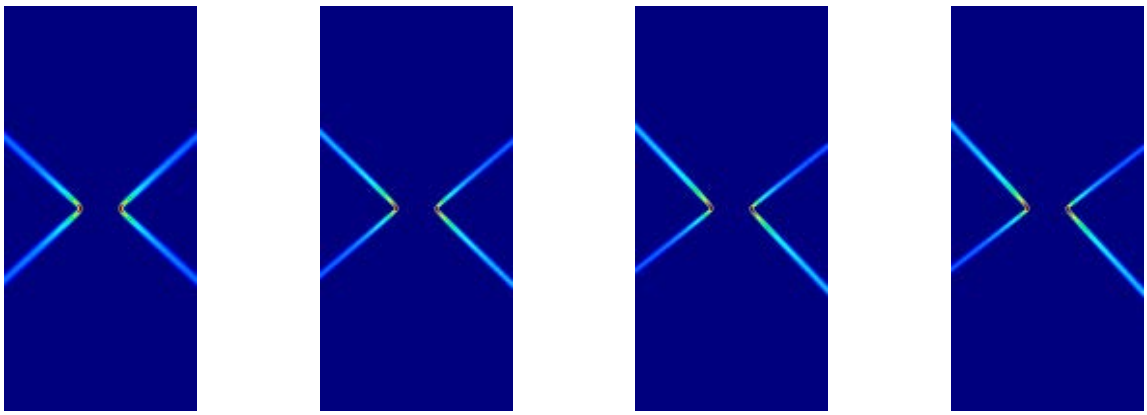

(**a**) (**b**) (**c**) (**d**)

Figure B2. Strip under vertical **plane strain tension** (Hoffman, $\kappa = 1.5$): (**a**) $\alpha = 0°$; (**b**) $\alpha = 30°$; (**c**) $\alpha = 45°$; (**d**) $\alpha = 60°$.

Table B2. Analytical and numerical Lode and strain localization angles for **Hoffman** under **plane strain tension**, $\kappa = 1.5$

α	ϑ_{ana}	ϑ_{num}	θ_{ana}^{slip}	θ_{num}^{slip}
0°	40.8934°	42.5043°	41.3843°, 41.3843°	41.5891°, 41.5891°
30°	35.4964°	35.5087°	39.4100°, 43.0613°	39.5226°, 43.1524°
45°	30.0000°	30.0031°	37.4491°, 45.0000°	37.7757°, 45.0000°
60°	24.5036°	24.8814°	36.9016°, 45.7565°	36.8699°, 45.7073°

Finally, Figure B3 shows the effect of the tilting of the material axes in Prandtl's punch test (Plane Strain, Hoffman model, $\kappa = 3.0$).

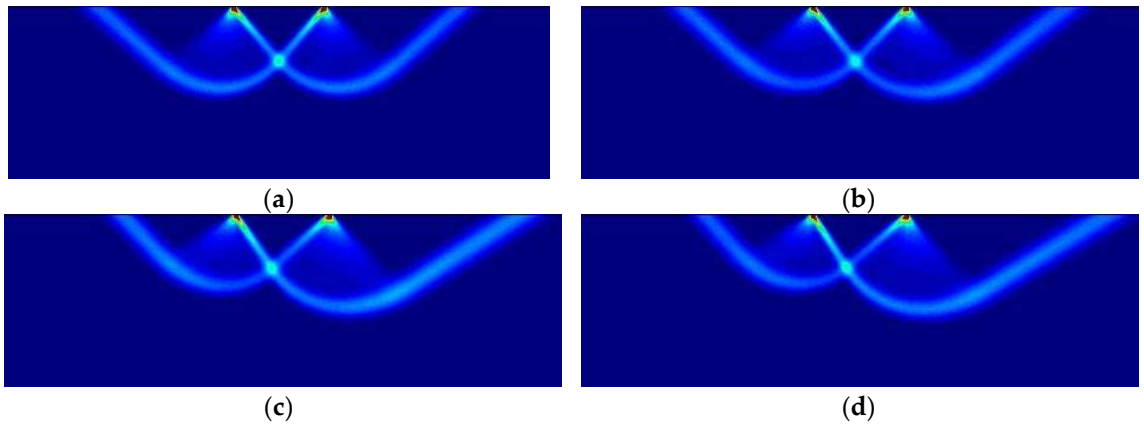

(**a**) (**b**) (**c**) (**d**)

Figure B3. Prandtl's Punch test (Plane Strain, Hoffman, $\kappa = 3.0$): (**a**) $\alpha = 0°$; (**b**) $\alpha = 30°$; (**c**) $\alpha = 45°$; (**d**) $\alpha = 60°$.

References

1. Hill, R. Constitutive modelling of orthotropic plasticity in sheet metals. *Journal of the Mechanics and Physics of Solids* **1990**, Volume 38, Issue 3, pp. 405–417. https://doi.org/10.1016/0022-5096(90)90006-P
2. Hill, R. A user-friendly theory of orthotropic plasticity in sheet metals. *Journal of the Mechanics and Physics of Solids* **1993**, Volume 35, Issue 1, pp. 19-25. https://doi.org/10.1016/0020-7403(93)90061-X
3. Hill, R. On the mechanics of localized necking in anisotropic sheet metals. *Journal of the Mechanics and Physics of Solids* **2001**, Volume 49, Issue 9, pp. 2055-2070. https://doi.org/10.1016/S0022-5096(01)00031-X
4. Drucker, D.C; Prager, W; Greenberg, H. Extended limit design theorems for continuous media. *Quarterly of Applied Mathematics* **1952**, Volume 9, pp. 381-389. https://doi.org/10.1090/qam/45573
5. Drucker, D.C; Prager, W. Soil Mechanics and Plastic Analysis on Limit Design. *Journal of applied Mathematics* **1952**, Volume 10, pp. 157-165.
6. Drucker, D.C. Limit analysis of two and three dimensional soil mechanics problems. *Journal of the Mechanics and Physics of Solids* **1953**, Volume 1, Issue 4, pp. 217-226. https://doi.org/10.1016/0022-5096(53)90001-5
7. Drucker, D.C.; Gibson, R.E.; and Henkel, DJ. Soil Mechanics and Work-Hardening Theories of Plasticity. *Transactions of the American Society of Civil Engineers* **1957**, Volume 122, Issue 1, pp. 338-346
8. Hoffman, O. The Brittle Strength of Orthotropic Materials. *Journal of Composite Materials* **1967**, Volume 1, Issue 2, pp. 200-206. https://doi.org/10.1177/002199836700100210
9. Tsai, S.W.; Wu, E.M. A General Theory of Strength for Anisotropic Materials. *Journal of Composite* Materials **1971**, Volume 5, Issue 1, pp. 58-80. https://doi.org/10.1177/002199837100500106
10. Karafillis, A.P.; Boyce, M.C. A general anisotropic yield criterion using bounds and a transformation weighting tensor. *Journal of the Mechanics and Physics of Solids* **1993**, Volume 41, Issue 12, pp. 1859–1886. https://doi.org/10.1016/0022-5096(93)90073-O
11. Deshpande, V.S.; Fleck, N.A.; Ashby, M. F. Effective properties of the octet-truss lattice material. *Journal of the Mechanics and Physics of Solids* **2001**, Volume 49, Issue 8, pp. 1747–1769. https://doi.org/10.1016/S0022-5096(01)00010-2
12. Cazacu, O.; Plunkett, B.; Barlat, F. Orthotropic yield criterion for hexagonal closed packed metals. *International Journal of Plasticity* **2001**, Volume 22, Issue 7, pp. 1171–1194. https://doi.org/10.1016/j.ijplas.2005.06.001
13. Galavi, V; Schweiger, H.F. Nonlocal Multilaminate Model for Strain Softening Analysis. *International Journal of Geomechanics* **2010**, Volume 10, Issue 1, pp. 30-44. https://doi.org/10.1061/(ASCE)1532-3641(2010)10:1(30)
14. Prandtl, L. Über die Härte plastischer Körper. *Nachrichten der Gesellschaft der Wissenschaften zu Göttingen, Mathematisch physikalische Klasse* **1920**, pp. 74–85 (In German). https://doi.org/10.1007/978-3-662-11836-8_7
15. Hencky, H. Über Einige Statisch Bestimmte Fälle Des Gleichgewichts In Plastischen Körpern. *Zeitschrift für Angewandte Mathematik und Mechanik* **1923**, Volume 3, Issue 4, pp. 241-251 (In German). https://doi.org/10.1002/zamm.19230030401
16. Hencky, H. Zur Theorie plastischer Deformationen und der hierdurch im Material hervorgerufenen Nachspannungen. *Zeitschrift für Angewandte Mathematik und Mechanik* **1924**, Volume 4, Issue 4, pp. 323-334 (In German). https://doi.org/10.1002/zamm.19240040405
17. Mandel, J. Sur les équilibres par tranches planes des corps solides à la limite d'écoulement. Thèses de docteur ès-sciences, Université de Lyon, Lyon, 1942. (In French). http://www.numdam.org/issue/THESE_1942__251__1_0.pdf
18. Hill, R. A general theory of uniqueness and stability in elastic-plastic solids. *Journal of the Mechanics and Physics of Solids* **1958**, Volume 6, Issue 3, pp. 236–249. https://doi.org/10.1016/0022-5096(58)90029-2
19. Hill, R. Acceleration waves in solids. *Journal of the Mechanics and Physics of Solids* **1962**, Volume 10, Issue 1, pp. 1–16. https://doi.org/10.1016/0022-5096(62)90024-8
20. Thomas, T.Y. *Plastic Flow and Fracture of Solids*. Academic Press, New York, USA, 1961
21. Rice, J.R. A path independent integral and the approximate analysis of strain concentration by notches and cracks. *Journal of Applied Mechanics* **1968**, Volume 35, Issue 2, pp. 379-386. https://doi.org/10.1115/1.3601206
22. Rice, J.R. Plane strain slip line theory for anisotropic rigid/plastic materials. *Journal of the Mechanics and Physics of Solids* **1973**, Volume 21, Issue 2, pp. 63-74. https://doi.org/10.1016/0022-5096(73)90030-6

23. Leroy, Y.; Ortiz, M. Finite element analysis of transient strain localization phenomena in frictional solids. *International journal for numerical and analytical methods in geomechanics* **1990**, Volume 14, Issue 2, pp. 93-124. https://doi.org/10.1002/nag.1610140203
24. Forest, S.; Blazy, J.-S.; Chastel, Y.; Moussy, F. Continuum modeling of strain localization phenomena in metallic foams. *Journal of Materials Science* **2005**, Volume 40, Issue 22, pp. 5903-5910. https://doi.org/10.1007/s10853-005-5041-6
25. Borja, R.I. A finite element model for strain localization analysis of strongly discontinuous fields based on standard Galerkin approximation. *Computer Methods in Applied Mechanics and Engineering* **2000**. Volume 190, Issues 11-12, pp. 1529-1549. https://doi.org/10.1016/S0045-7825(00)00176-6
26. Borja, R.I. Finite element simulation of strain localization with large deformation: capturing strong discontinuity using a Petrov–Galerkin multiscale formulation. *Computer Methods in Applied Mechanics and Engineering* **2002**. Volume 191, Issues 27-28, pp. 2949-2978. https://doi.org/10.1016/S0045-7825(02)00218-9
27. Kuhl, E; Ramm, E; Willam, K. Failure analysis of elasto-plastic material models on different levels of observation, *International Journal of Solids and Structures* **2000**, Volume 37, Issues 48–50, pp. 7259-7280. https://doi.org/10.1016/S0020-7683(00)00198-0
28. Liebe, T.; Willam, K. Localization Properties of Generalized Drucker-Prager Elastoplasticity. *Journal of Engineering Mechanics* **2001**, Volume 127, Issue 6, pp. 616–619. https://doi.org/10.1061/(ASCE)0733-9399(2001)127:6(616)
29. Vrech, S.M.; Etse, G. Geometrical localization analysis of gradient-dependent parabolic Drucker–Prager elastoplasticity. *International Journal of Plasticity* **2006**, Volume 22, Issue 5, pp. 943-964. https://doi.org/10.1016/j.ijplas.2005.07.002
30. Zhang, Y.Q.; Lu, Y.; Qiang, H.F. Influence of damage on properties of strain localization in geomaterials at plane stress and plane strain. *Archive of Applied Mechanics* **2004**, Volume 74, Issues 1-2, pp. 102–117. https://doi.org/10.1007/BF02637212
31. Tasan, C.C.; Hoefnagels, J.P.M.; Diehl, M.; Yan, D.; Roters, F.; Raabe, D. Strain localization and damage in dual phase steels investigated by coupled in-situ deformation experiments and crystal plasticity simulations. *International Journal of Plasticity* **2014**, Volume 63, pp. 198-210. https://doi.org/10.1016/j.ijplas.2014.06.004.
32. Simo, J.C.; Oliver, J.; Armero, F. An analysis of strong discontinuities induced by strain-softening in rate-independent inelastic solids. *Computational Mechanics* **1993**, Volume 12, Issues 5, pp. 277–296. https://doi.org/10.1007/bf00372173
33. Oliver, J. Modelling strong discontinuities in solid mechanics via strain softening constitutive equations. Part 1: Fundamentals. *International Journal for Numerical Methods in* Engineering **1996**, Volume 39, Issues 21, pp. 3575-3600. https://doi.org/10.1002/(SICI)1097-0207(19961115)39:21<3575::AID-NME65>3.0.CO;2-E
34. Oliver, J. Modelling strong discontinuities in solid mechanics via strain softening constitutive equations. Part 2: Numerical simulation. *International Journal for Numerical Methods in Engineering* **1996**, Volume 39, Issues 21, pp. 3601-3623. https://doi.org/10.1002/(SICI)1097-0207(19961115)39:21<3601::AID-NME64>3.0.CO;2-4
35. Oliver, J.; Cervera, M; Manzoli, O. Strong discontinuities and continuum plasticity models: the strong discontinuity approach. *International Journal of Plasticity* **1999**, Volume 15, Issue 3, pp. 319-351. https://doi.org/10.1016/S0749-6419(98)00073-4
36. Oliver, J. On the discrete constitutive models induced by strong discontinuity kinematics and continuum constitutive equations. *International Journal of Solids and Structures* **2000**, Volume 37, Issues 48–50, pp. 7207-7229. https://doi.org/10.1016/S0020-7683(00)00196-7
37. Cervera, M; Chiumenti, M.; Capua, D.D. Benchmarking on bifurcation and localization in J2 plasticity for plane stress and plane strain conditions. *Computer Methods in Applied Mechanics and Engineering* **2012**, Volumes 241–244, pp. 206-224. https://doi.org/10.1016/j.cma.2012.06.002
38. Cervera, M; Wu, J.Y.; Chiumenti, M; Kim, S. Strain localization analysis of Hill's orthotropic elastoplasticity: analytical results and numerical verification. *Computational Mechanics* **2020**, Volume 65, pp. 533–554. https://doi.org/10.1007/s00466-019-01782-4
39. Wu, J.Y.; Cervera, M. On the equivalence between traction- and stress-based approaches for the modeling of localized failure in solids. *Journal of the Mechanics and Physics of Solids* **2015**, Volume 82, pp. 137–163. https://doi.org/10.1016/j.jmps.2015.05.016

773 40. Wu, J.Y.; Cervera, M. A thermodynamically consistent plastic-damage framework for localized failure in
774 quasi-brittle solids: Material model and strain localization analysis. *International Journal of Solids and*
775 *Structures* **2016**, Volumes 88-89, Issues 227–247. https://doi.org/10.1016/j.ijsolstr.2016.03.005
776 41. Wu, J.Y.; Cervera, M. Strain Localization of Elastic-Damaging Frictional-Cohesive Materials: Analytical
777 Results and Numerical Verification. *Materials* **2017**, Volume 10, Issue 4, pp. 434.
778 https://doi.org/10.3390/ma10040434
779 42. Hughes, T. J. R. Generalization of selective integration procedures to anisotropic and nonlinear media.
780 *International Journal for Numerical Methods in Engineering* **1980**, Volume 15, Issue 9, pp. 1413–1418.
781 https://doi.org/10.1002/nme.1620150914

On the mechanics of strain localization in plasticity: Isotropic and orthotropic, elasto and rigid-plastic, associated and non-associated models (under review)

M. Cervera, J.Y. Wu, S. Kim and M. Chiumenti

Mechanics of Materials

Editor-in-Chief: Prof. Ghatu Subhash and Prof. Dr. Jean-Francois Molinari

PRINT ISSN: 0167-6636

Journal Editors - Elsevier

On the mechanics of strain localization in plasticity: Isotropic and orthotropic, elasto- and rigid-plastic, associated and non-associated models

Miguel Cervera[b], Jian-Ying Wu[a,*], Sungchul Kim[b], Michele Chiumenti[b]

[a] *State Key Laboratory of Subtropic Building Science, South China Univeristy of Technology, 510641 Guangzhou, China.*
[b] *CIMNE, Technical University of Catalonia, Edificio C1, Campus Norte, Jordi Girona 1-3, 08034 Barcelona, Spain.*

Abstract

As strain localization is usually prognostics of localized failure in solids and structures, prediction of its occurrence and quantification its adverse effects are of both theoretical and practical significance. Regarding plastic solids, onset of strain localization was presumed to be coincident with strain bifurcation, and the discontinuous bifurcation analysis was usually adopted to determine the discontinuity orientation though it does not apply to rigid-plastic solids. However, recent studies indicate that strain bifurcation and localization correspond to distinct stages of localized failure and should be dealt with separately. In this work the mechanics of strain localization is addressed for perfect and softening plasticity in the most general context. Both isotropic and orthotropic, elasto- and rigid-plastic solids with associated and non-associated flow rules are analytically considered and numerically validated, extending our previous work on softening plasticity with associated evolution laws. In addition to Maxwell's kinematics and continuity of the traction rate for strain bifurcation, a novel necessary condition, i.e., the stress rate objectivity (independent from the discontinuity bandwidth), and the resulting kinematic and static constraints, are derived for the occurrence of strain localization. In particular, the localization angles of the discontinuity band (surface) depend only on the specific stress state and the plastic flow tensor, relevant neither to the material elastic constants nor to the plastic yield function. Moreover, it is found that a transition stage generally exists in the case of plane strain during which the orientation of plastic flow rotates progressively such that strain localization may occur. Back-to-back numerical predictions of some benchmark problems, involving both perfect and softening plasticity, sufficiently justify the analytical results.

Keywords:
Localized failure, plasticity, strain localization, strain bifurcation, discontinuities.

1. Introduction

As a typical phenomenon of localized failure in solids and structures, strain localization is manifested by highly non-uniform deformations concentrated within narrow bands of dimensions much smaller than the structural size. It leads to strain (weak) or even displacement (strong) discontinuities across the localization band, triggering substantial

*Tel.: (+86) 20-87112787
Email address: jywu@scut.edu.cn (Jian-Ying Wu)

loss of integrity and safety or even collapse of structures. Consequently, quantification of strain localization is of both theoretical and practical significance in the prevention of localized failure for structural designs.

In the context of shear-driven "slip lines" in pressure independent rigid-plastic solids, strain localization was first studied in the seminal works of Prandtl (1920); Hencky (1923, 1924); Mandel (1942). This problem was later revisited by Hill (1950) and the "slip lines" were interpreted as the characteristic lines of the underlying governing equations of hyperbolic type. In these early works, only rigid-plasticity with no elastic deformations was considered, and incompressible behavior prior to shear-driven plastic yielding was assumed.

Strain localization in elastoplastic solids was later investigated by Hill (1958, 1962); Thomas (1961); Rice (1968) as a bifurcation problem. Upon the assumption of linear comparison (artificial) solids (i.e., plastic loading both inside and outside the discontinuity band), a strain bifurcation condition, i.e., singularity of the elastoplastic acoustic tensor, is derived from the combination of Maxwell's kinematics and traction rate continuity condition across the discontinuity band. One noteworthy result is that strain bifurcation always occurs at the hardening stages, i.e., $H_b \geq 0$, for non-associated plastic materials (Rudnicki and Rice, 1975). Moreover, closed-form results for the discontinuity orientation and the associated hardening/softening moduli were obtained for the 2-D plane stress and plane strain conditions (Runesson et al., 1991). In the computational context, the above bifurcation condition with null hardening modulus was recommended to determine the discontinuity orientation in embedding weak or strong discontinuities into finite elements (Simó et al., 1993; Oliver, 1996; Oliver et al., 1999).

Though the above bifurcation analysis has been widely adopted, two issues cannot be overlooked. On the one hand, the strain bifurcation analysis does not apply to rigid-plastic solids since there is no elastic strain and the stiffness tensor is undetermined. Consequently, the stress cannot be directly given from the elastoplastic constitutive relation, and the elastoplastic acoustic tensor is no longer well-defined. This makes unseemly the strain bifurcation analysis in rigid-plastic solids since it cannot be formulated as an equilibrium/stiffness problem.

On the other hand, the elastoplastic acoustic tensor depends on the hardening/softening modulus H, so do the bifurcation condition and the resulting discontinuity orientation. As clarified in Rice and Rudnicki (1980); Borré and Maier (1989), for the more frequently encountered incrementally nonlinear (real) material (i.e., inelastic loading inside the discontinuity band and elastic unloading outside it) the standard bifurcation analysis gives only the upper bound of strain localization. That is, though the initial bifurcation point corresponding to the largest hardening/softening modulus H_b can be uniquely determined, strain localization is still indefinite and it can occur at any instant for $H \leq H_b$. Moreover, even if the hardening/softening modulus H is specified *a priori* in an *ad hoc* manner, there may exist several solutions that fulfill the bifurcation condition. For instance, regarding the non-associated Mohr elastoplastic material, at least two valid solutions, one corresponding to Mohr's solution (Mohr, 1900) and the other to Roscoe's solution (Roscoe, 1970), exist at the peak of the stress – strain relation ($H = 0$); see Ottosen and Runesson (1991). Consequently, if the discontinuity orientation is fixed at such detected bifurcation points, it is unavoidable to get pathological results in the computational context (Oliver et al., 1999). In particular, stress locking occurs due to the mis-prediction of the discontinuity orientation (Oliver et al., 2012).

As the standard bifurcation analysis is not sufficient to determine the occurrence of strain localization, a more stringent condition needs to be introduced. To this end, the authors (Cervera et al., 2012) proposed using the stress (rate) boundedness condition to determine the discontinuity orientation of associated von Mises (J_2) plastic materials. This condition was extended to isotropic elastoplastic models with general failure criteria (e.g., Rankine, von Mises, Mohr-Coulomb, Drucker-Prager, and other more complex ones) (Wu and Cervera, 2014, 2015, 2016), to orthotropic plastic ones (Cervera et al., 2020; Kim et al., 2021), and also to strain-based damage models (Wu and Cervera, 2017). Not only the discontinuity orientation but also the localized model upon strain localization, i.e., constitutive relations, evolution equations, traction-based failure criterion, softening functions, etc., can be determined consistently from a given material model (Wu and Cervera, 2015, 2016).

For the case of inelastic loading inside the discontinuity band and elastic unloading outside it, the stress (rate) boundedness condition is more constrictive than the traction (rate) continuity adopted in the strain bifurcation one. Remarkably, for isotropic and orthotropic elasto-plastic materials with associated evolution laws, the discontinuity orientation predicted from the stress (rate) boundedness condition depends exclusively on the plastic flow tensor, independent of the elastic properties and the hardening/softening modulus. This is contradicting from the predictions given by the strain bifurcation condition. Extensive numerical simulations (Cervera et al., 2012, 2015; Li et al., 2018; Cervera et al., 2020) confirmed the analytical solutions with no *a priori* known information in the finite element simulations. These numerical results justify the stress (rate) boundedness condition for strain localization in plastic solids with associated flow rules and under the loading/unloading scenarios. Nevertheless, the not unusual loading/loading scenarios and the practically more encountered non-associated plastic flow rules remain to be investigated.

In this work the mechanics of strain localization is addressed in the more general cases. Isotropic and orthotropic, rigid-plastic or elastoplastic solids with associated or non-associated evolution laws are analytically considered and numerically validated, extending our previous work on softening plasticity with associated evolution laws. An extra necessary condition, i.e., the stress rate objectivity (independent of the discontinuity bandwidth), in addition to Maxwell's kinematics and continuity of the traction (rate) for strain bifurcation, is postulated for the occurrence of strain localization in perfectly or softening plastic solids. Both the loading/unloading and loading/loading scenarios are accounted for. This incorporates the "slip-line" or "zero rate of extension" for rigid-plastic solids (Hill, 1950) and elastoplastic soils (Roscoe, 1970) as particular cases. And the previously proposed stress rate boundedness condition is also recovered as a particular case of strong discontinuities or regularized ones with a vanishing bandwidth, respectively, under the loading/unloading scenario.

The remainder of this paper is structured as follows. Section 2 presents briefly the kinematics, constitutive relations and statics for the analysis of strain localization. Section 3 is devoted the mechanics of strain localization in the continuum setting. Plastic yielding, strain bifurcation and strain localization are regarded as distinct stages of the whole failure process of elasto- and rigid-plastic solids. The difference and correlation between stain bifurcation and strain localization is discriminated. The analytical results for the localization angles in 2-D plane stress and plane strain conditions are also presented. Numerical validation of the proposed strain localization condition and the derived

analytical results is addressed in Section 4 using the stabilized mixed $\boldsymbol{u}/p$ finite elements, regarding the von Mises and Hill models with associated and non-associated plastic flow rules. A horizontal slit under vertical stretch and the Prandtl punch test, with or without tilt angle between the material local axes and the global ones, are further considered in Section 5, further justifying the proposed condition for strain localization. The most relevant conclusions are drawn in Section 6 to close the paper.

2. General setting of discontinuities

Let us consider the reference configuration of an inelastic (elasto- and rigid-plastic in this work) solid $\Omega \subset \mathbb{R}^{n_{\text{dim}}}$ ($n_{\text{dim}} = 1, 2, 3$). The external boundary is denoted by $\partial\Omega \subset \mathbb{R}^{n_{\text{dim}}-1}$, with $\boldsymbol{n}^*$ being the outward unit normal vector. Deformations of the solid are characterized by the displacement field $\boldsymbol{u}(\boldsymbol{x})$ and infinitesimal strain field $\boldsymbol{\epsilon}(\boldsymbol{x}) := \nabla^{\text{sym}}\boldsymbol{u}(\boldsymbol{x})$, for the symmetric gradient operator $\nabla^{\text{sym}}(\cdot)$ with respect to the spatial coordinate $\boldsymbol{x}$. Prescribed displacements $\boldsymbol{u}^*(\boldsymbol{x})$ and tractions $\boldsymbol{t}^*(\boldsymbol{x})$ are applied to two disjointed parts $\partial\Omega_u$ and $\partial\Omega_t$ of the boundary $\partial\Omega$, respectively. The distributed body forces (per unit volume) are denoted by $\boldsymbol{b}^*$.

2.1. Kinematics of discontinuities

Initially both the displacement and strain fields are continuous everywhere in the solid. In this case, the standard kinematics applies.

Upon a specific condition and thereafter, either a discontinuity band or a discontinuity surface may form, depending on the width of the localization band. A discontinuity band can be regarded as a geometric regularization of a discontinuity surface (line) while the latter is recovered as bandwidth of the former vanishes in the limit.

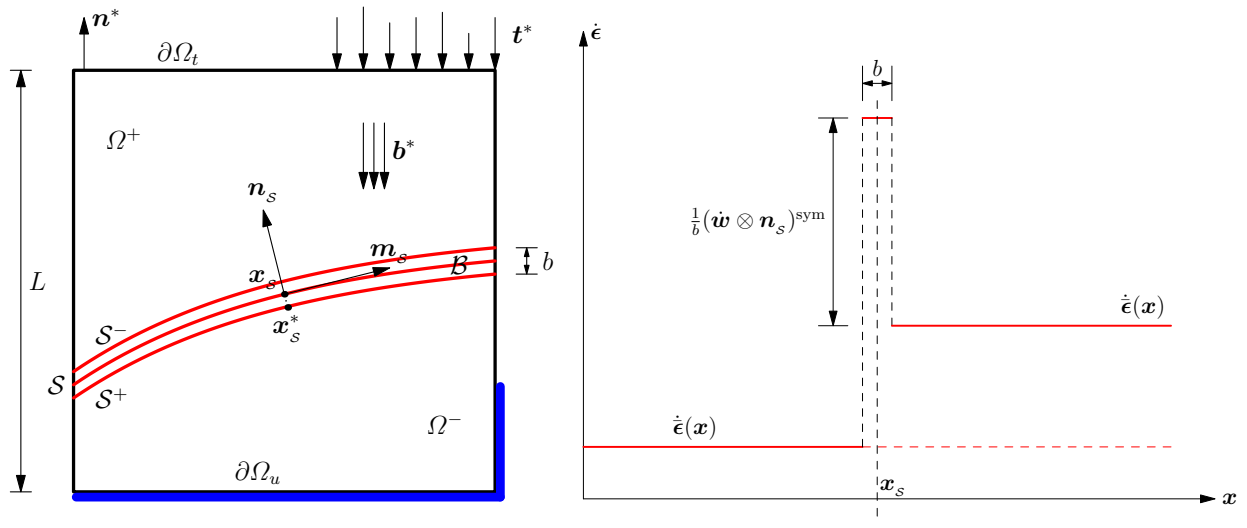

(a) A discontinuity band

(b) Kinematics of the discontinuity band

Figure 1: An inelastic solid with a discontinuity band.

2.1.1. Discontinuity band

As shown in Fig. 1(a), let us first consider the discontinuity band $\mathcal{B}$ of a finite width $b \ll L$, with L being the structural characteristic length. Note that in the continuum setting the bandwidth b is a numerical regularization parameter so that its value can be taken as small as possible. In the discrete (finite element) setting, b may be dependent on the mesh resolution. The discontinuity band $\mathcal{B}$ is delimited by two parallel surfaces $\mathcal{S}^+$ and $\mathcal{S}^-$, with the center one denoted by $\mathcal{S}$, i.e., $\Omega^+ \cup \Omega^- \cup \mathcal{B} = \Omega$. Let (n, m, t) be a set of orthogonal local axes, with $\boldsymbol{n}_{\mathcal{S}}$, $\boldsymbol{m}_{\mathcal{S}}$ and $\boldsymbol{t}_{\mathcal{S}}$ being the normal vector, the in-plane and out-of-plane tangential ones of the surface $\mathcal{S}$, respectively.

In this case, the displacement rate (velocity) field $\dot{\boldsymbol{u}}(\boldsymbol{x})$ is continuous, with an apparent velocity jump $\dot{\boldsymbol{w}} := \dot{\boldsymbol{u}}(\boldsymbol{x} \in \Omega^+ \cap \mathcal{S}^+) - \dot{\boldsymbol{u}}(\boldsymbol{x} \in \Omega^- \cap \mathcal{S}^-)$ across the discontinuity band $\mathcal{B}$, where $\dot{(\cdot)}$ signifies the time derivative. The resulting strain rate field can be given by

$$\dot{\boldsymbol{\epsilon}}(\boldsymbol{x}) = \bar{\dot{\boldsymbol{\epsilon}}}(\boldsymbol{x}) + \dot{\tilde{\boldsymbol{\epsilon}}}(\boldsymbol{x}), \qquad \dot{\tilde{\boldsymbol{\epsilon}}}(\boldsymbol{x}) = \frac{1}{b}\big(\dot{\boldsymbol{w}} \otimes \boldsymbol{n}_{\mathcal{S}}\big)^{\text{sym}}\, \Xi_{\mathcal{B}}(\boldsymbol{x}) \tag{2.1}$$

for the collocation function $\Xi_{\mathcal{B}}(\boldsymbol{x})$ within the discontinuity band $\mathcal{B}$

$$\Xi_{\mathcal{B}}(\boldsymbol{x}) = \begin{cases} 1 & \boldsymbol{x} \in \mathcal{B} \\ 0 & \boldsymbol{x} \in \Omega \backslash \mathcal{B} \end{cases} \tag{2.2}$$

Note that the strain rate field $\bar{\dot{\boldsymbol{\epsilon}}}(\boldsymbol{x})$ outside the discontinuity band $\mathcal{B}$ is independent of the bandwidth b, while the magnitude of the localized one $\dot{\tilde{\boldsymbol{\epsilon}}}$ is inversely proportional to it: the smaller the bandwidth b is, the larger the localized strain becomes; see Figure 1(b). Hereafter, the bar-symbols $\bar{(\cdot)}$ are associated with the material points outside the discontinuity band (surface).

Remark 2.1 Note that in the kinematics (2.1) the collocation function $\Xi_{\mathcal{B}}(\boldsymbol{x})$ can be replaced by a bell-shaped continuous function localized within the discontinuity band $\mathcal{B}$. In this case the localized strain rate $\dot{\tilde{\boldsymbol{\epsilon}}}(\boldsymbol{x})$ is continuous across the localization band, but it is still inversely proportional to the bandwidth b. □

2.1.2. Discontinuity surface

As mentioned, the bandwidth b is a numerical parameter that can be made as small as desired. In the limit case $b \to 0$, the discontinuity band $\mathcal{B}$ becomes a discontinuity surface $\mathcal{S}$. It then follows that

$$\lim_{b \to 0} \frac{1}{b} \Xi_{\mathcal{B}}(\boldsymbol{x}) = \delta_{\mathcal{S}}(\boldsymbol{x}) = \begin{cases} +\infty & \boldsymbol{x} \in \mathcal{S} \\ 0 & \boldsymbol{x} \in \Omega \backslash \mathcal{S} \end{cases} \tag{2.3}$$

for the Dirac-delta $\delta_{\mathcal{S}}(\boldsymbol{x})$ defined at the discontinuity surface $\mathcal{S}$.

Accordingly, the strain rate field becomes singular

$$\dot{\boldsymbol{\epsilon}}(\boldsymbol{x}) = \bar{\dot{\boldsymbol{\epsilon}}}(\boldsymbol{x}) + \dot{\tilde{\boldsymbol{\epsilon}}}(\boldsymbol{x}), \qquad \dot{\tilde{\boldsymbol{\epsilon}}}(\boldsymbol{x}) = \big(\dot{\boldsymbol{w}} \otimes \boldsymbol{n}\big)^{\text{sym}}\, \delta_{\mathcal{S}}(\boldsymbol{x}) \tag{2.4}$$

Similarly, the strain rate field $\bar{\dot{\boldsymbol{\epsilon}}}(\boldsymbol{x})$ outside the discontinuity band $\mathcal{B}$ is independent of the bandwidth b, while the localized one $\dot{\tilde{\boldsymbol{\epsilon}}}(\boldsymbol{x})$ is singular. The above kinematics is shown in Figure 2.

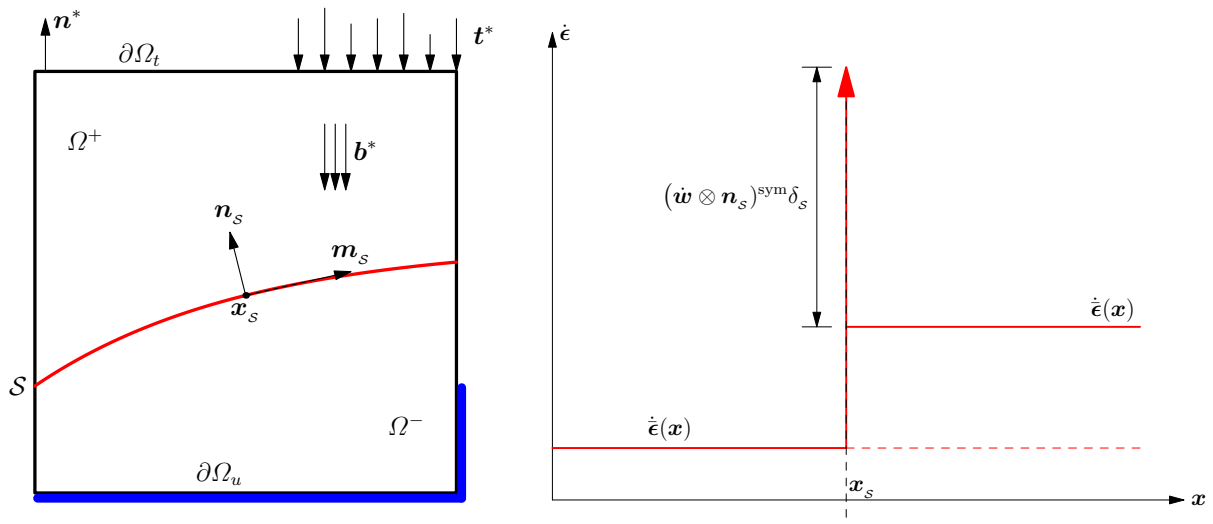

(a) A discontinuity surface

(b) Kinematics of the discontinuity surface

Figure 2: An inelastic solid with a discontinuity surface.

Remark 2.2 As the discontinuity surface can be recovered from the discontinuity band upon a vanishing bandwidth $b \to 0$, hereafter only the kinematics of the discontinuity band is considered. □

2.2. *Stress-strain relations*

For elastoplastic models, the constitutive relation is expressed in rate form as

$$\dot{\boldsymbol{\epsilon}} = \dot{\boldsymbol{\epsilon}}^e + \dot{\boldsymbol{\epsilon}}^p, \qquad \dot{\boldsymbol{\sigma}} = \mathbb{E}_0 : \dot{\boldsymbol{\epsilon}}^e = \mathbb{E}_0 : \left(\dot{\boldsymbol{\epsilon}} - \dot{\boldsymbol{\epsilon}}^p\right) \tag{2.5}$$

where the second-order tensors $\boldsymbol{\sigma}$ and $\boldsymbol{\epsilon}$ represent the stress and strain, respectively, with $\boldsymbol{\epsilon}^e$ and $\boldsymbol{\epsilon}^p$ being the elastic and plastic parts of the latter; the fourth-order material elasticity tensor $\mathbb{E}_0$ can be either isotropic or orthotropic.

Without loss of generality, the plastic strain rate is given by the following evolution laws

$$\dot{\boldsymbol{\epsilon}}^p = \dot{\lambda}\boldsymbol{\Lambda}^p, \qquad \dot{\kappa} = \dot{\lambda}h^p \tag{2.6}$$

for the plastic multiplier $\dot{\lambda}$ satisfying the classical Karush-Kuhn-Tucker conditions

$$\dot{\lambda} \geq 0, \qquad f(\boldsymbol{\sigma}, q) \leq 0, \qquad \dot{\lambda} f(\boldsymbol{\sigma}, q) \equiv 0 \tag{2.7}$$

where a stress-based yield function $f(\boldsymbol{\sigma}, q) \leq 0$, with q being the stress-like internal variable (yield stress) conjugate to the strain-like one κ which measure the plastic state, is introduced. The flow tensor $\boldsymbol{\Lambda}^p := \partial f^p/\partial\boldsymbol{\sigma}$ and the derivative $h^p := -\partial f^p/\partial q$ are normal to the potential function $f^p(\boldsymbol{\sigma}, q)$ — if the latter is identical (or more generally, proportional) to the yield function $f(\boldsymbol{\sigma}, q)$, the plastic flow is associated, and is non-associated otherwise. In absence of plastic flow or in the case of elastic unloading, i.e., $\dot{\lambda} = 0$, the yield condition is not activated, i.e., $f(\boldsymbol{\sigma}, q) < 0$; otherwise, plastic flow occurs. In this work, both perfect plasticity and softening one are addressed.

2.3. Statics of discontinuities

For elastoplastic solids, the stress rates inside the discontinuity band (surface) and outside it are given by

$$\dot{\boldsymbol{\sigma}} = \mathbb{E}_0 : \left(\dot{\boldsymbol{\epsilon}} - \dot{\boldsymbol{\epsilon}}^p\right) = \mathbb{E}_0 : \left(\dot{\boldsymbol{\epsilon}} - \dot{\lambda}\boldsymbol{\Lambda}^p\right) \tag{2.8a}$$

$$\dot{\bar{\boldsymbol{\sigma}}} = \mathbb{E}_0 : \left(\dot{\bar{\boldsymbol{\epsilon}}} - \dot{\bar{\boldsymbol{\epsilon}}}^p\right) = \mathbb{E}_0 : \left(\dot{\bar{\boldsymbol{\epsilon}}} - \dot{\bar{\lambda}}\bar{\boldsymbol{\Lambda}}^p\right) \tag{2.8b}$$

where the elastoplastic relations (2.5) and (2.6) have been recalled for both material points inside and outside the discontinuity band.

Accordingly, the resulting jump in the stress rate, $[\![\dot{\boldsymbol{\sigma}}]\!]$, is expressed as

$$[\![\dot{\boldsymbol{\sigma}}]\!] := \dot{\boldsymbol{\sigma}} - \dot{\bar{\boldsymbol{\sigma}}} = \mathbb{E}_0 : \left([\![\dot{\boldsymbol{\epsilon}}]\!] - \dot{\lambda}\boldsymbol{\Lambda}^p + \dot{\bar{\lambda}}\bar{\boldsymbol{\Lambda}}^p\right) = \mathbb{E}_0 : \left[\frac{1}{b}\left(\dot{\boldsymbol{w}} \otimes \boldsymbol{n}\right)^{\text{sym}} - \dot{\lambda}\boldsymbol{\Lambda}^p + \dot{\bar{\lambda}}\bar{\boldsymbol{\Lambda}}^p\right] \tag{2.9}$$

where the following Maxwell's kinematic condition has been considered

$$[\![\dot{\boldsymbol{\epsilon}}]\!] := \dot{\boldsymbol{\epsilon}} - \dot{\bar{\boldsymbol{\epsilon}}} = \frac{1}{b}\left(\dot{\boldsymbol{w}} \otimes \boldsymbol{n}_s\right)^{\text{sym}} \tag{2.10}$$

Equilibrium across the discontinuity band (surface) gives the following continuity condition of the traction rate

$$\boldsymbol{n}_s \cdot [\![\dot{\boldsymbol{\sigma}}]\!] = \boldsymbol{0} \qquad \Longrightarrow \qquad [\![\dot{\boldsymbol{\sigma}}]\!] = \dot{\alpha}_{mm}\boldsymbol{m}_s \otimes \boldsymbol{m}_s + \dot{\alpha}_{tt}\boldsymbol{t}_s \otimes \boldsymbol{t}_s + \dot{\alpha}_{mt}\left(\boldsymbol{m}_s \otimes \boldsymbol{t}_s\right)^{\text{sym}} \tag{2.11}$$

where the scalars $\dot{\alpha}_{mm}$, $\dot{\alpha}_{tt}$ and $\dot{\alpha}_{mt}$ can be either dependent on or independent of the bandwidth b, according to the deformation stage and stress state. Therefore, though stress rate discontinuities may occur, they can take place only on the plane of the discontinuity surface $\mathcal{S}$.

Remark 2.3 For rigid-plastic solids, the elastic strain $\boldsymbol{\epsilon}^e$ vanishes such that

$$\dot{\boldsymbol{\epsilon}} = \dot{\boldsymbol{\epsilon}}^p = \dot{\lambda}\boldsymbol{\Lambda}^p \tag{2.12}$$

In this case the stress (rate) cannot be directly determined from the constitutive relation $(2.5)_2$. Consequently, only the compatibility condition, rather than the equilibrium one, applies to rigid-plastic solids. □

3. The mechanics of strain localization: Continuum setting

In this section the mechanics of strain localization in plasticity is addressed in the continuum setting. The kinematics of discontinuities in an inelastic solid is first considered. After the classical concepts of plastic yielding (PY) and strain bifurcation (SB) are recalled, strain localization (SL) is further elaborated to general plastic models with associated and non-associated evolution laws.

3.1. Plastic yielding (PY)

Plastic yielding implies termination of linear elastic behavior. Plastic yielding occurs when the yield condition $f(\boldsymbol{\sigma}, q) = 0$ is activated, i.e. $\dot{\lambda} > 0$. It then follows from the consistency condition $\dot{f} = 0$ that

$$\dot{\lambda} = \frac{\boldsymbol{\Lambda} : \mathbb{E}_0 : \dot{\boldsymbol{\epsilon}}}{\boldsymbol{\Lambda} : \mathbb{E}_0 : \boldsymbol{\Lambda}^p + h \cdot H \cdot h^p} \tag{3.1}$$

for the derivatives $\boldsymbol{\Lambda} := \partial f/\partial \boldsymbol{\sigma}$ and $h := -\partial f/\partial q$ of the yield function $f(\boldsymbol{\sigma}, q)$. Note that the hardening/softening modulus $H := \partial q/\partial \kappa$ is null for perfect plasticity and negative for softening one. Internal snap-back is ruled out *a priori* with satisfaction of the condition $H > H_c := -\boldsymbol{\Lambda} : \mathbb{E}_0 : \boldsymbol{\Lambda}^p/(h \cdot h^p)$.

The corresponding constitutive relation in rate form then reads

$$\dot{\boldsymbol{\sigma}} = \mathbb{E}_0 : \left(\dot{\boldsymbol{\epsilon}} - \dot{\boldsymbol{\epsilon}}^p\right) = \mathbb{E}^{ep} : \dot{\boldsymbol{\epsilon}} \tag{3.2}$$

where the fourth-order elastoplasticity tangent $\mathbb{E}^{ep}$ is expressed as

$$\mathbb{E}^{ep} = \mathbb{E}_0 - \frac{\mathbb{E}_0 : \boldsymbol{\Lambda}^p \otimes \boldsymbol{\Lambda} : \mathbb{E}_0}{\boldsymbol{\Lambda} : \mathbb{E}_0 : \boldsymbol{\Lambda}^p + h \cdot H \cdot h^p} \tag{3.3}$$

For non-associated plasticity, i.e., $\boldsymbol{\Lambda}^p \neq \boldsymbol{\Lambda}$, the material tangent is not of major symmetry.

3.2. Strain bifurcation (SB)

Upon strain bifurcation, the strains inside and outside a small subdomain starts deviating from each other, resulting in a discontinuity band with the strain rate jump given by Maxwell's kinematics (2.10).

In this case, the material points inside the discontinuity band are in plastic loading, whereas those outside it can be either in plastic loading or elastic unloading, leading to the following *continuous* and *discontinuous* bifurcation scenarios, respectively:

- Loading–loading (i.e., the material is in loading both inside and outside the discontinuity band) or continuous bifurcation, i.e., $\dot{\lambda} > 0$ and $\dot{\bar{\lambda}} > 0$. Maxwell's kinematics (2.10) and the traction (rate) continuity (2.11) give the following continuous bifurcation condition (Rice, 1976)

  $$\det \boldsymbol{Q}^{ep}(\boldsymbol{n}_s) = 0 \tag{3.4}$$

  for the elastoplastic acoustic tensor $\boldsymbol{Q}^{ep} := \boldsymbol{n}_s \cdot \mathbb{E}^{ep} \cdot \boldsymbol{n}_s$ related to some normal vector $\boldsymbol{n}_s$.

- Loading–unloading (i.e., the material is in loading inside the band and in elastic unloading outside it) or discontinuous bifurcation, i.e., $\dot{\lambda} > 0$ and $\dot{\bar{\lambda}} = 0$. Discontinuous strain bifurcation may occur provided the following condition holds (Rice and Rudnicki, 1980; Borré and Maier, 1989)

  $$\det \boldsymbol{Q}^{ep}(\boldsymbol{n}_s) \leq 0 \tag{3.5}$$

  for some normal vectors $\boldsymbol{n}_s$.

Note that the condition (3.4) of continuous bifurcation is the upper bound for that of discontinuous one (3.5). Accordingly, for incrementally nonlinear (real) materials, strain bifurcation is possible for *any* hardening/softening modulus $H_c < H \leq H_b$ where the maximum value H_b is determined from the criterion (3.4) for incrementally linear comparison (artificial) solids Benallal and Comi (1996); see (Runesson et al., 1991) for the 2-D case of plane stress and plane strain.

As the hardening/softening modulus H evolves with ongoing inelastic deformations, bifurcation first occurs as a continuous one at a point in the body where conditions are locally favorable. Once the continuous bifurcation is surpassed, deformations and strain concentrate further so that the discontinuous one becomes possible (Rice and Rudnicki, 1980).

Remark 3.1 Regarding rigid-plastic solids, Young's modulus goes to infinity, such that the elastoplastic acoustic tensor cannot be defined. The concept of strain bifurcation does not apply and the bifurcation analysis is unseemly. For isotropic elastoplastic models with associated or non-associated flow rules, Runesson et al. (1991) derived the analytical results for the bifurcation angle and the corresponding hardening/softening modulus H_b in 2-D plane stress and plane strain conditions. It is found that the material under plane stress is more prone to strain localization compared to that under plane strain, and the bifurcation angle in the later case generally depends on Poisson's ratio. Moreover, the occurrence of strain bifurcation depends on the hardening/softening modulus and is thus usually indefinite. Sometimes, multiple solutions exist at a given moment (with the hardening/softening modulus H_b specified *a priori*) as discussed in Ottosen and Runesson (1991). The above facts imply that a more stringent condition is needed to determine the discontinuity band, motivating the strain localization criterion introduced in the next section. □

3.3. Strain localization (SL)

After strain bifurcation occurs, deformations within the discontinuity band become more and more localized, affecting the stress rate (2.8a). Compared to the strain rate $\dot{\bar{\boldsymbol{\epsilon}}}$ outside the band that is independent of the bandwidth b, the strain rate jump (2.10), inversely proportional to b, is much larger. Consequently, if it were not to cancel out by the third term, the stress rate $\dot{\boldsymbol{\sigma}}$ would become unbounded for a vanishing bandwidth $b \to 0$, which is physically not allowable due to the plastic yielding condition $f(\boldsymbol{\sigma}, q) \leq 0$.

Therefore, additionally to Maxwell's kinematics (2.10) and continuity of the traction rate (2.11), **for the occurrence of strain localization, the stress rate within the discontinuity band has to be independent of the bandwidth whatever the localized strain rate is**.

Remark 3.2 As the strain rate $\dot{\bar{\boldsymbol{\epsilon}}}$ and stress rate $\dot{\bar{\boldsymbol{\sigma}}}$ outside the discontinuity band are always independent of the bandwidth b, the above strain localization condition implies that the stress rate jump $[\![\dot{\boldsymbol{\sigma}}]\!]$ across the band has also to be independent of it. □

3.3.1. Kinematic conditions

Now let us consider the kinematic conditions upon which the afore-defined strain localization occurs. As the strain rate $\dot{\bar{\boldsymbol{\epsilon}}}$ outside the discontinuity band does not localize, for the stress rate (2.8a) inside the band to be independent of the bandwidth b, the plastic multiplier $\dot{\lambda} > 0$ has to admit the following additive expression

$$\dot{\lambda} = \dot{\lambda}_0 + \frac{1}{b}\dot{\tilde{\lambda}} \qquad \Longrightarrow \qquad \dot{\boldsymbol{\sigma}} = \mathbb{E}_0 : \left[\dot{\bar{\boldsymbol{\epsilon}}} - \dot{\lambda}_0 \boldsymbol{\Lambda}^p + \frac{1}{b}\left(\dot{\boldsymbol{w}} \otimes \boldsymbol{n}\right)^{\text{sym}} - \frac{1}{b}\dot{\tilde{\lambda}}\boldsymbol{\Lambda}^p\right] \tag{3.6}$$

where the regular part $\dot{\lambda}_0 \geq 0$ and the localized one $\dot{\tilde{\lambda}} > 0$ are both independent of the discontinuity bandwidth b.

Accordingly, for the stress rate (3.6) to be physically meaningful, the localized terms inversely proportional to the bandwidth b have to cancel out upon strain localization, i.e.,

$$\boxed{\left(\dot{\boldsymbol{w}} \otimes \boldsymbol{n}_s\right)^{\text{sym}} = \dot{\tilde{\lambda}} \boldsymbol{\Lambda}^p} \qquad \Longleftrightarrow \qquad [\![\dot{\boldsymbol{\epsilon}}]\!] = \frac{1}{b}\left(\dot{\boldsymbol{w}} \otimes \boldsymbol{n}_s\right)^{\text{sym}} = \frac{1}{b}\dot{\tilde{\lambda}} \boldsymbol{\Lambda}^p \tag{3.7}$$

That is, **upon strain localization all the strain rate jump, which *is inversely proportional to the bandwidth* b, has to be inelastic (plastic in this work)**. Note that the above kinematic condition depends only on the specific plastic flow tensor $\boldsymbol{\Lambda}^p$ regardless it is associated or non-associated.

Remark 3.3 For rigid-plastic solids, the strain rate within the discontinuity band is purely plastic, such that

$$\dot{\boldsymbol{\epsilon}} = \dot{\bar{\boldsymbol{\epsilon}}} + \frac{1}{b}\left(\dot{\boldsymbol{w}} \otimes \boldsymbol{n}\right)^{\text{sym}} = \dot{\lambda} \boldsymbol{\Lambda}^p = \dot{\lambda}_0 \boldsymbol{\Lambda}^p + \frac{1}{b}\dot{\tilde{\lambda}} \boldsymbol{\Lambda}^p \tag{3.8}$$

where the identity Eq. $(3.6)_1$ has been considered. As the strain rate $\dot{\bar{\boldsymbol{\epsilon}}}$ does not localize, it follows that

$$\frac{1}{b}\left(\dot{\boldsymbol{w}} \otimes \boldsymbol{n}\right)^{\text{sym}} = \frac{1}{b}\dot{\tilde{\lambda}} \boldsymbol{\Lambda}^p \qquad \Longrightarrow \qquad \left(\dot{\boldsymbol{w}} \otimes \boldsymbol{n}\right)^{\text{sym}} = \dot{\tilde{\lambda}} \boldsymbol{\Lambda}^p \tag{3.9a}$$

as well as

$$\dot{\bar{\boldsymbol{\epsilon}}} = \dot{\lambda}_0 \boldsymbol{\Lambda}^p = \dot{\lambda}_0 \dot{\tilde{\lambda}}^{-1} \left(\dot{\boldsymbol{w}} \otimes \boldsymbol{n}\right)^{\text{sym}} \tag{3.9b}$$

where the localized plastic multiplier $\dot{\tilde{\lambda}} > 0$ does not vanish by definition. As can be seen, the strain rate (3.9b) outside the discontinuity is compatible with the assumed rigid behavior, if and only if the following condition is fulfilled

$$\dot{\lambda}_0 = 0 \qquad \Longleftrightarrow \qquad \dot{\bar{\boldsymbol{\epsilon}}} = \boldsymbol{0} \tag{3.10}$$

That is, in this case strain localization occurs only for the loading/unloading scenarios, which is consistent with the classical result for rigid-plastic solids (Hill, 1950). Note that there is no need to consider the equilibrium equation for strain localization in rigid-plastic solids. □

3.3.2. Stress rate constraints

Upon satisfaction of the strain localization condition (3.7), the stress rate jump (2.9) is independent of the bandwidth b as expected

$$[\![\dot{\boldsymbol{\sigma}}]\!] = \mathbb{E}_0 : \left[\dot{\tilde{\lambda}} \bar{\boldsymbol{\Lambda}}^p - \dot{\lambda}_0 \dot{\tilde{\lambda}}^{-1} \left(\dot{\boldsymbol{w}} \otimes \boldsymbol{n}_s\right)^{\text{sym}}\right] \tag{3.11}$$

Similarly to strain bifurcation, the material points outside the discontinuity band can be in plastic loading or elastic unloading/neutral loading, while those interior points are in plastic loading all along, i.e., $\dot{\tilde{\lambda}} > 0$ and $\dot{\tilde{\lambda}} \geq 0$. Accordingly, the following two cases are distinguished:

- Loading–loading case (i.e., $\dot{\lambda} > 0$ and $\dot{\tilde{\lambda}} > 0$). In this case, the stress rate jump is either null or orthogonal to the normal vector $\boldsymbol{n}_s$, i.e.,

$$[\![\dot{\boldsymbol{\sigma}}]\!] = \dot{\tilde{\alpha}}_{mm} \boldsymbol{m}_s \otimes \boldsymbol{m}_s + \dot{\tilde{\alpha}}_{tt} \boldsymbol{t}_s \otimes \boldsymbol{t}_s + \dot{\tilde{\alpha}}_{mt} \left(\boldsymbol{m}_s \otimes \boldsymbol{t}_s\right)^{\text{sym}} \tag{3.12}$$

where the scalars $\dot{\alpha}_{mm}$, $\dot{\alpha}_{tt}$ and $\dot{\alpha}_{mp}$ are all independent of the discontinuity bandwidth b. This is a particular case of Eq. $(2.11)_2$ for strain bifurcation.

- Loading–unloading/neutral loading case (i.e., $\dot{\lambda} > 0$ and $\dot{\tilde{\lambda}} = 0$): It then follows that

$$[\![\dot{\boldsymbol{\sigma}}]\!] = -\dot{\lambda}_0 \dot{\tilde{\lambda}}^{-1} \mathbb{E}_0 : \left(\dot{\boldsymbol{w}} \otimes \boldsymbol{n}_s\right)^{\text{sym}} \qquad \Longrightarrow \qquad \boldsymbol{n}_s \cdot [\![\dot{\boldsymbol{\sigma}}]\!] = -\dot{\lambda}_0 \dot{\tilde{\lambda}}^{-1} \boldsymbol{Q}_0 \cdot \dot{\boldsymbol{w}} = \boldsymbol{0} \tag{3.13}$$

As the elastic acoustic tensor $\boldsymbol{Q}_0 := \boldsymbol{n}_s \cdot \mathbb{E}_0 \cdot \boldsymbol{n}_s$ is symmetric and strictly positive-definite, this condition is fulfilled *if and only if*

$$\dot{\lambda}_0 = 0 \qquad \Longleftrightarrow \qquad [\![\dot{\boldsymbol{\sigma}}]\!] = \boldsymbol{0} \tag{3.14}$$

Namely, **in the loading-unloading/neutral loading case, the stress rate is continuous upon strain localization**, even though the stress itselft might be discontinuous due to the accumulation ever since strain bifurcation. This is the case we previously considered for *strain softening solids with associated inelastic laws* (Cervera et al., 2012; Wu and Cervera, 2015, 2016); see Wu and Cervera (2014).

Note that the above condition for strain localization, i.e., independence of the stress rate jump of the bandwidth b, applies to strain discontinuity bands and, in the limit of a vanishing bandwidth b, to strain localization surfaces.

3.3.3. Localization angles: Analytical 2-D results

The strain localization condition (3.7) determines the structure of the flow tensor. More specifically, it implies the existence of a *plastic flow vector* $\boldsymbol{\gamma}$ satisfying (Oliver, 2000; Wu and Cervera, 2015, 2016)

$$\dot{\boldsymbol{w}} = \dot{\tilde{\lambda}} \boldsymbol{\gamma} \qquad \Longrightarrow \qquad \boxed{\boldsymbol{\Lambda}^p = \left(\boldsymbol{\gamma} \otimes \boldsymbol{n}_s\right)^{\text{sym}}} \tag{3.15}$$

or in component form of the local axes system (n, m, t) defined at the discontinuity surface $\mathcal{S}$

$$\Lambda^p_{nn} = \gamma_n, \qquad \Lambda^p_{nm} = \frac{1}{2}\gamma_m, \qquad \Lambda^p_{nt} = \frac{1}{2}\gamma_t \tag{3.16a}$$

$$\Lambda^p_{mm} = 0, \qquad \Lambda^p_{tt} = 0, \qquad \Lambda^p_{mt} = 0 \tag{3.16b}$$

From the kinematic constraint (3.15) or (3.16), the orientation of the discontinuity surface can be determined.

Regarding the 2-D case of plane stress and plane strain, the localization angle θ_ℓ can be determined from the condition (3.16b). Interestingly, our previous analytical results for isotropic (Wu and Cervera, 2014, 2015, 2016) and orthotropic (Cervera et al., 2020) plasticity with associated evolution laws also applies to the non-associated case. Here these results are summarized for the sake of later validations.

- Orthotropic plasticity. As shown in Figure 3(a), let us consider the problem in the material axes $(1, 2, 3)$. The orientation of the discontinuity band is characterized by the inclination angle (counter-clockwise) $\theta_\ell \in [-\pi/2, \pi/2]$ between the normal vector $\boldsymbol{n}_s$ and the material axis 1.

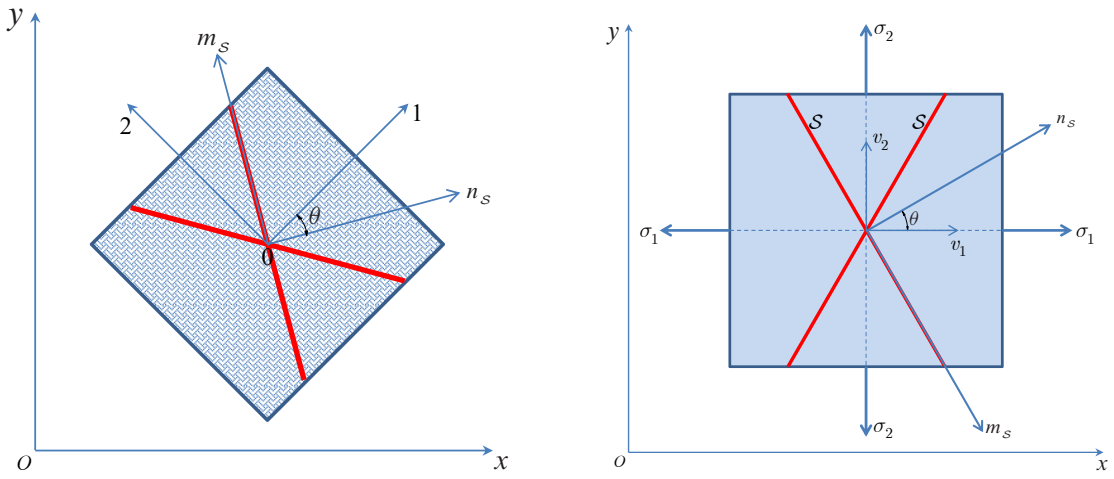

(a) Orthotropic plastic solids

(b) Isotropic plastic solids

Figure 3: Definitions of the discontinuity angle θ in isotropic and orthotropic plastic solids

In this case, the condition (3.16b)$_2$ gives (Cervera et al., 2020)

$$\tan\theta_\ell = -\frac{\Lambda^p_{12}}{\Lambda^p_{11}} \pm \sqrt{\left(\frac{\Lambda^p_{12}}{\Lambda^p_{11}}\right)^2 - \frac{\Lambda^p_{22}}{\Lambda^p_{11}}} \tag{3.17}$$

As can be seen, the discontinuity angle θ_ℓ depends on the stress state upon strain localization.

- Isotropic plasticity. In this case, it is more convenient to define the discontinuity angles in the principal axes of the flow tensor $\boldsymbol{\Lambda}^p$ (coincident with those of the stress tensor $\boldsymbol{\sigma}$) as shown in Figure 3(b). The in-plane components along these principal axes are defined as $(\Lambda^p_1, \Lambda^p_2)$, while Λ^p_3 are associated with the out-of-plane principal direction. The discontinuity angle (counter-clockwise) $\theta_\ell \in [-\pi/2, \pi/2]$ between the normal vector $\boldsymbol{n}_S$ and the principal vector $\boldsymbol{v}_1$ of the stress tensor $\boldsymbol{\sigma}$ is determined by (Wu and Cervera, 2015, 2016)

$$\tan\theta_\ell = \pm\sqrt{-\frac{\Lambda^p_2}{\Lambda^p_1}} \tag{3.18}$$

which corresponds exactly to the case of $\Lambda^p_{12} = 0$ for the orthotropic result (3.17). Here axes are labeled so that $\Lambda^p_1 \geq \Lambda^p_2$, and the magnitude of the out-of-plane components Λ^p_3 is not related directly to the magnitude of those in-plane.

For the plane stress case, Eq. (3.16b)$_2$ is automatically satisfied and thus Eq. (3.17) or Eq. (3.18) alone determines the localization angle θ_ℓ. Contrariwise, in the plane strain condition, the localization angle given by Eq. (3.17) or Eq. (3.18) is further constrained by the out-of-plane stress σ_3 that satisfies (Wu and Cervera, 2016)

$$\Lambda^p_{33}(\theta_\ell) = 0 \tag{3.19}$$

upon strain localization.

Remark 3.4 The out-of-plane stress satisfying (3.19) is in general different from the elastic value

$$\sigma_3 = \nu_0(\sigma_1 + \sigma_2) \tag{3.20}$$

Therefore, in the case of plane strain, except for very particular cases, strain localization does not occur at the onset of plastic yielding. Rather, substantial plastic flows have to occur after plastic yielding (and possibly, strain bifurcation), until the out-of-plane stress fulfills Eq. (3.19). □

Remark 3.5 As the localization angle θ_ℓ is not affected by the elastic constants like Young's modulus and Poisson's ratio, the above results also apply to orthotropic elasticity. □

3.4. Discussion

From the above analyses, the following comments can be made:

(1) For both strain bifurcation and localization, the strain (rate) field exhibits discontinuities and the corresponding jump across the discontinuity band is given by Maxwell's kinematics. Moreover, the material inside the band is in plastic loading, but the one outside it can be either in plastic/neutral loading or elastic unloading.

(2) For both strain bifurcation and localization, continuity of the traction rate implies that stress rate discontinuities can take place only on the plane parallel to the discontinuity surface.

(3) Strain bifurcation is only a necessary condition for strain localization, while the latter is more demanding with the extra condition that the stress rate within the discontinuity band has to be independent of the bandwidth.

(4) In the plane strain condition there is a transition stage between plastic yielding (and possibly, strain bifurcation) and strain localization. During this stage the stress rate within the discontinuity band may depend on the bandwidth.

(5) The occurrence of strain localization depends only on the plastic potential function, regardless of the flow rule is associated or non-associated. It depends neither on the plastic yield function (provided it is activated) nor on the elastic constants like Poisson's ratio as that for strain bifurcation.

4. The mechanics of strain localization: Discrete setting

In this section the above strain localization condition and the analytical results for the discontinuity angles presented in 3.3.3 are numerically verified by finite element simulations. In particular, full boundary value problems (BVPs) are set up, discretized and solved, completed with the corresponding boundary conditions and increasing applied loading. Consequently, the obtained solutions have spatial variation and time evolution. Also, they are subjected to approximation errors (discretization in space and time, nonlinear tolerances, etc). Therefore, the comparison of the analytical results to the discrete solutions has to be interpreted on this regard.

In the numerical simulations, the plastic potential functions of the von Mises and the Hill criteria are considered, both being pressure independent and producing perfectly isochorich plastic flow by definition. Accordingly, for the

occurrence of strain localization the plastic flow needs to be well developed and, at that stage, the incompressible plastic deformation is dominant over the elastic one. Standard displacement-based finite elements are not well suited to cope with this quasi-incompressibility situation in particular, if low-order finite elements are used. Mixed displacement/pressure ($\mathbf{u}/p$) finite elements are far more suitable (Simó and Hughes, 1998); see our previous works on this topic (Chiumenti et al., 2002, 2004; Cervera et al., 2003b,a, 2004; Cervera and Chiumenti, 2009; Cervera et al., 2012).

4.1. The stabilized mixed $\boldsymbol{u}/p$ formulation

The strong form of the mixed $\boldsymbol{u}/p$ formulation for mechanical problems is stated as: Given the elastic properties (G_0, K_0) and prescribed body forces $\boldsymbol{b}^*$, find the displacement $\boldsymbol{u}$ and pressure p, such that

$$\begin{cases} \nabla \cdot \boldsymbol{s} + \nabla p + \boldsymbol{b}^* = \boldsymbol{0} \\ \nabla \cdot \boldsymbol{u} - \dfrac{1}{K_0} p = 0 \end{cases} \tag{4.1}$$

where $\boldsymbol{s} = 2G_0\big(\boldsymbol{e} - \boldsymbol{e}^p\big)$ is the deviatoric stress tensor, with $\boldsymbol{e}$ and $\boldsymbol{e}^p$ being the deviatoric strain tensor and its plastic component; G_0 and K_0 denote the shear and bulk moduli, respectively.

Standard arguments yield the following discrete form

$$\begin{cases} \displaystyle\int_\Omega \nabla^{\text{sym}} \delta\boldsymbol{u}_h : \boldsymbol{s}_h \, \mathrm{d}V + \int_\Omega \big(\nabla \cdot \delta\boldsymbol{u}_h\big) p_h \, \mathrm{d}V = \int_\Omega \delta\boldsymbol{u}_h \cdot \boldsymbol{b}^* \, \mathrm{d}V + \int_{\partial\Omega_t} \delta\boldsymbol{u}_h \cdot \boldsymbol{t}^* \, \mathrm{d}A & \forall \delta\boldsymbol{u}_h \\ \displaystyle\int_\Omega \delta p_h \, \big(\nabla \cdot \boldsymbol{u}_h\big) - \int_\Omega \delta p_h \frac{1}{K_0} p_h \, \mathrm{d}V = 0 & \forall \delta p_h \end{cases} \tag{4.2}$$

where $(\boldsymbol{u}_h, p_h)$ and $(\delta\boldsymbol{u}_h, \delta p_h) \in \mathscr{V}_h \times \mathscr{Q}_h$ denote the discrete displacement and pressure fields and their variations.

In mixed formulations, it is challenging to construct appropriate interpolating finite element spaces that satisfy the stability requirements on the spaces $\mathscr{V}_h$ and $\mathscr{Q}_h$ (Brezzi and Fortin, 1991). For instance, standard mixed elements with continuous equal-order linear/linear interpolation for both fields are not stable. Fortunately, stabilization methods (Hughes, 1995; Hughes et al., 1998) can be developed to attain global stability with the desired choice of interpolation spaces. An appealing stabilization method is the orthogonal sub-grid scale method (Codina and Blasco, 1997; Codina, 2000), previously applied to the problem of incompressible elasto-plasticity (Chiumenti et al., 2002, 2004; Cervera et al., 2003b,a, 2004; Cervera and Chiumenti, 2009; Cervera et al., 2012).

The basic idea of the orthogonal sub-grid scale approach is to split the continuous displacement field into a coarse scale component and a fine one, corresponding to different scales or levels of resolution, i.e.,

$$\boldsymbol{u} = \boldsymbol{u}_h + \boldsymbol{u}_\perp \tag{4.3}$$

where $\boldsymbol{u}_h \in \mathscr{V}_h$ is the displacement field of the (coarse) finite element scale; $\boldsymbol{u}_\perp$ is the enriched displacement field corresponding to the fine sub-grid scale, located in the space orthogonal to the finite element space and given by

$$\boldsymbol{u}_\perp = \tau_e\big(\boldsymbol{r}_h - P_h(\boldsymbol{r}_h)\big) \qquad \text{with} \qquad \boldsymbol{r}_h = \nabla \cdot \boldsymbol{s}_h + \nabla p_h + \boldsymbol{b}^* \tag{4.4}$$

where P_h is the L_2-projection onto $\mathcal{V}_h$; the stabilization parameter is determined by $\tau_e = ch_e^2/(2G_0)$ with h_e being the characteristic length of the element and $c = \mathcal{O}(1)$ being a constant.

Accordingly, the resulting stabilized mixed system of equations is expressed as

$$\begin{cases} \displaystyle\int_\Omega \nabla^{\text{sym}}\delta\boldsymbol{u}_h : \boldsymbol{s}_h \,\mathrm{d}V + \int_\Omega \left(\nabla\cdot\delta\boldsymbol{u}_h\right) p_h \,\mathrm{d}V = \int_\Omega \delta\boldsymbol{u}_h\cdot\boldsymbol{b}^* \,\mathrm{d}V + \int_{\partial\Omega_t} \delta\boldsymbol{u}_h\cdot\boldsymbol{t}^* \,\mathrm{d}A & \forall\delta\boldsymbol{u}_h \\ \displaystyle\int_\Omega \delta p_h \left(\nabla\cdot\boldsymbol{u}_h\right) - \int_\Omega \delta p_h \frac{1}{K_0} p_h \,\mathrm{d}V - \int_\Omega \delta p_h \tau_e\left(\nabla p_h - \pi_h\right) \mathrm{d}V = 0 & \forall\delta p_h \end{cases} \tag{4.5}$$

where the nodal variable $\pi_h = P_h(\nabla p_h)$ is the L_2-projection of the pressure gradient.

4.2. Benchmark verification

The above mixed stabilized $\boldsymbol{u}/p$ element is then applied to the strain localization analysis. The benchmark example is a 2-D strip loaded in uniaxial tension by stretching via imposed vertical displacements at the top and bottom ends; horizontal movement is not restrained. Figure 4(a) depicts the geometry of the problem with dimensions 10 m $\times$ 20 m $\times$1 m (width $\times$ height $\times$ thickness). A sharp horizontal slit of length 2 m is inserted in the strip to introduce the perturbation necessary to trigger strain localization. As the plane stress condition has been previously numerically studied in Cervera et al. (2012) for isotropic plasticity and in Cervera et al. (2020) for orthotropic one, only the plane strain condition is considered in this work. The remote stress state corresponds to

$$\sigma_{xx} = 0, \qquad \sigma_{yy} = \sigma, \qquad \sigma_{xy} = 0 \tag{4.6}$$

The numerical results are then used to validate the proposed strain localization criterion and verify the analytical results for the discontinuity orientation.

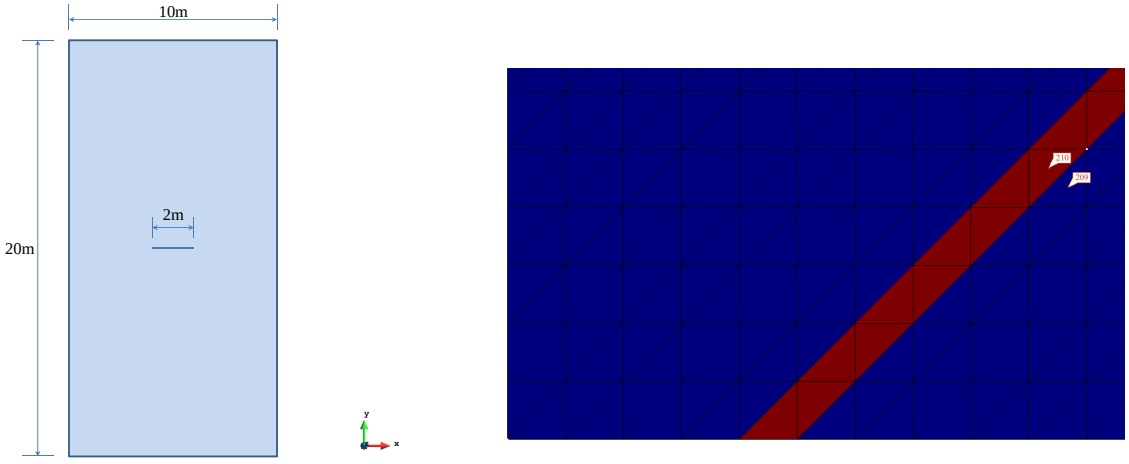

(a) Geometry (b) Finite element mesh and material points inside and outside the discontinuity band

Figure 4: A plane strain strip under vertical stretching: Dimensions and finite element mesh. The bottom and top edges are vertically stretched along opposite directions but with equal magnitude.

Several elastoplastic models, i.e., the isotropic von Mises model and the orthotropic Hill model with associated flow rules, and the von Mises model with the non-associated Hill evolution law, all being isochoric, are considered for the material. Without loss of generality, the yield function is of the following form

$$f(\boldsymbol{\sigma}, q) := \phi(\boldsymbol{\sigma}) - q \leq 0 \tag{4.7}$$

for the loading function $\phi(\boldsymbol{\sigma})$ and the yield strength q

$$\phi(\boldsymbol{\sigma}) = \sqrt{\frac{3}{2}\boldsymbol{\sigma}^{\mathrm{T}}\,\mathbf{P}\,\boldsymbol{\sigma}}, \qquad q = \frac{3}{2}\big(F+G+H\big)^{-1} \tag{4.8}$$

where $\boldsymbol{\sigma} := \big\{\sigma_{11}, \sigma_{22}, \sigma_{33}, \sigma_{12}, \sigma_{13}, \sigma_{23}\big\}^{\mathrm{T}}$ represents the stress vector in the Voigt notation, with $\sigma_{11}, \sigma_{22}, \sigma_{33}, \sigma_{12}, \sigma_{13}$ and σ_{23} denoting the stress components in the material axes $(1, 2, 3)$. Regarding the orthotropic Hill model, the projection matrix $\mathbf{P}$ is given by

$$\mathbf{P} = \frac{1}{F+G+H}\begin{bmatrix} F+G & -F & -G & 0 & 0 & 0 \\ -F & F+H & -H & 0 & 0 & 0 \\ -G & -H & G+H & 0 & 0 & 0 \\ 0 & 0 & 0 & 2L & 0 & 0 \\ 0 & 0 & 0 & 0 & 2M & 0 \\ 0 & 0 & 0 & 0 & 0 & 2N \end{bmatrix} \tag{4.9}$$

for the following material parameters F, G, H, L, M and N

$$F = \frac{1}{2}\left[\left(\frac{1}{\sigma_{Y,11}}\right)^2 + \left(\frac{1}{\sigma_{Y,22}}\right)^2 - \left(\frac{1}{\sigma_{Y,33}}\right)^2\right], \qquad L = \frac{1}{2}\left(\frac{1}{\sigma_{Y,12}}\right)^2 \tag{4.10a}$$

$$G = \frac{1}{2}\left[\left(\frac{1}{\sigma_{Y,11}}\right)^2 + \left(\frac{1}{\sigma_{Y,33}}\right)^2 - \left(\frac{1}{\sigma_{Y,22}}\right)^2\right], \qquad M = \frac{1}{2}\left(\frac{1}{\sigma_{Y,13}}\right)^2 \tag{4.10b}$$

$$H = \frac{1}{2}\left[\left(\frac{1}{\sigma_{Y,22}}\right)^2 + \left(\frac{1}{\sigma_{Y,33}}\right)^2 - \left(\frac{1}{\sigma_{Y,11}}\right)^2\right], \qquad N = \frac{1}{2}\left(\frac{1}{\sigma_{Y,23}}\right)^2 \tag{4.10c}$$

where those entities embellished by subscripts "Y" representing the corresponding yield strengths. The isotropic von Mises model is recovered with $\sigma_{Y,11} = \sigma_{Y,22} = \sigma_{Y,33} = \sqrt{3}\sigma_{Y,12} = \sqrt{3}\sigma_{Y,13} = \sqrt{3}\sigma_{Y,23} = \sigma_Y$ and $q = \sigma_Y$.

The following material properties are assumed in the numerical simulations: Young's modulus $E_0 = 10$ MPa, the yield strength $\sigma_Y = 10$ KPa for isotropic plastic models and $\sigma_{Y,11} = 15$ KPa with all the others equal to 10 kPa for orthotropic ones (no tilt is considered such that the material axes coincide with the global ones). It then follows that

$$\begin{cases} F = G = H = \frac{1}{2}\left(\frac{1}{\sigma_Y}\right)^2, \quad M = N = L = \frac{3}{2}\left(\frac{1}{\sigma_Y}\right)^2 & \text{the von Mises yield function} \\ F = G = \frac{2}{9}\left(\frac{1}{\sigma_Y}\right)^2, \quad H = \frac{7}{9}\left(\frac{1}{\sigma_Y}\right)^2, \quad L = M = N = \frac{3}{2}\left(\frac{1}{\sigma_Y}\right)^2 & \text{the Hill yield function} \end{cases} \tag{4.11}$$

The double symmetry of the problem and the solution allows to discretize a quarter of the domain. Various Poisson's ratio ν_0 are discussed for comparison purposes.

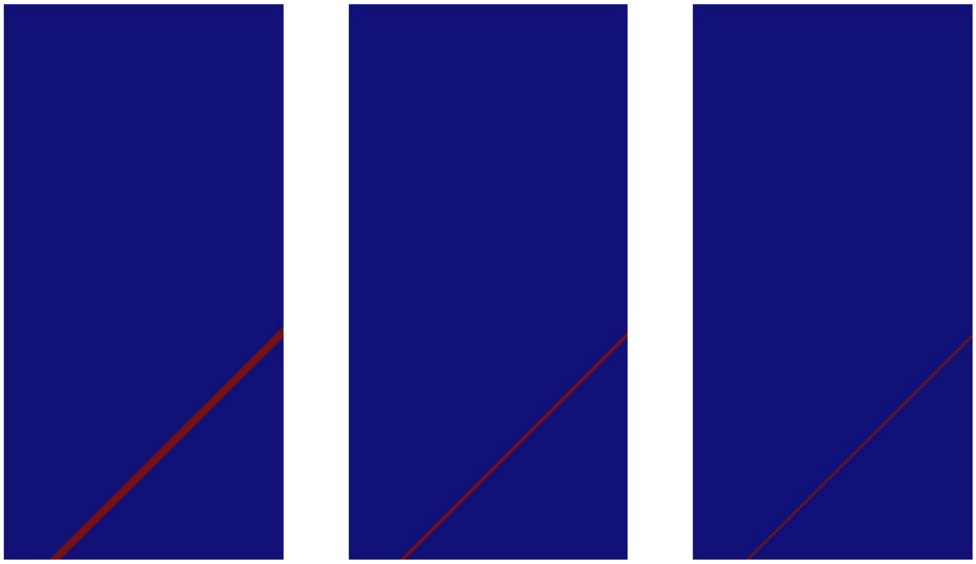

(a) Mesh M1 (b) Mesh M2 (c) Mesh M3

Figure 5: Localization angles for the finite element meshes with various sizes.

As the identity $\Lambda^p_{12} = 0$ holds for the von Mises potential function and the Hill one with no tilt, it follows from Eq. (4.16) that the localization angles are both $\theta_\ell = 45°$; see Remark 4.1. Accordingly, structured triangular meshes are used in all the simulations to optimize the capacity of the linear triangles to represent a pure sliding mode, in parallel to one of the element sides; see Figure 4(b). In each example, three meshes of various sizes, i.e., $h_e = 0.02$ m, 0.01 m and 0.005 m, are considered. As can been shown in Figure 5, for all cases the deformations are localized into narrow discontinuity bands of one single row of elements along $\pm 45°$ directions, with the bandwidth proportional to the mesh size, i.e., $b = \sqrt{2}\, h_e$.

Calculations are performed with an enhanced version of the finite element program COMET (Cervera et al., 2002), developed by the authors at the International Center for Numerical Methods in Engineering (CIMNE). Pre- and post-processing is done with GiD, also developed at CIMNE (CIMNE, 2009). Loading is applied by imposed vertical displacements at both ends of the strip. The Newton–Raphson method is used to solve the nonlinear system of equations arising from the spatial and temporal discretization of the problem. An automatic procedure is used to adjust the step size, and about 200 steps are necessary to complete the analyses. Convergence of a time step is attained when the ratio between the norms of the residual and the total forces is smaller than 10^{-3}.

The purpose of these benchmark examples is two-fold: *(i)* to validate the proposed strain localization condition by comparing the mesh size (or, equivalently, bandwidth) independence of the stress (rate) inside the discontinuity band, and *(ii)* to identify plastic yielding (PY), strain bifurcation (SB) and strain localization (SL) by monitoring stress and strain evolution of two neighboring points inside and right outside of the discontinuity band (see Figure 4(b)):

- Plastic yielding (PY): PY is identified as the linear elastic limit of the stress – strain curves of the material

point inside the discontinuity band. It can be determined by the change of slope observed in the evolution of the stresses and the Lode angle as plastic strains start to develop. For the current stress state and material parameters, it occurs when the vertical stress reaches

$$\sigma_{yy} = \begin{cases} \dfrac{\sigma_Y}{\sqrt{1-\nu_0+\nu_0^2}} & \text{the von Mises yield function} \\ \dfrac{\sigma_Y}{\sqrt{1-\frac{14}{9}\nu_0+\nu_0^2}} & \text{the Hill yield function} \end{cases} \tag{4.12}$$

- Strain bifurcation (SB): SB is identified by definition as the moment right after the curves of the strain components of the material points inside and outside the discontinuity band start deviating. However, as the corresponding strains are small, the onset of strain bifurcation is not always easy to determine by inspection: it comes soon after plastic yielding and it triggers the transition phase into strain localization.

  Regarding the current example involving perfectly plasticity, SB is identified as the moment when the discontinuity band is passing through the material point, manifested by a local peak of the stress curves. After that, rotation of the discontinuity orientation occurs until the SL condition is activated.

- Strain localization (SL): SL is identified as the moment upon which the Lode angle corresponding to the strain localization condition $\Lambda_{33}^p(\theta_\ell) = 0$ is fulfilled at the material point inside the discontinuity band. This is feasible because plastic flow depends only on the deviatoric stresses and the strain localization condition is determined also by the corresponding Lode angle $\tilde{\theta}$. More specifically, for the von Mises and Hill potential functions, the out-of-plane stress σ_3 fulfilling the condition (3.19) is given by

$$\sigma_3 = \begin{cases} \dfrac{1}{2}\sigma & \text{the von Mises potential function} \\ \dfrac{7}{9}\sigma & \text{the Hill potential function} \end{cases} \tag{4.13}$$

  Regarding the stress state (4.6) and (4.13), the Lode angle (positive cosine) $\tilde{\theta} \in [0, \pi/3]$ is determined as

$$\tilde{\theta} = \frac{1}{3}\arccos\left[\frac{J_3}{2}\left(\frac{3}{J_2}\right)^{3/2}\right] = \begin{cases} 30° & \text{the von Mises potential function} \\ 47.78° & \text{the Hill potential function} \end{cases} \tag{4.14}$$

  where J_2 and J_3 denote the second and third invariants of the deviatoric stress tensor $\boldsymbol{s}$.

Perfect plasticity is considered in Section 4.2.1 $\sim$ Section 4.2.4, while the results presented in Section 4.2.5 indicate that the proposed strain localization condition also applies to softening plasticity (Wu and Cervera, 2016).

Remark 4.1 For the plastic models with Eqs. (4.8)$\sim$(4.10) being the potential functions, in the plane strain cases ($\epsilon_3 = 0$) the condition (3.19) gives the following out-of-plane stress

$$\sigma_{33} = \frac{G\sigma_{11} + H\sigma_{22}}{G+H}, \qquad \Lambda_{11}^p + \Lambda_{22}^p = -\Lambda_{33}^p = 0 \tag{4.15}$$

Accordingly, Eq. (3.17) becomes

$$\tan\theta_\ell = -\frac{\Lambda^p_{12}}{\Lambda^p_{11}} \pm \sqrt{\left(\frac{\Lambda^p_{12}}{\Lambda^p_{11}}\right)^2 + 1} \tag{4.16}$$

for the ratio

$$\frac{\Lambda^p_{12}}{\Lambda^p_{11}} = \frac{(G+H)L}{FG+FH+GH} \cdot \frac{\sigma_{12}}{\sigma_{11}-\sigma_{22}} \tag{4.17}$$

It follows from Eq. (4.16) that

$$\tan\theta_{\ell 1} \cdot \tan\theta_{\ell 2} = -1 \qquad \Longrightarrow \qquad \left|\theta_{\ell 1} - \theta_{\ell 2}\right| = 90^\circ \tag{4.18}$$

Accordingly, in the plane strain condition the discontinuity bands are perpendicular to each other. For the particular case of isotropic von Misese model, it follows from $\Lambda^p_{12} = 0$ that $\theta_\ell = \pm 45^\circ$. □

4.2.1. The associated von Mises model with Poisson's ratio $\nu_0 = 0.0$

Let us first consider the associated von Mises model with Poisson's ratio $\nu_0 = 0.0$. For the material point within the discontinuity band, the evolution curves of the vertical strain, the vertical and out-of-plane stresses, and the Lode angle given by various mesh sizes are shown in Figure 6.

As expected, the vertical strain ϵ_{yy} depends on the discontinuity bandwidth (or, equivalently, the mesh size): the less the bandwidth b is, the larger strain it reaches. Moreover, except during the intermediate transition stage, the stress components σ_{yy} and σ_{zz}, and the Lode angle $\tilde{\theta}$, are all independent of the bandwidth b, validating the assumption postulated before: for the occurrence of strain localization, the stress rate inside the discontinuity band is independent from the mesh size and the resulting discontinuity bandwidth. Accordingly, termination of the transition stage can be identified as the strain localization point.

In order to identify plastic yielding (PY), strain bifurcation (SB) and strain localization (SL), the evolution curves of stress and strain at two neighboring points inside and right outside of the discontinuity band are considered in Figure 7. Here only the results given by the mesh size $h_e = 0.005$ m are presented. In Figure 7(a) the evolution curves of the stress σ_{yy} is shown. Plastic yielding is identified as the loss of linearity. For this case of vanishing Poisson's ratio $\nu_0 = 0.0$, another signal of plastic yielding is the occurrence of non-vanishing out-of-plane stress σ_{zz} as depicted in Figure 7(b).

The evolution curves of the strain ϵ_{yy} are depicted in Figure 7(c). Though strain bifurcation is defined as the deviation of the strains inside and outside of the band, it corresponds to the peak points of the stress curves. The evolution curves of Lode angle $\tilde{\theta}$ are shown in Figure 7(d). Strain localization is identified as the moment upon which the Lode angle $\tilde{\theta} = 30^\circ$ for the material point inside the discontinuity band. Compared to strain bifurcation, strain localization occurs much later and there is a transition stage between them allowing the out-of-plane stress (3.19) to be attained.

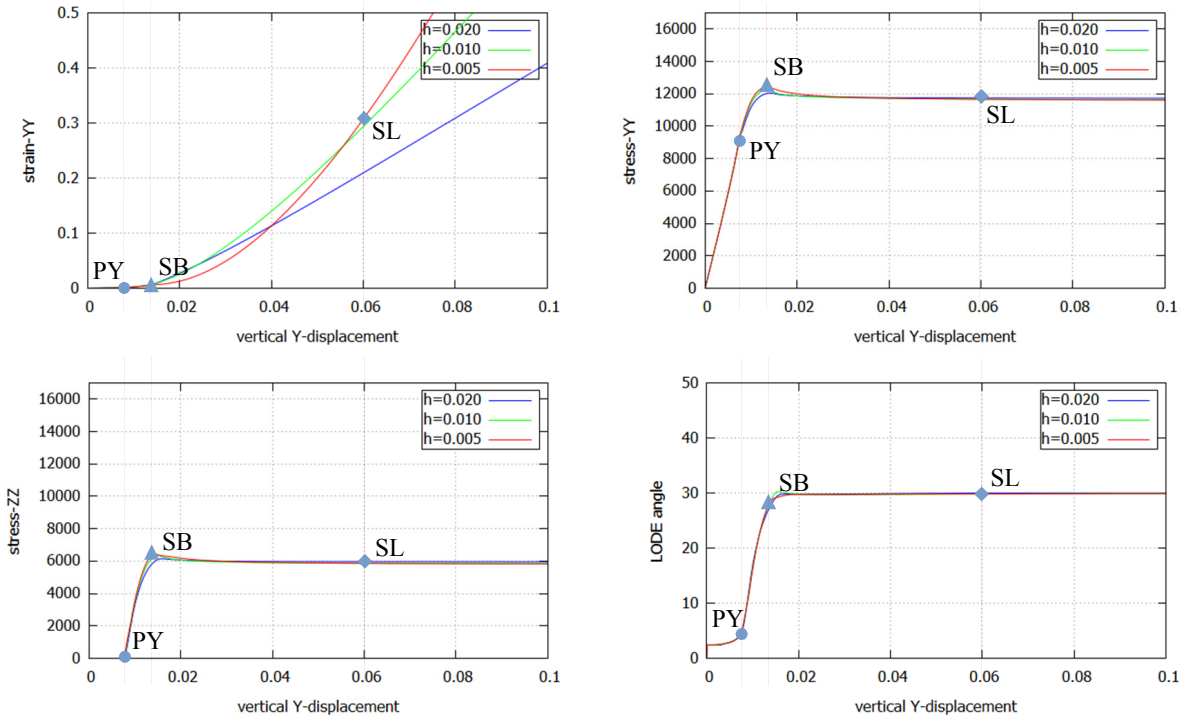

Figure 6: Strain, stresses and Lode angle of the von Mises model with Poisson's ratio $\nu_0 = \mathbf{0.0}$: Effect of the bandwidth (mesh size)

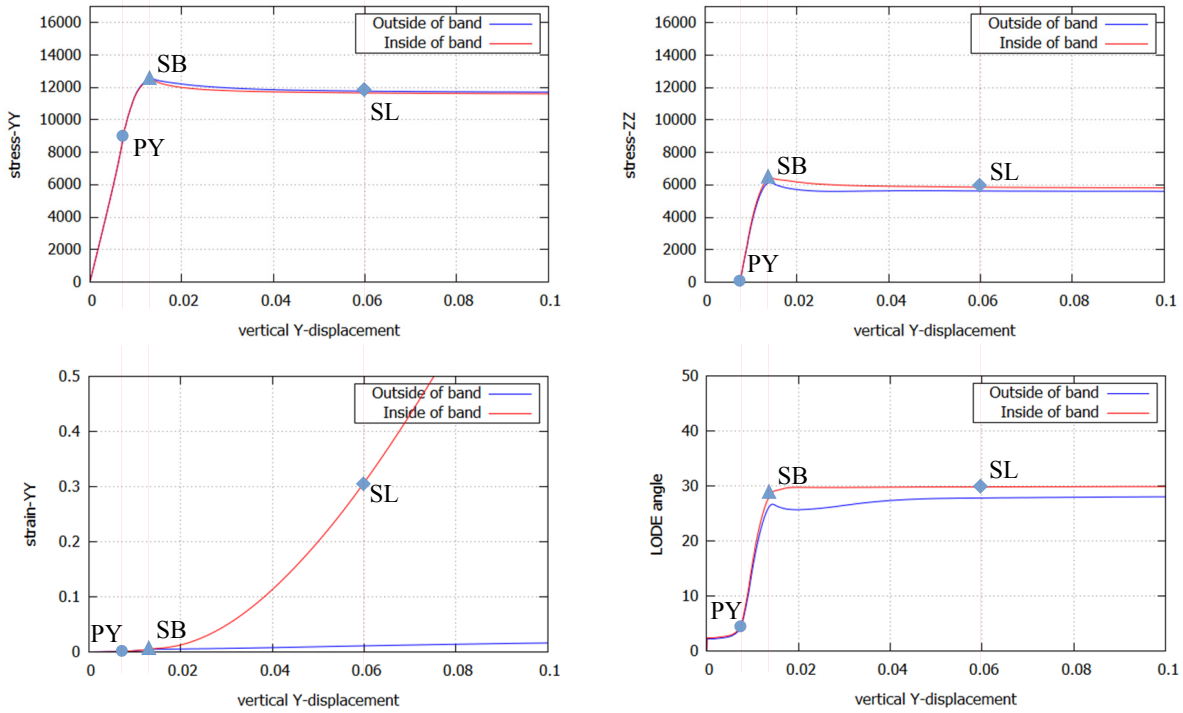

Figure 7: Evolution curves of the von Mises model with Poisson's ratio $\nu_0 = \mathbf{0.0}$.

As can be seen from the evolution curves of σ_{yy} and σ_{zz}, upon strain bifurcation the stresses inside and outside the discontinuity band start deviating from each other. This stress jump that evolves during the transition phase from strain bifurcation to straing localization, remains constant, i.e., $[\![\dot{\boldsymbol{\sigma}}]\!] = \boldsymbol{0}$, after strain localization, validating the stress rate continuity condition (3.14). This is because the material point outside the discontinuity band is in neutral loading.

4.2.2. The associated von Mises model with Poisson's ratio $\nu_0 = 0.5$

Let us next consider the associated von Mises model with Poisson's ratio $\nu_0 = 0.5$. As shown in Figure 8, except for the vertical strain ϵ_{yy}, the vertical and lateral stresses $(\sigma_{yy}, \sigma_{zz})$ as well as the Lode angle $\tilde{\theta}$ are all independent of the discontinuity bandwith b almost during the whole deformation process. The observed very minor deviations are caused by stress perturbations during the formation of the discontinuity band and its passing through the sampling point.

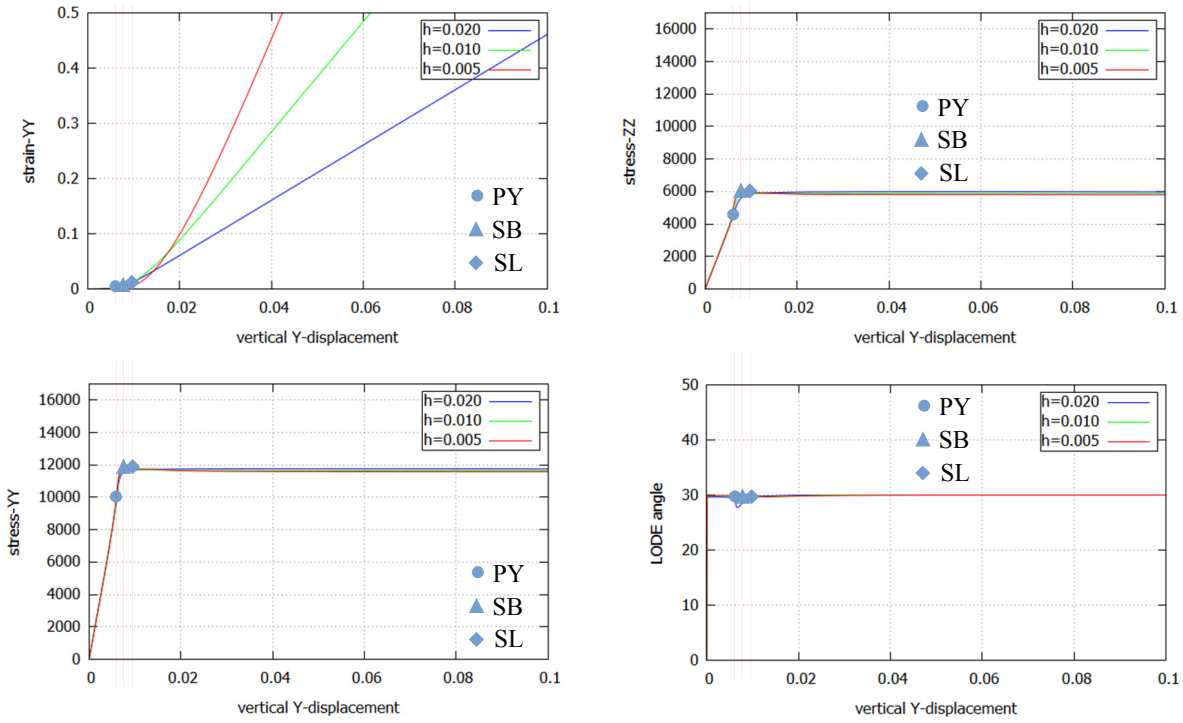

Figure 8: Strain, stresses and Lode angle of the von Mises model with Poisson's ratio $\nu_0 = 0.5$: Effect of the bandwidth (mesh size)

As shown in Figure 9 , in this case plastic yielding (PY), strain bifurcation (SB) and strain localization (SL) are very close to each other. This is because the out-of-plane stress (3.19) for $\nu_0 = 0.5$ is coincident with the elastic value (3.20) and no transition stage exists. The minor differences in-between them is caused by the crossing of the discontinuity band through the material point. As there is no transition stage allowing stress discontinuities to develop, the stresses are continuous across the discontinuity band and the stress continuity holds together with the stress rate continuity, i.e., $[\![\boldsymbol{\sigma}]\!] = [\![\dot{\boldsymbol{\sigma}}]\!] = \boldsymbol{0}$.

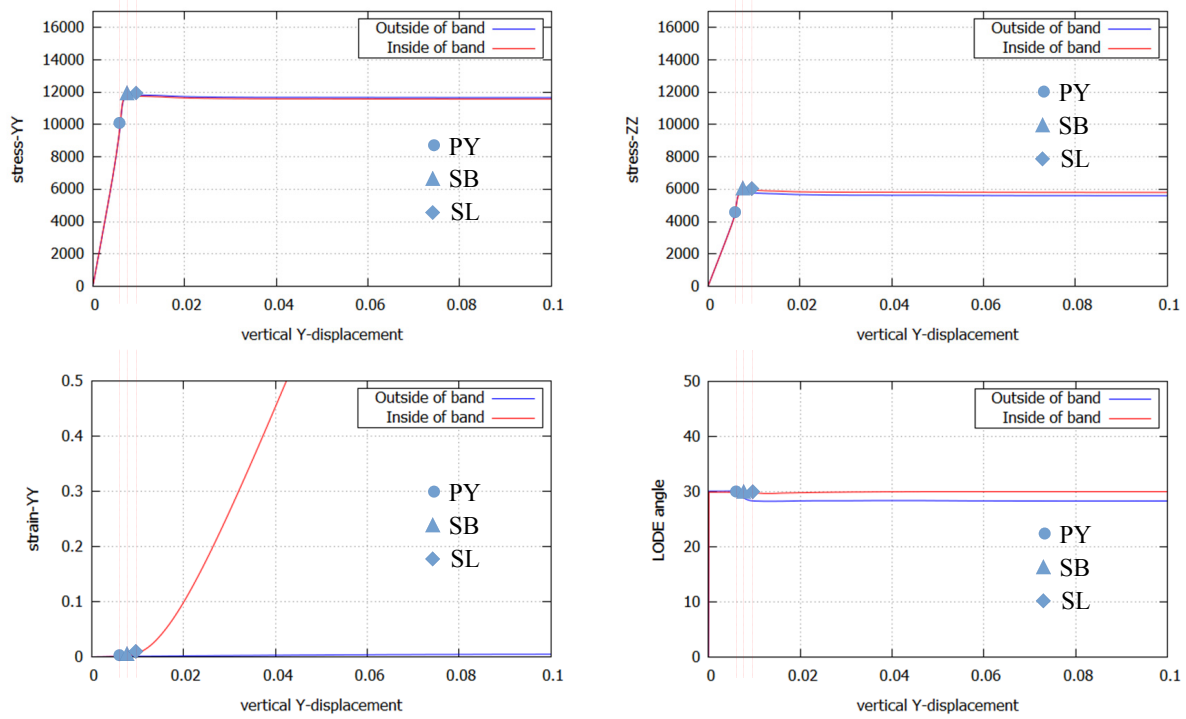

Figure 9: Evolution curves of the von Mises model with Poisson's ratio $\nu_0 = 0.5$.

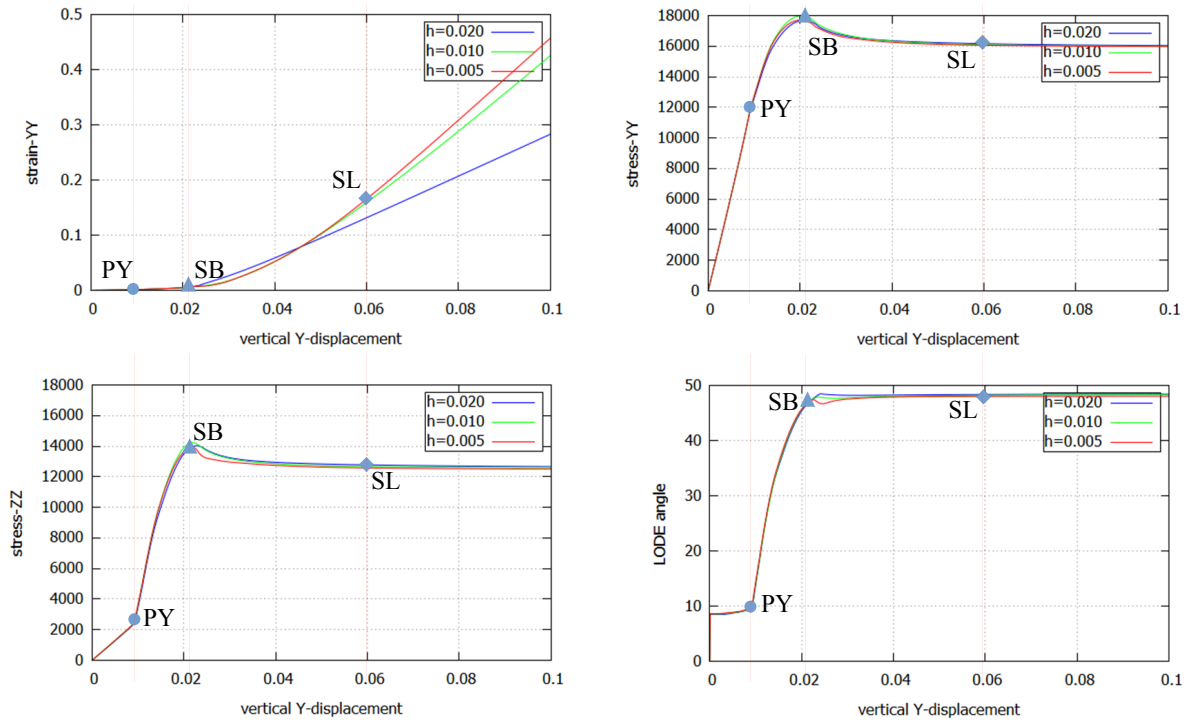

Figure 10: Strain, stresses and Lode angle of the associated Hill model with Poisson's ratio $\nu_0 = 0.2$: Effect of the bandwidth (mesh size)

4.2.3. The associated Hill model with Poisson's ratio $\nu_0 = 0.2$

Next the associated Hill model with Poisson's ratio $\nu_0 = 0.2$ is considered. Again, Figure 10 confirms that the strain field inside the discontinuity band is dependent of the bandwidth b as expected, but the non-vanishing stress components σ_{yy} and σ_{zz} as well as the Lode angle $\tilde{\theta}$ are all independent of it except during the intermediate transition stage between strain bifurcation and localization.

In this case, plastic yielding (PY) and strain bifurcation (SB), which are identified from the evolution curves of σ_{yy} and σ_{zz} shown in the Figure 11(a, b) as the loss of linearity of these curves and from Figure 11(c, d) as the deviation of the strains inside and outside the discontinuity band, respectively. The latter is more easily identified as the peak points of the stress curves. As the out-of-plane stress $(4.13)_2$ cannot be attained at the onset of plastic yielding, there is a transition stage until the plane strain localization occurs with a Lode angle $\tilde{\theta} = 47.78°$; see Figure 11(d).

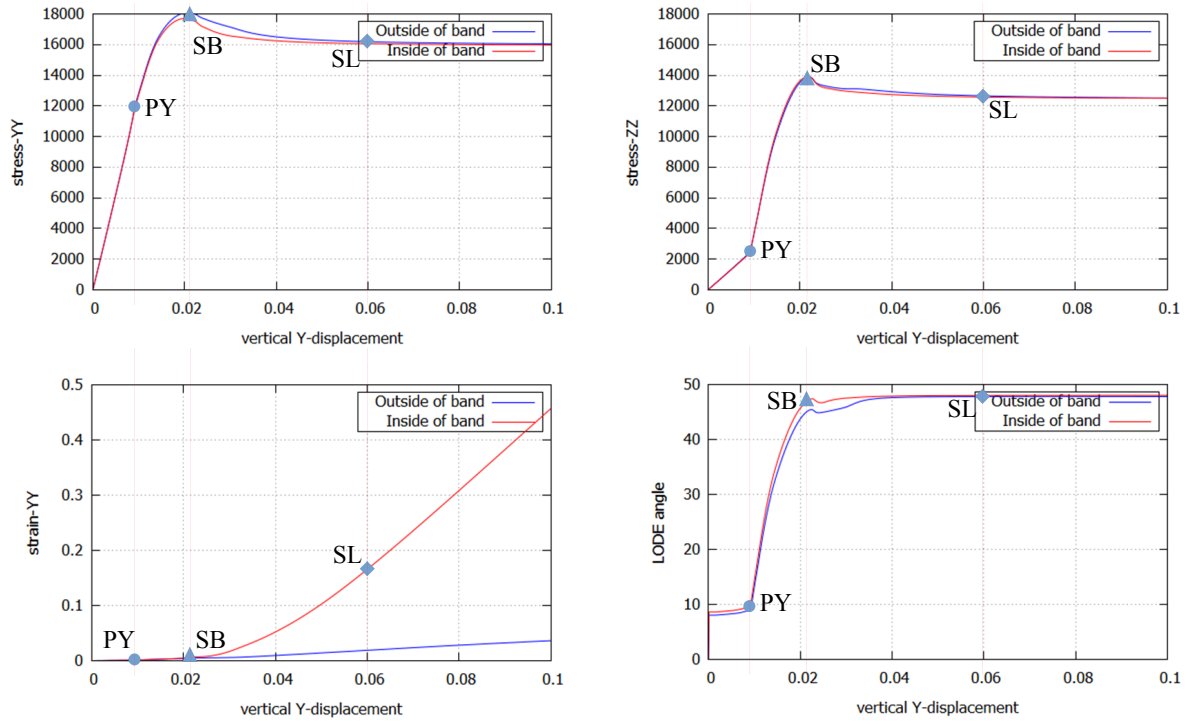

Figure 11: Evolution curves of the Hill model with Poisson's ratio $\nu_0 = 0.2$.

Moreover, though the gaps between the stresses inside and outside the discontinuity band vary during the transition stage, the stress rate continuity condition $[\![\dot{\boldsymbol{\sigma}}]\!] = \boldsymbol{0}$ holds upon strain localization (SL) and thereafter. That is, the postulated assumption of stress (rate) objectivity upon strain localization also applies to orthotropic plastic solids.

4.2.4. The non-associated von Mises/Hill model with Poisson's ratio 0.2

Finally, let us consider the non-associated plastic model with the von Mises yield function and the Hill potential function. Poisson's ratio $\nu_0 = 0.2$ is assumed. Figure 12 depicts the evolution curves of the vertical strain, the non-

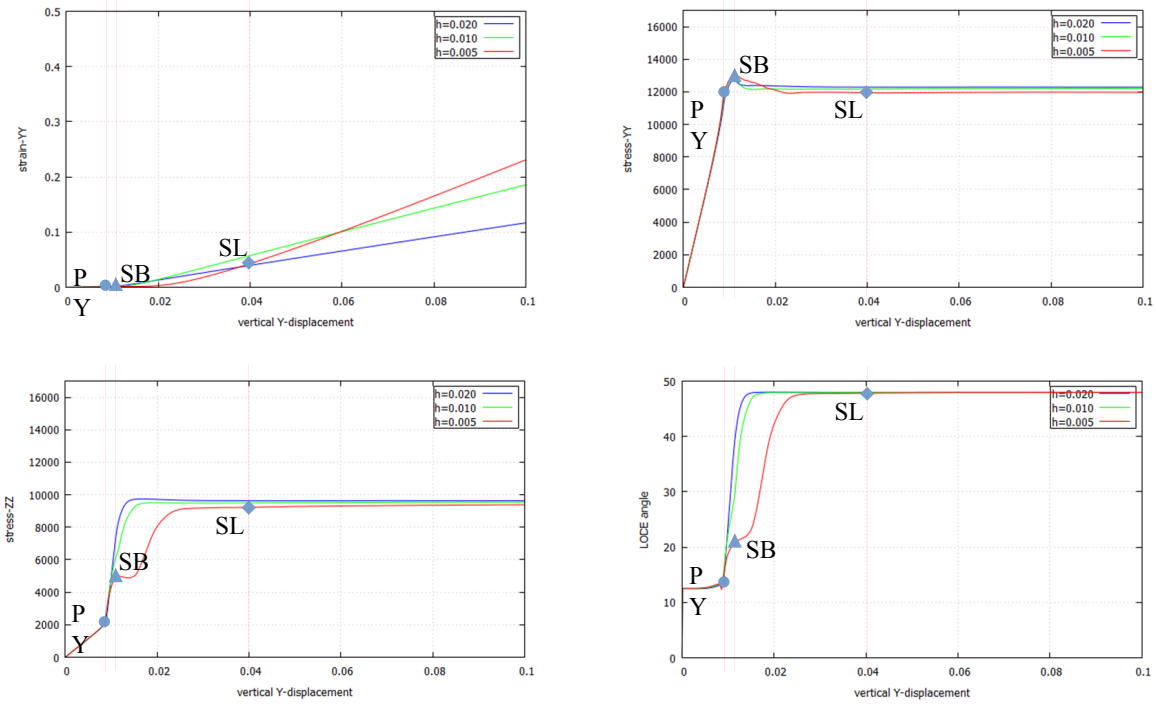

Figure 12: Strain, stresses and Lode angle of the non-associated von Mises/Hill model with Poisson's ratio $\nu_0 = 0.2$: Effects of the bandwidth

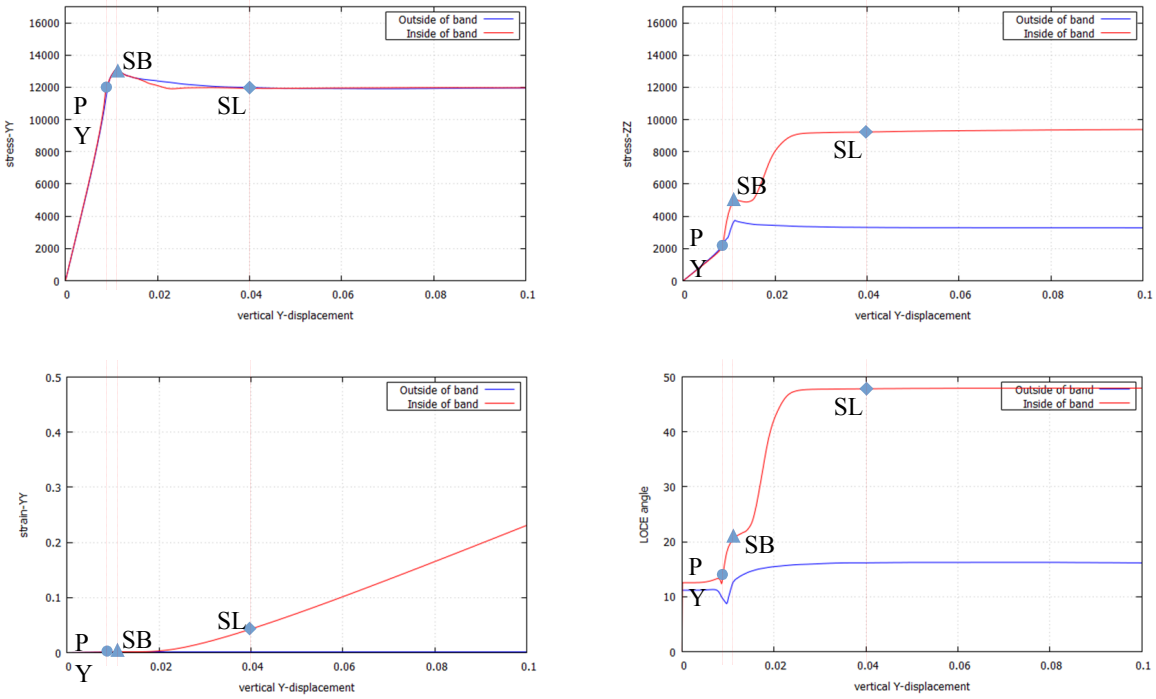

Figure 13: Evolution curves of the non-associated von Mises/Hill model with Poisson's ratio $\nu_0 = 0.2$.

vanishing stresses and the Lode angle inside the discontinuity band. As can be seen, for this non-associated plastic solid the stresses are also independent of the bandwidth upon strain localization and thereafter, though the strain becomes larger as the mesh size decreases.

Plastic yielding and strain bifurcation are easily identified from the loss of linearity and the peak load of the stress curves shown in Figure 13(a). Similarly, as the out-of-plane stress $(4.13)_2$ upon strain localization is not equal to the elastic one upon plastic yielding and strain bifurcation, a transition stage presents in Figure 13(d) during which substantial deviatoric plastic flow occurs until the stress state inside the band corresponds to a Lode angle $\tilde{\theta} = 47.78°$. Again, as can be seen from the evolution curves of σ_{yy} and σ_{zz}, upon strain localization the stress discontinuities inside and outside the band stop increasing and the stress gaps maintain constant, i.e., $[\![\dot{\boldsymbol{\sigma}}]\!] = \boldsymbol{0}$.

4.2.5. Localization in softening plasticity

In this subsection, the four cases studied in the preceding subsections for perfect plasticity are computationally re-analyzed for softening plasticity. For each case, three meshes of various sizes, i.e., $h_e = 0.02$ m, 0.01 m and 0.005 m, respectively, are considered as in the case of perfect plasticity.

Exponential softening is considered for the yield-stress q in Eq. (4.7). Dissipation in the discrete problem is controlled by relating the softening parameters to the fracture energy (Wu and Cervera, 2016), with the bandwidth b proportional to the mesh size, i.e., $b = \sqrt{2}h_e$. A fracture energy $G_{\mathrm{f}} = 1,250$ J/m^2 is used in all cases.

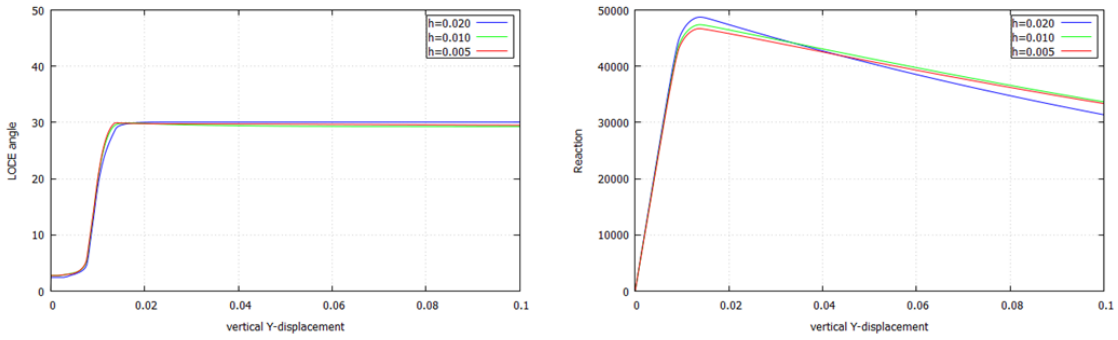

(a) Associated von Mises model with $\nu_0 = 0.0$

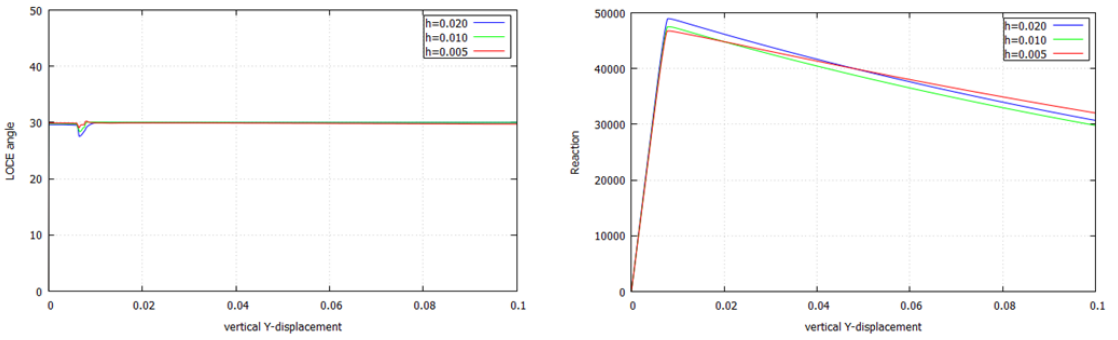

(b) Associated von Mises model with $\nu_0 = 0.5$

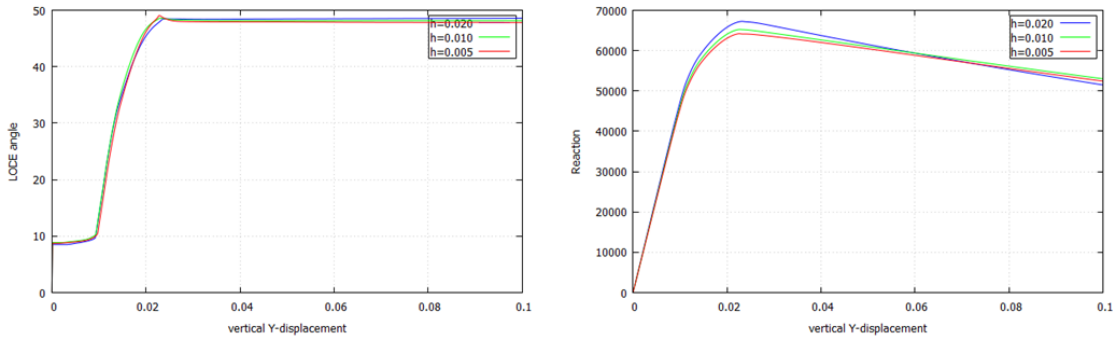

(c) Associated Hill model with $\nu_0 = 0.2$

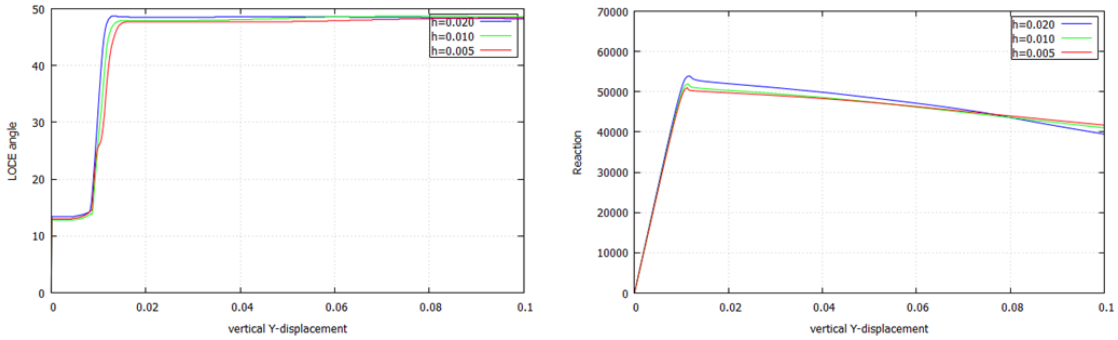

(d) Non-associated von Mises/Hill model with $\nu_0 = 0.2$

Figure 14: Evolution curves of Lode angle and vertical reaction for softening plasticity

For all the considered cases, the discontinuity bands form along as shown in Figure 5, along the 45° direction. Figure 14 shows the corresponding results. In the left column, the computed Lode angles for the elements inside the localization band are shown, corresponding exactly to the stress states that stem from satisfaction of the localization condition, i.e., 30° for the isotropic von Mises potential function and 47.78° for the Hill potential function. Note the resemblance to the corresponding results for the case of perfect plasticity shown in Figure 6, 8, 10 and 12, respectively. In the right column, the global vertical reaction — displacement curves are shown; in all cases, the softening responses and the convergence upon mesh refinement are observed.

5. Numerical examples

In this section, two extra numerical examples are presented to further validate the obtained strain localization condition under more general conditions.

5.1. The plane strain strip under uniaxial stretching

Firstly, the plane strain strip under uniaxial stretching presented in Section 4.2 is re-analyzed. Different from the previous simulations, here quadrilateral $\boldsymbol{u}/p$ elements are used to discretize the full computational domain. The mesh

size is adopted as $h = 0.005$ m. In this way, two discontinuity bands that both satisfy the strain localization condition may form. Additionally, mesh alignment independence is also demonstrated for the discrete solution.

Four different models, i.e., the associated von Mises and Hill models, and the non-associated Hill/von Mises model (with the Hill criterion as the yielding function and the von Mises criterion as the potential one) and von Mises/Hill model (vice versa), are adopted in the simulation.

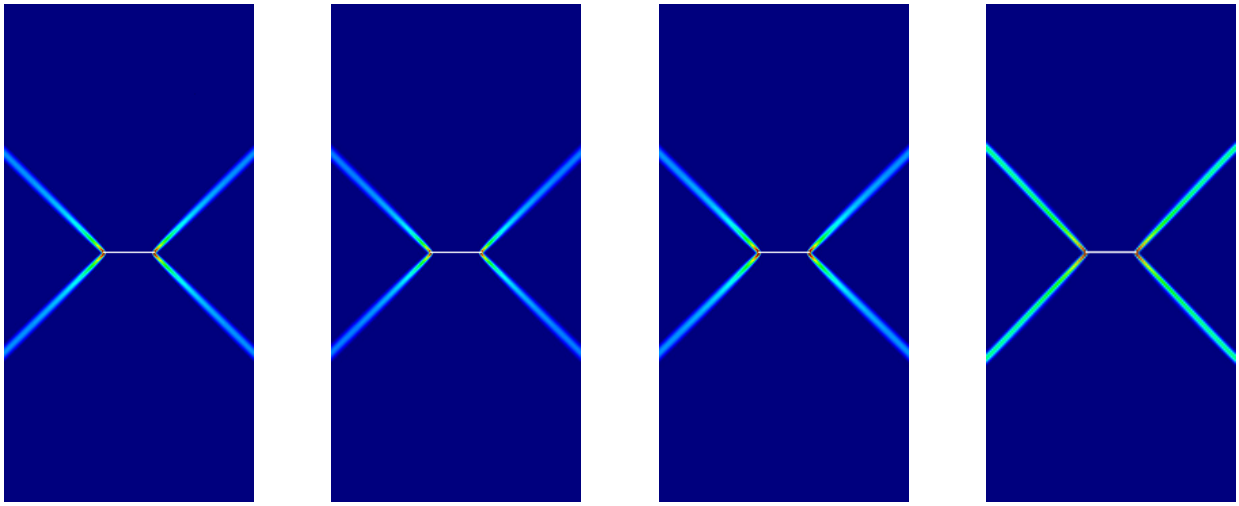

(a) von Mises model (b) Hill/von Mises model (c) Hill model (d) von Mises/Hill model

Figure 15: A plane strain strip under uniaxial stretching: Localization angles for various models with no tilting

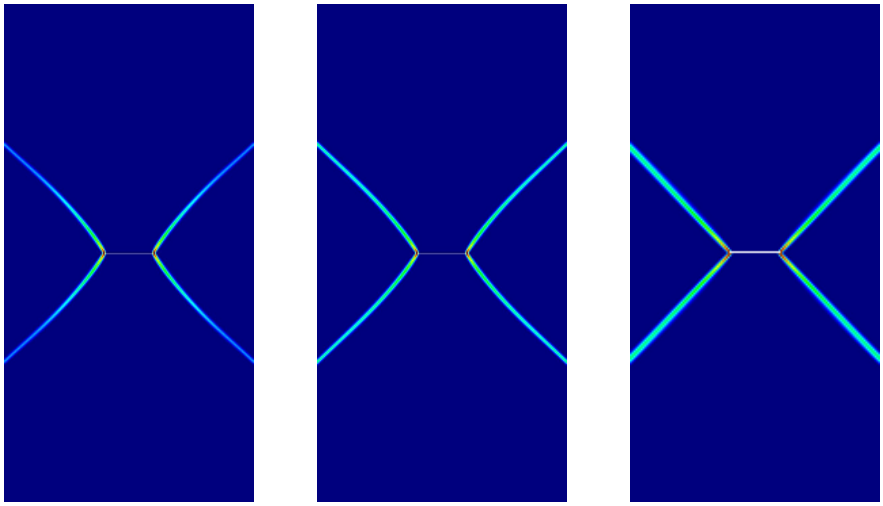

(a) $u^* = 0.010$ m (b) $u^* = 0.015$ m (c) $u^* = 0.030$ m

Figure 16: Snapshots of the equivalent plastic strain at various applied displacements, showing rotation of the discontinuity orientation for the non-associated von Mises/Hill model.

Let us first consider perfect plasticity. As mentioned before, for the case of no tilting, i.e., $\alpha = 0°$, the analytical

results predict discontinuity bands of $\pm 45^\circ$ directions for plastic models with either the von Mises or Hill potential function, and the yielding function does not alter the localization angle. The above results are exactly reproduced by the numerical simulations shown in Figure 15. It is worthy to note that even if the four final snapshots may look identical, they are not. The localization condition is identical for the four models, but the transition phases are different; distinct plastic strains accumulate during these phases. Minor differences can be observed around the horizontal slit, where plastic flows start.

Figure 16 presents three snapshots of the equivalent plastic strain at various applied displacements for the last model with the von Mises yielding function and the Hill potential one. The transition from plastic yielding/strain bifurcation to strain localization is evident, with the plastic strain evolving with increasing loading and the discontinuity angle eventually fixed at $\theta_\ell = 45^\circ$. Let us recall that for the von Mises model, the strain bifurcation angle θ_b depends on Poisson's ratio, and $\theta_b > 45^\circ$ for $\nu_0 < 0.5$ (Runesson et al., 1991).

Let us now consider the tilt angle $\alpha = 60^\circ$. For the von Mises potential function, the flow tensor is isotropic and the same localization angles $\theta_\ell = \pm 45^\circ$ apply. As shown in Figure 17(a) and Figure 17(b), the non-associated Hill/von Mises model shows the same localization as the associated von Mises model. The yield function does not alter the localization angle. Comparatively, for the Hill potential function, it follows from Eq. (4.16) that

$$\theta_\ell = -8.5^\circ;\ 81.5^\circ, \qquad \theta_\ell + \alpha = 51.5^\circ;\ 141.5^\circ \tag{5.1}$$

where $\theta_\ell + \alpha$ denotes the slopes of the upper discontinuity bands. As can be seen from Figure 17(c) and Figure 17(d), the above analytical results are correctly predicted by the numerical simulations. Moreover, the non-associated von Mises/Hill model exhibits a localization pattern similar to that of the associated Hill model. Dependence of the localization angles only on the plastic potential function regardless the yield one is again confirmed.

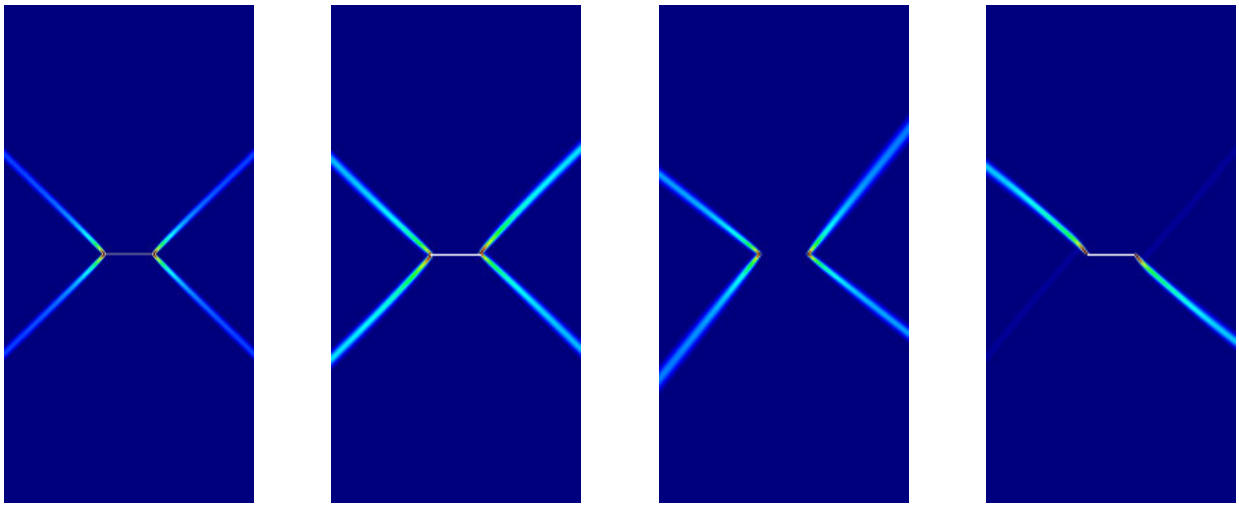

(a) von Mises model (b) Hill/von Mises model (c) Hill model (d) von Mises/Hill model

Figure 17: A plane strain strip under uniaxial stretching: Localization angles for various models with tilting angle $\alpha = 60^\circ$.

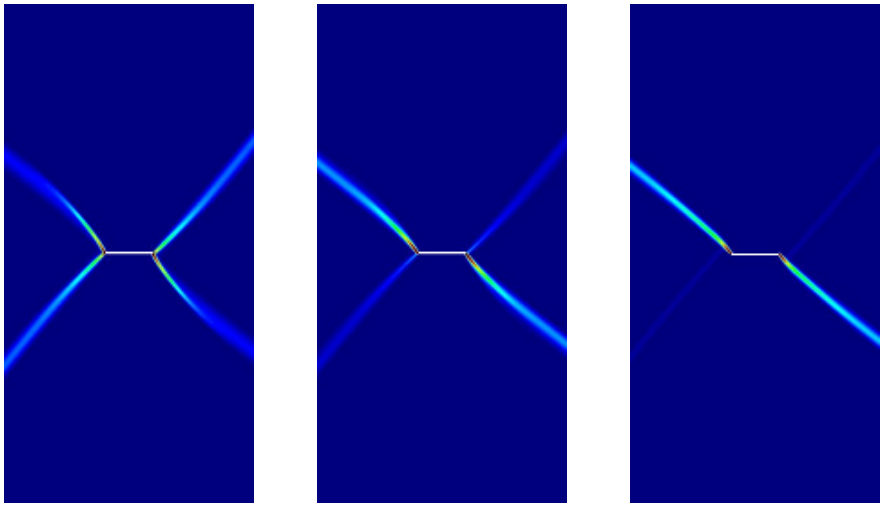

(a) $u^* = 0.010$ m (b) $u^* = 0.015$ m (c) $u^* = 0.030$ m

Figure 18: Snapshots of the equivalent plastic strain at various applied displacements, showing rotation of the discontinuity orientation for the non-associated von Mises/Hill model (with tilt angle $\alpha = 60°$).

Figure 18 presents three snapshots of the equivalent plastic strain at various applied displacements for the non-associated von Mises/Hill model. In this peculiar instance, the four initial symmetric plastic bands rotate during the transition phase until two of them eventually localize at an angle compatible with the localization condition while the other two, orthogonal to the former, progressively fade into desactivation. As mentioned previously, even if the localization conditions of cases (a) and (b), and cases (c) and (d), are identical respectively, the corresponding transition phases are not. This accounts for the slight curvature of the sliding lines in cases (b) and (d) around the slits.

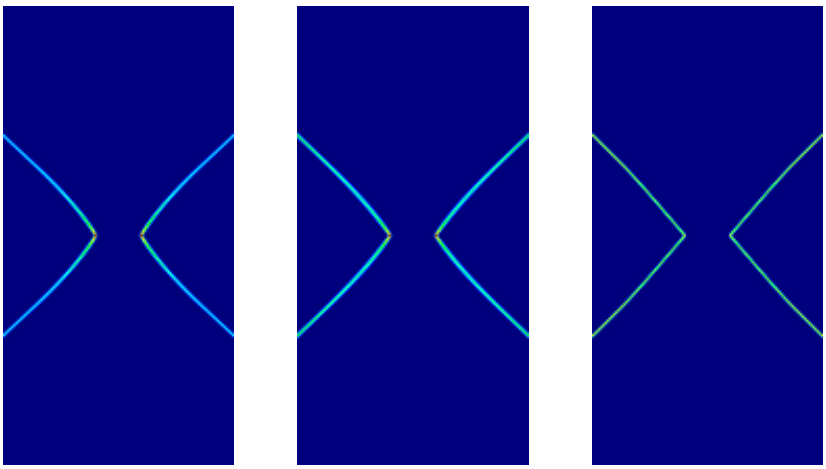

(a) $u^* = 0.010$ m (b) $u^* = 0.015$ m (c) $u^* = 0.030$ m

Figure 19: Snapshots of the equivalent plastic strain at various applied displacements, showing rotation of the discontinuity orientation for the softening non-associated von Mises/Hill model (with tilt angle $\alpha = 0°$).

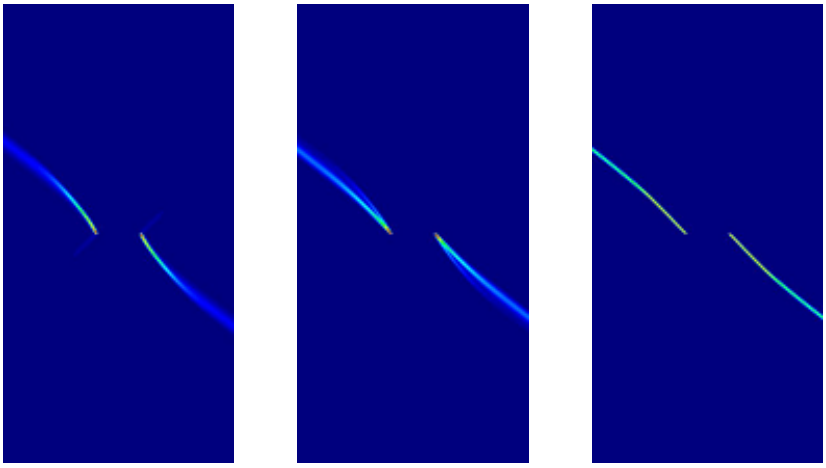

(a) $u^* = 0.010$ m (b) $u^* = 0.015$ m (c) $u^* = 0.030$ m

Figure 20: Snapshots of the equivalent plastic strain at various applied displacements, showing rotation of the discontinuity orientation for the softening non-associated von Mises/Hill model (with tilt angle $\alpha = 60°$).

Finally, let us consider softening plasticity. Figure 19 and Figure 20 show the discontinuity bands obtained for the non-associated von Mises/Hill model, for tilting angles (a) $\alpha = 0°$, (b) $\alpha = 60°$, respectively. The adopted softening properties are the same as in Section 4.2.5. The resemblance with the corresponding results for perfect plasticity, Figure 15(d) and Figure 17(d), respectively, is evident.

5.2. A plane strain punch test: Elasto- and rigid-plastic models

The second example is the punch indentation test by a flat rigid die shown in Figure 21. This is a well-known 2-D plane strain problem often used in the literature to test the ability of plastic models in capturing the failure modes. The problem was first studied by Prandtl (1920) for rigid-plastic bodies and then by Hill (1950) and Rice (1973) for elasto-plastic materials.

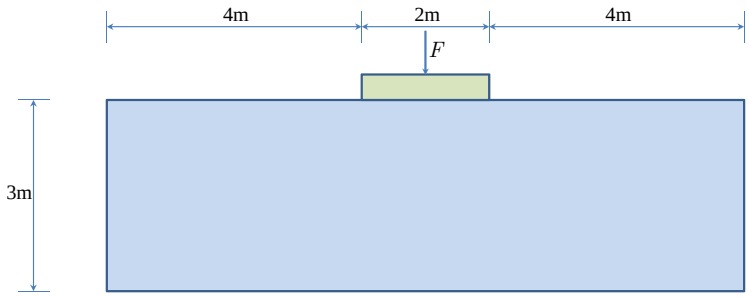

Figure 21: Indentation by a flat rigid die: Dimensions and loading. The bottom edge is fixed in both direction, while the left and right edges are constrained horizontally.

As the non-associated models have been discussed in the previous sections, only the associated von Mises and Hill models are considered. The reference material parameters adopted in the simulations are: Young's modulus $E_0 = 10$

MPa, Poisson's ratio $\nu_0 = 0.2$ and the yield strength $\sigma_Y = 10$ kPa for isotropic plasticity and $\sigma_{Y,11} = 15$ KPa with all the others equal to 10 kPa for orthotropic ones (a tilt angle 60° is assumed for the material axes). Perfect plasticity is used.

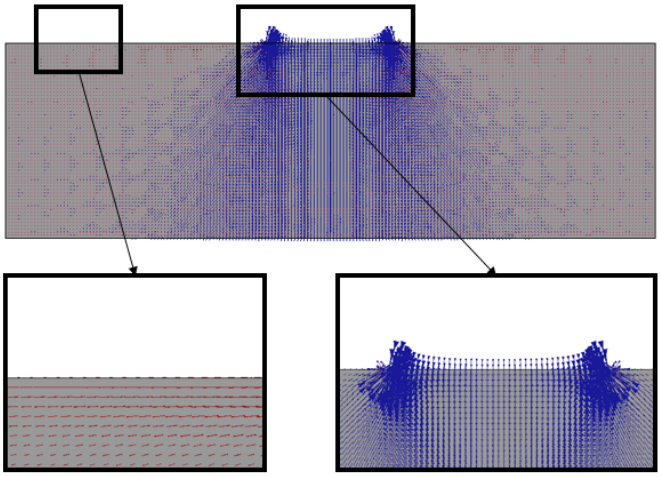

Figure 22: Indentation by a flat rigid die: Directions of principal stresses around the rigid footing.

Note that the material right under the rigid die is almost under uniaxial vertical loading in the global axes, i.e., $\sigma_{xy} = 0$; similarly, the material around the top surface (not under the die) is subjected to uniaxial horizontal stresses; see Figure 22. Therefore, the analytical results given in Eq. (5.1) apply here, with the localization angle depending only on the tilt of the material axes and the potential function.

5.2.1. Rough punch: Prandtl's solution

A rough punch is first studied; that is, the material directly under the punch is not allowed to move horizontally, corresponding to so-called Prandtl's solution.

We first consider the associated elasto-plastic models. As shown in Figure 23, the localization angle under the footing and close to the free surface is fixed $\theta^{\text{cr}} = \pm 45°$ with respect to the material axes, whatever the plastic yield function is. It is worth noting that the failure modes correspond to the claimed Prandtl's solution for rigid-plastic models. This coincidence confirms the the analytical prediction that rigid-plastic and elasto-plastic failure follow similar mechanics.

As demonstrated in Hill (1950), the failure mode is completely independent from the elastic constants. In the following, independence from the magnitude of the elastic modulus is shown. To this end, the analysis are performed with various values of Young's modulus, ranging three orders of magnitude. The computed load – displacement curves are shown in Figure 24. As can be seen, the global response is progressive stiffer, but the failure loads are identical as predicted analytically. The corresponding failure modes are exactly identical. Moreover, the stiffer the material, the

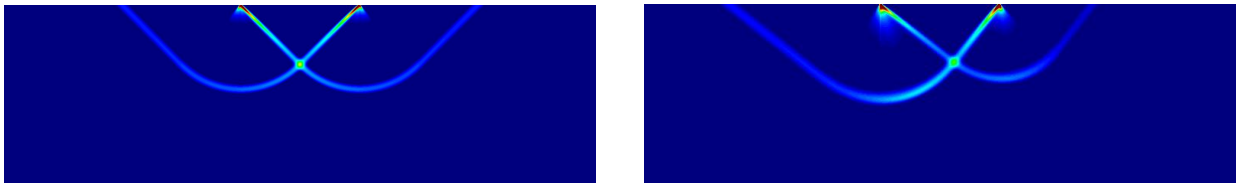

(a) Associated von Mises model (b) Associated Hill model

Figure 23: Indentation by a flat rigid die (rough punch): Localization angles for the associated von Mises and Hill models with tilting angle $\alpha = 60°$.

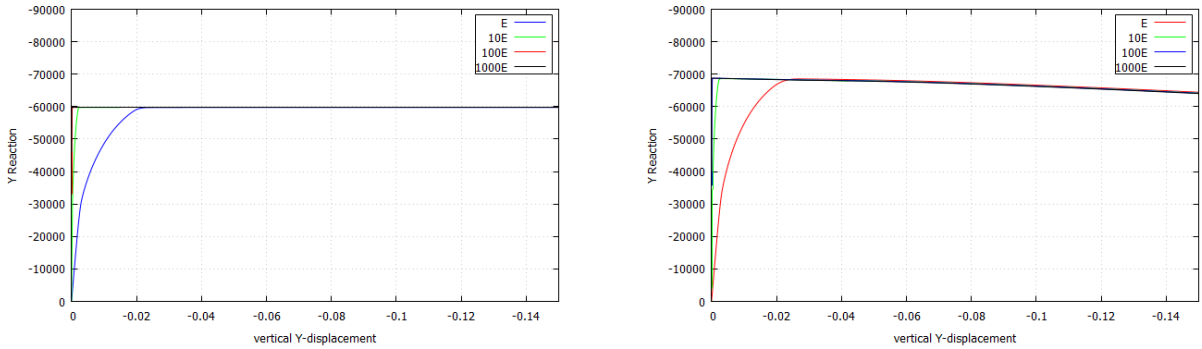

(a) Associated von Mises model (b) Associated Hill model

Figure 24: Indentation by a flat rigid die: Load – displacement curves for the associated von Mises and Hill models with tilting angle $\alpha = 60°$.

shorter the transition phase appears to be.

Finally, Figure 25 shows the discontinuity bands obtained for the associated von Mises and Hill models with the tilting angle $\alpha = 60°$, when softening plasticity is considered. The same softening properties as in Section 4.2.5 are adopted. The failure mechanisms are identical to those corresponding to perfect plasticity. Figure 26 shows the computed load–displacement curves for progressively increasing Youngs moduli. As can be seen, the global response is stiffer, but failure mechanisms and the softening branches are unaffected.

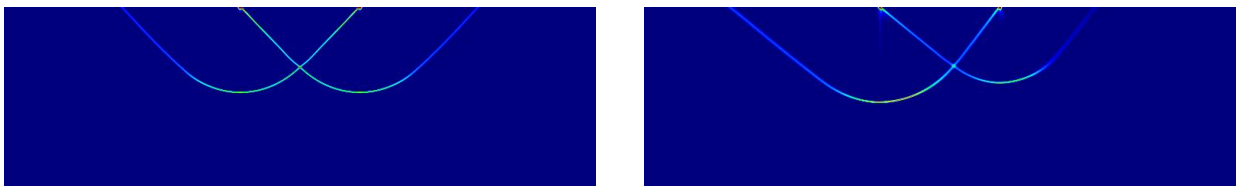

(a) Associated von Mises model (b) Associated Hill model

Figure 25: Indentation by a flat rigid die (rough punch): Localization angles for the softening associated von Mises and Hill models with tilting angle $\alpha = 60°$.

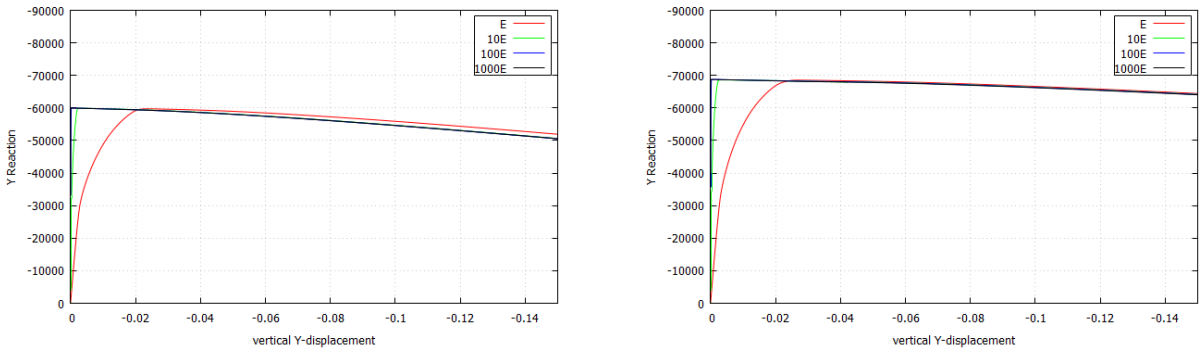

(a) Associated von Mises model

(b) Associated Hill model

Figure 26: Indentation by a flat rigid die: Load – displacement curves for the softening associated von Mises and Hill models with tilting angle $\alpha = 60°$.

Remark 5.1 For the von Mises rigid-plastic model, the limit load is given by (Hill, 1950)

$$F = 2a\frac{\sigma_Y}{\sqrt{3}}(\pi + 2) = 59370 \text{ N} \tag{5.2}$$

for $a = 1$ m here, coincident with the numerical predictions. □

5.2.2. Smooth punch: Hill's solution

A smooth punch is now investigated; that is, the material points locating directly under the punch are allowed to move horizontally. The only difference from the previous rough case is the boundary conditions at the base of the punch.

The corresponding failure patterns for the associated von Mises and the Hill models are shown in Figure 27. The former one corresponds to so-called Hill's solution for the punch problem (Hill, 1950).

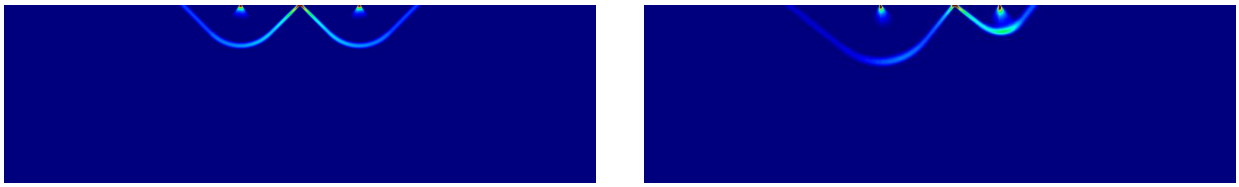

(a) Associated von Mises model

(b) Associated Hill model

Figure 27: Indentation by a flat rigid die (smooth punch): Localization angles for the associated von Mises and Hill models with tilting angle $\alpha = 60°$.

It can be seen that in these new solutions, the localization angles under the footing and close to the free surface are also fixed as $\theta^{\text{cr}} = \pm 45°$ with respect to the material axes.

Remarkably, the analytical and numerical load capacities of these solutions are exactly the same as those obtained for the rough punch. Additionally, the failure modes and load are independent from the elastic moduli and apply both

to elasto-plastic and rigid-plastic materials.

This last example illustrates that the localization condition applies locally, but the formation of global failure modes depends crucially on the global equilibrium and the kinematic boundary conditions. These are the basis of classical plastic limit analyses.

6. Conclusions

In this work the mechanics of strain localization is addressed both analytically and numerically for isotropic and orthotropic, elasto- and rigid-plastic solids with associated or non-associated flow laws. More specifically, we postulated the stress (rate) objectivity (i.e., independent of the discontinuity bandwidth) as the necessary condition for the occurrence of strain localization, in addition to Maxwell's kinematics and continuity of the traction (rate) for strain bifurcation. Consequently, strain localization is more demanding than the classical continuous/discontinuous strain bifurcation, though both accounts for the plastic loading/unloading and loading/loading scenarios. For the plane strain condition, there generally exists a transition stage between plastic yielding/strain bifurcation and strain localization. Moreover, regarding the stress (rate) within the discontinuity band, the boundedness condition (Oliver, 1996, 2000; Cervera et al., 2012) and the continuity condition (Wu and Cervera, 2014, 2015, 2016), both assuming plastic loading/unloading with associated evolution laws in strain softening solids, are recovered as particular cases of strong discontinuities with a vanishing bandwidth and of regularized ones with a finite bandwidth, respectively. The concept of "slip-line" or "zero rate of extension" is also incorporated for rigid-plastic solids (Hill, 1950) and soils (Roscoe, 1970).

The kinematic and static constraints upon strain localization were then derived analytically. In particular, the localization angles of the discontinuity band (surface) depend only on the specific stress state and the plastic flow tensor, relevant neither to the elastic material constants nor to the plastic yield function. During the transition stage the orientation of the discontinuity band (surface) rotates progressively to the localization angle. For the plane strain condition, the yield function affects evolution process upon which the out-of-plane stress for strain localization is achieved and consequently the transition stage, but not the localization angle.

The above strain localization condition and analytical results for the localization angle are validated numerically by several benchmark examples. The stabilized mixed finite element formulation is adopted to deal with the quasi-incompressible deformations resulting from the von Mises and Hill potential functions. It is found that for perfectly and softening plastic solids with either associated or non-associated evolution laws, upon strain localization and thereafter the stresses inside the discontinuity band are indeed independent of the bandwidth, validating the postulated assumption. Moreover, similarly to our previous work on plastic or damaging solids, the numerically predicted localization angles are coincident with those given by the analytical results, further justifying the proposed strain localization condition.

As it applies to isotropic and orthotropic rigid-/elasto-plastic solids with associated or non-associated flow rules,

the proposed strain localization condition can be used to determine the discontinuity orientation in the numerical modeling of localized failure in solids. In particular, it would be very helpful to track crack propagation paths, which is a challenging and open issue in the discontinuous approach like extended or enriched finite element methods (i.e., XFEM, EFEM); see Feist and Hofstetter (2006); Dumstorff and Meschke (2007); Jäger et al. (2008); Wu (2011); Wu et al. (2015); Wu and Li (2015). This will be explored in forthcoming jobs.

Acknowledgments

Financial support from the Spanish Government-MINECO-Proyectos de I + D (Excelencia)-DPI2017-85998-P-ADaMANT-Computational Framework for Additive Manufacturing of Titanium Alloy, the Severo Ochoa Programme for Centres of Excellence in R&D (CEX2018-000797-S) and the Catalan Government ACCIÓ - Ris3cat Transport and PRO^2 Project is gratefully acknowledged as well as the support of the Agència de Gestió dAjuts Universitaris i de Recerca (AGAUR) and the European Social Fund (ESF) to S. Kim through the predoctoral FI grants (ref. num. 2019FI-B00727). This work is also supported by the National Natural Science Foundation of China (51878294; 51678246), the State Key Laboratory of Subtropical Building Science (2018ZC04) to J.Y. Wu.

References

Benallal, A., Comi, C., 1996. Localization analysis via a geometrical method. Int. J. Solids Structures 33 (1), 99–119. 8

Borré, G., Maier, G., 1989. On linear versus nonlinear flow rules in strain localisation analysis. Meccanica 24, 36–41. 2, 8

Brezzi, F., Fortin, M., 1991. Mixed and Hybrid Finite Element Methods. Springer, Berlin. 14

Cervera, M., Agelet de Saracibar, C., Chiumenti, M., 2002. Comet: Coupled mechanical and thermal analysis. data input manual, version 5.0. Tech. Rep. Technical Report IT-308, CIMNE, Technical University of Catalonia, Available from: http://www.cimne.upc.es. 17

Cervera, M., Chiumenti, M., 2009. Size effect and localization in j_2 plasticity. International Journal of Solids and Structures 46, 3301–3312. 14

Cervera, M., Chiumenti, M., Benedetti, L., Codina, R., 2015. Mixed stabilized finite element methods in nonlinear solid mechanics. part iii: Compressible and incompressible plasticity. Comput. Methods Appl. Mech. Eng. 285, 752–775. 3

Cervera, M., Chiumenti, M., de Saracibar, C. A., 2003a. Softening, localization and stabilization: capture of discontinuous solutions in j2 plasticity. Int. J. Numer. Anal. Methods Geomech. 28, 373–393. 14

Cervera, M., Chiumenti, M., de Saracibar, C. A., 2004. Shear band localization via local j2 continuum damage mechanics. Comput. Method Appl. Mech. Eng. 193, 849–880. 14

Cervera, M., Chiumenti, M., Di Capua, D., 2012. Benchmarking on bifurcation and localization in j_2 plasticity for plane stress and plane strain conditions. Comput. Methods Appl. Mech. Eng. 241244, 206224. 3, 11, 14, 15, 34

Cervera, M., Chiumenti, M., Valverde, Q., de Saracibar, C. A., 2003b. Mixed linear/linear simplicial elements for incompressible elasticity and plasticity. Computer Methods in Applied Mechanics and Engineering 192, 5249–5263. 14

Cervera, M., Wu, J.-Y., Chiumenti, M., Kim, S., 2020. Strain localization analysis of hills orthotropic elastoplasticity: analytical results and numerical verification. Computational Mechanics 65, 533–554. 3, 11, 12, 15

Chiumenti, M., Valverde, Q., de Saracibar, C. A., Cervera, M., 2002. A stabilized formulation for incompressible elasticity using linear displacement and pressure interpolations. Computer Methods in Applied Mechanics and Engineering 191, 5253–5264. 14

Chiumenti, M., Valverde, Q., de Saracibar, C. A., Cervera, M., 2004. A stabilized formulation for incompressible plasticity using linear triangles and tetrahedra. Int. J. Plasticity 20, 1487–1504. 14

CIMNE, 2009. Gid: The personal pre and post processor Available from: http://www.gidhome.com. 17

Codina, R., 2000. Stabilization of impressibility and convection through orthogonal sub-scales in finite element methods. Comput. Method Appl. Mech. Eng. 190, 1579–1599. 14

Codina, R., Blasco, J., 1997. A finite element method for the stokes problem allowing equal velocity-pressure interpolations. Comput. Method Appl. Mech. Eng. 143, 373–391. 14

Dumstorff, P., Meschke, G., 2007. Crack propagation criteria in the framework of x-fem-based structural analyses. International Journal For Numerical And Analytical Methods In Geomechanics 31, 239–259. 35

Feist, C., Hofstetter, G., 2006. An embedded strong discontinuity model for cracking of plain concrete. Computer Methods in Applied Mechanics and Engineering 195, 7115–7138. 35

Hencky, H., 1923. Über einige statisch bestimmte fälle des gleichgewichts in plastischen körpern. Z. Angew. Math. Mech. 3, 241–251. 2

Hencky, H., 1924. Zur theorie plastischer deformationen und der hierdurch im material hervorgerufenen nachspannungen. Z. Angew. Math. Mech. 4, 323–334. 2

Hill, R., 1950. The Mathematical Theory of Plasticity. Oxford University Press, New York. 2, 3, 10, 30, 31, 33, 34

Hill, R., 1958. General theory of uniqueness and stability of elasto-plastic solids. J. Mech. Phys. Solids 6, 236–249. 2

Hill, R., 1962. Acceleration waves in solids. J. Mech. Phys. Solids 10, 1–16. 2

Hughes, T., 1995. Multiscale phenomena: Green's function, dirichlet-to neumann formulation, subgrid scale models, bubbles and the origins of stabilized formulations. Comput. Method Appl. Mech. Eng. 127, 187–401. 14

Hughes, T., Feijoó, G., Mazzei, L., Quincy, J., 1998. The variational multiscale method – a paradigm for computational mechanics. Comput. Method Appl. Mech. Eng. 166, 3–28. 14

Jäger, P., Steinmann, P., Kuhl, E., 2008. On local tracking algorithms for the simulation of three-dimensional discontinuities. Comput. Mech. 42 (3), 395–406. 35

Kim, S., Cervera, M., Wu, J. Y., Chiumenti, M., 2021. Strain localization of orthotropic elastoplastic cohesivefrictional materials: Analytical results and numerical verification. Materials 14 (8), 2040. 3

Li, M., Füssl, J., Lukacevic, M., Eberhardsteiner, J., 2018. A numerical upper bound formulation with sensibly-arranged velocity discontinuities and orthotropic material strength behavior. Journal of Theoretical and Applied Mechanics 56 (2), 417–433. 3

Mandel, J., 1942. Equilibre par trasches planes des solides à la limite d'écoulement. Ph.D. thesis, Thèse, Paris. 2

Mohr, O., 1900. Welche umstande bedingen der bruch und der elasizitätsgrenze des materials. Z. Verins Deutscher Ingenieure, 1524. 2

Oliver, J., 1996. Modeling strong discontinuities in solid mechanics via strain softening constitutive equations. part i: Fundamentals; part ii: Numerical simulation. International Journal for Numerical Methods in Engineering 39, 3575–3600; 3601–3623. 2, 34

Oliver, J., 2000. On the discrete constitutive models induced by strong discontinuity kinematics and continuum constitutive equations. International Journal of Solids and Structures 37, 7207–7229. 11, 34

Oliver, J., Cervera, M., Manzoli, O., 1999. Strong discontinuities and continuum plasticity models: the strong discontinuity approach. Int. J. Plast. 15, 319–351. 2

Oliver, J., Huespe, A. E., Dias, I. F., 2012. Strain localization, strong discontinuities and material fracture: Matches and mismatches. Comput. Methods Appl. Mech. Eng. 241-244, 323–336. 2

Ottosen, N., Runesson, K., 1991. Discontinuous bifurcation in a nonassoicated mohr material. Mechanics of Materials 12, 255–265. 2, 9

Prandtl, L., 1920. Über die häete plastistischer körper. Nachr. Ges. Wisensch, Göttingen, math. phys. Klasse, 74–85. 2, 30

Rice, J., 1976. The localisation of plastic deformations. In: Koiter, W. (Ed.), Theoretical and Applied Mechanics. North-Holland, Amsterdam, pp.

207–220. 8

Rice, J. R., 1968. A path independent integral and the approximate analysis of strain cncentrations by notches and cracks. J. Appl. Mech.-T. ASME 35, 379–386. 2

Rice, J. R., 1973. Plane strain slip line theory for anisotropic rigid/plastic materials. J. Mech. Phys. Solids 21, 63–74. 30

Rice, J. R., Rudnicki, J. W., 1980. A note on some features of the theory of localization of deformation. Int. J. Solids Structures 16, 597–605. 2, 8, 9

Roscoe, K., 1970. The influence of strains in soil mechanics. Géotechnique 20 (2), 129–170. 2, 3, 34

Rudnicki, J. W., Rice, J. R., 1975. Conditions of the localization of deformation in pressure-sensitive dilatant material. J. Mech. Phys. Solids 23, 371–394. 2

Runesson, K., Ottosen, N., Peric, D., 1991. Discontinuous bifurcations of elastic-plastic solutions at plane stress and plane strain. Int. J. Plast. 7, 99–121. 2, 8, 9, 28

Simó, J., Hughes, T., 1998. Computational inelasticity. Springer, New York. 14

Simó, J., Oliver, J., Armero, F., 1993. An analysis of strong discontinuities induced by strain-softening in rate-independent inelastic solids. Comput. Mech. 12, 277–296. 2

Thomas, T., 1961. Plastic Flow and Fracture of Solids. Academic Press, New York. 2

Wu, J. Y., 2011. Unified analysis of enriched finite elements for modeling cohesive cracks. Comput. Methods Appl. Mech. Engrg. 200 (45-46), 3031–3050. 35

Wu, J. Y., Cervera, M., 2014. Strain localization and failure mechanics for elastoplastic damage solids. Monograph CIMNE M147, Barrcelona, Spain. 3, 11, 34

Wu, J. Y., Cervera, M., 2015. On the equivalence between traction- and stress-based approaches for the modeling of localized failure in solids. Journal of the Mechanics and Physics of Solids 82, 137–163. 3, 11, 12, 34

Wu, J. Y., Cervera, M., 2016. A thermodynamically consistent plastic-damage framework for localized failure in quasi-brittle solids: Material model and strain localization analysis. International Journal of Solids and Structures 88-89, 227–247. 3, 11, 12, 18, 25, 34

Wu, J. Y., Cervera, M., 2017. Strain localization of elastic-damaging frictional-cohesive materials: Analytical results and numerical verification. Materials 10, 434; doi:10.3390/ma10040434. 3

Wu, J. Y., Li, F. B., 2015. An improved stable xfem (is-xfem) with a novel enrichment function for the computational modeling of cohesive cracks. Comput. Methods Appl. Mech. Engrg. 295, 77–107. 35

Wu, J. Y., Li, F. B., Xu, S. L., 2015. Extended embedded finite elements with continuous displacement jumps for the modeling of localized failure in solids. Comput. Methods Appl. Mech. Engrg. 285, 346–378. 35